FINAL REPORT

Scientific Understanding of the Mechanisms of Non-Chromate Corrosion Inhibitors

SERDP Project WP-1621

JANUARY 2014

Florent Bocher
James Dante
Southwest Research Institute

John R. Scully
Samuel Madden
Arwen Wilson
University of Virginia

Distribution Statement A
This document has been cleared for public release

SERDP
DOD ▪ EPA ▪ DOE

REPORT DOCUMENTATION PAGE

Form Approved
OMB No. 0704-0188

Public reporting burden for this collection of information is estimated to average 1 hour per response, including the time for reviewing instructions, searching existing data sources, gathering and maintaining the data needed, and completing and reviewing this collection of information. Send comments regarding this burden estimate or any other aspect of this collection of information, including suggestions for reducing this burden to Department of Defense, Washington Headquarters Services, Directorate for Information Operations and Reports (0704-0188), 1215 Jefferson Davis Highway, Suite 1204, Arlington, VA 22202-4302. Respondents should be aware that notwithstanding any other provision of law, no person shall be subject to any penalty for failing to comply with a collection of information if it does not display a currently valid OMB control number. **PLEASE DO NOT RETURN YOUR FORM TO THE ABOVE ADDRESS.**

1. REPORT DATE *(31-01-2013)*

2. REPORT TYPE Draft Final Report

3. DATES COVERED *(July 2008 – Jan 2013)*

4. TITLE AND SUBTITLE

Scientific Understanding of the Mechanisms of Non-Chromate Corrosion Inhibitors

5a. CONTRACT NUMBER: W912HQ08C0043

5b. GRANT NUMBER

5c. PROGRAM ELEMENT NUMBER

5d. PROJECT NUMBER WP-1621

5e. TASK NUMBER

5f. WORK UNIT NUMBER

6. AUTHOR(S)

Florent Bocher & James Dante, SwRI®

John R. Scully, Samuel Madden and Arwen Wilson, UVA

7. PERFORMING ORGANIZATION NAME(S) AND ADDRESS(ES)

Southwest Research Institute
6220 Culebra Road
San Antonio, TX 78238-5166

University of Virginia (Materials Science & Engineering)
116 Engineer's Way
PO Box 400745 • Charlottesville, VA 22904-4745

8. PERFORMING ORGANIZATION REPORT

9. SPONSORING / MONITORING AGENCY NAME(S) AND ADDRESS(ES)

Strategic Environmental Research and Development Program
901 North Stuart Street, Suite 303
Arlington, VA 22203

10. SPONSOR/MONITOR'S ACRONYM(S)
SERDP

SERDP

11. SPONSOR/MONITOR'S REPORT NUMBER(S)

12. DISTRIBUTION / AVAILABILITY STATEMENT

13. SUPPLEMENTARY NOTES

14. ABSTRACT

The mechanisms of selected alternative inhibitors to chromate under realistic metallurgical and environmental conditions were investigated. Permanganate was shown to be both an anodic and cathodic inhibitor for AA2024, and an inhibitor of copper replating at OCP. The vanadate species in solutions were identified, and vanadate was found to inhibit the oxygen reduction reaction in solution under a critical concentration. Higher concentrations of NaVO3 were required to raise the average pitting potential. Cerium, vanadate and molybdate were partially successful corrosion inhibitors for AA7075 and carbon steel 1018. All three compounds acted as anodic inhibitor with AA7075, while only cerium and vanadate behaved as cathodic inhibitors. Molybdate acted as an anodic and a cathodic inhibitor for carbon steel. Synergistic behaviors have been proven to be occurring partially for Ce/Mo and Ce/V and were especially successful for carbon steel 1018.An aluminum/copper multielectrode array mimicked an aluminum alloy containing copper-rich intermetallic particles. Composition, concentration and pretreatment were found to have an impact on the effectiveness of the inhibitor. Vanadate was the sole successful inhibitor when combined with NaCl. All inhibitors were successful when pretreated, but better results were obtained at lower concentration. EDS and Auger electron spectrometry showed that cerium, molybdate and vanadate are all present on the surface of AA7075. However, only cerium was found to be dependent on the quantity of the inhibitor using surface EDS. Atmospheric test using the Al/Cu MEA were performed and only vanadate and cerium performed successfully at lower relative humidity (60 and 70%). At higher relative humidity, none of the compounds inhibited corrosion, due to the vanadate concentration being above the maximum value at higher relative humidity

15. SUBJECT TERMS

16. SECURITY CLASSIFICATION OF:			**17. LIMITATION OF ABSTRACT**	**18. NUMBER OF PAGES**	**19a. NAME OF RESPONSIBLE PERSON** Florent Bocher
a. REPORT	**b. ABSTRACT**	**c. THIS PAGE**		175	**19b. TELEPHONE NUMBER** *(include area code)* 210-522-6559

Standard Form 298 (Rev. 8-98)

Contents

Contents i
List of Tables vii
List of Figures ix
List of Acronyms xxviii
Keywords xxx
Acknowledgements xxx
Abstract 1
Objective 3
Background 5
Materials and Methods 15
Description of Individual Tasks 15
Task 1 – Effect of Individual Inhibitors under Controlled Hydrodynamic Conditions 15
Task 2 – Effect of Combinations of Inhibitors 20
Task 3 – Effect of Microstructural Heterogeneity on Inhibitor Action 20
Task 4 – Effect of Alternate Wet & Dry Conditions 21
Materials and Test Electrolytes 22
Techniques – Corrosion Inhibition of AA2024 using Permanganate 23
Open Circuit Measurements and Electrochemical Impedance Spectroscopy during Open Circuit Exposure Periods 23
Microscopic Analysis after Open Circuit Exposures 24
Anodic and Cathodic Cyclic Potentiodynamic Polarization Scans 24
Cyclic Voltammetry Tests to Assay Copper Redeposition 25
Raman Spectroscopy 25
Techniques – Corrosion Inhibition of AA2024 using Vanadate 25
Nuclear Magnetic Resonance 25
Open Circuit Exposures 26
E–log(i) Polarization Experiments 26

Techniques – Corrosion Inhibition of AA2024 with Inhibitors Combination.....28
Cerium-Permanganate Combinations.....28
Materials and Test Electrolytes.....28
Open Circuit Measurements During Open Circuit Exposure Periods.....28
Microscopic Analysis after Open Circuit Exposures.....29
Anodic and Cathodic Cyclic Potentiodynamic Polarization Scans.....29
Cyclic Voltammetry Tests to Assay Copper Redeposition.....29
Vanadate-Cerium and Vanadate-Molybdate Combinations.....30
Materials and Solutions.....30
Nuclear Magnetic Resonance.....30
Open Circuit Exposures.....30
E–log(i) Polarization Experiments.....31
Techniques – Effect of Molybdate on Repassivation of AA2024.....33
Techniques – Corrosion Inhibition of AA7075 and 1018 Carbon Steel.....35
Anodic and Cathodic Potentiodynamic Scans.....35
Chronoamperometric Measurements.....38
Electrochemical Tests Performed on Electrode Arrays.....38
Multi Electrode Array Study of Inhibitors.....40
Techniques – Surface Interaction with Inhibitors.....41
Auger Electron Spectroscopy and Surface EDS.....41
Scanning Kelvin Probe.....42
Techniques – Mott-Schottky.....43
Techniques – Atmospheric MEA.....44
Results and Discussion.....45
Results.....45
Thermodynamic Calculations of Inhibitor Solutions (Speciation).....45
Corrosion Inhibition of AA2024 using Permanganate and Vanadate.....49
Effects of Permanganate during OCP exposures of AA2024 in 50 mM NaCl Solution.....50
Inhibition of Copper Replating.....55

Anodic Inhibition by Permanganate Ions 58
Localized Corrosion Behavior on Pretreated 2024-T351 58
Localized Corrosion Behavior of AA2024-T351 with Permanganate in Solution.....59
Investigation of Cathodic Inhibition with KMnO4.....62
The Oxygen Reduction Reaction on AA2024-T4 and Pure Copper.....62
The Effects of Potassium Permanganate on Oxygen Reduction Reaction on AA2024-T4 63
Manganese Oxide Valence State Determination 68
Vanadate Species Present in NMR and Speciation Diagrams 70
Effect of Vanadate Inhibitors on Suppressing Open Circuit Pitting Corrosion of AA2024-T3 73
24 Hour Immersion Experiments on AA2024–T3.....73
Inhibition of Localized Corrosion during Anodic Polarization 77
Effects of Vanadate Pretreatment on Anodic Behavior of AA2024–T3 82
Effects of Vanadate Inhibitors on Oxygen Reduction Reaction and Hydrogen Evolution Rates on Different Materials 83
Effects of Vanadate on Reducing the Oxygen Reduction and Hydrogen Evolution Reactions.....86
Corrosion Inhibition of AA2024 with Inhibitors Combination 92
Cerium-Permanganate Combinations 92
Effects of Cerium-Permanganate Pretreatment on OCP Exposures of AA2024 in 50 mM NaCl Solution.....95
Open Circuit Behavior of Pretreated AA2024-T351 103
Inhibition of Copper Replating 104
Anodic Inhibition of AA2024-T351 by Cerium-Permanganate Pretreatments 105
Investigation of Cathodic Inhibition with Cerium-Permanganate Pretreatments 107
Vanadate-Cerium and Vanadate-Molybdate Combinations 111
Species Present in NMR and Speciation Diagrams 112
Effect of Vanadate Inhibitors on Suppressing Open Circuit Pitting Corrosion of AA2024-T3 114
24 Hour Immersion Experiments on AA2024-T3 117

Inhibition of Localized Corrosion of Aluminum during Anodic Polarization 121
Effect of Vanadate Inhibitor Combinations on Reducing the Oxygen Reduction and Hydrogen Evolution Reactions 141
Effect of Molybdate on Repassivation of AA2024.....148
The Inhibition of Pitting Potential 148
The Inhibitor Buffer Capacity.....149
The Inhibition of Net Current Density During Scratch Repassivation 150
The Oxide Film Capacitance 158
Corrosion Inhibition of AA7075 and Carbon Steel 1018 161
Effect of Individual Inhibitors on AA7075.....161
Anodic Inhibition 161
Cathodic Inhibition 161
Effect of Individual Inhibitors on 1018 Carbon Steel.....168
Anodic Inhibition 168
Cathodic Inhibition 169
Effect of Inhibitor Combinations on AA7075 and 1018 Carbon Steel.....170
Cerium and Vanadate Combination.....170
1018 Carbon Steel.....171
Aluminum Alloy 7075 172
Cerium and Molybdate Combination.....174
1018 Carbon Steel.....174
Aluminum Alloy 7075 175
Investigation of the Effect of the Inhibitors on the Microstructural Heterogeneity of AA2024.....176
Rotating Disc Arrays.....176
Aluminum/Copper Multi-Electrode Array Study of Inhibitor.....180
Inhibitor Interaction with AA7075 183
Scanning Kelvin Probe (SKP) 193
Mott-Schottky (M-S) 194
Atmospheric MEA 196

Discussion 202
Corrosion Inhibition of AA2024 using Permanganate and Vanadate 202
Oxidation States of Manganese 202
Active Corrosion Inhibition 202
Modes of MnO_4^- Inhibition: Anodic 203
Modes of MnO_4^- Inhibition: Cathodic 203
Vanadate Speciation 207
Open Circuit Potential Inhibition with Coupled Anodic and Cathodic Reactions 209
Anodic Inhibition Upon Anodic Polarization 209
Cathodic Inhibition due to Vanadate Solutions 210
Corrosion Inhibition of AA2024 with Inhibitors Combination 214
Cerium-Permanganate Combinations 214
Open circuit and Anodic Inhibition by Cerium Permanganate Pretreatments 214
Diffusion Limited Current Density Inhibition by Cerium-Permanganate Pretreatments 215
Vanadate-Cerium and Vanadate-Molybdate Combinations 216
Vanadate Speciation 216
Open Circuit Potential Inhibition with Coupled Anodic and Cathodic Reactions 217
Anodic Inhibition Upon Anodic Polarization 218
Cathodic Inhibition due to Vanadate Binary Combinations Solutions 220
Effect of Molybdate on Repassivation AA2024 Using Scratch Repassivation Experiments 224
Corrosion Inhibition of AA7075 and Carbon Steel 1018 225
Corrosion Inhibition with Single Inhibitors 225
Corrosion Inhibition with Inhibitor Combinations 226
Investigation of the Effect of the Inhibitors on the Microstructural Heterogeneity of AA2024 226
Rotating Disc Arrays 226
Aluminum/Copper Multi-Electrode Array Study of Inhibitor 226
Inhibitor Interaction with AA7075 227

Mott-Schottky 227
Atmospheric MEA 227
Conclusions and Implications for Future Research/Implementation 228
Conclusions 228
Implications for Future Research/Implementation 230
Transfer of technology to other metallic alloys 230
Development of application techniques with combination of inhibitors 231
Study of inhibitor combinations for aggressive atmospheric conditions 231
Literature Cited 233
Appendices 244
List of Scientific/Technical Publications 244
Talks 244
Papers 245
Posters 245

List of Tables

Table 1. Hypothesized inhibition mechanisms of Cr(VI) ions and CCCs. 6

Table 2. The chemical formulas associated with aqueous vanadate subtypes. 11

Table 3. Compositions of Alloys Used in the Study. 23

Table 4. Elemental peak energy used for determining atomic percentages. 26

Table 5. Composition Variables of the Mo/Ce Solutions. 35

Table 6. Composition Variables of the V/Ce Solutions. 35

Table 7. Ce and V Combination Solutions Used for AA7075, Solution A. 36

Table 8. Ce and V Combination Solutions Used for AA7075, Solution B. 36

Table 9. Ce and Mo Combination Solutions Used for AA7075, Solution A. 36

Table 10. Ce and Mo Combination Solutions Used for AA7075, Solution B. 36

Table 11. Ce and V Combination Solutions Used for CS1018. 37

Table 12. Ce and Mo Combination Solutions Used for CS 1018, Solution A. 37

Table 13. Ce and Mo Combination Solutions Used for CS 1018, Solution B. 37

Table 14. Potential Values Used in Chronoamperometric Measurements. 38

Table 15. Rotating Disk Array Dimensions. 38

Table 16. Solution Compositions Used to Study the Effect of the Microstructural Heterogeneity. 39

Table 17. MEA experimental matrix. 41

Table 18. MEA atmospheric testing experimental matrix. 44

Table 19. Compilation of EDS data for AA2024-T351 intermetallic particles in Figure 24 a) and b), before and after pretreatment in 0.1 M $KMnO_4$. 50

Table 20. The predicted five greatest vanadate species percentage for each total vanadate concentration in 50 mM NaCl 71

Table 21. The ^{51}VNMR peaks for different $NaVO_3$ concentrations in 50 mM NaCl. 72

Table 22. The ^{51}VNMR determined abundance of vanadate species for different $NaVO_3$ concentrations in 50 mM NaCl. 72

Table 23. The average open circuit potentials for AA2024–T3 in 50 mM NaCl with various concentrations of $NaVO_3$ in open to the air solutions at the 1st and 23rd hours. 73

Table 24. Compilation of EDS data for AA2024-T351 intermetallic particles in Figure 81, before and after pretreatment in 0.1 M $KMnO_4$. 97

Table 25. The ^{51}VNMR peaks for different inhibitor concentrations in 50 mM NaCl solution at room temperature 113

Table 26. Abundance of vanadate species and solution pH for different inhibitor concentrations in 50 mM NaCl 113

Table 27. The average open circuit potentials for AA2024–T3 in 50 mM NaCl solution with various concentrations of inhibitor in naturally aerated solution and as a 2 hour pretreatment at the 1st and 23rd hours 114

Table 28. The average open circuit potentials for AA2024–T3 in naturally aerated 50 mM NaCl solution with various concentrations of inhibitor in aerated solution at the 1st and 23rd hours 116

Table 29. Fitting parameters for 99.999% aluminum at -0.8 VSCE.....152

List of Figures

Figure 1. Summary of proposed tasks.....4

Figure 2. (a) The E-pH diagrams for 0.005 M permanganate with addition of 0.05 M chloride. (b) The speciation diagrams for 0.005 M permanganate + 0.05 M Cl^- at -0.5 V_{SCE}, the open circuit of AA-2024 in the presence of permanganate. 10

Figure 3. Example of M-S plots of I825, I625 and C22 alloys. (a) The x-intercept of the extrapolated line is the flatband potential. (b) Shift in flatband potential for I825 alloy as a function of molybdate and chloride concentration. 17

Figure 4. Schematic of an oxide covered surface after a scratch. The bare metallic electrode undergoes oxide nucleation and an increase in oxide surface coverage, followed by thickening of the oxide film as repassivation occurs. The thickness of the oxide layer is d_{ox}. 18

Figure 5. Theoretical model of Bode impedance for depassivated and passive aluminum electrodes. Values were determined assuming a passivated R_{film} value of 10^4 Ω-cm^2, depassivated R_{film} of 10 Ω-cm^2, and $R_{solution}$ of 350Ω. Capacitance of 1 μF/cm^2 and 100 μF/cm^2 were used for the passivated and bare electrodes, respectively. Values corrected for electrode surface area of $2x10^{-4}$ cm^2. 19

Figure 6. Schematic model of potential effects of cathodic inhibitors on IMCs.[29] 21

Figure 7. SKP image of bimetallic substrate after partial exposure to VCI (left), and cross-section through feature showing potential shift for VCI exposed metal (right).[110] 22

Figure 8. Schematic of scratched electrode cell with wiring diagram for data capture devices.....33

Figure 9 . Detailed 3-D scratch topography for calculating area of exposed electrode during scratched electrode testing. 34

Figure 10. Schematic of the exposed surface of the copper multi-electrode array rotating disk electrode. 38

Figure 11. Photographs of different multielectrode arrays. 39

Figure 12. Schematic of the RDE array cell setup. 39

Figure 13. Schematic operating principle of MEA. 40

Figure 14. (a) Assembled aluminum/copper MEA and (b) schematic of the aluminum/copper MEA. 40

Figure 15. Schematic of the aluminum/copper MEA used for atmospheric testing. 44

Figure 16. Bulk solution pH as a function of inhibitor concentration. 45

Figure 17. Speciation diagram of a. 0.01 M and b. 0.05 M sodium vanadate solution. The natural pH of the inhibitor solution is within the pink shaded area. 46

Figure 18. Speciation diagram of a. 0.01 M and b. 0.05 M cerium acetate solution. The natural pH of the inhibitor solution is within the pink shaded area. 46

Figure 19. Speciation diagram of a. 0.01 M and b. 0.05 M sodium molybdate. The natural solution pH range is shaded in pink. 47

Figure 20. E-pH diagrams of permanganate calculated at 0.1, 0.05 and 0.005 M concentrations. 48

Figure 21. Speciation diagrams of manganese calculated at -0.5 V vs. SCE for two different concentrations: 0.1 and 0.05 M. 48

Figure 22. Speciation diagram of 0.05 M cerium acetate. The pink highlights the region that would be present in and near an active anodic pit. The blue highlights the region present over a cathodic intermetallic particle. 49

Figure 23 (a) The as-polished (1200 grit) AA2024-T351 and the subsequent surface damage caused by 24 hour exposure to 0.05 M NaCl solution. (b) The damaged specimen image is distorted laterally but includes a secondary electron image and a backscattered electron image. It clearly shows intermetallic trenching. 51

Figure 24 (a) AA2024-T351 polished to 1200 grit with indication of EDS sites labeled 1-8. (b) after 24 hours pretreatment in 0.1M $KMnO_4$. Indication of EDS sites labeled 1-8. 51

Figure 25 (a) Intermetallic particle 1 from Figure 24. (b) Intermetallic particle 5 from Figure 24. The left spectrum is taken from an untreated sample, the right, a pretreated sample. 52

Figure 26. (a) AA2024-T351 pretreated with 0.1 M $KMnO_4$ for 24 hours (secondary electron image). (b) AA2024-T351 pretreated with 0.05 M $KMnO_4$ for 24 hours (secondary electron image). (c) AA2024-T351 pretreated with 0.005 M $KMnO_4$ for 24 hours (backscattered image). 53

Figure 27 (a) AA2024-T351 exposed to 0.05 M NaCl for 24 hours after pretreatment in 0.1 M $KMnO_4$ for 24 hours. (b) AA2024-T351 exposed to 0.05 M NaCl for 24 hours after pretreatment in 0.05 M $KMnO_4$ for 24 hours. (c) AA2024-T351 exposed to 0.05 M NaCl for 24 hours after pretreatment in 0.005 M $KMnO_4$ for 24 hours....53

Figure 28 (a) AA2024-T351 exposed to 0.05 M NaCl with 0.1 M $KMnO_4$ in-situ for 24 hours. (b) AA2024-T351 exposed to 0.05 M NaCl with 0.05 M $KMnO_4$ in-situ for 24 hours. (c) AA2024-T351 exposed to 0.05 M NaCl with 0.005 M $KMnO_4$ in-situ for 24 hours....53

Figure 29. AA2024-T351 exposed to 0.05 M NaCl solution with 0.05 M $KMnO_4$ in-situ for 24 hours with manganese oxide caps removed. The manganese caps reduce intermetallic trenching and leave the matrix that was covered looking pristine. 54

Figure 30. The OCP was recorded for one hour after 24 hours at OCP in 50 mM sodium chloride solution with inhibitor the concentrations reported. 54

Figure 31. OCP measurements for pretreated AA2024-T351 after 24 hours in varying concentrations of $KMnO_4$. OCP measured in 0.05 m NaCl solution. Experiments have been run 10 times and show great reproducibility. 55

Figure 32. Baseline CV of high-purity Cu, high-purity Al, AA2024-T351, and AA2024-T351 etched for 24 hours in 0.05 M NaCl solution. 56

Figure 33. (a) CVs of AA2024-T351 etched for 24 hours in 0.05 M NaCl solution with varying inhibitor concentration in solution, 0.4 M, 0.05 M, 0.005 M KMnO4, and no inhibitor. (b) CVs of AA2024-T351 etched in 0.05 M NaCl solution for 24 hours after pretreatment for 24 hours in varying inhibitor concentration: 0.1 M, 0.05 M, 0.005 M $KMnO_4$. 57

Figure 34. The relative intensities of the Cu^{1+} reduction on the AA2024-T351 surface when corroded with the MnO_4^- ion in solution for 24 H in 0.05 M NaCl (A) and with MnO_4^- inhibitor pretreatment followed by exposure for 24 H in 0.05 M NaCl (B). 57

Figure 35. Optical microscopy of AA2024-T351 after exposure to 0.05 M sodium chloride solution. (a) Exposure to 0.05 M NaCl with 0.1 M MnO_4^- in solution. (b) Exposure to 0.05 M NaCl with 0.05 M MnO_4^- in solution. (c) Exposure to 0.05 M NaCl with 0.005 M MnO_4^- in solution. (d) Exposure to 0.05 M NaCl after pretreatment in 0.1 M MnO_4^- in solution for 24 hours. (e) Exposure to 0.05 M NaCl after pretreatment in 0.05 M MnO_4^- in solution for 24 hours. (f) Exposure to 0.05 M NaCl after pretreatment in 0.005 M MnO_4^- in solution for 24 hours. 58

Figure 36. The anodic polarization behavior for AA2024-T351 after pretreatment in $KMnO_4$ for 24H. Scan run in 0.05 M sodium chloride solution. (a) Pretreatment in 0.1 M $KMnO_4$, (b) Pretreatment in 0.05 M $KMnO_4$, (c) Pretreatment in 0.005 M $KMnO_4$. 59

Figure 37. The anodic polarization behavior for AA2024-T351 after 24 hours of exposure to 50 mM sodium chloride solution with the inhibitor in-situ. Scans conducted in 50 mM sodium chloride solution with varied inhibitor concentrations. (a) 100 mM $KMnO_4$, (b) 50 mM $KMnO_4$, (c) 5 mM $KMnO_4$. 59

Figure 38. S-phase ingot with large lighter regions corresponding to higher copper content and higher Z. (a) Sample as polished. (b) Sample held potentiostatically in 100 mM MnO_4^- and 50 mM Cl^- solution for 200 seconds. Note the growth of a protective manganese oxide over the S-phase particles. (c) Sample held potentiostatically in 50 mM Cl^- solution for 200 seconds. Insert of EDS line scan shows the enrichment of copper in proximity of visible S-phase damage. 60

Figure 39. AA2024 exposed to 0.005 M $KMnO_4$ + 0.05 M NaCl for 24 hours and then anodically polarized to potentials above E_{pit} (+0.3 V vs. SCE) in fresh 0.005 M $KMnO_4$ + 0.05 M NaCl solution. (a) Sample as removed from anodic polarization solution. (b) sample after removal of manganese oxide caps over intermetallic particles. 60

Figure 40. Representative anodic polarization behavior for AA2024-T351 in 25 mM $MnCl_2$ solution (—■—) compared to 50 mM NaCl (—●—). 61

Figure 41. Cumulative probability of pitting as a function of potential for both (a) pretreatment and (b) in-situ solution phase permanganate inhibitor concentration. Probability of pitting in 0.05 M NaCl. 61

Figure 42. The average difference between pitting and open circuit potentials for Mn pretreatment (a) and in-situ solution phase additions (b), as a function of inhibitor concentration. The error bars indicate one standard deviation. 62

Figure 43. Cathodic E vs. log(*i*) data for AA2024-T4 (a) and high-purity copper (b) samples run at various rotation rates from 100 rpm to 2500 in pH 8.4 borate buffer. Solutions were aerated naturally. 63

Figure 44. Cathodic E vs. log(*i*) data for AA2024-T4 (a) and high-purity copper (b) samples run at various rotation rates from 100 rpm to 2500 in 0.05 M NaCl. Solutions were aerated naturally. 63

Figure 45. Cathodic polarization behavior of AA2024-T4 and pure copper samples ground to 1200 grit, tested at 1000 rpm in pH 8.4 borate buffer solution after 100 H pretreatment (a) and run at 1500 rpm in 0.05 M NaCl solution with in-situ inhibitor additions (b) Rotation rate has been kept constant and inhibitor concentration is tested at different levels. All data collected under natural aeration. 64

Figure 46 (a) Total current at -1 V vs. SCE for AA2024-T4 and pure copper compared with the Levich prediction (i_d) in pH 8.4 borate buffer solution. (b) Diffusion limited current extracted from i_{total} at -1V vs. SCE for AA2024-T4 and pure copper compared with the Levich prediction in pH 8.4 borate buffer. Data extracted from Figure 44. 65

Figure 47. Total current at -1V vs. SCE for AA2024-T4 for the inhibitor pretreatment tests in inhibitor free environment (a) and with the inhibitor present in-situ (b). (a) and (b) have an order of magnitude difference in the ordinate. Total current densities for pure copper, bare AA2024-T4 and the Levich prediction i_d values are included for comparison. Data extracted from Figure 45. 66

Figure 48. Diffusion limited current extracted from i_{total} at -1V vs. SCE for AA2024-T4 after pretreatment at various inhibitor concentration compared with pure copper, bare AA2024-T4, and the Levich prediction. Tests were conducted in borate buffer solution at pH = 8.4. Data extracted from Figure 47. 66

Figure 49: Potentiodynamic scan of high-purity copper with Mn-oxide grown at a potential of -0.5 V vs. SCE. 67

Figure 50. (a) Extracted activation controlled current density over a range of potentials for high-purity Cu , AA2024-T351, and AA2024-T351 pretreated in 0.05 M MnO_4^- and 0.1 M MnO_4^-. (b) Calculated copper coverage, Θ_{Cu}^{Kaeshe} , at -0.6 V using Equation 17. Cu (1), AA2024-T351(2), and AA2024-T351 pretreated in 0.05 M MnO_4^- (3) and 0.1 M MnO_4^- (4). 68

Figure 51. Constant current discharge curves of electrodeposited manganese oxide coated copper (-▲-) and uncoated copper (-■-). High-purity Copper with Mn oxide deposited at -0.5 V SHE from 0.1 m KMnO4 with a pH of 6. Galvanostatic reduction performed at 20 mA in pH 8.4 borate buffer. The red dotted line (· ·) indicates the reversible potential of

$MnO_4^- + 4H^+ + 3e^- \leftrightarrow MnO_2 + 2H_2O$ at 0.54 V vs. SCE. The blue dashed (– –) line indicates the reversible potential for $MnO_2 + H_2O + e^- \leftrightarrow MnOOH + OH^-$ at 0.187 V vs. SCE. The green dash-dotted line (– · –) indicates the reversible potential for $MnOOH + H_2O + e^- \leftrightarrow Mn(OH)_2 + OH^-$ at -0.385 V vs. SCE.....69

Figure 52. Raman spectra for AA2024-T351, AA2024-T351 pretreated in 0.005 M $KMnO_4$, copper pretreated in 0.1 M $KMnO_4$ at -0.5 V vs. SCE, manganese metal held potentiostatically at 0.35 V vs. SCE, and MnO_2 powder.....70

Figure 53. Graph of vanadate speciation with time at room temperature. No great change in species present occurred over 28 days for 5 mM $NaVO_3$ plus 50 mM NaCl in D_2O solvent. 71

Figure 54. SEM micrographs of AA2024-T3 on the transverse-lateral surface after 24 hours of exposure in open to the air 50 mM NaCl solutions with 0, 5, 10, 50, and 150 mM $NaVO_3$ at room temperature. Decreasing pit density and depth is observed with increasing $NaVO_3$ concentration. No visible pits on the 150 mM $NaVO_3$ plus 50 mM NaCl exposed specimen were seen with optical methods, but parts of the copper intermetallic particles have change color from copper to blue.....74

Figure 55. Secondary electron image obtained at 15 kV of AA2024–T3 specimen exposed to 50 mM NaCl solution for 24 hours. The yellow arrow indicates location and direction of EDS. (a) represents the unattacked matrix composition way from a pitting site. (b) shows a pitting site above an Al–Cu–Fe–Mn intermetallic particle.....75

Figure 56. Higher magnification secondary electron image taken at 15 kV of AA2024–T3 specimen exposed to 5 mM $NaVO_3$ plus 50 mM NaCl for 24 hours. The yellow arrow indicates location and direction of EDS scan. Precipitated products are shown to be vanadium rich. There appears to be a dual phase intermetallic particle at the EDS line scan in the right hand image. Both Al–Cu–Mg and Al–Cu–Fe–Mn compositions exist. 76

Figure 57. Backscattered electron image, in the compositional mode, taken at 15 kV with 184 second collection time of AA2024–T3 specimen exposed to 5 mM $NaVO_3$ plus 50 mM NaCl for 24 hours. Yellow arrow indicates location and direction of EDS scan. The vanadium concentration of an intermetallic particle away from the pitting site is approximately the same as that of the matrix near the pitting site (Figure 56). 77

Figure 58. Typical anodic E-log(i) polarization behavior for Al (99.9%) specimens in open to the air 50 mM NaCl solution containing 0, 5, and 150 mM $NaVO_3$ [(a) after 1 hour open circuit; and (b) after 24 hour open circuit].....78

Figure 59. Cumulative probability plot of E_{pit} for Al 99.99% in open to the air 50 mM NaCl solutions plus various concentrations of $NaVO_3$. Data points indicate cumulative probability of pitting before potential reversal at 0 or 0.2 V_{SCE}. Arrows indicate specimens that did not pit at the potential indicated.....79

Figure 60. Cumulative probability plot of E_{pit} for Al 99.99% after 24 hours of exposure in open to the air 50 mM NaCl solutions plus various concentrations of $NaVO_3$. Data points indicate cumulative probability of pitting before potential reversal at 0 V_{SCE}. Arrows indicate specimens that did not pit at the potential indicated. 79

Figure 61. Typical anodic E-log(i) polarization behavior for AA2024–T3 specimens in open to the air 50 mM NaCl solution containing 0, 5, and 150 mM NaVO3 [(a) after 1 hour open circuit exposure; (b) after 24 hour open circuit exposure]. 80

Figure 62. Cumulative probability plot for AA2024-T3 after 1 hour in open to the air 50 mM NaCl solution plus various concentrations of $NaVO_3$. Data points indicate cumulative probability of pitting before potential reversal at 0 or 0.2 V_{SCE}. Arrows indicate specimens that did not pit at the potential indicated. 81

Figure 63. Cumulative Probability plot for AA2024–T3 after 24 hours in open to the air 50 mM NaCl solution plus various concentrations of $NaVO_3$. A single test was conducted with 1 mM $NaVO_3$. Data points indicate cumulative probability of pitting before potential reversal at 0 V_{SCE}. Arrows indicate specimens that did not pit at the potential indicated. 81

Figure 64. Anodic E–log(i) polarization behavior for AA2024-T3 specimens: (a) 24 hours, 5 mM $NaVO_3$ inhibitor pretreated and exposed in inhibitor free 50 mM NaCl; (b) exposed in 50 mM NaCl plus 5 mM $NaVO_3$. 1 hour open circuit exposure in the test solution occurred prior to polarization scans. Arrows indicate the direction of polarization. 82

Figure 65. E_{pit} cumulative probability plot for AA2024–T3 pretreated for 24 hours in various concentrations of $NaVO_3$ open to the air solutions then tested in open to the air 50 mM NaCl solutions. An 1 hour open circuit in test solution occurred prior to anodic E–log (i) polarization scan. 83

Figure 66. Cathodic E-Log(i) polarization behavior for high-purity Al, AA2024-T4,and high-purity Cu in open to the air 50 mM NaCl solution with an electrode rotation speed of 0 rpm. A 1 hour open circuit with specimen in the test solution occurred prior to cathodic polarization. Data not corrected for ohmic resistance. 84

Figure 67. Koutecky–Levich plot for Cu in open to the air 50 mM NaCl at three different potentials of -0.8 V_{SCE} and -1 V_{SCE}. Data was not corrected for ohmic resistance. 85

Figure 68. Levich plot of i_{Lim} extracted from i_{Total} on Cu and AA2024 in 50 mM NaCl showing comparison of experimental results to theoretical mass transport limited ORR rates. 85

Figure 69. Effect of rotation rate for open to the air 0 (left column) and 150 (right column) mM $NaVO_3$ plus 50 mM NaCl solutions on the cathodic polarization behavior of high-purity Al, AA2024–T4, and high-purity Cu. The data were corrected for ohmic resistance. (a) Al in 50 mM NaCl, (b) Al in 150 mM $NaVO_3$ plus 50 mM NaCl, (c) AA2024-T4 in 50 mM NaCl, (d) AA2024-T4 in 150 mM $NaVO_3$ plus 50 mM NaCl, (e) Cu in 50 mM NaCl, and (f) Cu in 150 mM $NaVO_3$ plus 50 mM NaCl. 87

Figure 70. Effect of various $NaVO_3$ concentrations in open to the air 50 mM NaCl solution on the cathodic polarization behavior of high-purity Al, AA2024–T4, and Cu at 0 (left) and 2500 (right) RPM. Data is not corrected for ohmic resistance. (a) Al at 0 rpm, (b) Al at 2500 rpm, (c) AA2024-T4 at 0 rpm, (d) AA2024-T4 at 2500 rpm, (e) Cu at 0 rpm, and (f) Cu at 2500 rpm. 88

Figure 71. Koutecky–Levich plot for Cu in open to the air 50 mM NaCl plus various concentrations of $NaVO_3$ at a potential of -0.8 V_{SCE}. Data was not corrected for Ohmic resistance. 89

Figure 72. The Koutecky–Levich plot for AA2024–T4 in open to the air 50 mM NaCl plus various concentrations of $NaVO_3$ at a potential of -0.8 V_{SCE}. 90

Figure 73. Levich plot (i_{Lim} extracted from i_{Total}) of Cu using data from the ORR region only (potential of -0.8 V_{SCE}) shows a loss of ideal mass transport controlled behavior. Tests performed open to the air 50 mM NaCl plus $NaVO_3$ solutions. 91

Figure 74. Levich plot (i_{Lim} extracted from i_{Total}) for AA2024–T4 using data taken in the ORR region. All analyzed data was taken at -0.8 V_{SCE}. Tests performed at ambient temperature in open to the air solutions of 50 mM NaCl plus various $NaVO_3$ concentrations. (b) emphasizes the effect of $NaVO_3$ on current density. 91

Figure 75. Cathodic polarization of (a) AA2024-T3 or (b) Cu in open to the air 50 mM NaCl solution with 0, 5, or 150 mM $NaVO_3$. The black line representing no addition inhibitor is the only the current associated with charge transfer kinetics. 92

Figure 76. (a) The E-pH behavior of 0.05 M Ce3+ in aqueous solution. (b) The concentrations of cerium species in the cerium-H_2O system at -0.5 V vs. SCE, near OCP of AA2024. 93

Figure 77. (a) The E-pH behavior of 0.05 M MnO_4^- in aqueous solution. (b) The concentrations of manganese species in the manganese-H_2O system at -0.5 V vs. SCE, near OCP of AA2024. 93

Figure 78. Concentrations of species in the cerium-chloride-H_2O system at 0.78 V vs. SCE, the E_o of Equation 19. The cerium oxide species (CeO_2) is stable above pH 3.3 at this potential. 94

Figure 79. (a) The as-polished (1200 grit) AA2024-T351 and the subsequent surface damage caused by 24 hour exposure to 0.05 M NaCl solution in a naturally aerated state at room temperature. (b) The damaged specimen image is compressed horizontally to include a secondary electron and backscattered electron image. 95

Figure 80. (a) AA2024-T351 pretreated with 0.01 M Ce3+ for 100 hrs. and 0.04 M MnO4- for 24 hrs. (secondary electron image). (b) Same pretreatment times with inhibitor concentrations of 0.025 M Ce3+ and 0.025 MnO4-. (c) Same pretreatment times with inhibitor concentrations of 0.04 M Ce3+ and 0.01 MnO4-. (d) Same pretreatment times with inhibitor concentrations of 0.05 M Ce3. (e) Same pretreatment time with inhibitor concentration of 0.05 MnO4-. 96

Figure 81. (a) AA2024-T351 with indication of EDS sites labeled 1-8. (b) Same sample and area as (a) Sample has been pretreated for 24 hours in 0.1M $KMnO_4$. Indication of EDS sites labeled 1-8. 97

Figure 82. (a) Intermetallic particle 1 from Figure 81. (b). Intermetallic particle 5 from Figure 81. The left spectrum is taken from an untreated sample, the right, a pretreated sample. The cerium-permanganate dual inhibitor pretreatments produced a wide array of

surface features as seen in Figure 80. In order to analyze the chemical composition of the complex oxide structures observed, EDS line scans for oxygen, magnesium, aluminum, chloride, manganese, iron, copper, and cerium were performed. Manganese is the only element that is found both in the pretreatment solution, and the alloy. The alloy contains 0.6% manganese by weight as shown in Table 3. This complicates the analysis of the manganese EDS results because the element is concentrated in certain intermetallic compounds in the alloy. However, manganese enrichment is clearly visible in the microscopy due to the unique oxide formations that have been observed. 98

Figure 83. EDS at 15 kV accelerating potential of AA2024-T351 pretreated in 10 mM Ce^{3+} + 40 mM MnO_4^-(a), 25 mM Ce^{3+} + 24 mM MnO_4^- (b), 40 mM Ce^{3+} + 10 mM MnO_4^-. All cerium pretreatments lasted for 100 hours. All permanganate pretreatments lasted for 24 hours.....100

Figure 84. (a) AA2024-T351 pretreated with 0.01 M Ce^{3+} for 100 hrs. and 0.04 M MnO_4^- for 24 hours and exposed to 0.05 M Cl^- for 24 hrs. (secondary electron image). (b) Same pretreatment with inhibitor concentrations of 0.025 M Ce^{3+} and 0.025 MnO_4^- and exposed to 0.05 M Cl^- for 24 hrs. (c) Same pretreatment with inhibitor concentrations of 0.04 M Ce^{3+} and 0.01 MnO_4^- and exposed to 0.05 M Cl^- for 24 hrs. (d) Same pretreatment with inhibitor concentrations of 0.05 M Ce^{3+} and exposed to 0.05 M Cl^- for 24 hrs.(e) Same pretreatment with inhibitor concentrations of 0.05 MnO_4^- and exposed to 0.05 M Cl^- for 24 hrs. Samples were not cleaned post exposure. 101

Figure 85. EDS at 15 kV accelerating potential of AA2024-T351 exposed for 24 hours in 50 mM NaCl after pretreatment in 10 mM Ce^{3+} + 40 mM MnO_4^- (a), 25 mM Ce^{3+} + 24 mM MnO_4^- (b). All cerium pretreatments lasted for 100 hours. All permanganate pretreatments lasted for 24 hours.....102

Figure 86. Surface damage revealed by abrasive removal of cerium oxide after pretreatment in 0.05 M Ce^{3+} for 100 hrs. and subsequent exposure to 0.05 M NaCl for 24 hours.....103

Figure 87. Open circuit test of pretreated AA2024-T351 in 50 mM NaCl solution with ambient aeration. Test included 100 hrs. pretreatment in Ce^{3+} followed by 24 hrs. pretreatment in MnO_4^- at the indicated concentrations. Pretreatments are Cl^- free. 104

Figure 88. CVs of pretreated AA2024-T351 after a 24 hour exposure in 50 mM NaCl solution.....104

Figure 89. The relative intensities of the Cu^{1+} reduction peak on the AA2024-T351 surface pretreated in cerium for 100 hours and subsequently in permanganate for 24 hrs. followed by exposure for 24 hrs. in 0.05 M NaCl are shown. Combined inhibitor concentrations tested had ratios of cerium to permanganate of 0.2 and 0.8 with a total inhibitor concentration of 0.05 M. Results are compared to permanganate pretreatments and cerium pretreatments. A large decrease in the copper surface coverage is evident for the combined inhibitor pretreatment over either single inhibitor pretreatment. 105

Figure 90. Anodic E-log(*i*) behavior of AA2024 with cerium-permanganate pretreatments at stated concentrations tested in 5 mM sodium chloride. 106

Figure 91. Cumulative probability of pitting on AA 2024-T351 as a function of potential for both permanganate-cerium combinations and in-situ solution phase permanganate inhibitor concentration. Combined inhibitor concentrations tested had ratios of cerium to permanganate of 0, 0.2, 0.5, 0.8, and 1 with a total inhibitor concentration of 0.05 M. Cumulative probability of pitting in 0.05 M NaCl solution.....107

Figure 92. Cathodic E vs. log(*i*) data for AA2024-T4 (a) and high purity copper (b) samples run at various rotation rates from 100 rpm to 2500 in pH 8.4 borate buffer. Solutions were aerated naturally and no pretreatment was performed.....108

Figure 93. Rotating disk cathodic polarizations experiments on AA 2024-T351 at a rotation rate of 2500 rpm in pH 8.4 borate buffer. Combined inhibitor concentrations tested had ratios of cerium to permanganate of 0.2, 0.5, and 0.8 with a total inhibitor concentration of 0.05 M. Total current densities for bare AA2024, cerium treated, and permanganate treated have been included for reference. 108

Figure 94. (a) RPM Ramp 500 to 2500 (increments of 500) of AA2024-T351 in pH 8.4 borate buffer after stated pretreatments When manganese deposits are present it reacts electrochemically effecting the current density at each rotation rate. (b) RPM Ramp 500 to 2500 (increments of 500) of high purity copper in pH 8.4 borate buffer after stated pretreatments.....109

Figure 95. Diffusion limited current density on high purity copper compared to AA2024-T351 at rotation rates from 500 to 2500 rpm in pH 8.4 borate buffer. Combined inhibitor concentrations tested had ratios of cerium to permanganate of 4, 1, and 0.2 with a total inhibitor concentration of 0.05 M. 110

Figure 96. Diffusion limited current density on high purity copper at rotation rates from 500 to 2500 rpm in pH 8.4 borate buffer. Combined inhibitor concentrations tested had ratios of cerium to permanganate of 4, 1, and 0.2 with a total inhibitor concentration of 0.05 M. 111

Figure 97. Vanadate speciation as a function of time. Insignificant changes in vanadate species present occurred for a) 50 mM $NaVO_3$ plus 50 mM NaCl in D_2O solvent; b) 40 mM Na_2MoO_4 plus 10 mM $NaVO_3$ plus 50 mM NaCl in D_2O solvent. 112

Figure 98. Typical OCP behavior for AA2024-T3 specimens in naturally aerated 50 mM NaCl solutions after a) 1st Hour and b) 23rd Hour. A pretreatment in various concentrations of $Ce(C_2H_3O_2)_3$ followed by testing in various concentrations of $NaVO_3$ in 50 mM NaCl solutions. 115

Figure 99. Typical OCP behavior for AA2024-T3 specimens in naturally aerated 50 mM NaCl solutions after a) 1st Hour and b) 23rd Hour. The test solution contained 50 mM $NaVO_3$ and Na_2MoO_4 inhibitors in addition to 50 mM NaCl. The ratio of $NaVO_3$ and Na_2MoO_4 varied, but total inhibitor concentration was kept constant at 50 mM. 116

Figure 100. Optical micrographs of AA2024-T3 on the transverse-lateral surface after 24 hours of exposure in naturally aerated 50 mM NaCl solutions with different combinations of inhibitors at room temperature. 50 mM NaCl solution containing cerium acetate was in

contact with the surface for 2 hours prior to testing in the chloride containing test solutions for 24 hours for the cerium acetate pretreatment specimens. The scale bars are all 50μm. 118

Figure 101. Backscattered electron image, in the compositional mode, taken at 20 kV with 180 second collection time of AA2024–T3 specimen exposed to a) 50 mM $Ce(C_2H_3O_2)_3$ or b) 10 mM $Ce(C_2H_3O_2)_3$ for 2 hours. The arrows indicate location and direction of EDS scan over Al-Cu-Fe-Mn particles.....119

Figure 102. Backscattered electron image, in the compositional mode, taken at 20 kV with 180 second collection time of AA2024–T3 specimen exposed to a) 40 mM $Ce(C_2H_3O_2)_2$ for 2 hours or b) 40 mM $Ce(C_2H_3O_2)_2$ for a 2 hour pretreatment then a 24 hour immersion in 10 mM $NaVO_3$ + 50 mM NaCl. The arrows indicate location and direction of EDS scan. 120

Figure 103. Backscattered electron image, in the compositional mode, taken at 20 kV with 180 second collection time of AA2024–T3 specimen exposed to a) 50 mM Na_2MoO_4 or b) 25 mM Na_2MoO_4 + 25 mM $NaVO_3$ for a 24 hour immersion in 50 mM NaCl. The arrows indicate location and direction of EDS scans. 121

Figure 104. Backscattered electron image, in the compositional mode, taken at 20 kV with 180 second collection time of AA2024–T3 specimen exposed to a) 50 mM Na_2MoO_4 or b) 10 mM Na_2MoO_4 + 40 mM $NaVO_3$ for a 24 hour immersion in 50 mM NaCl. The arrows indicate location and direction of EDS scans. 122

Figure 105. Typical anodic E-log(i) polarization behavior for Al (99.99%) specimens in aerated 50 mM NaCl solutions after an 1 hour open circuit. A pretreatment in various concentrations of $Ce(C_2H_3O_2)_3$ followed by testing in various concentrations of $NaVO_3$ in the 50 mM NaCl solution lead to each surface having been exposed to a constant total of 50 mM of inhibitor between the two solutions. 123

Figure 106. Typical anodic E-log(i) polarization behavior for Al (99.99%) specimens in aerated 50 mM NaCl solutions after a 24 hour open circuit. A pretreatment in various concentrations of $Ce(C_2H_3O_2)_3$ followed by testing in various concentrations of $NaVO_3$ in the 50 mM NaCl solution lead to each surface having been exposed to a constant total of 50 mM of inhibitor between the two solutions. 124

Figure 107. Typical anodic E-log(i) polarization behavior for Al (99.99%) specimens in aerated 50 mM NaCl solutions after an 1 hour open circuit. The test solution contained 50 mM of $NaVO_3$ and Na_2MoO_4 inhibitors in addition to 50 mM NaCl. The ratio of $NaVO_3$ and Na_2MoO_4 varied, but the total inhibitor concentration was kept constant at 50 mM. 126

Figure 108. Typical anodic E-log(i) polarization behavior for Al (99.99%) specimens in aerated 50 mM NaCl solutions after a 24 hour open circuit. The test solution contained 50 mM of $NaVO_3$ and Na_2MoO_4 inhibitors in addition to 50 mM NaCl. The ratio of $NaVO_3$ and Na_2MoO_4 varied, but the total inhibitor concentration was kept constant at 50 mM. 127

Figure 109. Typical anodic E-log(i) polarization behavior for AA2024–T3 specimens in naturally aerated 50 mM NaCl solutions after an 1 hour open circuit. A pretreatment in various concentrations of $Ce(C_2H_3O_2)_3$ followed by testing in various concentrations of $NaVO_3$ in the 50 mM NaCl solution lead to each surface having been exposed to a total of 50 mM of inhibitor between the two solutions. 128

Figure 110. Typical anodic E-log(i) polarization behavior for AA2024–T3 specimens in naturally aerated 50 mM NaCl solutions after a 24 hour open circuit period. A pretreatment in various concentrations of $Ce(C_2H_3O_2)_3$ was followed by testing in various concentrations of $NaVO_3$ in the 50 mM NaCl solution lead to each surface having been exposed to a total of 50 mM of inhibitor between the two solutions.....130

Figure 111. Typical anodic E-log(i) polarization behavior for AA2024–T3 specimens in naturally aerated 50 mM NaCl solutions after a 24 hour open circuit period. A pretreatment of 10 mM $Ce(C_2H_3O_2)_3$ was followed by testing in various concentrations of $NaVO_3$ in the 50 mM NaCl solution.....131

Figure 112. Average Epit for AA2024-T3 specimens in aerated 50 mM NaCl solutions after a 24 hour open circuit. A 2 hour $Ce(C_2O_3H_2)_3$ pretreatment was followed by testing in various concentration of $NaVO_3$ in the 50 mM NaCl solution.....132

Figure 113. Typical anodic E-log(i) polarization behavior for AA2024-T3 specimens in naturally aerated 50 mM NaCl solutions after a 1 hour open circuit. The test solution contained a combined concentration of 50 mM of $NaVO_3$ and Na_2MoO_4 inhibitors in addition to 50 mM NaCl. The ratio of $NaVO_3$ and Na_2MoO_4 varied.....133

Figure 114. Typical anodic E-log(i) polarization behavior for AA2024-T3 specimens in naturally aerated 50 mM NaCl solutions after a 24 hour open circuit. The test solution contained a combined concentration of 50 mM of $NaVO_3$ and Na_2MoO_4 inhibitors in addition to 50 mM NaCl. The ratio of $NaVO_3$ and Na_2MoO_4 varied.....135

Figure 115. Cumulative probability plot for Al (99.99%) after 1 hour in aerated 50 mM NaCl solution plus various 50 mM inhibitor mixtures; a) a $Ce(C_2H_3O_2)_3$ 2 hour pretreatment then tested with the remainder of the inhibitor concentration as $NaVO_3$ dissolved in the test solution; b) $NaVO_3$ and Na_2MoO_4 mixtures dissolved into the test solution. Data points indicate cumulative probability of pitting before potential reversal.....136

Figure 116. Cumulative probability plot for Al (99.99%) after 24 hours in aerated 50 mM NaCl solution plus various 50 mM inhibitor mixtures; a) a $Ce(C_2H_3O_2)_3$ 2 hour pretreatment then tested with the remainder of the inhibitor concentration as $NaVO_3$ dissolved in the test solution; b) $NaVO_3$ and Na_2MoO_4 mixtures dissolved into the test solution. Data points indicate cumulative probability of pitting before potential reversal.....137

Figure 117. Cumulative probability plot for AA2024-T3 after 1 hour in aerated 50 mM NaCl solution plus various concentrations of $NaVO_3$. Average E_{pit} values of AA2024-T3 after 1 hour in aerated 50 mM NaCl solution plus various 50 mM inhibitor mixtures; a) a $Ce(C_2H_3O_2)_3$ 2 hour pretreatment then tested with the remainder of the inhibitor concentration as $NaVO_3$ dissolved in the test solution; b) $NaVO_3$ and Na_2MoO_4 mixtures dissolved into the test solution. Data points indicate cumulative probability of pitting before potential reversal. Arrows indicate specimens that did not pit at the potential indicated.....139

Figure 118. Cumulative probability plot for AA2024-T3 after 24 hours in aerated 50 mM NaCl solution plus various concentrations of $NaVO_3$. Average E_{pit} values of AA2024-T3 after 1 hour in aerated 50 mM NaCl solution plus various 50 mM inhibitor mixtures; a) a $Ce(C_2H_3O_2)_3$ 2 hour pretreatment then tested with the remainder of the inhibitor

concentration as $NaVO_3$ dissolved in the test solution; b) $NaVO_3$ and Na_2MoO_4 mixtures dissolved into the test solution. Data points indicate cumulative probability of pitting before potential reversal. Arrows indicate specimens that did not pit at the potential indicated.....140

Figure 119. Cathodic E–log(i) polarization behavior for high purity Cu in aerated 50 mM NaCl solution with various concentrations of vanadate after a 2 hour cerium acetate pretreatment. An electrode rotation speed of 2500 rpm was used. A 1 hour open circuit in the test solution occurred prior to cathodic polarization. Data was not corrected for ohmic resistance.....142

Figure 120. Cathodic E–log(i) polarization behavior for high purity Cu in aerated 50 mM NaCl solution with various concentrations of vanadate and molybdate. An electrode rotation speed of 2500 rpm was used. A 1 hour open circuit in the test solution occurred prior to cathodic polarization. Data was not corrected for ohmic resistance.....143

Figure 121. Cathodic E–log(i) polarization behavior for AA2024–T4 in aerated 50 mM NaCl solution with various concentrations of vanadate and a 2 hour cerium acetate pretreatment. An electrode rotation speed of 2500 rpm was used. A 1 hour open circuit in the test solution occurred prior to cathodic polarization. Data was not corrected for ohmic resistance.....144

Figure 122. Cathodic E–log(i) polarization behavior for AA2024–T4 in aerated 50 mM NaCl solution with various concentrations of vanadate and a 2 hour cerium acetate pretreatment. An electrode rotation speed of 2500 rpm was used. A 1 hour open circuit in the test solution occurred prior to cathodic polarization. Data was not corrected for ohmic resistance.....145

Figure 123. Koutecky–Levich plot for Cu in aerated 50 mM NaCl plus various 50 mM inhibitor combinations at a potential of -0.8 V_{SCE} after a 1 hour open circuit. a) Cu specimens were pretreated for 2 hours in various $Ce(C_2O_3H_2)_3$ followed by testing in various $NaVO_3$ plus 50 mM NaCl solutions. b) Cu specimens were tested in various 50 mM combinations of Na_2MoO_4/ $NaVO_3$ plus 50 mM NaCl. Data was not corrected for Ohmic resistance.....146

Figure 124. Koutecky–Levich plot for AA2024-T4 in aerated 50 mM NaCl plus various 50 mM inhibitor combinations at a potential of -0.8 V_{SCE} after a 1 hour open circuit. a) AA2024-T4 specimens were pretreated for 2 hours in various Cerium followed by testing in various $NaVO_3$ plus 50 mM NaCl solutions. b) AA2024-T4 specimens were tested in various 50 mM combinations of Na_2MoO_4/ $NaVO_3$ plus 50 mM NaCl. Data was not corrected for Ohmic resistance. 146

Figure 125. Levich plot (i_{Lim} extracted from i_{Total}) of Cu using data from the ORR region only (potential of -0.8 V_{SCE}) shows a loss of ideal mass transport controlled behavior. A 1 hour open circuit was used. Test preformed in aerated 50 mM NaCl plus $NaVO_3$ binary inhibitor combinations. a) Cu specimens were pretreated for 2 hours in various $Ce(C_2H_3O_2)_3$ followed by testing in various $NaVO_3$ plus 50 mM NaCl solutions. b) Cu specimens were tested in various 50 mM combinations of Na_2MoO_4/ $NaVO_3$ plus 50 mM NaCl. Data was not corrected for Ohmic resistance.....147

Figure 126. Levich plot (i_{Lim} extracted from i_{Total}) of AA2024-T4 using data from the ORR region only (potential of -0.8 V_{SCE}) shows a loss of ideal mass transport controlled

behavior. A 1 hour open circuit was used. Test preformed in aerated 50 mM NaCl plus $NaVO_3$ binary inhibitor combinations. a) AA2024-T4 specimens were pretreated for 2 hours in various $Ce(C_2H_3O_2)_3$ followed by testing in various $NaVO_3$ plus 50 mM NaCl solutions. b) AA2024-T4 specimens were tested in various 50 mM combinations of Na_2MoO_4/ $NaVO_3$ plus 50 mM NaCl. Data was not corrected for Ohmic resistance. 148

Figure 127. Anodic inhibitors of interest for EFCP inhibition. Potentiodynamic scan of AA2024-T351 in molybdate and chromate containing 0.05 M NaCl solution. Lines to the left of polarization curves indicate scratch potentials investigated ranging from -0.8 V to -0.3 V vs. SCE. 148

Figure 128. Molybdate buffer capacity.[141] Initial pH was 9.3 for 0.1 M MoO_4^{2-} solutions. Solution pH from titration of (0.01 M, 0.05 M, and 0.1 M) sodium molybdate + 0.6 M NaCl with 0.25 mL of 1 M HCl reported as HCl concentration in mM. Molybdate concentration varied from 0.1 to 0.01 M and results are compared against uninhibited 0.6 M NaCl. Molybdate chemical reactions are shown with relevant predominant species in the measured pH range. 149

Figure 129. Scratch of 99.999% Al in 1 M NaCl at pH 6.5 potentiostatically held at -0.8 V SCE. 151

Figure 130. Scratch of 99.999% Al in 1 M NaCl at pH 6.5 potentiostatically held at -0.8 V SCE. The ohmic potential drop at the working electrode is 0.2 V increasing the hydrogen over-potential. 151

Figure 131. Current transients from 99.999% aluminum scratched electrodes. Potentials from -0.5 to -0.8 V vs. SCE are shown at three chloride concentrations from 0.05 to 1 M. The pH for all tests was 6.5. 152

Figure 132. Calculated IR limit as compared to peak net current density of scratched 99.999% aluminum electrodes in various chloride concentrations at time zero after scratch. 153

Figure 133. Net current transients from AA7075 (a) and AA2024 (b) in aqueous 1 M NaCl with pH adjusted to 6.5 with NaOH. Scratch potentials vary from -0.5 to -0.8 V vs. SCE. Current transients from AA7075 (c) and AA2024 (d) in aqueous 1 M NaCl with pH adjusted to 6.5. Scratch potentials vary from -0.5 to -0.8 V vs. SCE for (c) and -0.4 to -0.8 V vs. SCE for (d). 154

Figure 134. (a) Scratched electrode net anodic current densities for AA7075-T6 in 0.05 M NaCl solution with pH 6.5. (b) Calculated IR limit as compared to peak current density of scratched AA7075 electrodes at time zero after scratch. IR limit is calculated for an aqueous 0.05 M NaCl solution, a 0.1 M CrO_4^{2-} and 0.05 M NaCl solution, and 0.1 M MoO_4^{2-} and 0.05 M NaCl solution. (c) and (d) show scratched electrode current transients for AA7075-T6 with 0.1 M MoO_4^{2-} and 0.1 M CrO_4^{2-} additions, respectfully.....155

Figure 135. (a) Scratched electrode charge passed for AA7075-T6 in 0.05 M NaCl solution with a pH of 6.5 and 0.1 M CrO_4^{2-} and 0.05 M NaCl solution. (b) Scratched electrode charge passed for AA2024-T351 in 0.05 M NaCl solution with a pH of 6.5 and 0.1 M Na_2MoO_4 and 0.05 M NaCl solution. Integration of current over three periods from 0.05 milliseconds to 0.01 second, 0.01 to 0.1 second, and 0.1 to 1 second. 156

Figure 136. (a) Scratched electrode net anodic current densities for AA2024-T6 in 0.05 M NaCl solution with pH 6.5. (b) Calculated IR limit as compared to peak current density of scratched AA2024 electrodes at time zero after scratch. IR limit is calculated for an aqueous 0.05 M NaCl solution, 0.1 M CrO_4^{2-} and 0.05 M NaCl solution, and 0.1 M MoO_4^{2-} and 0.05 M NaCl solution. (c) and (d) show scratched electrode current transients for AA2024-T351 with 0.1 M $MoO_4^{2-}$and 0.1 M CrO_4^{2-} additions, respectfully. 157

Figure 137. (a) Scratched electrode charge passed for AA2024-T351 in 0.05 M NaCl solution with a pH of 6.5 and 0.1 M CrO_4^{2-} and 0.05 M NaCl solution. (b) Scratched electrode charge passed for AA2024-T351 in 0.05 M NaCl solution with a pH of 6.5 and 0.1 M MoO_4^{2-} and 0.05 M NaCl solution. Integration of current over three periods from 0.05 milliseconds to 0.01 second, 0.01 to 0.1 second, and 0.1 to 1 second. 158

Figure 138. (a) Single frequency impedance measurements on AA2024 taken at -0.8 V_{SCE} in aqueous 1 M NaCl with a range of MoO_4^{2-} concentrations, all with adjusted pH of 6.5 at frequency 1000 Hz. These are impedance values as collected by the frequency response analyzer. (b) Single frequency impedance measurements from (a) corrected for scratched electrode area. (c) Calculated capacitance values from area corrected impedance values. (d) Oxide thickness calculated from film capacitance. The 1 M NaCl did not repassivate. 159

Figure 139. (a) Single frequency impedance measurements taken at -0.8 V_{SCE} in an aqueous 1 M NaCl and 5 mM CrO_4^{2-} solution corrected for scratched electrode area. Instrument limitations prevent data acquisition at long times in the solution shown and at all times at higher concentrations of chromate. This is due to small sample area and large oxide thickness. (b) Calculated capacitance values from area corrected impedance values. (c) Oxide thickness calculated from film capacitance. The 1 M NaCl solution did not repassivate. 160

Figure 140. Representative anodic potentiodynamic polarization scans measured in 0.05 M NaCl solutions containing inhibitors at different concentrations. 162

Figure 141. Cathodic potentiodynamic polarization scans of AA7075 in non-deaerated, 0.05 M NaCl solution containing various inhibitors at different concentrations.....163

Figure 142. Chronoamperometric curves of AA7075 measured in non-deaerated, 0.05 M NaCl solution with and without inhibitors. 164

Figure 143. Cathodic current densities measured after 60 seconds of potentiostatic hold during chronoamperometric tests as a function of inhibitor concentrations. 164

Figure 144. Measured open circuit potential, E_{pit} and resulting ΔE_{pass} for AA7075 in non-deaerated, 0.05 M NaCl solution containing cerium at different concentrations. 166

Figure 145. Measured open circuit potential, E_{pit} and resulting ΔEpass for AA7075 in non-deaerated, 0.05 M NaCl solution containing vanadate at different concentrations. 167

Figure 146. Measured open circuit potential, E_{pit} and resulting ΔEpass for AA7075 in non-deaerated, 0.05 M NaCl solution containing molybdate at different concentrations.....167

Figure 147. Passive current density (A/cm^2) of carbon steel 1018 in deaerated, 0.05 M NaCl solution containing molybdate at different concentrations, as a function of the concentration of sodium molybdate. 168

Figure 148. Anodic potentiodynamic polarization scans of 1018 carbon steel in deaerated, 0.05 M NaCl solution containing various inhibitors at different concentrations. 169

Figure 149. Cathodic potentiodynamic polarization scans of 1018 carbon steel measured in non-deaerated, 0.05 M NaCl solutions containing various inhibitors at different concentrations. 170

Figure 150. OCP of 1018 CS in non-deaerated, 0.05 M NaCl with single Ce and V inhibitors and V/Ce inhibitor combinations as a function of the total inhibitor concentration. 171

Figure 151. Cathodic current densities of 1018 CS at -0.2 V vs. OCP in 0.05 M NaCl with single Ce and V inhibitors and V/Ce inhibitor combinations as a function of the total inhibitor concentration. 171

Figure 152. OCP of AA 7075 in non-deaerated, 0.05 M NaCl with single Ce and V inhibitor and V/Ce inhibitor combinations as a function of the total inhibitor concentration. 172

Figure 153. Cathodic current densities of AA 7075 at -0.2 V vs. OCP in 0.05 M NaCl with single Ce and V inhibitors and V/Ce inhibitor combinations as a function of the total inhibitor concentration. 173

Figure 154. E_{pit} of AA 7075 in 0.05 M NaCl with single Ce and V inhibitors and V/Ce inhibitor combinations as a function of the total inhibitor concentration. 173

Figure 155. OCP of 1018 CS in 0.05 M NaCl with single Ce and Mo inhibitors and Ce/Mo inhibitor combinations as a function of the total inhibitor concentration. 174

Figure 156. Cathodic currents of 1018 CS at -0.2 V vs. OCP in 0.05 M NaCl with single Ce and Mo inhibitors and Ce/Mo inhibitor combinations as a function of the total inhibitor concentration. 175

Figure 157. OCP of AA 7075 in 0.05 M NaCl with single Ce and Mo inhibitors and Ce/Mo inhibitor combinations as a function of the total inhibitor concentration. 175

Figure 158. Cathodic currents of AA 7075 at -0.2 V vs. OCP in 0.05 M NaCl with single Ce and Mo inhibitors and Ce/Mo inhibitor combinations as a function of the total inhibitor concentration. 176

Figure 159. E_{pit} of AA 7075 in 0.05 M NaCl with single Ce and Mo inhibitors and Ce/Mo inhibitor combinations as a function of the total inhibitor concentration. 176

Figure 160. Cathodic polarization scans of array 1 at 1000 rpm with and without the presence of inhibitors. 177

Figure 161. Cathodic polarization scans of array 2 at 1000 rpm. 177

Figure 162. Cathodic polarization scans of array 3 at 1000 rpm. 178

Figure 163. Cathodic polarization scans of array 4 at 1000 rpm. 178

Figure 164. Cathodic polarization scans of all arrays in V solution at 1000 rpm.....179

Figure 165. Cathodic polarization scans of all arrays in Ce solution at 1000 rpm. 179

Figure 166. Effect of the type of inhibitors combined to 0.05 M NaCl on the measured anodic (Al, in red) and cathodic (Cu, in blue) total current as a function of time. 180

Figure 167. Effect of the concentration of vanadate combined to 0.05 M NaCl on the measured anodic (Al, in red) and cathodic (Cu, in blue) total current as a function of time.....181

Figure 168. Comparison between pre-exposure and combination with cerium on the measured anodic (Al, in red) and cathodic (Cu, in blue) total current as a function of time.....181

Figure 169. Comparison between pre-exposure and combination with molybdate on the measured anodic (Al, in red) and cathodic (Cu, in blue) total current as a function of time.....182

Figure 170. Effect of the concentration of pre-exposure vanadate on the measured anodic (Al, in red) and cathodic (Cu, in blue) total current as a function of time. 182

Figure 171. Auger electron Spectroscopy Scans of AA7075 after exposure to (a) 0.05 mol/L and (b) 0.005 mol/L cerium for 24 hours. 183

Figure 172. Auger electron Spectroscopy Scans of AA7075 after exposure to (a) 0.05 mol/L and (b) 0.005 mol/L cerium for 24 hours and 10 seconds at 400 Å/min sputtering. 184

Figure 173. Auger electron Spectroscopy Scans of AA7075 after exposure to (a) 0.05 mol/L and (b) 0.005 mol/L cerium for 24 hours and 30 seconds at 400 Å/min sputtering. 184

Figure 174. Auger electron Spectroscopy Scans of AA7075 after exposure to (a) 0.05 mol/L and (b) 0.005 mol/L vanadate for 24 hours. 184

Figure 175. Auger electron Spectroscopy Scans of AA7075 after exposure to (a) 0.05 mol/L and (b) 0.005 mol/L vanadate for 24 hours and 10 seconds at 400 Å/min sputtering. 185

Figure 176. Auger electron Spectroscopy Scans of AA7075 after exposure to (a) 0.05 mol/L and (b) 0.005 mol/L vanadate for 24 hours and 30 seconds at 400 Å/min sputtering. 185

Figure 177. Auger electron Spectroscopy Scans of AA7075 after exposure to (a) 0.05 mol/L and (b) 0.005 mol/L molybdate for 24 hours. 185

Figure 178. Auger electron Spectroscopy Scans of AA7075 after exposure to (a) 0.05 mol/L and (b) 0.005 mol/L molybdate for 24 hours and 10 seconds at 400 Å/min sputtering....186

Figure 179. Auger electron Spectroscopy Scans of AA7075 after exposure to (a) 0.05 mol/L and (b) 0.005 mol/L molybdate for 24 hours and 30 seconds at 400 Å/min sputtering....186

Figure 180. EDS of AA7075 after exposure to (a) 0.05 mol/L and (b) 0.005 mol/L cerium for 24 hours. 186

Figure 181. EDS of AA7075 after exposure to (a) 0.05 mol/L and (b) 0.005 mol/L molybdate for 24 hours. 187

Figure 182. EDS of AA7075 after exposure to (a) 0.05 mol/L and (b) 0.005 mol/L vanadate for 24 hours. 187

Figure 183. Surface analysis performed using EDS on AA7075 after 24 hours exposure to 0.05 mol/L (*inh*1) and 0.005 mol/L (*inh*2) molybdate, cerium and vanadate. 187

Figure 184. EDS mapping of AA 7075 before 24 hours immersion in 0.05 mol/L cerium acetate. 200 μm^2 frame. 188

Figure 185. EDS mapping of AA 7075 after 24 hours immersion in 0.05 mol/L cerium acetate. 200 μm^2 frame. The hypothesized inhibitor precipitates are indicated with the red arrows. 189

Figure 186. EDS mapping of AA 7075 after 24 hours immersion in 0.05 mol/L cerium acetate. 25 μm^2 frame. 189

Figure 187. EDS mapping of AA 7075 before 24 hours immersion in 0.05 mol/L sodium vanadate. 200 μm^2 frame. 190

Figure 188. EDS mapping of AA 7075 after 24 hours immersion in 0.05 mol/L sodium vanadate. 200 μm^2 frame. 190

Figure 189. EDS mapping of AA 7075 after 24 hours immersion in 0.05 mol/L sodium vanadate. 25 μm^2 frame. 191

Figure 190. EDS mapping of AA 7075 before 24 hours immersion in 0.05 mol/L sodium molybdate. 200 μm^2 frame. 191

Figure 191. EDS mapping of AA 7075 after 24 hours immersion in 0.05 mol/L sodium molybdate. 200 μm^2 frame. The hypothesized inhibitor precipitates are indicated with the red arrows. 192

Figure 192. EDS mapping of AA 7075 after 24 hours immersion in 0.05 mol/L sodium molybdate. 25 μm^2 frame. 192

Figure 193. (a) topographic scan and (b) work function scan of a pure copper specimen before being exposed to 0.05 M sodium molybdate. 193

Figure 194. (a) topographic scan and (b) work function scan of a pure copper specimen after being exposed to 0.05 M sodium molybdate. 193

Figure 195. (a) topographic scan and (b) work function scan of a pure copper specimen before being exposed to 0.05 M sodium vanadate. 194

Figure 196. (a) topographic scan and (b) work function scan of a pure copper specimen after being exposed to 0.05 M sodium vanadate. 194

Figure 197. Mott-Schottky analysis results in 0.05 M cerium acetate. (a) Evolution of $1/C^2$ as a function of the applied potential at various frequencies. (b) Flatband potential (V vs. $HgSO_4$) as a function of the frequency. 195

Figure 198. Donor density and flatband potential for 0.05 M and 0.005 M cerium acetate and vanadate. 196

Figure 199. Total current measured on Al/Cu MEA treated with 0.05 M cerium acetate for 24 hours. The current are measured during (a) 3 hours at 60% RH and 2.5 hours at 45% RH, (b) 3 hours at 70% RH and 2.5 hours at 45% RH, (c) 3 hours at 80% RH and 2.5 hours at 45% RH, and (d) 3 hours at 90% RH and 2.5 hours at 45% RH. The test chamber relative humidity and temperature, and room temperature are also plotted. 197

Figure 200. Total current measured on Al/Cu MEA treated with 0.05 M sodium vanadate for 24 hours. The current are measured during (a) 3 hours at 60% RH and 2.5 hours at 45% RH, (b) 3 hours at 70% RH and 2.5 hours at 45% RH, (c) 3 hours at 80% RH and 2.5 hours at 45% RH, and (d) 3 hours at 90% RH and 2.5 hours at 45% RH. The test chamber relative humidity and temperature, and room temperature are also plotted. 198

Figure 201. Total current measured on Al/Cu MEA treated with 0.05 M sodium molybdate for 24 hours. The current are measured during (a) 3 hours at 60% RH and 2.5 hours at 45% RH, (b) 3 hours at 70% RH and 2.5 hours at 45% RH, (c) 3 hours at 80% RH and 2.5 hours at 45% RH, and (d) 3 hours at 90% RH and 2.5 hours at 45% RH. The test chamber relative humidity and temperature, and room temperature are also plotted. 199

Figure 202. Total current measured on Al/Cu MEA untreated. The current are measured during (a) 3 hours at 60% RH and 2.5 hours at 45% RH, (b) 3 hours at 70% RH and 2.5 hours at 45% RH, (c) 3 hours at 80% RH and 2.5 hours at 45% RH, and (d) 3 hours at 90% RH and 2.5 hours at 45% RH. The test chamber relative humidity and temperature, and room temperature are also plotted.....200

Figure 203. Total anodic charge as a function of the relative humidity and inhibitor treatment after 150 minutes exposure at high relative humidity.....201

Figure 204. Total anodic charge as a function of the relative humidity and inhibitor treatment after 330 minutes exposure at high relative humidity.....201

Figure 205. (a) Gueshi model showing effect of IMC special geometry in AA2024-T351 on modeled ORR kinetics and actual data values. (b) A schematic showing effect of decreasing active area in an inactive matrix. 204

Figure 206. Optical (left) and scanning electron microscopy (right) of manganese oxide film grown over high-purity copper.....205

Figure 207. Membrane modeling of cathodic reaction kinetics in mass transport and mixed ORR regime for high-purity copper with a manganese oxide film grown on its surface from 0.1 M $KMnO_4$ solution at -0.5 V vs. SCE. 206

Figure 208. The limiting current density extracted from the total current for AA2024-T4 in open to the air 50 mM NaCl plus (0, 1, 5, 10, 50, 150 mM $NaVO_3$). δ is the O_2 diffusion boundary layer thickness perpendicular to the planer surface. L is the spacing between intermetallic compounds. The copper coverage θ is determined by the difference in current for the inhibited vs. uninhibited specimen divided by the current of the uninhibited specimen at a single potential in the ORR dominated potential range. Data place on top of theoretical limiting current density generated using the Gueshi model.[90] 212

Figure 209. Plot of θ/(1-θ) versus C_{NaVO3}: (a) AA2024-T4 or (b) Cu in open to the air 50 mM NaCl plus various (1, 5, 10, 50, 150 mM) $NaVO_3$ solutions at different potentials. θ is the vanadate coverage on the surface. The rotation rate was 2,500 rpm. 213

Figure 210. Plot of θ versus Log C_{NaVO3}: (a) AA2024-T4 or (b) Cu in open to the air 50 mM NaCl plus various (1, 5, 10, 50, 150 mM) $NaVO_3$ solutions at different potentials. The rotation rate was 2,500 rpm. 214

Figure 211. Schematic of different cathodic reaction inhibition mechanisms for the reduction of permanganate, the chemical precipitation of cerium hydroxide, and the effect of dual inhibitor pretreatment. 215

Figure 212. Plots of E_{pit} and E_{corr} for Al (99.99%) exposed to 50 mM of inhibitor plus 50 mM NaCl and with a 1 or 24 hour open circuit prior to an anodic polarization scan. a) A pretreatment in various concentrations of $Ce(C_2H_3O_3)$ followed by testing in various concentrations of $NaVO_3$ in the 50 mM NaCl solution lead to each surface having been exposed to a total of 50 mM of inhibitor between the two solutions. b) The test solution contained 50 mM of $NaVO_3$ and Na_2MoO_4 inhibitors in addition to 50 mM NaCl. The ratio of $NaVO_3$ and Na_2MoO_4 varied, but the total inhibitor concentration was kept constant at 50 mM. 219

Figure 213. Plots of E_{pit} and E_{corr} for AA2024-T3 exposed to 50 mM of inhibitor plus 50 mM NaCl and with a 1 or 24 hour open circuit prior to an anodic polarization scan. a) A pretreatment in various concentrations of $Ce(C_2H_3O_3)$ followed by testing in various concentrations of $NaVO_3$ in the 50 mM NaCl solution lead to each surface having been exposed to a total of 50 mM of inhibitor between the two solutions. b) The test solution contained 50 mM of $NaVO_3$ and Na_2MoO_4 inhibitors in addition to 50 mM NaCl. The ratio of $NaVO_3$ and Na_2MoO_4 varied, but the total inhibitor concentration was kept constant at 50 mM. 219

Figure 214. The competition of anions on a positively charged AA2024 surface. The cerium precipitate blocks anions from reaching the surface. 221

Figure 215. Coverage versus concentration of $NaVO_3$ at various cathodic potentials. Total inhibitor concentration of vanadate and molybdate equals 50 mM in 50 mM sodium chloride. a) AA2024-T4 and b) Cu. 222

Figure 216. Coverage versus Log C_{NaVO3} at various cathodic potentials. Metals exposed to 50 mM sodium chloride with increasing vanadate concentration: a) AA2024-T4; and c) Cu. Total inhibitor concentration of vanadate and molybdate equals 50 mM in 50 mM sodium chloride: b) AA2024-T4 and d) Cu. 223

Figure 217. (a) E-pH diagram for 0.1 M molybdate and 1 M chloride solution showing the stability of molybdenum oxide over a large region of potential and pH with high potential stability in the low pH region. (b) Speciation of molybdate-chloride system at previously stated concentrations at -0.8 V vs. SCE. 225

List of Acronyms

a – One Half of the Scratched Electrode Area's Width
b – One Half of the Scratched Electrode Area's Length
BSE – Back-scattered Electron Microscopy
C – Concentration
C_{bare} – Capacitance from Ruptured Surface
C_{ox} – Capacitance from Passive Surface
C_{total} – Total Capacitance
C_{SC} – Space Charge Region Capacitance
CCC – Chromate Conversion Coating
CS – Carbon Steel
CV – Cyclic Voltammetry
d_{ox}– Oxide Thickness
D – Diffusion Rate
DI – Deionized Water
DoD – Department of Defense
E_{app} – Applied Potential
E_{bare} – Ruptured Electrode Potential
E_{corr} – Corrosion Potential
E_{repass} – Repassivation Potential
e – Dielectric Constant of the Passive Film
e_0 – Free Space Permittivity
EDS – Energy Dispersive X-ray Spectroscopy
E_{FB} – Flatband Potential
EIS – Electrochemical Impedance Spectroscopy
E_{pit} – Pitting Potential
f – Applied AC Frequency
F – Faraday Constant
HER – Hydrogen Evolution Reaction
$i_{crack\ tip}^{anodic}$ – Anodic current density from rupture surface
$i_{passive\ surface}^{cathodic}$ – Cathodic current density from surrounding passive surface
$i_{crack\ tip}^{cathodic}$ – Cathodic current density from ruptured surface
i_{corr} – Corrosion Current
i_{ct} - Charge Transfer Limited Cathodic Current Density
i_{net} – Net Current Density
i_o– Peak Bare Surface Current Density
i_{ohmic} – Ohmic Limited Current Density
i_D - Diffusion Limited Cathodic Current Density
i_{HER} – Hydrogen Evolution Reaction Current
i_{ORR} – Oxygen Reduction Reaction Current
i_T – Total Cathodic Current Density
IMC – Intermetallic Compound
l – Geometric term describing the active-inactive array

L – Distance between wires of rotating disk array
m – Repassivation time constant
M – Molar
M-S – Mott-Schottky
MEA – Multi-electrode array
MSE – Mercury Sulfate Electrode
n – Number of Electrons Transferred
N – donor density (in the case of M-S)
NMR – Nuclear Magnetic Resonance
OCP – Open Circuit Potential
ORR – Oxygen Reduction Reaction
OSHA – Occupational Safety and Health Administration
PEL – Permissible Exposure Limit
RDE – Rotating Disk Electrode
RPM – Revolutions per Minute
SCE – Saturated Calomel Electrode
SEM – Scanning Electron Microscope
SERS – Surface Enhanced Raman Spectroscopy
SKP – Scanning Kelvin Probe
t – Time
t_o – Time at Peak Current Density
UVA – University of Virginia
V – Volts
VCI- Volatile Corrosion Inhibitor
^{51}VNMR – Nuclear Magnetic Resonance of Vanadium
V_{SCE} – Volts vs. Saturated Calomel Reference Electrode
ν – Kinematic Viscosity
Z number – Atomic Number
ZRA – Zero Resistance Ammeter
ΔE_{pass} – Pitting Potential minus Open Circuit Potential
δ – Diffusion Affected Zone
κ – Solution Conductivity
σ – Term that relates to the coverage of aluminum matrix
Θ – Surface Coverage
χ_{ox} – Oxide thickness
Ω – Ohm
ω – Angular Velocity

Keywords

Corrosion, Corrosion Inhibitor, Environmentally Friendly Inhibitor, Green Inhibitor, Permanganate, Cerium, Vanadate, Molybdate, Aluminum Alloy 2024, Aluminum Alloy 7075, Carbon Steel 1018, In-situ Raman, Chromate Replacement, Pitting Corrosion, Mass Transport Control Current, Multi Electrode Array, Electrochemistry.

Acknowledgements

This project was a collaborative effort between Southwest Research Institute and the University of Virginia (UVA). Dr. Marta Jakab spearheaded the project at SwRI alongside Prof. John R. Scully at UVA. Dr. Jakab left SwRI in 2010 and Dr. Florent Bocher has taken the lead at in her place with the help and guidance of James Dante.

Two graduate students, Arwen Wilson and Sam Madden, performed the research at UVA under the guidance of Prof. Scully. They performed the research relating to the effect of vanadate and permanganate on corrosion of AA2024. The team at SwRI was composed of multiple technicians and senior technicians, with a special mention to Brian Derby who has been working on this project throughout its duration.

The contributions of the support staff at SwRI and UVA are greatefully acknowledged.

D.J. Moosbauer, instrumentation chemist at Gamry Instruments, is thanked for his contributions to the repassivation studies.

The project team would also like to acknowledge and thank Bruce Sartwell, as well as Jeff Houff and Cailtin Rohan, at SERDP/ESTCP for their support during this project.

Abstract

Objectives: Hexavalent chromium [Cr(VI)] has been extensively used in conversion coatings and paints to protect against corrosion of aluminum and iron-based alloys in Department of Defense (DoD) systems. However, chromate-based inhibitor systems are being eliminated as Cr(VI) is toxic and carcinogenic leading to the development of non-chromate alternatives. Most of those are individually not as effective as chromate, however, a combination of them may be found to be a suitable replacement. The objective of this program was to gain understanding of the mechanism of selected alternative inhibitors under realistic metallurgical and environmental conditions in order to facilitate the development of non-chromate inhibitor systems that possess effectiveness comparable to that of chromates. With the fundamental understanding of individual compounds, inhibitor systems with combinations of inhibitors whose individual properties are synergistically enhanced were studied.

Technical Approach: The program addressed this objective by (1) assessing the anodic and cathodic inhibition functions of non-chromate inhibitors (using standard and multielectrode electrochemical techniques and scratching electrode techniques), (2) determining the adsorption characteristics and concentration of adsorbed species on the alloy surfaces, (3) investigating the interactions between the inhibitors and heterogeneities in the microstrucures (using multielectrode and microelectrochemical techniques), and (4) analyzing the effect of alternating wet and dry conditions and the drying process on inhibition mechanisms.

Results: The inhibition of corrosion on AA2024-T351 in NaCl solutions, mitigated by either in-situ permanganate ions (MnO_4^-) or MnO_4^- pretreatment, was examined. The anodic and cathodic inhibition effects were studied as a function of inhibitor concentration. Inhibition of open circuit corrosion under conditions where anodic and cathodic reactions are coupled was also examined. The oxygen reduction reaction (ORR) was modeled using the Gueshi and Membrane models after the Koutecky-Levich correction was applied to experimental cathodic data. The oxidation states of the inhibiting manganese oxides were determined using potentiometric electrochemical reduction and in-situ Raman Spectroscopy. The thermodynamics of the Mn-water system was also considered over a range of concentrations. Permanganate was shown to be both an anodic and cathodic inhibitor, and an inhibitor of copper replating at open circuit potential (OCP).

Vanadate was investigated as a corrosion inhibitor for AA2024 fully immersed in NaCl solutions. Nuclear Magnetic Resonance (NMR) was used to determine the vanadate species in solutions. The dominant species was $V_4O_{12}^{4-}$ in 50 mM NaCl + 5 to 150 mM $NaVO_3$. Vanadate was found to inhibit the ORR for both AA2024-T4 and high-purity copper. Vanadate anions in solution reduced both charge transfer and mass transport current densities. Less than 1 mM $NaVO_3$ was needed for cathodic inhibition on AA2024-T4. Higher concentrations of $NaVO_3$ were required to raise the average pitting potential. Modeling of the cathodic inhibition mechanisms was pursued using the Gueshi analysis representing an array of active cathodic sites, as well as Langmuir and Temkin adsorption isotherms. The vanadate coverage on copper containing intermetallic particles was found to be dependent on the over-potential. After 24 hour exposures at open circuit potential, anodic inhibition of pitting increased with increasing vanadate concentration in solution for both AA2024-T3 and high-purity aluminum suggesting that tetrahedrally coordinated vanadate species affect pure aluminum as well as intermetallics in AA2024-T3.

Corrosion inhibitor combinations were studied on AA2024. Vanadate-molybdate combinations acted as cathodic inhibitor, unlike cerium-vanadate. Ce precipitates blocked cathodic sites from vanadate adsorption. This is consistent with modeling of competitive adsorption of anions on copper intermetallic particles. Vanadate-molybdate was as effective as vanadate as anodic inhibitor, and cerium addition to vanadate provided no benefit. Cathodic inhibition of a cerium-permanganate combination was equivalent to that of permanganate and superior to cerium. Cerium-permanganate also increased OCP corrosion inhibition at a level comparable to that of the single inhibitors. No anodic inhibition was found.

Scratch repassivation of AA2024-T351, AA7075-T6, and 99.999% aluminum in molybdate and chromate containing NaCl solutions was performed. Chromate suppressed scratched electrode current transients at high potentials. Furthermore the rapid growth of a thick, protective oxide was measured. Molybdate did not suppress transient current but did promote the rapid growth of a passive film.

Cerium, vanadate and molybdate acted as anodic inhibitor with AA7075, while only cerium and vanadate behaved as cathodic inhibitors. Molybdate was found to behave as an anodic and a cathodic inhibitor for carbon steel 1018. Synergistic behaviors were proven to be occurring partially for Ce/Mo and Ce/V and were especially successful for carbon steel 1018. However, they were not accurately predicted during this project.

Rotating disc arrays were used to study the impact of the density and size of copper intermetallic particles on the cathodic effectiveness of the inhibitor. This was consistent with the comparison between AA2024 and AA7075, based upon the potentiodynamic analysis and scanning electron microscope (SEM) studies. Aluminum/copper multi-electrode array (MEA) was used to simulate copper-rich intermetallic particles in an aluminum-rich matrix. Composition, concentration and pretreatment were found to have an impact on the effectiveness of the inhibitor. Vanadate was the sole successful inhibitor when testing in NaCl solutions. All inhibitors were successful when pretreated, but better results were obtained at lower concentration, consistent with the Levich analysis performed on AA2024, which concluded that the critical inhibitor concentration needed to suppress ORR is below 0.005 mol/L sodium vanadate. Energy dispersive X-ray spectroscopy (EDS) and Auger electron spectrometry showed that cerium, molybdate and vanadate are all present on the surface of AA7075. However, only cerium was found to be dependent on the quantity of the inhibitor. Based upon the surface EDS, it appears that the role of concentration observed for the Al/Cu MEA is not due to the amount of inhibitor on the surface but may be due to the species of inhibitors. This would be due to the fact that the pH of the solution is dependent on the concentration of the inhibitor and the inhibitor speciation is directly related to the pH.

Atmospheric tests using the Al/Cu MEA were performed to assess the performance of various inhibitors at various relative humidity. Vanadate and cerium performed successfully only at lower relative humidity (60 and 70%). At higher relative humidity, vanadate and cerium concentration may be too low to perform as cathodic inhibitors.

Benefits: The results of this program can be applicable to a variety of weapons systems and ground support equipment. Cerium, vanadate and molybdate, which had been successfully applied to AA2024, were shown to be partially transferable to AA7075 and carbon steel 1018. Inhibitor behavior was also found to depend on the type of treatment, e.g. in solution vs. pretreatment. Furthermore, inhibitor combinations have been shown to be beneficial under certain circumstances (e.g. cerium and vanadate efficiently inhibit corrosion under atmospheric corrosion at lower relative humidity).

Objective

Hexavalent chromium has been a widely used corrosion inhibitor for both ferrous (e.g., mild steel, stainless steel) and nonferrous (e.g., aluminum, zinc, cadmium) alloys for over 50 years.[1] It is commonly used in chromate conversion coatings (CCCs) in, for example, the aerospace and automobile industries. Hexavalent chrome and CCCs have been found to be excellent corrosion inhibitors of both the anodic and cathodic corrosion processes.[2,3] In addition, CCCs provide active corrosion inhibition via the release of hexavalent chromium ions upon the increase of pH of the environment.[4] However, hexavalent chromium is a known human carcinogen that is associated with lung cancer.[5] Due to its carcinogenicity, Occupational Safety and Health Administration (OSHA) recently lowered the permissible exposure limit (PEL) by a factor of twenty.[6] This new regulation affects all hexavalent chromium applications, especially the aging aircraft program. The long-term goal of OSHA is the elimination of hexavalent chromium and replacing it with new, environmentally-friendly, non-toxic coatings.

To date, none of the environmentally-friendly chrome replacement inhibitors proposed has been found to be as effective as hexavalent chrome treatments. It is believed that a combination of non-chromate inhibitors may be functionally equivalent to hexavalent chrome treatments. Several combinatorial and other empirical methods have been used in the literature to identify non-chromate inhibitors that are effective under realistic operating conditions. This research focuses on mechanistic studies of selected non-chromate inhibitors on aluminum alloys and steel to develop a model that will enable a more effective selection of non-chromate inhibitors for real-world applications.

The objective of the program was to gain an understanding of the mechanisms of selected alternative inhibitors under realistic metallurgical and environmental conditions in order to facilitate the development of non-chromate inhibitor systems that possess effectiveness comparable to that of hexavalent chrome.

The program was divided into five tasks:

1. Effect of individual inhibitors under controlled hydrodynamic conditions;
2. Effect of combinations of inhibitors;
3. Effect of microstructural heterogeneity on inhibitor action;
4. Effect of alternate wet and dry conditions; and
5. Modeling and verification using commercial alloys.

The effectiveness of any inhibitor system is a function of its inherent inhibitive efficiency under various environmental conditions and its ability to be packaged in an efficient delivery system (coating, conversion coat, etc.). While both are important to the success of a chromate replacement, we have chosen to focus primarily on inhibitor efficiency. This program, led by SwRI in partnership with the University of Virginia, addressed the gaps outlined above by investigating the following issues:

- <u>How do individual non-chromate inhibitors work</u>? Little is known about why these inhibitors are highly effective in preventing corrosion of certain alloys and not others and what the prevalent inhibiting mechanisms are. These issues will be addressed in Task 1.

- Can we intelligently design combinations of non-chromate inhibitors based on our knowledge gained in Task 1? Synergistic effects between the inhibitors have been reported in the literature, however, they were found by trial-and-error.[7,8] The design of the non-chromate inhibitor systems can be greatly improved by utilizing a mechanistic approach in combining the individual inhibitors. This approach was investigated in Task 2.
- How do inhibitors work on realistic alloys under realistic exposure conditions? The alloys that need to be protected are not homogeneous. They contain varying numbers and types of microstructural features and impurities that significantly affect their corrosion resistance, e.g., intermetallic particles in high-strength aluminum alloys and inclusions in steels. The interaction of the inhibitors with these heterogeneities needed to be investigated in order to be able to predict the performance of the inhibitors for potential applications. The exposure conditions also vary in many applications during service, often resulting in alternate wet and dry environments. Evaluating the potential inhibitors and their combinations provides a more accurate assessment of their performance in the field. Tasks 3 and 4 addressed these issues.

The overall approach is summarized in Figure 1.

The project focused on promising non-chromate inhibitors along with a limited study of chromate and uninhibited systems as a benchmark and control, respectively. The inhibitors included were Ce(III), MnO_4^-, MoO_4^{2-}, and VO_3^-. The substrate metals chosen for the mechanistic study included both model metals, commercially pure aluminum, pure copper, pure iron, synthesized intermetallic particles, commercially available heterogeneous alloys, AA2024-T3, and carbon steel. The heterogeneous alloys were mainly used to validate mechanistic information derived from model metals.

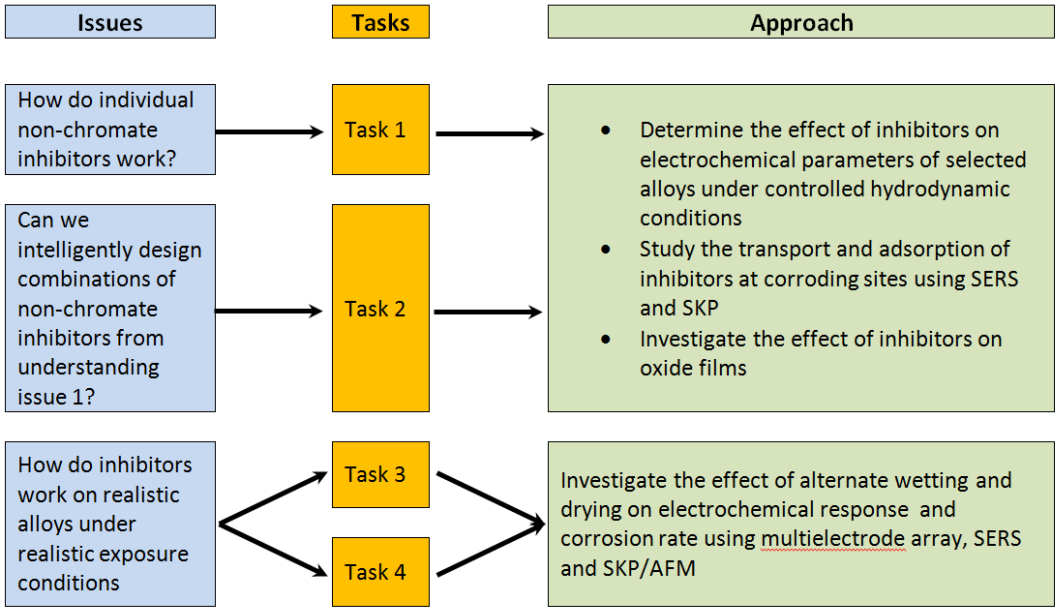

Figure 1. Summary of proposed tasks.

Background

Hexavalent chromium has been a widely used corrosion inhibitor for both ferrous (e.g., mild steel, stainless steel) and nonferrous alloys (e.g., aluminum, zinc, cadmium) for over 50 years.[1] It is commonly used in CCCs in, for example, the aerospace and automobile industries.

The corrosion inhibition mechanism of chromates has been studied intensively in the past 20 years. They have been found to be excellent inhibitors of the ORR in near-neutral and alkaline environments through the formation of an irreversibly adsorbed $Cr(OH)_3$ surface layer that acts as a bipolar barrier inhibiting the electron transfer.[2] In high-strength aluminum alloys, the ORR rate on the Cu-rich intermetallic particles is significantly reduced and the rotation rate dependence of the diffusion limited current density disappears in the presence of chromates.[3] It is believed that the chromate ions not only affect the ORR, but also interact with the intermetallic particles to passivate them.[9]

Chromates have also been found to inhibit the anodic corrosion processes.[3,10] The effectiveness of the anodic inhibition, however, is highly dependent upon environmental and metallurgical factors (e.g., chloride:chromate ratio, pH, degree of aeration, alloy chemistry and temper). Chromates were found not only to raise the pitting potential ($E_{pit)}$ of pure aluminum in chloride containing solutions,[11] but also to suppress metastable pitting.[12] Chromates also affect the repassivation process by accelerating the kinetics of repassivation, suppressing the reactivation and elevating the repassivation potential (E_{repass}).[13] The anodic inhibition is believed to be due to nonreductive adsorption of hexavalent chromate, which lowers the zeta potential of the oxide surface thereby hindering the chloride adsorption.[14,15]

Hexavalent chromium is also present in CCCs reversibly bound to a $Cr(OH)_3$ polymer backbone structure. Upon pH increase due to a corrosion process, the hexavalent chromium is released from the CCC as $HCrO_4^-$ and is transported to the locally corroding areas, where it is reduced and adsorbed on the defect surface as an insoluble Al(III)-Cr(III) precipitate or it is adsorbed as Cr(VI) onto the hydrous alumina gel corrosion product.[4,16] The hypothesized inhibition mechanisms of hexavalent chromium oxoanions and CCC are summarized in Table 1.

Hexavalent chromium is a known human carcinogen that is associated with lung cancer.[5] It enters the cells through the phosphate-sulfate transport channels, where it is reduced to Cr(III) generating molecular debris.[17] This molecular debris causes DNA damage through OH* radical[17] or Cr(V)/Cr(IV) peroxo complex[18] formation. Due to the carcinogenicity of the hexavalent chromium species, OSHA recently lowered the PEL by a factor of twenty.[6] This new regulation affects all hexavalent chromium applications, especially the aging aircraft program. The long-term goal of OSHA is the elimination of hexavalent chromium and its replacement with new, environmentally friendly, non-toxic coatings.

Table 1. Hypothesized inhibition mechanisms of Cr(VI) ions and CCCs.

Hexavalent Chromium Oxoanions	CCC
inhibition of ORR after reduction to Cr(III) and by irreversible adsorption	acting as hydrophobic barrier, as $Cr(OH)_3$
inhibition of pit initiation and dissolution of active IMCs in Al alloys	storage of releasable Cr(VI) ions, which migrate to and interact at anodic defects to interfere with stabilization of corrosion
modification of the composition of passive oxides via adsorption and buffering	inhibition of anodic and cathodic corrosion reactions
lowering the zeta potential via adsorption, which discourages Cl^- adsorption	

The need to eliminate Cr(VI) containing materials from the metal finishing operations has led to worldwide research with the aim of finding alternative, non-toxic corrosion inhibitors. Several potential alternatives have been identified.

The MeO_4^{n-} anions, where "Me" stands for metallic elements, (e.g., molybdates, vanadates, tungstates, and permanganates) are attractive, because they are structural analogs of chromates.

The molybdate ion (MoO_4^{2-}) acts as an anodic inhibitor for aluminum, aluminum alloys and steel. In aerated solutions, it has been found to be an effective anodic inhibitor of steel by promoting the passivation of the actively corroding steel, reducing the passive current density, extending the anodic passive range and promoting the repassivation of pits.[19] On aluminum alloys, it has been found to be a moderately effective anodic and very effective cathodic inhibitor.[20] When introduced into the solution as an oxoanion, it is believed to adsorb on the aluminum oxide surface via a competitive adsorption mechanism, thereby inhibiting the adsorption of oxygen and/or chloride ions on the surface.

Implantation of molybdenum ions into the upper 13 nm of the surface of both pure aluminum (99.99%) and AA7075-T6 led to an increase in OCP and the breakdown potential for both materials in the presence of chloride with the alloy demonstrating the largest potential change.[21] Mass loss studies over an eight-month time period have not found molybdate to be aa effective a corrosion inhibitor as chromate.[22] The mass loss of AA2024-T351 and AA7075-T7451 coupons were compared after 8 months in aerated pH 8.2 3.5% NaCl solutions with and without inhibitor additions of 50 mM Na_2CrO_4 or 50 mM Na_2MoO_4. For AA7075-T7451, solutions containing chromate and molybdate reduced mass loss with chromate containing solution giving superior results compared to molybdate containing solutions.[22] However, AA2024-T351 only had reduced mass loss from the chromate inhibitor.[22] The mechanism of molybdate passivation was unknown, but the addition of molybdate into the passive film, chemically as an absorbed ionic species, or physical as a precipitate was suggested as possible factors influencing inhibition.[21] The break down potential can be increased so that OCP is more negative, if an adequate molybdate concentration is maintained in solution.[23] Other authors have found that molybdenum must be

incorporated into the passive film to increase E_{pit} of aluminum rather than just being in solution.[24] In solutions with pH less than 4.5, a polymeric molybdate species dominates and it does not inhibit corrosion.[24] The molybdate species, MoO_4^{2-} in solutions at pH 6 or higher was found to inhibit aluminum corrosion. As the pH of the solution decreases, the dominant Mo species changes from MoO_4^{2-} to $H_XMo_7O_{24}^{X-6}$ ($x \sim 0$ - 2) to β-$[Mo_8O_{26}]^{4-}$ to $Mo_{36}O_{112}^{8-}$ to MoO_2^{2+} at near zero pH.[25] The presence of 0.1 M Na_2MoO_4 was not as effective as 0.1 M Na_2CrO_4 in 0.5 M NaCl in impeding the corrosion of aluminum once pitting had started, however it was more effective at increasing E_{pit}.[26] The main species that mediate inhibition was determined by X-ray Photoelectron Spectroscopy (XPS) to be MoO_4^{2-}.

This species, MoO_4^{2-}, inhibits by adsorbing onto the surface of aluminum and creating a film that is an electrostatic barrier for Cl^- absorption.[26] When chloride is already present at the surface, the addition of MoO_4^{2-} leads to a competition between Cl^- and MoO_4^{2-} for surface sites and thus reduced inhibition of pitting.[26] The oxide covering the surface is bilayered with an inner aluminum oxide layer and an outer molybdate oxide layer.[27] The molybdate inhibits by first reducing the concentration of Cl^- that reaches the surface, thereby reducing the likelihood that a critical concentration of chloride ions exists for pit initiation.[27] In addition, molybdate participates in a reaction in which exposed Al is oxidized to an aluminum hydroxide and molybdate is reduced to MoO_2 or MoO_3.[27]

The effect of molybdate at reducing the ORR reaction was also studied and found to be both pH and potential dependent. Reducing the potential leads to the reduction of MoO_4^{2-} into MoO_2.[28] This reaction is counter balanced by the oxidation of MoO_2 on the surface to MoO_4^{2-} at pH values above 9.[28] Molybdate was only an effective cathodic inhibitor in the pH range 8 to 9.[28] Molybdate was found to be an effective cathodic inhibitor for AA2024-T3, and Al-Cu-Mg and Al-Cu-Mn-Fe phases when it was in solution and the over potentials with respect to ORR were low.[29]

Vanadates were found to be good inhibitors of corrosion on AA2024-T3.[30] It was recently found that the solution pH plays a very important role in determining the inhibitor efficiency of vanadates. While under neutral and slightly alkaline conditions the metavanadates provide good corrosion inhibition of Al alloys, upon acidification, decavanates form, which show no inhibiting effect.[31] Iannuzzi and coworkers investigated the inhibition mechanisms of metavanadates and found that they act as cathodic inhibitors through the physisorption of metavanadate ions.[32] The effect of vanadates on the anodic behavior of Al alloys and their effect on the corrosion of steel have not been studied in detail. It must be noted that the toxicity of vanadium is an important issue that is yet to be resolved in the use of these inhibitors.

Very limited information can be found in the literature regarding the effectiveness and corrosion inhibiting mechanism of permanganate (MnO_4^-). One study suggests that the permanganate ions raise E_{pit} of AA2024-T3 in chloride containing solutions.[33]

Cerous (Ce(III)) salts are non-toxic and relatively cheap, which makes them an attractive alternative to chromates. They have been shown to inhibit corrosion on stainless steel,[34] mild steel,[35] galvanized steel,[36] zinc,[35,37] aluminum, and aluminum alloys.[38–41]

Cerium(III) ions were found to be only marginally effective or ineffective anodic inhibitors in the case of high Cu containing Al alloys, especially AA2024-T3.[20] They are, however, very

effective cathodic inhibitors.[29,40] It was found that the corrosion inhibition of Ce^{3+} ions is associated with the formation of a Ce-rich film over the copper-rich intermetallic particles.[40,42] Due to the presence of different oxidation states in cerium and their different solubilities, active corrosion inhibition triggered by pH changes caused by local corrosion processes has been demonstrated for this inhibitor by several authors.[43,44]

Cerium increases E_{pit} of aluminum and its alloys by changing the passive film due to the integration of cerium oxide and hydroxides into the film.[45] Inhibition is derived from the reduction in available cathodic sites, which decreases the cathodic current density and hence, from charge balance, reduces the anodic current density and the rate of anodic dissolution of aluminum.[20,29,40] Cerium conversion coatings have been shown to reduce copper replating for alloy exposures in sodium chloride.[20,29] Research suggested a possible preference for cerium deposition on certain intermetallics such that the S-phase (Cu-Mg-Al) showed higher coverage than $(Cu,Fe,Mn)Al_3$.[40,46] As the coverage of each type of intermetallic compound varied, it was hypothesized that cerium coverage varied due to differences in the local pH over the particular intermetallic compound. Since a basic local pH is needed for cerium to precipitate on the intermetallic sites, dealloying of the intermetallics is seen as an important step. This is because this anodic mechanism results in locally increased pH due to enhanced ORR at cathodic intermetallics sites on the dealloying particle. As the S-phase has a higher dealloying rate, it naturally has a higher cerium concentration on average than $(Cu,Fe,Mn)Al_3$.[46] Codeposition of chloride along with cerium was seen at the intermetallic sites.[46] While the Ce(IV) [i.e., $Ce(OH)_4$ and CeO_2] precipitate has been found to inhibit corrosion, the ability of Ce(IV) precipitate to protect is dependent on the precipitation conditions including pH, potential, oxidizing agent, and oxygen content, which control the "morphology, degree of agglomeration, and surface chemical activity".[47,48] The Ce(IV) precipitate is in equilibrium with Ce^{3+} in solution.[47,48] The addition of millimolar amounts of chloride during the dissolution process will increase the rate of precipitation by removing the oxide layer on the copper.[49] Recent studies of cerium conversion coatings that form when aluminum-copper alloys are either cathodically polarized in cerium solutions or left at open circuit and allowed to have local pH increases at the cathodic sites proved that older Pourbaix diagrams of the cerium in water were incorrect and provided modifications.[47,48] When the precipitation of aluminum hydroxides along with cerium compounds was evaluated, the aluminum hydroxides were shown to have little to no effect on the cerium precipitation as the aluminum hydroxides precipitated at a lower pH and the precipitate was no longer the majority precipitate once the pH rose to a favorable value for cerium precipitation.[50] Also as noted by Hughes, the removal of chloride ion from the cerium conversion coating led to precipitation of cerium only on intermetallic particles and not on the aluminum matrix.[50] Overall, the anodic and cathodic sites found on AA 2024-T3 will have different hydroxide coverage. The S–phase is expected to be covered with a mixed aluminum hydroxide/oxide with copper and cerium oxide, the $(Fe, Cu, Mn)Al_3$ compounds covered with cerium oxide, and the anodic sites covered with aluminum oxide under a cerium hydroxide.[51]

Other rare-earth salts (e.g., lanthanum, praseodymium compounds) have also been investigated and found to possess similar inhibiting qualities to that of Ce(III).[38,39]

Trivalent chromium (Cr(III)) has been investigated as an alternative coating pretreatment method mainly on zinc substrates.[52,53] The preliminary results were promising, indicating good corrosion inhibition properties, however, the effectiveness of Cr(III)-inhibitor as a long-term protective

agent under realistic metallurgical and environmental conditions is yet to be demonstrated. Although, it may act as an effective inhibitor of the ORR as much as a part of the Cr(VI) chain does, the ability to maintain releasable concentration of Cr(III) species needs further evaluation.

Precipitation-hardened aluminum alloys containing copper and iron are highly susceptible to corrosion due to local galvanic coupling between intermetallic phases and the surrounding aluminum matrix.[54–60] Localized corrosion of alloys such as AA2024-T351 results from the presence of intermetallic compounds in a solute lean α-Al matrix that are either noble with respect to their surrounding matrix or particles that tend to be initiation sites for pitting.[54,57] Particles such as Al_2CuMg and Cu_2Al can also be detrimental to the corrosion resistance of the alloy because of their tendency to dealloy at the open circuit potential.[60] This process has many damaging consequences including the creation of catalytic high surface area copper enriched intermetallic remnants and the associated deposition of copper on the alloy surface,[61] both of which result in increased ORR rates. This increase in ORR supports increased aluminum matrix dissolution in the form of localized trenching around the intermetallic phases and subsequently leading to pit initiation and growth that can produce nucleation sites for subsequent crack growth.[62–64] Effective inhibition of these constituent-particle-related damage modes in this class of alloys is of strong interest.

One aspect of current research in the field of corrosion inhibition has focused on oxoanions of the form $MeO_4^{(n-8)}$ (such as molybdates, tungstates, and vanadates),[21,31,32,65–72] structural analogues of hexavalent chromium. In this study permanganate (MnO_4^-) has been evaluated as a potential replacement for CrO_4^-.

Permanagate (Mn^{+7}) is a very strong oxidizer due to its high potential as seen in Figure 2(a). When permanganate is added to solution in contact with AA2024-T351 at a lower potential, it will be reduced and undergo serveral possible electrochemical reactions. Over all ranges of pH, MnO_4^- in the +7 valence state will likely first be reduced to manganese (IV) dioxide by the electrochemical ½ cell reaction shown in Equation 1.[73]

$$nO_4^- MnO_4^- + 4\,H^+ + 3e^- \leftrightarrow MnO_2 + 2H_2O \qquad \textbf{Equation 1}$$

Several additional electrochemical reactions can further reduce the oxide to Mn(*III*), a mixed valence oxide, and finally the Mn(*II*) state; see Equation 2 and Equation 3.[73]

$$2MnO_2 + 4\,H^+ + 2e^- \leftrightarrow Mn_2O_3 + 2H_2O \qquad \textbf{Equation 2}$$

$$3Mn_2O_3 + 4H^+ + 2e^- \leftrightarrow 2\,Mn_3O_4 + 2H_2O \qquad \textbf{Equation 3}$$

$$Mn_3O_4 + 2H^+ + 2e^- \leftrightarrow 3MnO + H_2O \qquad \textbf{Equation 4}$$

At low pH and low potential the oxides will disolve as Mn^{2+}. However, at higher pH above 8 a stable hydroxyde exists in an insoluble form.[73]

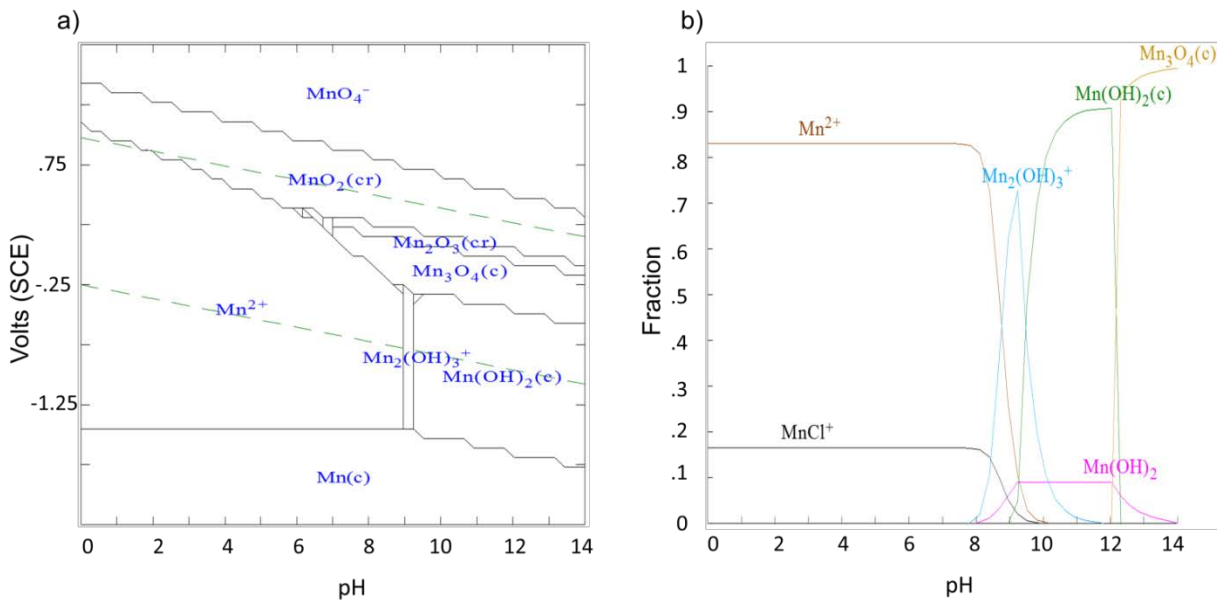

Figure 2. (a) The E-pH diagrams for 0.005 M permanganate with addition of 0.05 M chloride. (b) The speciation diagrams for 0.005 M permanganate + 0.05 M Cl^- at -0.5 V_{SCE}, the open circuit of AA-2024 in the presence of permanganate.

The equilibrium speciation predictions can be seen in Figure 2(b). These speciation diagrams indicate predominant species ratios at -0.5 V_{SCE}. This potential is approximately the value of the observed OCP for AA2024-T351 in 0.05 M sodium chloride solution with the permanganate ion in solution. The stable Mn(II) species is $Mn(OH)_2$ above a pH of 8.5. Half-cell reactions (Equation 1 through Equation 4) substantiate that Mn(II) could deposit electrochemically and remain stable at high pH cathodic sites such as present over copper-rich constituent particles.[9,74]

Permanganate-based coating products have been in commercial production for many years and several patents exist.[75,76] Previous scientific studies of MnO_4^- on AA2024 have focused on open circuit electrochemical properties, barrier layer properties, exposure tests such as ASTM B-117[77] neutral salt spray testing, as well as on the oxidation states of protective manganese oxides.[78–80] The mechanism by which MnO_4^- inhibits corrosion on AA2024 has been shown to be the growth of manganese oxides over copper-rich intermetallic particles.[80] The oxidation state of the manganese deposits is difficult to determine with no definitive proof of the valence state in the literature,[80,81] and little electrochemical information has been provided with regards to the effect of the manganese deposits on the ORR on AA2024-T351. It is useful to review the electrochemical and chemical dynamics of the aqueous-manganese system that apply to MnO_4^- in treatments on AA2024-T351.

The inhibition of localized corrosion (pitting) on AA2024 by permanganate has been studied by Danilidis.[82] The effect of manganese oxides on the ORR has not been reported in the literature. Moreover, a fundamental understanding of the mechanism that leads to anodic inhibition is lacking. Release and transport of manganese species for active inhibition has not been studied. The manganese system has multiple valence states between +7 and +2 which, in a similar way to the chromate system, may provide mechanisms for storage release and transport of the soluble oxidizing inhibiting species to sites for additional reduction leading to self-healing capabilities.

Initially, soluble permanganate, manganese in the +7 valence state, can be electrochemically deposited on Cu-rich intermetallic sites. MnO_2 and ($MnOH_2$) are relatively insoluble.[83] Moreover, incomplete MnO_4^- reduction could lead to a reservoir of the Mn(VII) species trapped in a lower valence state oxide. Release of the Mn^{2+} species is also possible from the oxide caps if a solution is present at a pH lower than approximately 8. The pH will rise when a cathodic reaction occurs above a finite rate over a Cu-rich site. The Mn^{2+} could again be chemically deposited by a homogeneous chemical reaction over the active cathodic site. In this manner the manganese species can protect actively corroding areas on AA2024-T351. However, prevailing oxide states after MnO_4^- treatments are unclear. X-Ray Photoelectron Spectroscopy, Raman, and X-ray Absorption Near Edge Structure studies on platinum, gold, and additional aluminum alloy substrates have also been conducted, mainly to elucidate oxide stoichiometry.[81,82,84–89]

These papers illustrate the difficulty in reporting definitive results determining oxide valence states in manganese oxides. No reliable *in situ* surface analytical probe has determined the oxidation state of electrodeposited manganese oxides.[90]

In aqueous solutions, vanadate (vanadium in a +5 chemical valence state) speciation is strongly dependant on solution pH.[91] The general groups of vanadate species, in increasing pH order, are decavanadate, metavanadate, pyrovanadate, and vanadate.[91] All of these species are in the +5 valence state except decavanadate, which are present in the +5 and +6 valence states. These vanadate groups and associated species are presented in Table 2. As the pH of the solution increases, the number of vanadate atoms in each molecule decreases from 10 in highly acidic solutions to 1 in highly alkaline solutions. Prefixes of mono-, di-, tri-, tetra-, penta-, and deca- are used to describe the number of vanadium atoms per molecule. Between pH 6 to 9, metavanadate species are dominant.[91] Upon acidification to a pH below 6, the metavanadate species quickly convert into decavanadate species with a change from tetrahedral coordination to octahedral coordination.[92] However, it has been shown that reversing the pH back into the metavanadate range by adding NaOH, did not convert all of the decavanadate back into metavanadate. A substantial amount of the decavanadate species remained in solution at the new higher pH range.[31] Quite often, a colorless solution changes to yellow with the formation of decavanadate species. However, decavanadate species can be present in colorless solution.

Table 2. The chemical formulas associated with aqueous vanadate subtypes.

Vanadate Subtype	Chemical Formula	Vanadate Coordination
Decavanadate	$V_{10}O_{26}(OH)_2^{4-}$, $V_{10}O_{27}(OH)^{5-}$, $V_{10}O_{28}^{6-}$	Octahedral
Metavanadate	$VO(OH)_3$, $VO_2(OH)_2^-$, $V_3O_9^{3-}$, $V_4O_{12}^{4-}$	Tetrahedral
Pyrovanadate	$VO_3(OH)^{2-}$, $HV_2O_7^{3-}$, $V_2O_7^{4-}$	Tetrahedral
Vanadate	VO_2^+, $VO(OH)_3$, $VO_2(OH)_2^-$, $VO_3(OH)^{2-}$, VO_4^{3-}	Tetrahedral

Source: Baes[91]

Few studies exist on the effectiveness of vanadate for reducing corrosion of AA2024. Ralston et al.,[67] evaluated anodic inhibition of AA2024-T3 in aerated and deaerated solutions containing 50 mM NaCl plus 0, 3.2, or 320 mM $NaVO_3$ (the latter was not used at pH 3) at pH 3,

5, 8, and 10. Anodic inhibition was independent of aeration of the solution.[67] The corrosion potential (E_{corr}) increased, the corrosion current (i_{corr}) decreased, and E_{pit} increased as compared to those for 50 mM NaCl solutions, for basic pH (8 and 10) 50 mM NaCl solutions in the presence of various vanadate concentrations.[67] At acidic pH (3 and 5), there was minimal to no change in E_{pit}. In deaerated solutions, the addition of vanadate increased E_{pit}, with a greater increase for the 320 mM $NaVO_3$ plus 50 mM NaCl than the 3.2 mM $NaVO_3$ plus 50 mM NaCl solution.[67] Ralston et al.,[71] performed a second set of anodic experiments on elemental, and phase components of AA2024-T3 including 99.999% Al, 99.9% Cu, Al_7Cu_2Fe, $Al_{20}Cu_2Mn$, Al4%Cu, Al_2CuMg, and Al_2Cu. Tests were performed in 10 mM $NaVO_3$ plus 500 mM NaCl or in 500 mM NaCl raised to pH 9.2. Vanadate did not reduce E_{corr} for Cu but did reduce, to some extent, E_{corr} for all other tested materials (AA2024-T3, 99.999% Al, Al_7Cu_2Fe, $Al_{20}Cu_2Mn$, Al4%Cu, Al_2CuMg, and Al_2Cu). Except for Al_2CuMg and Cu, all materials showed an increase in E_{pit}.[71]

Ralston et al.,[67] also evaluated cathodic inhibition of AA2024-T3 in aerated and deaerated solutions of 50 mM NaCl plus 0, 3.2 mM, and 320 mM $NaVO_3$ (the latter was not used at pH 3) at pH 3, 5, 8, and 10. There was a negligible inhibition effect at pH 3 and 5 in aerated solutions, but a factor of ten decrease in cathodic current density at alkaline pH of 8 and 10. The lower concentration of vanadate, 3.2 mM, was more effective at lowering the cathodic current compared to the higher concentration, 320 mM at all pH values except at pH 10. In the deaerated experiments, vanadates did not decrease the cathodic current of deaerated solutions below that of 50 mM NaCl except at pH 10, and at that pH the cathodic current values for solutions with and without vanadate overlapped. The deaerated solution experiments showed that the ORR was suppressed, but not the hydrogen evolution reaction (HER). Inhibition of the ORR explains the decrease in E_{corr} in the aerated solution tests.[67] While cathodic inhibition of more than 80% was observed in aerated 500 mM NaCl solutions with 0.007 mM monovanadate or more in solution, some inhibition was observed with an inhibitor concentration of 0.005 mM monovanadate. Monovanadate, a subgroup of the vanadate species, was identified by NMR.[93] Iannuzzi and Frankel[32] also performed cathodic polarization tests to determine the effect of tetrahedrally coordinated vanadate and octahedrally coordinated decavanadate. The solution without octahedrally coordinated decavanadates showed better inhibition. The current density in the presence of 10 mM $NaVO_3$ decreased by two orders of magnitude with the tetrahedrally coordinated vanadate solutions producing the lower current density and the mixed solution having a higher current density.[32] The cathodic current density increased in solutions of the mixed coordinated species with solution aging time, but did not in the tetrahedral species only solutions. Thus, it was proposed that tetravanadates, the aging product of decavanadates, did not inhibit ORR.[32] Ralston et al.,[71] performed a set of cathodic experiments on elements and phases of the AA2024-T3. Vanadate reduced the current density on all materials at high over potentials except for Al for which a higher current density was seen.[71] At -0.8 V_{SCE}, for AA2024-T3, an increase in the tetrahedrally coordinated vanadate species in solution decreased the cathodic current density in comparison to octahedrally coordinated decavanadate species.[71]

Iannuzzi et al.,[31] performed a split cell experiment to evaluate galvanic couples with separate anodes and cathodes. The resulting conditions lead to formation of a net cathode and net anode, but the AA2024-T3 specimens had both cathodic and anodic sites on the specimen; thus, the arrangement did not completely separate the reactions on AA2024-T3 specimens. Inhibitor was injected onto one side of Al/Cu, AA2024–T3/Cu or AA2024-T3/ AA2024-T3 couples to assess

its impact on the galvanic current density. A reduction in galvanic current density for the cathode was taken as evidence that the tetrahedrally coordinated vanadate solutions inhibited ORR by adsorption onto the surface instead of reduction of V^{+5} at the surface of AA2024-T3, as no current peak associated with vanadate oxidation state reduction was observed. The anodic cell side of AA2024-T3/ AA2024-T3 showed no inhibition with addition of either tetrahedrally coordinated vanadates or the octahedrally coordinated decavanadates with tetrahedrally coordinated vanadate species.

Nuclear Magnetic Resonance of vanadium (^{51}VNMR) has been the identification method of choice for vanadate speciation due to its ability to identify different molecules. Much of the past work on vanadate inhibitors looked at the inhibition of AA2024 in aqueous solutions containing vanadate species at pH above and below the 7-9 pH range used in the present work. As reported in those papers, evaluation of vanadate speciation by ^{51}VNMR was completed in NaCl free solutions. Ralston[67] and Iannuzzi[93] of Ohio State University (OSU) completed different types of speciation studies on sodium vanadate, but did not evaluate the effect of chloride or sodium ion concentration on the vanadate speciation. In all of those studies, except for the pigment studies, chloride ions were not in solution with vanadate ions. The effect of changing the pH of a 100 mM $NaVO_3$ solution from basic to acid and back to basic was evaluated. These tests showed that vanadate solutions quickly transformed from tetrahedrally coordinated vanadates to octahedrally coordinated decavanadate species with the addition of acid, but transformed very slowly (and there was incomplete conversion) from octahedrally coordinated decavanadate species back to tetrahedrally coordinated vanadates species with the addition of base.[67,93] For both low (1-5mM) and high concentration (upper limit was 150 mM) vanadate solutions, decavanadate was the dominant species after returning to a basic pH. The main metavanadate species changed from divanadate to tetravanadate as the concentration of sodium vanadate in solution was increased. The alkalinity addition tests, which evaluated speciation when a source of alkalinity was present, showed that the mixed octahedrally and tetrahedrally coordinated vanadate species in solution increased in the ratio of “simple tetrahedral” to octahedral structures, and an increase in larger molecular weight tetrahedrally coordinated vanadate species. However, at greater additions of base above pH 9, the tested solutions did not have decavanadate species. Results of these tests showed that as the pH was increased, the concentration of pentavanadate and tetravanadate species decreased and these species were no longer present in solution at a pH greater than 9, which is in agreement with the chemical literature.[91,94,95] At the same time, the concentration of monovanadate and divanadate species increased and monovanadate species became the dominant species. The effect of aluminum (99.999%) on vanadate speciation was evaluated. Solution exposed to aluminum had increased tetrahedral vanadates, which was inferred to be the result of decomposition of decavanadates by aluminum. Results of aging studies showed that the relative speciation of tetrahedrally and octahedrally coordinated species did not show changes with time.[67,71]

Several unresolved issues associated with vanadate inhibition of AA2024-T3 corrosion exist. The mechanisms governing the anodic inhibition processes have not been determined. Iannuzzi and Frankel[32] modeled the cathodic inhibition mechanism using the Langmuir Isotherm, but only compared data over a limited potential range.[32] Broad potential cathodic behavior has suggested potential dependent adsorption. The effect of pretreating the surface with vanadates prior to testing in inhibitor free solutions has not been evaluated. Further, testing with modified pH solutions resulted in test solutions that are not representative of equilibrium speciation

conditions because of the slow reaction rate for the conversion of species back to equilibrium. Vanadates in aqueous solutions may also function as buffers. Moreover, the concentration of sodium chloride in solution impacts vanadate speciation and yet only two concentrations of sodium chloride, 50 or 500 mM, have been evaluated. Past measured cathodic currents on AA2024-T3 in sodium chloride solutions combine effects of corrosion, vanadate reduction, mass and charge transfer controlled ORR and HER. Therefore, while separation of the ORR and HER reactions for cathodic polarization has been completed, no test examined the effects of vanadate on the rate limiting step for ORR.

When evaluating the effectiveness of the chromate alternative corrosion inhibitors, it was often found that the chromate is superior to these individual alternatives. Upon the investigation of combinations of the potential replacements, however, several authors reported synergistic effects between certain combinations. Mansfeld and coworkers found that a combination of cerium and molybdate treatments provide exceptional corrosion resistance to aluminum and aluminum alloys.[7] Chambers and coworkers found that the combination of cerium and molybdate, cerium and lanthanum as well as that of metavanadate and phosphate was superior to the equivalent concentration of chromate.[8] However, such investigations are purely empirical and do not provide a systematic and fundamentally grounded method to identify new, more effective combinations.

In order to develop new inhibitors and/or find a combination of existing non-chromate inhibitors that show performance equivalent or superior to that of chromates, the mechanisms of the corrosion inhibition on different materials needs to be elucidated. Synergistic effects, for example, have only been found using random, combinatorial techniques that are material extensive and time consuming.[8] Recently, several efforts were made to understand the inhibition mechanism of non-chromate alternatives.[1,29,68] Despite these efforts, significant gaps remain in the understanding of the mechanism of non-chromate corrosion inhibitors, including:

- Their effects on different regimes of anodic and cathodic kinetics of matrix alloy and intermetallic precipitates – a previous study by Jakab et al.[29] has shown that the mechanism of inhibition can vary from blocking cathodic sites on precipitates to cathodic sites on the matrix depending on whether the cathodic reaction is mass transport-controlled or activation controlled. Further understanding of these effects is necessary to tailor inhibitors to different alloy systems and environmental conditions.
- A considerable paucity of mechanistic data on steels, where the kinetics are significantly different from those on aluminum.
- The synergy or competition between different inhibitors when present together.
- The effect of mechanical damage and creation of un-filmed surface on inhibition kinetics – there is a great difference in the adsorption characteristics of inhibitors on freshly exposed surfaces. Kinetics of adsorption of inhibitors will be relatively fast compared to other transport steps. However, coverage as a function of bulk concentration of inhibitor in solution is very important.
- The speciation and electrochemical behavior of inhibitors under alternating wet and dry conditions – it is known that the hydration of some inhibitors change with drying, but the effect on electrochemical behavior has been poorly characterized. The concentration changes during drying may also influence speciation of inhibitors.

Materials and Methods

Description of Individual Tasks

Task 1 – Effect of Individual Inhibitors under Controlled Hydrodynamic Conditions

The purpose of this task was to determine the prevalent corrosion inhibition mechanism of the individual inhibitors in order to understand why they are effective in inhibiting corrosion of certain alloys. As described in detail below, we proposed to study first the effect of inhibitors on anodic and cathodic behavior. This understanding was supplemented by using Mott-Schottky analysis to determine the adsorption properties of chosen inhibitors onto oxide surface as a function of surface properties. The above techniques were used to generally define inhibitor efficiency. Important to film healing processes are the kinetics of inhibitor adsorption/incorporation and corrosion protection. In order to measure this kinetics, scratching electrode techniques combined with Surface Enhanced Raman Spectroscopy were used.

The effects of inhibitors on both the anodic and cathodic reactions were evaluated using traditional potentiodynamic polarization tests and chronoamperometry. The anodic potentiodynamic polarization tests provided insight into the effect of inhibitors on the barrier properties of the selected alloys, while the cathodic polarization curves were used to measure the changes in the kinetics of ORR and hydrogen evolution upon exposure to solutions containing inhibitors. The cathodic scans were carried out under controlled hydrodynamic conditions using rotating disk electrodes so that the effect of inhibitor under activation and mass-transport controlled conditions could be delineated.[29] Chronoamperometry was also used to investigate the cathodic kinetics, since the current measured as a function of time after a potential step can be used to measure the cathodic behavior at a wide range of boundary layer thicknesses. The effect of the inhibitors on the “ideal” mass transport limited, or Levich behavior was also evaluated, since it has been observed that the cathodic kinetics does not follow the Levich behavior in the presence of certain inhibitors.[28,29] Chronoamperometry upon the introduction of inhibitors into solution was also carried out to measure the time dependence of the inhibitor-surface interaction.[32]

Pure aluminum, copper and iron, as well as multi-electrode arrays were used as substrates in these tests. The multi-electrode arrays were used to mimic the heterogeneous structure of AA2024 alloy.

Corrosion measurements were carried out using 100-channel potentiostats. This enabled the measurement of individual E_{corr}, potentiodynamic polarization scans and chronoamperometric scans on up to 100 individual electrodes simultaneously. This high-throughput technique allowed us to investigate the effect of exposure time, inhibitor type and concentration on the inhibitor effectiveness in a wide time and concentration range.

In addition to the standard polarization and chronoamperometric techniques, we used an MEA probe to further elucidate the effect of various inhibitors on the relationship between anodic and cathodic sites. Unlike the 100-channel potentiostat, where each channel is isolated, the system at SwRI provides a common connection that each element contacts through a current measuring resistor. In this manner, electrons can flow from anodic sites to cathodic sites through the

common connection. The current flowing through each element can then be measured to determine whether the element is acting as a cathode or an anode under open circuit conditions. Thus, a direct measure of both the anodic and cathodic current at OCP is obtained (corrosion current density). Other than the ability to directly measure the corrosion current density under open circuit conditions, this technique has the advantage that the effect of environment, inhibitor, exposure time, etc. can be measured at each individual element and thus the relationship between individual elements can be directly assessed (relative size, spatial separation, number density, etc.).

The adsorption of inhibitor species on the surface and/or their incorporation into the oxide layer can alter the electrical properties of the surface oxide thereby changing the barrier properties thereof by making it less susceptible to chloride ion adsorption and penetration into the oxide.[99] These passive oxide films on metal alloys are known to exhibit semiconductor properties. For example, n-type oxides (Fe_2O_3, Al_2O_3, and TiO_2) can support cathodic current but under anodic polarization, they are highly polarizable. The opposite is true for p-type oxide (NiO, Cr_2O_3, CuO, Cu_2O) films. Throughout the last several decades, numerous studies have exploited the semiconductor nature of these metal oxides to explain their behavior as catalysts, their corrosion behavior, and basic physical properties of solid liquid interfaces.[100] At the interface between a semiconductor and an electrolyte, the need to establish equilibrium of the charge carriers between the solid and electrolyte phases results in electron or hole depletion (band bending) in the solid depending on whether the semiconductor is n-type (excess electrons in the conduction band) or p-type (excess holes in the valence band) and on the position of the band edges (the flat band potential). Much work has focused on the use of semiconductor physics to explore the relationship between oxide and corrosion properties of iron,[101] aluminum,[102] stainless steel,[103] titanium,[104] and nickel and its alloys.[104,105] The interface between a liquid and a semiconductor is analogous to a metal/semiconductor interface. An applied potential to the liquid metal interface results in a potential drop across a space charge region within the oxide in electrolytes with high conductivity. Thus by controlling the potential, one can control the degree of band bending within the space charge region. The degree of band bending and the energy of an oxide surface govern both thermodynamics and kinetics of charge transfer within the system. Mott-Schottky (M-S) measurements can be performed on oxide thin films on the surface of alloys in solution under passivating conditions. M-S data provides information regarding the charge carrier density and the flatband potential (E_{FB}) which is closely related to the surface energy of the solid. As an example, three M-S curves are shown in Figure 3a. The flat band potential is taken as the point where the extrapolated line crosses the x-axis. As the molybdate concentration increases from alloy I825 < I625 < C22, a marked shift in the flatband potential can be seen; -0.380 V, -0.461 V, and -0.485 V respectively. This shift in flatband potential is accompanied by an increase in the localized E_{corr}. In Figure 3b., it is shown that both an increase in chloride and molybdate concentration result in a shift in the flatband potential towards more negative values for I825. This shift is a result of surface adsorption of these species. In the case of the localized corrosion behavior of I825, a competitive adsorption process between chloride and molybdate ions occurs. The presence of adsorbed molybdate likely results in the electrostatic repulsion of chloride ions as described by Natishan and coworkers.[106]

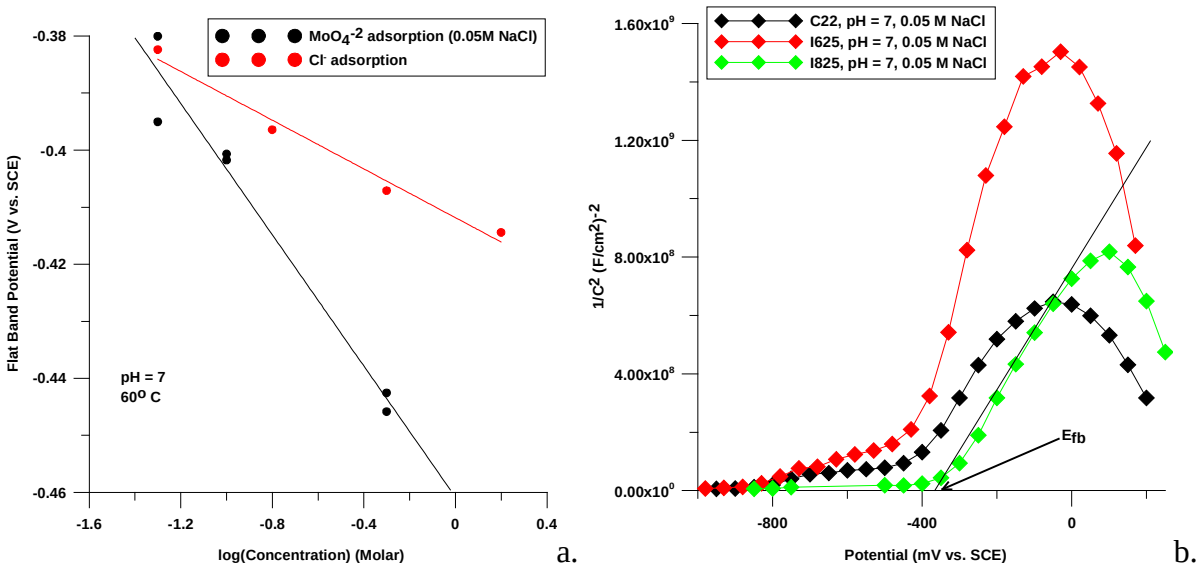

Figure 3. Example of M-S plots of I825, I625 and C22 alloys. (a) The x-intercept of the extrapolated line is the flatband potential. (b) Shift in flatband potential for I825 alloy as a function of molybdate and chloride concentration.

In this work, the shift in the flatband potential was measured as a function of the type of inhibitor and their concentrations in solution. M-S scans were performed on aluminum alloys.

The Mott-Schottky measurements were supplemented by energy dispersive spectroscopy and Auger electron spectroscopy measurements were used to investigate the effect of the inhibitors on the oxide layer. Some inhibitors have been shown to be incorporated in the oxide,[29] while others are adsorbed to form a surface layer.[32] Both scenarios can be evaluated using EDS and Auger electron spectroscopy. Auger electron spectroscopy was carried out to detect any incorporation of inhibitor and/or chloride ions into the surface oxide layer.

Although electrochemical measurements outlined above provided important information on the fundamental processes affected by non-chromate inhibitors, in-situ analyses are necessary to characterize the state of association of the inhibitor molecule with the surface and the kinetics of interactions. In-situ analysis of localized corrosion and inhibitors in conversion coatings has been successfully conducted using Raman spectroscopy.[107,108]

However, traditional Raman spectroscopy was not be sufficiently sensitive to identify adsorbed layers of inhibitors on electrodes. Surface Enhanced Raman Spectroscopy (SERS) is highly sensitive to even sub-monolayers of inhibitors adsorbed on surfaces.[109,110] However, SERS requires the deposition of nanoparticles of silver or gold on the surface, which may influence the electrochemical behavior of the surface of interest.

Scratch testing has been demonstrated in the literature to be useful in determining rates of metal dissolution, proton reduction, E_{pit}, and oxide growth on many substrates including aluminum and aluminum alloys,[111,112] titanium,[113] and steels.[114–116] However, there is a very limited body of research addressing the influence of corrosion inhibitors such as chromate and molybdate on the processes that lead to the repassivation of scratched electrodes.[112,117–119] One difficulty with analyzing scratched electrode experiments is the presence of sizable local cathodic reactions

which obscure the true anodic reaction rate when recording the net current density as seen in Equation 5. The addition of inhibitors to the repassivation process creates additional difficulty in analyzing current transients because of additional cathodic current resulting from possible inhibitor reduction. Therefore the addition of oxidizing inhibitors can add greatly to the cathodic components of Equation 5.[120] In Equation 5, i_{net} is the total current, $i_{pit\ tip}^{anodic}$ is the true anodic current generated from the dissolution of aluminum, the cathodic terms represent the current from the reduction of oxygen, the evolution of hydrogen, or the reduction of an inhibitor, and the $C\frac{dV}{dt}$ term represents the capacitive current generated from the rapid changes in potential, V.

$$i_{net} = i_{pit\ tip}^{anodic} - (i_{pit\ tip}^{cathodic} + i_{passive\ surface}^{cathodic}) \pm C\frac{dV}{dt} \qquad \textbf{Equation 5}$$

To address the ambiguity inherent to the scratched electrode current transient due to the difficulty in extracting the true anodic current from the measured net current, a complimentary technique to examine oxide capacitance has been developed. The well-known relationship between oxide thickness (d_{ox}) and capacitance (C_{ox}) were used to monitor oxide growth. Several stages of growth are predicated after scratching a metallic electrode, as shown in Figure 4. The nucleation of oxide on the bare metallic surface can be exploited because it has an effect on the capacitance as described by Equation 6, where θ is the fraction of bare metallic electrode.

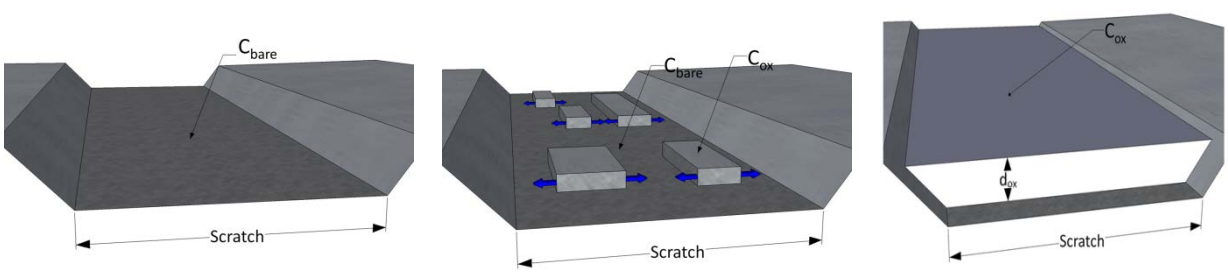

Figure 4. Schematic of an oxide covered surface after a scratch. The bare metallic electrode undergoes oxide nucleation and an increase in oxide surface coverage, followed by thickening of the oxide film as repassivation occurs. The thickness of the oxide layer is d_{ox}.

$$c_{total} = \theta C_{bare} + (1-\theta)C_{ox} \qquad \textbf{Equation 6}$$

The measurement of the capacitance was performed by using a fast single frequency impedance measurement (3-5 impedance measurements per second) in the capacitive region of frequency response. The method relies on the fact that C_{bare} is much larger than C_{ox} for aluminum.[121] C_{bare} was on the order of the double layer or Helmholtz layer capacitance which is between 40 and 100 μF/cm^2 [121,122] while the Al_2O_3 oxide capacitance was on the order of 1-2 μF/cm^2.[123] Therefore, C_{total} during repassivation should decrease by at least an order of magnitude as the electrode repassivates. Figure 5 presents a theoretical Bode impedance plot under passive and mechanically depassivated conditions. These calculations were used to determine the single frequency at which capacitive data would be easily extractable. A frequency of 1000 Hz was

selected because it was well within the capacitive region of both the passive and depassivated surfaces. The capacitive region has a negative slope with a value close to -1 on the Bode impedance plot.[124] In the capacitive dominated region, the impedance magnitude were inversely proportional to the oxide thickness, and the effects of inhibitors on oxide thickness will be accessible.

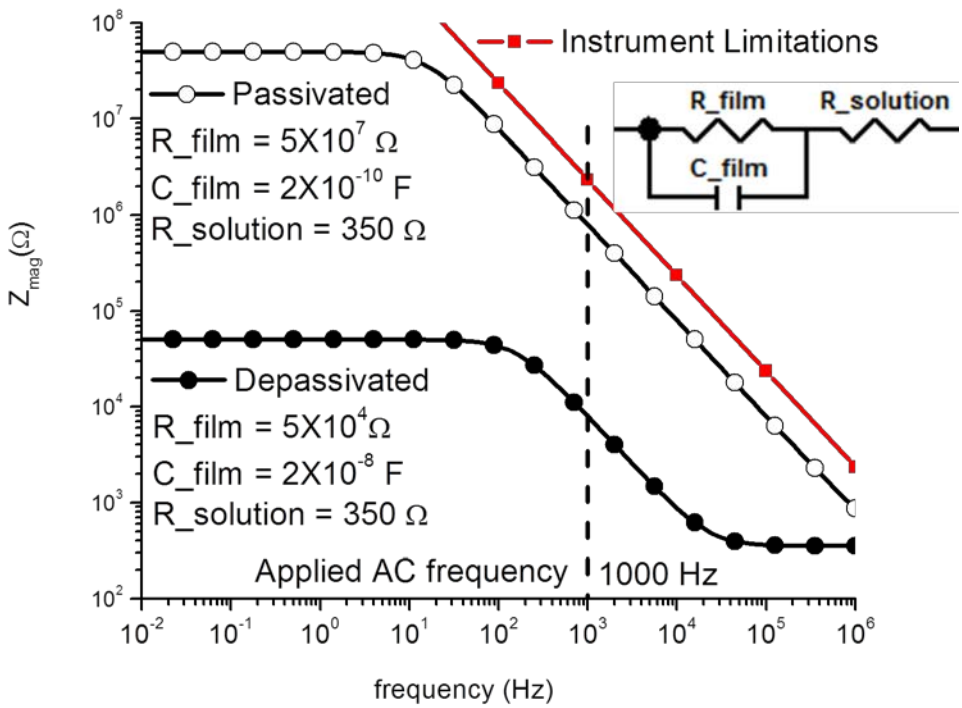

Figure 5. Theoretical model of Bode impedance for depassivated and passive aluminum electrodes. Values were determined assuming a passivated R_{film} value of 10^4 Ω-cm^2, depassivated R_{film} of 10 Ω-cm^2, and $R_{solution}$ of 350Ω. Capacitance of 1 μF/cm^2 and 100 μF/cm^2 were used for the passivated and bare electrodes, respectively. Values corrected for electrode surface area of 2x10^{-4} cm^2.

Chromate and molybdate enhance repassivation and oxide barrier growth after mechanical depassivation. The regrowth of oxide films over freshly bared aluminum surfaces in the presence of aqueous inhibitors and chloride were examined.

Task 2 – Effect of Combinations of Inhibitors

As mentioned before, combining the beneficial properties of two or more non-chromate inhibitors was the key to improving their performance due to synergistic interactions between them.[7,8] An example was the combination of Ce(III), which is a cathodic inhibitor with Mo(VI) which is an anodic inhibitor. An empirical combinatorial method has been used by others to find the inhibitor pairs that exhibit synergy.[8] However, such methods did not help to identify new combinations that are not included in the experimental matrix and are very time consuming. Therefore, a critical aspect of our proposed study was to examine the electrochemical behavior of various substrates described in Task 1, when a second inhibitor is added to a given inhibitor. This unearthed mechanistic information that can then be used to explore combinations of inhibitors not examined through prior experiments. The synergistic effect in many cases can result from a co-adsorption mechanism of the inhibitor ions. In this case, the introduction of a second inhibitor lowers the number of available adsorption sites on the surface for Cl^- or O_2 adsorption. Another possibility is that the simultaneous adsorption of two negatively charged inhibitors uniformly covers the surface with negative charge providing a charge barrier to Cl^- ions. The inhibitors can also precipitate on the surface due to local pH changes as in the case of Ce(III).[29,40] Upon the introduction of a second inhibitor a co-precipitation reaction is possible during which a denser precipitate layer can form. The different non-chromate inhibitors can also react with each other in a redox reaction, as in case of Ce(III) and MoO_4^{2-} (see Equation 7).

$$MoO_4^{2-} + 2Ce^{3+} + 2H_2O \rightarrow MoO_2 + 2CeO_2 + 4H^+ \qquad \textbf{Equation 7}$$

In the above reaction, molybdenum(IV) oxide and cerium(IV) oxide form, both of which are highly insoluble in water. All these possible synergistic mechanisms need to be examined and evaluated in order to gain an understanding of the interactions between the different inhibitor groups on different alloys.

Task 3 – Effect of Microstructural Heterogeneity on Inhibitor Action

As mentioned before, secondary phases significantly impact both the electrochemical properties of the alloys, as well as the effectiveness of an inhibitor. The mechanism of inhibitor action on a secondary phase is often difficult to access using an alloy containing the secondary phase, since contribution of the matrix to the electrochemical behavior cannot be isolated. In this task, an Al/Cu multielectrode array, containing 100 addressable elements, was fabricated to simulate both the matrix and second phase. Since they are electrically isolated, the electrochemical interactions between them can be studied. The effect of these microstructural parameters on the efficiency of the inhibitors can then be studied. This approach is particularly important in case of the inhibitors that affect the cathodic kinetics, since the Al_2Cu intermetallic particles have been shown to be responsible for the majority of the cathodic current via supporting the ORR[90] and certain inhibitors have been shown to interact with these intermetallic compounds (IMCs) thereby affecting the cathodic kinetics.[29] One hypothesis is that the cathodic inhibitors selectively block the IMCs that support ORR, e.g., Al_2Cu, thereby changing the distribution of these particles on the surface.[29] It is not clear yet, however, whether these inhibitors partially block all the IMCs or completely block select IMCs to increase the distance between them and lower their surface coverage.[29] A schematic of the possible scenarios is shown in Figure 6.

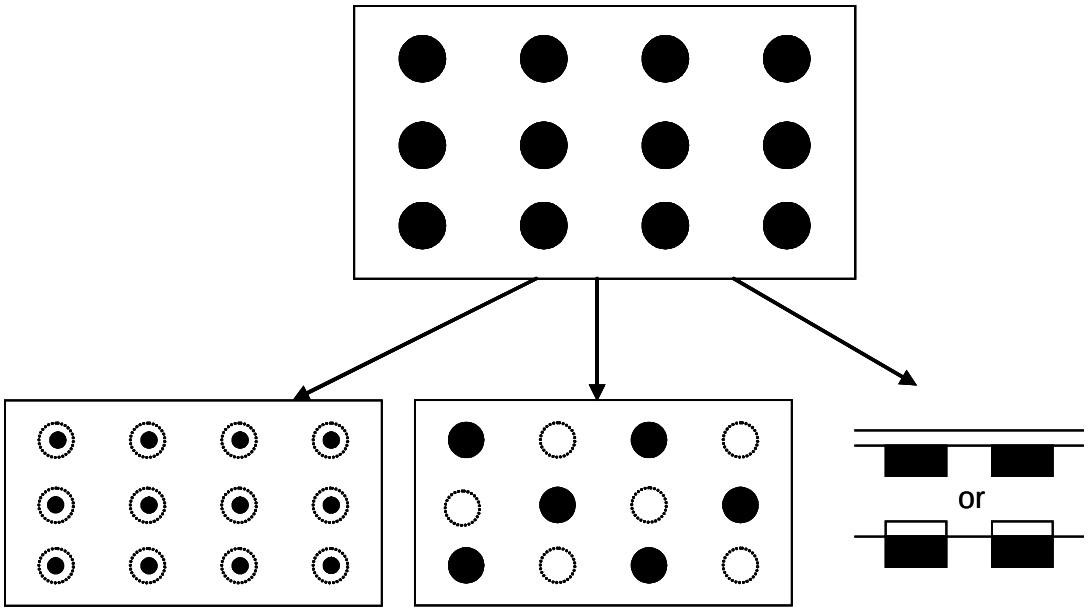

Figure 6. Schematic model of potential effects of cathodic inhibitors on IMCs.[29]

Task 4 – Effect of Alternate Wet & Dry Conditions

In real applications involving aluminum alloys and steel, alternating wet and dry environments usually prevail. It is suspected that under drying conditions the electrolyte film thins causing changes in the boundary layer thickness and in the concentrations of both the inhibitor and aggressive ions. The ion concentrations increased, as well as the oxygen uptake. Moreover, the gel-like hydrated inhibitor film that forms under wet conditions may undergo physical and chemical alterations. Changes in ionic strength of the electrolyte due to evaporation may affect the speciation of the inhibitors. It has been shown recently that the speciation of inhibitors play a very important role in determining their effectiveness in case of some non-chromate inhibitors, e.g., vanadates.[31] Iannuzzi and coworkers found that while metavanadates are highly effective cathodic inhibitors, decavanadates, which form upon acidification of metavanadate solutions, are practically ineffective.[32] Some of these changes may be irreversible and affect the performance of inhibitors in subsequent wet cycles. However, such changes have not been studied in-situ for either chromate or non-chromate inhibitors. A challenge is the ability to monitor electrochemical behavior under relatively dry conditions where only a thin water layer is present. To address this, potential mapping of electrode arrays prepared with the thin film technique was used. The potential mapping was carried out using Scanning Kelvin Probe (SKP). The Scanning Kelvin Probe measures the Volta potential between the probe and the sample under a thin electrolyte layer. The effect of inhibitors on the electrochemical behavior of the surface can be measured from the Volta potential difference between the inhibitor treated and untreated surfaces. SKP has recently been used at SwRI to show the ennoblement of a bimetallic surface due to adsorption of volatile corrosion inhibitors (VCIs) as shown in Figure 7.[125]

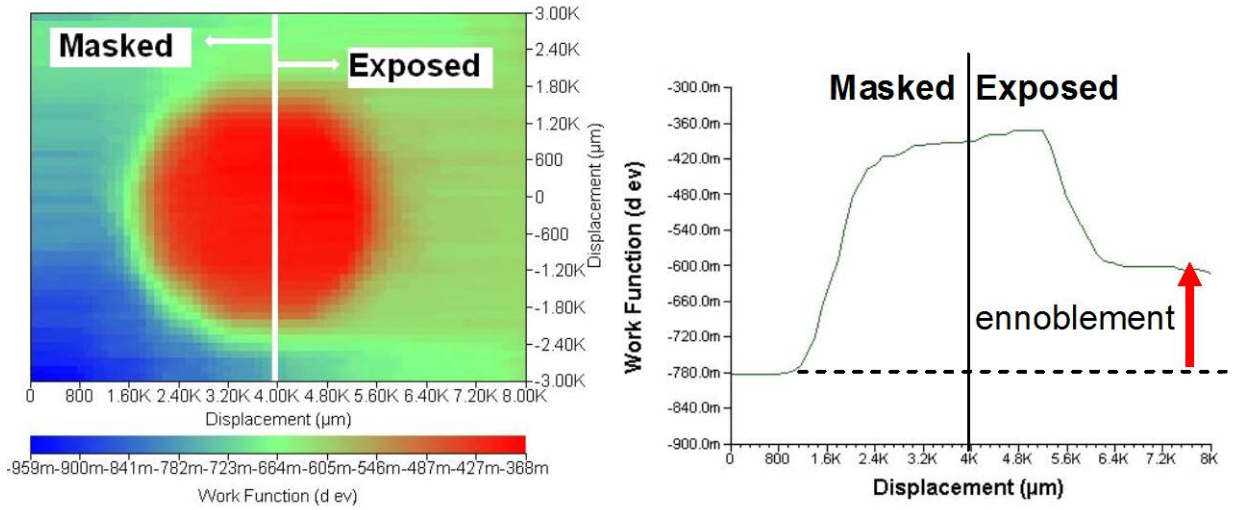

Figure 7. SKP image of bimetallic substrate after partial exposure to VCI (left), and cross-section through feature showing potential shift for VCI exposed metal (right).[110]

Measuring changes in the electrode potential or potential profile of the electrical double layer resulting from either wet or dry conditions, as well as shifts in potentials for subsequent wet conditions during cycling indicated whether the above changes occur, and if so, whether or not they are irreversible. This was used to identify changes in the inhibitor ion speciation that occurs due to wet-dry cycling and associate the change in speciation with their electrochemical effects. These phenomena were probed on multi electrode arrays consisting of electrodes simulating the matrix and IMCs. These electrode arrays allowed for potentiodynamic polarization data to be obtained from each individual electrode separately, therefore combining determination of inhibitor species and the resulting effects on electrochemical behavior of the matrix, IMCs and matrix/IMC interfaces individually, as well as spatio-temporal information for the substrate-inhibitor interaction to be obtained under a thin electrolyte film.

Materials and Test Electrolytes

Aluminum alloys 2024, 7075 and 1018 carbon steel, as well as pure aluminum (99.998%) and pure copper (99.999%) were used in the experiments. The alloy compositions are presented in Table 3. The 2024 aluminum alloy was used in T3 and T4 tempers.

The specimens were used in as-received condition or they were wet polished through 600 or 1200 grit silicon carbide paper. All specimens were cleaned, first in 18.2 MΩ deionized water and then in methanol, and finally air-dried. The cathodic tests used AA2024-T4 rod material with a surface area of 1.29 cm^2, and 99.998% pure aluminum and 99.999% pure copper of surface area 0.196 cm^2. The anodic and electrochemical impedance spectroscopy (EIS) tests used plate material of AA2024-T3 with a surface area of 6.45 cm^2, and 99.99% Al plate with a surface area of 0.0602 cm^2. Surface evaluations were performed on AA2024-T3 specimens. Cyclic voltammetry (CV) tests used coupon specimens of AA2024-T3 and Cu (C11000).

Table 3. Compositions of Alloys Used in the Study.

Al Alloys	Mg	Mn	Fe	Cu	Zn	Cr	Ti	Si	V	Al
2024-T3	1.260	0.590	0.220	4.56		0.010	0.020	0.080	0.010	93.25
2024-T4*	1.20-1.80	0.30-0.90	0.50 max	3.80	0.25 max	0.10 max	0.15 max	0.50 max		90.7-94.7
7075-T6*	2.10-2.90	≤ 0.30	≤ 0.50	1.20-2.00	5.10-6.10	0.18-0.28	≤ 0.20	≤ 0.40		87.1-91.4
99.999% Al	<0.1	<0.1	<0.1	<0.1	<0.1	<0.1	<0.1	<0.1	<0.1	Balance

Carbon Steel	C	Mn	P	S	Fe
1018*	0.14	0.60	0.04	0.05	99.17

*Nominal compositions

Test solutions were made using 18.2 MΩ deionized water with additions of sodium metavanadate ($NaVO_3$), cerium acetate ($Ce(CH_3COO)_3$), sodium molybdate (Na_2MoO_4), potassium permanganate ($KMnO_4$) and sodium chloride (NaCl). pH 8.4 and 8.2 borate buffers (sodium tetraborate decahydrate + boric acid and sodium hydroxide + boric acid, respectively) were also used. The reference electrode used was a saturated calomel electrode (SCE) except for chloride free electrochemical tests, in which a mercury sulfate electrode (MSE) was used.

Techniques – Corrosion Inhibition of AA2024 using Permanganate

Open Circuit Measurements and Electrochemical Impedance Spectroscopy during Open Circuit Exposure Periods

OCP measurements were used to study the effect of the inhibitor on corrosion events when anodic and cathodic reactions were allowed to occur at uncontrolled rates on AA2024-T351. The potential measurements were carried out in three ways. One hour OCP measurements were taken while the sample was exposed to a 50 mM sodium chloride solution in the presence of the inhibitor in the previously discussed concentrations. OCP measurements were also taken in permanganate free 50 mM sodium chloride after a 24 hour pretreatment with permanganate at room temperature. The pretreatment consisted of emersion in aerated potassium permanganate solution with the concentrations previously discussed for 24 hours at room temperature and OCP. Care was taken to insure that none of the faces of the sheet AA2024 were allowed to rest against the walls or bottom of the chloride free glass beakers. After 24 hours the pretreated samples were

rinsed thoroughly in 18.2 MΩ deionized water, blotted dry with cotton lab tissue, and attached to a standard 3 electrode cell within 5 minutes. After attachment the sample was thoroughly dried with compressed nitrogen to ensure that only the desired area was exposed to electrolyte. Following the pretreatment, the OCP was measured for 1 hour in 50 mM sodium chloride solution.

The third measurement was a 1 hour OCP measurement at the beginning and end of a 24 hour continuous OCP exposure to 50 mM sodium chloride solution with varied inhibitor concentrations in-situ (0 mM, 5 mM, 10 mM, and 100 mM permanganate solutions). Tests were run for each concentration in a 3 electrode cell, EIS data was gathered after the OCP measurement. EIS measurements ranged from 10^6 to 10^{-3} Hz taking six data points per decade with a root mean square voltage amplitude of 20 mV. A slight variation on the pretreatment procedure (disregard for Cl^- contamination) was used when EIS data was not needed.

Microscopic Analysis after Open Circuit Exposures

Scanning electron microscopy was used to examine samples after open circuit exposures, pretreatment, and pretreatment followed by exposure. Examination focused on intermetallic trenching and general pitting of the aluminum matrix as well as oxide growth on the sample. S-phase was examined at -0.5 V vs. SCE, approximately the OCP of AA2024-T351 in permanganate and chloride solutions. Potentiostatic holds at -0.5 V vs. SCE were conducted for 200 seconds to determine the effect of permanganate on S-phase attack. The short time period was chosen to minimize damage to the singular S-phase ingot.

Anodic and Cathodic Cyclic Potentiodynamic Polarization Scans

Upward anodic scans were run immediately following the OCP measurements described above. The samples were scanned from -0.05 V vs. OCP to 1 V vs. SCE or until the current density (*i*) reached $5X10^{-3}$ mA/cm^2. The scan then reversed direction and proceeded to -0.5 V vs. OCP. These anodic scans were repeated on replicate specimens to give a statistical probability of pitting. All measurements were taken with respect to a saturated calomel electrode. E_{pit} were taken when the current density reached 10^{-4} A/cm^2.

Cathodic reaction kinetics were studied using the rotating disk electrode (RDE) method. Samples were examined with permanganate and chloride in the test solution and also after a pretreatment in permanganate with the test scan solution consisting of 50 mM sodium chloride or a pH 8.4 borate buffer solution. The permanganate and sodium chloride tests were measured using saturated calomel reference electrode. The pretreated samples that were scanned in pH 8.4 borate buffer were measured with a Hg/Hg_2SO_4 reference electrode. Rotation rates of 100, 500, 1000, 1500, 2000, 2500 revolutions per minute (RPM) were used. Samples included high-purity copper and AA2024-T4. The RDE samples were mounted in Polytetrafluoroethylene with BONDiT B-4811 from Reltek™. This epoxy is resistant to harsh chemical environments and is needed in the presence of permanganate, a strong oxidizer.

Galvanostatic reduction experiments were performed on high-purity copper samples that were both untreated and pretreated in a 0.1 M $KMnO_4$ solution at a potential of -0.5 V vs. SCE. These experiments were conducted to observe valence state changes in the electrodeposited

manganese oxide on the pretreated copper samples. The galvanostatic tests were conducted in pH 10 borate buffer. The galvanostatic reduction was run at a rate of 20 $\mu A/cm^2$.

Cyclic Voltammetry Tests to Assay Copper Redeposition

CV experiments were performed on exposed, pretreated, and pretreated then exposed AA2024-T351 to assay the surface copper redeposition process after inhibitor pretreatment.[68] CV experiments were performed after transferring specimens to pH 8.4 borate buffer solution in chloride and copper (I and II) free cells using Hg/Hg_2SO_4 reference electrodes. The procedure for the test can be found in the literature.[68] The anodic current that resulted from the scans is dependent on the surface coverage of copper and thus the area coverage of the active Cu-rich cathodic reaction sites. Metallic copper on the surface can be oxidized to Cu_2O (Cu I) and CuO (Cu II). There can be interference with this assay if $Mn(OH)_2$ is oxidized to Mn_2O_3 during the potential sweep but this has been avoided by choosing the pH 8.4 buffer solution such that the reversible potential for the Mn(II) to Mn(III) reaction is -0.117 vs. Hg/Hg_2SO_4. Several manganese oxidation reduction reactions could potentially occur between -0.1 and -1.6 V Hg/Hg_2SO_4. However, none of them occur near the reduction peak for Cu seen in our experiments of around -0.4 V Hg/Hg_2SO_4.

Raman Spectroscopy

Raman spectroscopy experiments were conducted on copper, pretreated copper, AA2024-T351, pretreated AA2024-T351, manganese metal, and a series of manganese oxide powders purchased from Alfa Aesar including MnO_2 (99.999%), Mn_2O_3 (98%), and Mn_3O_4 (99.9%). Copper was pretreated in 0.1 M $KMnO_4$ at a potential of -0.5 V vs. SCE to mimic the OCP of the intermetallic particles in AA2024-T351 exposed to a similar solution. Manganese metal was held at a series of potentials ranging from -1.84 V to 1 V vs. SCE in pH 10 borate buffer solution for 24 hours to grow stable manganese oxides on the surface of the metal. Raman spectroscopy was taken in-situ for the manganese metal, pretreated copper, and pretreated AA2024-T351. Raman spectroscopy was conducted ex-situ for the manganese oxide powders.

Techniques – Corrosion Inhibition of AA2024 using Vanadate

Nuclear Magnetic Resonance

NMR was employed to determine vanadate speciation of the sodium vanadate–sodium chloride solutions. Four mL samples were made using deuterium oxide, D_2O (99.98%, Cambridge Isotope Laboratory) as the solvent with sodium metavanadate (99.9% by metals basis, Sigma Aldrich) and sodium chloride (98% reagent grade Fisher Scientific). Five different molarities (1, 5, 10, 50, 150 mM) of vanadate were tested in 50 mM sodium chloride solutions that were aged for 1, 2, 3, 4, 5, 7, 14, 21, and 28 days. A Unity Inova spectrometer at 500MHz (11 T), was used to capture 200 transients with a $90°$ pulse width of $18\,\mu s$, relaxation delay of 0.2 s and a spectrum width of 100,000 Hz for a ^{51}V frequency of 131.480 MHz. An external reference solution of neat $VOCl_3$ ($\delta^{51}V = 0$ ppm) was used to compare the ^{51}V chemical shifts. The probe temperature was 22°C ± 3°C. Peak identifications were made by comparison to the available ^{51}VNMR literature.

The vanadate species in solution were determined as a function of aging time. The areas under the NMR peaks were compared to each other to calculate the percentage of each species.

All calculations and frequency analyses were performed with the MestRENova version v6.0.3–5640 software using the standard settings. The baseline and integral calculations were performed automatically by the software. During integral analysis, some peak widths were reduced from default settings to compensate for large and overlapping peaks. The absolute area calculated for each peak was used to determine its contribution to the total area. The percentage of the total area is equal to the peak's area divided by the total area multiplied by 100%. Graphs were generated showing the change in peak area over time.

Open Circuit Exposures

Ground AA2024-T3 coupons (2.54 cm by 2.54 cm) were immersed in beakers of approximately 30 mL of (0, 1, 5, 10, 50, 150 mM) sodium vanadate plus 50 mM sodium chloride solution for 24 hours. The specimens were then removed and rinsed in 18.2 MΩ deionized water. The surfaces of the specimens were imaged using optical and electron microscopy techniques. For optical measurements, a detection limit in determining pit formation was 30 µm, which was obtained by scanning the surface of the specimen at 700x magnification. SEM, and back-scattered electron microscopy (BSE) in conjunction with EDS were used to examine pitting sites and surface compositions. Secondary electron images were obtained at 15 kV with 184 second collection time. Peak keV energies used for determining relative atomic percentages are presented inTable 4. While anodic and cathodic polarization tests assess a set of net anodic or cathodic reactions, respectively, open circuit exposures were conducted in order to assess the ability of the inhibitor to function in the presence of a mix of anodes and cathodes on the surface of the specimens.

Table 4. Elemental peak energy used for determining atomic percentages.

Element	**Al**	**Cu**	**Fe**	**Mn**	**Mg**	**V**	**Cl**
Energy (keV)	1.486955	8.01	6.398	5.894	1.253779	4.949	2.622087

E–log(i) Polarization Experiments

Cathodic and anodic [E–log(i)] polarization experiments were undertaken to determine the effect of vanadate inhibitors on the ORR and E_{pit} at room temperature.

Cathodic polarization scans, using RDEs, were performed on AA2024-T4, as well as Al and Cu specimens in 50 mM NaCl solutions containing additions of 0, 1, 5, 10, 50, or 150 mM $NaVO_3$, which resulted in solutions of pH 5.7, 6.5, 7.6, 7.8, 8.4, and 8.7 respectively. The RDEs were rotated at 0, 500, 1000, 1500, or 2500 RPM with ambient aeration.A limited number of experiments were performed on aluminum. OCP was measured for one hour, starting at specimen immersion in the test solution (referred to as 1 hour OCP measurement), prior to performing a cathodic potentiodynamic scan.These scans were conducted from 0 versus V_{ocp} to -1.9 versus V_{ref} with a return scan to 0 versus V_{ocp} at a rate of 0.1 mV/s (V_{ocp} is the open circuit potential; V_{ref} is the voltage of the reference electrode versus the standard hydrogen electrode (SHE).

The effective cathodic current density as well as the mass transfer-limited current density for ORR was calculated. Calculations were made for each material and inhibitor combination using the Koutechy-Levich equation. The Koutechy-Levich equation relates the total cathodic current density (i_T) to the mass transfer-limited ORR current density (i_{Lim}) using Equation 8, where i_{lim} is given by Equation 9.

$$\frac{1}{i_T} = \frac{1}{i_{act}} + \frac{1}{i_{Lim}} \qquad \textbf{Equation 8}$$

$$\frac{1}{i_{Lim}} = k\omega^{-1/2} \qquad \textbf{Equation 9}$$

After combining these equations, i_{act}, the charge transfer cathodic current density that is independent of rotation rate, was obtained from the y intercept of a graph of a plot [Koutechy-Levich plot ($1/i_T$ *vs.* $\omega^{-1/2}$)] for Equation 10(k is a constant and the slope).

$$\frac{1}{i_T} = \frac{1}{i_{act}} + k\omega^{-1/2} \qquad \textbf{Equation 10}$$

Three different anodic experiments were performed on both inhibitor pretreated and untreated specimens. One type of anodic test consisted of 1 hour OCP measurement followed by anodic potentiodynamic scans from -0.05 V versus V_{ocp} to 0 V versus V_{ref} to -1 V versus V_{ref} at a scan rate of 0.1 mV/s. These tests were conducted in 50 mM NaCl solutions containing additions of 0, 5, 10, 50, or 150 mM $NaVO_3$. This test was repeated using multiple specimens.

A second type of anodic test consisted of 24 hour OCP measurements (measurement of OCP from the 0 to 1st hour and 23rd to the 24th hour after specimen immersion) followed by anodic potentiodynamic scans using the identical procedure. In addition to the previous solutions, a solution containing 1mM $NaVO_3$ was employed.

The third type of anodic test consisted of immersion of AA2024-T3 for 24 hours in room temperature chloride free 0, 5, 10, 50, or 150 mM $NaVO_3$ solutions prior to a 1 hour OCP measurement. This was followed by anodic potentiodynamic scans in inhibitor free 50 mM NaCl solutions. This test was repeated using six specimens.

The average OCP was calculated at each time interval using OriginPro 7.5. The average open circuit potentials were compared to each other. The E_{pit} was chosen as the voltage corresponding to a current density of 10^{-4} A/cm^2. If the corresponding current density was not reached during the experiment, the highest potential tested was used as the value for E_{pit}. The range and 3-standard deviation of E_{pit} were also calculated. Graphs of cumulative frequency distribution were made from the E_{pit} data for each vanadate concentration. Cumulative frequency distributions, also known as cumulative probability graphs, were used to determine the likelihood that a value was within a set of data.[126,127]

Techniques – Corrosion Inhibition of AA2024 with Inhibitors Combination

Cerium-Permanganate Combinations

Materials and Test Electrolytes

AA2024-T351 (1 mm sheet) and T4 (rod) precipitation age hardened aluminum alloys, and copper (99.994%) were investigated. Specific chemical compositions (wt. %) of the aluminum alloy can be found in Table 3. All sheet metal samples were tested on their LT surfaces, rod samples were tested on their S-T surfaces. Sample preparation varied by experimental technique depending on surface roughness requirements for imagining. These preparations fall into two categories; refinished and polished. The refinishing process consisted of a single polishing step using 600 grit silicon-carbide paper and was intended to restore the specimens to as-received condition. Polishing was carried out in 18.2 MΩ deionized water. The samples were subsequently rinsed in 18.2 MΩ deionized water, methanol, and again in 18.2 MΩ deionized water for degreasing before being dried on cotton lab tissue. When a finer surface roughness was desired to resolve constituent particles at micrometer scale resolution, the samples were ground sequentially to 1200 grit Si-C paper resulting in a partially reflective surface on AA2024 and high purity copper. The degreasing procedure was identical.

The test solutions were prepared with 18.2 MΩ deionized water. Solutions were prepared with (in wt.%) sodium chloride (99.8% NaCl), potassium permanganate (99.5% $KMnO_4$), cerium acetate (99.99%), sodium tetraborate decahydrate 101.3%, and boric acid, 99.99%. All solutions were aerated and at room temperature unless otherwise noted. Several solution preparations were used. Pretreatment solutions consisted of chloride free cerium or permanganate solutions with concentrations of 0 mM, 10 mM, 25 mM, 40 mM, and 50 mM. The naturally occurring pH of the solutions ranged from 5.8 for the 5 mM permanganate solution to 7.4 for the 100 mM concentration. Post-pretreatment exposure was carried out in 50 mM sodium chloride at its natural pH of 6 in an ambient environment.

Open Circuit Measurements During Open Circuit Exposure Periods

OCP measurements were used to study the effect of the inhibitor on corrosion events when anodic and cathodic reactions were allowed to occur at uncontrolled rates on AA2024-T351. OCP measurements were taken in permanganate and cerium free 50 mM sodium chloride after a pretreatment that consisted of sequential cerium and then permanganate treatments. The first step of the pretreatment was a 100 hour treatment in a cerium solutions with a concentration stated above. The next step was a 24 hour treatment with permanganate in at a concentration that when added with the prior treatment in cerium came to a total inhibitor concentration of 50 mM. As an example, if the first treatment was in 10 mM Ce-acetate, the second treatment was in 40 mM permanganate. If the first treatment was in 25 mM cerium-acetate, the second treatment was in 25 mM permanganate. All treatments were carried out at room temperature and at the natural open circuit potential. Care was taken to insure that none of the faces of the sheet AA2024 were allowed to rest against the walls or bottom of the chloride free glass beakers. After the pretreatment the samples were rinsed thoroughly in 18.2 MΩ deionized water, blotted dry with cotton lab tissue, and attached to a standard 3 electrodes cell within 5 minutes. After attachment the sample was thoroughly dried with compressed nitrogen to ensure that only the desired area

was exposed to electrolyte. Following the pretreatment, the OCP was measured for 1 hour in 50 mM sodium chloride solution.

Microscopic Analysis after Open Circuit Exposures

Scanning electron microscopy was used to examine samples after pretreatment, and pretreatment followed by exposure. Examination focused on intermetallic trenching and general pitting of the aluminum matrix as well as oxide growth on the sample. Images were recorded using the secondary electron LEI detector at 5 kV and a working distance of 6 mm. EDS analysis was carried out at 15 kV accelerating voltage with a working distance of 15 mm. The K-alpha characteristic emission was recorded for all species with the exception of cerium whose L and M-alpha characteristic emissions were recorded.

Anodic and Cathodic Cyclic Potentiodynamic Polarization Scans

Upward anodic scans were run immediately following the OCP measurements described above. The samples were scanned from -0.05 V vs. OCP to 1 V vs. SCE or until the current density (*i*) reached 5.0×10^{-3} mA/cm^2. The scan was then reversed in direction to -0.5 V vs. OCP. These anodic scans were repeated on replicate specimens to give a statistical probability of pitting reported in cumulative probability plots. All measurements were taken with respect to a saturated calomel electrode. E_{pit} were taken when the current density reached 10^{-4} A/cm^2.

Cathodic reaction kinetics were studied using the RDE method. Samples were examined after a pretreatment described above with the test scan solution consisting of pH 8.4 borate buffer solution. The reference electrode used was mercury/mercury sulfate (Hg/Hg_2SO_4). However, all data has been converted to the saturated calomel scale for ease of use. Two types of scans were carried out. The first type was a potentiodynamic scan carried out at 2500 RPM from 0.05 V above OCP to -1.5 V vs. SCE. The second type of cathodic kinetics experiment was a potentiostatic hold at -1.0 V vs. SCE. This potential was in the ORR dominated region of the cathodic reaction path. Rotation rate was varied during the potentiostatic hold at the following rpm: 100, 500, 1000, 1500, 2000, and 2500. Samples included high purity copper and AA2024-T4. The RDE samples were mounted in PTFE with BONDiT B-4811 from Reltek™. This epoxy is resistant to harsh chemical environments and is needed in the presence of permanganate, a strong oxidizer.

Cyclic Voltammetry Tests to Assay Copper Redeposition

CV experiments were performed on pretreated samples that had been exposed to 50 mM NaCl for 24 hours to assay the surface copper redeposition process after inhibitor pretreatment.[20] CV experiments were performed after transferring specimens to pH 8.4 borate buffer solutions in chloride and copper (I and II) free cells using Hg/Hg_2SO_4 reference electrodes. All potentials have been reported on the saturated calomel scale for ease of use. The procedure for the test can be found in the literature.[20] The anodic current that resulted from the scans is dependent on the surface coverage of copper and thus the area coverage of the active Cu-rich cathodic reaction sites. Metallic copper on the surface can be oxidized to Cu_2O (Cu I) and CuO (Cu II). There can be interference with this assay if $Mn(OH)_2$ is oxidized to Mn_2O_3 during the potential sweep but this has been avoided by choosing the pH 8.4 buffer solution such that the reversible potential for the Mn(II) to Mn(III) reaction is -0.117 vs. Hg/Hg_2SO_4. Several manganese oxidation reduction

reactions could potentially occur between -0.1 and -1.6 vs. V Hg/Hg_2SO_4. However, none of them occur near the reduction peak for Cu seen in our experiments of around -0.4 V vs. Hg/Hg_2SO_4.

Vanadate-Cerium and Vanadate-Molybdate Combinations

Materials and Solutions

Aluminum alloy AA2024 in the T3 or T4 temper (compositions presented in Table 3), high purity aluminum, and high purity copper specimens were prepared in the same fashion described in Materials and Test Electrolytes (see page 22).

Test solutions were made using 18.2 MΩ deionized water with additions of sodium metavanadate, $NaVO_3$, 99.9%, sodium molybdate, Na_2MoO_4, 99.5-103.0%, sodium chloride, NaCl, 99.8% and cerium acetate, $Ce(C_2H_3O_2)_3$, 99.9%. The reference electrode used was a saturated calomel electrode (SCE). In reference to the standard hydrogen electrode (SHE), SCE is +0.2415 V.[122]

Nuclear Magnetic Resonance

NMR was employed to determine vanadate speciation of the sodium vanadate–sodium chloride solutions. Four mL samples were made using deuterium oxide, D_2O (99.98%) as the solvent with sodium metavanadate (99.9%), sodium molybdate (99.5-103.0%) and sodium chloride (98% reagent grade). Four different molarities (40 mM Na_2MoO_4 + 10 mM $NaVO_3$, 25 mM Na_2MoO_4 + 25 mM $NaVO_3$, 10 mM Na_2MoO_4 + 40 mM $NaVO_3$, 50 mM $NaVO_3$) of vanadate were tested in 50 mM sodium chloride solutions that were aged for 1, 3, 6, 7, 14, 21, and 29 days. A Unity Inova spectrometer at 500MHz (11 T), was used to capture 200 transients with a *90°* pulse width of *18 μs*, relaxation delay of 0.2 s and a spectrum width of 100,000 Hz for a ^{51}V frequency of 131.480 MHz. An external reference solution of neat $VOCl_3$ ($\delta^{51}V = 0$ ppm) was used to compare the ^{51}V chemical shifts. The probe temperature was 22°C ± 3°C. Peak identifications were made by comparison to the available ^{51}VNMR literature.

The vanadate species in solution were determined as a function of aging time. The areas under the NMR peaks were compared to each other to calculate the percentage of each species. All calculations and frequency analyses were performed with the MestRENova version v6.0.3–5640 software using the standard settings. The baseline and integral calculations were performed automatically by the software. During integral analysis, some peak widths were reduced from default settings to compensate for large and overlapping peaks. The absolute area calculated for each peak was used to determine its contribution to the total area. The percentage of the total area is equal to the peak's area divided by the total area multiplied by 100%. Graphs were generated showing the change in peak area over time.

Open Circuit Exposures

Ground AA2024-T3 coupons (2.54 cm by 2.54 cm) were pretreated by immersion for 2 hours in a chloride free cerium acetate solution (10, 25, 40 or 50 mM; 5.6 ± 0.1 pH) or used as polished. These cerium pretreated rotating disk electrodes (RDEs) were then rinsed clean using 18.2 MΩ deionized water and dried. The specimens were then immersed in beakers of approximately 30 mL of solution for 24 hours. For the cerium pretreated coupons, the test solution was

composed of (0, 10, 25, or 40, mM; 5.7, 7.8, 8.2, and 8.4 pH, respectively) sodium vanadate plus 50 mM sodium chloride, and for the as polished specimens, the test solution was composed of (50 mM Na_2MoO_4, 40 mM Na_2MoO_4 + 10 mM $NaVO_3$, 25 mM Na_2MoO_4 + 25 mM $NaVO_3$, 10 mM Na_2MoO_4 + 40 mM $NaVO_3$ or 50 mM $NaVO_3$; 7.5, 7.9, 8.3, 8.4, and 8.4 pH, respectively) plus 50 mM sodium chloride. The pretreatment and test solutions were paired so that the surface of a specimen was exposed to a total inhibitor concentration of 50 mM. The specimens were then removed and rinsed in 18.2 MΩ deionized water. The surfaces of the specimens were imaged using optical and electron microscopy techniques. For optical measurements, a detection limit in determining pit formation was 30 μm, which was obtained by scanning the surface of the specimen at 700x magnification. Secondary electron microscopy (SEM), and BSE in conjunction with energy dispersive x-ray spectroscopy (EDS) were used to examine pitting sites and surface compositions. Secondary electron images were obtained at 20 kV with 180 second collection time. Peak keV energies used for determining relative atomic percentages are presented in Table 4. While anodic and cathodic polarization tests assess a set of net anodic or cathodic reactions, respectively, open circuit exposures were conducted in order to assess the ability of the inhibitor to function in the presence of a mix of anodes and cathodes on the surface of the specimens.

E–log(i) Polarization Experiments

Cathodic and anodic E–log(i) polarization experiments were undertaken to determine the effect of vanadate inhibitors on the ORR and E_{pit} at room temperature.

Cathodic polarization scans, using RDEs, were performed on AA2024-T4, as well as Cu specimens in both cerium pretreated or as polished conditions. RDEs had a cerium acetate pretreatment during which the surface of the RDE was submerged for 2 hours in a chloride free cerium acetate solution (10, 25, 40 or 50 mM) which were all 5.6 ± 0.1 pH (indistinguishable with instrument error). These cerium pretreated RDEs were then rinsed clean using 18.2 MΩ deionized water and dried. The test solutions for the cerium pretreated RDEs were 50 mM NaCl solutions containing additions of 0, 10, 25, or 40 mM $NaVO_3$, which resulted in solutions of pH 5.7, 7.8, 8.2, and 8.4, respectively. The pretreatment and test solutions were paired so that the surface of a specimen was exposed to a total inhibitor concentration of 50 mM. The test solutions for the as polished RDEs were 50 mM NaCl solutions containing additions of 50 mM Na_2MoO_4, 40 mM Na_2MoO_4 + 10 mM $NaVO_3$, 25 mM Na_2MoO_4 + 25 mM $NaVO_3$, 10 mM Na_2MoO_4 + 40 mM $NaVO_3$ or 50 mM $NaVO_3$, which resulted in solutions of pH 7.5, 7.9, 8.3, 8.4 and 8.4, respectively.

The RDEs were rotated at 2500 RPM with ambient aeration. OCP was measured for one hour, starting at specimen immersion in the test solution (referred to as 1 hour OCP measurement), prior to performing a cathodic potentiodynamic scan. These scans were conducted from 0 vs. V_{ocp} to -1.9 vs. V_{ref} at a rate of 0.1 mV/s (V_{ref} is the voltage of the reference electrode versus the standard hydrogen electrode, SHE). Additionally, potentiostatic hold experiments at applied potentials of -0.9 V_{SCE}, -0.8 V_{SCE}, -0.58 V_{SCE} where the rotation rate of the RDE was increased after 60 minutes at steady state with a 5 minute window for the electrode to come up to speed with increasing rotation rate were conducted. The open circuit measurements for these experiments started with the electrode rotating at 500 rpm and then the rotation speed increased

to 1000, 1500, and 2500 rpm with each 65 minute applied potential hold period for a total experimental time of 5 hours and 20 minutes.

The effective cathodic current density as well as the mass transfer-limited current density for ORR was calculated. Calculations were made for each material and inhibitor combination using the Koutechy-Levich equation. The Koutechy-Levich equation relates the net cathodic current density (i_T) to the mass transfer-limited ORR current density (i_{Lim}) using Equation 11.

$$\frac{1}{i_T} = \frac{1}{i_{act}} + \frac{1}{i_{Lim}}$$ **Equation 11**

i_{act}, the charge transfer cathodic current density that is independent of rotation rate, is obtained from the y intercept of a graph of a plot (Koutechy-Levich plot) for Equation 12(k is a constant).

$$\frac{1}{i_{Lim}} = k\omega^{-1/2}$$ **Equation 12**

Two different anodic experiments were performed on both inhibitor pretreated and untreated specimens. One type of anodic test consisted of 1 hour OCP measurement followed by anodic potentiodynamic scans from -0.05 V versus V_{ocp} to 0 V vs. V_{ref} to -1 V vs. V_{ref} at a scan rate of 0.1 mV/s. The aluminum or AA2024-T3 coupons had a cerium acetate pretreatment during which the surface of the coupon was submerged for 2 hours in a chloride free cerium acetate solution (10, 25, 40 or 50 mM) which were all 5.6 ± 0.1 pH (indistinguishable with instrument error). These cerium pretreated coupons were then rinsed clean using 18.2 MΩ deionized water and dried. The test solutions for the cerium pretreated coupons were 50 mM NaCl solutions containing additions of 0, 10, 25, or 40 mM $NaVO_3$, which resulted in solutions of pH 5.7, 7.8, 8.2, and 8.4, respectively. The pretreatment and test solutions were paired so the surface of a specimen was exposed to a total inhibitor concentration of 50 mM. The test solution for the as polished RDEs were 50 mM NaCl solutions containing additions of 50 mM Na_2MoO_4, 40 mM Na_2MoO_4 + 10 mM $NaVO_3$, 25 mM Na_2MoO_4 + 25 mM $NaVO_3$, 10 mM Na_2MoO_4 + 40 mM $NaVO_3$ or 50 mM $NaVO_3$, which resulted in solutions of pH 7.5, 7.9, 8.3, 8.4 and 8.4, respectively. This test was repeated using multiple specimens.

A second type of anodic test consisted of 24 hour OCP measurements (measurement of the OCP from the 0 to 1st hour and 23rd to the 24th hour after specimen immersion) followed by anodic potentiodynamic scans using the identical procedure. In addition to the previous solutions, 50 mM NaCl solutions containing 10, 25, or 40 mM $NaVO_3$ were employed to compare the effect of molybdate and vanadate solutions to vanadate solutions of the same vanadate concentration. Similarly, 10 mM $Ce(C_2H_3O_2)_2$ pretreatments were tested at various vanadate concentrations of 0, 10, 25, and 50 mM $NaVO_3$ to separate the inhibition effect of the cerium pretreatment from the effect of vanadate.

The average OCP was calculated at each time interval using curve fixing software (OriginPro 7.5). The average open circuit potentials were compared to each other. E_{pit} was chosen as the voltage corresponding to a current density of 10^{-4} A/cm^2. If the corresponding current density was not reached during the experiment, the highest potential tested was used as the value for E_{pit}. The range and 3-standard deviation of E_{pit} were also calculated. Graphs of cumulative frequency

distribution were made from the E_{pit} data for each vanadate concentration. Cumulative frequency distributions, also known as cumulative probability graphs, were used to determine the likelihood that a value was within a set of data.[126,127]

Techniques – Effect of Molybdate on Repassivation of AA2024

The procedure for conducting a scratch depassivation experiment has been reported.[128] AA2024-T351, AA7075-T6, and 99.999% aluminum were cut and ground to 0.03 cm width and 0.8 cm length. Chemical composition for the alloys is reported in Table 3. Samples were bonded with highly chemically resistant epoxy to polytetrafluoroethylene (PTFE) mounts that had been etched with an activated sodium solution. Electrical connection was made with heavy gauge copper wire through the back of the mount using high silver content epoxy. The sample mounts were inserted into a three electrode cell so that the face of the sample was vertical (Figure 8). A saturated calomel electrode (SCE) and platinized niobium mesh counter-electrode were used throughout all electrochemical experiments. The reference electrode was placed far enough away from the working electrode to be considered at an infinite distance to facilitate the calculation of the theoretically limited ohmic current density.

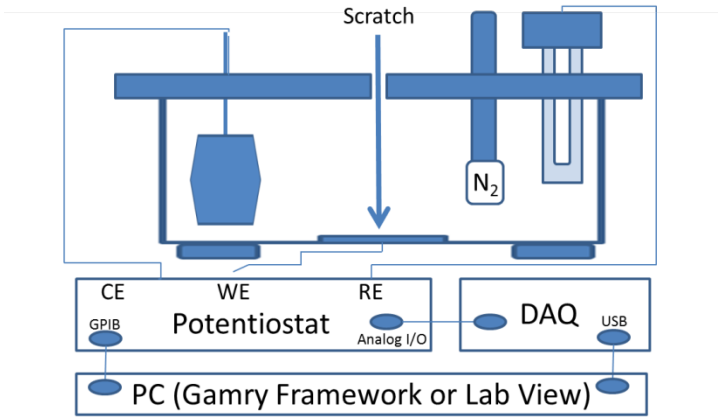

Figure 8. Schematic of scratched electrode cell with wiring diagram for data capture devices.

The scratch was made with a diamond-tip scribing stylus. Scratches were examined with an optical 3D tiling microscope to determine the width, depth, and area of the scratch (Figure 9). The exposed sample face was lightly coated with vacuum grease prior to the scratch to eliminate capacitive current contributions from adjacent areas as indicated in Equation 5.[128] Scratches were examined with an optical microscope after every scratch to ensure that there was no vacuum grease or Teflon contamination. The width of the sample across (the length of the scratch) was small to minimize the time that the stylus was in contact with the sample.[120] The rise time for current transients was on the order of 0.5 ms.

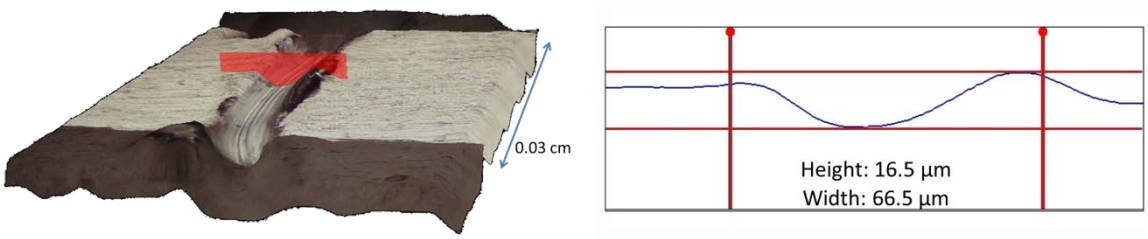

Figure 9 . Detailed 3-D scratch topography for calculating area of exposed electrode during scratched electrode testing.

Solutions investigated include aqueous molybdate and chromate with concentrations from 0.1 mM to 0.1 M in NaCl solution concentrations from 0.05 M to 1.0 M. All solutions were prepared with 18.2 MΩ water. All solutions were adjusted to pH 6.5 with concentrated NaOH and HCl. All solutions were deaerated with high purity nitrogen for one hour prior to testing and an N_2 blanket was maintained over the cell.

The working electrodes were held potentiostatically at applied potentials ranging from -0.8 V to -0.3 V vs. SCE. A PAR 273A potentiostat was used to apply potentials and collect net current. The current data was sampled through the potentiostat's analog outputs and collected with an NI SCXI-1140 DAQ and a SCXI-1600 with sampling capability of 200 kilosamples per second (kS/s). Auto-ranging of the potentiostat was disabled. Successive scratches were performed until a range at which peak current was captured could be determined. Auto-ranging was enabled and short time data was sacrificed when long term data was collected.

A Gamry G 300 series potentiostat was used when single frequency impedance was collected to hold the sample potentiostatically and perform the impedance measurements. A fast single frequency impedance script was developed to increase the sampling rate capabilities of the standard EIS software. The frequency applied was 1000 Hz with an amplitude of 20 mV RMS. The measurements were taken at a DC offset of -0.8 V_{SCE} unless otherwise stated. These tests were conducted in 1 M NaCl with various concentrations of molybdate and chromate. Solutions were all adjusted to pH 6.5.

Techniques – Corrosion Inhibition of AA7075 and 1018 Carbon Steel

Electrochemical tests performed on AA7075 and 1018 carbon steel (CS) alloys were utilized to investigate the inhibiting effect of vanadate, cerium, molybdate and permanganate ions as well as that of selected inhibitor combinations. Anodic and cathodic potentiodynamic polarization scans and chronoamperometric measurements were carried out.

Anodic and Cathodic Potentiodynamic Scans

Anodic potentiodynamic polarization scans on as-received, 1” x 1” x 1/8” AA7075 and 1018 carbon steel sheets were performed in deaerated, 0.05 M NaCl solutions with the additions of 0, 0.005, 0.01, 0.25, 0.05 M $Ce(CH_3COO)_3$ or 0, 0.005, 0.01, 0.05, 0.1, 0.5 M $NaVO_3$ or Na_2MoO_4. The scans were performed after 1 hr. OCP measurement in a traditional three electrode cell using SCE as reference electrode and platinized niobium mesh as a counter electrode. The potential was scanned from -0.1 V vs. OCP to a vertex current of 1 mA and back to -0.1 V vs. OCP at a scan rate of 0.1 mV/s.

The cathodic scans were measured in non-deaerated, 0.05 M NaCl solutions with the same inhibitor additions as the anodic scans. The tests were performed after 1 hr. OCP measurement from 0.1 V vs. OCP to -1.5 V vs. SCE at a scan rate of 0.1 mV/s.

Two inhibitor combinations were investigated: sodium molybdate and cerium acetate (Mo/Ce) and sodium vanadate and cerium acetate (V/Ce). The two variables were the total quantity of inhibitor and the ratio of concentration. Table 5 and Table 6 present the different values of the variables for the Mo/Ce and the V/Ce combinations, respectively. The choice of total concentration and concentration ratio were based on the synergy observed between inhibitors by Chambers.[8,129] Furthermore, 0.05 M NaCl was always present in the solution investigated.

Table 5. Composition Variables of the Mo/Ce Solutions.

Solution ID	Mo ratio	Ce ratio	Total concentration (mol/L)
CeMo1	50%	50%	0.005
CeMo2	20%	80%	0.005
CeMo3	50%	50%	0.05
CeMo4	20%	80%	0.05

Table 6. Composition Variables of the V/Ce Solutions.

Solution ID	V ratio	Ce ratio	Total concentration (mol/L)
CeV1	50%	50%	0.05
CeV2	20%	80%	0.05
CeV3	80%	20%	0.05
CeV4	50%	50%	0.5
CeV5	20%	80%	0.5
CeV6	80%	20%	0.5

In some cases, the samples had to be pretreated in the Ce solution to prevent the formation of Ce precipitates when mixed with Mo or V. In these instances, the test and pretreatment solutions are designated “A” and “B”. Table 7 and Table 8 present the compositions of the solutions used to investigate the effect of the combination of Ce and V on AA 7075. Table 9 and Table 10 show the composition of solutions used to study the effect of the combination of Ce and Mo on AA 7075. The composition of the Ce, V and Mo solutions used for carbon steel 1018 are presented in Table 11, Table 12 and Table 13.

Table 7. Ce and V Combination Solutions Used for AA7075, Solution A.

Solution ID	[NaCl] (mol/L)	[$NaVO_3$] (mol/L)	Total Inhibitor (mol/L)
CeV1-a	0.05	0.025	0.05
CeV2-a	0.05	0.01	0.05
CeV3-a	0.05	0.04	0.05
CeV4-a	0.05	0.25	0.5
CeV5-a	0.05	0.1	0.5
CeV6-a	0.05	0.4	0.5

Table 8. Ce and V Combination Solutions Used for AA7075, Solution B.

Solution ID	[$Ce(CH_3COO)_3$] (mol/L)
CeV1-b	0.025
CeV2-b	0.04
CeV3-b	0.01
CeV4-b	0.25
CeV5-b	0.4
CeV6-b	0.1

Table 9. Ce and Mo Combination Solutions Used for AA7075, Solution A.

Solution ID	[NaCl] (mol/L)	[Na_2MoO_4] (mol/L)
CeMo1-a	0.05	0.0025
CeMo2-a	0.05	0.001
CeMo3-a	0.05	0.025
CeMo4-a	0.05	0.01

Table 10. Ce and Mo Combination Solutions Used for AA7075, Solution B.

Solution ID	[$Ce(CH_3COO)_3$] (mol/L)	Total Inhibitors (mol/L)
CeMo1-b	0.0025	0.005
CeMo2-b	0.004	0.005
CeMo3-b	0.025	0.05
CeMo4-b	0.04	0.05

Table 11. Ce and V Combination Solutions Used for CS1018.

Solution ID	[NaCl] (mol/L)	[$Ce(CH_3COO)_3$] (mol/L)	[$NaVO_3$] (mol/L)	Total Inhibitors (mol/L)
CeV1	0.05	0.025	0.025	0.05
CeV2	0.05	0.04	0.01	0.05
CeV3	0.05	0.01	0.04	0.05
CeV4	0.05	0.25	0.25	0.5
CeV5	0.05	0.4	0.1	0.5
CeV6	0.05	0.1	0.4	0.5

Table 12. Ce and Mo Combination Solutions Used for CS 1018, Solution A.

Solution ID	[NaCl] (mol/L)	[Na_2MoO_4] (mol/L)
CeMo1-a	0.05	0.0025
CeMo2-a	0.05	0.001
CeMo3-a	0.05	0.025
CeMo4-a	0.05	0.01

Table 13. Ce and Mo Combination Solutions Used for CS 1018, Solution B.

Solution ID	[$Ce(CH_3COO)_3$] (mol/L)	Total Inhibitors (mol/L)
CeMo1-b	0.0025	0.005
CeMo2-b	0.004	0.005
CeMo3-b	0.025	0.05
CeMo4-b	0.04	0.05

The specimens were machined out of AA7075 and 1018 carbon steel plates (see compositions in Table 3). The coupons were approximately 1” by 1” with a thickness of approximately 1/8”. They were ground to 600 grit, then degreased in methylene chloride in an ultrasonic bath for 5 minutes, rinsed with DI water and air-dried.

Anodic and cathodic potentiodynamic scans were performed in triplicates for all inhibitor combinations. During pretreatments, the samples were immersed in the Ce solution (solution “B”) for two hours. The coupons were then rinsed with DI water and mounted in a cylindrical electrochemical cell. The potentiodynamic scans were performed in solution “A”. In the case of 1018 CS in Ce/V solutions, no precipitation was observed, therefore, the potentiodynamic scans were performed in test solutions containing NaCl, $Ce(CH_3COO)_3$ and $NaVO_3$.

For the anodic scans, the test solutions were deaerated for at least one hour prior to measurement by bubbling nitrogen through them and then they were transferred into a nitrogen-purged electrochemical cell. OCP was measured for one hour, which was followed by the anodic potentiodynamic scan at a scan rate of 0.1 mV/sec. The potential was increased from -0.1 V vs. OCP to a vertex current of 1 mA, and was then reversed back to -0.1 V vs. OCP.

The cathodic scans were carried out in non-deaerated solutions after 1 hr of OCP measurement. The scan was run from 0.1 V vs. SCE to -1.5 V vs. SCE at a scan rate of 0.1 mV/sec.

Chronoamperometric Measurements

To further elucidate the effect of inhibition in cases where ORRs were inhibited, chronoamperometric measurements were performed. These tests were carried out in non-deaerated, 0.05 M NaCl solutions containing 0, 0.001, 0.025 or 0.05 M $Ce(CH_3COO)_3$ or 0, 0.005, 0.05 or 0.1 M $NaVO_3$. After a 1-hr hold at OCP, the potential was stepped down and held at values summarized in Table 14. These values corresponded to the mass-transport controlled ORR potential ranges and were determined from the cathodic scans described above. During the potentiostatic hold, the current was measured and recorded as a function of time.

Table 14. Potential Values Used in Chronoamperometric Measurements.

Material/Inhibitor	1018 Carbon Steel	7075 Aluminum Alloy
Cerium	-0.8 V vs. SCE	-1.1 V vs. SCE
Vanadate	-0.9 V vs. SCE	

Electrochemical Tests Performed on Electrode Arrays

Rotating disk electrodes were made out of an array of electrochemically active copper wires embedded in an inactive Teflon matrix in order to simulate the heterogeneous microstructure of the high strength aluminum alloys in a well-defined fashion. Table 15 summarizes the dimensions of the electrode arrays. These array electrodes we prepared using polyimide-coated pure (>99%) copper wires mounted in Teflon shims. A diagram shown in Figure 10 presents the arrangement of the electrodes in the array, while the actual arrays are shown in Figure 11.

Table 15. Rotating Disk Array Dimensions.

Array	Distance between wires (L) (mm)	Wire diameter (D) (microns)
1	2	500
2	5	500
3	2	100
4	5	100

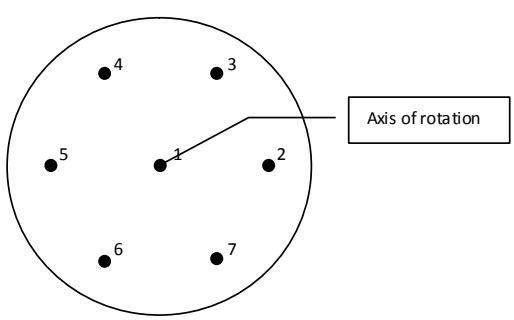

Figure 10. Schematic of the exposed surface of the copper multi-electrode array rotating disk electrode.

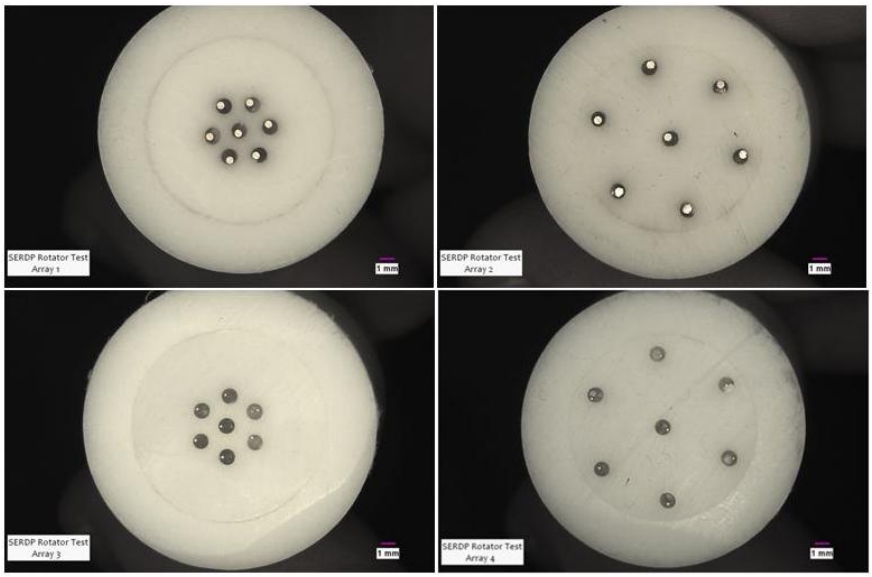

Figure 11. Photographs of different multielectrode arrays.

The arrays were polished to 600 grit, then rinsed with ethanol and air-dried. The arrays were then placed in a RDE cell setup as shown in Figure 12. Mercury/mercury sulfate reference electrodes were used to avoid contamination with chloride ions.

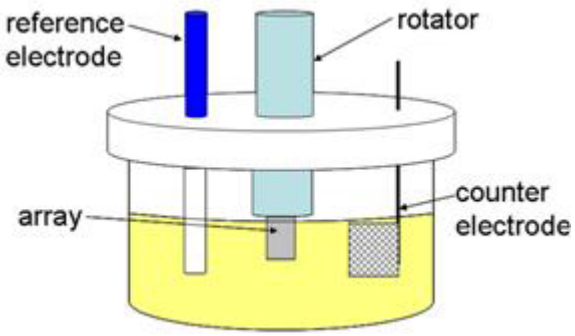

Figure 12. Schematic of the RDE array cell setup.

Four solutions were investigated as presented in Table 16. Cathodic scans were performed in non-deaerated solutions, from 0.1 V vs. OCP to -1.9 V vs. MSE at 0 rpm, 100 rpm and 1000 rpm rotation rates. All scans were performed in triplicates. The arrays were polished and reused after each test.

Table 16. Solution Compositions Used to Study the Effect of the Microstructural Heterogeneity.

Solution	Compound	Concentration (mol/L)
Ce	$Ce(CH_3COO)_3$	0.1
V	$NaVO_3$	0.1
Borate buffer (pH 8.2)	H_3BO_3	0.1

Multi Electrode Array Study of Inhibitors

An array of microelectrodes was constructed in order to replicate copper-rich intermetallics in an aluminum-rich matrix. The MEA allowed the measure of the individual current of each electrodes while they are galvanically connected through zero resistance ammeters. Figure 13(a) shows the local electrochemical behavior observed on an aluminum alloy suffering from pitting corrosion. Local anodes and local cathodes result in local electrochemical cell. Figure 13(b) shows how using MEA with microelectrodes (represented in gray) can allow the measurement of the local current while keeping the anodes and cathodes galvanically coupled.

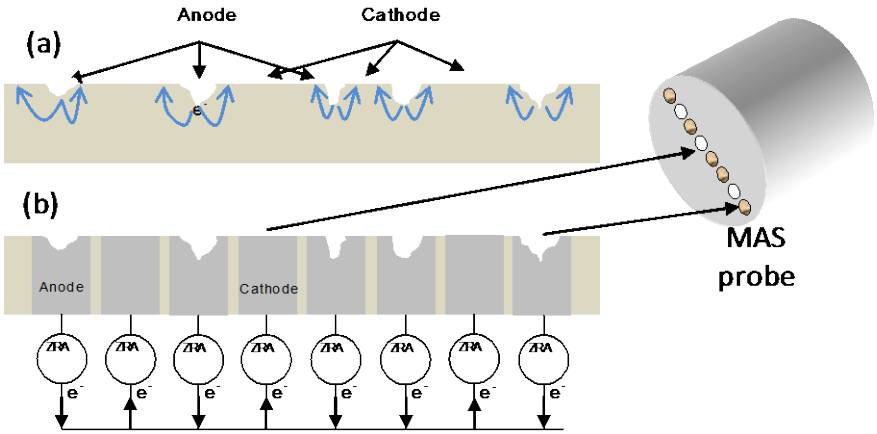

Figure 13. Schematic operating principle of MEA.

A 100 electrode MEA was assembled, containing 80 pure aluminum electrodes and 20 pure copper electrodes; 250 microns diameter wires coated with polyimide coating were used to build the array. The array simulated a planar electrode, with 100 flush mounted close packed electrodes electrically coupled through in line zero resistance ammeters. The electrodes were insulated from each other by a polyimide coating to avoid any unintended short circuit. The polyimide coating also minimized crevice corrosion between the assembly epoxy and the electrode so that attack only initiated on the polished surface. Figure 14 shows the schematic and the assembled MEA. The position of the copper electrodes was chosen so that they would be equidistant from each other and replicate homogeneously distributed intermetallic particles that could be found in aluminum copper alloys.

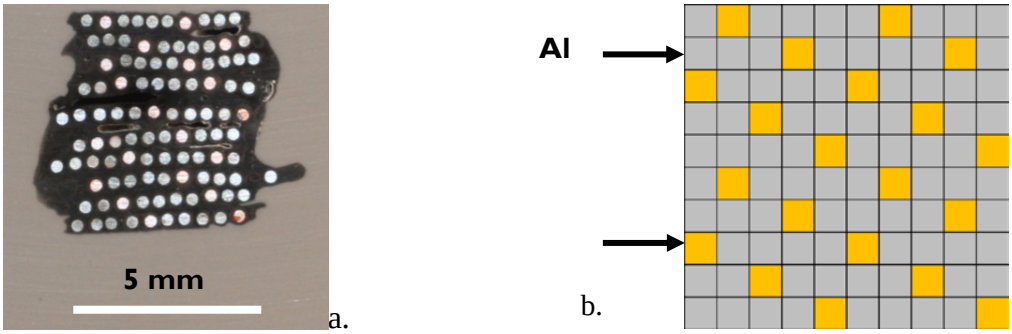

Figure 14. (a) Assembled aluminum/copper MEA and (b) schematic of the Al/Cu MEA.

The MEA was polished to 1000 grit, rinsed with DI water and air-dried shortly before any tests in order to avoid any corrosion before exposure. The MEA were polarized at -0.8 V vs. SCE and the current was measured for each electrodes. The experimental matrix for the MEA tests is shown in Table 17. Experiments were performed in triplicate at each condition. They were performed in solutions combining 0.05 M NaCl and the inhibitors ("Combined"), or the specimens were pre-treated in the inhibitor solution for twenty four hours, followed by the test in the 0.05 M NaCl ("24 hours Pre-treatment"). All inhibitors were investigated at 0.05 M under combined and 24 hours pre-treatment conditions. Experiments were also performed using vanadate at lower concentrations when combined with NaCl. The effect of pre-treatment was investigated for all inhibitors at 0.005 M.

Table 17. MEA experimental matrix.

Inhibitor concentration (mol/L)	**Combined**			**24 hours Pre-treatment**		
	Mo	**V**	**Ce**	**Mo**	**V**	**Ce**
0.05	√	√	√	√	√	√
0.01		√				
0.005		√		√	√	√

The results were analyzed by summing the current measured to determine the total anodic and cathodic current as a function of time.

Techniques – Surface Interaction with Inhibitors

Auger Electron Spectroscopy and Surface EDS

Auger electron spectroscopy and EDS were performed on 1"x1" specimens of aluminum alloys 7075 polished to 1000 grit that had been exposed to cerium acetate, sodium vanadate or sodium molybdate solutions. The 0.05 mol/L and 0.005 mol/L solutions were investigated in order to assess the effect of the inhibitors concentration on their interaction with the surface. The solutions were prepared and stored in nitric acid decontaminated glassware. The specimens were polished, rinsed with DI water and dried with compressed air. The specimens were stored in individual sample plastic bags containing desiccant bags. The specimens were treated in the inhibitor solutions for 24 hours.

Auger electron spectroscopy was performed on freshly treated specimens in order to measure the presence of vanadium, cerium or molybdenum on the surface of exposed panels. This was directly followed by EDS surface analysis. In order to assess the possible absorption vs. adsorption mechanism, sputtering was performed on the same specimens using Auger electron

spectroscopy. Sputtering is performed at a known removal rate, allowing the removal of a known thickness from the surface of the specimen. This was performed for 10 seconds and a further 30 seconds at 400 Å/min.

EDS mapping was also performed on specimens exposed to 0.05 mol/L of cerium acetate, sodium molybdate or sodium vanadate. EDS mapping is used to measure qualitatively the amount of a compound as a function of the location over a predetermined area. This results in a monochrome image for each compound with the intensity being proportional to the amount of the compound present. Multiple specimens were prepared from sheets of AA7075 and mounted in conductive epoxy. Each specimen was polished, rinsed with ethanol and air-dried. The specimens were marked in order to be able to compare the same area and assess whether the inhibitors were precipitating preferentially on intermetallic particles and what may be the composition of those intermetallic particles. Two horizontal and two vertical scribes were marked on the specimens to highlight an area one to two millimeters across. An additional line was marked in order to indicate the loading direction of the specimen in the SEM.

Multiple sets of images were taken, one large-scale image (approximately 20 μm x 20 μm) was used to clearly identify the zone of interest. The large-scale image was chosen so that it would contain multiple intermetallic particles. EDS mapping was performed on the large-scale area to investigate aluminum, copper and iron. No thorough study has been performed in the case of AA7075 to identify the composition of the intermetallic particles that may have an active role in corrosion mechanism. However, it is well documented that copper and iron containing particles play a role in corrosion of AA2024. Consequently, those two elements were chosen in addition to aluminum for EDS mapping of AA7075. Higher scale images and map scans of individual intermetallic particles were taken in order to obtain better quality EDS data.

The specimens were then exposed to 0.05 mol/L cerium acetate, sodium vanadate or sodium molybdate solutions for twenty four hours. The specimens were then rinsed with DI water and air-dried, before being stored in dry sample plastic bags containing desiccant bags. EDS mapping was then performed again on the same area and intermetallic particles in order to identify the interaction of the inhibitor with AA7075.

Scanning Kelvin Probe

The interaction between the corrosion inhibitor and copper was studied using a SKP before and after exposure to inhibitor and a controlled atmospheric corrosive environment. The SKP is a non-contact non-destructive technique used to measure the work function which can be related to the surface condition.

The specimens were 1cm x 1cm coupons from a pure copper sheet. Specimens were attached to an electric cable using conductive epoxy. This was done in order to connect the specimens to the SKP equipment. The specimens were then mounted in epoxy and marked with an individual identification number inscribed on the side of the mount. The specimens were polished manually to 1000 grit before being rinsed with deionized water (DI), cleaned with acetone and air-dried. All the specimens were stored in a desiccator before the experiments.

The specimens were marked with one horizontal and one vertical line using a razor blade in order to be able to perform the scans on the same areas. The first series of scans were performed on the untreated specimens. Two types of scans were performed: topographic and work function.

The topographic scan was performed in order to identify any physical defect on the surface. The work function scan was performed to measure the effect of the inhibitor.

The specimens were then exposed to 0.05 M sodium vanadate, sodium molybdate or cerium acetate for 24 hours. The inhibitor solutions were prepared in diluted nitric acid cleaned glassware in order to avoid any contamination with outside chemicals or cross-contamination between inhibitors.

The specimens were kept in the sealed container with a well-controlled environment for 7 days. Scans were then performed in order to determine the topography of the surface as well as the impact of the exposure to the inhibitors and the humid environment on the work function.

Techniques – Mott-Schottky

Mott-Schottky testing was performed on 1” x 1” specimens of aluminum alloys 7075 polished to 1000 grit, followed by rinsing with ethanol and air-dried. The test cell and the additional non-metallic and non-plastic fittings in contact with the solutions were cleaned using nitric acid solution (50% diluted with water) in order to avoid any potential chloride contamination. The metallic and plastic fittings were replaced with new parts to avoid contamination. The large plastic parts that make the test cell were thoroughly cleaned with water and detergent before being rinsed with DI water. The test solutions were prepared in decontaminated glassware that had been prepared in the same way described above. The tests were performed in borate buffer, cerium acetate, and sodium vanadate. Tests in borate buffer provided control data in the absence of inhibitors. The borate buffer was required in order to support charge transfer in the electrolyte in the absence of other ions. The effect of the inhibitor concentration was studied by performing the experiments in 0.05 M and 0.005 M cerium or vanadate solutions. A mercury/mercury sulfate reference electrode was used inside a Luggin probe filled with borate solution in order to avoid any chloride contamination.

Mott-Schottky analysis was performed within the passive range of the alloy where the capacitance is primarily the result of the oxide space charge layer. It is therefore important to identify the potential range of the passive region. Potentiodynamic scans were first performed in the deaerated tests solution in order to determine the passive range potential. The test solutions were deaerated with nitrogen for one hour before being transferred to the purged test cell. The OCP was measured for one hour and the anodic scan was performed from -0.1 V vs. OCP to a current of 1 mA. The passive range was identified when the current density was below 10^{-5} $A \cdot cm^{-2}$, and the relevant potential range was used for the Mott-Schottky analysis.

Mott-Schottky analysis is a combination of EIS scans performed at various frequencies and at various potentials. The first EIS scan is performed at the highest potential within the passive range. The potential is decreased down to the lowest value in a step by step manner while EIS scans are performed at each step. The test solution and test cell are both individually deaerated with nitrogen for one hour before the solution is transferred to the test cell. The specimen is left at OCP and the current is measured for twenty hours, until the current is steady. The Mott-Schottky experiment was performed within the passive range identified using potentiodynamic scans, with 50 mV steps. Each EIS scan was performed at frequencies of 3, 10, 30, 100, 300, and 1000 Hz.

Techniques – Atmospheric MEA

An aluminum/copper MEA was exposed to an environment of controlled relative humidity and temperature after being treated with various inhibitors. The MEA was composed of 12 copper electrodes and 48 aluminum electrodes. The arrangement of the electrodes is shown in Figure 15. All the electrodes were connected to each other through individual zero resistance ammeters (ZRAs). The details of the MEA are described in the chapter "Multi Electrode Array Study of Inhibitors".

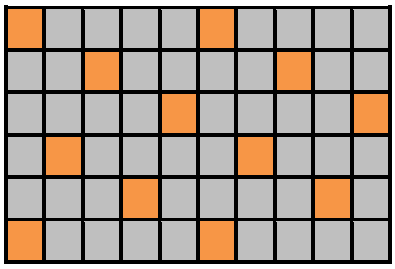

Figure 15. Schematic of the aluminum/copper MEA used for atmospheric testing.

The array was hand polished to 1000 grit, rinsed with DI water and air-dried. This was performed just prior to the experiments in order to avoid unwanted deterioration of the electrodes. The MEA was exposed to the inhibitor solution for 24 hours. The inhibitor solutions were 0.05 M sodium vanadate, 0.05 M sodium molybdate or 0.05 M cerium acetate. Experiments were also performed on a bare MEA to be used as a control.

NaCl (2.7 mg) was placed over the MEA within a 0.24 inch ID o-ring. This was done to create an aggressive atmospheric environment. The loaded MEA was then put in an environmental chamber. The relative humidity of the chamber was measured by using an internal sensor. The data was relayed to a laptop running Labview which controlled a water atomizer that injected aerosol into the chamber. The water was atomized away from the specimens in order to avoid droplets on the specimen surface. The specimens were only inserted in the chamber when the relative humidity reached its desired value. Data acquisition was started 5 minutes prior to placing the MEA into the chamber for each test. Data was collected every 60 seconds.

The MEA was exposed to a high relative humidity for 3 hours before being decreased to 45% for 2.5 hours. The experimental matrix is shown in Table 18.

Table 18. MEA atmospheric testing experimental matrix.

	2.5 hrs 60% RH 3 hrs 40% RH	**2.5 hrs 70% RH 3 hrs 40% RH**	**2.5 hrs 80% RH 3 hrs 40% RH**	**2.5 hrs 90% RH 3 hrs 40% RH**
0.05 M vanadate	√	√	√	√
0.05 M molybdate	√	√	√	√
0.05 M cerium	√	√	√	√
No inhibitors	√	√	√	√

Results and Discussion

Results

Thermodynamic Calculations of Inhibitor Solutions (Speciation)

The composition of inhibitor solutions at different concentrations was calculated using a thermodynamic software package. These calculations were essential to enable the determination of the dominant species and potential precipitates that can form during pretreatment or electrochemical measurements. Once the chemical composition of the inhibitor solution is known, the elucidation of the inhibiting mechanism becomes possible.

The bulk solution pH varies slightly as a function of the concentration of the various inhibitors. Measured pH for various concentration are shown in Figure 16.

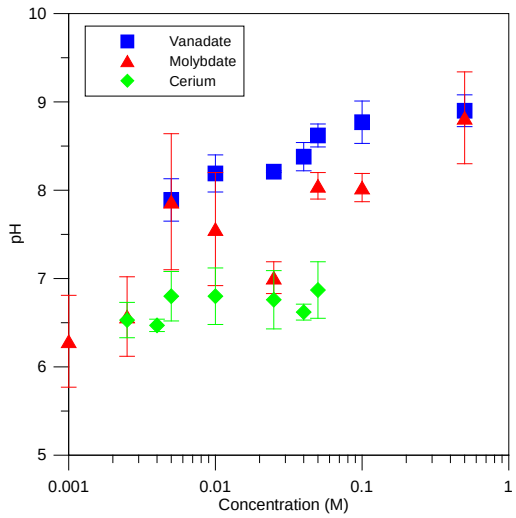

Figure 16. Bulk solution pH as a function of inhibitor concentration.

The chemical species vs. pH (speciation) diagram of 0.01 M and 0.05 M sodium vanadate solution is shown in Figure 17.

As Figure 17 indicates, the solution chemistry of vanadates is very complex. Several oxo- and hydroxo- ions form as the pH of the solution changes. Slight changes in pH can cause significant changes in solution composition.

The speciation diagram of 0.01 M cerium acetate solution is shown in Figure 18.

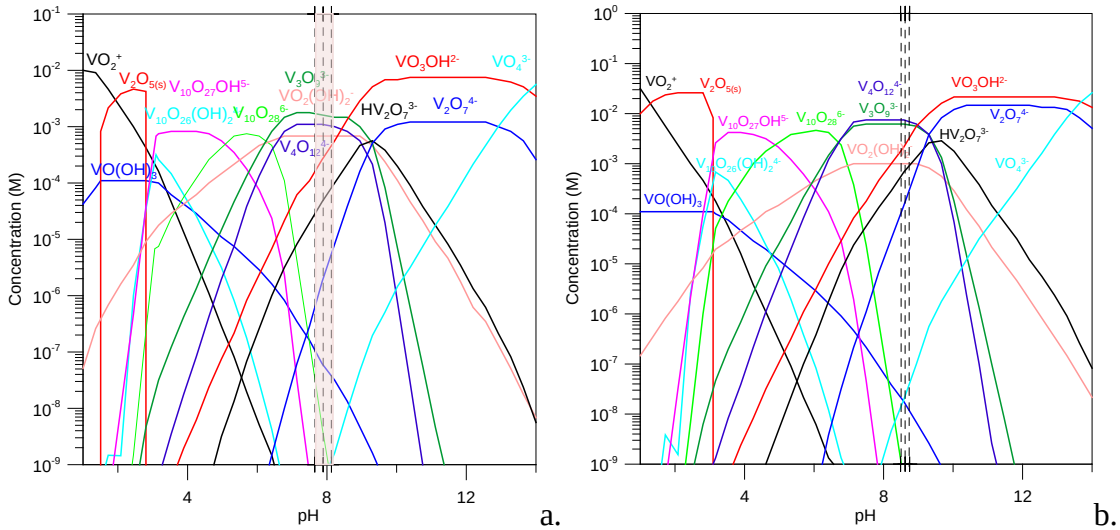

Figure 17. Speciation diagram of a. 0.01 M and b. 0.05 M sodium vanadate solution. The natural pH of the inhibitor solution is within the pink shaded area.

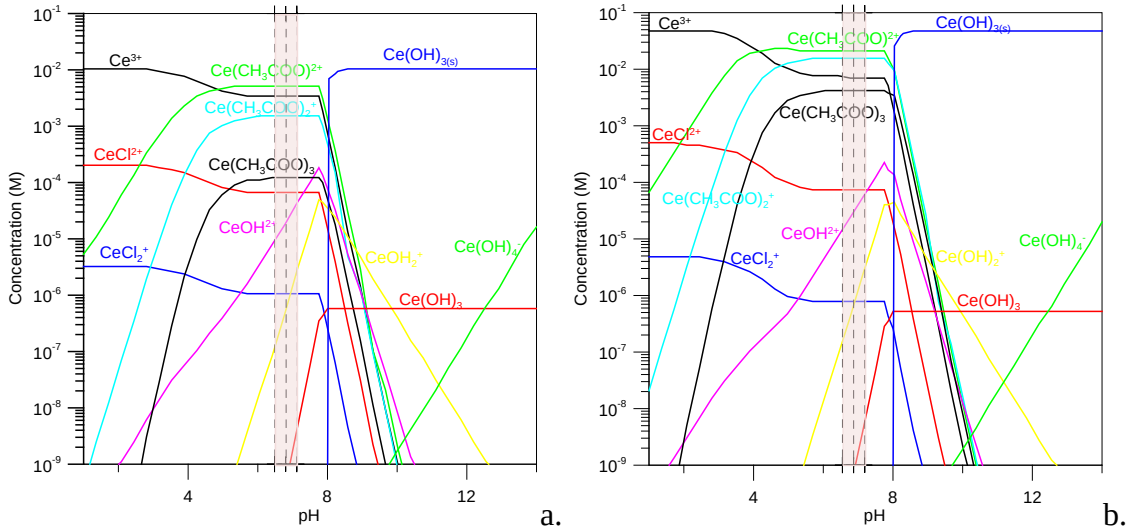

Figure 18. Speciation diagram of a. 0.01 M and b. 0.05 M cerium acetate solution. The natural pH of the inhibitor solution is within the pink shaded area.

The predominant species at the natural pH of the bulk solution are soluble Ce-acetate complex ions. As the pH increases, however, insoluble cerium hydroxide ($Ce(OH)_3$) occurs, which forms a precipitate film on the surface that can act as a barrier for the diffusion of aggressive ions and oxygen. This film formation has been observed on top of certain intermetallic particles upon local pH increase that occurred due to the ORR (see Equation 13).

$$O_2 + 2H_2O + 4e \rightarrow 4OH^- \qquad \textbf{Equation 13}$$

Figure 19 shows the speciation diagram of 0.01 M and 0.05 M sodium molybdate.

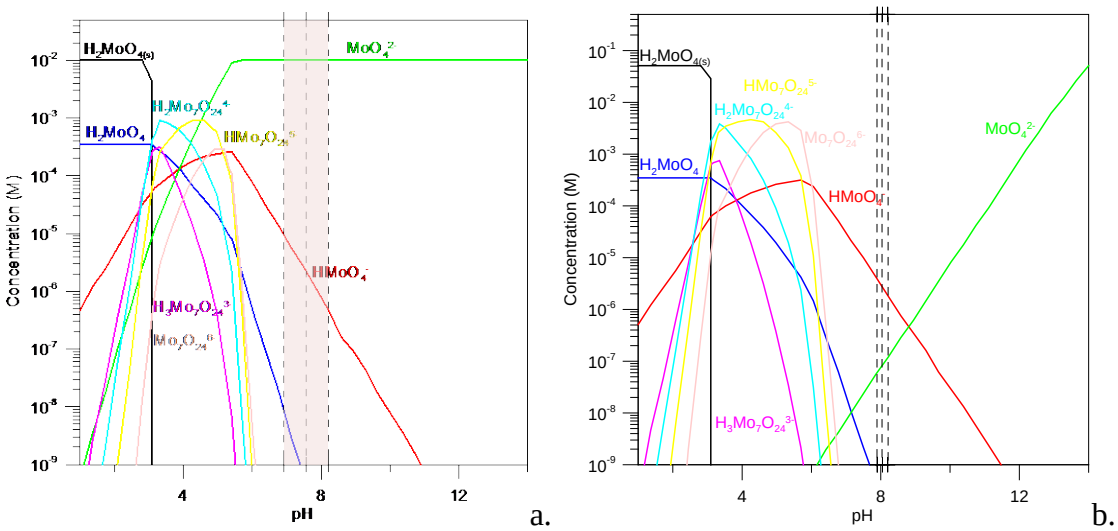

Figure 19. Speciation diagram of a. 0.01 M and b. 0.05 M sodium molybdate. The natural solution pH range is shaded in pink.

The predominant species in the case are MoO_4^{2-} ions, which are most likely adsorbed on the surface layer of the oxide film of the alloy during exposure.

The permanganate is a very strong oxidizer due to its very high potential as shown in Figure 20. When permanganate is added to solution in contact with AA2024-T351 at a lower potential, it is reduced and undergoes several possible electrochemical reactions. Over all the ranges of pH, MnO_4^- is likely to be reduced to manganese dioxide (see Equation 14).

$$MnO_4^- + 4H^+ + 3e^- \rightarrow MnO_2 + 2H_2O \qquad \textbf{Equation 14}$$

Several additional electrochemical reactions can further reduce the oxide to form Mn_2O_3. At low pH and potential, the oxides most likely dissolve as Mn^{2+}, however, experimental data on exact values has not been determined. The results of the equilibrium speciation calculations are shown in Figure 21. These speciation diagrams indicate predominant species at -0.5 V vs. SCE, the approximate value of the observed OCP for AA2024-T351 in 0.05 M NaCl solution with permanganate. It can be seen that at pH values above 8.5, the stable species are $Mn(OH)_2$, which is a precipitate. This suggests that this precipitate can form electrochemically and can remain stable at high pH cathodic sites associated with certain intermetallic particles.

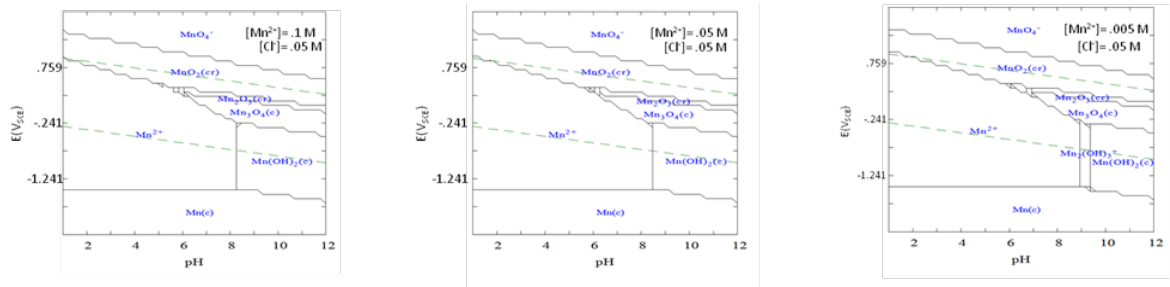

Figure 20. E-pH diagrams of permanganate calculated at 0.1, 0.05 and 0.005 M concentrations.

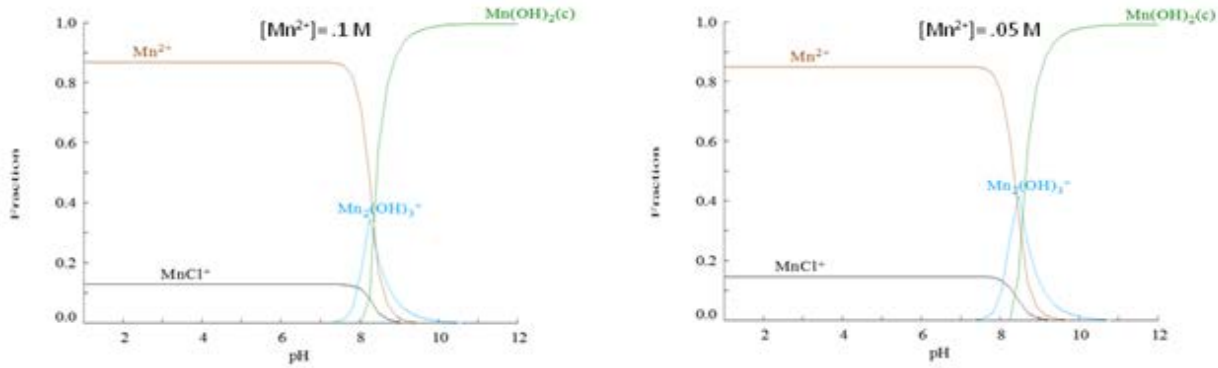

Figure 21. Speciation diagrams of manganese calculated at -0.5 V vs. SCE for two different concentrations: 0.1 and 0.05 M.

In the case of aluminum alloy 2024, the corrosion process is highly dependent on local electrochemical cells surrounding intermetallic particles such as S-phase (Al_2CuMg). Due to pitting corrosion and the resulting separation of the anode and the cathode, the local pH can change drastically between highly acidic (pH<2 in the pit) and highly alkaline (pH>9 over cathodic sites). Consequently, the inhibitor-based compounds present will vary greatly as a function of the location. An example of the impact of the localized pH on the compounds present is shown for cerium in Figure 22.

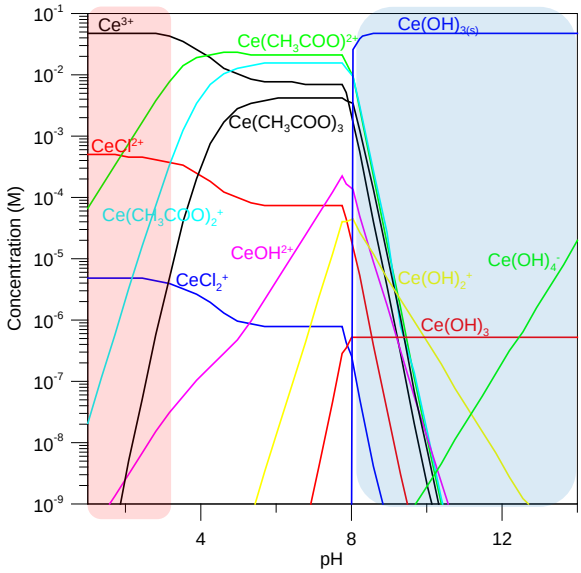

Figure 22. Speciation diagram of 0.05 M cerium acetate. The pink highlights the region that would be present in and near an active anodic pit. The blue highlights the region present over a cathodic intermetallic particle.

Corrosion Inhibition of AA2024 using Permanganate and Vanadate

The objective of this work was to understand the viability of permanganate and vanadate as stand-alone inhibitors in full immersion. We examined both pretreatments with permanganate, to examine the effects of the protective manganese oxide barriers, and exposures in the presence of the permanganate ion to distinguish the effects of the soluble ion from the manganese oxides. Open circuit full immersion exposure experiments were conducted. Surface chemical compositions and deposit morphologies were also investigated. Copper replating was investigated to indirectly explore the inhibition of Cu-rich phase dealloying. E_{pit} were determined and ORR kinetics were extracted using the Koutecky-Levich correction. Theoretical modeling with Guishi and membrane models was performed to analyze ORR kinetics obtained from RDE experiments. Electron transport through the solid/electrolyte-interface was also characterized. Raman spectroscopy and galvanostatic reductions were used to attempt to characterize the valence states of protective manganese oxides.

The inhibition mechanism of vanadate on AA2024 was investigated. A comprehensive study of the speciation of vanadate in aqueous solutions of sodium chloride other than those used in prior NMR studies was completed. Potentiodynamic testing was performed to determine the effect of vanadate inhibition on cathodic current density and E_{pit}. Cathodic results were analyzed using the Koutecky-Levich approach to separate charge and mass transport contributions to ORR, Gueshi modeling, and absorption isotherms.[32,90,130–133]

Effects of Permanganate during OCP exposures of AA2024 in 50 mM NaCl Solution

Figure 23 shows as-polished AA2024-T351 and the subsequent surface damage caused by 24 hour exposure to 0.05 M NaCl solution.[54,57] Figure 24(a) shows the distribution of intermetallic particles (the lighter regions, higher Z number) on bare AA2024-T351. Figure 24(b)shows the effects of pretreatment with 0.1 M potassium permanganate on the same region of intermetallic constituent particles as Figure 24. The particles studied by energy dispersive spectroscopy can be seen in the secondary electron image shown in Figure 24 (a and b). Table 19 and Figure 25(a and b) show the EDS qualitative chemical analysis of the intermetallic particles before and after pretreatment. Manganese oxide growth is apparent on many of the intermetallics and is shown to be deposited specifically on the Cu-rich phases as opposed to the aluminum matrix phase. Qualitative chemical data from EDS shows coverage of theta, sigma, and Cu-Mn-Fe-Al phases by a manganese oxide of unknown valence state. Permanganate forms thick oxide deposits over copper-rich intermetallics in AA2024-T351 when pretreated. The deposition is characterized by spherical caps over small (~0.5 μm) intermetallics and conformal layers with terraces over larger particles (5 μm) (Figure 24(b).

Table 19. Compilation of EDS data for AA2024-T351 intermetallic particles in Figure 24 a) and b), before and after pretreatment in 0.1 M $KMnO_4$.

Intermetallic phase	**Particle #**	**Manganese Oxide Cap**	**Mn enrichment (EDS)**
AlCuMg phase	5, 6	Yes	Yes
Al(Cu,Mn,Fe,Si) phase	1, 2, 3	Yes	Yes
AlCu phase	4	Yes	Yes
Al(Cu,Mn,Fe,Mg) phase	7, 8	Yes	Yes

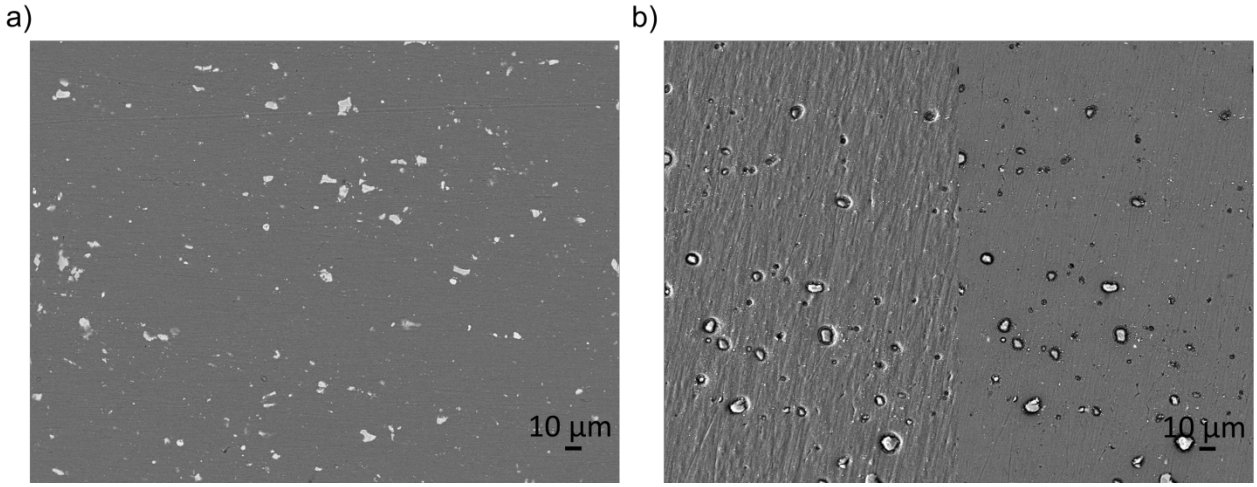

Figure 23 (a) The as-polished (1200 grit) AA2024-T351 and the subsequent surface damage caused by 24 hour exposure to 0.05 M NaCl solution. (b) The damaged specimen image is distorted laterally but includes a secondary electron image and a backscattered electron image. It clearly shows intermetallic trenching.

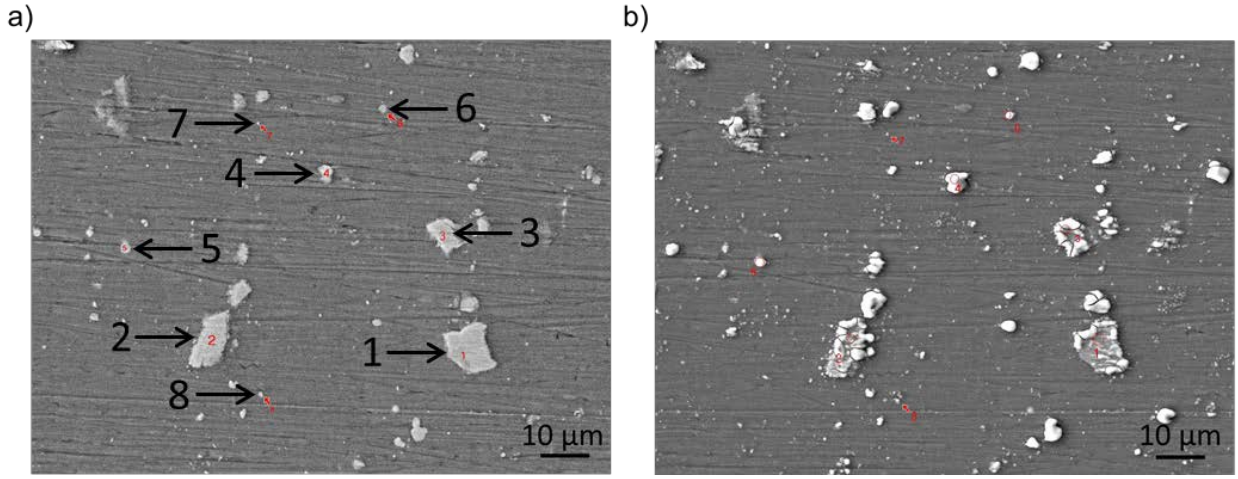

Figure 24 (a) AA2024-T351 polished to 1200 grit with indication of EDS sites labeled 1-8. (b) after 24 hours pretreatment in 0.1M $KMnO_4$. Indication of EDS sites labeled 1-8.

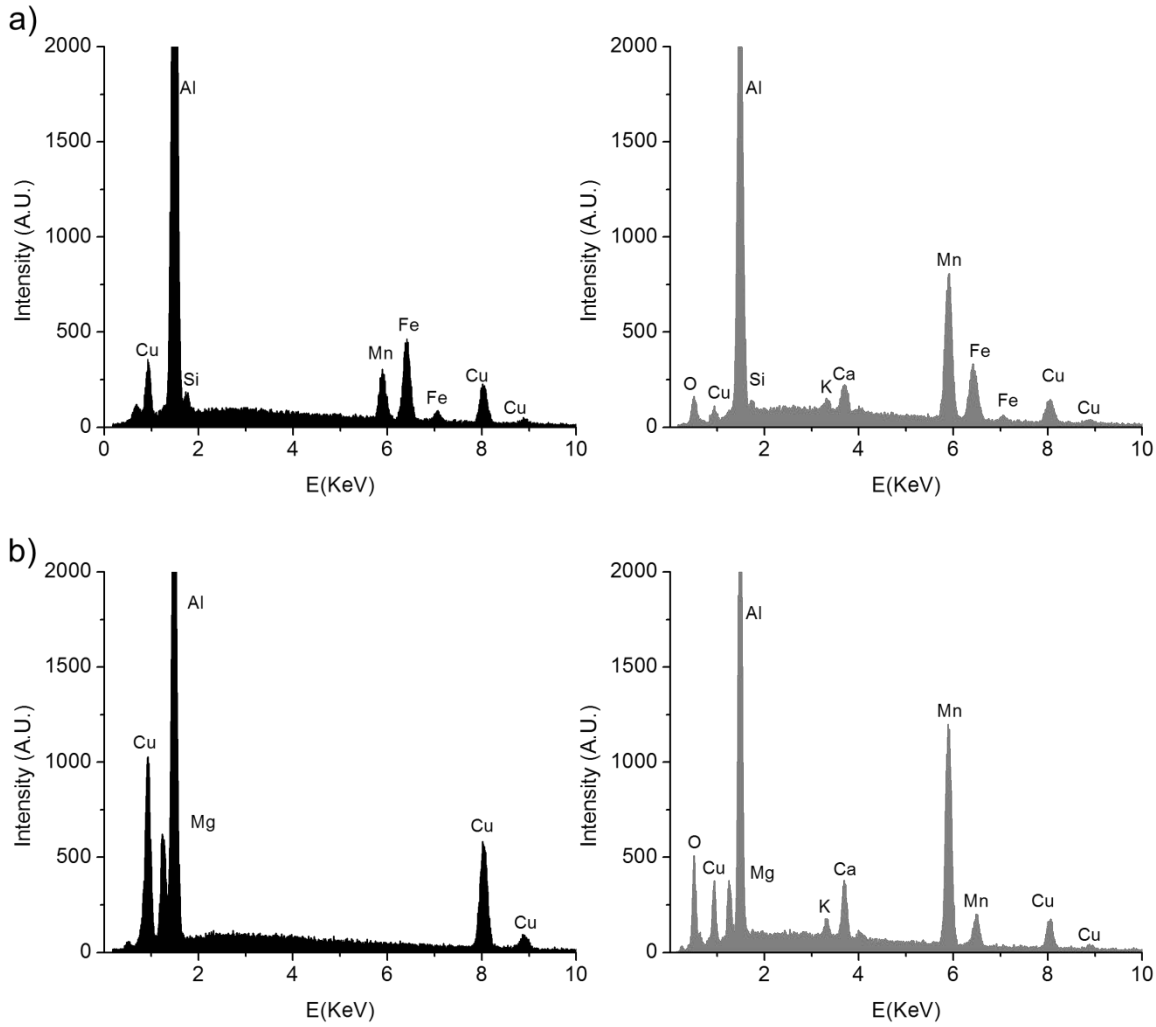

Figure 25 (a) Intermetallic particle 1 from Figure 24. (b) Intermetallic particle 5 from Figure 24. The left spectrum is taken from an untreated sample, the right, a pretreated sample.

Figure 26 shows the result of 24 hours of pretreatment in permanganate in a Cl^--free environment. As the concentration of permanganate increases, the size of the intermetallic cap decreases. Figure 27 shows the results of subsequent exposure to 0.05 M sodium chloride solution after 24 hour pretreatment in potassium permanganate. Intermetallic trenching has been inhibited at high concentrations of permanganate (0.1 M) while the lower concentrations did not produce similar inhibition.

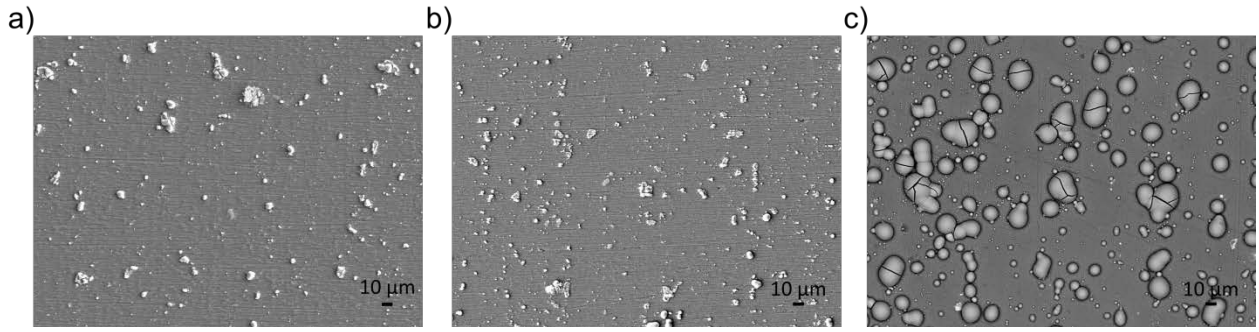

Figure 26. (a) AA2024-T351 pretreated with 0.1 M $KMnO_4$ for 24 hours (secondary electron image). (b) AA2024-T351 pretreated with 0.05 M $KMnO_4$ for 24 hours (secondary electron image). (c) AA2024-T351 pretreated with 0.005 M $KMnO_4$ for 24 hours (backscattered image).

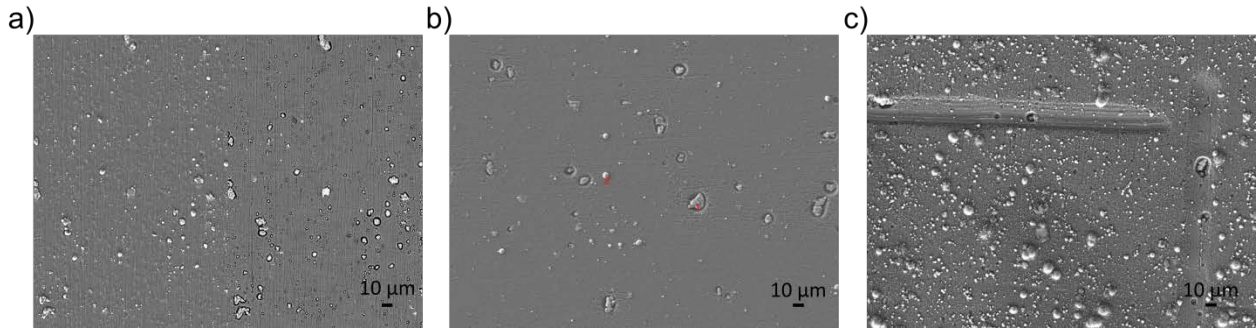

Figure 27 (a) AA2024-T351 exposed to 0.05 M NaCl for 24 hours after pretreatment in 0.1 M $KMnO_4$ for 24 hours. (b) AA2024-T351 exposed to 0.05 M NaCl for 24 hours after pretreatment in 0.05 M $KMnO_4$ for 24 hours. (c) AA2024-T351 exposed to 0.05 M NaCl for 24 hours after pretreatment in 0.005 M $KMnO_4$ for 24 hours.

Figure 28 shows the results of exposure to aggressive solution (0.05 M sodium chloride) with the inhibitor in-situ at the previously stated concentrations. Figure 29 shows the intact aluminum matrix surrounding the intermetallic particles after the manganese oxide caps have been removed by a hard-bristled brush.

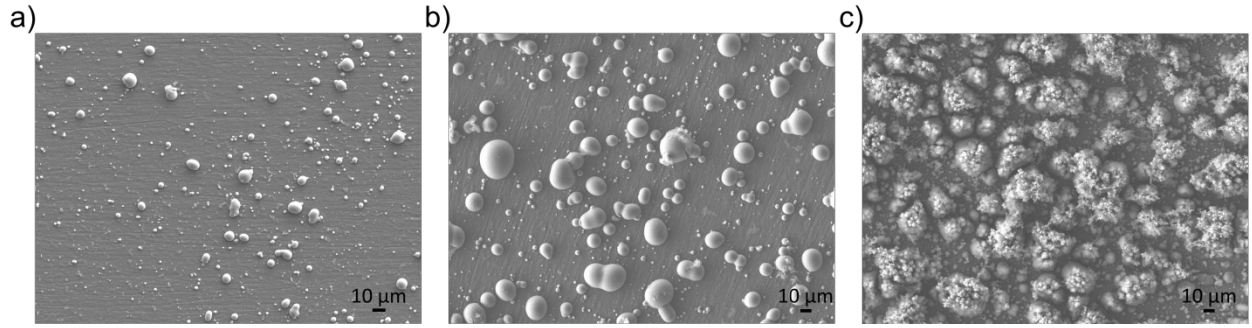

Figure 28 (a) AA2024-T351 exposed to 0.05 M NaCl with 0.1 M $KMnO_4$ in-situ for 24 hours. (b) AA2024-T351 exposed to 0.05 M NaCl with 0.05 M $KMnO_4$ in-situ for 24 hours. (c) AA2024-T351 exposed to 0.05 M NaCl with 0.005 M $KMnO_4$ in-situ for 24 hours.

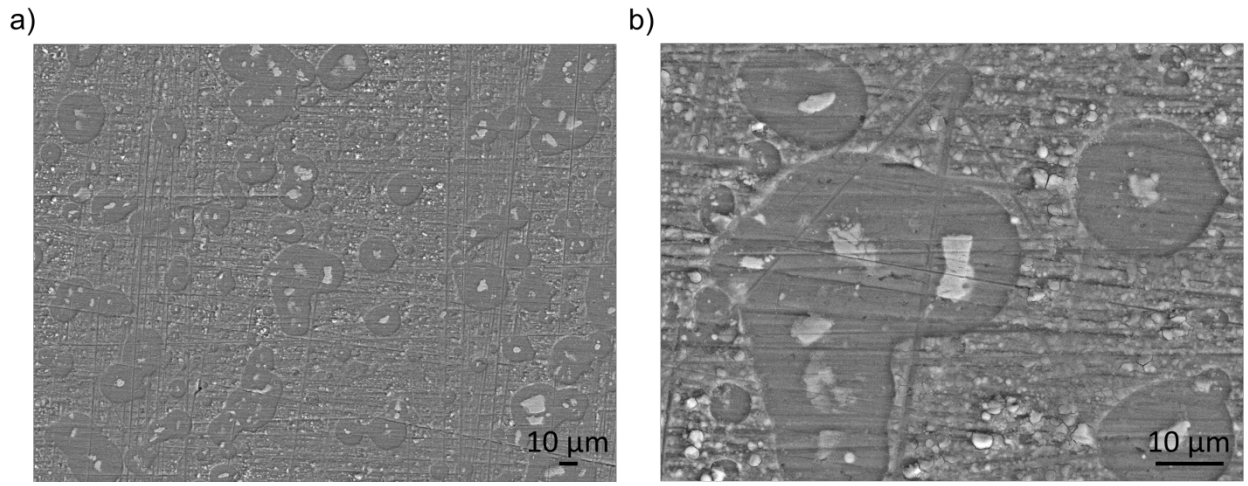

Figure 29. AA2024-T351 exposed to 0.05 M NaCl solution with 0.05 M $KMnO_4$ in-situ for 24 hours with manganese oxide caps removed. The manganese caps reduce intermetallic trenching and leave the matrix that was covered looking pristine.

OCP data was collected for 1 hour after a 24 hour exposure to 0.05 M sodium chloride solution with inhibitor in solution (Figure 30). The OCP was measured in the same solution. The OCP for all cases with in-situ permanganate are slightly higher than for AA2024-T351 in 0.05 M sodium chloride solution (-0.53 V vs. SCE). The average OCP for 6 samples from the highest permanganante concentration to the lowest was as follows: -0.46 V,-0.48 V, and -0.49 V vs. SCE. The lower the concentration the less stable the OCP was. The higher the concentration, the higher the OCPs tend to be which is expected given the oxidizing capability of MnO_4^-.

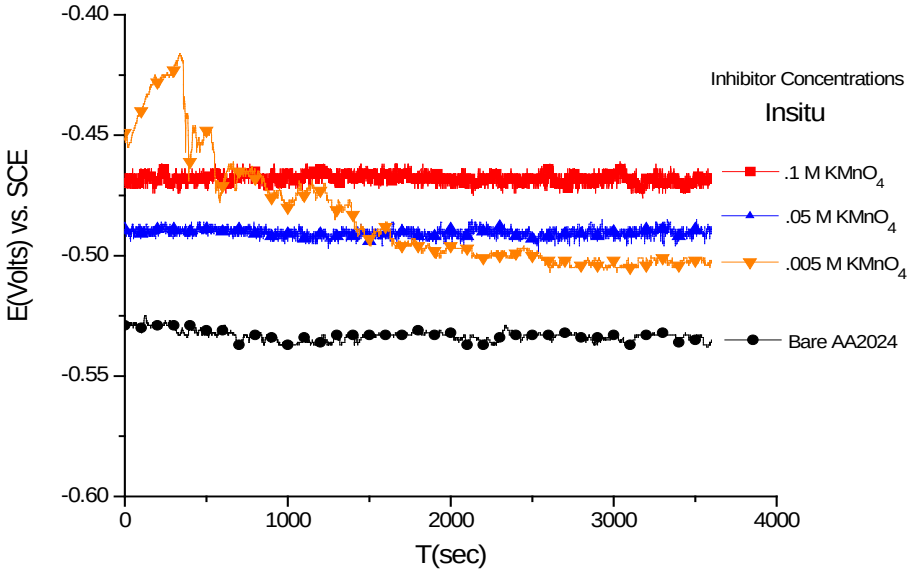

Figure 30. The OCP was recorded for one hour after 24 hours at OCP in 50 mM sodium chloride solution with inhibitor the concentrations reported.

The OCP was also measured for one hour after pretreatment for 24 hours in potassium permanganate but without MnO_4^- in the OCP test solution. The samples were removed from pretreatment, rinsed thoroughly, and open circuit was measured in 0.05 M sodium chloride solution. As Figure 31 shows, the OCP after such a pretreatment decreases to lower potentials over time, relative to when it is first exposed to the full immersion test. This may be the result of residual permanganate, stored in the oxide, being reduced. As the source is depleted the reduction reaction slows and the OCP drops. Quite negative potentials are reached after this process has occurred. However, the Al alloy is not attacked. This is shown by the anodic upward scan after the open circuit measurement and will be discussed in the section on anodic polarization behavior.

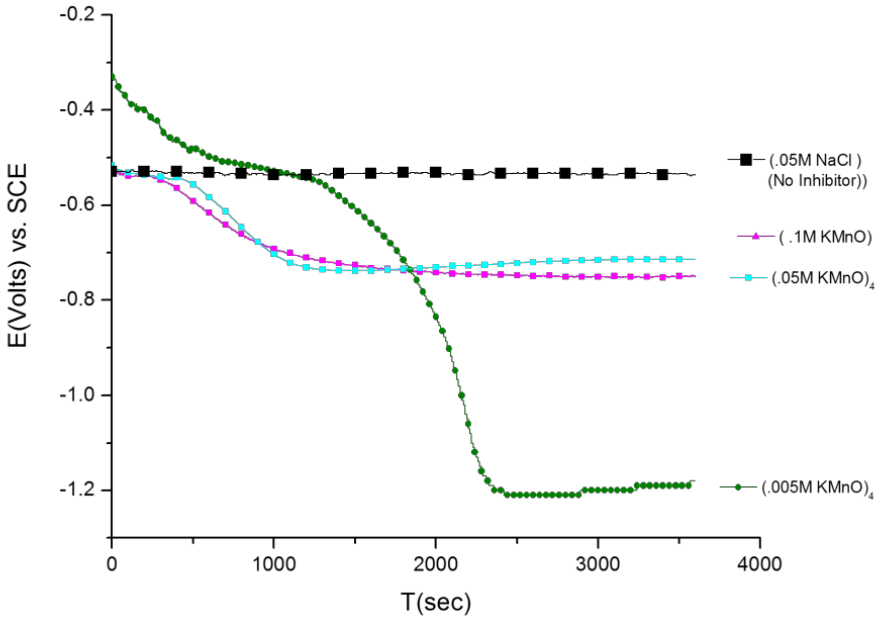

Figure 31. OCP measurements for pretreated AA2024-T351 after 24 hours in varying concentrations of $KMnO_4$. OCP measured in 0.05 m NaCl solution. Experiments have been run 10 times and show great reproducibility.

Inhibition of Copper Replating

Copper replating was also investigated on AA2024-T351 surfaces after OCP exposures using the CV method to assay the copper coverage. Figure 32 shows the cyclic voltammetric analysis of high-purity copper, high-purity aluminum, untreated AA2024-T351, and AA2024-T351 etched in 0.05 M NaCl solution for 24 hours.

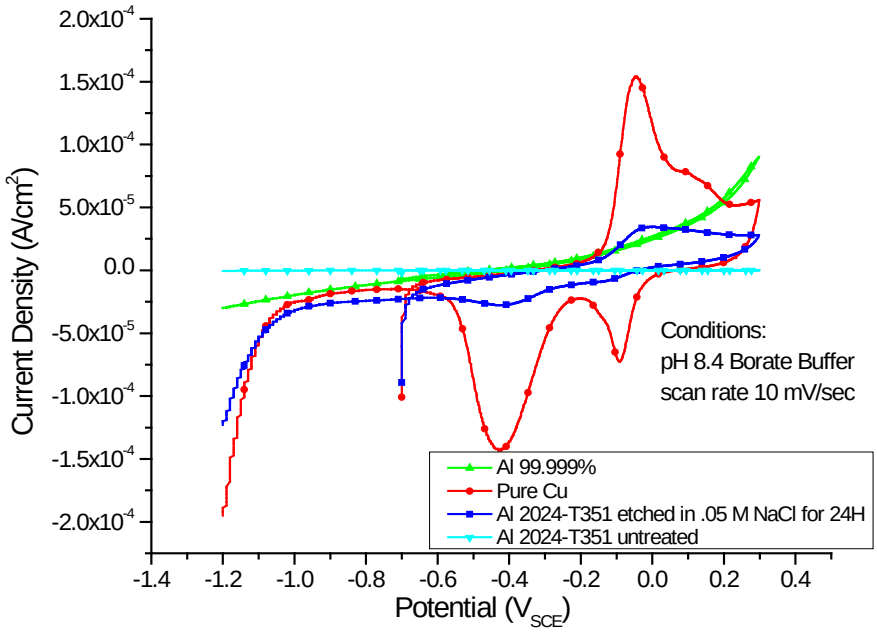

Figure 32. Baseline CV of high-purity Cu, high-purity Al, AA2024-T351, and AA2024-T351 etched for 24 hours in 0.05 M NaCl solution.

As expected, the high-purity copper shows large current peaks when copper changes valence state from 0 to (I) and then to (II). The etched AA2024-T351 shows a marked increase in the 0 V_{SCE} oxidation peak as compared to the freshly polished AA2024. The anodic peaks reflect the surface coverage of copper brought about by corrosion and thus is an indication of copper replating.[68] Figure 33 shows the results of 24 hour exposure with inhibitor in-situ and after 24 hours of pretreatment. The results of the CV tests are summarized in the bar plots of Figure 34. Permanganate solution phase additions are the most effective at reducing Cu release by corrosion and/or replating. The suppression of copper replating increases with concentration in solution. This agrees with observations of corrosion damage. Optical microscopy after exposure (Figure 35) shows pitting in the pretreated samples exposed to 0.05 M chloride while none is evident for the in-situ experiments. The worst case of pitting is seen after pretreatment in 100 mM MnO_4^- solution followed by exposure to 0.05 M chloride solution. This pretreatment was shown to have the smallest manganese oxide caps in Figure 26 A.

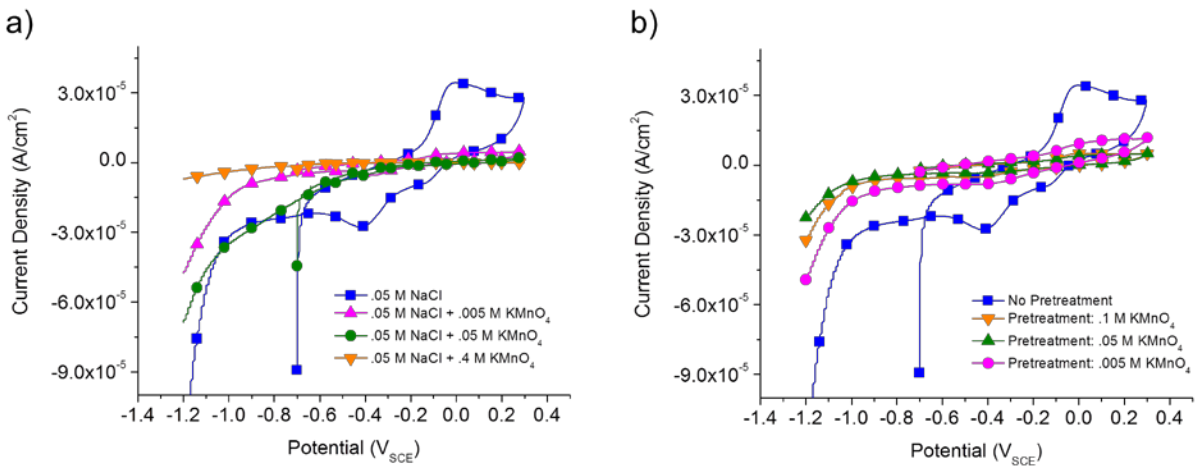

Figure 33. (a) CVs of AA2024-T351 etched for 24 hours in 0.05 M NaCl solution with varying inhibitor concentration in solution, 0.4 M, 0.05 M, 0.005 M KMnO4, and no inhibitor. (b) CVs of AA2024-T351 etched in 0.05 M NaCl solution for 24 hours after pretreatment for 24 hours in varying inhibitor concentration: 0.1 M, 0.05 M, 0.005 M $KMnO_4$.

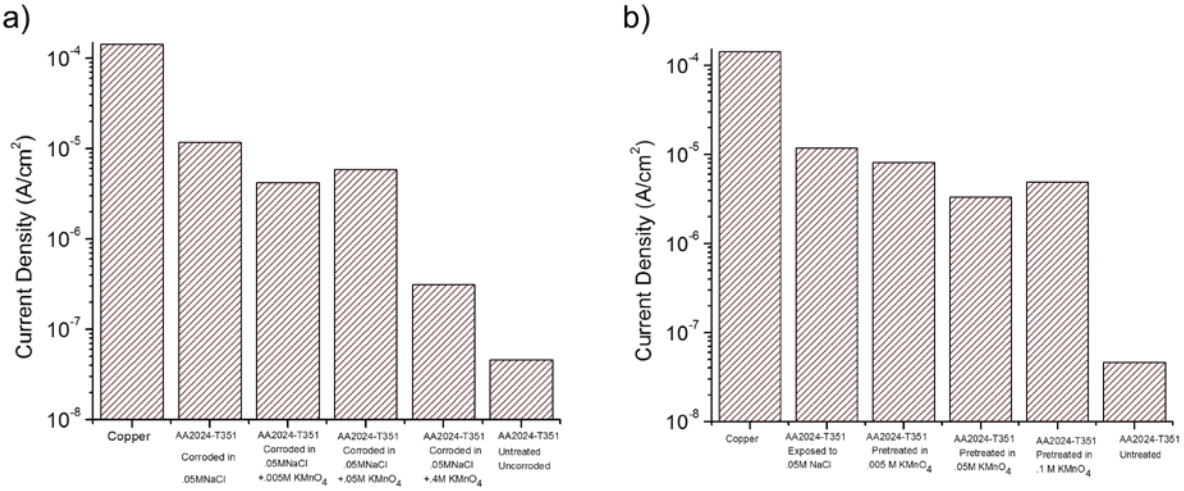

Figure 34. The relative intensities of the Cu^{1+} reduction on the AA2024-T351 surface when corroded with the MnO_4^- ion in solution for 24 H in 0.05 M NaCl (A) and with MnO_4^- inhibitor pretreatment followed by exposure for 24 H in 0.05 M NaCl (B).

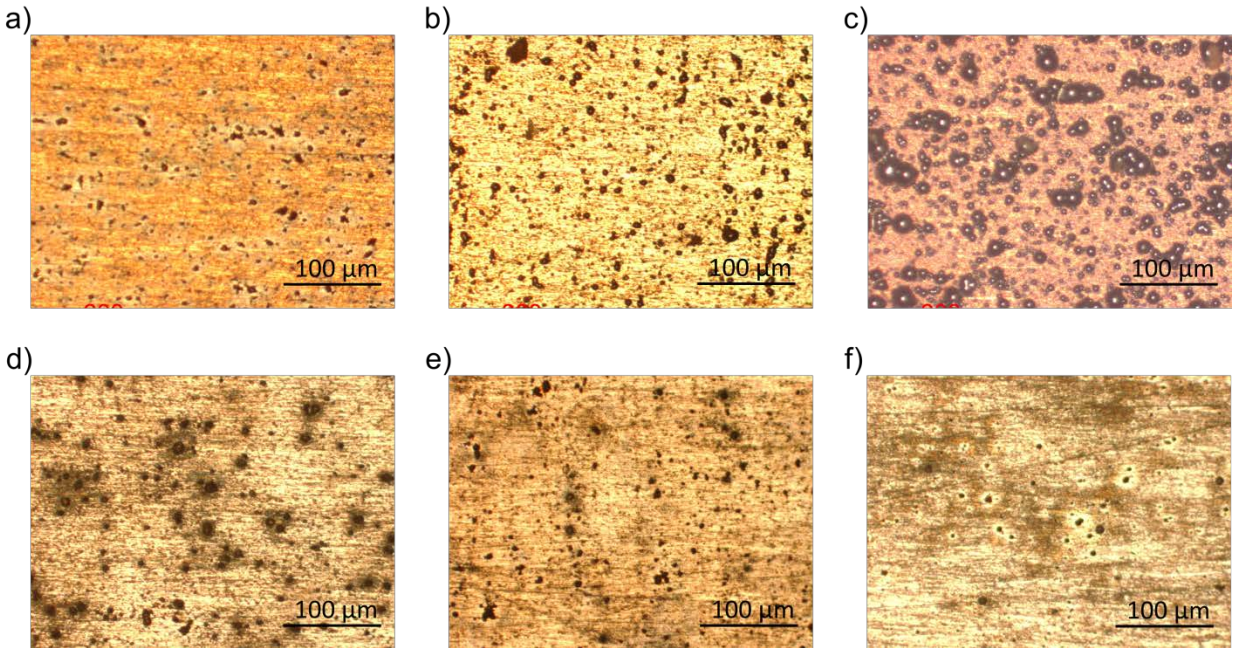

Figure 35. Optical microscopy of AA2024-T351 after exposure to 0.05 M sodium chloride solution. (a) Exposure to 0.05 M NaCl with 0.1 M MnO_4^- in solution. (b) Exposure to 0.05 M NaCl with 0.05 M MnO_4^- in solution. (c) Exposure to 0.05 M NaCl with 0.005 M MnO_4^- in solution. (d) Exposure to 0.05 M NaCl after pretreatment in 0.1 M MnO_4^- in solution for 24 hours. (e) Exposure to 0.05 M NaCl after pretreatment in 0.05 M MnO_4^- in solution for 24 hours. (f) Exposure to 0.05 M NaCl after pretreatment in 0.005 M MnO_4^- in solution for 24 hours.

Anodic Inhibition by Permanganate Ions

Localized Corrosion Behavior on Pretreated 2024-T351

Figure 36(a-c) shows anodic E-log*i* behavior for AA2024-T351 in 0.05 M sodium chloride solution during upward cyclic potentiodynamic scans. AA2024-T351 samples were first pretreated for 24 hours in a chloride-free environment with various inhibitor concentrations and then exposed to 50 mM NaCl solution without inhibitor. The dotted curve (—●—) shows the results on an untreated control specimen.

Pretreated samples exposed at OCP showed suppression of OCP and uncovered a passive region. The open circuit suppression consistently occurred at the lowest concentration; at higher concentrations the suppression was statistically distributed. Only a small increase in E_{pit} was observed for pretreatment in 0.005 M potassium permanganate. The 50 and 100 mM concentrations showed no increase in E_{pit}. In summary, pretreatments showed the largest effect on the ΔE defined as E_{pit}- OCP. However the effect was mainly associated with lowering the OCP.

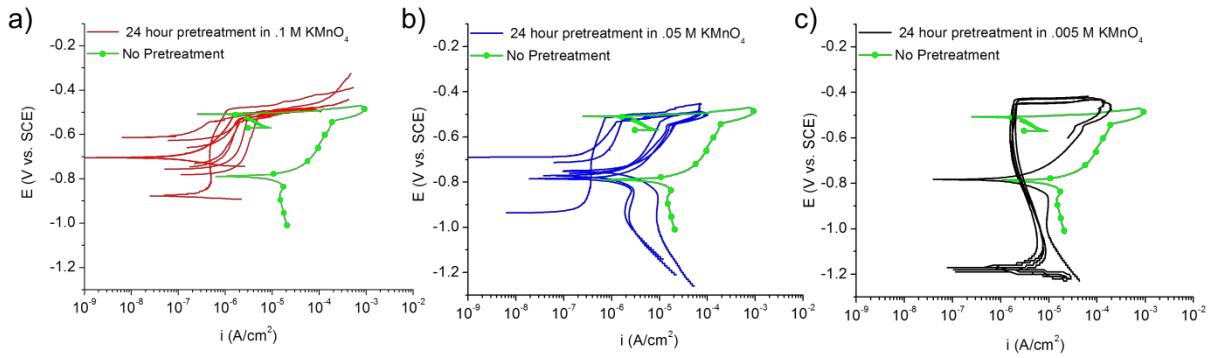

Figure 36. The anodic polarization behavior for AA2024-T351 after pretreatment in $KMnO_4$ for 24H. Scan run in 0.05 M sodium chloride solution. (a) Pretreatment in 0.1 M $KMnO_4$, (b) Pretreatment in 0.05 M $KMnO_4$, (c) Pretreatment in 0.005 M $KMnO_4$.

Localized Corrosion Behavior of AA2024-T351 with Permanganate in Solution

Experiments were also conducted in-situ or with the inhibitor added concurrently to the 50 mM NaCl solution. Aluminum 2024-T351 was exposed for 24 hours with the inhibitor in solution. Figure 37 shows the behavior of AA2024-T351 in 50 mM sodium chloride solution with the inhibitor as an in-situ addition.

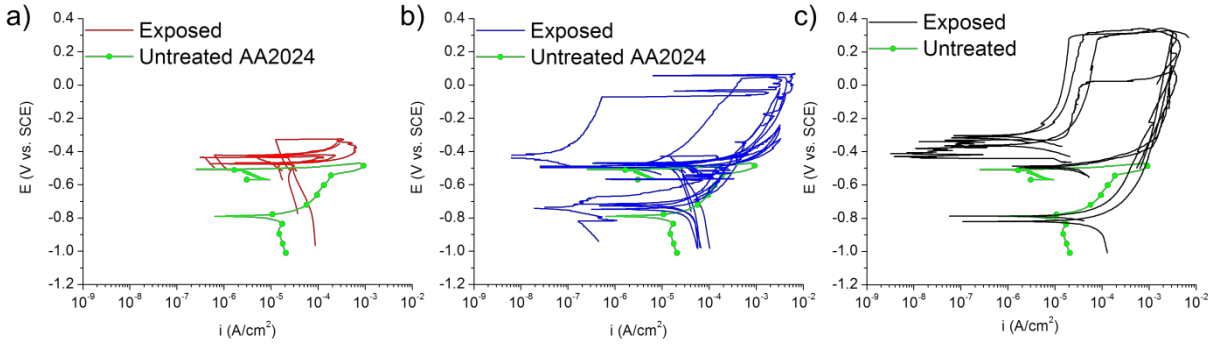

Figure 37. The anodic polarization behavior for AA2024-T351 after 24 hours of exposure to 50 mM sodium chloride solution with the inhibitor in-situ. Scans conducted in 50 mM sodium chloride solution with varied inhibitor concentrations. (a) 100 mM $KMnO_4$, (b) 50 mM $KMnO_4$, (c) 5 mM $KMnO_4$.

When the in-situ MnO_4^- inhibitor was investigated at 100 mM concentration (Figure 37(a)), little to no anodic inhibition was observed. This lack of anodic inhibition was further exacerbated by the fact that OCP was raised slightly because of the oxidizing nature of in-situ permanganate while E_{pit} was minimally affected. At lower concentrations (5 mM) the inhibitor significantly raised E_{pit} of AA2024-T351. Interestingly, the experiments in which an increase in E_{pit} was observed all had elevated OCP levels. This could be the result of deposition of a high valence state oxide with a high redox potential covering the surface of the AA2024. When the OCP remained at -0.5 V vs. SCE, no increase in E_{pit} was observed. Microscopy on samples that experienced very high E_{pit} showed substantial manganese oxide coverage of the entire surface.

Microscopy of synthesized Al_2CuMg S-phase held at -0.5 V vs. SCE in both 50 mM chloride solution and 100 mM $KMnO_4$ and 50 mM chloride solution are shown in Figure 38. Figure 39 shows a sample that exhibited a very high E_{pit}. The manganese oxide coverage not only covered the intermetallic particles but also the aluminum matrix.

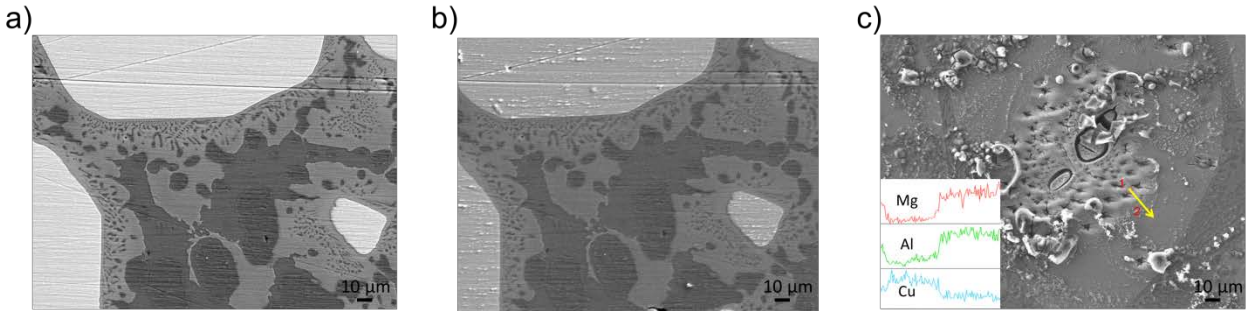

Figure 38. S-phase ingot with large lighter regions corresponding to higher copper content and higher Z. (a) Sample as polished. (b) Sample held potentiostatically in 100 mM MnO_4^- and 50 mM Cl^- solution for 200 seconds. Note the growth of a protective manganese oxide over the S-phase particles. (c) Sample held potentiostatically in 50 mM Cl^- solution for 200 seconds. Insert of EDS line scan shows the enrichment of copper in proximity of visible S-phase damage.

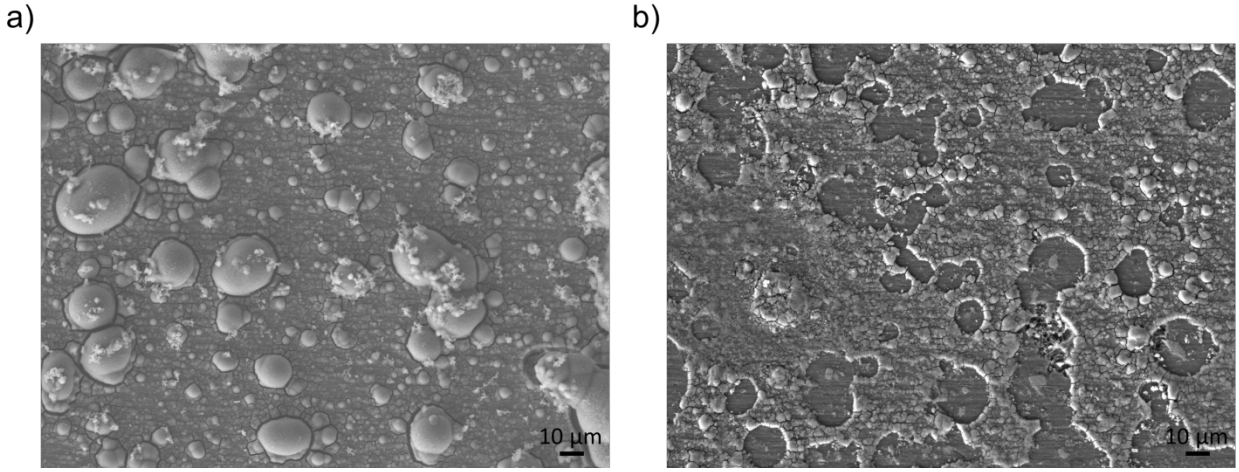

Figure 39. AA2024 exposed to 0.005 M $KMnO_4$ + 0.05 M NaCl for 24 hours and then anodically polarized to potentials above E_{pit} (+0.3 V vs. SCE) in fresh 0.005 M $KMnO_4$ + 0.05 M NaCl solution. (a) Sample as removed from anodic polarization solution. (b) sample after removal of manganese oxide caps over intermetallic particles.

Anodic polarization scans were also carried out in 25 mM manganese (II) chloride solution to determine if the reduced form of manganese had any effect on E_{pit} of AA2024-T351. The concentration of 25 mM was chosen so that the total chloride concentration was the same as the previous tests. A representative example of an anodic polarization of AA2024-T351 in 25 mM $MnCl_2$ can be seen in Figure 40. No increase in E_{pit} was seen with 25 mM Mn^{2+} in solution.

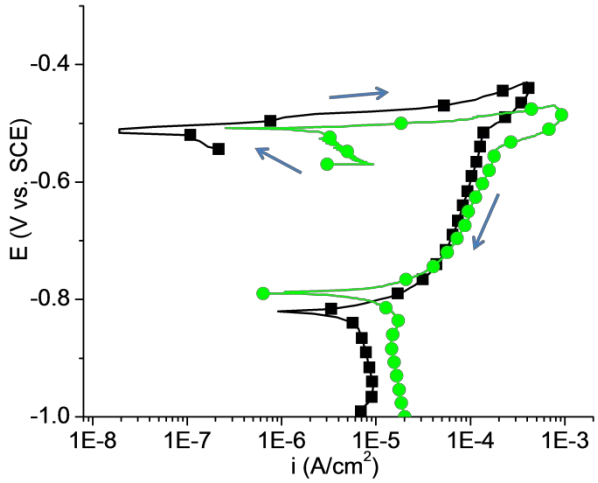

Figure 40. Representative anodic polarization behavior for AA2024-T351 in 25 mM $MnCl_2$ solution (—■—) compared to 50 mM NaCl (—●—).

Figure 41 presents the cumulative probability of pitting as a function of potential for both pretreatment and in-situ solution phase inhibitor studies. Figure 42 presents the average difference between E_{pit} and the open circuit for both pretreatment and solution phase permanganate procedures on AA2024-T351. No significant increase in E_{pit} is observed for pretreated AA2024-T351 tested in 50 mM NaCl solution except at 5 mM $KMnO_4$. In-situ MnO_4^- additions at low concentrations in the presence of an activating ion, like Cl^-, produce a statistically significant increase in E_{pit}.

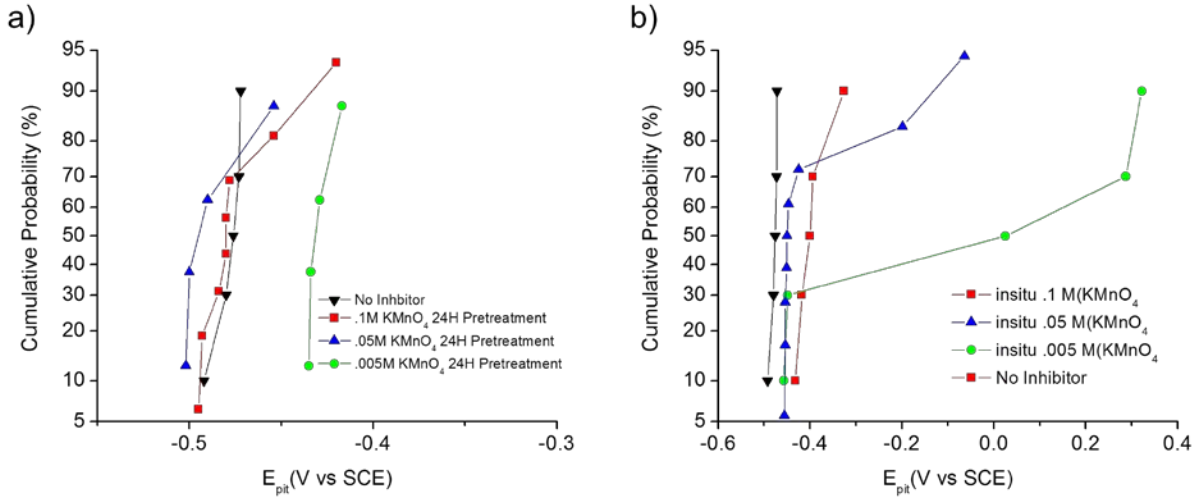

Figure 41. Cumulative probability of pitting as a function of potential for both (a) pretreatment and (b) in-situ solution phase permanganate inhibitor concentration. Probability of pitting in 0.05 M NaCl.

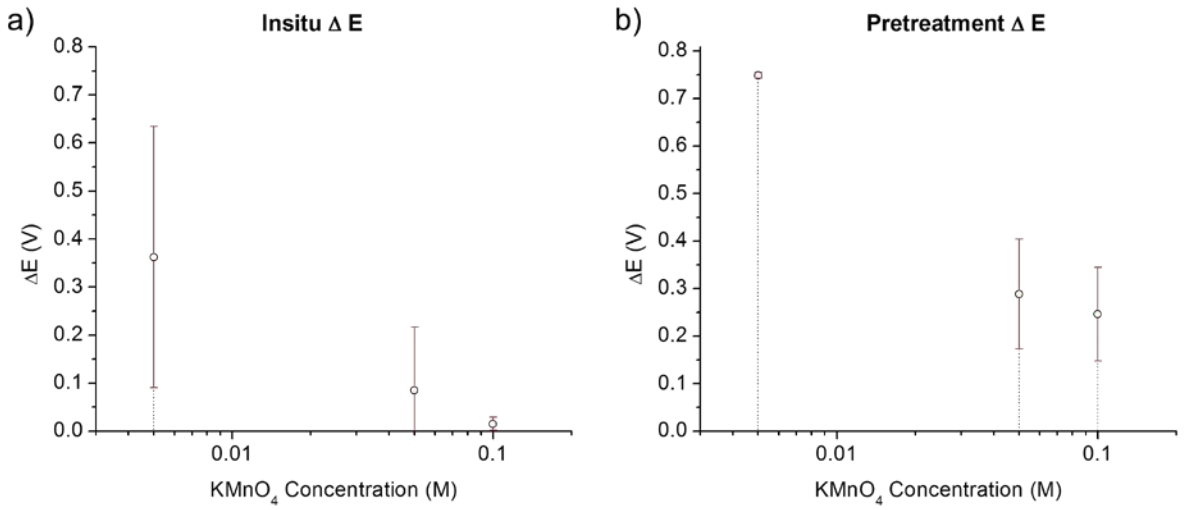

Figure 42. The average difference between pitting and open circuit potentials for Mn pretreatment (a) and in-situ solution phase additions (b), as a function of inhibitor concentration. The error bars indicate one standard deviation.

Investigation of Cathodic Inhibition with KMnO4

The Oxygen Reduction Reaction on AA2024-T4 and Pure Copper

The RDE method was used to examine cathodic reaction kinetics of both AA2024-T4 and pure copper in pH 8.4 borate buffer solution to limit pH changes during the test (Figure 44). Tests were also conducted in 0.05 M sodium chloride (Figure 43). Figures 43 and 44 shows cathodic polarization data collected as a function of rotation rate. AA2024-T4 exposed in 50 mM NaCl showed mixed charge transfer-mass transfer controlled ORR from OCP to approximately -0.9 V vs. SCE at which point diffusion limited control dominated until the HER dominated the total cathodic current density around -1.2 V vs. SCE. Pure copper showed slightly different behavior in borate buffer than in sodium chloride. In borate buffer, the mixed charge transfer-mass transfer control region extends to -0.8 V vs. SCE with mass transfer control of the ORR dominating to -1.3 V vs. SCE followed by the HER. In 0.05 M sodium chloride solution, the oxygen reduction mass transfer control region was slightly larger and operates in the range -0.6 to -1.3 V vs. SCE.

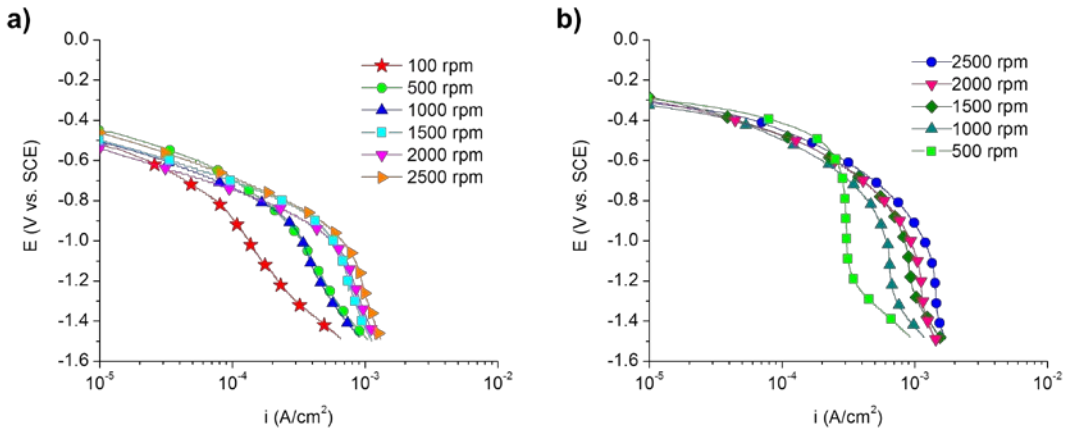

Figure 43. Cathodic E vs. log(*i*) data for AA2024-T4 (a) and high-purity copper (b) samples run at various rotation rates from 100 rpm to 2500 in pH 8.4 borate buffer. Solutions were aerated naturally.

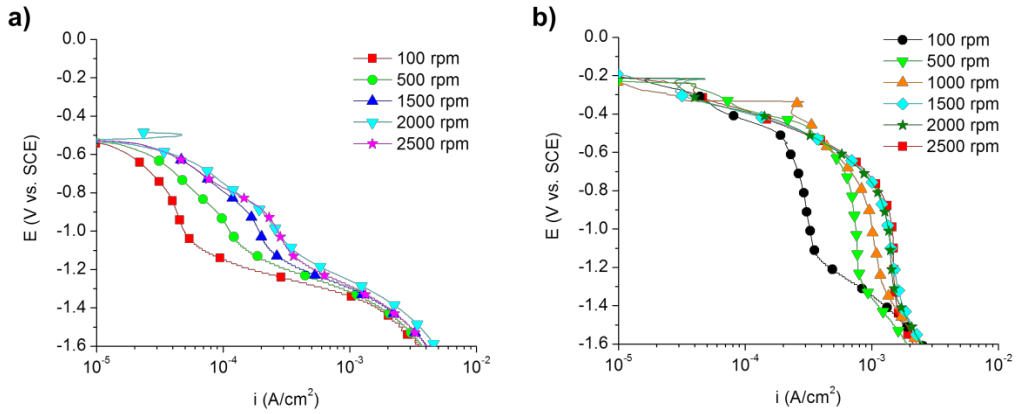

Figure 44. Cathodic E vs. log(*i*) data for AA2024-T4 (a) and high-purity copper (b) samples run at various rotation rates from 100 rpm to 2500 in 0.05 M NaCl. Solutions were aerated naturally.

As shown previously, the AA2024-T4 did not follow the Levich prediction because of the nature of its distributed array of local cathodic reaction sites.[90]

The Effects of Potassium Permanganate on Oxygen Reduction Reaction on AA2024-T4

Figure 45 shows the cathodic polarization data collected using the RDE method to examine the effects of potassium permanganate ($KMnO_4$) on the ORR kinetics on AA2024-T4. Two approaches were used to examine the inhibitors effect on the ORR; an inhibitor pretreatment and inhibitor addition in-situ (Figure 45(a) and (b), respectively). It should be noted that $KMnO_4$ provides a strong cathodic reactant with a very high redox potential in addition to dissolved O_2 and H_2O as discussed in the introduction. In the in-situ experiments there is an increase in cathodic current density resulting from this additional cathodic reaction compared to the pretreated condition and no inhibitor.

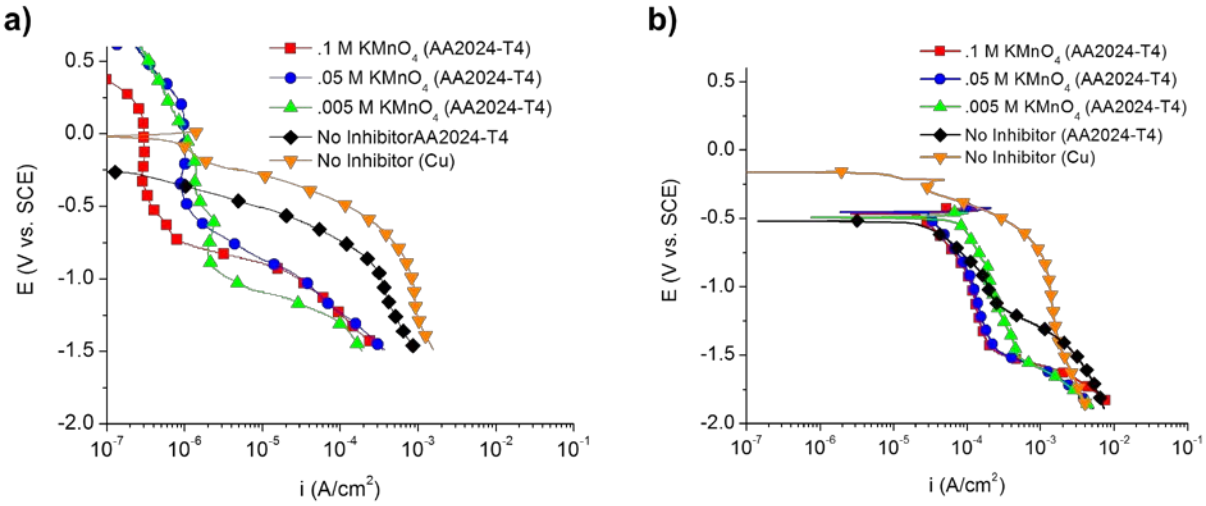

Figure 45. Cathodic polarization behavior of AA2024-T4 and pure copper samples ground to 1200 grit, tested at 1000 rpm in pH 8.4 borate buffer solution after 100 H pretreatment (a) and run at 1500 rpm in 0.05 M NaCl solution with in-situ inhibitor additions (b) Rotation rate has been kept constant and inhibitor concentration is tested at different levels. All data collected under natural aeration.

Potassium permanganate changes the regions of mass and charge transfer control on AA2024-T4. In the pretreatment case, mass transfer control begins around 0.2 V vs. SCE and the HER is dominant between -0.06 and -1.1 V vs. SCE because the ORR is slow. When the inhibitor is used in-situ, mass transport control occurs from -0.6 V to -1.4 V vs. SCE at which point the HER begins to dominate.

Plots of $1/i_{\mathrm{Tot}}$ vs. $\omega^{1/2}$ at -1 V vs. SCE (a potential dominated by oxygen reduction mass transfer control) show that uninhibited AA2024-T4 has a lower current density than high-purity copper; this is due to the array of active electrodes surrounded by inactive aluminum matrix as described by the Gueshi model [90,132] to be considered later. The Koutecky-Levich method,[130] as shown in Equation 15, was used to extract i_D from i_T (Figure 46) at -1 V vs. SCE, where i_D is the diffusion limited cathodic current density and i_{ct} is the charge transfer limited cathodic current density. At this potential i_{HER} is much lower than i_{ORR}.

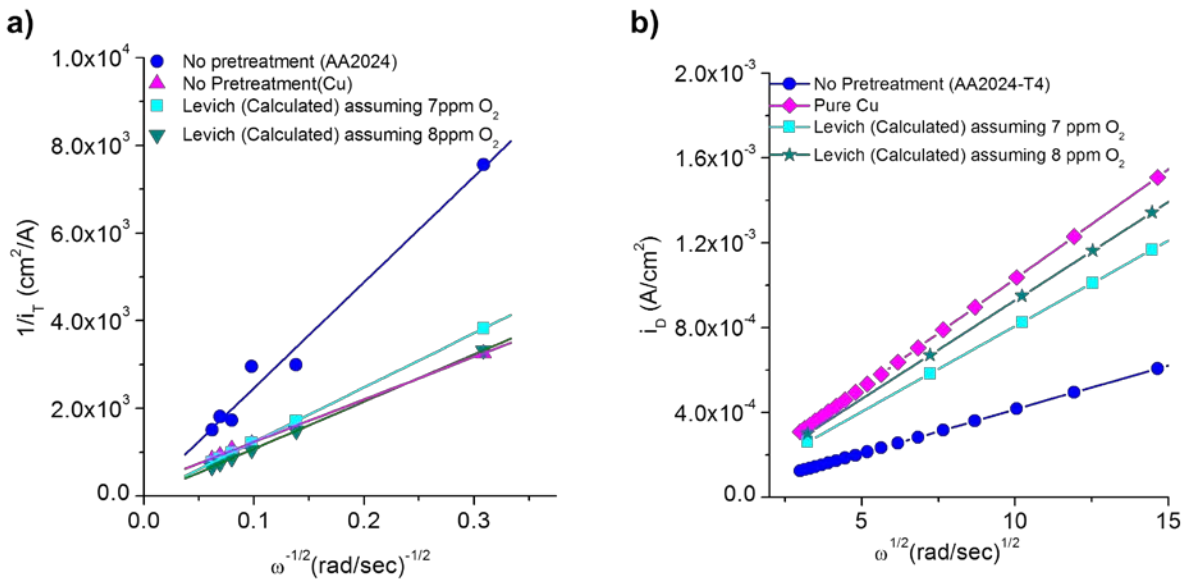

Figure 46 (a) Total current at -1 V vs. SCE for AA2024-T4 and pure copper compared with the Levich prediction (i_d) in pH 8.4 borate buffer solution. (b) Diffusion limited current extracted from i_{total} at -1V vs. SCE for AA2024-T4 and pure copper compared with the Levich prediction in pH 8.4 borate buffer. Data extracted from Figure 44.

$$\frac{1}{i_{Tot}} = \frac{1}{i_{ct}} + \frac{1}{i_D} \qquad \textbf{Equation 15}$$

Where i_D is given by Equation 16.

$$i_D = 0.62nFD^{2/3}v^{1/6}C\omega^{1/2} \qquad \textbf{Equation 16}$$

The results on high-purity copper can be compared with the Levich description of mass-transport limited O_2 reduction given by Equation 16. Using a value for the diffusion of O_2 in water, D = $1.9 \cdot 10^{-5}$ cm^2/s (diffusion rate), a value of n = 4, the concentration of O_2 in solution, C = 7-9 ppm, *F* being the Faraday constant and the kinematic viscosity, $\nu = 1x10^{-2}$ cm^2/s, good agreement is found between theoretical values and experimental data.[28] This suggests that at -1 V vs. SCE the current due to the HER is a small fraction of the ORR current.

The diffusion limited current density was extracted from the total current density (Figure 47) using the Koutecky-Levich method (Equation 15) for the pretreated case at -1 V vs. SCE. The extracted diffusion limited current density is shown in Figure 48. Pretreated AA2024 has a lower cathodic current density than untreated AA2024-T4 over all rotation rates with a weaker rotation rate dependency. In-situ inhibitor use only suppresses total current density at high rotation rates or low $\omega^{-1/2}$. At low rotation rates the additional oxidizer raises the total cathodic reaction rate during the in-situ tests. In contrast, when the inhibitor is used as a pretreatment and no additional cathodic reaction is present the total current density is suppressed as much as 2 orders of magnitude at all rotation rates.

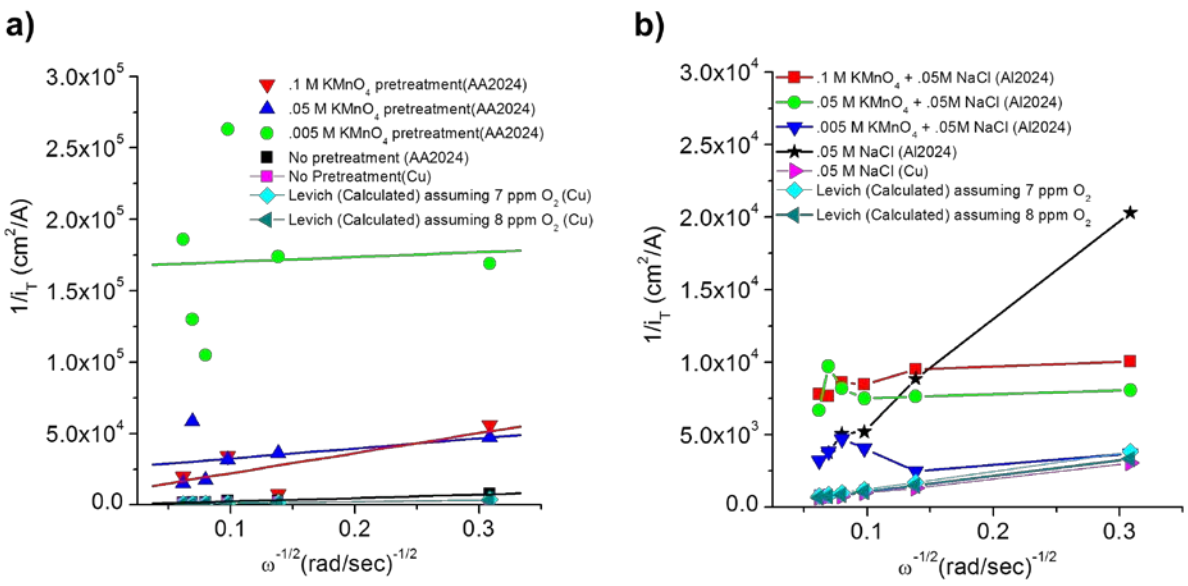

Figure 47. Total current at -1V vs. SCE for AA2024-T4 for the inhibitor pretreatment tests in inhibitor free environment (a) and with the inhibitor present in-situ (b). (a) and (b) have an order of magnitude difference in the ordinate. Total current densities for pure copper, bare AA2024-T4 and the Levich prediction i_d values are included for comparison. Data extracted from Figure 45.

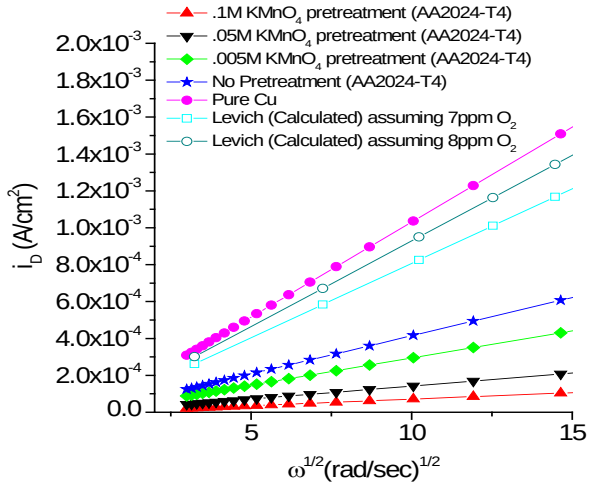

Figure 48. Diffusion limited current extracted from i_{total} at -1V vs. SCE for AA2024-T4 after pretreatment at various inhibitor concentration compared with pure copper, bare AA2024-T4, and the Levich prediction. Tests were conducted in borate buffer solution at pH = 8.4. Data extracted from Figure 47.

The cathodic polarization behavior of a copper sample pretreated in 50 mM $KMnO_4$ at -0.5 V vs. SCE can be seen in Figure 49. The manganese oxide has been electroplated onto high-purity copper at -0.5 V vs. SCE to mimic OCP of AA2024-T351. This experiment shows the effects of the reduction of the manganese oxide on the cathodic current density compared to samples with no pretreatment. These additional reduction reactions obscure analysis of oxygen on copper-rich intermetallic particles in AA2024-T351. However, the reduction of the manganese oxide provides a mechanism for active inhibition that will be addressed in the discussion.

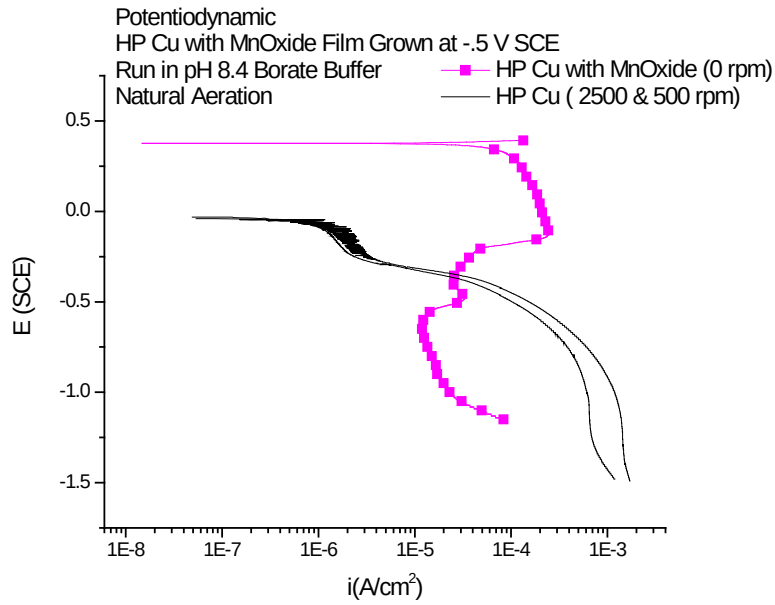

Figure 49: Potentiodynamic scan of high-purity copper with Mn-oxide grown at a potential of -0.5 V vs. SCE.

The activation controlled cathodic current density is a linear function of the copper surface coverage described by Kaesche [29] by Equation 17.

$$i_{act,heterogeneous} = \Theta_{Cu}^{Kaeshe} i_{homogeneous}. \qquad \textbf{Equation 17}$$

Where Θ_{Cu}^{Kaeshe} is the copper surface coverage or Cu-rich IMC coverage and $i_{homogeneous}$ is exponentially dependent on the cathodic potential. Activation current density has been extracted and can be seen in Figure 50, along with estimated copper coverage.

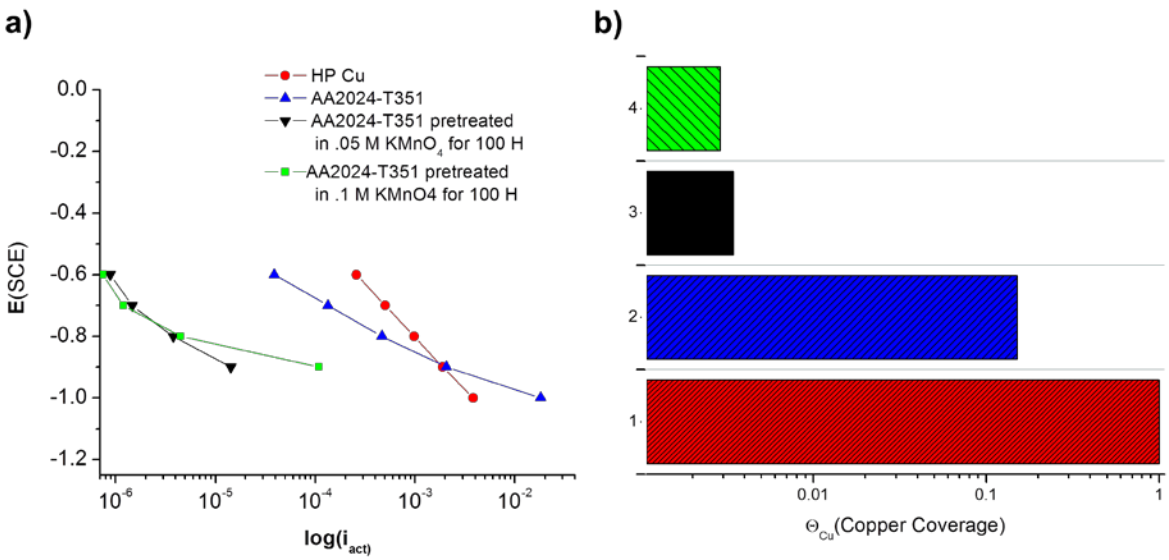

Figure 50. (a) Extracted activation controlled current density over a range of potentials for high-purity Cu , AA2024-T351, and AA2024-T351 pretreated in 0.05 M MnO_4^- and 0.1 M MnO_4^-. (b) Calculated copper coverage, Θ_{Cu}^{Kaeshe} , at -0.6 V using Equation 17. Cu (1), AA2024-T351(2), and AA2024-T351 pretreated in 0.05 M MnO_4^- (3) and 0.1 M MnO_4^- (4).

Manganese Oxide Valence State Determination

Galvanostatic reduction curves of electrodeposited manganese oxides on copper have been conducted to probe the valence state of the manganese oxide and can be seen in Figure 51. The multiple potential waves compared to untreated copper indicate that the oxide is present in a high valence state. The reduction of CuO is observed in the uncoated copper sample.[134] The manganese reduction potential waves are indicative of changes in the oxide's valence state as the reduction proceeds. The reversible potentials of several likely manganese reduction reactions are indicated in the figure by the dotted lines. A break in the abscissa is necessary as the reduction of the manganese oxide requires more charge to be passed than the reduction of the copper oxide, necessitating much longer times. All of the prominent features of the manganese oxide reduction are shown to the right of the break. The potential decays linearly until 5000 seconds have passed at which point two reduction waves occur in quick succession.

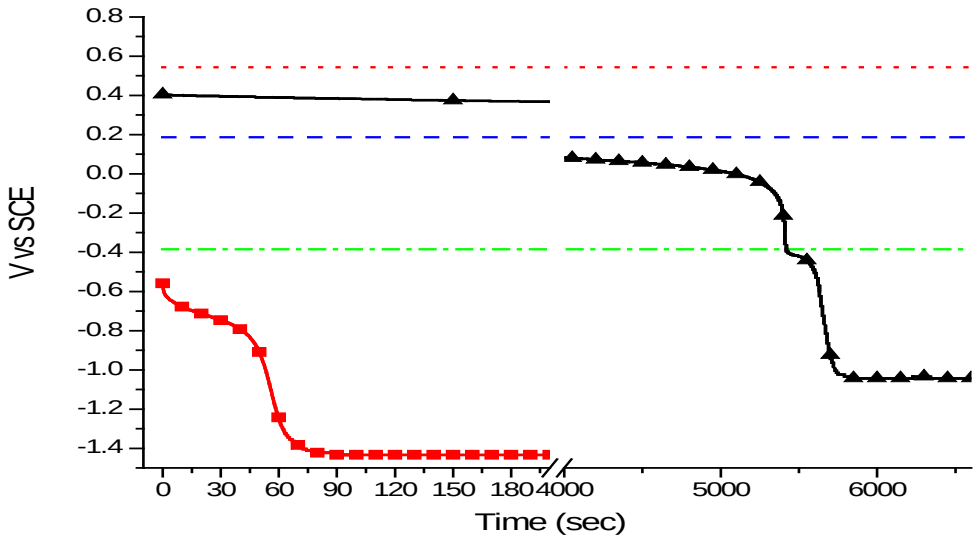

Figure 51. Constant current discharge curves of electrodeposited manganese oxide coated copper (-▲-) and uncoated copper (-■-). High-purity Copper with Mn oxide deposited at -0.5 V SHE from 0.1 m KMnO4 with a pH of 6. Galvanostatic reduction performed at 20 mA in pH 8.4 borate buffer. The red dotted line (· ·) indicates the reversible potential of $MnO_4^- + 4H^+ + 3e^- \leftrightarrow MnO_2 + 2H_2O$ at 0.54 V vs. SCE. The blue dashed (– –) line indicates the reversible potential for $MnO_2 + H_2O + e^- \leftrightarrow MnOOH + OH^-$ at 0.187 V vs. SCE. The green dash-dotted line (–·–) indicates the reversible potential for $MnOOH + H_2O + e^- \leftrightarrow Mn(OH)_2 + OH^-$ at -0.385 V vs. SCE.

Raman spectroscopy was conducted on high-purity copper, pretreated AA2024-T351, and high-purity metallic manganese. The spectra for a selection of the data are presented in Figure 52. The figure shows two common peaks shared between the MnO_2 powder, the manganese metal potentiostatically held at 0.35 V vs. SCE, the copper treated in 0.1 M $KMnO_4$ at -0.5 V vs. SCE, and the AA2024-T351 pretreated at OCP in 0.1 M $KMnO_4$. The potential of the potentiostatic hold of the manganese metal was chosen with the intention of growing MnO_2. The first peak is centered on 500 wavenumbers (cm^{-1}). The second common peak is centered on 630 wavenumbers. The E-pH diagram in Figure 2 shows that at a pH of 10, the chosen potential is solidly within the MnO_2 phase.

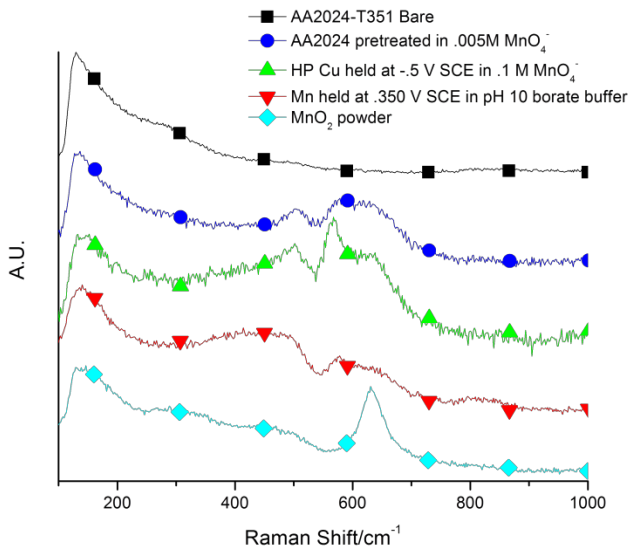

Figure 52. Raman spectra for AA2024-T351, AA2024-T351 pretreated in 0.005 M $KMnO_4$, copper pretreated in 0.1 M $KMnO_4$ at -0.5 V vs. SCE, manganese metal held potentiostatically at 0.35 V vs. SCE, and MnO_2 powder.

The steady drop in potential in Figure 31 indicates a reduction of manganese oxides after they are deposited on AA2024-T351. As the reduction from manganese (VI) to (III) to (II) occurs, the potential of the system drops towards the Nernst potential of the lower valence oxide until all of the oxide has been reduced and the rate of the HER dominates the OCP of AA2024-T351.

Vanadate Species Present in NMR and Speciation Diagrams

The speciation of vanadate in aqueous solutions is known to vary with both ionic concentration and pH.[135,136] To determine the species of vanadate in solution, both thermodynamic prediction using Medusa Chemical Equilibrium Database and Plotting Software[137] and NMR were utilized. Medusa software predicted little variation between vanadate species found in 5, 10, 50, and 150 mM sodium vanadate in solution with 50-mM NaCl in the pH range from 7.6 to 8.7. Table 20 shows the five greatest vanadate species percent in the given pH range for the vanadate concentrations tested based on Medusa.[137]

Table 20. The predicted five greatest vanadate species percentage for each total vanadate concentration in 50 mM NaCl.

Dissolved $NaVO_3$	5 mM	10 mM	50 mM	150 mM
V^{5+} species in decreasing abundance	$V_3O_9^{3-}$	$V_3O_9^{3-}$	$V_4O_{12}^{4-}$	$V_4O_{12}^{4-}$
	$VO_2(OH)^{2-}$	$V_4O_{12}^{4-}$	$V_3O_9^{3-}$	VO_3OH^{2-}
	$V_4O_{12}^{4-}$	$VO_2(OH)^{2-}$	VO_3OH^{2-}	$V_3O_9^{3-}$
	VO_3OH^{2-}	VO_3OH^{2-}	$VO_2(OH)^{2-}$	$HV_2O_7^{3-}$
	$HV_2O_7^{3-}$	$HV_2O_7^{3-}$	$HV_2O_7^{3-}$	$V_2O_7^{4-}$

^{51}VNMR was used to experimentally determine the species present in $NaVO_3$ plus 50 mM NaCl solutions and any change in speciation with time. While slight differences were seen between the minor peaks for different concentrations of vanadate, the peak at -577 ppm was dominant in all solutions except for the 1 mM $NaVO_3$ plus 50 mM NaCl solution, for which it was the second most prevalent peak. This peak corresponded to $(V_4O_{12})^{-4}$ which was predicted to be dominant in the high vanadate concentration range (50 to 150 mM) by the Medusa software. However, other experimentally observed minor peaks (-586 ppm $(V_5O_{15})^{-5}$ and -589 ppm $(V_6O_{18})^{-6}$),[94,95,136] were not predicted by the software. Solution age did not appear to be a factor in speciation. Figure 53 demonstrates that vanadate speciation was stable after 24 hours. Some of the experimental peaks have yet to be identified, given available literature.

Table 21 shows the experimentally observed peaks in order of abundance for each vanadate concentration tested. Table 22 contains the species, estimated percent of total species present and the pH of the solution.

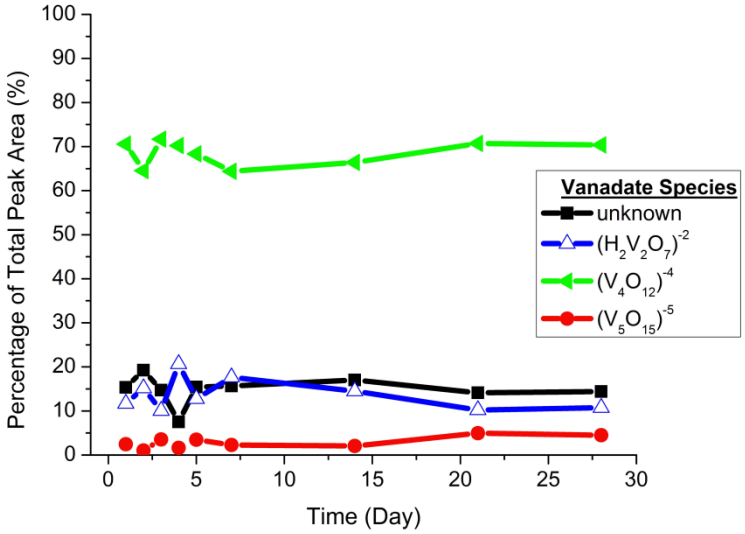

Figure 53. Graph of vanadate speciation with time at room temperature. No great change in species present occurred over 28 days for 5 mM $NaVO_3$ plus 50 mM NaCl in D_2O solvent.

Table 21. The ^{51}VNMR peaks for different $NaVO_3$ concentrations in 50 mM NaCl.

Dissolved $NaVO_3$	**1 mM**	**5 mM**	**10 mM**	**50 mM**	**150 mM**
V^{5+} species in decreasing abundance	-558 ± 1 ppm $V_2O_7^{4-}$	-577 ppm $V_4O_{12}^{4-}$	-577 ppm $V_4O_{12}^{4-}$	-577 ppm $V_4O_{12}^{4-}$	-577 ppm $V_4O_{12}^{4-}$
	-577 ppm $V_4O_{12}^{4-}$	-572 ± 1 ppm $H_2V_2O_7^{2-}$	-572 ± 1 ppm $H_2V_2O_7^{-2}$	-586 ppm $V_5O_{15}^{5-}$	-586 ppm $V_5O_{15}^{5-}$
	-572 ± 1 ppm $H_2V_2O_7^{2-}$	-558 ± 1 ppm $V_2O_7^{4-}$	-557 ± 1 ppm $V_3O_{10}^{5-}$	-572 ± 1 ppm $H_2V_2O_7^{2-}$	-544 ± 1 ppm Unknown
		-586 ppm $V_5O_{15}^{5-}$	-586 ppm $V_5O_{15}^{5-}$	-550 ppm Unknown	-568 ± 1 ppm $HV_4O_{13}^{5-}$ or $V_4O_{13}^{6-}$
					-589 ppm $V_6O_{18}^{4-}$

Source: [94,95,136,138,139]

Table 22. The ^{51}VNMR determined abundance of vanadate species for different $NaVO_3$ concentrations in 50 mM NaCl.

Species	**Species Code**	**1 mM**	**5 mM**	**10 mM**	**50 mM**	**150 mM**
$V_4O_{12}^{4-}$	V_4	35-26%	64-72%	77-74%	76-81%	76-79%
$H_2V_2O_7^{2-}$	V_2	21-18%	10-20%	8-11%	3-12%	
$V_2O_7^{4-}$	V_2	46-53%	8-19%			
$V_5O_{15}^{5-}$	V_5		1-5%	6-5%	4-13%	14-16%
$V_3O_{10}^{5-}$	V_3			9-11%		
-550 ppm Unknown					1-6%	
-544 ± 1 ppm Unknown						2-3%
$HV_4O_{13}^{5-}$ or $V_4O_{13}^{6-}$	V_4					2-4%
$V_6O_{18}^{4-}$	V_6					1-4%
pH		6.5	7.6	7.8	8.4	8.7

Effect of Vanadate Inhibitors on Suppressing Open Circuit Pitting Corrosion of AA2024-T3

The results of the 24 hour open circuit potentials exposures prior to anodic scanning conducted in 50 mM NaCl plus various concentrations of $NaVO_3$ in solution are presented in Table 23 for AA2024-T3. During the first hour of exposure, only the AA2024–T3 specimen in the 50 mM NaCl solution with 5 mM $NaVO_3$ demonstrated an OCP higher than that of a similar specimen exposed in the salt solution without inhibitor. After 23 hours of AA2024-T3 exposure in solutions, the open circuit potentials of all specimens exposed in salt solutions with either 5, 10, 50, or 150 mM $NaVO_3$, were higher than those of the specimens exposed in 50 mM NaCl solution without inhibitor. Specimens exposed in 1 mM $NaVO_3$ plus 50 mM NaCl solution were exceptions and followed the trend of those exposed in 50 mM NaCl solution by having a reduced potential. This apparent difference in potential values was due to the decrease in OCP of the specimen exposed to the salt solution in the absence of the inhibitor, as a result of pitting and trenching around intermetallic compounds, without any significant change in OCP of those specimens exposed in the presence of the inhibitor. Twenty-four hour immersion tests in 50 mM NaCl without inhibitor confirm corrosion of AA2024-T3 at open circuit. For both the 1 hour and 24 hour open circuit, the vanadate concentration did not correlate with the open circuit potential.

Table 23. The average open circuit potentials for AA2024–T3 in 50 mM NaCl with various concentrations of $NaVO_3$ in open to the air solutions at the 1st and 23rd hours.

Concentration of $NaVO_3$	Open Circuit Potential at the 1st Hour (V_{SCE})	Open Circuit Potential at the 23rd Hour (V_{SCE})
0 mM	-0.536	-0.667
1 mM	-0.637	-0.792
5 mM	-0.500	-0.542
10 mM	-0.570	-0.584
50 mM	-0.634	-0.649
150 mM	-0.614	-0.642

24 Hour Immersion Experiments on AA2024–T3

Open circuit or freely corroding immersion experiments were conducted to evaluate the effect of various concentrations of $NaVO_3$ in 50 mM NaCl solutions on corrosion of AA2024-T3 sheet where all anodic and cathodic sites were in close proximity. As shown in Figure 54, the number of pits and the pit size were reduced by the addition of $NaVO_3$ to 50 mM NaCl solutions. The addition of 5 mM $NaVO_3$ reduced the number of pitting sites. At higher concentrations of 50 mM and 150 mM $NaVO_3$, the pitting sites could not be seen without the use of an optical microscope. AA2024-T3 exposed to 5 mM $NaVO_3$ in 50 mM NaCl solutions formed yellow precipitates around the pit. This yellow precipitate was not seen at higher concentrations of $NaVO_3$.

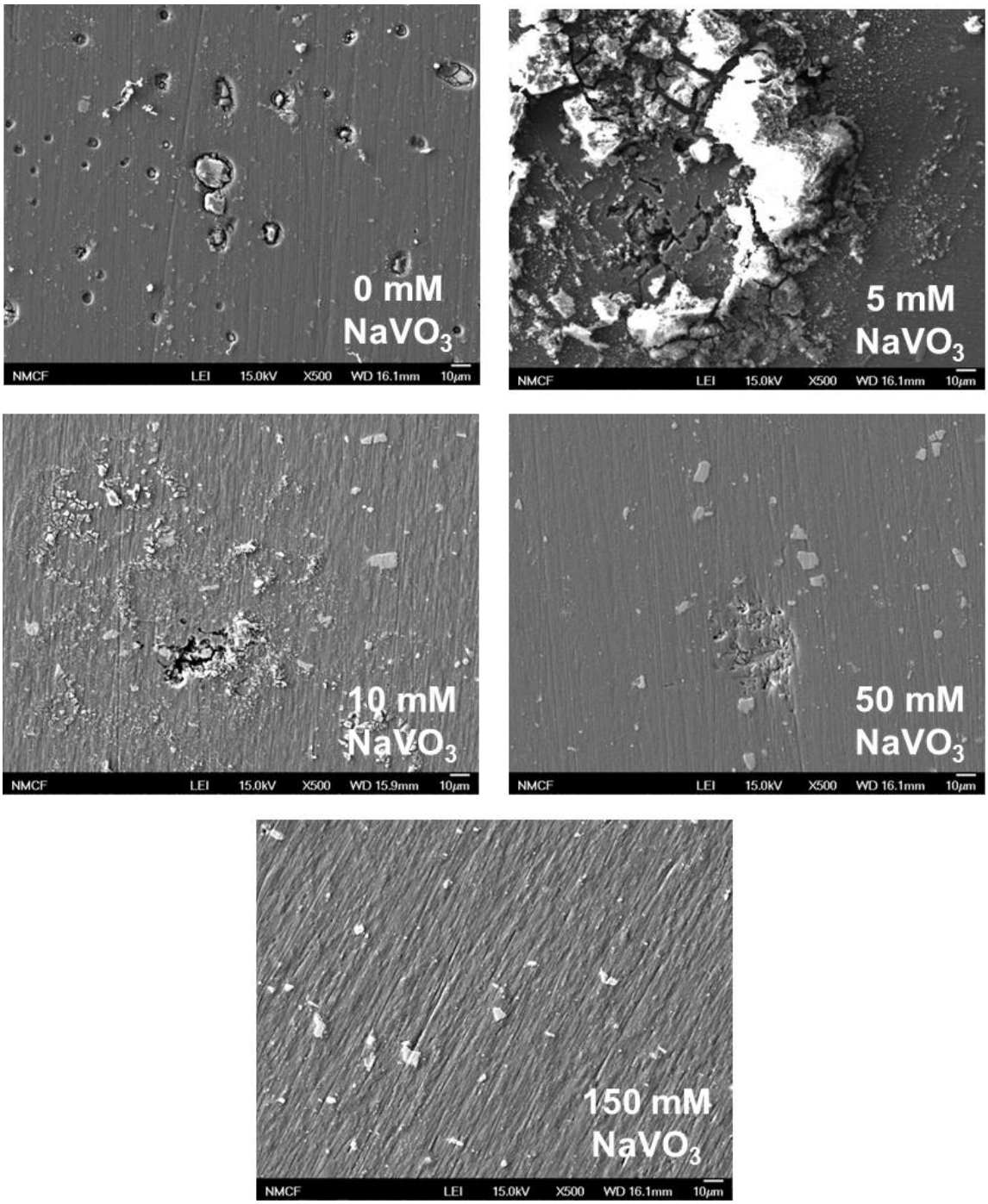

Figure 54. SEM micrographs of AA2024-T3 on the transverse-lateral surface after 24 hours of exposure in open to the air 50 mM NaCl solutions with 0, 5, 10, 50, and 150 mM $NaVO_3$ at room temperature. Decreasing pit density and depth is observed with increasing $NaVO_3$ concentration. No visible pits on the 150 mM $NaVO_3$ plus 50 mM NaCl exposed specimen were seen with optical methods, but parts of the copper intermetallic particles have change color from copper to blue.

Pits initiated on S phase Al–Cu–Mg particles or at the matrix adjacent to Al–Cu–Fe–Mn particles. After 24 hours, corrosion, which at first entrenched around the Al–Cu–Fe–Mn intermetallic particles, has progressed such that pitting of both the matrix and the intermetallic particles has occurred, as seen in Figure 55. EDS information, presented in Figure 55 (b), shows for the intermetallic particle, an increase in Mn, Fe, and Cu and a decrease in Al concentration as compared to the matrix [Figure 55(a)]. Additionally, salt precipitate was observed at the pitting site on AA2024-T3 specimens exposed to 50 mM NaCl solution for 24 hours, as shown in Figure 55. The pits in Figure 55 are typical regardless of type of local intermetallic particles.

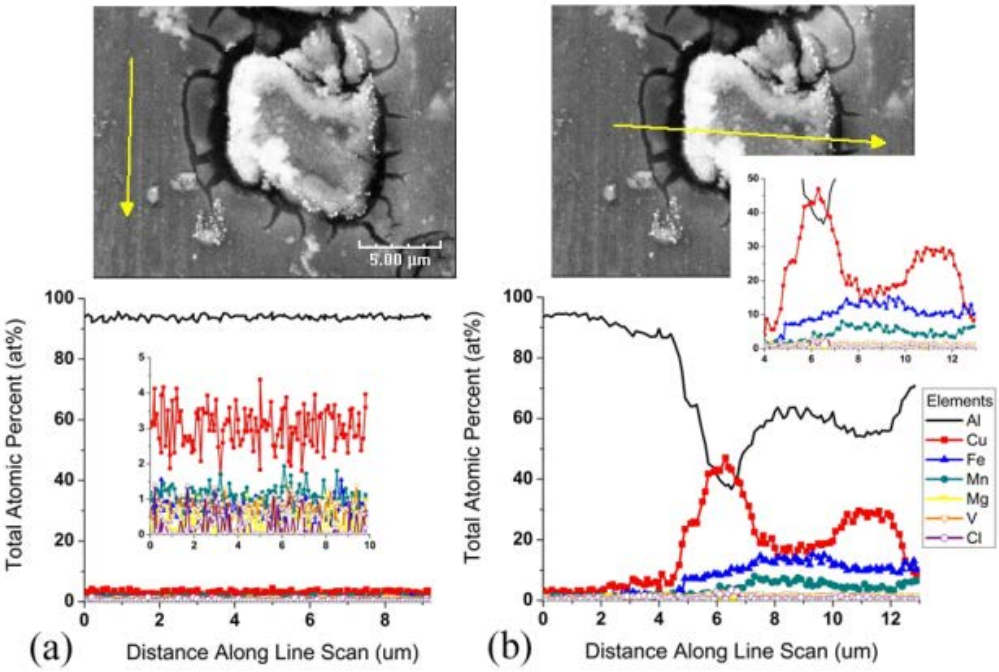

Figure 55. Secondary electron image obtained at 15 kV of AA2024–T3 specimen exposed to 50 mM NaCl solution for 24 hours. The yellow arrow indicates location and direction of EDS. (a) represents the unattacked matrix composition way from a pitting site. (b) shows a pitting site above an Al–Cu–Fe–Mn intermetallic particle.

Vanadium-rich precipitates were observed by EDS on the surface of the AA2024-T3 specimens exposed to the low 5 mM $NaVO_3$ plus 50 mM NaCl solutions. These precipitates surrounded the pit. Higher magnification images presented in Figure 56, indicate that these precipitate products contain vanadium. Figure 56 also shows the atomic composition of the surface near the pit, and that of the underlying surface, possibly an intermetallic particle. Figure 56 (a) shows an example of the unaffected matrix. There is no vanadium peak (EDS) for the unpitted matrix, even though it was exposed to vanadate containing solutions for 24 hours. Figure 56(b) shows a vanadium containing precipitate over a dual phase intermetallic particle—both Al–Cu–Mg and Al–Cu–Fe–Mn compositions exist. Boag et al.,[140] found that most intermetallic particles in AA2024–T3 were of multiple compositions.

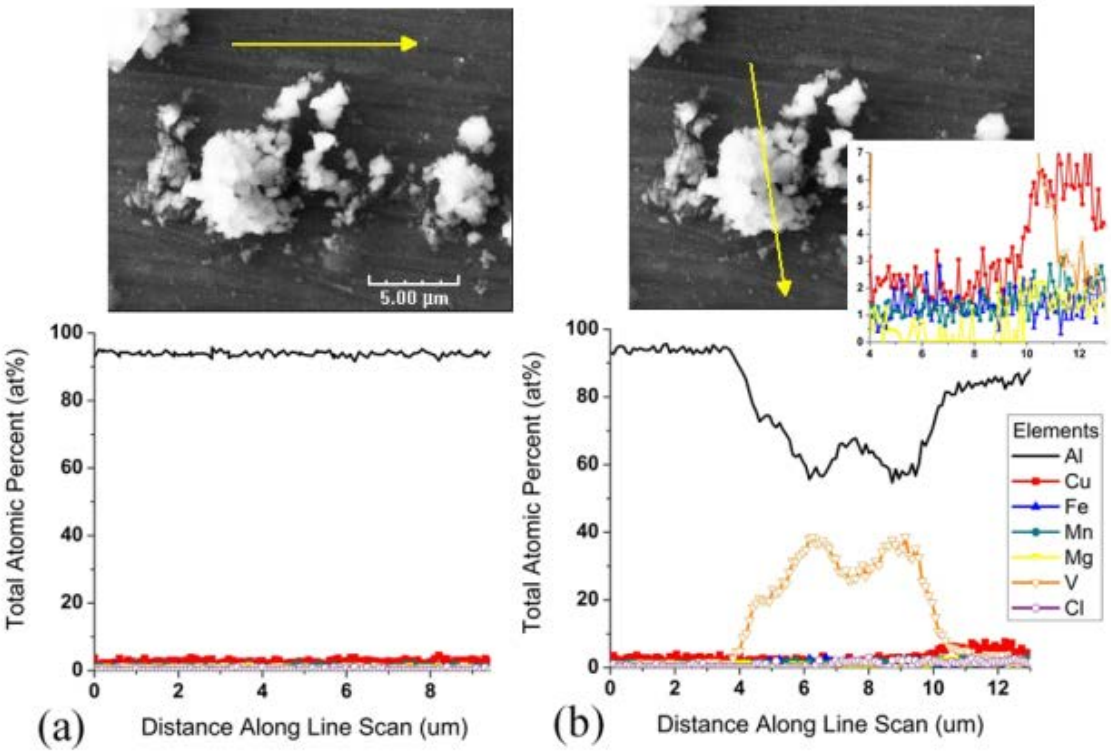

Figure 56. Higher magnification secondary electron image taken at 15 kV of AA2024–T3 specimen exposed to 5 mM $NaVO_3$ plus 50 mM NaCl for 24 hours. The yellow arrow indicates location and direction of EDS scan. Precipitated products are shown to be vanadium rich. There appears to be a dual phase intermetallic particle at the EDS line scan in the right hand image. Both Al–Cu–Mg and Al–Cu–Fe–Mn compositions exist.

Figure 57 shows the composition of an Al–Cu–Fe–Mn intermetallic particle away from the pitting site. There was little vanadium detected over the constituent particle. The level of vanadium on the intermetallic particle away from the pitting site was approximately the same as that of the matrix near the pitting site [Figure 56(a)]. The intermetallic particles did not show a corresponding increase in vanadium concentration as was seen for the corrosion product formed at the pit site [Figure 56(b)].

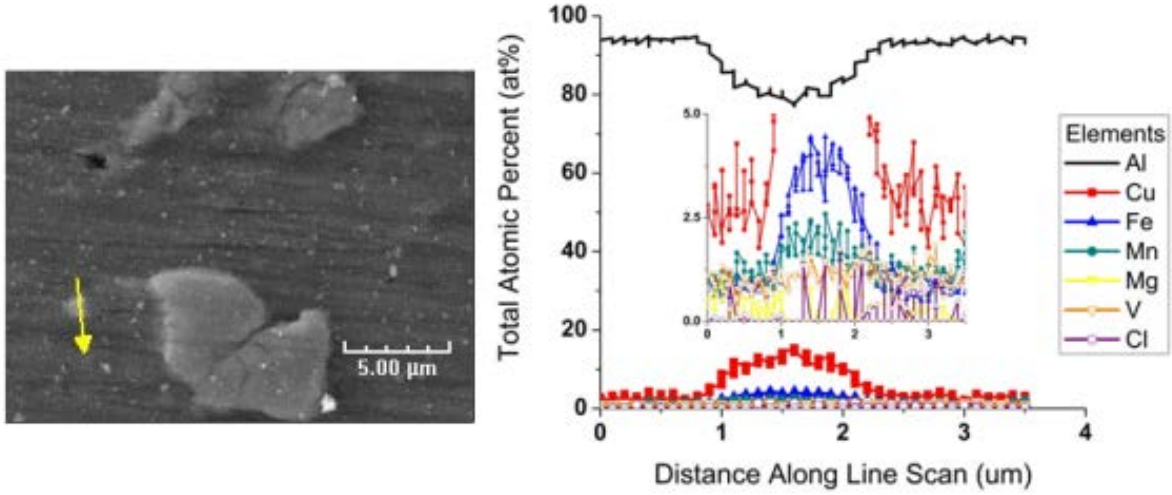

Figure 57. Backscattered electron image, in the compositional mode, taken at 15 kV with 184 second collection time of AA2024–T3 specimen exposed to 5 mM $NaVO_3$ plus 50 mM NaCl for 24 hours. Yellow arrow indicates location and direction of EDS scan. The vanadium concentration of an intermetallic particle away from the pitting site is approximately the same as that of the matrix near the pitting site (Figure 56).

AA2024-T3 exposed to 150 mM $NaVO_3$ plus 50 mM NaCl also showed an increase of vanadium at the pitting site, which is associated with an intermetallic particle containing aluminum, manganese, and iron. This increase in vanadium concentration at the pitting site was not observed on intermetallic particles that are not associated with pits in this post-test analysis. At higher $NaVO_3$ concentrations, a yellow precipitate was not evident at the pitting sites. There was no increase in vanadium on the intermetallic particle. In summary, for all vanadate concentrations, vanadium was detected by EDS at pitting sites as a precipitate or deposit but was not observed at unattacked intermetallic particles or on the matrix.

Inhibition of Localized Corrosion during Anodic Polarization

In the case of pure aluminum specimens, the mean E_{pit} increased with $NaVO_3$ concentration (Figure 58). There was a greater difference between E_{pit} for different vanadate concentrations after the 24 hour open circuit exposure [Figure 58(b)] as compared to the 1 hour open circuit exposure [Figure 58(a)].

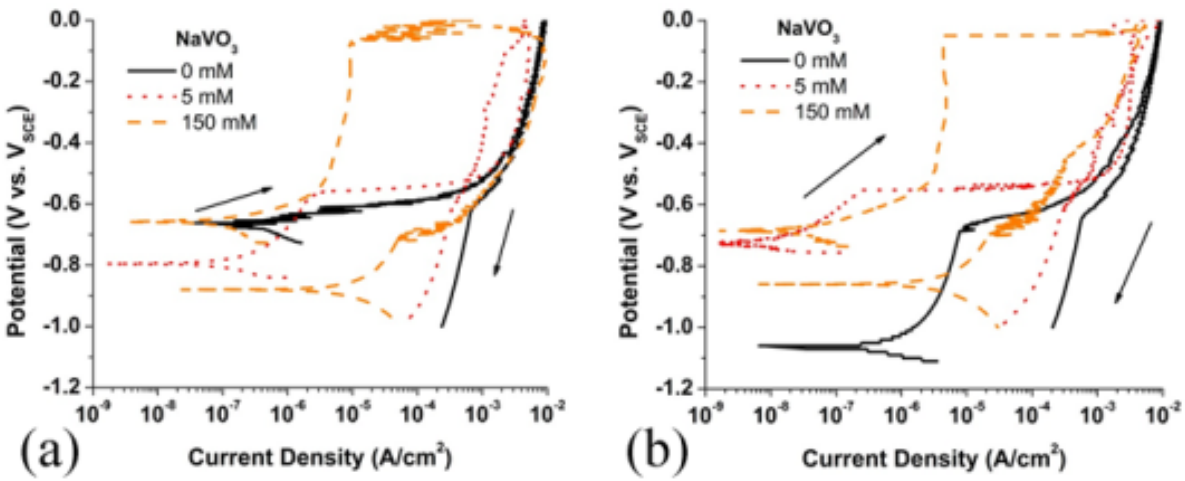

Figure 58. Typical anodic E-log(i) polarization behavior for Al (99.9%) specimens in open to the air 50 mM NaCl solution containing 0, 5, and 150 mM $NaVO_3$ [(a) after 1 hour open circuit; and (b) after 24 hour open circuit].

The E_{corr} and E_{pit} for the aluminum specimens increased with the addition of vanadate into 50 mM NaCl solutions. There was a change in the width of potential covered in the passive range. The passivation current density, i_{pass}, was approximately 10^{-6} A/cm^2 irrespective of inhibitor concentration or exposure time. Increasing the exposure time from 1 to 24 hours raised the E_{pit} and thus the range of passivity for all vanadate concentrations. In comparison, after 24 hours at the open circuit potential, aluminum specimens in 50 mM NaCl solution also had increases in the passive region, but these increases were related to a reduction in E_{corr} rather than a further increase in E_{pit}.

The high-purity Al E_{pit} cumulative probability diagrams for 1 and 24 hour open circuit showed a monotonic relationship between the average E_{pit} and the vanadate concentration. After 1 hour at open circuit potential, significant improvement in E_{pit} is seen at 75th percentile but below 20th percentile, the improvement is small (Figure 59). After 24 hours at OCP in 50 mM NaCl solutions containing vanadate, the effect of different vanadate inhibitor concentrations on E_{pit} was more visible (Figure 60). A significant increase in E_{pit} below the 20th percentile was seen with 150 mM $NaVO_3$ compared to that in 50 mM NaCl without inhibitor. For this 150 mM $NaVO_3$ concentration, the increase in E_{pit} at the 10th percentile is similar to that for the 70th percentile for the 10 and 50 mM $NaVO_3$ concentrations and is greater than those for 5 mM $NaVO_3$ concentration. This strong effect of inhibition is not seen for anodic scans after the 1 hour open circuit exposure. Above the 30th percentile, all vanadate concentrations above 5 mM $NaVO_3$ in solution exhibited more than a 100 mV increase in E_{pit}.

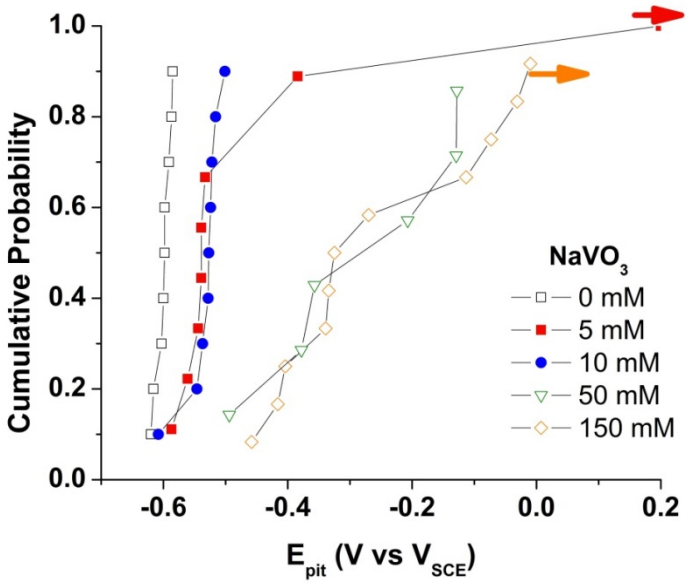

Figure 59. Cumulative probability plot of E_{pit} for Al 99.99% in open to the air 50 mM NaCl solutions plus various concentrations of $NaVO_3$. Data points indicate cumulative probability of pitting before potential reversal at 0 or 0.2 V_{SCE}. Arrows indicate specimens that did not pit at the potential indicated.

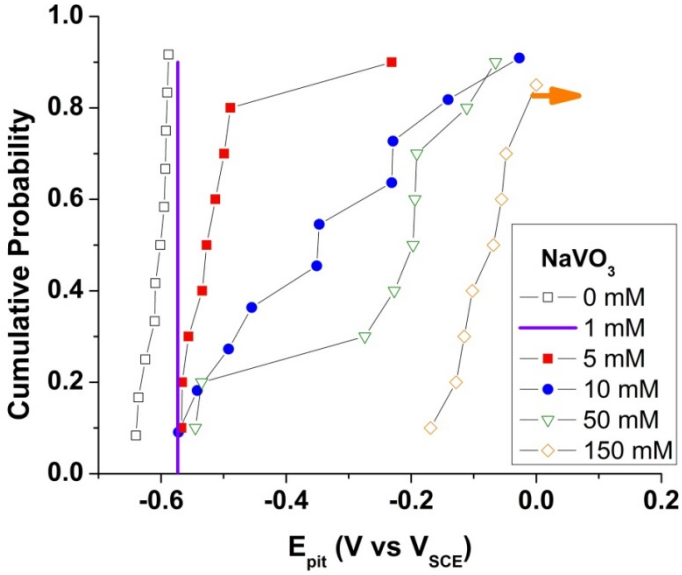

Figure 60. Cumulative probability plot of E_{pit} for Al 99.99% after 24 hours of exposure in open to the air 50 mM NaCl solutions plus various concentrations of $NaVO_3$. Data points indicate cumulative probability of pitting before potential reversal at 0 V_{SCE}. Arrows indicate specimens that did not pit at the potential indicated.

In summary, vanadate concentration did not affect the i_{pass} value for high-purity aluminum, but did affect E_{pit} and the passive potential range. Longer exposure times to inhibitor concentrations or high inhibitor concentration for short exposure times were tied to an overall increase in resistance to pit formation and stabilization.

An increase in E_{pit} was observed on AA2024–T3 when both $NaVO_3$ and NaCl are in solution (Figure 61). The 5 mM $NaVO_3$ plus 50 mM NaCl tests showed the most significant increase in E_{pit} compared to the other $NaVO_3$ in 50 mM NaCl solutions. However, the increase in E_{pit} is not monotonic with $NaVO_3$ additions in the case of AA2024-T3.

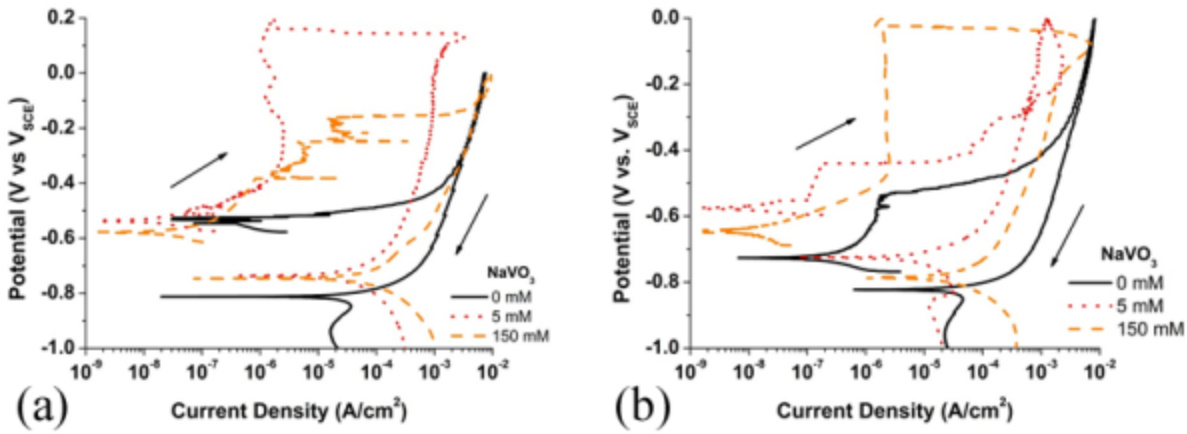

Figure 61. Typical anodic E-log(i) polarization behavior for AA2024–T3 specimens in open to the air 50 mM NaCl solution containing 0, 5, and 150 mM NaVO3 [(a) after 1 hour open circuit exposure; (b) after 24 hour open circuit exposure].

Passive current density was observed when the addition of vanadate inhibitor to the solution raised E_{pit} above the open circuit potential, E_{corr}. The average passive current, i_{pass}, was approximately 10^{-6} A/cm^2. AA2024-T3 specimens tested in 50 mM NaCl solutions with a 1 hour open circuit exhibited pitting near E_{corr}. Solutions containing 5 mM $NaVO_3$ plus 50 mM NaCl had the largest range of passive current density and the greatest variability in range. After 1 hour, AA2024–T3 exposed to 50 and 150 mM $NaVO_3$ plus 50 mM NaCl solutions exhibited similar passive current density. There was a trend of AA2024-T3 specimens exposed to higher inhibitor concentrations having greater passive potential ranges due to the increase in E_{pit} above E_{corr}. The anodic E–log(i) polarization behavior after 24 hours of solution exposure for AA2024-T3 is shown in Figure 61. After 24 hours of exposure to similar $NaVO_3$ concentrations, an i_{pass} of 10^{-6} A/cm^2 was observed. Vanadate concentration and time of the open circuit exposure did not affect the observation of a -0.8 V_{SCE} E_{repass}.

Twenty-four hours of exposure to $NaVO_3$ plus NaCl solutions raised E_{pit} of AA2024-T3, as presented in Figure 61. Fifty percent of the AA2024-T3 specimens in 50 and 150 mM $NaVO_3$ plus 50 mM NaCl solutions did not reach E_{pit} as determined by a current density of 10^{-4} A/cm^2 during the upward polarization scan, which was reversed at 0 V_{SCE}. This was unlike the1 hour anodic E–log(i) polarization behavior for which 5 mM $NaVO_3$ plus 50 mM NaCl solution showed the largest increase in E_{pit}. As in the case of the 1 hour open circuit exposures, the increase in E_{pit} was not monotonic with inhibitor concentration after 24 hour open circuit exposures. Similar E_{pit} relationships were observed after both 1 hour and 24 hour exposure at low

inhibitor concentration. The 5 mM $NaVO_3$ solution exhibited a higher average E_{pit} as compared to the 10 mM $NaVO_3$ solution, as shown in Figure 62 and Figure 63.

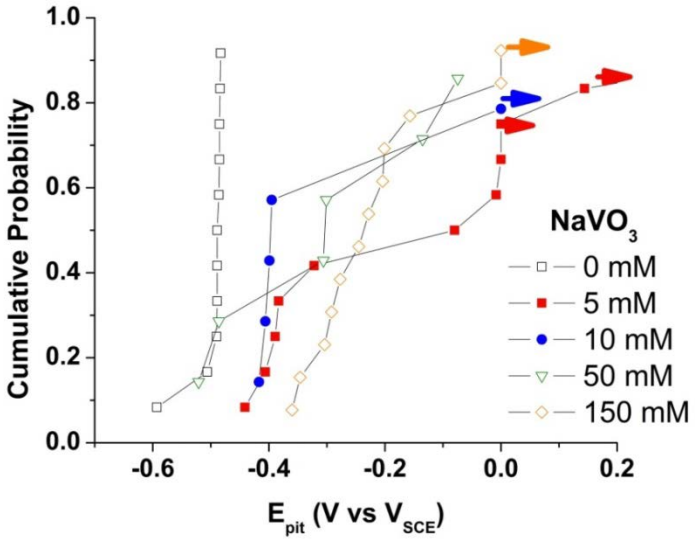

Figure 62. Cumulative probability plot for AA2024-T3 after 1 hour in open to the air 50 mM NaCl solution plus various concentrations of $NaVO_3$. Data points indicate cumulative probability of pitting before potential reversal at 0 or 0.2 V_{SCE}. Arrows indicate specimens that did not pit at the potential indicated.

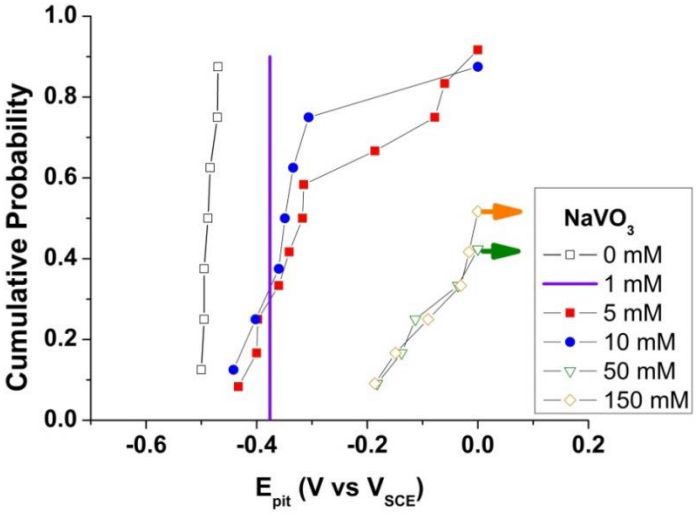

Figure 63. Cumulative Probability plot for AA2024–T3 after 24 hours in open to the air 50 mM NaCl solution plus various concentrations of $NaVO_3$. A single test was conducted with 1 mM $NaVO_3$. Data points indicate cumulative probability of pitting before potential reversal at 0 V_{SCE}. Arrows indicate specimens that did not pit at the potential indicated.

Cumulative probability plots of E_{pit} after one-hour exposures showed that median E_{pit} was greater than 0 mM $NaVO_3$ but did not increase monotonically with inhibitor concentration. The improvement in E_{pit} is statistically significant but the trend indicates that the upper populations improved significantly while the worst performing AA2024-T3 coupons were only slightly improved over those with no inhibitor (Figure 62). Significant improvement was seen at 75th percentile but at below 20th percentile, the improvement was small (Figure 62). The greatest increase in E_{pit} was not at the higher concentrations of $NaVO_3$ but with 5 mM $NaVO_3$.

Figure 63 presents E_{pit} cumulative probability plot for AA2024-T3 exposed for 24 hours to 50 mM NaCl solution plus various concentrations of $NaVO_3$. E_{pit} increases above that for uninhibited 50 mM NaCl for all specimens exposed in $NaVO_3$ concentrations plus 50 mM NaCl solutions. As shown in Figure 63, after 24 hours at open circuit potential, E_{pit} for low and high inhibitor concentrations began to separate. AA2024-T3 specimens exposed to 50 or 150 mM $NaVO_3$ plus 50 mM NaCl solutions have a higher E_{pit} range than the 1, 5, or 10 mM $NaVO_3$ plus 50 mM NaCl solutions. Such a strong relationship between inhibitor concentration and E_{pit} was not seen after 1 hour exposure.

Effects of Vanadate Pretreatment on Anodic Behavior of AA2024–T3

The upward anodic E–log(i) polarization behavior for AA2024-T3 specimens that were pretreated in the 5 mM $NaVO_3$ inhibitor solution and exposed in 50 mM NaCl without inhibitor additions showed only a slight increase in E_{pit} compared to AA2024-T3 specimens in 50 mM NaCl solutions. However, AA2024-T3 specimens exposed in 50 mM NaCl plus 5 mM $NaVO_3$ showed an increase in E_{pit} up to 0.5 V, as shown in Figure 64. The pretreated specimens did not exhibit a passive current density range and a similar E_{repass} of -0.8 V_{SCE} as seen in the case of the 50 mM NaCl solution.

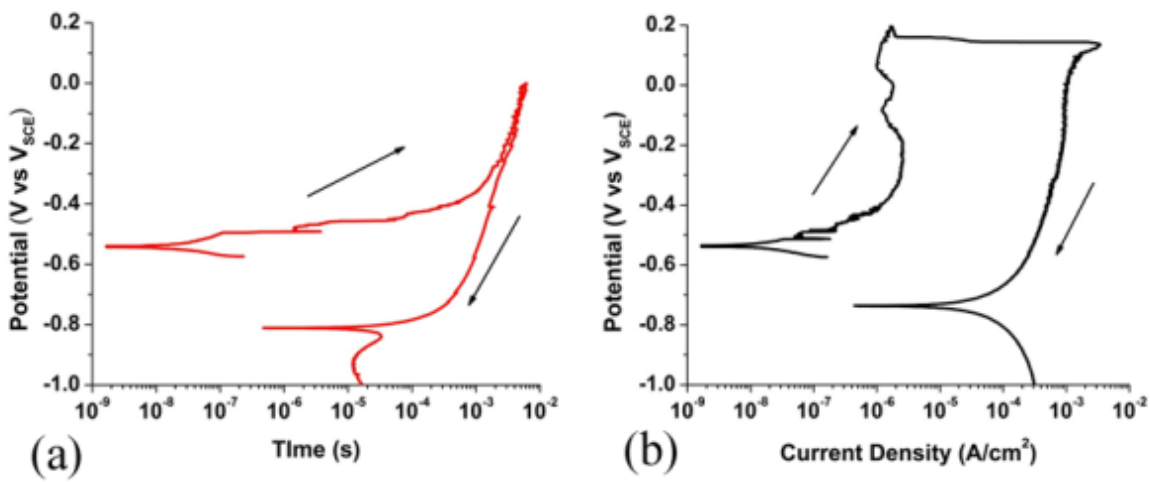

Figure 64. Anodic E–log(i) polarization behavior for AA2024-T3 specimens: (a) 24 hours, 5 mM $NaVO_3$ inhibitor pretreated and exposed in inhibitor free 50 mM NaCl; (b) exposed in 50 mM NaCl plus 5 mM $NaVO_3$. 1 hour open circuit exposure in the test solution occurred prior to polarization scans. Arrows indicate the direction of polarization.

The cumulative probability plot for E_{pit}, Figure 65, for the pretreated samples demonstrates that pretreatment did little to improve E_{pit} of AA2024-T3. The inhibitor $NaVO_3$ must be in solution with NaCl to increase E_{pit} significantly.

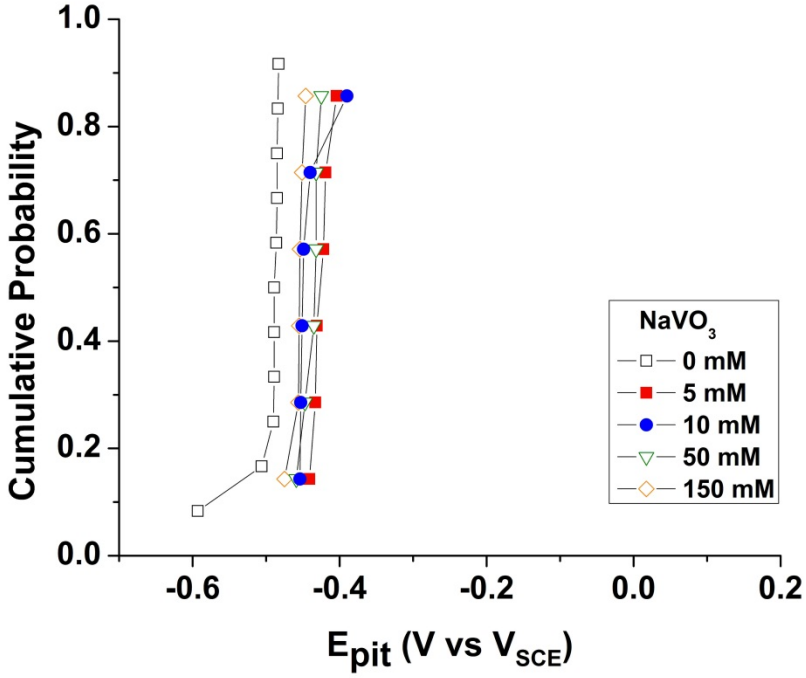

Figure 65. E_{pit} cumulative probability plot for AA2024–T3 pretreated for 24 hours in various concentrations of $NaVO_3$ open to the air solutions then tested in open to the air 50 mM NaCl solutions. An 1 hour open circuit in test solution occurred prior to anodic E–log (i) polarization scan.

Effects of Vanadate Inhibitors on Oxygen Reduction Reaction and Hydrogen Evolution Rates on Different Materials

Both the ORR and HER were investigated in cathodic E–log(i) polarization scans under controlled rotation rates. In Figure 66, the effect of different materials on the cathodic current density in 50 mM NaCl solutions is presented. Aluminum has the lowest current density due to an insulating, high-bandgap, surface oxide film, which acts as a barrier to electron transfer to the aluminum cathode.[9] As high-purity copper does not have a significant oxide barrier to prevent electron transfer to the cathode, the rate of the ORR on copper was determined by the rate of oxygen diffusion and its concentration in solution. AA2024-T4 contains an Al-Cu solid solution and copper-rich intermetallic particles, which support ORR, in an aluminum matrix.[90] The magnitude of the resulting cathodic current density was between that for high-purity aluminum and high-purity copper, because an array of copper-rich sites on a benign aluminum matrix has a lower surface area to support ORR when compared to a homogenous copper surface of similar area.

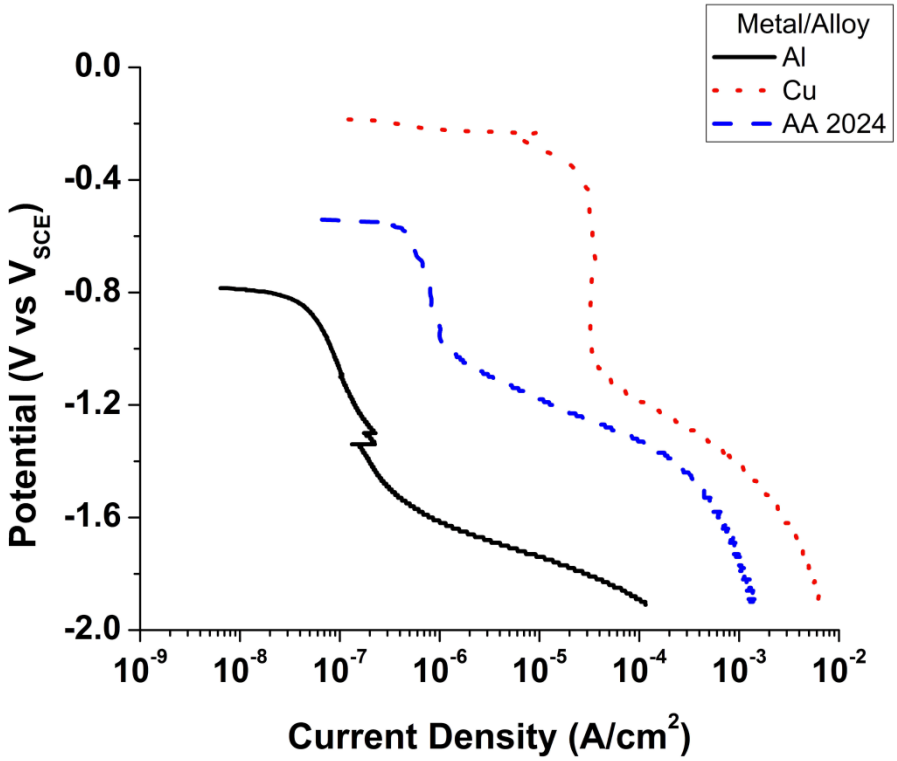

Figure 66. Cathodic E-Log(i) polarization behavior for high-purity Al, AA2024-T4,and high-purity Cu in open to the air 50 mM NaCl solution with an electrode rotation speed of 0 rpm. A 1 hour open circuit with specimen in the test solution occurred prior to cathodic polarization. Data not corrected for ohmic resistance.

The Koutecky-Levich method was used to extract i_{act} values which were used to calculate i_{Lim} for the Levich plots. The Koutecky-Levich plot, shown in Figure 67, is for Cu in open to air 50 mM NaCl at two different potentials of -0.8 V_{SCE} and -1 V_{SCE}. While the data were taken in the mixed ORR and HER region, ORR is dominant. As shown, the high-purity copper specimen followed ideal behavior with the inverse of the total cathodic current density increasing linearly with the inverse square root of rotation rate. Even when both the HER and ORR are occurring simultaneously on Cu, the cathodic reaction, lying between the theoretical lines for 8 and 7 ppm of oxygen dissolved in the solution, followed ideal Levich behavior, as shown in Figure 68 (Koutecky–Levich plot is shown in Figure 67). In contrast, AA2024–T4, also shown in Figure 68, the cathodic reaction falls below that for copper due to the limited number of Cu-rich sites. However, there is still a weak effect of rotation rate.

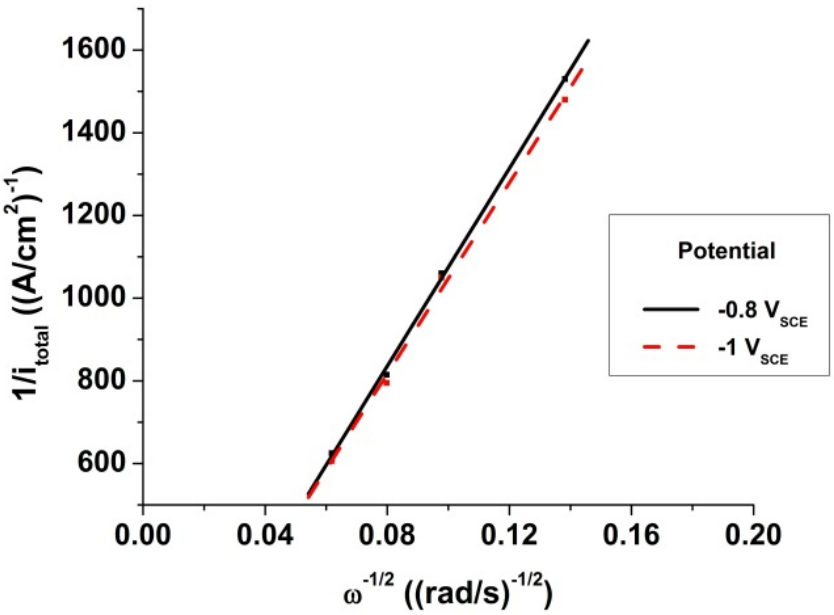

Figure 67. Koutecky–Levich plot for Cu in open to the air 50 mM NaCl at three different potentials of -0.8 V_{SCE} and -1 V_{SCE}. Data was not corrected for ohmic resistance.

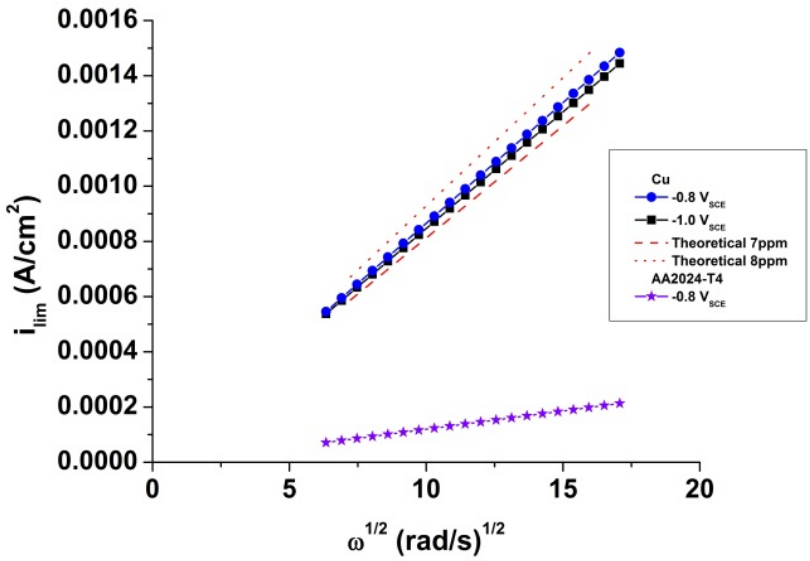

Figure 68. Levich plot of i_{Lim} extracted from i_{Total} on Cu and AA2024 in 50 mM NaCl showing comparison of experimental results to theoretical mass transport limited ORR rates.

Effects of Vanadate on Reducing the Oxygen Reduction and Hydrogen Evolution Reactions

The effect of $NaVO_3$ on current density for high-purity Al was minimal compared to the effect on AA2024–T4 and high-purity Cu. This was interpreted to result from the presence, on high-purity aluminum, of an insulation layer of Al_2O_3, which limits cathodic current density. For the high-purity copper specimens, the addition of $NaVO_3$ decreased the current density during ORR (Figure 69). AA2024–T4 also had a current density strongly affected by the inhibitor. There was a strong correlation between vanadate concentration in the 50 mM NaCl and current density for Cu and AA2024–T4 specimens. The current density was reduced stepwise from the lowest to the highest vanadate concentration with the highest concentration showing the greatest effect (Figure 70). The aluminum alloy AA2024-T4 had a significant response to the addition of $NaVO_3$ that was similar to that of copper. However, there was not a clear dose concentration–response relationship with current density decreasing with $NaVO_3$ concentration as was seen for high-purity copper. It is possible that the 5 mM $NaVO_3$ plus 50 mM NaCl solution is above the critical vanadate concentration need to limit the ORR on the surface for AA2024–T4.[32] No effect of the inhibitor is observed at very negative potentials where proton reduction occurs at a similar or higher rate as the ORR. As shown in Figure 69, for high-purity aluminum samples, all cathodic currents were in the mixed oxygen-hydrogen reduction region and could not be used to calculate Levich plots. For AA2024–T4 in 50 mM NaCl solution, high rotation rates and the resulting increased oxygen concentration gradient led to greater current density in the oxygen reduction region. However, only a small portion of the cathodic scan occurred before the start of significant HER. As can be seen in Figure 69, a slight change in current density occurred where HER begun due to the change in the pH of the solution. The magnitude of ORR current density, even below the HER start voltage, was greater and allowed for the calculation of Koutecky–Levich and Levich plots for Cu and AA2024–T4.

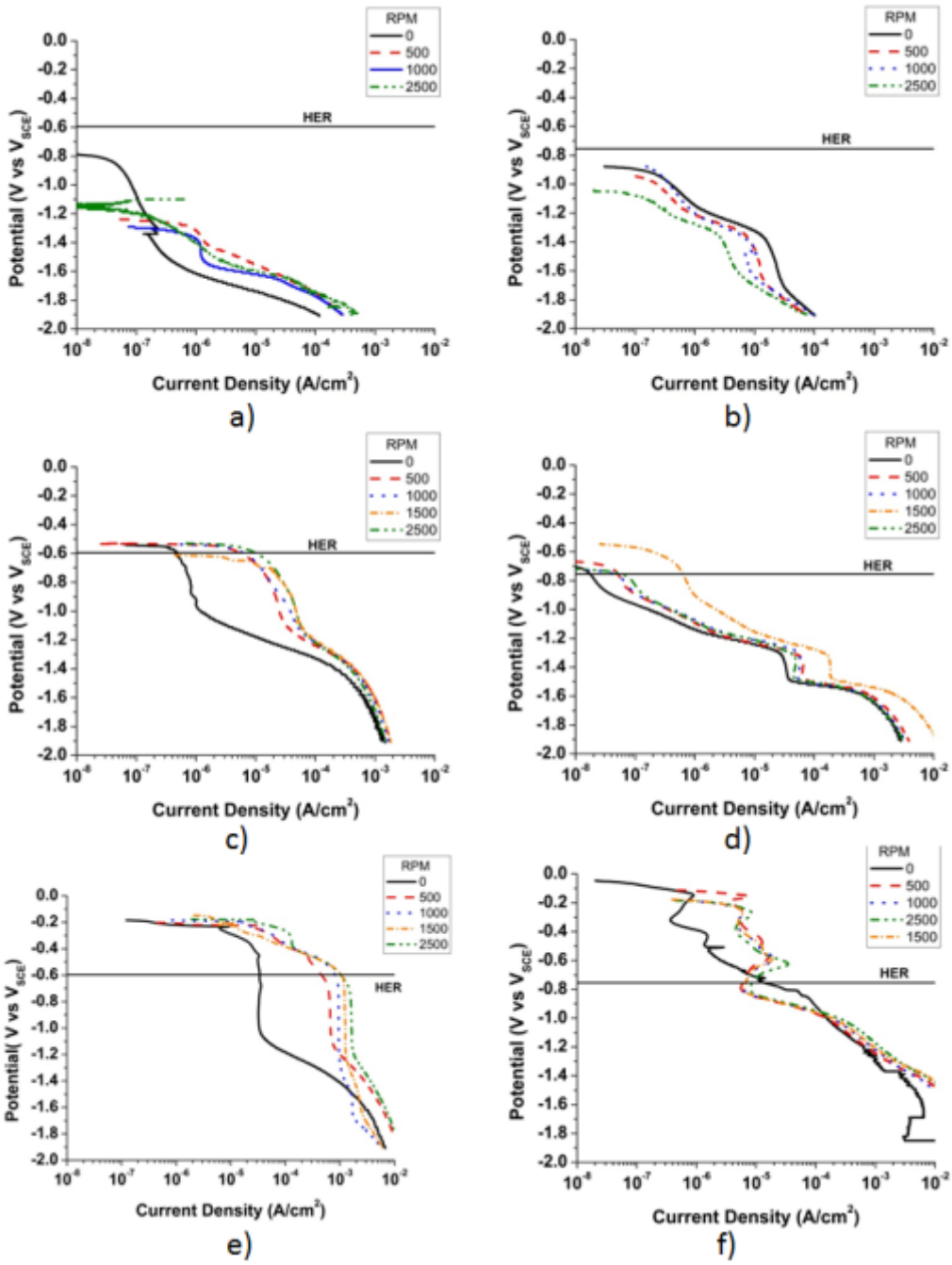

Figure 69. Effect of rotation rate for open to the air 0 (left column) and 150 (right column) mM $NaVO_3$ plus 50 mM NaCl solutions on the cathodic polarization behavior of high-purity Al, AA2024–T4, and high-purity Cu. The data were corrected for ohmic resistance. (a) Al in 50 mM NaCl, (b) Al in 150 mM $NaVO_3$ plus 50 mM NaCl, (c) AA2024-T4 in 50 mM NaCl, (d) AA2024-T4 in 150 mM $NaVO_3$ plus 50 mM NaCl, (e) Cu in 50 mM NaCl, and (f) Cu in 150 mM $NaVO_3$ plus 50 mM NaCl.

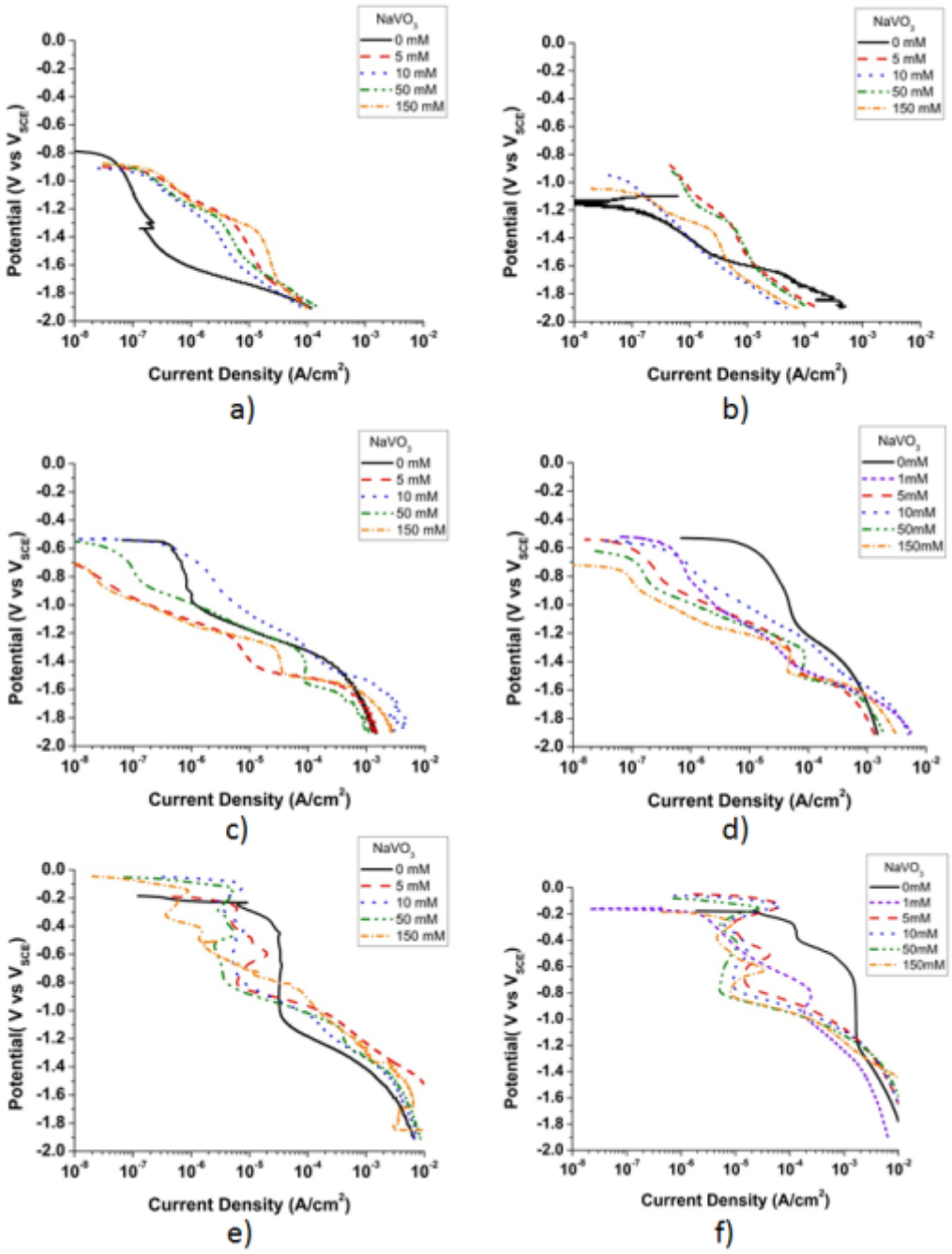

Figure 70. Effect of various $NaVO_3$ concentrations in open to the air 50 mM NaCl solution on the cathodic polarization behavior of high-purity Al, AA2024–T4, and Cu at 0 (left) and 2500 (right) RPM. Data is not corrected for ohmic resistance. (a) Al at 0 rpm, (b) Al at 2500 rpm, (c) AA2024-T4 at 0 rpm, (d) AA2024-T4 at 2500 rpm, (e) Cu at 0 rpm, and (f) Cu at 2500 rpm.

The Koutecky-Levich plot, shown in Figure 71, presents the data for Cu in open to the air 50 mM NaCl plus various concentrations of $NaVO_3$ at a potential of -0.8 V_{SCE}, a potential in the ORR region. Current densities decreased with increasing $NaVO_3$ concentrations, except for 150 mM $NaVO_3$ plus 50 mM NaCl solution. Vanadate concentrations in solution with 50 mM NaCl removed the effects of rotation rates.

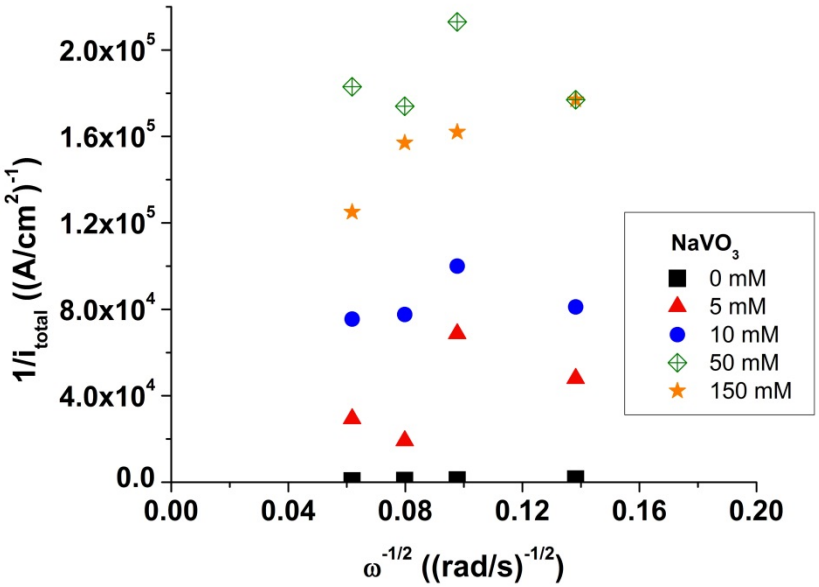

Figure 71. Koutecky–Levich plot for Cu in open to the air 50 mM NaCl plus various concentrations of $NaVO_3$ at a potential of -0.8 V_{SCE}. Data was not corrected for Ohmic resistance.

Figure 72 presents the Koutecky-Levich plot for AA2024–T4 in open to the air 50 mM NaCl solutions with various concentrations of vanadate at the potentials of -0.8 V_{SCE} (ORR dominant region). The effect of the $NaVO_3$ on the ORR is illustrated in Figure 72. It should also be noted that a V^{5+} reduction to V^{4+} can occur in the same potential range in which the ORR is dominant.[31] Vanadate significantly decreased the ORR rate and removed the effect of rotation rate (Figure 72).

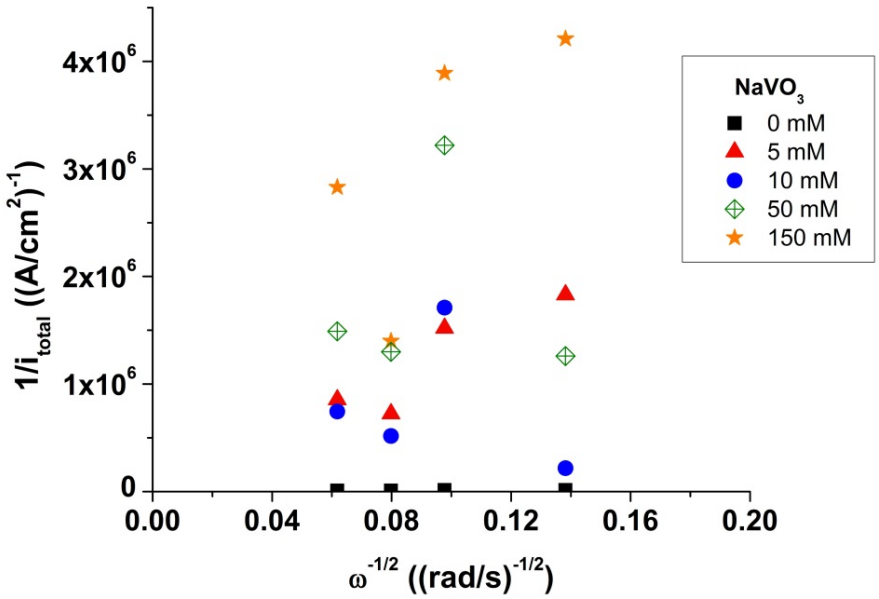

Figure 72. The Koutecky–Levich plot for AA2024–T4 in open to the air 50 mM NaCl plus various concentrations of $NaVO_3$ at a potential of -0.8 V_{SCE}.

The usual Levich correlation between an increasing limiting current density for ORR and rotation rate was not obtained for Cu with vanadate in solution with 50 mM NaCl. Figure 73 (Koutecky-Levich plot shown in Figure 71) showing extracted i_{Lim} versus $\omega^{1/2}$ demonstrates the effect of $NaVO_3$ on ORR in the mass transport-limited regime. Increasing the $NaVO_3$ concentrations caused ORR on Cu to deviate from idea Levich behavior in the ORR regime. Lower concentrations of $NaVO_3$ were more effective than higher concentrations at causing deviation from ideal behavior.

In Figure 74 (extracted i_{Lim} versus $\omega^{1/2}$), all of the different concentrations of $NaVO_3$ suppressed the ORR on AA2024–T4. Figure 74 demonstrates the effect of inhibitor on AA2024–T4 (Koutecky-Levich plot shown in Figure 72). The ORR is changed from ideal behavior on copper to non-ideal behavior on AA2024 in 50 mM NaCl solutions, as discussed by Jakab.[90] The $NaVO_3$ plus 50 mM NaCl solutions further suppressed ORR reaction on AA2024–T4. Based on Figures Figure 73 and Figure 70(d), it is likely that the critical inhibitor concentration needed to suppress ORR on AA2024–T4 is below the 5 mM $NaVO_3$ level.

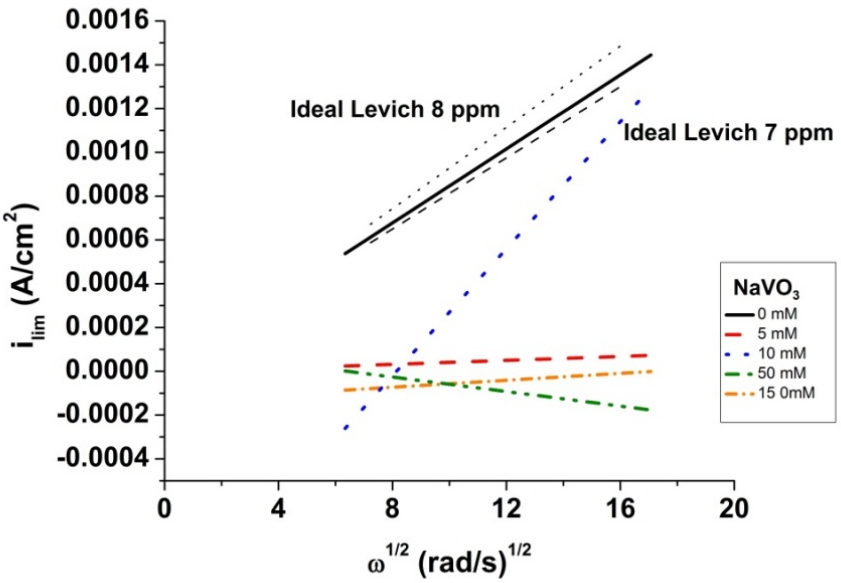

Figure 73. Levich plot (i_{Lim} extracted from i_{Total}) of Cu using data from the ORR region only (potential of -0.8 V_{SCE}) shows a loss of ideal mass transport controlled behavior. Tests performed open to the air 50 mM NaCl plus $NaVO_3$ solutions.

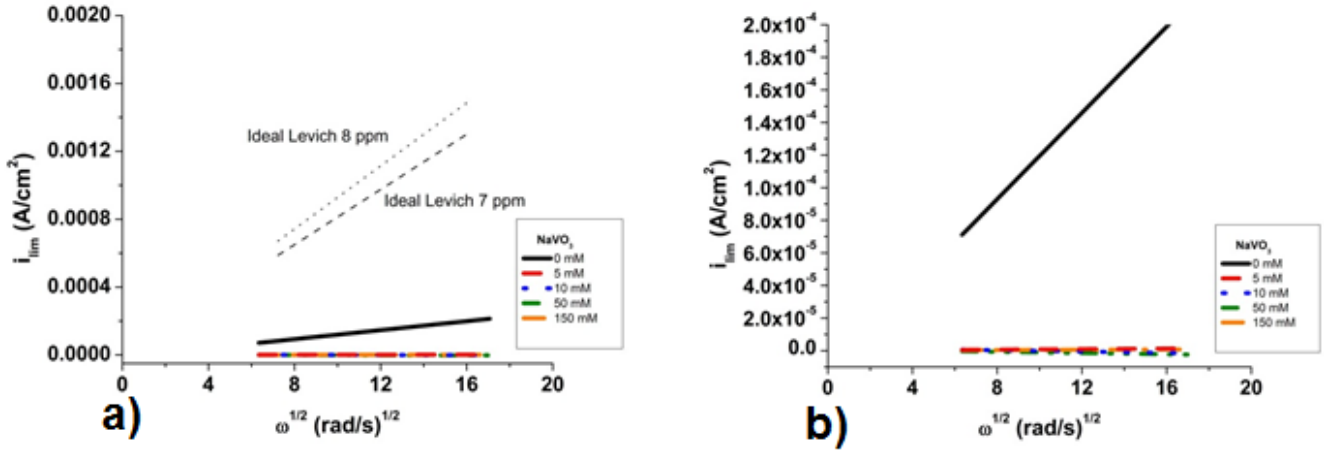

Figure 74. Levich plot (i_{Lim} extracted from i_{Total}) for AA2024–T4 using data taken in the ORR region. All analyzed data was taken at -0.8 V_{SCE}. Tests performed at ambient temperature in open to the air solutions of 50 mM NaCl plus various $NaVO_3$ concentrations. (b) emphasizes the effect of $NaVO_3$ on current density.

As seen in Figure 75, the total current density on the surface of AA2024-T3 or Cu was reduced below that of the extracted charge transfer controlled current for a specimen exposed only to sodium chloride solution. This result indicates that vanadate inhibits the charge transfer controlled current density as well.

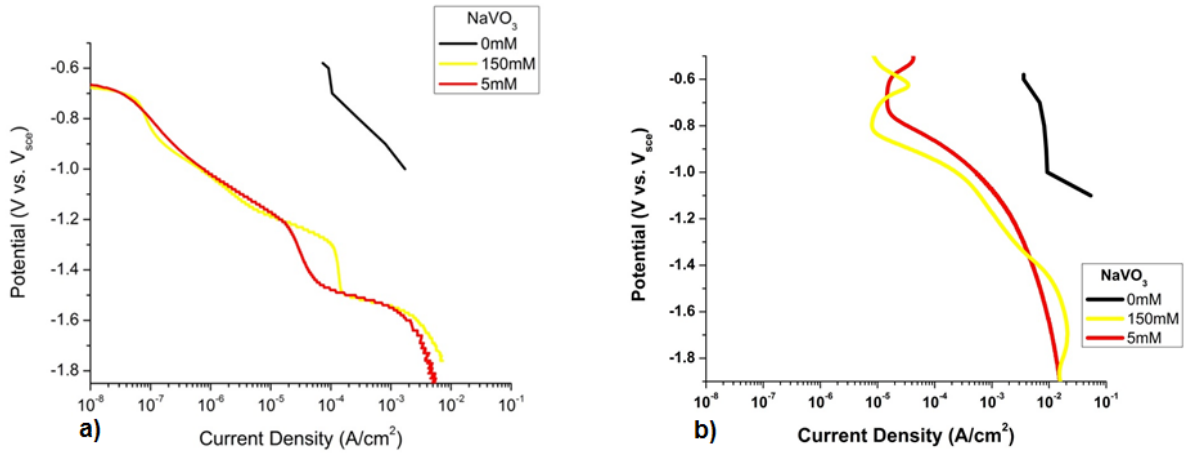

Figure 75. Cathodic polarization of (a) AA2024-T3 or (b) Cu in open to the air 50 mM NaCl solution with 0, 5, or 150 mM $NaVO_3$. The black line representing no addition inhibitor is the only the current associated with charge transfer kinetics.

Corrosion Inhibition of AA2024 with Inhibitors Combination

Cerium-Permanganate Combinations

Three possible inhibitors interaction mechanisms are suggested. The combination can act independently, acting to fill gaps where the other inhibitor provides insufficient protection. They can have a supportive chemical role by altering the species of the other inhibitor, for instance by oxidizing a species to a more stable state leading to enhanced corrosion protection. Thirdly, there could be a new combined species of ion or oxide that involves both inhibitors that provides corrosion protection in an expanded manner.

The E-pH speciation predictions for the cerium-water system can be seen in Figure 76(b). These speciation diagrams indicate predominante species ratios at -0.5 V_{SCE}. This potential is approximatly the value of the observed OCP for AA2024-T351 in 0.05 M sodium chloride solution with Ce^{3+} or the permanganate ion in solution. The stable cerium oxide is CeO_2 above a pH of 9.5 and $Ce(OH)_3$ between a pH of 7.3 and 9.5. When cerium acetate is added to solutions in contact with AA2024-T351, the species will undergo a chemical reaction near high pH regions such as at IMC where the ORR occurs. This behavior produces a precipitate oxide of $Ce(OH)_3$ at low potentials such as those seen on AA2024-T351 at -0.5 V vs. SCE. The chemical reaction can be seen in Equation 18.

$$\mathrm{Ce}^{3+} + 3\,OH^- \leftrightarrow Ce(OH)_3 \qquad \textbf{Equation 18}$$

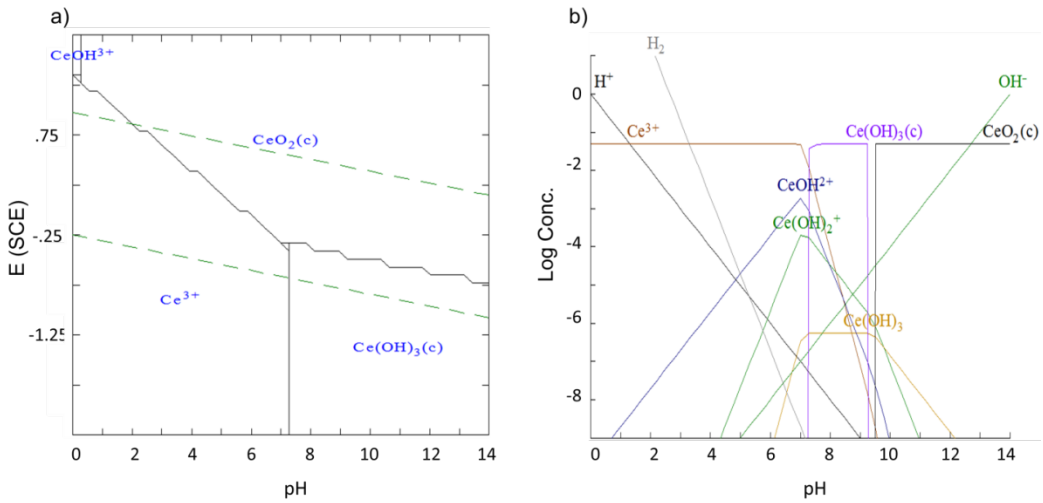

Figure 76. (a) The E-pH behavior of 0.05 M Ce3+ in aqueous solution. (b) The concentrations of cerium species in the cerium-H_2O system at -0.5 V vs. SCE, near OCP of AA2024.

The E-pH speciation predictions for the manganese-water system can be seen in Figure 77(b). The stable Mn(II) species is $Mn(OH)_2$ above a pH of 8.5 at -0.5 V(SCE). Permanganate (MnO_4^-) is a very strong oxidizer due to its high potential as seen in Figure 77(a). When permanganate is added to solution in contact with AA2024-T351 at a lower potential, it has been shown to be reduced through serveral possible electrochemical reactions. Over all ranges of pH, MnO_4^- in the +7 valence state will likely first be reduced to manganese (IV) dioxide by the following electrochemical ½ cell reaction (Equation 19).[73] Eo for this reaction at pH 8.4 is 0.54 V vs. SCE.

$$MnO_4^- + 4\,H^+ + 3e^- \leftrightarrow MnO_2 + 2H_2O \qquad \textbf{Equation 19}$$

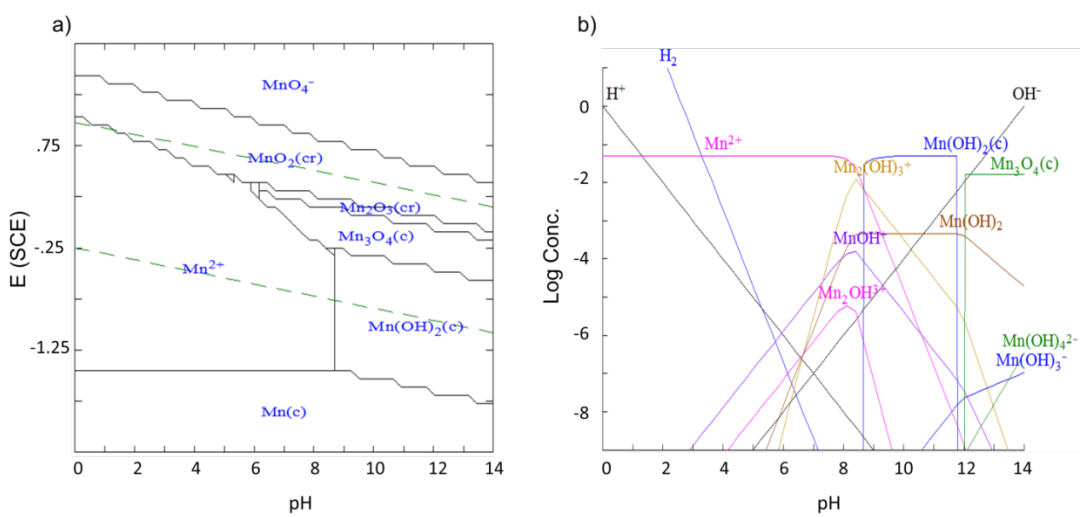

Figure 77. (a) The E-pH behavior of 0.05 M MnO_4^- in aqueous solution. (b) The concentrations of manganese species in the manganese-H_2O system at -0.5 V vs. SCE, near OCP of AA2024.

Several additional electrochemical reactions can further reduce the oxide to Mn(*III*), a mixed valence oxide, and finaly the Mn(*II*) state (Equation 20, Equation 21 and Equation 22).[73]

$$2MnO_2 + 4\,H^+ + 2e^- \leftrightarrow Mn_2O_3 + 2H_2O \qquad \textbf{Equation 20}$$

$$3Mn_2O_3 + 4H^+ + 2e^- \leftrightarrow 2\,Mn_3O_4 + 2H_2O \qquad \textbf{Equation 21}$$

$$Mn_3O_4 + 2H^+ + 2e^- \leftrightarrow 3MnO + H_2O \qquad \textbf{Equation 22}$$

At low pH and low potential the oxides may disolve as Mn^{2+}. However, at higher pH above 8 a stable hydroxyde exists in an insoluble form.[73] Half-cell reactions Equation 19 through Equation 22 substantiate that Mn(II) could be deposited electrochemically from MnO_4^- and remain stable at high pH cathodic sites such as present over copper rich constituent particles.[9,74]

Of interest is the interaction between the initial petreatment that leads to chemically deposited $Ce(OH)_3$ and the high valence state permangante ion used in the second step of the pretreatment. It is hypothesized that the cerium hydroxide will be oxidized to cerium oxide by the permanganate ion resulting in a cerium oxide coating that is stable over a larger range of pH than a cerium hydroxide coating Figure 76(a). The concentrations of the cerium species present at the redox potential of Equation 19 is shown in Figure 78. A litterature search shows no documentation of an ionic species or oxide that consistes of both cerium and manganese. The resulting manganese oxides are also expected to provide corrosion protection in this dual inhibitor scheme.

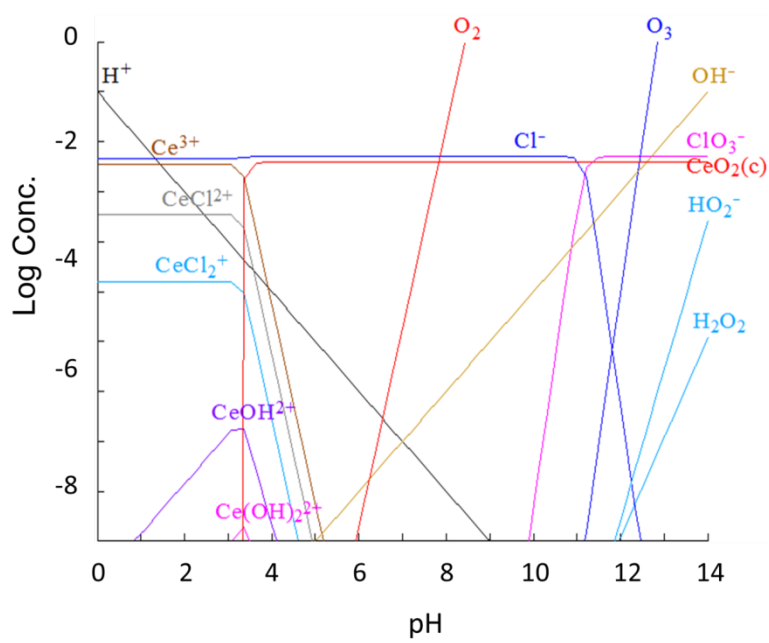

Figure 78. Concentrations of species in the cerium-chloride-H_2O system at 0.78 V vs. SCE, the E_o of Equation 19. The cerium oxide species (CeO_2) is stable above pH 3.3 at this potential.

Open circuit full immersion exposure experiments were conducted. Surface chemical compositions and deposit morphologies were also investigated. Cu replating was investigated to

indirectly explore the inhibition of Cu release and replating. E_{pit} were determined and ORR kinetics were extracted using the Koutecky-Levich correction.[90]

Effects of Cerium-Permanganate Pretreatment on OCP Exposures of AA2024 in 50 mM NaCl Solution

Figure 79 shows as-polished AA2024-T351 and the surface damage caused by a subsequent 24 hour exposure to 0.05 M NaCl solution. Figure 80 shows the effect of the pretreatment of AA2024-T351 with the cerium and permanganate solutions. In all pretreatment regimes where cerium was present above 10 mM there appears to be a thick deposit that covers a large percentage of the surface of the AA2024-T351. This is in contrast to the permanganate pretreatment (Figure 81). The permanganate is electrochemically reduced over copper rich intermetallic particles, the active cathodic sites on AA2024-T351, which mitigates corrosion.

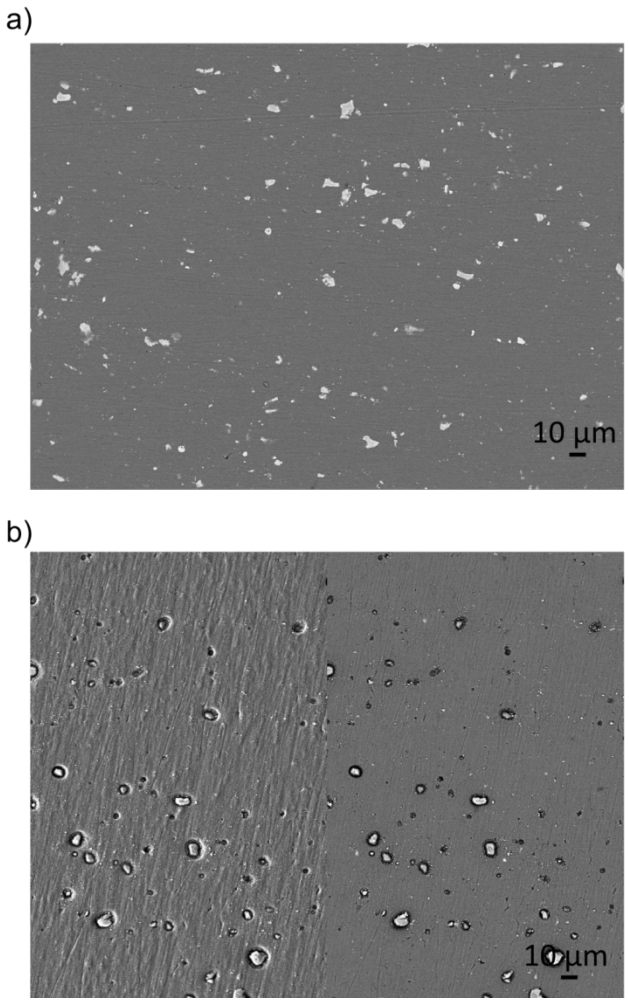

Figure 79. (a) The as-polished (1200 grit) AA2024-T351 and the subsequent surface damage caused by 24 hour exposure to 0.05 M NaCl solution in a naturally aerated state at room temperature. (b) The damaged specimen image is compressed horizontally to include a secondary electron and backscattered electron image.

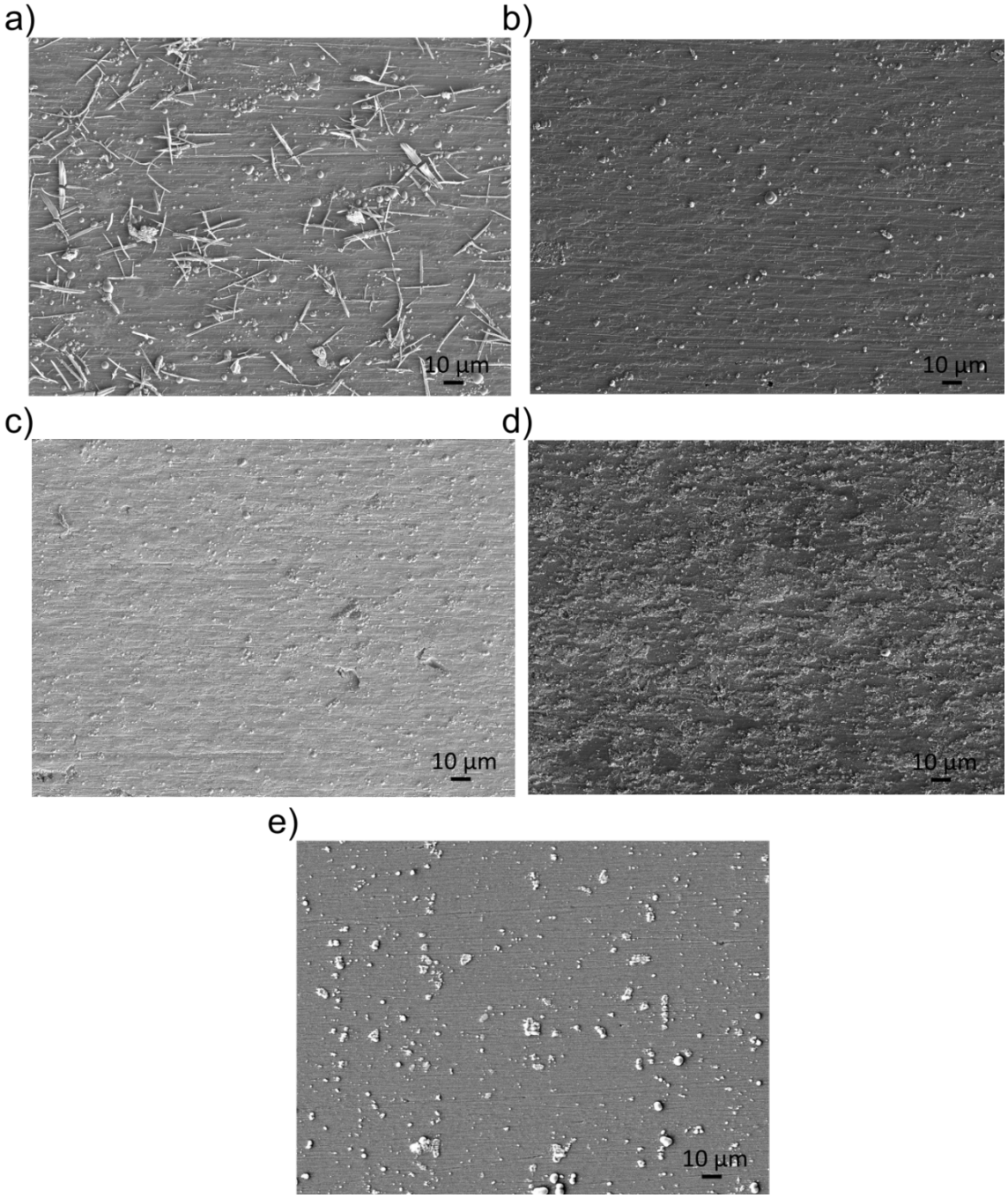

Figure 80. (a) AA2024-T351 pretreated with 0.01 M Ce3+ for 100 hrs. and 0.04 M MnO4- for 24 hrs. (secondary electron image). (b) Same pretreatment times with inhibitor concentrations of 0.025 M Ce3+ and 0.025 MnO4-. (c) Same pretreatment times with inhibitor concentrations of 0.04 M Ce3+ and 0.01 MnO4-. (d) Same pretreatment times with inhibitor concentrations of 0.05 M Ce3. (e) Same pretreatment time with inhibitor concentration of 0.05 MnO4-.

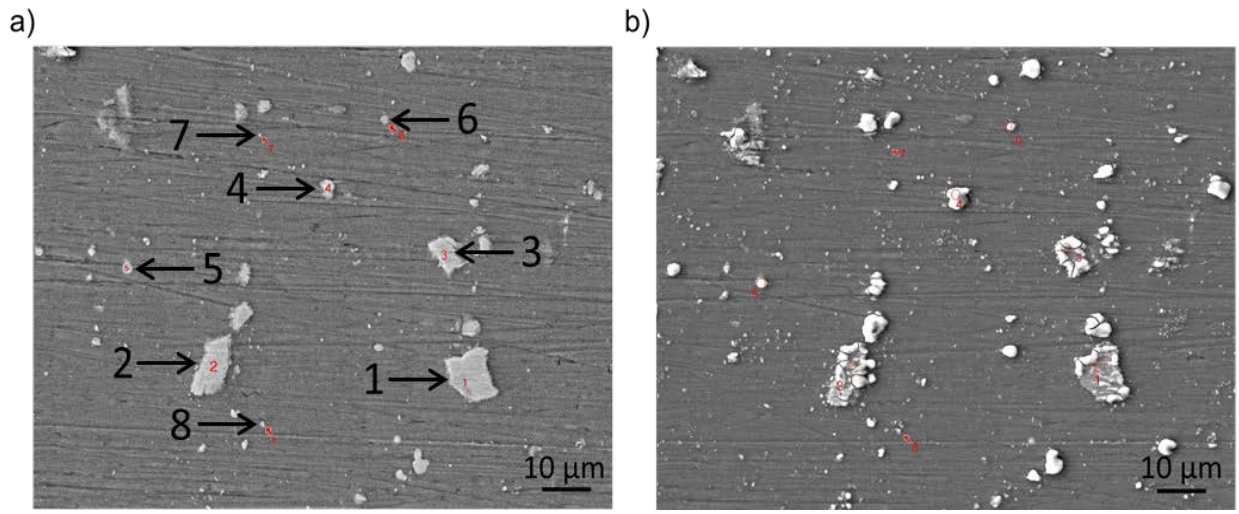

Figure 81. (a) AA2024-T351 with indication of EDS sites labeled 1-8. (b) Same sample and area as (a) Sample has been pretreated for 24 hours in 0.1M $KMnO_4$. Indication of EDS sites labeled 1-8.

The manganese oxide particles detected by energy dispersive spectroscopy can be seen in the secondary electron image shown in Figure 81 (a and b). Figure 82 show EDS point scans of two intermetallic particles before and after pretreatment. Qualitative chemical analyses of the intermetallic particles before and after pretreatment are summarized in Table 24. Manganese oxide growth is apparent on many of the intermetallics and is shown to be deposited specifically on the various types of Cu rich phases as opposed to the aluminum rich matrix phase. Qualitative chemical data from EDS shows coverage of θ, S, and Cu-Mn-Fe-Al phases by a manganese oxide of unknown valence state. An example of this is shown in Figure 82. Permanganate forms thick oxide deposits over copper rich intermetallics in AA2024-T351 when pretreated. The deposition is characterized by spherical caps over small (~0.5 μm) intermetallics and conformal layers with terraces over larger particles (5 μm).

Table 24. Compilation of EDS data for AA2024-T351 intermetallic particles in Figure 81, before and after pretreatment in 0.1 M $KMnO_4$.

Intermetallic phase	Particle #	Manganese Oxide Cap	Mn enrichment (EDS)
AlCuMg phase	5, 6	Yes	Yes
Al(Cu,Mn,Fe,SI) phase	1, 2, 3	Yes	Yes
AlCu phase	4	Yes	Yes
Al(Cu,Mn,Fe,Mg) phase	7,8	Yes	Yes

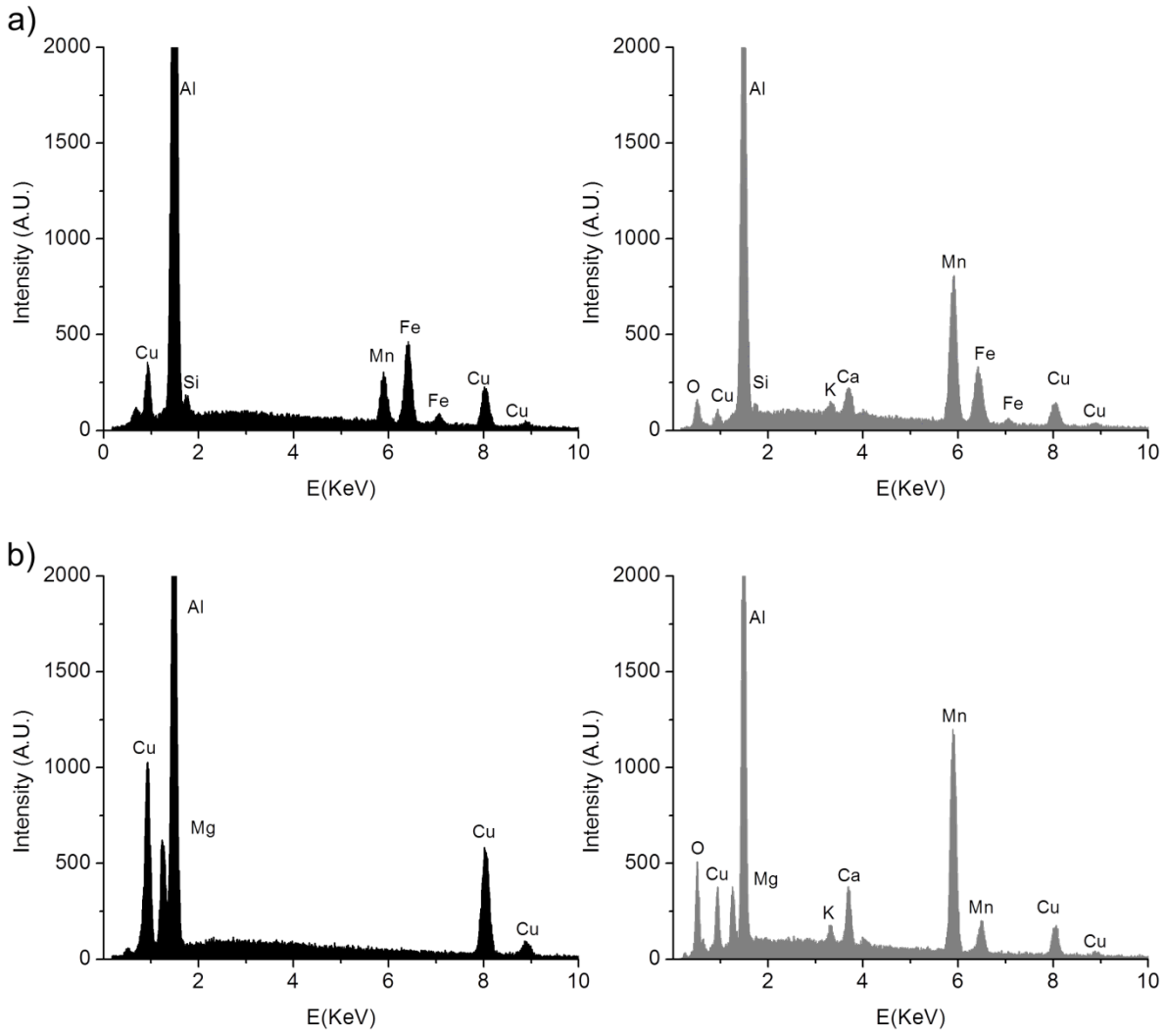

Figure 82. (a) Intermetallic particle 1 from Figure 81. (b). Intermetallic particle 5 from Figure 81. The left spectrum is taken from an untreated sample, the right, a pretreated sample. The cerium-permanganate dual inhibitor pretreatments produced a wide array of surface features as seen in Figure 80. In order to analyze the chemical composition of the complex oxide structures observed, EDS line scans for oxygen, magnesium, aluminum, chloride, manganese, iron, copper, and cerium were performed. Manganese is the only element that is found both in the pretreatment solution, and the alloy. The alloy contains 0.6% manganese by weight as shown in Table 3. This complicates the analysis of the manganese EDS results because the element is concentrated in certain intermetallic compounds in the alloy. However, manganese enrichment is clearly visible in the microscopy due to the unique oxide formations that have been observed.

EDS line scans are shown in Figure 83 for AA2024-T351 in one of the pretreated states used. There are three oxide formation structures visible for cerium and one structure visible for manganese. When the 10 mM Ce^{3+} + 40 mM MnO_4^- pretreatment was examined [Figure 80 (a) and Figure 83(b)], long cerium rich oxide needles were observed while manganese oxides appeared to deposit over intermetallic particles as seen in the permanganate only pretreatment (Figure 81). When the 25 mM Ce^{3+} + 24 mM MnO_4^- pretreatment was examined [Figure 80 (a) and (b)] cerium oxides no longer were in the form of long needles. The cerium deposits for this pretreatment regime are pellet shaped, clearly seen in Figure 83(b). Some permanganate deposits remain over the intermetallic particles. When the 40 mM Ce^{3+} + 10 mM MnO_4^- pretreatment was examined, cerium enrichment appears to be more widespread suggesting a more homogeneous cerium oxide or hydroxide covering the surface of the AA2024-T351. Manganese oxide deposits are still present but they appear to be smaller and less distinct. Finally, when a 50 mM cerium pretreatment is conducted, general cerium enrichment is observed over the surface of the AA2024-T351 as seen in Figure 80(d) and Figure 83(d). In all cases the cerium and permanganate enrichment location indicated in EDS line scans does not coincide indicating that they are not present in a single phase. In both the 10 mM Ce^{3+} + 40 mM MnO_4^- and the 25 mM Ce^{3+} + 24 mM MnO_4^- pretreatments the enrichment of cerium on the surface, as detected by EDS [Figure 83 (a) and (b)] appears to be minimal whereas the pretreatments with higher cerium concentrations [Figure 83 (c) and (e)] maintain some level of cerium enrichment covering the entire surface of the AA2024-T351.

Figure 84 shows the effects of a subsequent exposure of the pretreated samples to 0.05 M NaCl for 24 hours. The effect of the inhibitor pretreatment on visible exposure damage is significant. After the pretreated samples were exposed to 50 mM NaCl for 24 hours the morphology of the surfaces changes significantly. Figure 85 shows EDS line scans of pretreated AA2024-T351 that had been exposed to 50 mM NaCl for 24 hours.

The corrosion inhibition of each pretreatment regime can be visually assessed by observing the extent of intermetallic trenching and pitting that has occurred on the surface of the AA2024-T351. Figure 84 and Figure 85 indicates that as the concentration of cerium increases the pretreatment appears to be more effective at decreasing the extent of damage surrounding the intermetallic particles. In Figure 84(a), the 10 mM Ce^{3+} + 40 mM MnO_4^- pretreatment has slightly greater damage than any other cerium treated sample. As the concentration of cerium increases the visible damage decreases and is no longer observed once the 40 mM concentration is reached albeit without cleaning. In order to determine the extent of surface damage hidden by cerium deposits the cerium oxide formed during 50 mM Ce pretreatment was abrasively removed (Figure 86). When the oxide is removed it becomes apparent that the surface has been heavily damaged during the exposure. The dark spots in the microscopy indicate the presence of pervasive pitting attack to the sample surface below the cerium oxide layer. These pits can be seen to a lesser extent in Figure 84 (d) due to the presence of the cerium oxide layer. However, none are seen in Figure 84, (b) or (c), two samples there were also pretreated with permanganate.

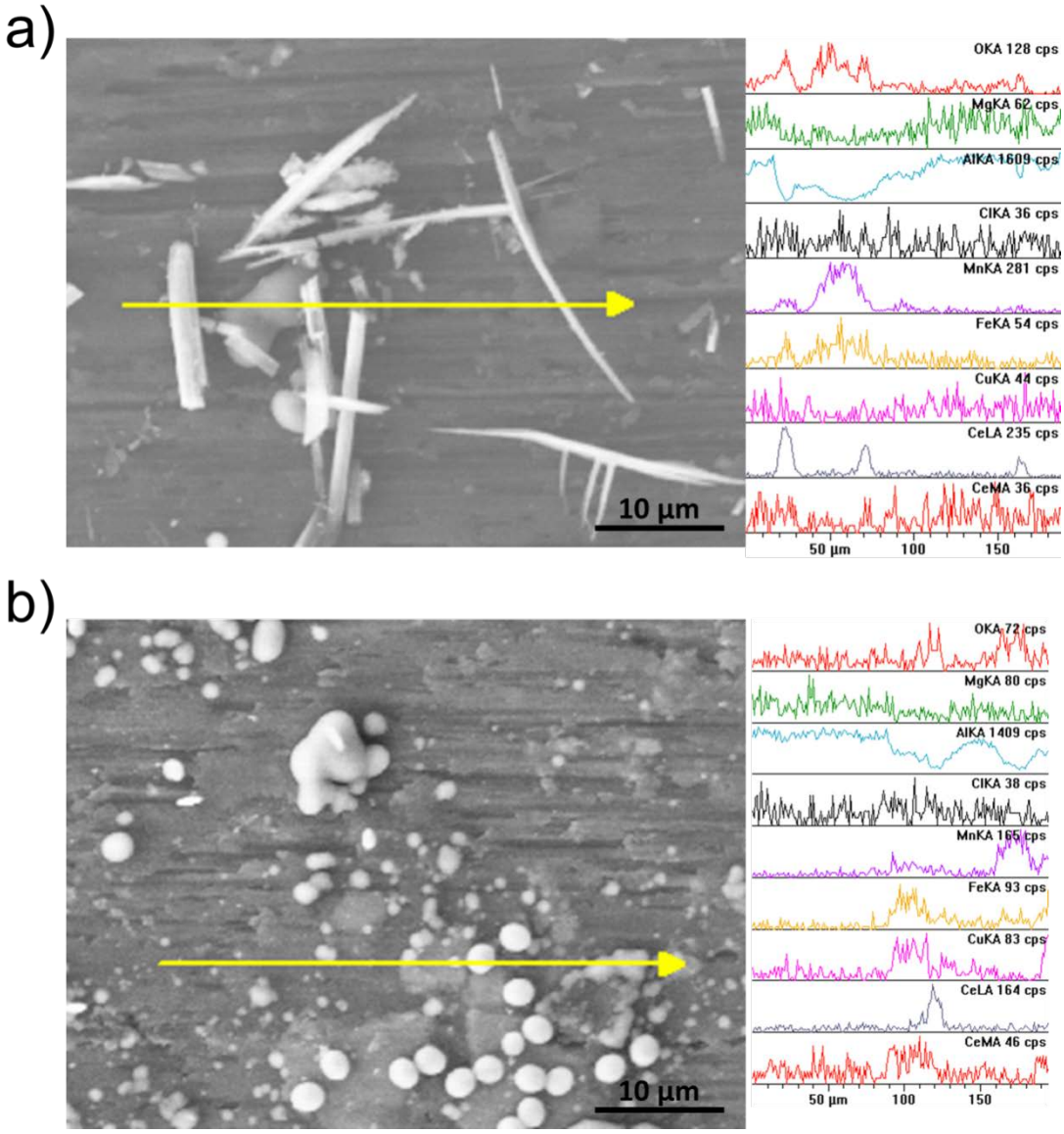

Figure 83. EDS at 15 kV accelerating potential of AA2024-T351 pretreated in 10 mM Ce^{3+} + 40 mM MnO_4^-(a), 25 mM Ce^{3+} + 24 mM MnO_4^- (b), 40 mM Ce^{3+} + 10 mM MnO_4^-. All cerium pretreatments lasted for 100 hours. All permanganate pretreatments lasted for 24 hours.

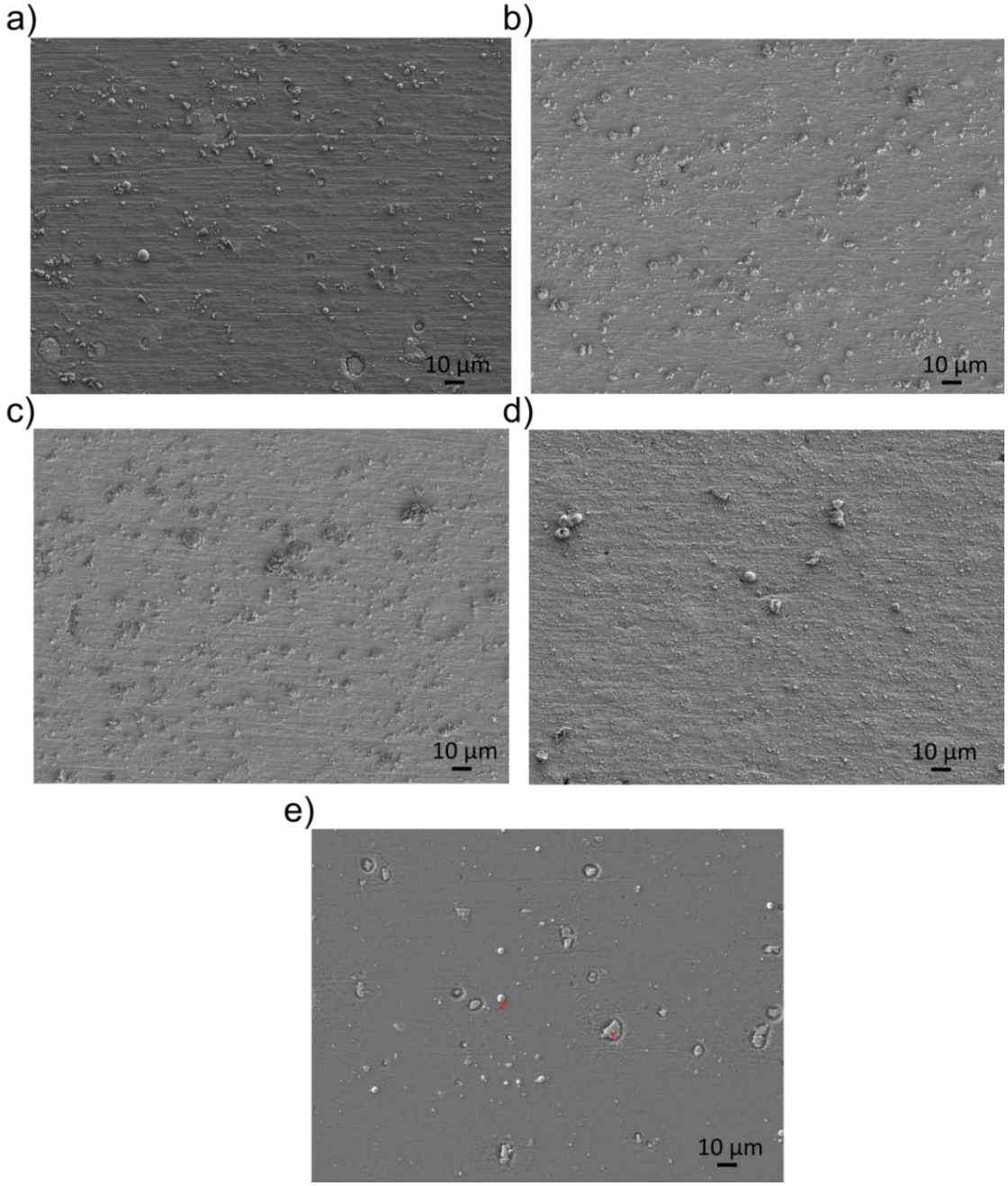

Figure 84. (a) AA2024-T351 pretreated with 0.01 M Ce^{3+} for 100 hrs. and 0.04 M MnO_4^- for 24 hours and exposed to 0.05 M Cl^- for 24 hrs. (secondary electron image). (b) Same pretreatment with inhibitor concentrations of 0.025 M Ce^{3+} and 0.025 MnO_4^- and exposed to 0.05 M Cl^- for 24 hrs. (c) Same pretreatment with inhibitor concentrations of 0.04 M Ce^{3+} and 0.01 MnO_4^- and exposed to 0.05 M Cl^- for 24 hrs. (d) Same pretreatment with inhibitor concentrations of 0.05 M Ce^{3+} and exposed to 0.05 M Cl^- for 24 hrs.(e) Same pretreatment with inhibitor concentrations of 0.05 MnO_4^- and exposed to 0.05 M Cl^- for 24 hrs. Samples were not cleaned post exposure.

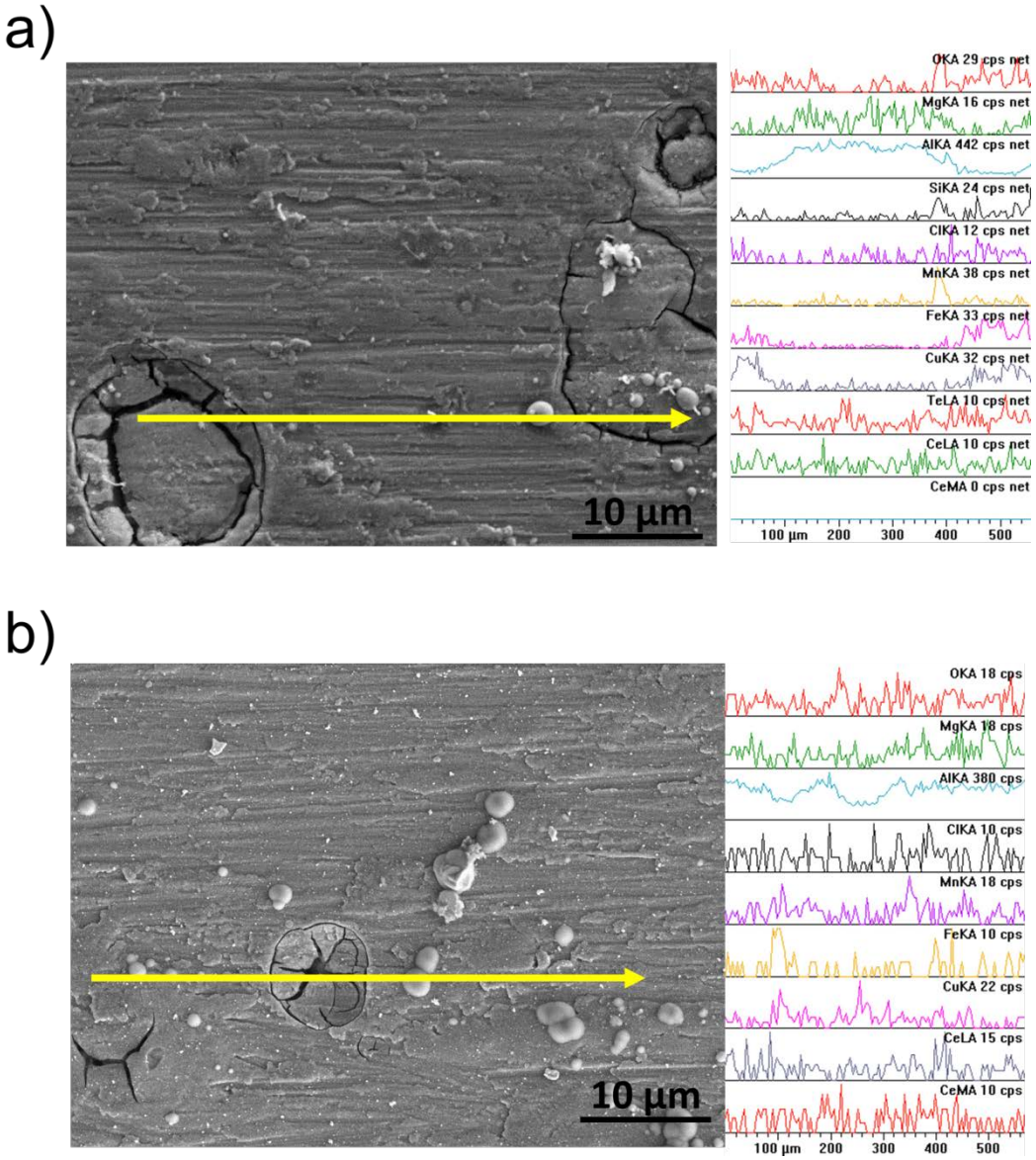

Figure 85. EDS at 15 kV accelerating potential of AA2024-T351 exposed for 24 hours in 50 mM NaCl after pretreatment in 10 mM Ce^{3+} + 40 mM MnO_4^- (a), 25 mM Ce^{3+} + 24 mM MnO_4^- (b). All cerium pretreatments lasted for 100 hours. All permanganate pretreatments lasted for 24 hours.

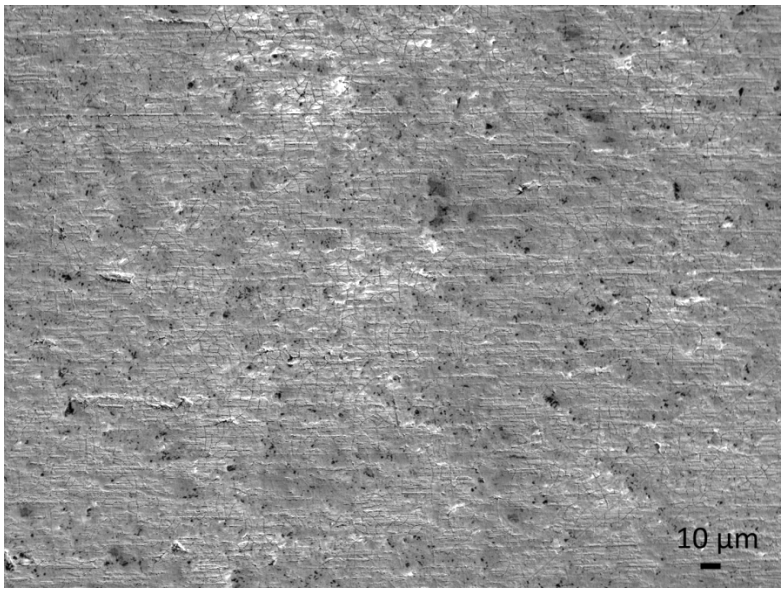

Figure 86. Surface damage revealed by abrasive removal of cerium oxide after pretreatment in 0.05 M Ce^{3+} for 100 hrs. and subsequent exposure to 0.05 M NaCl for 24 hours.

This is in contrast to the 50 mM permanganate pretreatment which is shown in Figure 84 (e). There does appear to be trenching around the intermetallic particles. However, there is a lack of heavy pitting of the aluminum matrix as seen in the 50 mM cerium pretreatment. In summary MnO_4^- alone is more effective than Ce^{3+} with Ce-Mn combinations intermediate.

Open Circuit Behavior of Pretreated AA2024-T351

OCP data was collected for 1 hour in ambient aerated 0.05 M NaCl solution after the dual inhibitor pretreatments were performed (Figure 87). The samples were removed from pretreatment, rinsed thoroughly, and the open circuit was measured in 0.05 M sodium chloride solution. The specimens that were treated with higher levels of permanganate tend to have lower OCP when compared with no pretreatment. Briefly, it is believed that the manganese oxide deposits initially contain some residual permanganate, which over the course of the first hour is reduced providing an additional cathodic reactant. As the residual permanganate is reduced the OCP drops as the result of the blockage of the intermetallic particles for fast ORR. As the manganese oxide deposits over the intermetallic caps degrade or dissolve, the open circuit recovers to the open circuit of the un-treated AA2024-T351 substrate. Figure 87 and Figure 84 (e) show this behavior. A significant result is that MnO_4^- is much more effective at lowering OCP than Ce^{+3} suggesting greater ORR inhibition.

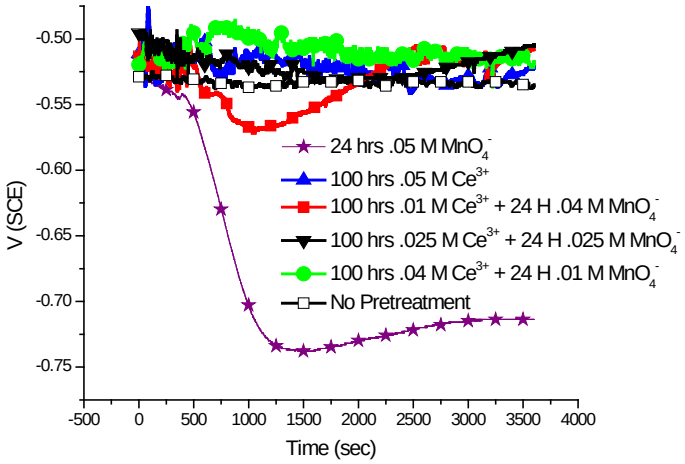

Figure 87. Open circuit test of pretreated AA2024-T351 in 50 mM NaCl solution with ambient aeration. Test included 100 hrs. pretreatment in Ce^{3+} followed by 24 hrs. pretreatment in MnO_4^- at the indicated concentrations. Pretreatments are Cl^- free.

Inhibition of Copper Replating

Copper replating was also investigated on pretreated AA2024-T351 surfaces after OCP exposures in 50 mM NaCl using the CV method to assay the copper coverage. Figure 88 shows the cyclic voltammetric analysis of pretreated AA2024-T351, and AA2024-T351 etched in 0.05 M NaCl solution for 24 hours. The charge associated with anodic Cu(I) to Cu(II) reaction peaks reflect the surface coverage of copper brought about by corrosion and are indicative of copper replating.[20] The results of the CV tests are summarized in the bar plots in Figure 89. These suggest that cerium-permanganate pretreatments reduce copper redeposition the most.

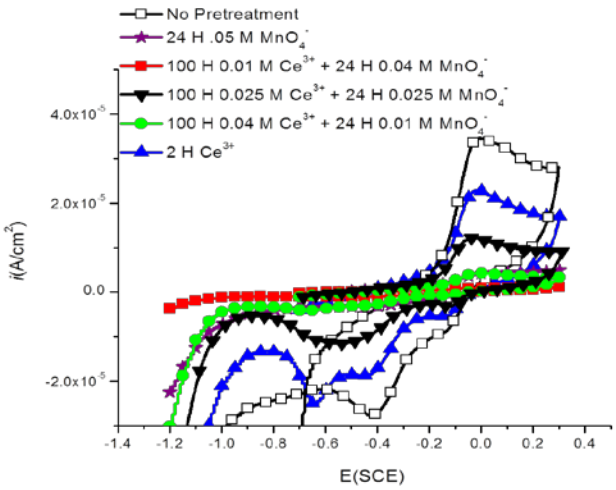

Figure 88. CVs of pretreated AA2024-T351 after a 24 hour exposure in 50 mM NaCl solution.

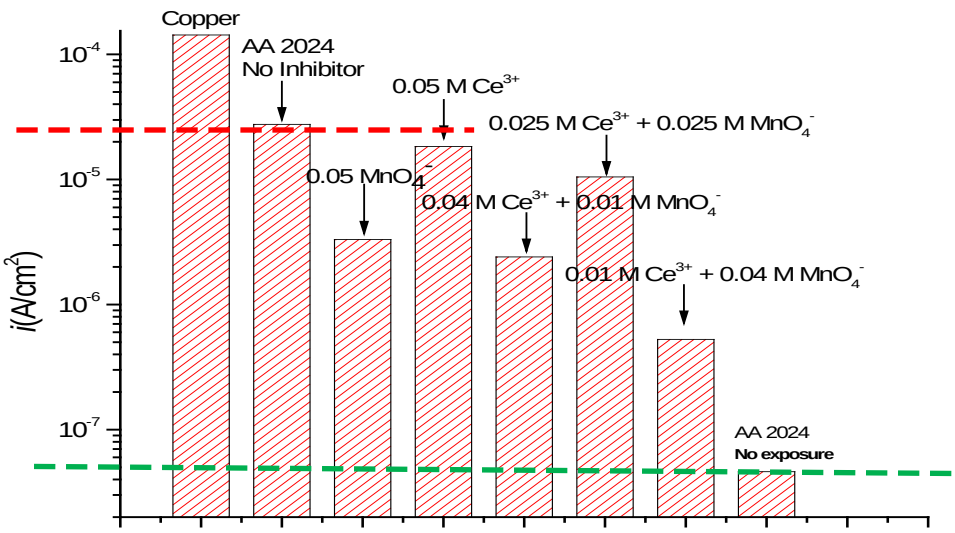

Figure 89. The relative intensities of the Cu^{1+} reduction peak on the AA2024-T351 surface pretreated in cerium for 100 hours and subsequently in permanganate for 24 hrs. followed by exposure for 24 hrs. in 0.05 M NaCl are shown. Combined inhibitor concentrations tested had ratios of cerium to permanganate of 0.2 and 0.8 with a total inhibitor concentration of 0.05 M. Results are compared to permanganate pretreatments and cerium pretreatments. A large decrease in the copper surface coverage is evident for the combined inhibitor pretreatment over either single inhibitor pretreatment.

Anodic Inhibition of AA2024-T351 by Cerium-Permanganate Pretreatments

Figure 90 (a-e) shows anodic E-log(*i*) behavior for pretreated AA2024-T351 in 0.05 M sodium chloride solution during upward cyclic potentiodynamic scans. Cerium-permanganate pretreatments had very little effect on E_{pit} of AA2024-T351. A very slight increase in E_{pit} is observed but it is not significant. As shown previously, the samples pretreated with permanganate alone experience a significantly suppressed OCP that exposes a passive region. E_{pit} of the exposed passive film is not affected. However ΔE_{pass} is significantly improved. Cerium pretreatments alone show little effect on E_{pit} or OCP. Therefore ΔE is not reduced.

Figure 91 presents the cumulative probability of pitting as a function of potential for pretreated AA2024-T351. No significant increase in E_{pit} is observed for pretreated AA2024-T351 tested in 50 mM NaCl solution.

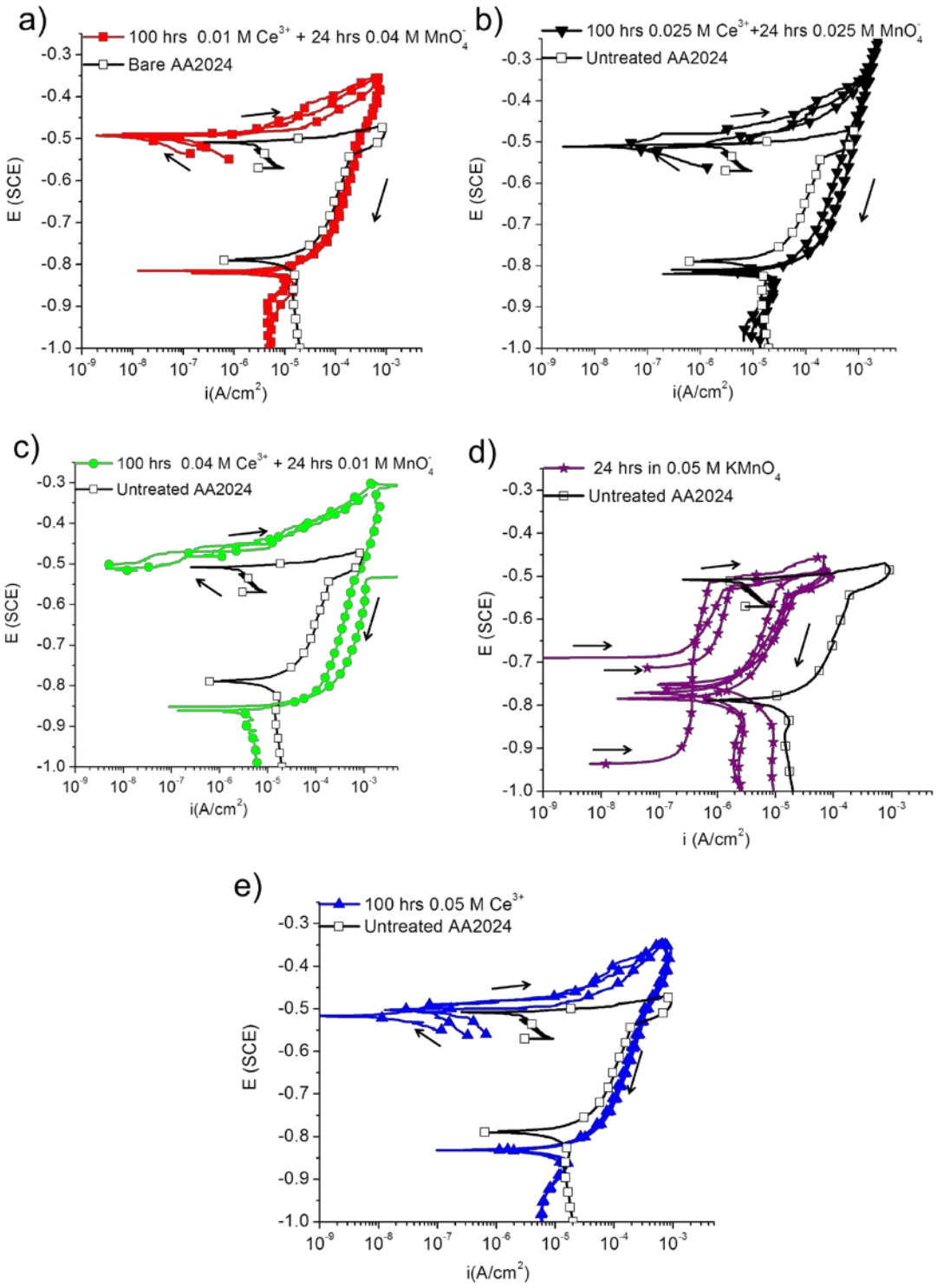

Figure 90. Anodic E-log(*i*) behavior of AA2024 with cerium-permanganate pretreatments at stated concentrations tested in 5 mM sodium chloride.

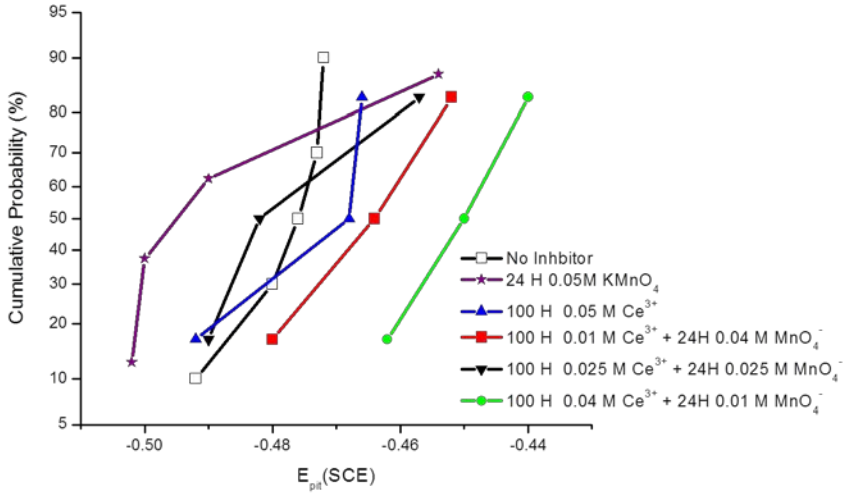

Figure 91. Cumulative probability of pitting on AA 2024-T351 as a function of potential for both permanganate-cerium combinations and in-situ solution phase permanganate inhibitor concentration. Combined inhibitor concentrations tested had ratios of cerium to permanganate of 0, 0.2, 0.5, 0.8, and 1 with a total inhibitor concentration of 0.05 M. Cumulative probability of pitting in 0.05 M NaCl solution.

Investigation of Cathodic Inhibition with Cerium-Permanganate Pretreatments

Figure 92 shows the cathodic polarization data collected using the RDE method to examine the effects of cerium-permanganate pretreatments on the ORR kinetics on AA2024-T4 in pH 8.4 borate buffer. The E-*i* behavior of untreated AA2024-T351 and high purity copper were run with traditional potentiodynamic control to illustrate the effect of rotation rate over all potentials. This can be seen in Figure 92. Figure 93 shows the results of potentiodynamic downward scans at a set rotation rate of 2500 rpm. Cerium-permanganate pretreatments change the regions of mass and charge transfer control on AA2024-T4. Cerium-permanganate inhibitor combinations show very similar behavior to that of permanganate pretreated samples. This begins with an elevated OCP in pH 8.4 borate buffer. The elevated potential can be explained by considering the half-cell reaction potentials for manganese oxide species at pH 8.4. As the potential is decreased these oxides are reduced resulting in the cathodic current density shoulder observed from 0.5 V vs. SCE to -0.5 V vs. SCE. As the potential continues downward the ORR begins to dominate the current density and becomes mass transport limited starting around -0.6 V vs. SCE. This cathodic kinetic behavior is not evident for two pretreatment systems: 10 mM Ce^{3+} +40 mM MnO_4^- and 25 mM Ce^{3+} + 24 mM MnO_4^-. These two systems show remarkable inhibition of the oxygen reduction reaction. The current density for these two systems is two and a half orders of magnitude lower than untreated AA2024-T351. The remaining E-log(*i*) scans show the onset of HER dominated current density between -1.2 and -1.5 V vs. SCE.

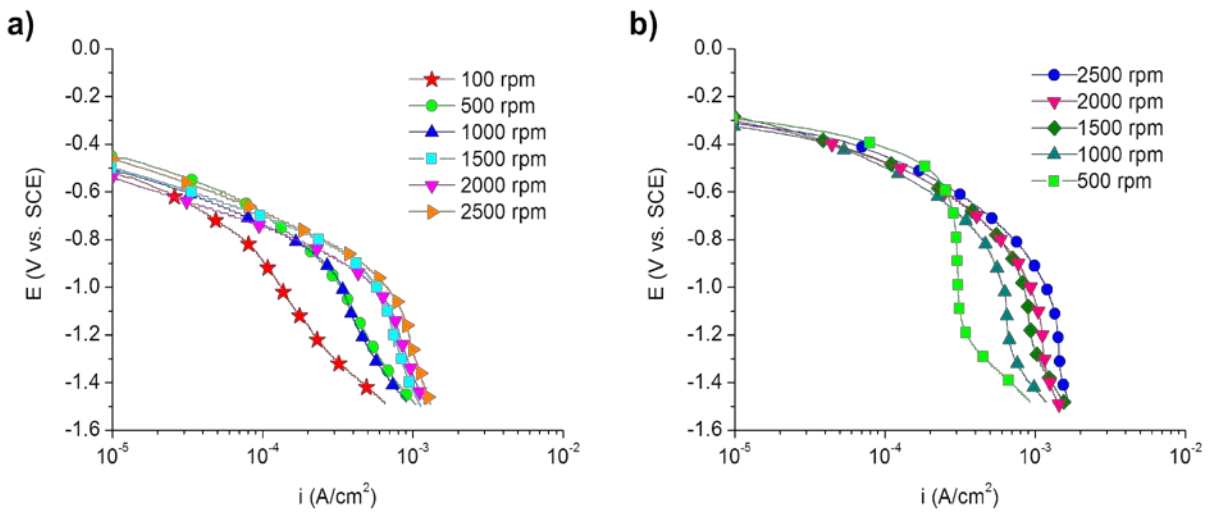

Figure 92. Cathodic E vs. log(*i*) data for AA2024-T4 (a) and high purity copper (b) samples run at various rotation rates from 100 rpm to 2500 in pH 8.4 borate buffer. Solutions were aerated naturally and no pretreatment was performed.

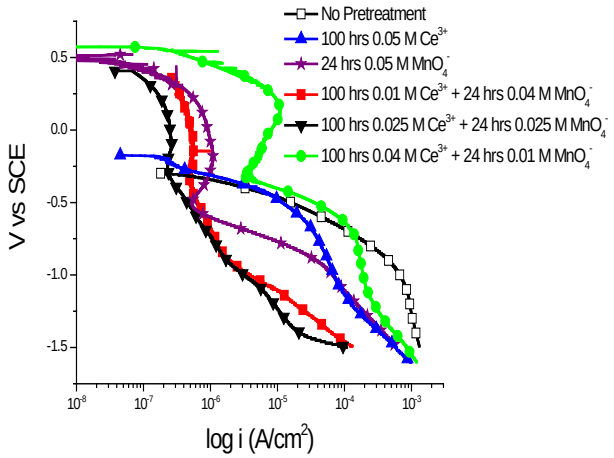

Figure 93. Rotating disk cathodic polarizations experiments on AA 2024-T351 at a rotation rate of 2500 rpm in pH 8.4 borate buffer. Combined inhibitor concentrations tested had ratios of cerium to permanganate of 0.2, 0.5, and 0.8 with a total inhibitor concentration of 0.05 M. Total current densities for bare AA2024, cerium treated, and permanganate treated have been included for reference.

A second RDE method was used to examine the ORR further. The working electrode was held at a potential of -1.0 V vs. SCE and the rotation rate of the sample was varied. The results can be seen in Figure 94. The primary finding is that cerium-permanganate is more effective at cathodic inhibition than cerium alone. The variable rotation rate results for AA2024-T351 pretreated in cerium-permanganate dual inhibitor pretreatments in Figure 94(a), suffer from the presence of an additional source of cathodic current, the reduction of manganese. The rotation rate dependent

cathodic current density changes manifest themselves as near instantaneous steps in current density that correlate exactly with the change in rotation rate. The ORR rotation dependence can be extracted by observing the instantaneous jump in current density that occurs when the rotation rate is increased after accounting for the additional manganese reduction current.

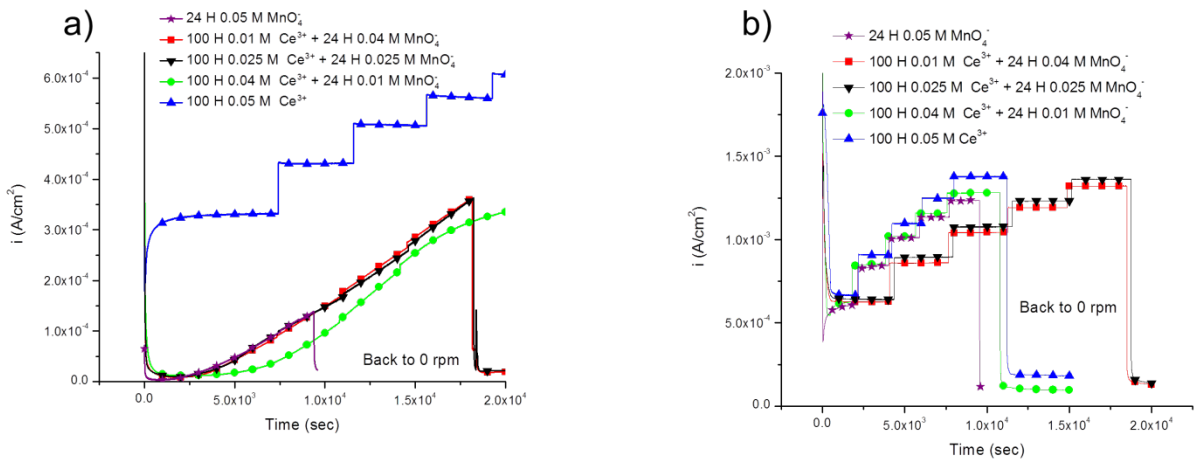

Figure 94. (a) RPM Ramp 500 to 2500 (increments of 500) of AA2024-T351 in pH 8.4 borate buffer after stated pretreatments When manganese deposits are present it reacts electrochemically effecting the current density at each rotation rate. (b) RPM Ramp 500 to 2500 (increments of 500) of high purity copper in pH 8.4 borate buffer after stated pretreatments.

The additional cathodic current from the reduction of manganese is not seen when pretreatments were conducted on high purity copper that was potentiostatically pretreated at the open circuit of the AA2024-T351 system (-0.5 V vs. SCE) in cerium and permanganate solutions. These pretreatments showed limited inhibition (Figure 94).

Plots of $1/i_{Tot}$ vs. $\omega^{-1/2}$ at -1.0 V vs. SCE (a potential dominated by oxygen reduction mass transfer control) show that uninhibited AA2024-T4 has a slightly lower current density than high purity copper, see Figure 95(a). This is due to the array of active electrodes surrounded by inactive aluminum matrix as described by the Gueshi model.[37,38] The Koutecky-Levich method,[130] as shown in Equation 23, was used to extract i_D from i_T at -1.0 V vs. SCE, where i_D is the diffusion limited cathodic current density and i_{ct} is the charge transfer limited cathodic current density, see Figure 95(b). At this potential i_{HER} is much lower than i_{ORR}.

$$\frac{1}{i_{Tot}} = \frac{1}{i_{ct}} + \frac{1}{i_D} \qquad \textbf{Equation 23}$$

Where i_D is given by Equation 24.

$$i_D = 0.62nFD^{2/3}v^{1/6}C\omega^{1/2} \qquad \textbf{Equation 24}$$

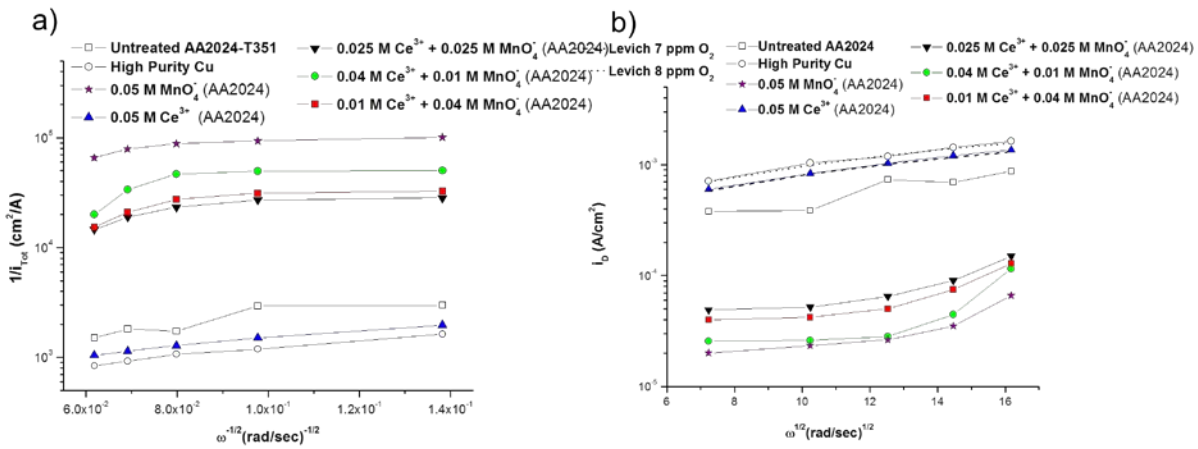

Figure 95. Diffusion limited current density on high purity copper compared to AA2024-T351 at rotation rates from 500 to 2500 rpm in pH 8.4 borate buffer. Combined inhibitor concentrations tested had ratios of cerium to permanganate of 4, 1, and 0.2 with a total inhibitor concentration of 0.05 M.

The results on high purity copper can be compared with the Levich description of mass-transport limited O_2 reduction given by Equation 16. Using a value for the diffusion of O_2 in water, $D = 1.9 \times 10^{-5}$ cm^2/s, a value of n = 4, the concentration of O_2 in solution, C = 7-9 ppm, and the kinematic viscosity, $\nu = 1 \times 10^{-2}$ cm^2/s. Good agreement is found between theoretical values and experimental data.[28] This suggests that at -1.0 V vs. SCE the current due to the HER is a small fraction of the ORR current.

The diffusion limited current density was extracted from the total current density using the Koutecky-Levich method for the pretreated case at -1.0 V vs. SCE. The extracted diffusion limited current density is shown in Figure 96(b). Pretreated AA2024 has a lower cathodic current density than untreated AA2024-T4 over all rotation rates with a weaker rotation rate dependency. Permanganate and Cerium-permanganate pretreatments suppress the diffusion limited current density significantly. Permanganate alone affords the best reduction in cathodic current on AA2024.

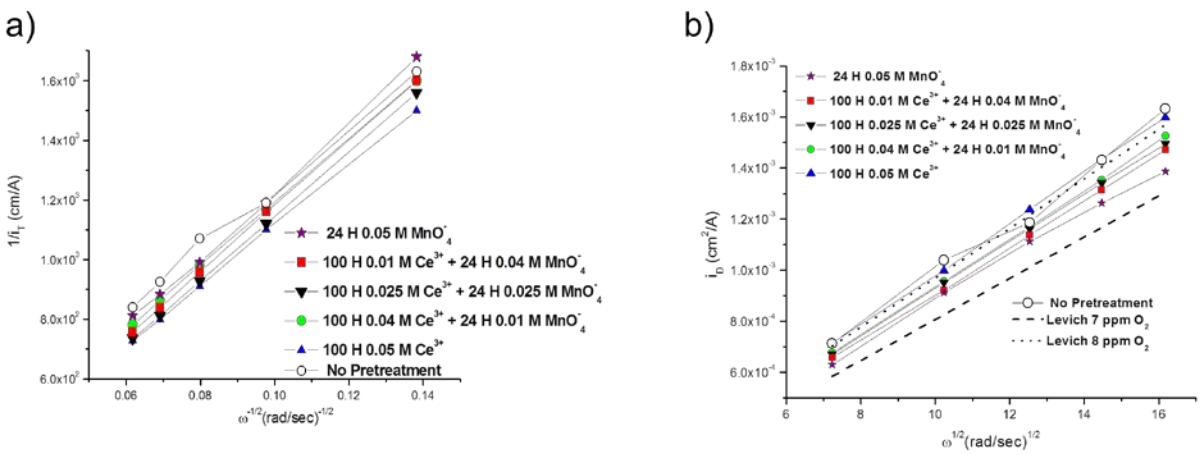

Figure 96. Diffusion limited current density on high purity copper at rotation rates from 500 to 2500 rpm in pH 8.4 borate buffer. Combined inhibitor concentrations tested had ratios of cerium to permanganate of 4, 1, and 0.2 with a total inhibitor concentration of 0.05 M.

Vanadate-Cerium and Vanadate-Molybdate Combinations

Candidates for combining with vanadate include Ce and Mo, which have been investigated as single inhibitors. While there is a basic understanding of vanadate speciation in aqueous solutions at various pH ranges, vanadate speciation with molybdate in solution has not been well demonstrated. It is important to determine if changes in species or groupings of vanadate molecules (tetrahedral versus octahedral coordination) occur and if these changes significantly impact inhibition. Additionally, the conditions under which inhibiting vanadate species become the dominant vanadate species in solution may also be affected by addition of molybdate in solution.

Inhibitor combination chemicals tested for AA2024 include cerium chloride and sodium molybdate. High throughput testing was used to examine two, three, or four inhibitors in combination.[8] AA2024-T3 wire was placed in 600 mM NaCl plus 3.4 mM total inhibitor concentration at a pH of 7 for one or seven days. The resultant test solution was then screened for Al^{3+} concentration using a florometric technique.[8] Additionally, CV was employed to test for copper replating on AA2024-T3 wires that had been immersed in the above solution for 24 hours. Cerium chloride in combination with sodium molybdate was more effective than sodium chromate alone at reducing copper replating.[96] Measurements were also made using a pair of AA2024-T3 wires held in solution for 9 hours with a 100 mV applied anodic DC voltage above open circuit. During this time the current was measured.Based on the current values of the last 2 hours of applied potential, the inhibition efficiency (one minus the ratio of inhibited current to uninhibited current) of sodium metavanadate plus sodium molybdate and sodium metavanadate plus cerium chloride were approximately 90% and 80%, respectively, as compared to 95% for sodium chromate.[96] The few studies of inhibitor combinations for AA2024 provide limited cathodic and anodic information and did not examine possible changes in mechanism governing inhibition.[8,96] Combinations of cerium acetate pretreatments followed by testing in vanadate solutions have not been studied. While there is a basic understanding of vanadate speciation in

aqueous solutions at various pH ranges, vanadate speciation with molybdate in solution has not been extensively demonstrated. Studies have found the existence of vanadium molybdenum molecules in the pH range 1.5–7.5.[92,97,98] It is important to determine if changes in species or groupings of vanadate molecules (tetrahedral versus octahedral coordination) occur and if these changes significantly impact inhibition. Additionally, the conditions under which inhibiting species become the dominant vanadate species in solution may also be affected by addition of molybdate in solution.

Species Present in NMR and Speciation Diagrams

The speciation of vanadate in aqueous solutions is known to vary with both ionic concentration and pH.[135,136] ^{51}VNMR was used to experimentally determine the species present in $NaVO_3$ plus 50 mM NaCl and $NaVO_3$ plus Na_2MoO_4 plus 50 mM NaCl solutions and, as well as, to check for any change in speciation with time. While slight differences were seen between the minor peaks for different concentrations of vanadate, the dominant peak at -577 ppm was found in all solutions regardless of MoO_4^{-2} content. This peak corresponded to the tetrahedrally coordinated vanadate species $(V_4O_{12})^{-4}$. Other experimentally observed minor peaks were (-586 ppm $(V_5O_{15})^{-5}$, -572 ppm $(H_2V_2O_7)^{-2}$, and -550 ppm $(V_2O_7)^{-4}$).[94,95,136] Solution age did not appear to be a factor in speciation. Figure 97 demonstrates that vanadate speciation was stable after 24 hours. Table 25 shows the experimentally observed peaks in order of abundance for each vanadate concentration tested. Adding molybdate to a 10 mM $NaVO_3$ 50 mM NaCl solution changes the ratio of minor species present but not what the minor species are, as seen in Table 25.

Table 26 contains the species, estimated percent of total species present and the pH of the solution. The addition of molybdate to 50 mM NaCl vanadate solutions increased the pH (but within the 6 - 9 range) and the concentration of $(V_4O_{12})^{-4}$ in solution.

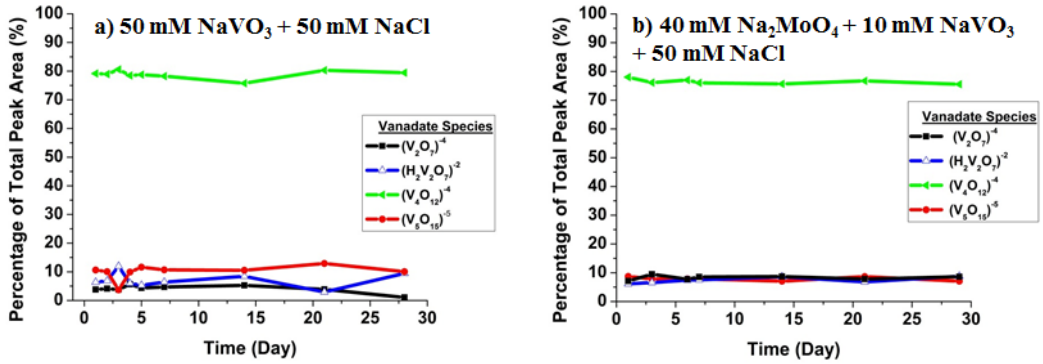

Figure 97. Vanadate speciation as a function of time. Insignificant changes in vanadate species present occurred for a) 50 mM $NaVO_3$ plus 50 mM NaCl in D_2O solvent; b) 40 mM Na_2MoO_4 plus 10 mM $NaVO_3$ plus 50 mM NaCl in D_2O solvent.

Table 25. The ^{51}VNMR peaks for different inhibitor concentrations in 50 mM NaCl solution at room temperature.

Dissolved Inhibitor	10 mM $NaVO_3$	40 mM Na_2MoO_4 + 10 mM $NaVO_3$	25 mM Na_2MoO_4 + 25 mM $NaVO_3$	10 mM Na_2MoO_4 + 40 mM $NaVO_3$	50 mM $NaVO_3$
V^{5+} species in decreasing abundance	-577 ppm	-577 ppm	-577 ppm	-577 ppm	-577 ppm
	$V_4O_{12}^{4-}$	$V_4O_{12}^{4-}$	$V_4O_{12}^{4-}$	$V_4O_{12}^{4-}$	$V_4O_{12}^{4-}$
	-572 ± 1 ppm	-550 ± 7 ppm	-586 ppm	-586 ppm	-586 ppm
	$H_2V_2O_7^{-2}$	$V_2O_7^{4-}$	$V_5O_{15}^{5-}$	$V_5O_{15}^{5-}$	$V_5O_{15}^{5-}$
	-550 ± 7 ppm	-586 ppm	-572 ± 1 ppm	-572 ± 1 ppm	-572 ± 1 ppm
	$V_2O_7^{4-}$	$V_5O_{15}^{5-}$	$H_2V_2O_7^{2-}$	$H_2V_2O_7^{2-}$	$H_2V_2O_7^{2-}$
	-586 ppm	-572 ± 1 ppm	-550 ± 5 ppm	-550 ± 3 ppm	-550 ppm
	$V_5O_{15}^{5-}$	$H_2V_2O_7^{2-}$	$V_2O_7^{4-}$	$V_2O_7^{4-}$	$V_2O_7^{4-}$

Source: [94,95,136,138,139]The dominant peak at -577 ppm is $V_4O_{12}^{4-}$

Table 26. Abundance of vanadate species and solution pH for different inhibitor concentrations in 50 mM NaCl.

Species	Species Abbreviation	50 mM Na_2MoO_4	40 mM Na_2MoO_4 + 10 mM $NaVO_3$	25 mM Na_2MoO_4 + 25 mM $NaVO_3$	10 mM Na_2MoO_4 + 40 mM $NaVO_3$	50 mM $NaVO_3$
$V_4O_{12}^{4-}$	V_4		76-78%	78-82%	80%	76-81%
$H_2V_2O_7^{2-}$	V_2		6-9%	4-7%	4-6%	3-12%
$V_2O_7^{4-}$	V_2		7-9%	4-6%	4-5%	1-6%
$V_5O_{15}^{5-}$	V_5		7-9%	9-10%	10-11%	4-13%
pH		7.5	7.9	8.3	8.4	8.4

Effect of Vanadate Inhibitors on Suppressing Open Circuit Pitting Corrosion of AA2024-T3

The results of the 24 hour open circuit potentials prior to anodic scan of cerium acetate pretreated specimens exposed in 50 mM NaCl plus various concentrations of $NaVO_3$ in solution are presented in Table 27 and Figure 98 for AA2024-T3. During the first hour of exposure, all the AA2024–T3 specimen in the 50 mM NaCl solution with 50 mM total inhibitor concentration (mixture of $Ce(C_2H_3O_2)_3$ pretreatment or $NaVO_3$) in test solution demonstrated an OCP higher than that of a similar specimen exposed in the salt solution without inhibitor. These specimens also pitted. The increase in OCP continued for the 24 hour time period. After 24 hours, all of the specimens exposed to the cerium acetate and vanadate inhibitor combinations had a decrease in OCP as did the specimens exposed to just 50 mM NaCl. Twenty-four hour immersion tests in 50 mM NaCl without inhibitor confirmed corrosion of AA2024-T3 at open circuit potential. For both the 1 hour and 24 hour open circuit, OCP did not correlate with the cerium acetate and vanadate ratio.

Table 27. The average open circuit potentials for AA2024–T3 in 50 mM NaCl solution with various concentrations of inhibitor in naturally aerated solution and as a 2 hours pretreatment at the 1st and 23rd hours.

Concentration of Inhibitor	**Open Circuit Potential at the 1st Hour (V_{SCE})**	**Open Circuit Potential at the 23rd Hour (V_{SCE})**
50 mM $Ce(C_2H_3O_2)_3$ pretreatment	-0.502	-0.517
40 mM $Ce(C_2H_3O_2)_3$ pretreatment + 10 mM $NaVO_3$ in test solution	-0.501	-0.630
25 mM $Ce(C_2H_3O_2)_3$ pretreatment + 25 mM $NaVO_3$ in test solution	-0.488	-0.567
10 mM $Ce(C_2H_3O_2)_3$ pretreatment + 40 mM $NaVO_3$ in test solution	-0.498	-0.600
0 mM	-0.536	-0.667

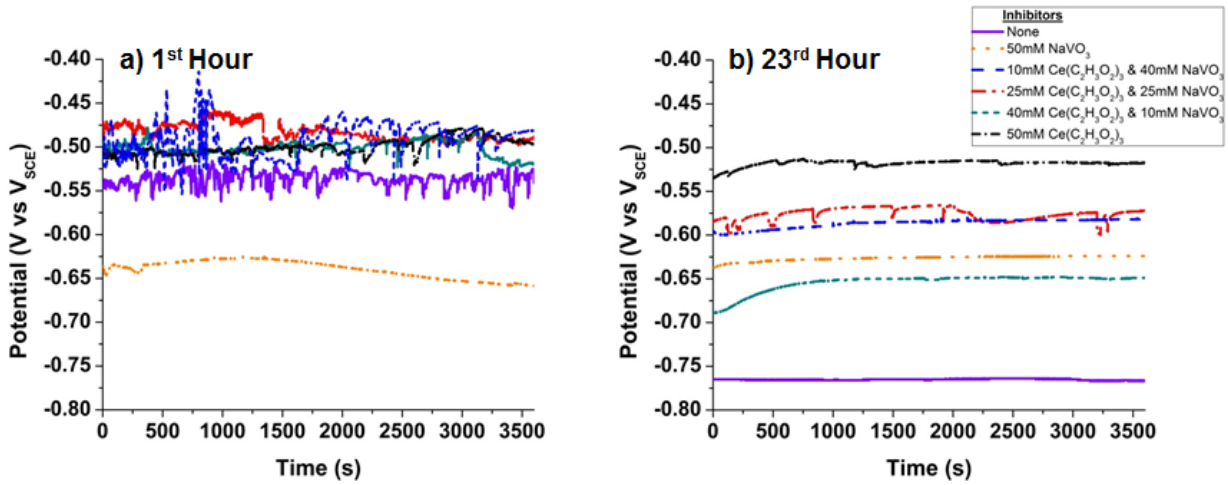

Figure 98. Typical OCP behavior for AA2024-T3 specimens in naturally aerated 50 mM NaCl solutions after a) 1st Hour and b) 23rd Hour. A pretreatment in various concentrations of $Ce(C_2H_3O_2)_3$ followed by testing in various concentrations of $NaVO_3$ in 50 mM NaCl solutions.

The results of the 24 hour open circuit potentials prior to anodic scan conducted in 50 mM NaCl plus various concentrations of Na_2MoO_4 and $NaVO_3$ in solution are presented in Table 28 and Figure 99 for AA2024-T3. During the first hour of exposure, only the AA2024–T3 specimen in the 50 mM NaCl solution with 50 mM Na_2MoO_4 demonstrated an OCP higher than that of a similar specimen exposed in the salt solution without inhibitor. This specimen also pitted. After 23 hours of AA2024-T3 exposure in solutions, the open circuit potentials of all specimens exposed in salt solutions with inhibitor, were higher than those of the specimens exposed in 50 mM NaCl solution without inhibitor with the exception of specimens exposed in 25 mM $NaVO_3$ plus 50 mM NaCl or 25 mM Na_2MoO_4 plus 25 mM $NaVO_3$ plus 50 mM NaCl solution. Only three solutions, (40 mM Na_2MoO_4 plus 10 mM $NaVO_3$ plus 50 mM NaCl, 10 mM Na_2MoO_4 plus 40 mM $NaVO_3$ plus 50 mM NaCl, and 40 mM $NaVO_3$ plus 50 mM NaCl), did not follow the trend of those exposed in 50 mM NaCl solution of having a reduced potential over time. For both the 1 hour and 24 hour open circuit, OCP did not correlate with the vanadate concentration. The 24 hour OCP did correlate with molybdate concentration wherein higher molybdate concentrations ratios had higher open circuit potentials.

Table 28. The average open circuit potentials for AA2024–T3 in naturally aerated 50 mM NaCl solution with various concentrations of inhibitor in aerated solution at the 1st and 23rd hours.

Concentration of Inhibitor	Open Circuit Potential at the 1st Hour (V_{SCE})	Open Circuit Potential at the 23rd Hour (V_{SCE})
0 mM	-0.536	-0.667
50 mM Na_2MoO_4	-0.459	-0.544
40 mM Na_2MoO_4 + 10 mM $NaVO_3$	-0.653	-0.577
10 mM $NaVO_3$	-0.570	-0.584
25 mM Na_2MoO_4 + 25 mM $NaVO_3$	-0.580	-0.681
25 mM $NaVO_3$	-0.621	-0.700
10 mM Na_2MoO_4 + 40 mM $NaVO_3$	-0.772	-0.665
40 mM $NaVO_3$	-0.657	-0.583
50 mM $NaVO_3$	-0.634	-0.649

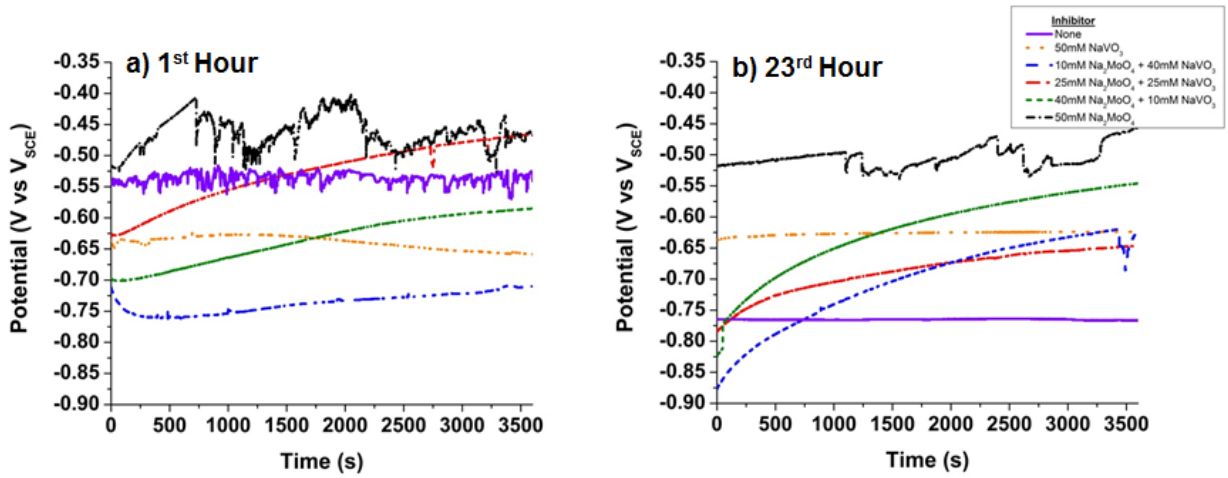

Figure 99. Typical OCP behavior for AA2024-T3 specimens in naturally aerated 50 mM NaCl solutions after a) 1st Hour and b) 23rd Hour. The test solution contained 50 mM $NaVO_3$ and Na_2MoO_4 inhibitors in addition to 50 mM NaCl. The ratio of $NaVO_3$ and Na_2MoO_4 varied, but total inhibitor concentration was kept constant at 50 mM.

24 Hour Immersion Experiments on AA2024-T3

Open circuit or freely corroding immersion experiments were conducted to evaluate the effect of various inhibitors on corrosion of AA2024-T3 sheet, where all anodic and cathodic sites were in close proximity, in 50 mM NaCl solutions. As shown in Figure 100, the number of pits and the pit size were reduced by the addition of $NaVO_3$ to 50 mM NaCl solutions. Both the specimens either pretreated in 50 mM $Ce(C_2H_3O_2)_2$ and then exposed in 50 mM NaCl test solution or that exposed in 50 mM Na_2MoO_4 plus 50 mM NaCl in test solution had a similar appearance to specimens exposed to 50 mM NaCl. The post exposure surfaces of specimens exposed to those two inhibitors had corrosion of and around copper intermetallic particles, as well as, discoloration of the alloy matrix, which was also seen with specimens exposed in 50 mM NaCl solutions. Neither the cerium acetate pretreatment nor the sodium molybdate inhibitors were as effective at reducing pitting as the 50 mM $NaVO_3$ inhibitor. For specimens exposed to solution containing 50 mM $NaVO_3$ solution, the pitting sites could not be seen without the use of a microscope. Also, the addition of 10 mM $NaVO_3$ to 40 mM of either of the other inhibitors reduced the number of pitting sites.

Vanadate precipitates out at pitting sites as a yellow substance. AA2024-T3 exposed to 5 mM $NaVO_3$ in 50 mM NaCl solutions formed yellow precipitates around pits. This yellow precipitate was not seen at higher concentrations of $NaVO_3$. In general, for exposure in solutions containing vanadate, the cerium pretreated specimens were more corroded than the specimens exposed in similar concentrations of vanadate solutions containing molybdate, as shown in Figure 100. Although, there was still wide spread attack of copper intermetallic particles at the 10 mM $Ce(C_2H_3O_2)_2$ pretreatment and 40 mM $NaVO_3$ plus 50 mM NaCl inhibitor combination ratio, vanadate precipitation only occurred at pitting sites for the 40 mM $Ce(C_2H_3O_2)_2$ pretreatment and 10 mM $NaVO_3$ plus 50 mM NaCl inhibitor combination ratio. It is unlikely that the 2 hour cerium acetate pretreatment would be an effective inhibitor against chloride assisted pitting at open circuit conditions. The AA2024-T3 surface post exposure to 50 mM Na_2MoO_4 plus 50 mM NaCl also had a precipitate at large pitting sites. This precipitate was white to brown in color. The mixtures of vanadate and molybdate have precipitate of both the white and yellow colors at large pits. SEM employing EDS was used to examine the difference in elemental composition between the different colored precipitates.

Figure 101 shows the elemental line profile of an Al–Cu–Fe–Mn intermetallic particles and the matrix of AA2024 specimens that were subjected to high and low cerium acetate pretreatment conditions. There was no discernible increase in cerium above the intermetallic particle as compared to the matrix. Both had low average cerium coverage ranging from 2 to 1 at%. An increase in the cerium acetate pretreatment concentration did not lead to a noticeable increase in the amount of cerium coating the matrix and Al–Cu–Fe–Mn intermetallic particle surfaces after the 2 hour pretreatment. The coverage in these tests was of a lower cerium percentage than those found at S–phase Al–Cu–Mg particles. Figure 100 (a-d) shows that the large Al–Cu–Fe–Mn particles had localized attack on the IMC surface, but large pits were found by Al–Cu–Mg particles. Figure 102 shows that the Al–Cu–Mg particles had an order of magnitude higher Ce coverage as compared to the matrix or Al–Cu–Fe–Mn particles. Pitting still occurred preferentially at these Al–Cu–Mg particles. During pitting, chloride and vanadium concentrations increased at the Al–Cu–Mg particle during a 24 hour exposure to 10 mM $NaVO_3$ plus 50 mM sodium chloride solution. Although a high concentration of cerium was deposited on

top of the S–phase, corrosion still occurred at these particles instead of at other metallurgical features with lower cerium coverage. High cerium concentrations on the more anodic Al–Cu–Mg particles did not change the method of AA2024-T3 pitting.

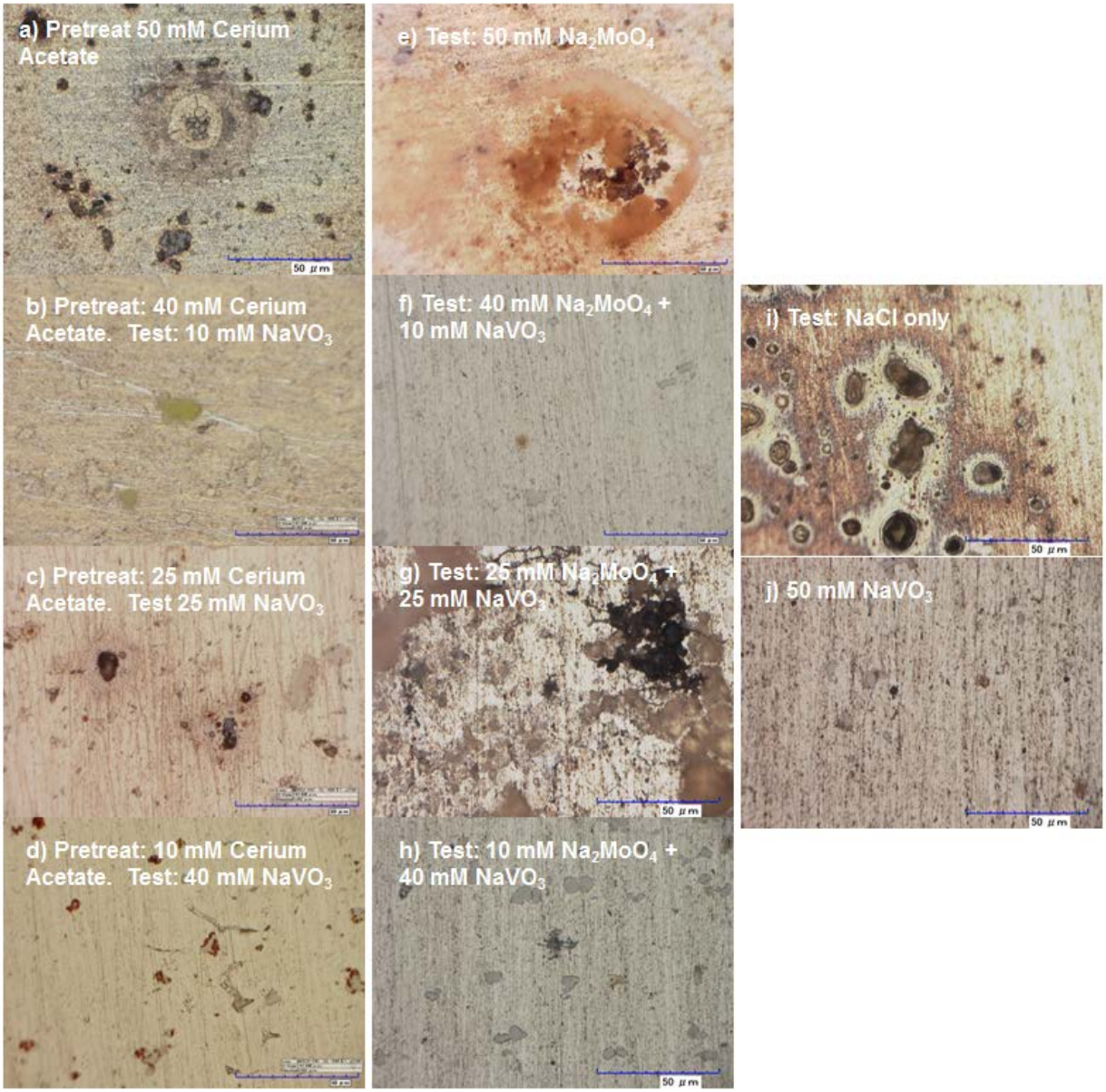

Figure 100. Optical micrographs of AA2024-T3 on the transverse-lateral surface after 24 hours of exposure in naturally aerated 50 mM NaCl solutions with different combinations of inhibitors at room temperature. 50 mM NaCl solution containing cerium acetate was in contact with the surface for 2 hours prior to testing in the chloride containing test solutions for 24 hours for the cerium acetate pretreatment specimens. The scale bars are all 50µm.

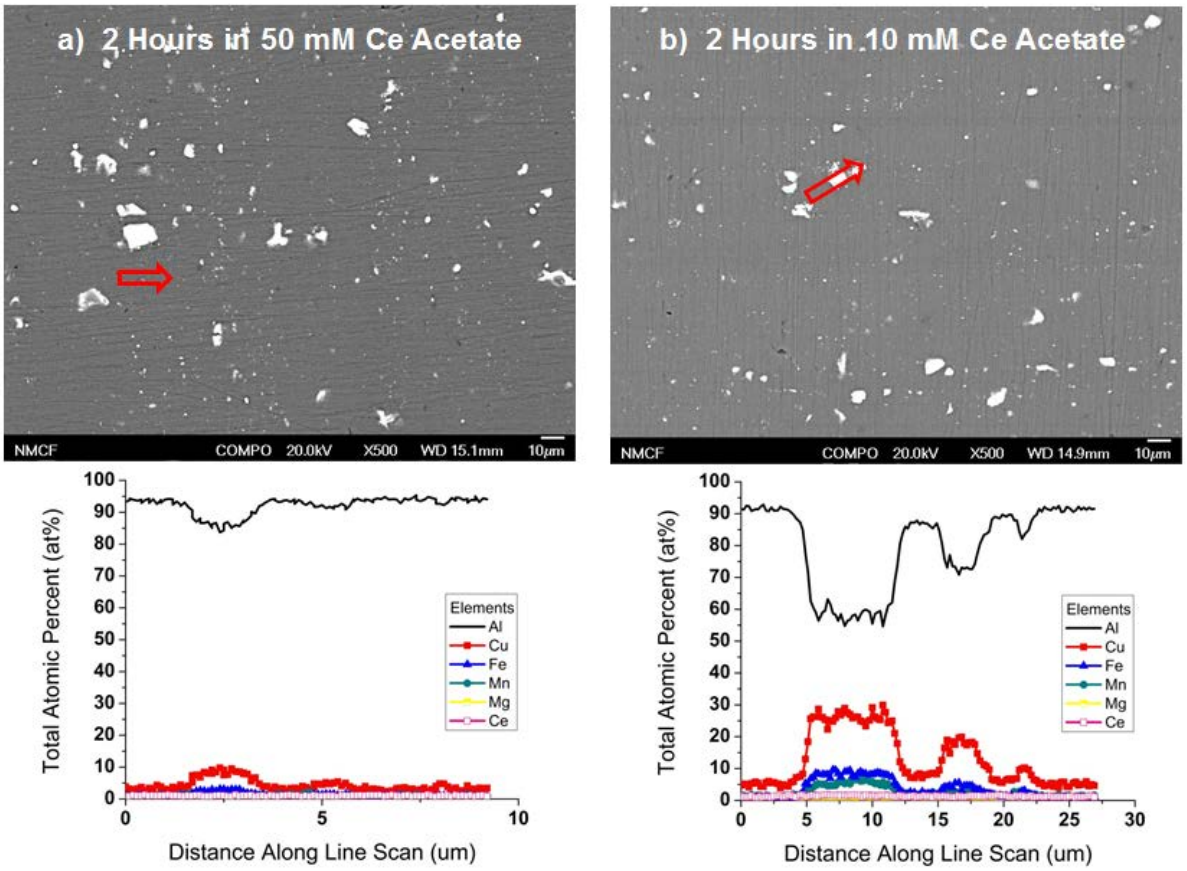

Figure 101. Backscattered electron image, in the compositional mode, taken at 20 kV with 180 second collection time of AA2024–T3 specimen exposed to a) 50 mM $Ce(C_2H_3O_2)_3$ or b) 10 mM $Ce(C_2H_3O_2)_3$ for 2 hours. The arrows indicate location and direction of EDS scan over Al-Cu-Fe-Mn particles.

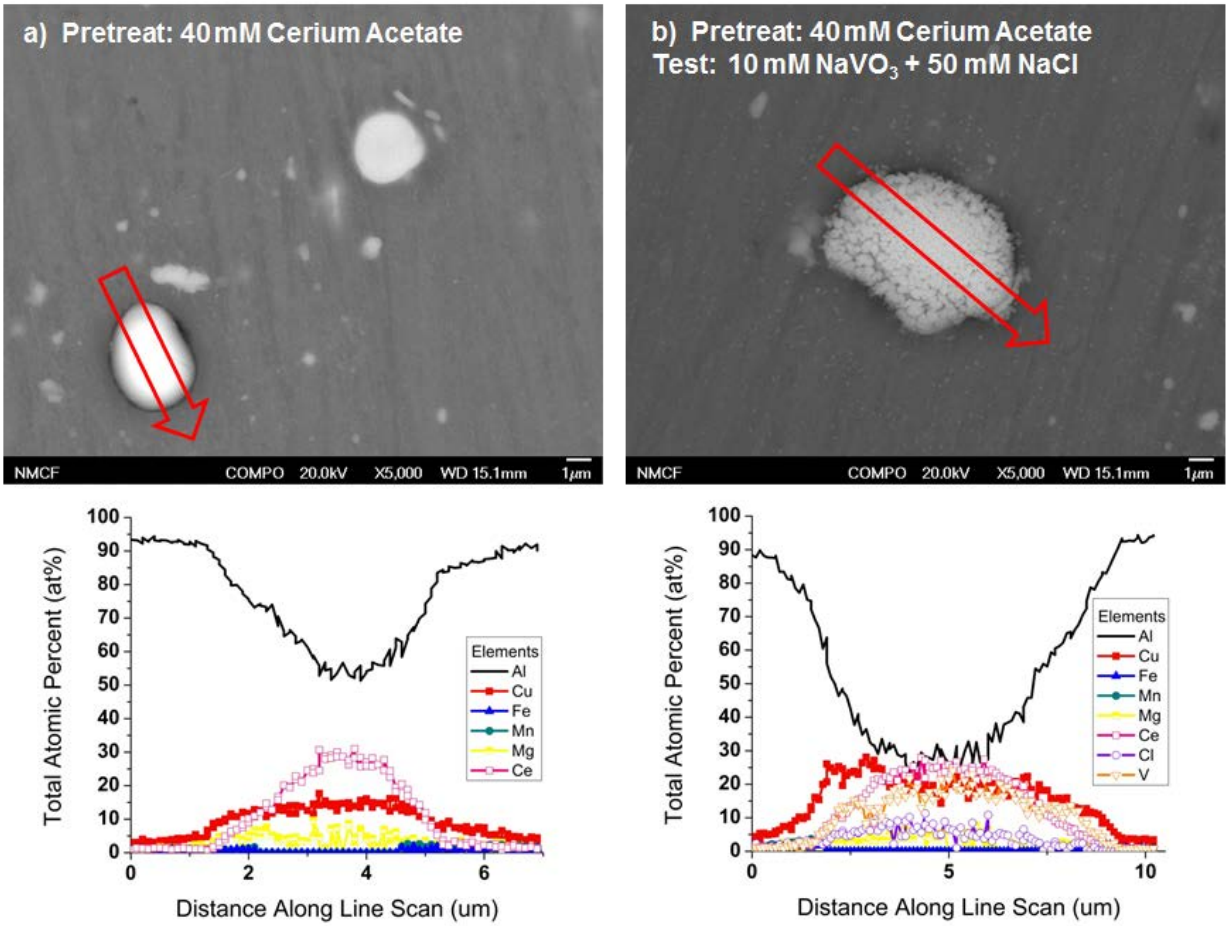

Figure 102. Backscattered electron image, in the compositional mode, taken at 20 kV with 180 second collection time of AA2024–T3 specimen exposed to a) 40 mM $Ce(C_2H_3O_2)_2$ for 2 hours or b) 40 mM $Ce(C_2H_3O_2)_2$ for a 2 hour pretreatment then a 24 hour immersion in 10 mM $NaVO_3$ + 50 mM NaCl. The arrows indicate location and direction of EDS scan.

For the vanadate molybdate mixtures, the pits initiated at the matrix adjacent to Al–Cu–Fe–Mn particles or at S–phase Al–Cu–Mg particles. Molybdenum and Vanadium rich precipitates were observed on the surface of the AA2024-T3 specimens exposed to the 50 mM mixtures of $NaVO_3$ and Na_2MoO_4 plus 50 mM NaCl solutions. These precipitates surrounded the pit. EDS scans presented in Figure 103, indicate that these precipitate products contain molybdenum and vanadium. The EDS scan in Figure 103 (a), 50 mM Na_2MoO_4 + 50 mM NaCl test solution, has a molybdenum rich precipitate on top and surrounding the pit. As seen in the EDS scans in Figure 103 (b) for the 25 mM $NaVO_3$ + 25 mM Na_2MoO_4 + 50 mM NaCl test solution, the molybdenum was preferentially deposited on top of the pit along with a small amount of vanadium and the composition of the precipitate further away from the pit had a composition that high in vanadium and low in molybdenum. Figure 104 (a) shows an example of the unaffected matrix. There is no molybdate peak for the unpitted matrix, even though it was exposed to molybdate containing solutions for 24 hours. Figure 104 (b) shows no molybdate or vanadate precipitate over a Al–Cu–Fe–Mn phase intermetallic particle. The increase in molybdenum and or vanadium concentration at the pitting site was not observed on intermetallic particles that are

not associated with pits in this post-test analysis. At higher $NaVO_3$ concentrations, a yellow precipitate was not evident at the pitting sites. In summary, for all vanadate or vanadate–molybdate concentrations, vanadium or molybdenum was detected at pitting sites as a precipitate but was not observed at unattacked intermetallic particles or on the matrix.

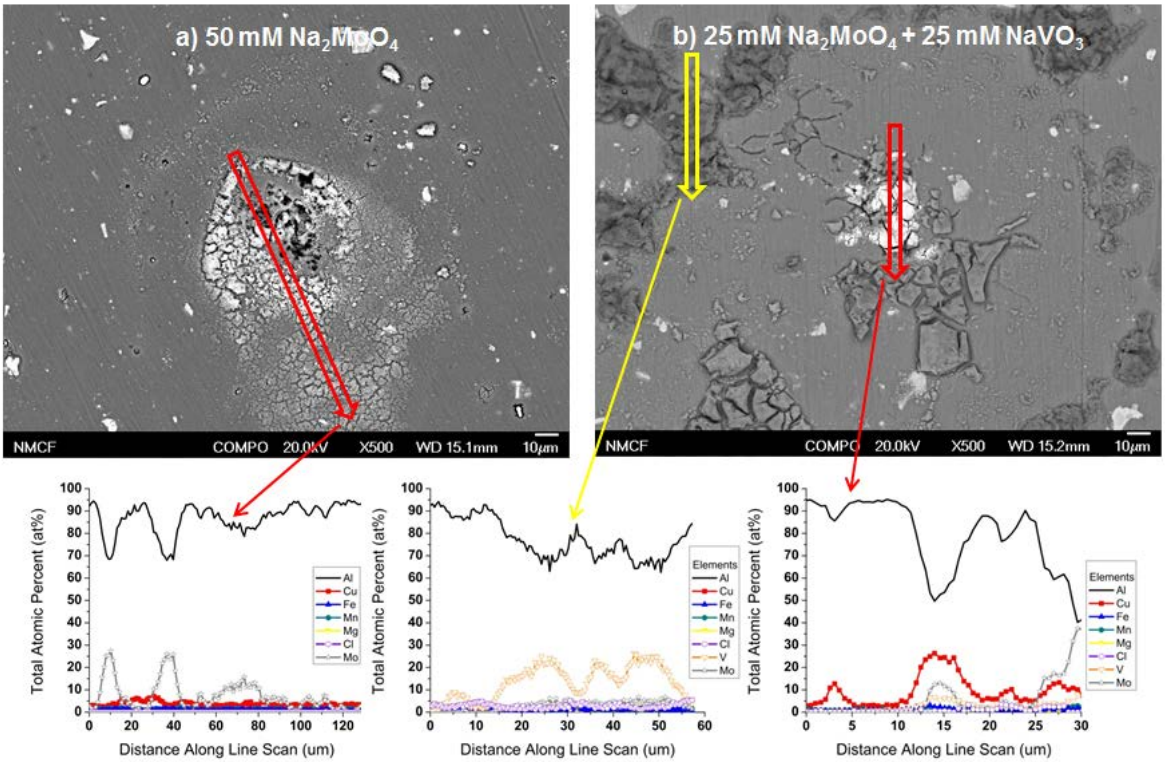

Figure 103. Backscattered electron image, in the compositional mode, taken at 20 kV with 180 second collection time of AA2024–T3 specimen exposed to a) 50 mM Na_2MoO_4 or b) 25 mM Na_2MoO_4 + 25 mM $NaVO_3$ for a 24 hour immersion in 50 mM NaCl. The arrows indicate location and direction of EDS scans.

Inhibition of Localized Corrosion of Aluminum during Anodic Polarization

All combinations of cerium acetate pretreatment and sodium vanadate in test solution reduced the open circuit potential. Pure aluminum specimens, pre-exposed to cerium acetate solutions and tested in sodium chloride plus sodium vanadate solutions (after a 1 hour open circuit exposure), showed an increase in the mean E_{pit} with increasing $NaVO_3$ concentration [Figure 105 (b, c, d, and e)]. In contrast, aluminum pre-exposed to 50 mM cerium acetate solutions and then tested in sodium chloride solutions (after a 1 hour open circuit exposure) did not show an increase in E_{pit} [Figure 105 (a and b)]. Aluminum tested in sodium chloride plus sodium vanadate solutions (after a 1 hour open circuit exposure) did display an increase in E_{pit} [Figure 105 (a and f)]. The latter E_{pit} increase was greater than those observed for all combinations of pre-exposures to cerium acetate solutions followed by testing in sodium chloride plus sodium vanadate solutions. There was a greater difference between E_{pit} for different vanadate combinations after the 24 hour open circuit exposure (Figure 106). The trend of increasing E_{pit} with increasing vanadate for aluminum specimens after 1 hour open circuit exposures was

similar to that for the 24 hour open circuit exposures for specimens after cerium acetate 2 hour pretreatment and tested in sodium vanadate plus sodium chloride solutions. As shown in Figure 106, the effectiveness of 50 mM cerium acetate as a 2 hour pretreatment was marginal at increasing the E_{pit} for aluminum specimens. The E_{corr} and E_{pit} for aluminum specimens increased with increasing vanadate concentration in 50 mM NaCl solutions. The passive potential range for specimens given the cerium acetate pretreatment and tested in vanadate containing solutions decreased as the exposure time at open circuit increased. There was a change in the passive potential range. The passive current density, i_{pass}, was approximately 10^{-6} A/cm^2 irrespective of inhibitor concentration or exposure time. The increasing ratio of the concentration of vanadate in solution to the concentration of cerium acetate pretreatment can be associated with a shift in the range of passive current for Al in 50 mM NaCl, for both 1 hour and 24 hour open circuit exposures.

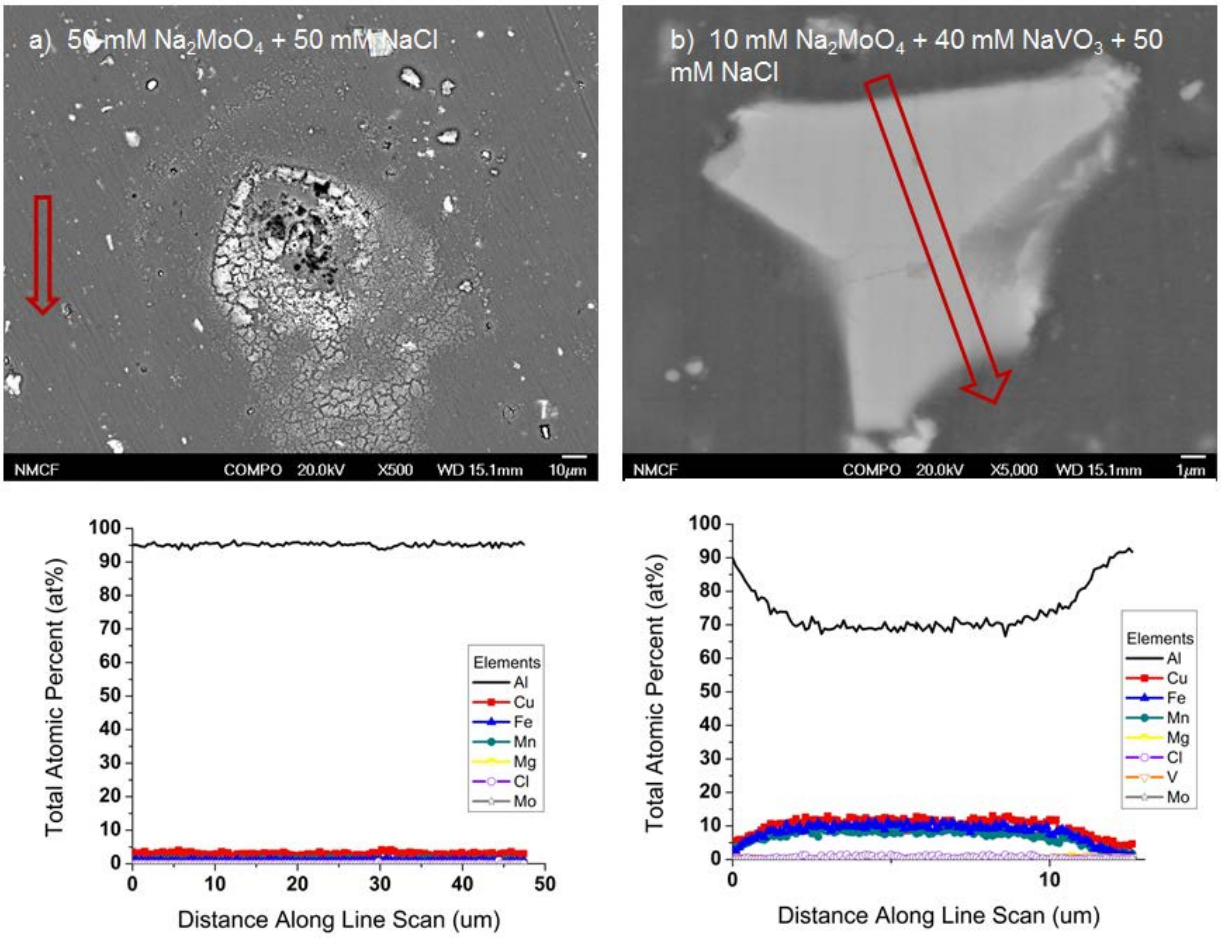

Figure 104. Backscattered electron image, in the compositional mode, taken at 20 kV with 180 second collection time of AA2024–T3 specimen exposed to a) 50 mM Na_2MoO_4 or b) 10 mM Na_2MoO_4 + 40 mM $NaVO_3$ for a 24 hour immersion in 50 mM NaCl. The arrows indicate location and direction of EDS scans.

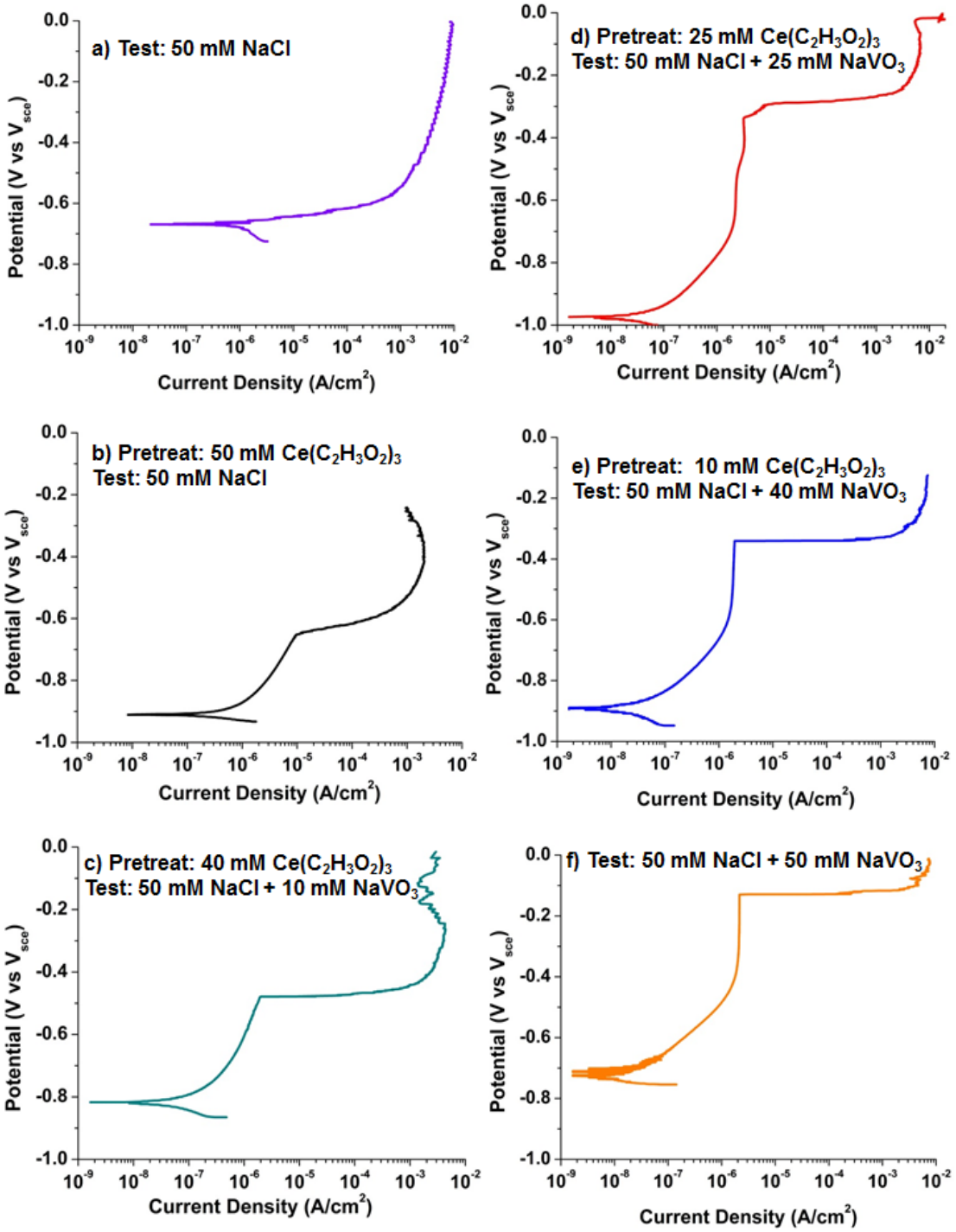

Figure 105. Typical anodic E-log(i) polarization behavior for Al (99.99%) specimens in aerated 50 mM NaCl solutions after an 1 hour open circuit. A pretreatment in various concentrations of $Ce(C_2H_3O_2)_3$ followed by testing in various concentrations of $NaVO_3$ in the 50 mM NaCl solution lead to each surface having been exposed to a constant total of 50 mM of inhibitor between the two solutions.

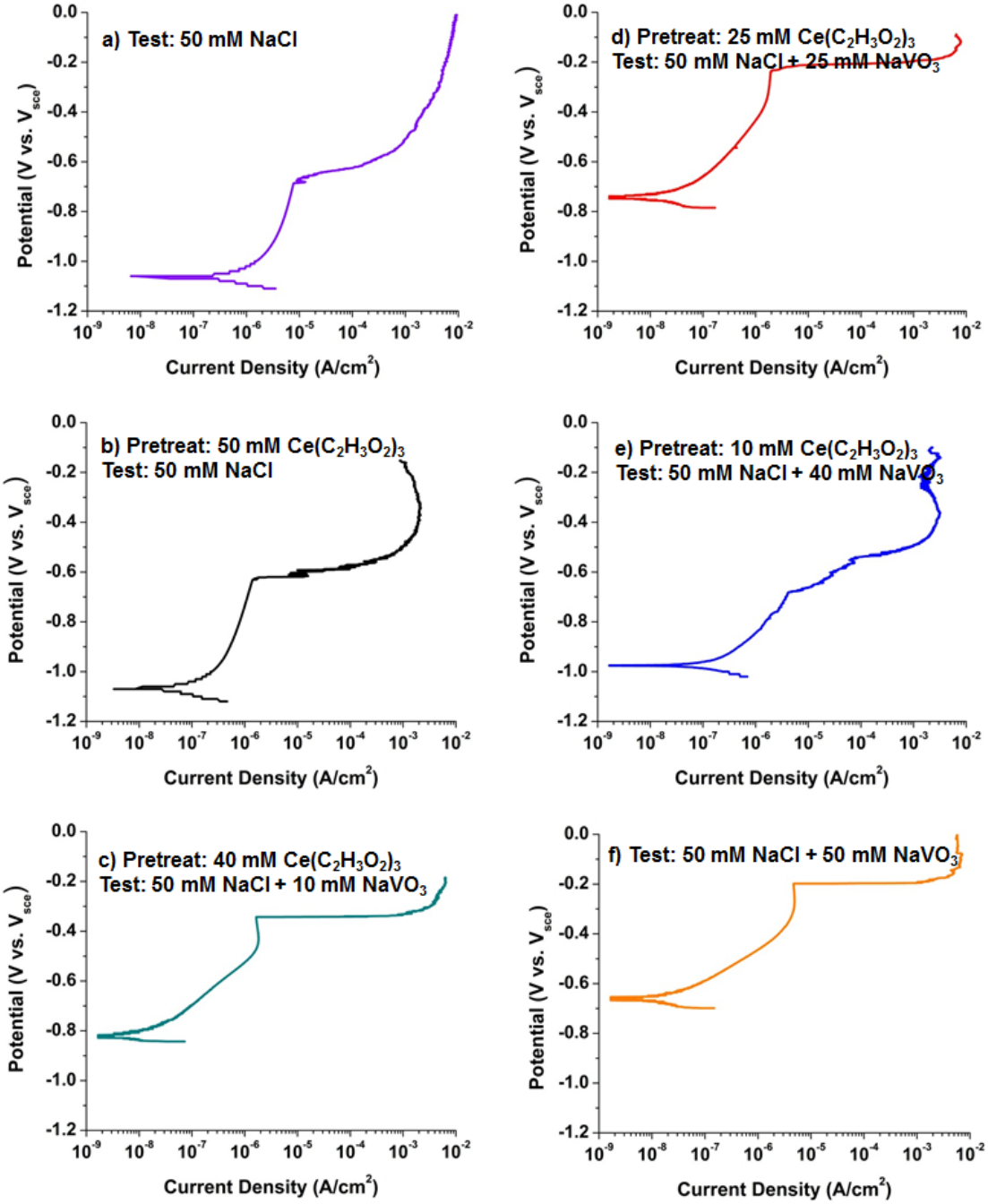

Figure 106. Typical anodic E-log(i) polarization behavior for Al (99.99%) specimens in aerated 50 mM NaCl solutions after a 24 hour open circuit. A pretreatment in various concentrations of $Ce(C_2H_3O_2)_3$ followed by testing in various concentrations of $NaVO_3$ in the 50 mM NaCl solution lead to each surface having been exposed to a constant total of 50 mM of inhibitor between the two solutions.

The anodic polarization behavior of aluminum specimens tested in sodium chloride plus various combinations of sodium vanadate and sodium molybdate after 1 hour open circuit exposures are presented in Figure 107. All combinations of vanadate-molybdate inhibitor mixtures were effective at raising E_{pit}, compared to the uninhibited case. The coupons exposed to 50 mM molybdate had the smallest increase in E_{pit}. An inhibitor combination of 40 mM sodium molybdate and 10 mM vanadate appears to be almost as effective at increasing E_{pit} as 50 mM vanadate by itself [Figure 107 (c and f)]. However, an inhibitor combination of 25 mM sodium molybdate and 25 mM sodium vanadate appears to be the least effective at increasing E_{pit} as compared to other combinations tested [Figure 107 (c, d and e)]. The molybdate-vanadate combination inhibitor was more effective at increasing E_{pit} on aluminum specimens than the cerium acetate pretreatment.

After 24 hours, for aluminum specimens, the molybdate-vanadate inhibitor combinations were more effective than the cerium pretreatment followed by testing in vanadate containing solutions at raising E_{pit} and E_{corr} values, as shown in Figure 108. Increasing the exposure time from 1 to 24 hours increased the range of passivity for all vanadate and molybdate concentrations. The greatest increase in i_{pass} potential range or difference in E_{pit} - E_{corr} values due to increased time at open circuit was observed for the 50 mM Na_2MoO_4 inhibitor in solution. For the 1 hour open circuit exposure, the 50 mM Na_2MoO_4 inhibitor had the smallest i_{pass} potential range, whereas this inhibitor concentration had the largest i_{pass} potential range after a 24 hour exposure. In comparison, after 24 hours at open circuit, aluminum specimens in 50 mM NaCl solution also had increases in the potential range of the passive region, but these increases were related to a reduction in E_{corr} rather than a further increase in E_{pit}.

There was an increase in E_{pit} on AA2024–T3 specimens whenever $NaVO_3$ was in solution with NaCl, as shown in Figure 109. After exposures to various concentrations of $NaVO_3$ in 50 mM NaCl solutions for 1 hour at open circuit potential, the increase in E_{pit} was not monotonic with $NaVO_3$ concentration. The specimens that had been exposed to a concentration of 50 mM $NaVO_3$ showed the most significant increase in E_{pit}.

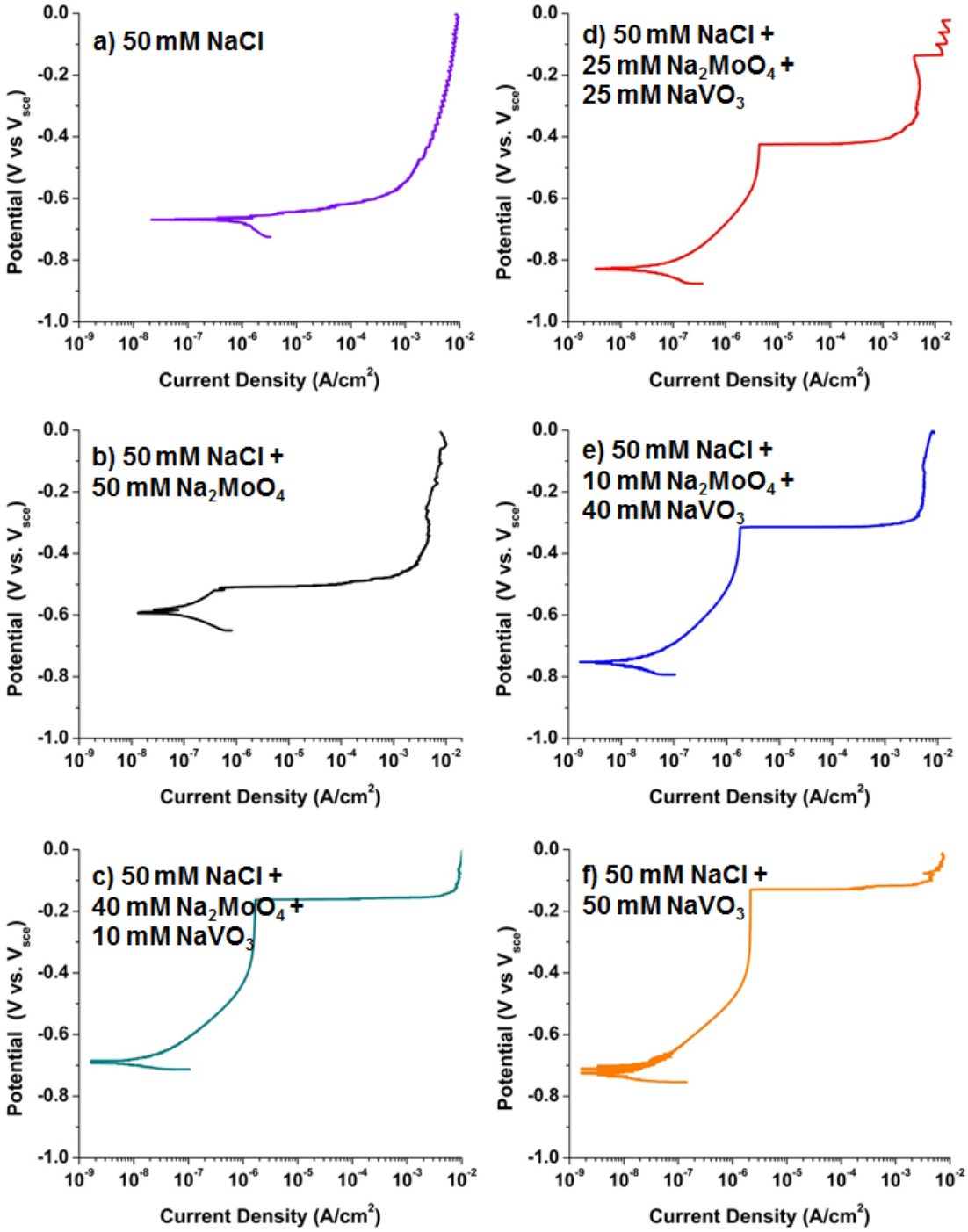

Figure 107. Typical anodic E-log(i) polarization behavior for Al (99.99%) specimens in aerated 50 mM NaCl solutions after an 1 hour open circuit. The test solution contained 50 mM of $NaVO_3$ and Na_2MoO_4 inhibitors in addition to 50 mM NaCl. The ratio of $NaVO_3$ and Na_2MoO_4 varied, but the total inhibitor concentration was kept constant at 50 mM.

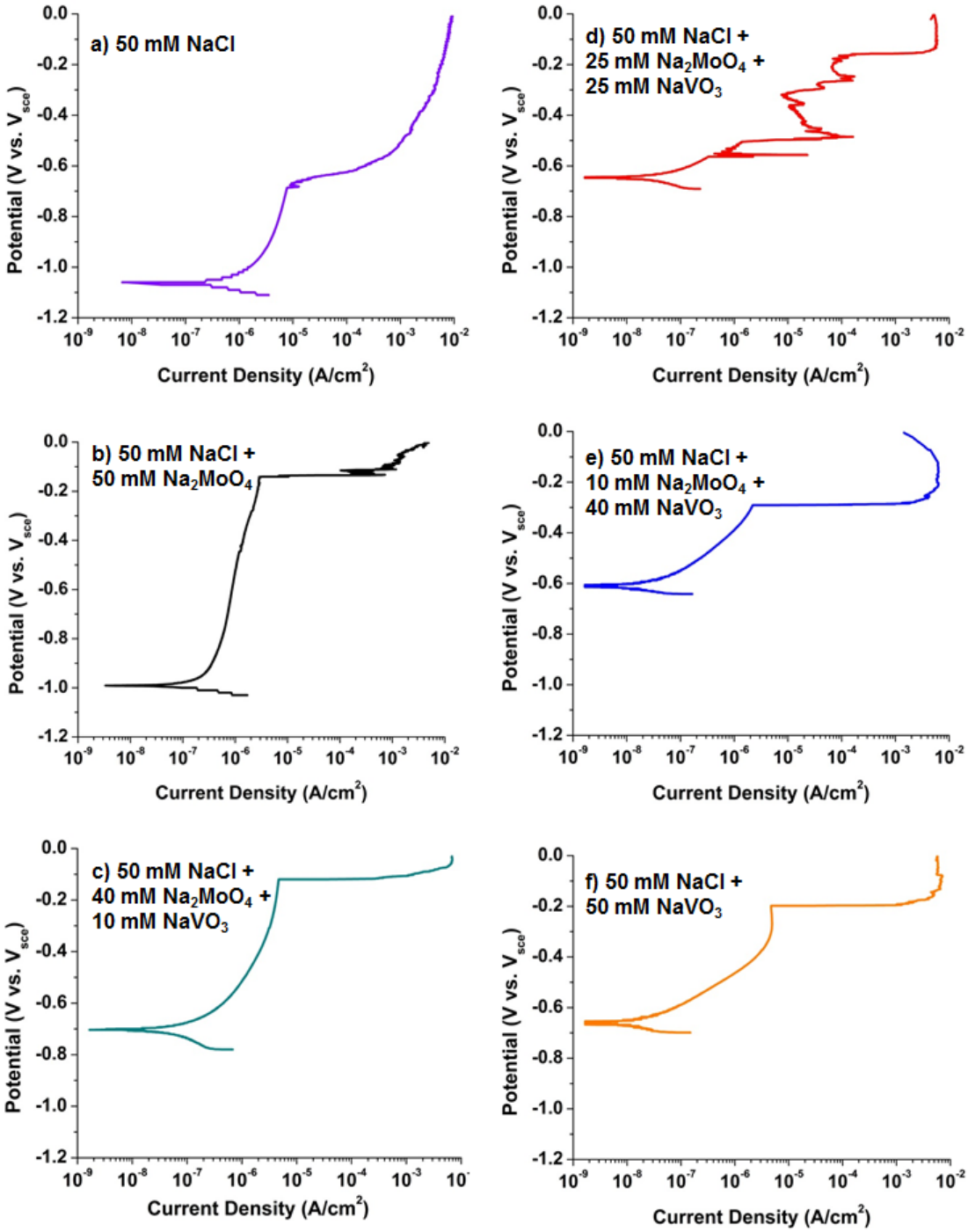

Figure 108. Typical anodic E-log(i) polarization behavior for Al (99.99%) specimens in aerated 50 mM NaCl solutions after a 24 hour open circuit. The test solution contained 50 mM of $NaVO_3$ and Na_2MoO_4 inhibitors in addition to 50 mM NaCl. The ratio of $NaVO_3$ and Na_2MoO_4 varied, but the total inhibitor concentration was kept constant at 50 mM.

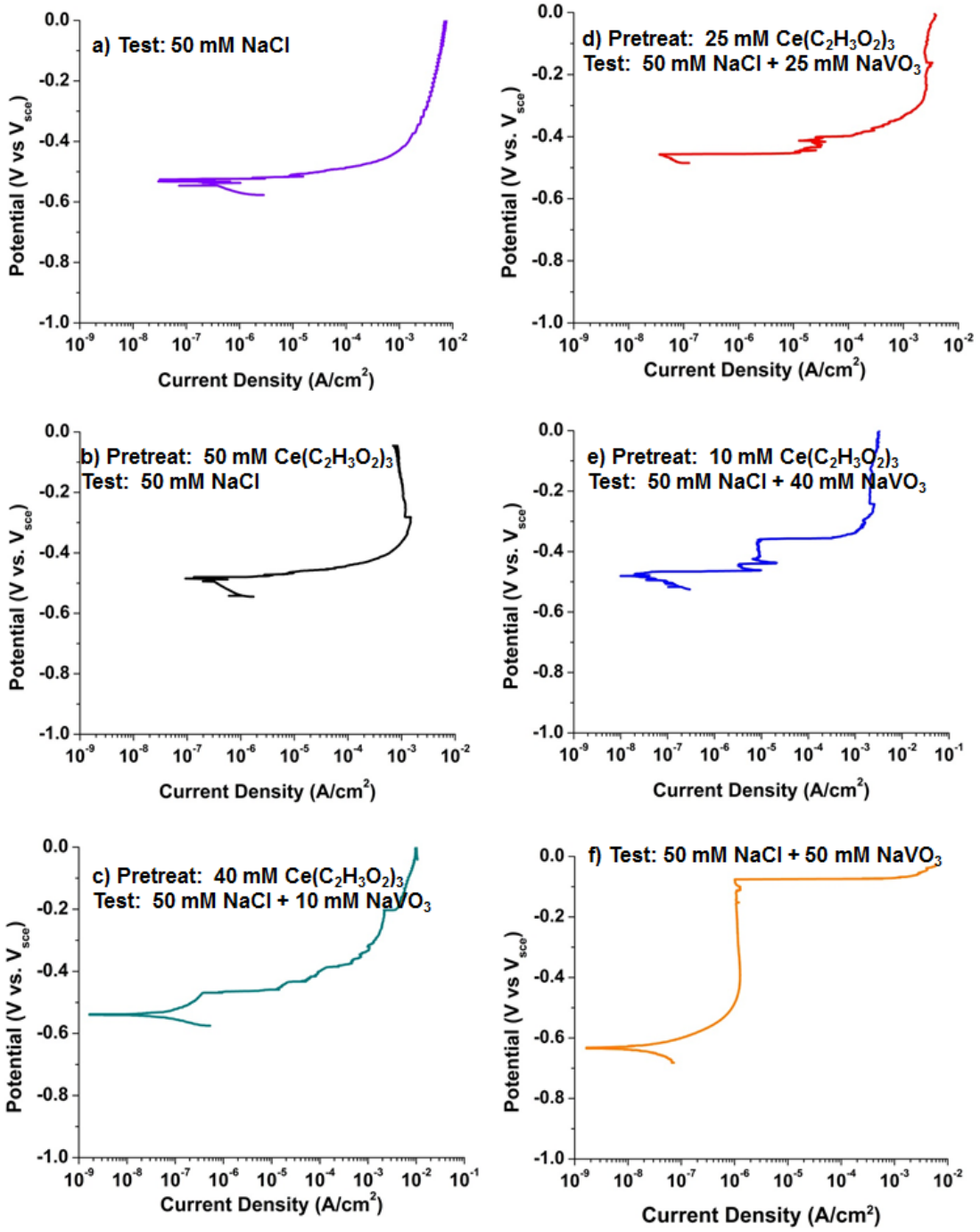

Figure 109. Typical anodic E-log(i) polarization behavior for AA2024–T3 specimens in naturally aerated 50 mM NaCl solutions after an 1 hour open circuit. A pretreatment in various concentrations of $Ce(C_2H_3O_2)_3$ followed by testing in various concentrations of $NaVO_3$ in the 50 mM NaCl solution lead to each surface having been exposed to a total of 50 mM of inhibitor between the two solutions.

The passive current density range, given by E_{pit} - E_{corr}, increased with vanadate concentration. AA2024-T3 specimens tested in 50 mM NaCl solutions with a 1 hour open circuit exhibited pitting near E_{corr}. Pretreating the AA2024-T3 specimens in $Ce(C_2H_3O_2)_3$ for two hours prior to testing also resulted in pitting near E_{corr} (Figure 109). E_{pit} increased with increasing vanadate in solution and decreasing cerium acetate pretreatment concentration. Specimens exposed only to solutions containing 50 mM $NaVO_3$ plus 50 mM NaCl had the largest range of passive current density and the greatest variability in range. The AA2024-T3 specimens exposed to higher vanadate inhibitor concentrations exhibited greater passive potential ranges due to the increase in E_{pit} above E_{corr}. The specimens given a cerium pretreatment and exposed to vanadate containing solutions showed a smaller passive potential range due to increases in E_{corr}, and showed more limited increases in E_{pit} than vanadate only inhibited specimens. The passive potential ranges on the cerium pretreated specimens occurred at current densities of approximately 10^{-6} A/cm^2. E_{repass} for specimens with or without the cerium acetate pretreatment and tested in vanadate containing solutions was approximately -0.8 V_{SCE}. This same approximately -0.8 V_{SCE} E_{repass} was observed for the specimens with or without a 2 hour cerium acetate pretreatment and exposed to 50 mM NaCl solution (Figure 109).

The anodic E–log(i) polarization behavior after 24 hours of solution exposure for AA2024-T3 is shown in Figure 110. Twenty-four hours of exposure to $NaVO_3$ plus NaCl solutions raised E_{pit} of AA2024-T3, as presented in Figure 110. A 2 hour cerium acetate pretreatment followed by testing in vanadate containing solutions produced the same trends in E_{pit} for the 1 hour solution exposed specimens. The increase in E_{pit} was related to a decrease in the cerium acetate pretreatment and an increase in vanadate in solution for the cerium acetate-vanadate 50 mM total of inhibitor. Also, similar to the 1 hour exposure, specimens pretreated in 50 mM $Ce(C_2H_3O_2)_3$ and then tested in 50 mM NaCl lacked a passive potential range because pitting occurred at E_{corr}. For these specimens in Ce-V inhibitor combinations, an i_{pass} of 10^{-6} A/cm^2 along with E_{repass} value of -0.8 V_{SCE} was observed. To determine the effect of vanadate concentration on raising E_{pit}, several experiments were completed with a 10 mM $Ce(C_2H_3O_2)_3$ 2 hour pretreatment and various concentrations of sodium vanadate in test solution. Figure 111 shows the resulting anodic E–log(i) polarization behavior after 24 hours of solution exposure for AA2024-T3 given a 10 mM $Ce(C_2H_3O_2)_3$ 2 hour pretreatment and various concentrations of sodium vanadate. Increases in E_{pit} and in the resulting passivation potential range were observed when the vanadate concentration was increased at a constant total inhibitor concentration (Figure 111). No effect on repassivation was demonstrated. It is likely that any increase in E_{pit} is due to vanadate concentration and not to the increase in cerium acetate pretreatment concentration as E_{pit} appeared to be independent of cerium acetate pretreatment concentration (Figure 112).

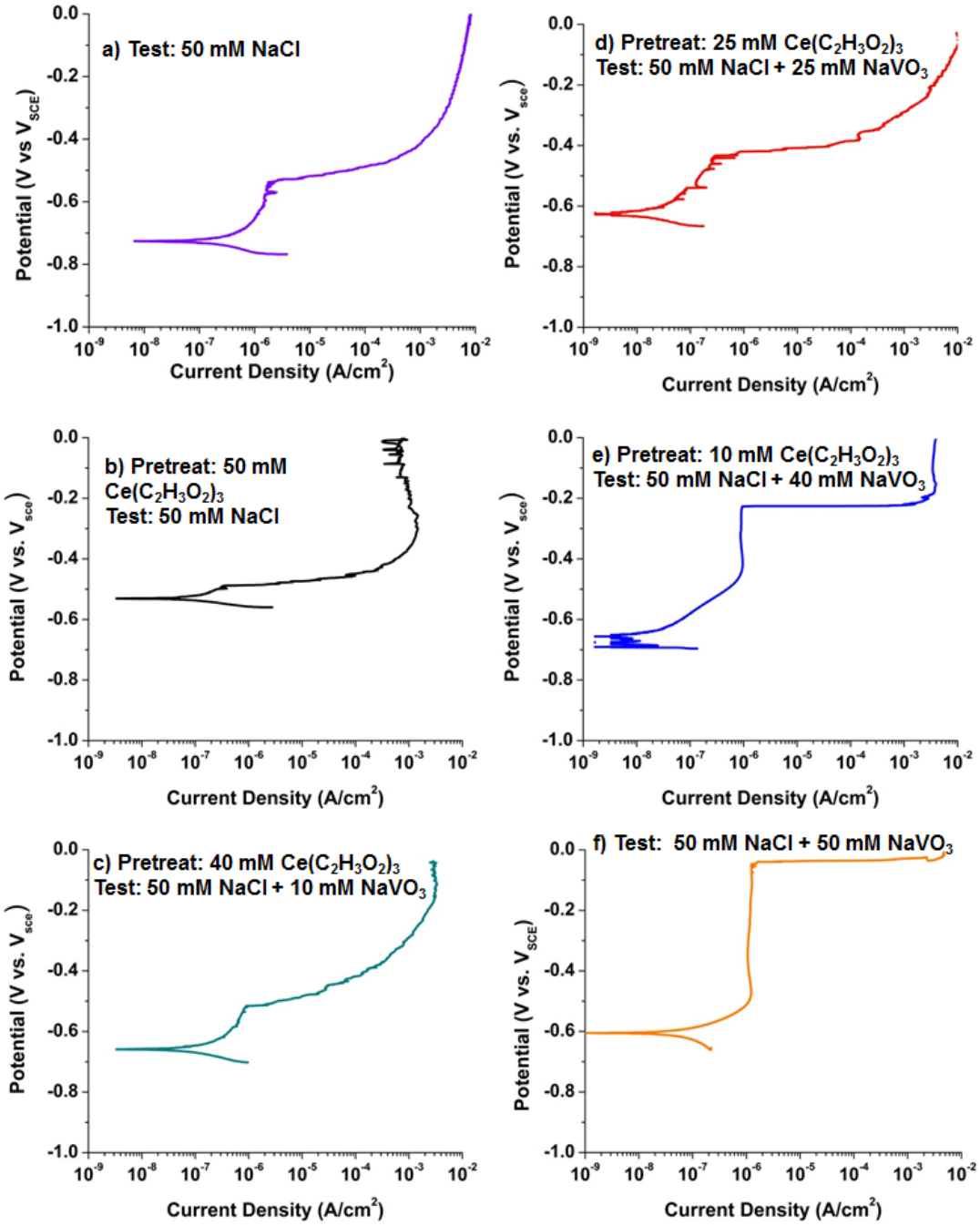

Figure 110. Typical anodic E-log(i) polarization behavior for AA2024–T3 specimens in naturally aerated 50 mM NaCl solutions after a 24 hour open circuit period. A pretreatment in various concentrations of $Ce(C_2H_3O_2)_3$ was followed by testing in various concentrations of $NaVO_3$ in the 50 mM NaCl solution lead to each surface having been exposed to a total of 50 mM of inhibitor between the two solutions.

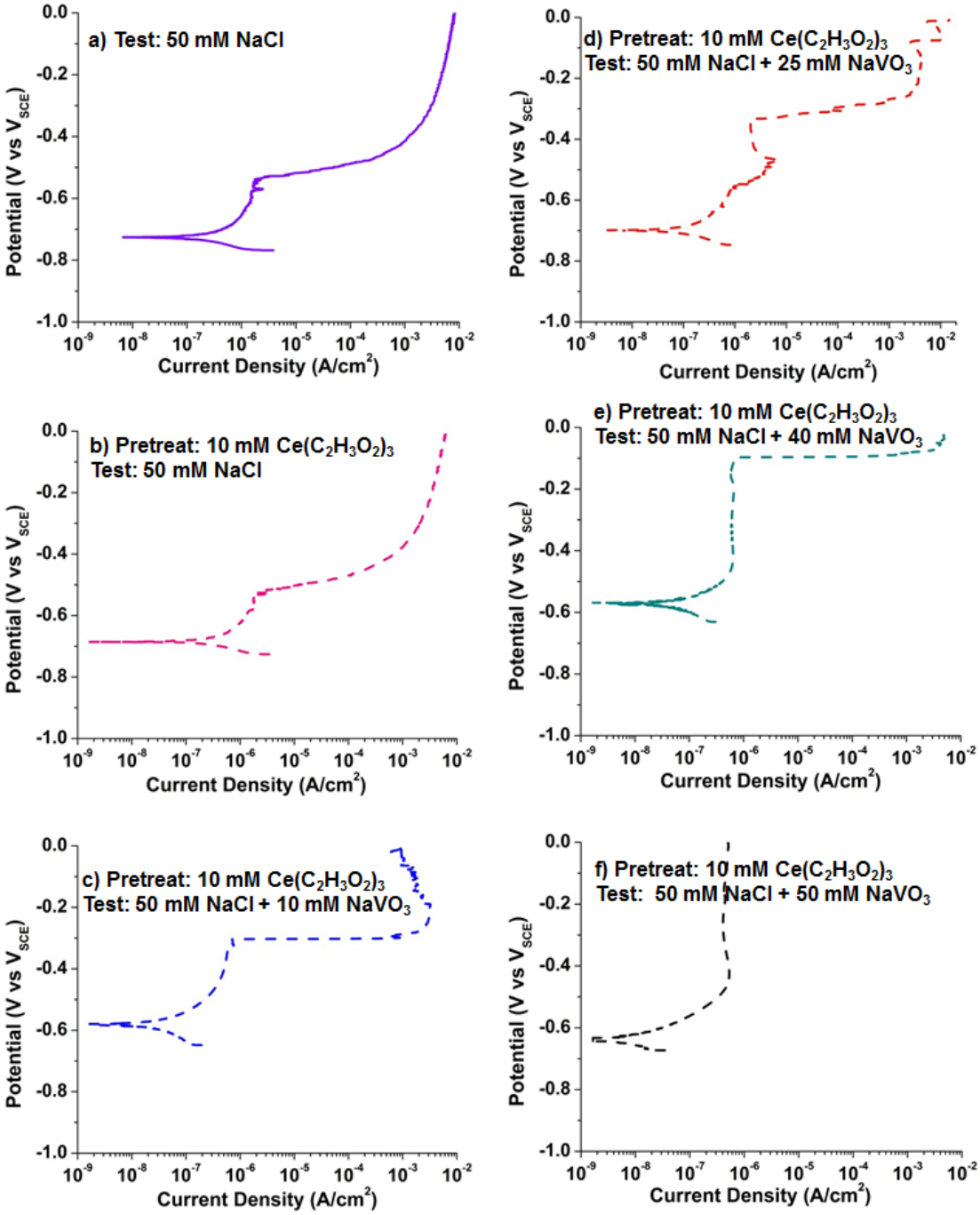

Figure 111. Typical anodic E-log(i) polarization behavior for AA2024–T3 specimens in naturally aerated 50 mM NaCl solutions after a 24 hour open circuit period. A pretreatment of 10 mM $Ce(C_2H_3O_2)_3$ was followed by testing in various concentrations of $NaVO_3$ in the 50 mM NaCl solution.

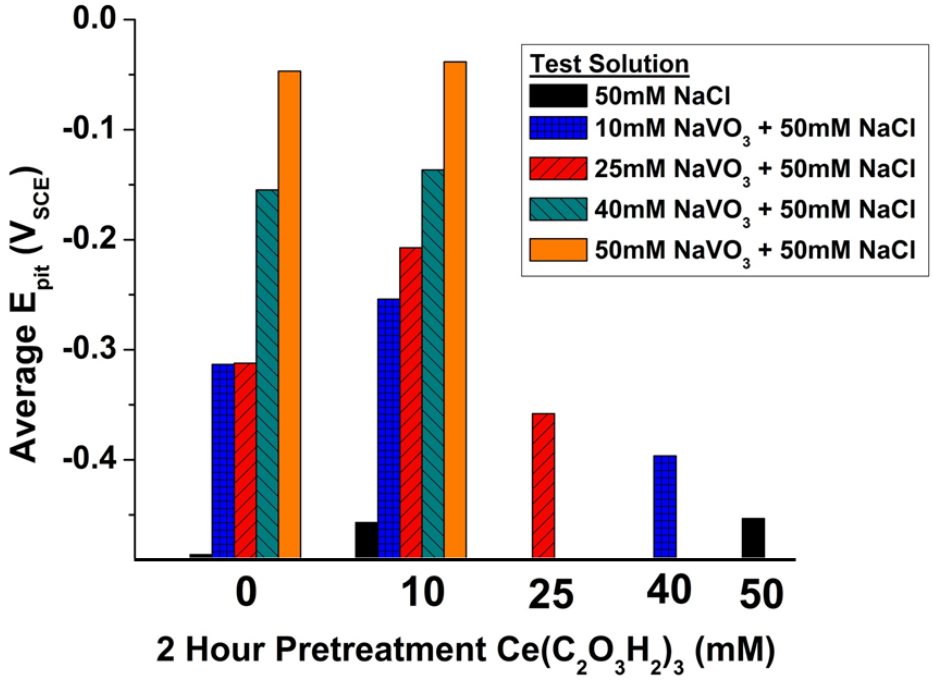

Figure 112. Average Epit for AA2024-T3 specimens in aerated 50 mM NaCl solutions after a 24 hour open circuit. A 2 hour $Ce(C_2O_3H_2)_3$ pretreatment was followed by testing in various concentration of $NaVO_3$ in the 50 mM NaCl solution.

The anodic polarization behavior for AA2024-T3 exposed to both 50 mM inhibitor (Na_2MoO_4 and $NaVO_3$) mixtures and 50 mM NaCl is presented in Figure 113. E_{pit} of AA2024–T3 increased with increasing ratios of $NaVO_3$ to Na_2MoO_4. The specimens exposed to Na_2MoO_4 and $NaVO_3$ solutions had E_{pit} values similar to those for exposure to the 50 mM $NaVO_3$ plus 50 mM NaCl solution, and slightly above those for exposure to 50 mM Na_2MoO_4 plus 50 mM NaCl solutions. However, the increase in E_{pit} is not monotonic with $NaVO_3$ additions. AA2024-T3 specimens tested in 50 mM NaCl solutions with a 1 hour open circuit exhibited pitting near E_{corr}. A passive current density range was observed when the addition of vanadate and molybdate inhibitors to the solution raised E_{pit} above the open circuit potential, E_{corr}. 50 mM $NaVO_3$ in solution was best at raising the average E_{pit} value and 50 mM Na_2MoO_4 in solution raised the average E_{corr} value. The average passive current, i_{pass}, was approximately 10^{-6} A/cm^2. E_{repass} of approximately -0.8 V_{SCE} was not affected by vanadate or molybdate in solution.

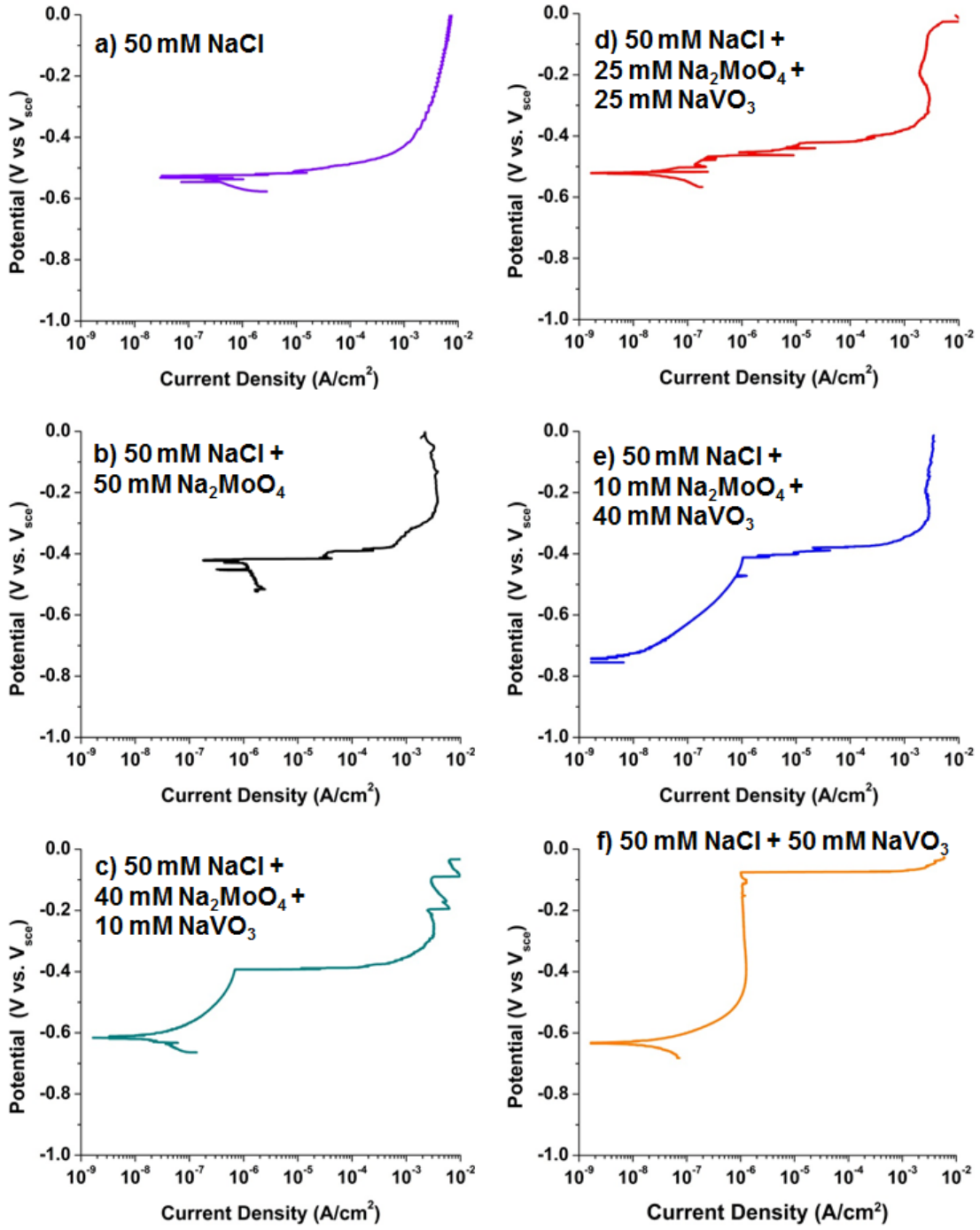

Figure 113. Typical anodic E-log(i) polarization behavior for AA2024-T3 specimens in naturally aerated 50 mM NaCl solutions after a 1 hour open circuit. The test solution contained a combined concentration of 50 mM of $NaVO_3$ and Na_2MoO_4 inhibitors in addition to 50 mM NaCl. The ratio of $NaVO_3$ and Na_2MoO_4 varied.

Twenty-four hours of exposure to 50 mM inhibitor mixtures (Na_2MoO_4 and $NaVO_3$) and 50 mM NaCl solutions raised E_{pit} of AA2024-T3, as presented in Figure 114. These specimens behaved like the 1 hour anodic E–log(i) polarization specimens. In this case, the increase in E_{pit} and decreases in OCP correlated with increasing vanadate inhibitor concentration in solution. However, the total range of passive current density was increased with increase time at open circuit. After 24 hours of exposure to 50 mM inhibitor (Na_2MoO_4 and $NaVO_3$) mixtures, an i_{pass} of 10^{-6} A/cm^2 was observed. Molybdate and vanadate concentration and time of the open circuit exposure did not affect the observation of a -0.8 V_{SCE} E_{repass}, nor the observation of an i_{pass} of 10^{-6} A/cm^2.

The cumulative probability plots afford the opportunity to compare vanadate to vanadate-molybdate and vanadate-cerium average E_{pit}. E_{pit} cumulative probability diagrams for high purity aluminum exposed to sodium chloride solutions containing various amounts of sodium vanadate after 1 hour and 24 hour open circuit exposures display monotonically increasing average E_{pit} with vanadate concentration. For the 1 hour open circuit exposures, significant improvement in E_{pit}, for various concentrations of vanadate in 50 mM NaCl was observed at the 75th percentile but below the 20th percentile, the improvement is small (Figure 115). The average E_{pit} values for the $Ce(C_2H_3O_2)_3$ pretreatment also show a monotonic increase in E_{pit} with an increase in vanadate concentration. These E_{pit} values also show that the average E_{pit} for aluminum specimens subjected to 50 mM $Ce(C_2H_3O_2)_3$ 2 hour pretreatment and then tested in 50 mM NaCl was slightly lower than that for the specimens tested in 50 mM NaCl without any prior exposure to inhibitors.

Likewise, for the 1 hour open circuit experiments using molybdate and vanadate mixtures with aluminum specimens, 50 mM Na_2MoO_4 underperformed 50 mM $NaVO_3$ in inhibiting E_{pit}. Only the 40 mM Na_2MoO_4 plus 10 mM $NaVO_3$ combination of inhibitors in solution outperformed the 50 mM $NaVO_3$ in increasing the average E_{pit} for the 1 hour open circuit experiments. This 40 mM Na_2MoO_4 plus 10 mM $NaVO_3$ combination of inhibitors had an average E_{pit} above the 50th percentile of the 50 mM $NaVO_3$ E_{pit} cumulative probability.

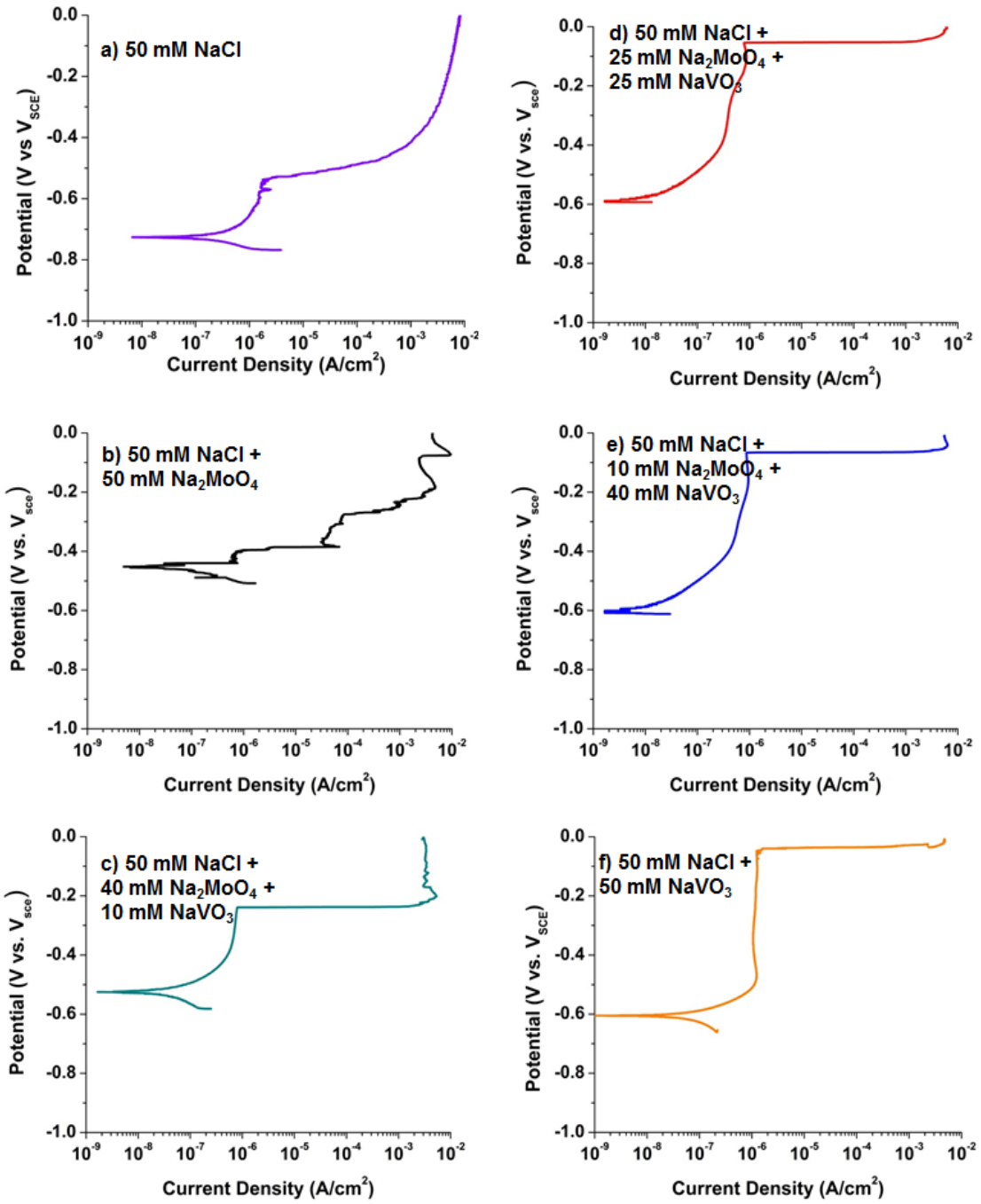

Figure 114. Typical anodic E-log(i) polarization behavior for AA2024-T3 specimens in naturally aerated 50 mM NaCl solutions after a 24 hour open circuit. The test solution contained a combined concentration of 50 mM of $NaVO_3$ and Na_2MoO_4 inhibitors in addition to 50 mM NaCl. The ratio of $NaVO_3$ and Na_2MoO_4 varied.

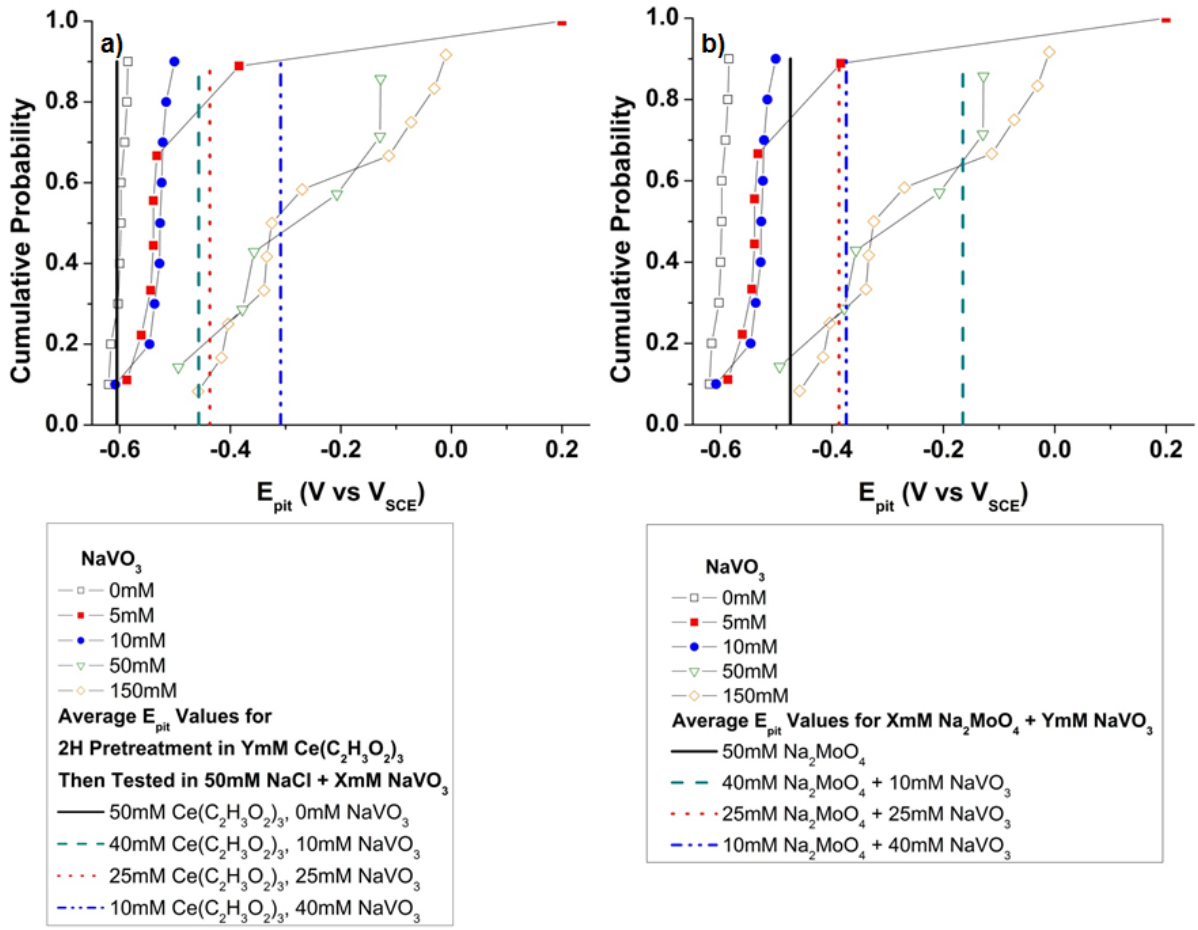

Figure 115. Cumulative probability plot for Al (99.99%) after 1 hour in aerated 50 mM NaCl solution plus various 50 mM inhibitor mixtures; a) a $Ce(C_2H_3O_2)_3$ 2 hour pretreatment then tested with the remainder of the inhibitor concentration as $NaVO_3$ dissolved in the test solution; b) $NaVO_3$ and Na_2MoO_4 mixtures dissolved into the test solution. Data points indicate cumulative probability of pitting before potential reversal.

After a 24 hour open circuit in 50 mM NaCl solutions containing vanadate, the strong effect of different vanadate inhibitor concentrations on E_{pit} was more obvious (Figure 116). A significant increase in E_{pit} below the 20th percentile was seen with 150 mM $NaVO_3$ compared to that in 50 mM NaCl without inhibitor. For this 150 mM $NaVO_3$ concentration, the increase in E_{pit} at the 10th percentile is similar to that for the 70th percentile for the 10 and 50 mM $NaVO_3$ concentrations and is greater than those for 5 mM $NaVO_3$ concentration. This strong effect of inhibition is not seen for anodic scans after the 1 hour open circuit exposure. Above the 30th percentile, all vanadate concentrations above 5 mM $NaVO_3$ in solution exhibited more than a 100 mV increase in E_{pit}. As observed with the 1 hour open circuit exposures, aluminum specimens subjected to the 50 mM $Ce(C_2H_3O_2)_3$ 2 hour pretreatment and then tested in 50 mM NaCl had a similar average E_{pit} value as that for the 50 mM NaCl solution without any exposure to inhibitors. The increase in average E_{pit} also correlates with a decrease in concentration of $Ce(C_2H_3O_2)_3$ for 2 hour pretreatment and an increase in concentration of vanadate in the test solution.

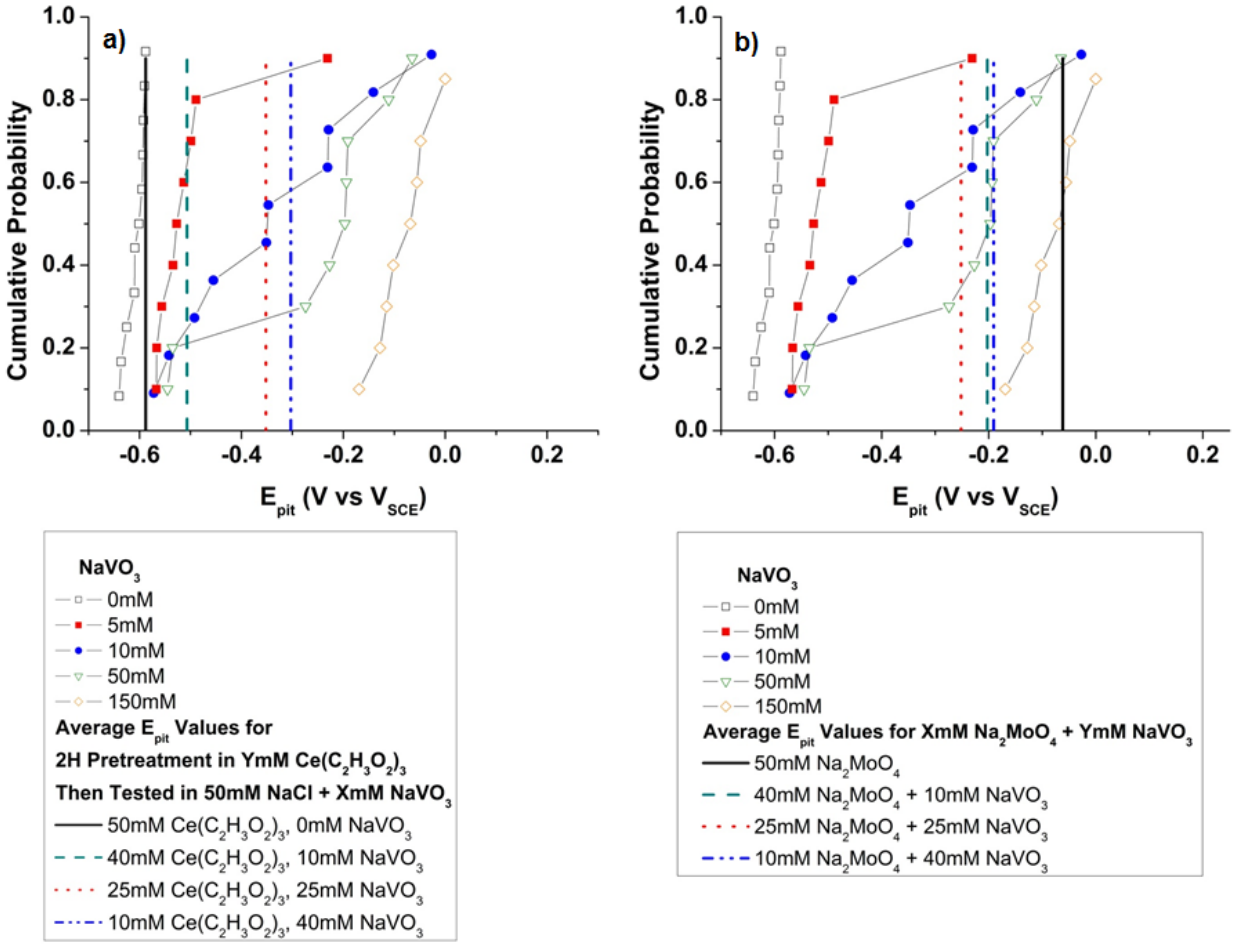

Figure 116. Cumulative probability plot for Al (99.99%) after 24 hours in aerated 50 mM NaCl solution plus various 50 mM inhibitor mixtures; a) a $Ce(C_2H_3O_2)_3$ 2 hour pretreatment then tested with the remainder of the inhibitor concentration as $NaVO_3$ dissolved in the test solution; b) $NaVO_3$ and Na_2MoO_4 mixtures dissolved into the test solution. Data points indicate cumulative probability of pitting before potential reversal.

The greatest change in effective inhibitor combinations is seen with molybdate and vanadate combinations. Except for 40 mM Na_2MoO_4 plus 10 mM $NaVO_3$ combination of inhibitors, all other combinations had a greater increase in E_{pit} for the 24 hour exposures as compared to the 1 hour exposures of the AA2024-T3. For the 40 mM Na_2MoO_4 plus 10 mM $NaVO_3$ combination of inhibitors, the average E_{pit} value was approximately the same (Figure 115 and Figure 116). Both the 40 mM Na_2MoO_4 plus 10 mM $NaVO_3$ and 10 mM Na_2MoO_4 plus 40 mM $NaVO_3$ combination of inhibitors resulted in average E_{pit} values comparable to those at the 50th percentile for 50 mM $NaVO_3$ alone. The greatest increase in average E_{pit} was seen for the 50 mM Na_2MoO_4 inhibitor solution, which changed order from being the least inhibiting concentration to most inhibition concentration after the 24 hour in solution.

In summary, inhibitor combinations tested did not affect the i_{pass} value for high purity aluminum, but did affect E_{pit} and the passive potential range. For vanadate alone, longer exposure times to

inhibitor concentrations or high inhibitor concentration for short exposure times resulted in an overall increase in resistance to pit formation and stabilization. Decreasing the ratio of $Ce(C_2H_3O_2)_3$ 2 hour pretreatment concentration to the $NaVO_3$ concentration in solution led to increased E_{pit}. This will be discussed further, but cerium precipitates appears to block vanadate adsorption. The larger passive potential ranges were obtained with the short open circuit exposure time of 1 hour. Increasing the ratio of $NaVO_3$ concentration in solution to the $Ce(C_2H_3O_2)_3$ 2 hour pretreatment concentration increased E_{pit} similarly to that observed for increasing vanadate concentration in 50 mM NaCl. As the open circuit exposure was increased from 1 to 24 hours, E_{pit} and the passive potential range increased for the molybdate-vanadate inhibitor mixtures.

Cumulative probability plots of E_{pit} for AA2024-T3 specimens after one hour exposures in vanadate containing solutions showed that the median E_{pit} was greater than that in the absence of $NaVO_3$ but did not increase monotonically with inhibitor concentration. The improvement in E_{pit} is statistically significant but the trend indicates that the upper population (75th percentile) of specimens showed significantly improved performance and the worst preforming AA2024-T3 specimens (below 20th percentile) showed only marginally improvement over those tested in the absence of the $NaVO_3$ inhibitor (Figure 117). The greatest increase in E_{pit} was obtained, not at the higher concentrations of $NaVO_3$, but at 5 mM $NaVO_3$.

All inhibitor combinations increased the average E_{pit} value for AA2024-T3 above the average E_{pit} value for AA2024–T3 exposed to 50 mM NaCl for 1 hour prior to the anodic scan (Figure 117). Also, all of the specimens subjected to the 2 hour cerium acetate pretreatment followed by testing in sodium vanadate and 50 mM sodium chloride had lower average E_{pit} values than the 50th percentile specimens tested in 50 mM $NaVO_3$ + 50 mM NaCl. Specimens given the 50 mM $Ce(C_2H_3O_2)_3$ pretreatment had a lower average E_{pit} value than the 50th percentile E_{pit} values for specimens tested at various concentration of sodium vanadate + 50 mM sodium chloride solutions. The increase in E_{pit} for specimens subjected to the cerium acetate and sodium vanadate combinations correlated with a decreasing cerium acetate pretreatment concentration and an increasing sodium vanadate concentration.

For the molybdate vanadate inhibitor mixtures, only one combination, 10 mM Na_2MoO_4 + 40 mM $NaVO_3$ + 50 mM NaCl, had an E_{pit} value higher than the 50th percentile value for 50 mM $NaVO_3$ + 50 mM NaCl. 40 mM Na_2MoO_4 + 10 mM $NaVO_3$ + 50 mM NaCl had an E_{pit} value that was equivalent to the 50th percentile value for 50 mM $NaVO_3$ + 50 mM NaCl. The E_{pit} values for both the 50 mM Na_2MoO_4 and 25 mM Na_2MoO_4 + 25 mM $NaVO_3$ were 100 mV below the average E_{pit} for 50 mM $NaVO_3$. The two vanadate mixtures had limited efficacy at increasing the average E_{pit} above the 50th percentile value for 50 mM $NaVO_3$ + 50 mM NaCl.

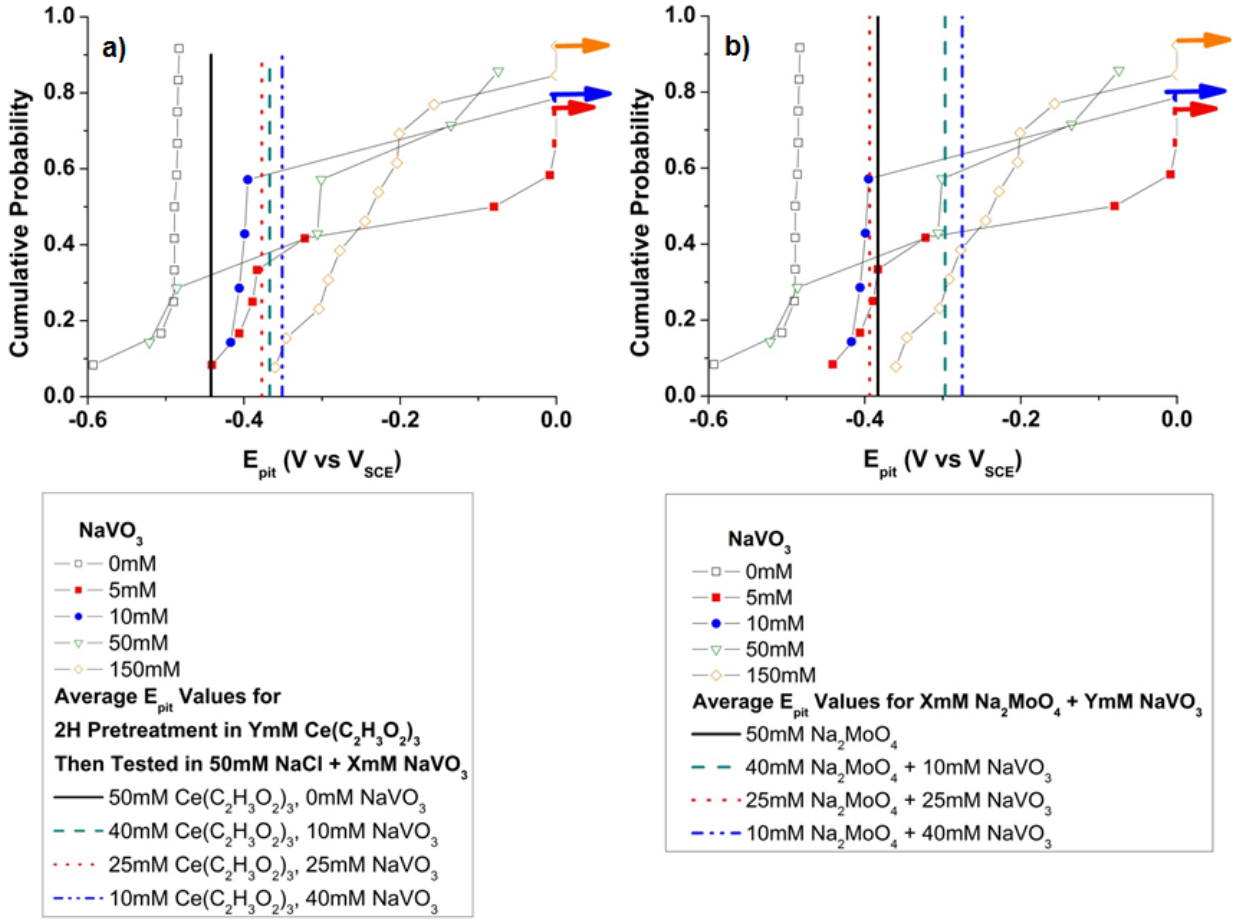

Figure 117. Cumulative probability plot for AA2024-T3 after 1 hour in aerated 50 mM NaCl solution plus various concentrations of $NaVO_3$. Average E_{pit} values of AA2024-T3 after 1 hour in aerated 50 mM NaCl solution plus various 50 mM inhibitor mixtures; a) a $Ce(C_2H_3O_2)_3$ 2 hour pretreatment then tested with the remainder of the inhibitor concentration as $NaVO_3$ dissolved in the test solution; b) $NaVO_3$ and Na_2MoO_4 mixtures dissolved into the test solution. Data points indicate cumulative probability of pitting before potential reversal. Arrows indicate specimens that did not pit at the potential indicated.

Fifty percent of the AA2024-T3 specimens in 50 and 150 mM $NaVO_3$ plus 50 mM NaCl solutions did not reach E_{pit} as determined by a current density of 10^{-4} A/cm^2 during the upward polarization scan, which was reversed at 0 V_{SCE}. This was unlike the1 hour anodic E–log(i) polarization behavior for which 5 mM $NaVO_3$ plus 50 mM NaCl solution showed the largest increase in E_{pit}. As in the case of the 1 hour open circuit exposures, the increase in E_{pit} was not monotonic with inhibitor concentration after 24 hour open circuit exposures. Similar E_{pit} relationships were observed after both 1 hour and 24 hour exposure at low inhibitor concentration. The 5 mM $NaVO_3$ solution exhibited a higher average E_{pit} as compared to the 10 mM $NaVO_3$ solution, as shown in Figure 117 and Figure 118. Figure 118 presents E_{pit} cumulative probability plot for AA2024-T3 exposed for 24 hours to 50 mM NaCl solution plus various concentrations of $NaVO_3$. E_{pit} for all specimens exposed to $NaVO_3$ concentrations plus 50 mM NaCl solutions were increased above that for specimens exposed to uninhibited 50 mM

NaCl. As shown in Figure 118, after 24 hours at open circuit, E_{pit} for specimens exposed to low and high inhibitor concentrations diverged. AA2024-T3 specimens exposed to 50 or 150 mM $NaVO_3$ plus 50 mM NaCl solutions have a higher E_{pit} range than the specimens exposed to 5 or 10 mM $NaVO_3$ plus 50 mM NaCl solutions. Such a strong relationship between inhibitor concentration and E_{pit} was not observed after the 1 hour exposures.

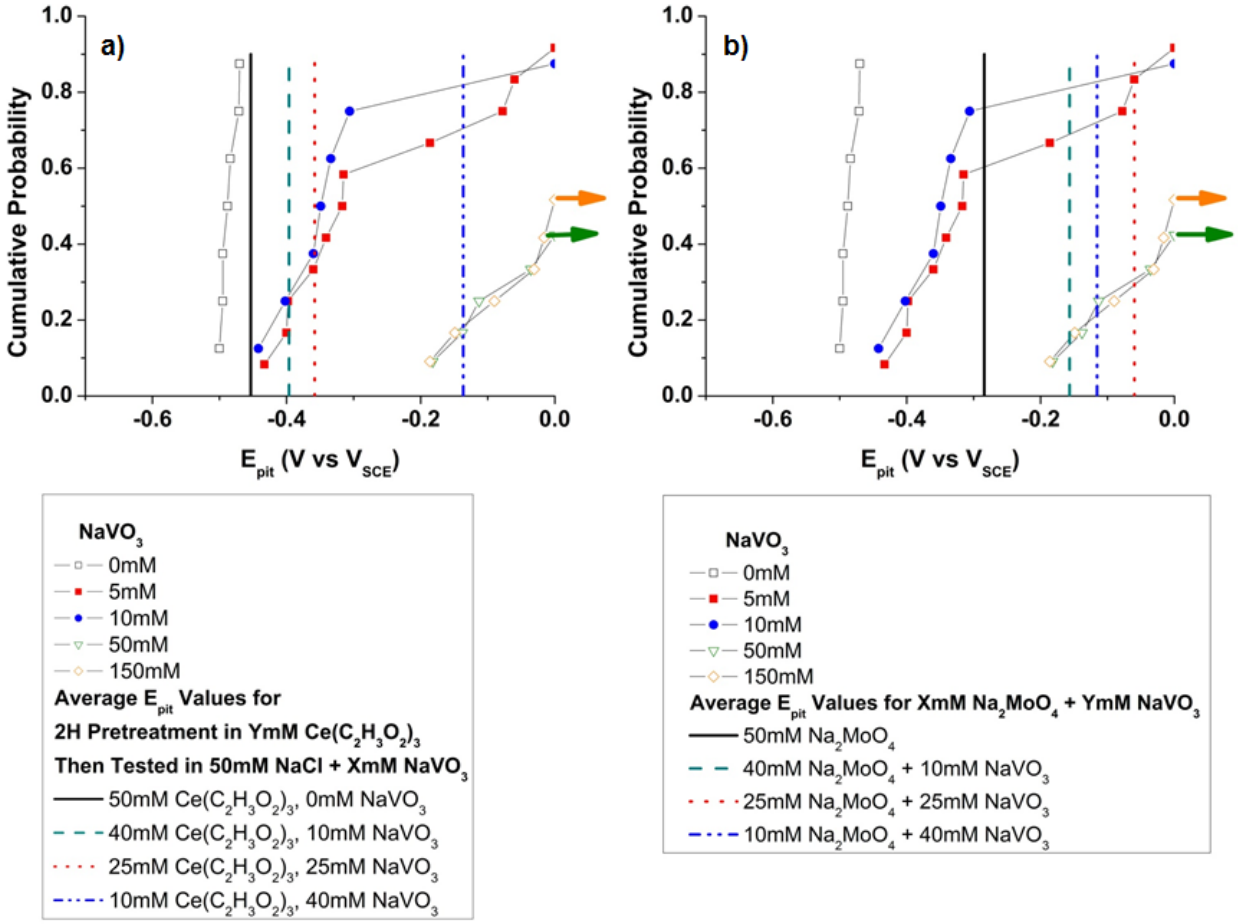

Figure 118. Cumulative probability plot for AA2024-T3 after 24 hours in aerated 50 mM NaCl solution plus various concentrations of $NaVO_3$. Average E_{pit} values of AA2024-T3 after 1 hour in aerated 50 mM NaCl solution plus various 50 mM inhibitor mixtures; a) a $Ce(C_2H_3O_2)_3$ 2 hour pretreatment then tested with the remainder of the inhibitor concentration as $NaVO_3$ dissolved in the test solution; b) $NaVO_3$ and Na_2MoO_4 mixtures dissolved into the test solution. Data points indicate cumulative probability of pitting before potential reversal. Arrows indicate specimens that did not pit at the potential indicated.

The AA2024-T3 E_{pit} values for all of the vanadate inhibitor combinations were lower than that for 50 mM $NaVO_3$. As with the 1 hour exposures, the cerium acetate pretreated specimens showed average E_{pit} that increased with increasing $NaVO_3$ concentration and decreasing $Ce(C_2H_3O_2)_3$ 2 hour pretreatment concentration. 50 mM cerium acetate 2 hour pretreatment specimens had an average E_{pit} value barely above that of the 50 mM NaCl tested specimens. Specimens subjected to the 10 mM $Ce(C_2H_3O_2)_3$ 2 hour pretreatment followed by testing in

40 mM $NaVO_3$ + 50 mM NaCl displayed the greatest increased E_{pit} for all the cerium vanadate combinations.

All specimens exposed to the various molybdate-vanadate combinations had E_{pit} values at least 100 mV above that of specimens given the 50 mM cerium acetate 2 hour pretreatment. The specimens exposed to the molybdate-vanadate combinations had E_{pit} values between those of the 50 mM Na_2MoO_4 and 50 mM $NaVO_3$ single inhibitor specimens. Unlike the cerium acetate pretreated specimens, the molybdate-vanadate combination specimens did not have an E_{pit} value that increased with increased vanadate concentration. The specimens tested in 25 mM Na_2MoO_4 + 25 mM $NaVO_3$ + 50 mM NaCl solution had the highest E_{pit} value among the different molybdate-vanadate combinations.

Effect of Vanadate Inhibitor Combinations on Reducing the Oxygen Reduction and Hydrogen Evolution Reactions

AA2024-T4 contains copper rich intermetallic particles, which can support ORR, in an aluminum matrix. The effect of inhibitor combinations on the ORR on copper was evaluated for comparison. For the high purity copper specimens, the addition of $NaVO_3$ decreased the current density during ORR (Figure 119). In the ORR dominant regime (below -0.2 V_{SCE}), Cu tested in vanadate containing solutions had a lower cathodic density than Cu subjected to cerium acetate pretreatments and tested in vanadate containing solutions. For instance, the greatest reduction in ORR cathodic current density for the cerium acetate 2 hour pretreated specimens, was one magnitude order as compared to the uninhibited 50 mM NaCl solutions. In contrast, there was a 3-order of magnitude decrease in ORR dominated cathodic current density for the specimens tested in vanadate containing solutions. Copper pretreated in 40 mM $Ce(C_2H_3O_2)_3$ for 2 hours and tested in 10 mM $NaVO_3$ plus 50 mM NaCl had two orders of magnitude larger cathodic current density in the ORR dominated current range than copper tested in 10 mM $NaVO_3$ plus 50 mM NaCl solutions. Therefore, in the ORR dominant regime, vanadate by itself was a better cathodic inhibitor than the combination inhibition of pretreatment with cerium acetate and testing in vanadate containing solutions. At large over potentials, where HER became the dominant cathodic reaction, specimens, whether pretreated or not pretreated and evaluated in solution containing or not containing vanadate showed similar behavior.

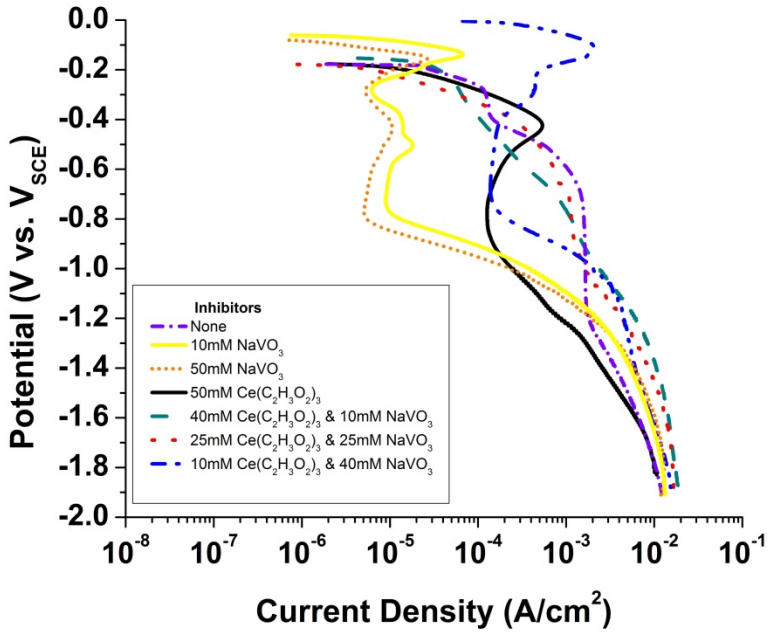

Figure 119. Cathodic E–log(i) polarization behavior for high purity Cu in aerated 50 mM NaCl solution with various concentrations of vanadate after a 2 hour cerium acetate pretreatment. An electrode rotation speed of 2500 rpm was used. A 1 hour open circuit in the test solution occurred prior to cathodic polarization. Data was not corrected for ohmic resistance.

As shown in Figure 120, the 50 mM molybdate-vanadate inhibitor combinations were as effective at reducing the ORR dominated cathodic current as vanadate only inhibitor of equal or lower concentration. All specimens exposed to vanadate and vanadate-molybdate inhibitor combination solutions had two orders of magnitude lower ORR cathodic current density compared to the uninhibited Cu specimen tested in 50 mM NaCl solution. The Cu specimen exposed to 50 mM Na_2MoO_4 plus 50 mM NaCl had the same magnitude cathodic current density as the specimen exposed to 50 mM NaCl only solutions. As all specimens exposed to 50 mM vanadate-molybdate combinations had cathodic current densities similar to specimens exposed to 50 mM $NaVO_3$ plus 50 mM NaCl and 10 mM $NaVO_3$ plus 50 mM NaCl, molybdate does not appear to be an effective inhibitor to ORR dominated cathodic current density after an 1 hour exposure.

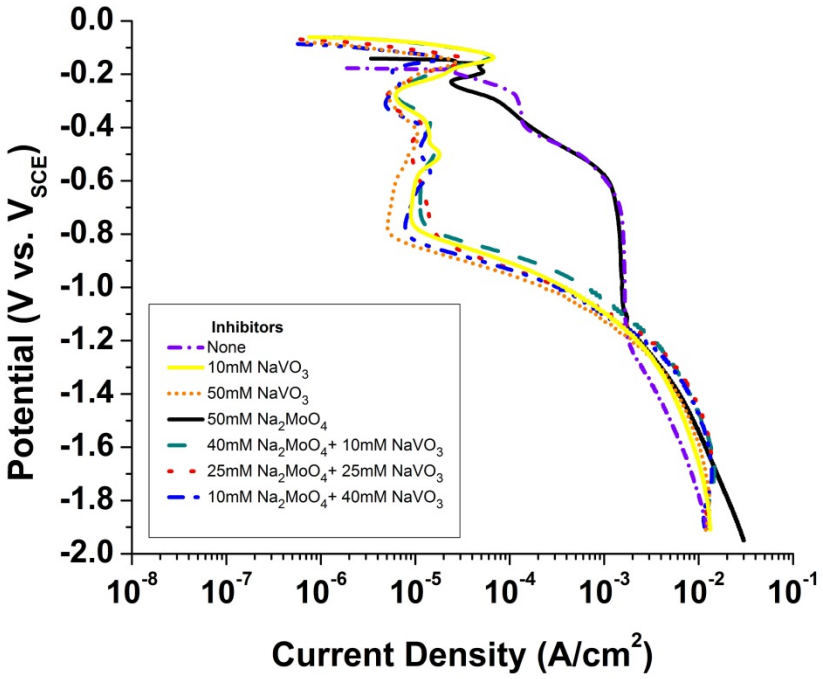

Figure 120. Cathodic E–log(i) polarization behavior for high purity Cu in aerated 50 mM NaCl solution with various concentrations of vanadate and molybdate. An electrode rotation speed of 2500 rpm was used. A 1 hour open circuit in the test solution occurred prior to cathodic polarization. Data was not corrected for ohmic resistance.

AA2024–T4 displayed current densities that were strongly affected by vanadate inhibitors. As for the copper specimens, the 50 mM cerium acetate 2 hour pretreated specimens had a cathodic current density of the same magnitude as the uninhibited AA2024–T4 specimen (Figure 121). All specimens, with or without a cerium acetate pretreatment and tested in vanadate containing solutions, had cathodic current densities of the same order of magnitude, which was three orders of magnitude less than that for uninhibited AA2024–T4 specimens. Two of the 50 mM cerium-vanadate inhibitor combination specimens [10 mM $Ce(C_2H_3O_2)_3$ pretreatment then tested in 40 mM $NaVO_3$ plus 50 mM NaCl and 25 mM $Ce(C_2H_3O_2)_3$ pretreatment then tested in 25 mM $NaVO_3$ plus 50 mM NaCl] had a slightly lower current density than the specimen tested in 50 mM $NaVO_3$ plus 50 mM NaCl.

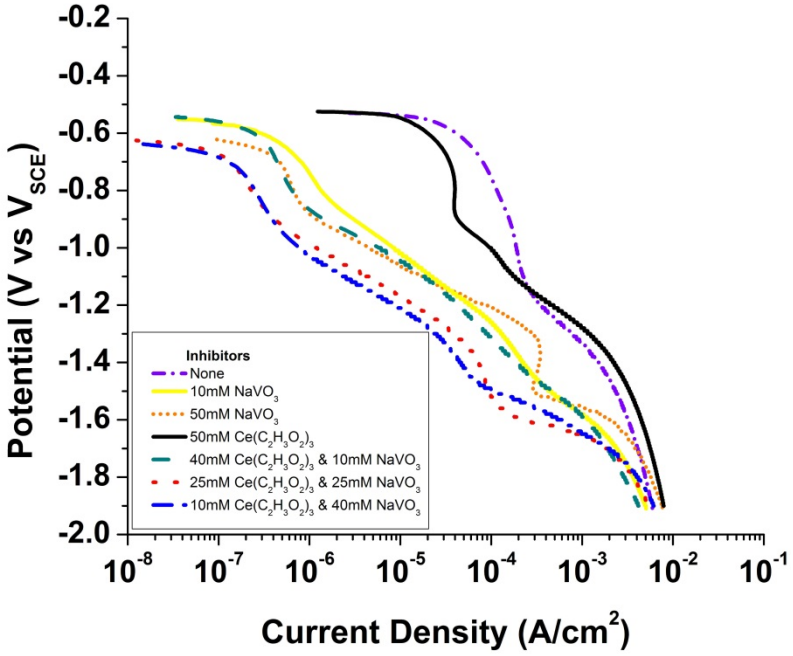

Figure 121. Cathodic E–log(i) polarization behavior for AA2024–T4 in aerated 50 mM NaCl solution with various concentrations of vanadate and a 2 hour cerium acetate pretreatment. An electrode rotation speed of 2500 rpm was used. A 1 hour open circuit in the test solution occurred prior to cathodic polarization. Data was not corrected for ohmic resistance.

There was a strong correlation between the molybdate-vanadate concentration in 50 mM NaCl solutions and the cathodic current density for AA2024–T4 specimens (Figure 122). All specimens exposed to molybdate-vanadate combinations had ORR cathodic current densities lower than those for specimens exposed to 50 mM (vanadate or molybdate) plus 50 mM NaCl solutions. The specimens exposed to 50 mM Na_2MoO_4 plus 50 mM NaCl had the highest cathodic current densities of all the inhibitor solutions tested. While AA202–T4 specimens exposed to molybdate-vanadate combinations inhibitors had a lower current density than 50 mM $NaVO_3$ specimens, the specimens' current densities more closely followed the vanadate cathodic current density trend rather than the much higher current density of the 50 mM Na_2MoO_4 exposed specimens. Molybdate, without vanadate additions, was an inferior inhibitor of the ORR dominated cathodic current for AA2024–T4 specimens.

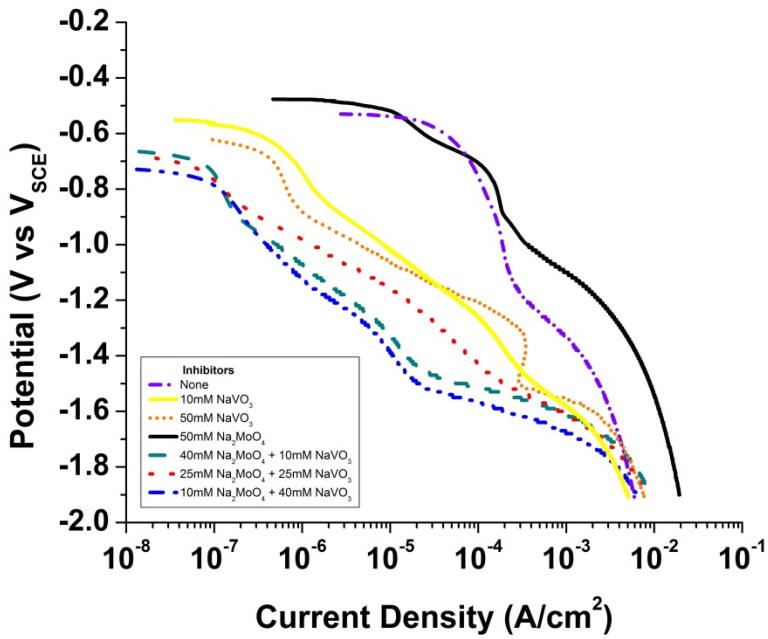

Figure 122. Cathodic E–log(i) polarization behavior for AA2024–T4 in aerated 50 mM NaCl solution with various concentrations of vanadate and a 2 hour cerium acetate pretreatment. An electrode rotation speed of 2500 rpm was used. A 1 hour open circuit in the test solution occurred prior to cathodic polarization. Data was not corrected for ohmic resistance.

In general, for both AA2024–T4 and Cu, no effect of the inhibitor combinations was observed at very negative potentials where proton reduction occurs at a similar or higher rate as the ORR. For AA2024–T4 in 50 mM NaCl solution, high rotation rates and the resulting reduced oxygen diffusion pathway led to greater current densities in the oxygen reduction region. However, only a small portion of the cathodic scan occurred before the onset of HER. The magnitude of ORR current, even below the HER start voltage, was sufficient to allow for the calculation of Koutecky–Levich and Levich plots for Cu and AA2024–T4.

The Koutecky-Levich plot, shown in Figure 123, presents the data for Cu in aerated 50 mM NaCl plus various combinations of 50 mM inhibitors at a potential of -0.8 V_{SCE}, a potential in the ORR region. The smallest cathodic current densities occurred on the Cu specimen exposed to 50 mM $NaVO_3$ plus 50 mM NaCl solution. Copper exposed to all other inhibitor combinations exhibited an order of magnitude higher current density values. The cerium acetate pretreatment-vanadate combinations [Figure 123 (a)] and the molybdate-vanadate combinations [Figure 123 (b)] were equally effective at reducing the cathodic current densities on the Cu specimens. Cu specimens exposed to the 50 mM cerium acetate pretreatment followed by testing in 50 mM NaCl solution and Cu specimens exposed to the 50 mM molybdate plus 50 mM sodium chloride solution exhibited cathodic current densities similar to the Cu specimen in the uninhibited solution.

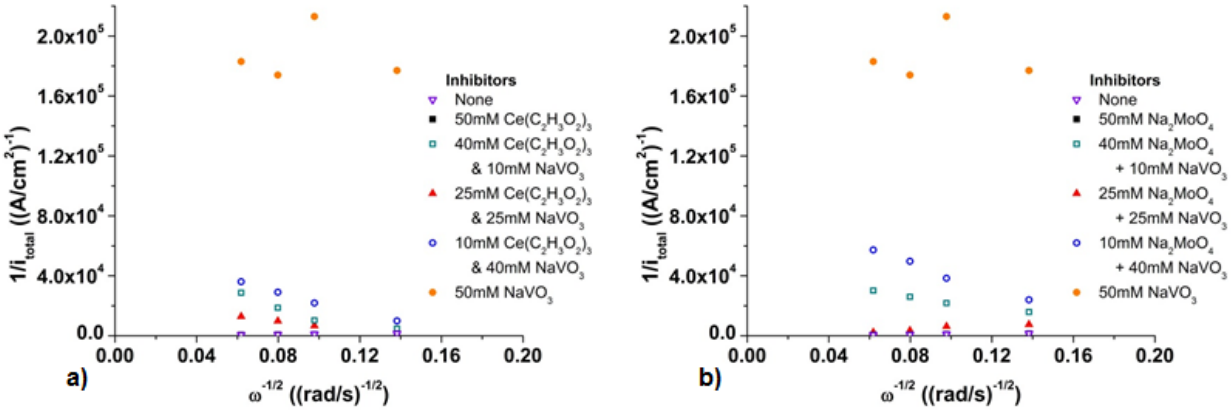

Figure 123. Koutecky–Levich plot for Cu in aerated 50 mM NaCl plus various 50 mM inhibitor combinations at a potential of -0.8 V_{SCE} after a 1 hour open circuit. a) Cu specimens were pretreated for 2 hours in various $Ce(C_2O_3H_2)_3$ followed by testing in various $NaVO_3$ plus 50 mM NaCl solutions. b) Cu specimens were tested in various 50 mM combinations of Na_2MoO_4/ $NaVO_3$ plus 50 mM NaCl. Data was not corrected for Ohmic resistance.

Figure 124 presents the Koutecky-Levich plot for AA2024–T4 in aerated 50 mM NaCl solutions with various binary 50 mM vanadate inhibitor combinations at the potentials of -0.8 V_{SCE} (ORR dominant region). AA2024–T4 specimens tested in the presence of the binary inhibitor combinations exhibited lower current densities as compared to specimens tested in 50 mM molybdate, vanadate or exposed to the cerium acetate pretreatment. AA2024–T4 specimens exposed to 50 mM molybdate or cerium acetate pretreatment exhibited similar current densities as specimens exposed to the uninhibited sodium chloride solutions. The best reduction on ORR was obtained from the 2 hour 25 mM cerium acetate pretreatment followed by testing in 25 mM $NaVO_3$. Also, that inhibition combination reduced the effect of rotation rate on current density [Figure 124 (a)].

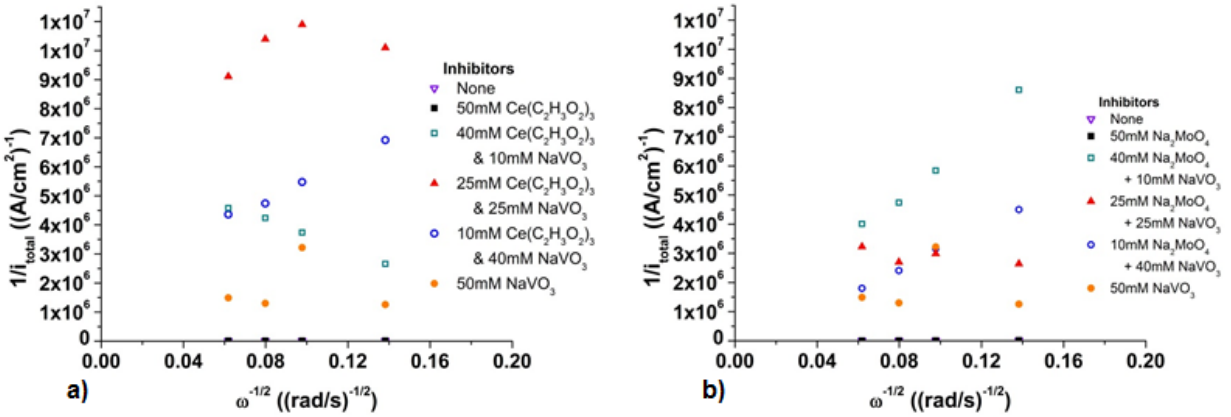

Figure 124. Koutecky–Levich plot for AA2024-T4 in aerated 50 mM NaCl plus various 50 mM inhibitor combinations at a potential of -0.8 V_{SCE} after a 1 hour open circuit. a) AA2024-T4 specimens were pretreated for 2 hours in various Cerium followed by testing in various $NaVO_3$ plus 50 mM NaCl solutions. b) AA2024-T4 specimens were tested in various 50 mM combinations of Na_2MoO_4/ $NaVO_3$ plus 50 mM NaCl. Data was not corrected for Ohmic resistance.

The usual Levich correlation between an increasing limiting current density for ORR and rotation rate was not obtained for Cu with vanadate in solution with 50 mM NaCl. Figure 125 (Koutecky-Levich plot shown in Figure 123) showing extracted i_{Lim} versus $\omega^{1/2}$ demonstrates the effect of $NaVO_3$ on ORR in the mass transport limited regime. All Cu specimens exposed to the two different 50 mM binary $NaVO_3$ containing solutions had an ORR cathodic current densities which deviate from ideal behavior in the ORR regime. In contrast, both the 50 mM $Ce(C_2H_3O_2)_3$ pretreatment and the 50 mM Na_2MoO_4 in solution inhibitor specimens had cathodic current densities which were similar to both the uninhibited Cu specimens and ideal Levich behavior at a normal oxygen concentration in water. Except for the specimen exposed to 25 mM Na_2MoO_4 plus 25 mM $NaVO_3$ inhibitor concentration, all the specimens exposed to binary inhibitor mixtures and the 50 mM $NaVO_3$ plus 50 mM NaCl solution exhibited ORR limiting current densities which were independent of rotation speed (i.e., oxygen diffusion path length).

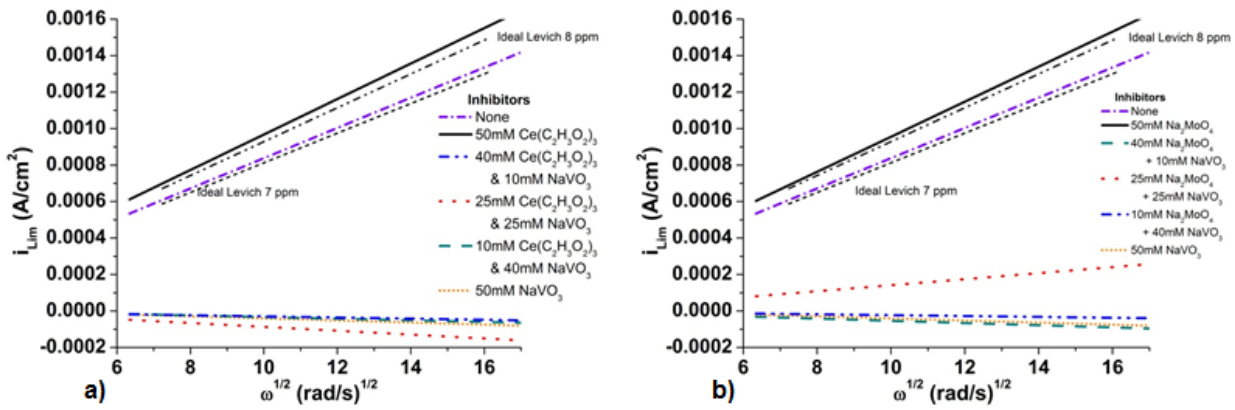

Figure 125. Levich plot (i_{Lim} extracted from i_{Total}) of Cu using data from the ORR region only (potential of -0.8 V_{SCE}) shows a loss of ideal mass transport controlled behavior. A 1 hour open circuit was used. Test preformed in aerated 50 mM NaCl plus $NaVO_3$ binary inhibitor combinations. a) Cu specimens were pretreated for 2 hours in various $Ce(C_2H_3O_2)_3$ followed by testing in various $NaVO_3$ plus 50 mM NaCl solutions. b) Cu specimens were tested in various 50 mM combinations of Na_2MoO_4/ $NaVO_3$ plus 50 mM NaCl. Data was not corrected for Ohmic resistance.

The ORR changed from ideal behavior on copper to non-ideal behavior on AA2024, as discussed by Jakab. Figure 126 (Koutecky-Levich plot shown in Figure 124) demonstrates the effect of the inhibitor mixtures on AA2024–T4. As shown in Figure 126 (extracted i_{Lim} versus $\omega^{1/2}$), all of the different binary combinations of $NaVO_3$ suppressed the ORR on AA2024–T4. Inhibitor combinations with $NaVO_3$ plus 50 mM NaCl further suppressed the ORR reaction on AA2024–T4. The suppression of the ORR with a 2 hour $Ce(C_2H_3O_2)_3$ pretreatment resulted in a similar ORR limiting current density as that for the uninhibited AA2024–T4 specimen [Figure 126 (a)]. Fifty mM Na_2MoO_4 was less effective at lowering the ORR limiting current density than the Na_2MoO_4 plus $NaVO_3$ inhibitor combinations; the AA2024–T4 limiting current density remained rotation rate dependent [Figure 126 (b)]. The effect of oxygen diffusion path length on the ORR limiting current density was eliminated only when $NaVO_3$ was in solution as the single inhibitor or as part of a binary mixture.

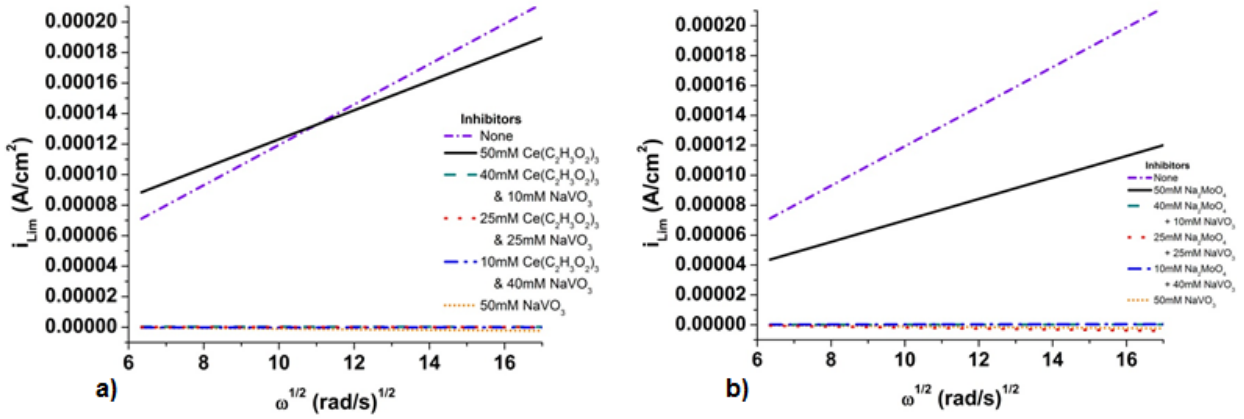

Figure 126. Levich plot (i_{Lim} extracted from i_{Total}) of AA2024-T4 using data from the ORR region only (potential of -0.8 V_{SCE}) shows a loss of ideal mass transport controlled behavior. A 1 hour open circuit was used. Test preformed in aerated 50 mM NaCl plus $NaVO_3$ binary inhibitor combinations. a) AA2024-T4 specimens were pretreated for 2 hours in various $Ce(C_2H_3O_2)_3$ followed by testing in various $NaVO_3$ plus 50 mM NaCl solutions. b) AA2024-T4 specimens were tested in various 50 mM combinations of Na_2MoO_4/ $NaVO_3$ plus 50 mM NaCl. Data was not corrected for Ohmic resistance.

Effect of Molybdate on Repassivation of AA2024

The Inhibition of Pitting Potential

The selected potentials for scratch repassivation tests are referenced against potentiodynamic scans showing the inhibitor effect on oxide stability in Figure 127. Molybdate and chromate were chosen for this study because they have stabilizing effects on barrier oxides.

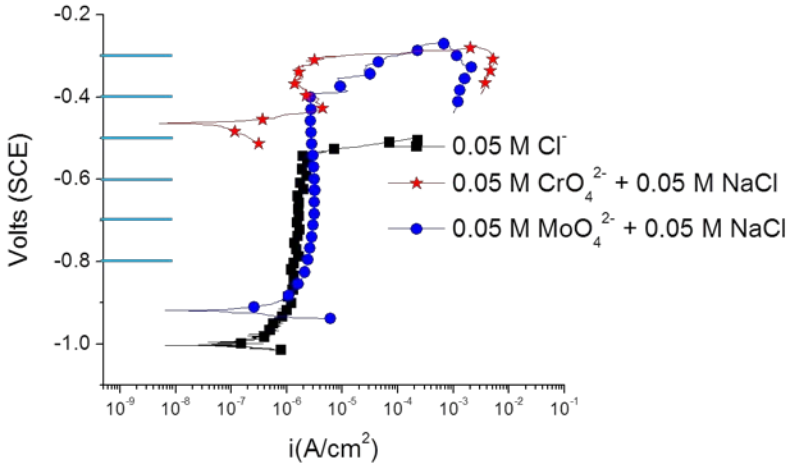

Figure 127. Anodic inhibitors of interest for EFCP inhibition. Potentiodynamic scan of AA2024-T351 in molybdate and chromate containing 0.05 M NaCl solution. Lines to the left of polarization curves indicate scratch potentials investigated ranging from -0.8 V to -0.3 V vs. SCE.

The Inhibitor Buffer Capacity

The buffering capacity of several molybdate concentration are shown in Figure 128.[141] At high concentrations of molybdate the buffer capacity below pH 6 is large. Chromate buffer capacity is unknown. It is hypothesized to be similar to molybdate due to the existence of protonated anions.[73] The limited buffer capacity of the chloride solution is hypothesized to be the result of carbonate.

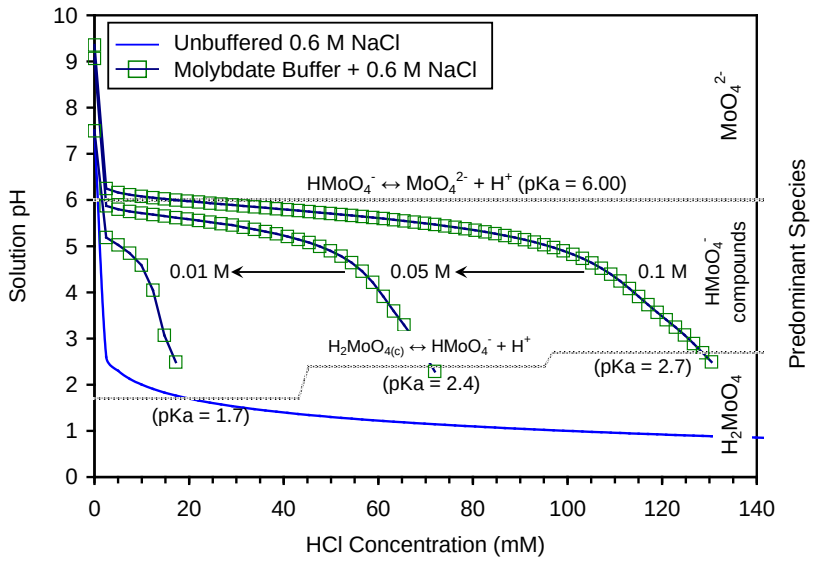

Figure 128. Molybdate buffer capacity.[141] Initial pH was 9.3 for 0.1 M MoO_4^{2-} solutions. Solution pH from titration of (0.01 M, 0.05 M, and 0.1 M) sodium molybdate + 0.6 M NaCl with 0.25 mL of 1 M HCl reported as HCl concentration in mM. Molybdate concentration varied from 0.1 to 0.01 M and results are compared against uninhibited 0.6 M NaCl. Molybdate chemical reactions are shown with relevant predominant species in the measured pH range.

The Inhibition of Net Current Density During Scratch Repassivation

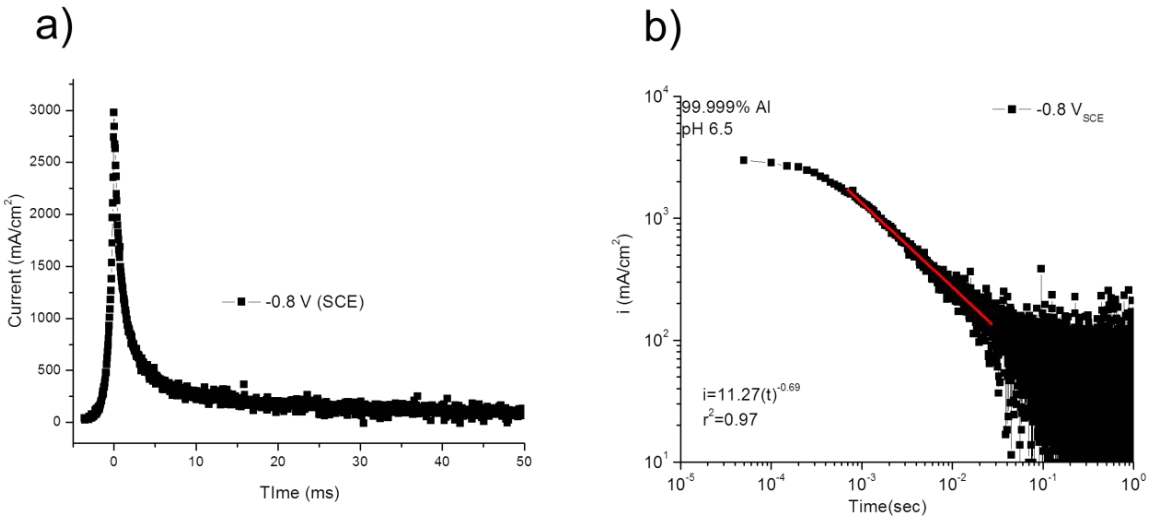

Figure 129 shows a typical repassivation event conducted on 99.999% pure aluminum. The repassivation shows a plateau at early times before the first millisecond. After this an expression for the current decay takes the form of Equation 25 where i is current density, i_o is peak bare surface current density, t is time elapsed for $t > t_o$ or $t = t_o$ for $t < t_o$.[113] Both t_o and m are constants.

$$i = i_o \left(\frac{t}{t_o}\right)^{-m} \qquad \textbf{Equation 25}$$

This decay expression is fit between 1 ms and 50 ms, after which the current decays into a region of lower precision due to the high current scale of the potentiostat and the 2% of range limitation on accuracy. Figure 130 shows the potential corrected for ohmic drop at the working electrode relative to the reversible hydrogen potential (SCE scale) at pH 3, 6, and 10.

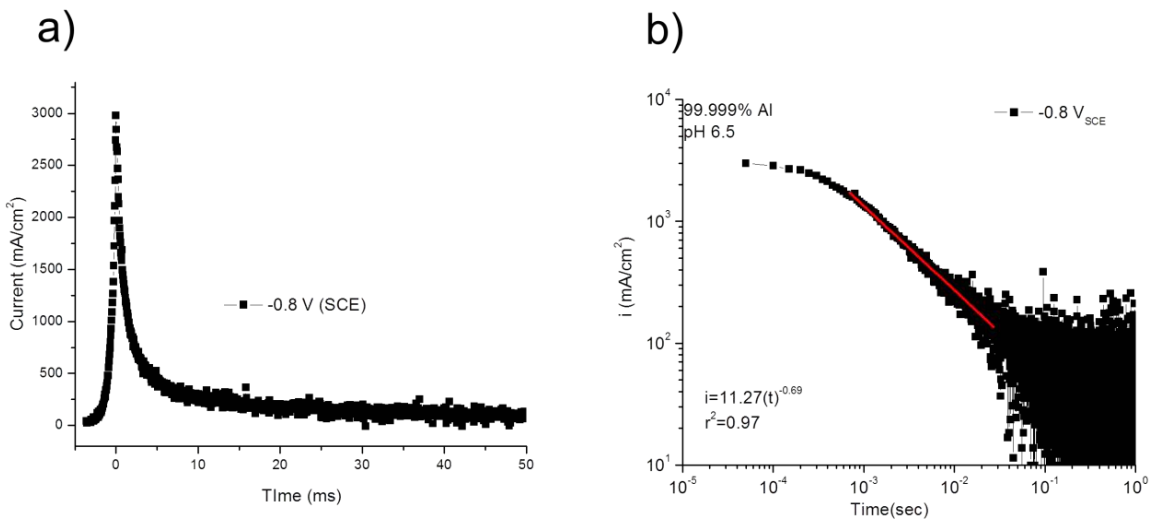

Figure 129. Scratch of 99.999% Al in 1 M NaCl at pH 6.5 potentiostatically held at -0.8 V SCE.

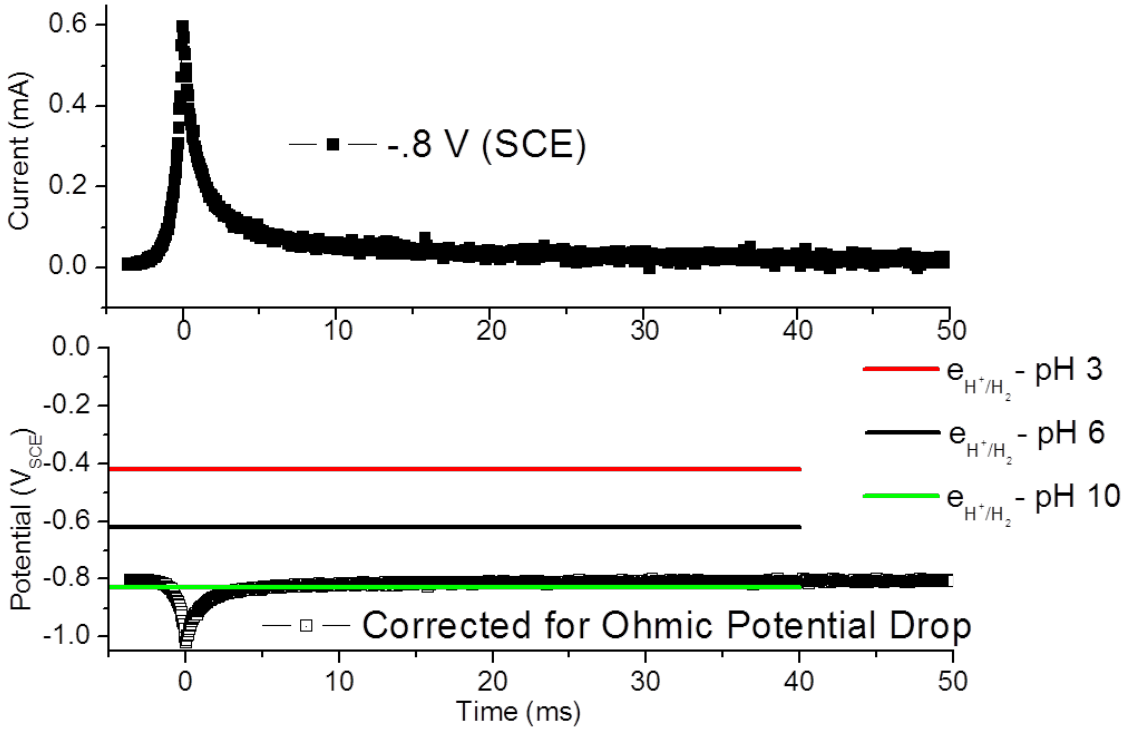

Figure 130. Scratch of 99.999% Al in 1 M NaCl at pH 6.5 potentiostatically held at -0.8 V SCE. The ohmic potential drop at the working electrode is 0.2 V increasing the hydrogen over-potential.

Figure 131 shows repassivation transients for 99.999% aluminum in 1 M, 0.5 M, and 0.05 M NaCl solution, indicating the effect of chloride concentration and potential on repassivation. In Figure 131(a), increased potential leads to onset of depassivated anodic behavior. The time of onset and the current density of the post-transient behavior are affected by the applied potential. As the chloride level decreases the depassivated anodic behavior is suppressed revealing repassivation transients of the form expressed by Equation 25.

Table 29 lists the fitting parameters for the scratch transients in Figure 131(d). General features in addition to the behavior described by Equation 25 include sustained depassivation at a threshold current density.

Table 29. Fitting parameters for 99.999% aluminum at -0.8 VSCE.

99.999% Al at -.8 V_{SCE}	1 M Cl^-	0.5 M Cl^-	0.05 M Cl^-
m	0.69	0.67	0.51

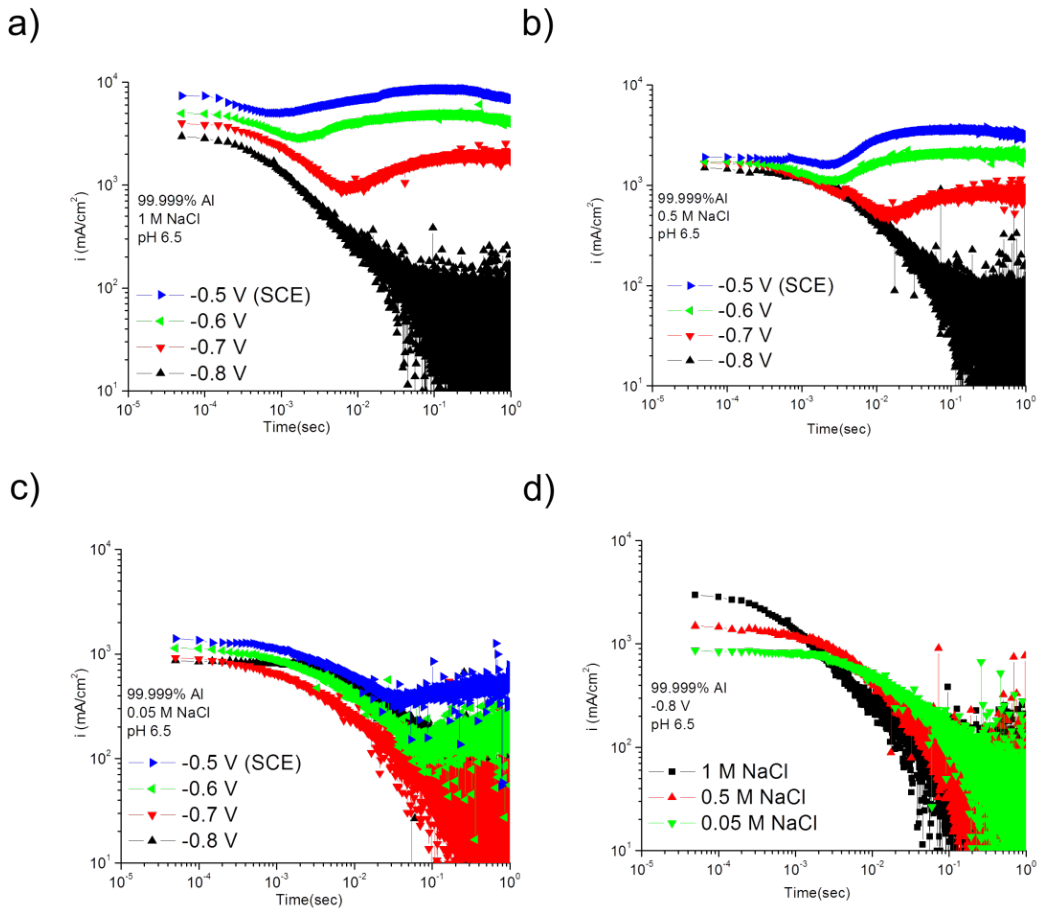

Figure 131. Current transients from 99.999% aluminum scratched electrodes. Potentials from -0.5 to -0.8 V vs. SCE are shown at three chloride concentrations from 0.05 to 1 M. The pH for all tests was 6.5.

Chloride concentration clearly has an effect on the onset of depassivated behavior. It also appears to have an effect on the maximum peak current at short times after the scratch. Figure 132 relates the maximum current density observed for each chloride-potential combination in relation to the theoretical ohmically limited current density for each solution, calculated using Equations 26 and 27.[113]

$$R_s = \left(\frac{1}{2\pi\kappa b}\right) ln\left(\frac{4b}{a}\right)$$ **Equation 26**

Where R_s is the solution resistance (Ω), κ is the solution conductivity (Ω-cm), a is one half of the bared areas width (cm), and b is one half of the bared areas length (cm). The ohmic current density was calculated.

$$i_{ohmic} = \frac{E_{app} - E_{bare\ OCP}}{(R_s)(Area)}$$ **Equation 27**

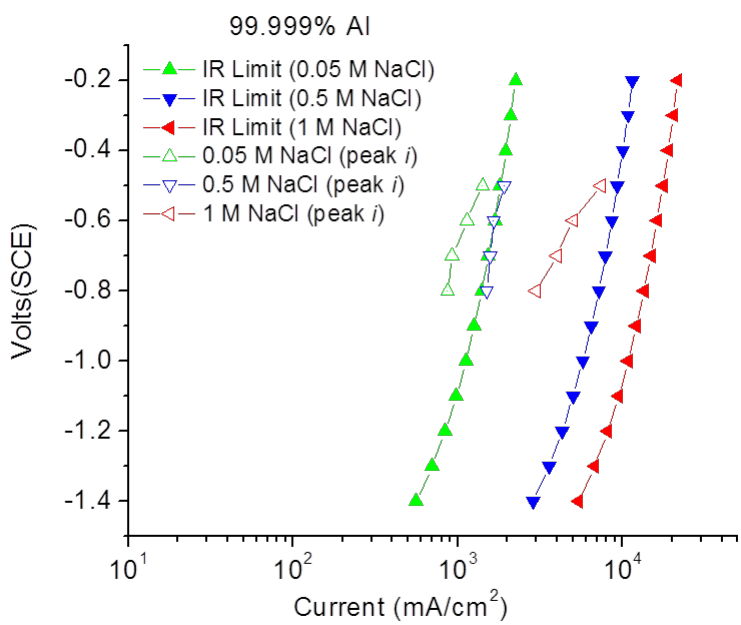

Figure 132. Calculated IR limit as compared to peak net current density of scratched 99.999% aluminum electrodes in various chloride concentrations at time zero after scratch.

In Equation 27, i is the theoretical ohmically limited current density, E_{app} is the applied potential, and $E_{bare,OCP}$ is OCP of the bare metal taken to be -1.8 V_{SCE}. The data suggests that at all chloride concentrations the peak current density is approaching the theoretical ohmically limited current density as seen in Figure 132. This would suggest that at very short times the ohmic influence on the current density might be substantial.

Figure 133 shows the scratched electrode current density transients for both AA2024-T351 and AA7075-T6 at two chloride levels and over multiple potentials. There are two important observations to be made in how these alloys differ from one another and from highly pure

aluminum. The first is that the peak current densities have some scatter which may result from the disruption of intermetallic compound particles during mechanical scratching. The second is that AA2024-T351 shows an onset of sustained depassivated current densities at higher potentials than AA7075-T6. This may result from the higher copper content in the alloy. A higher level of soluble copper in solid solution in the aluminum matrix has been shown to have an effect on E_{pit} and it is reasonable to believe the effect may also be seen in repassivation behavior in scratched electrode experiments.[142,143] AA7075 is richer in magnesium and zinc then AA2024 which may contribute to the observed onset of high depassivated current densities.

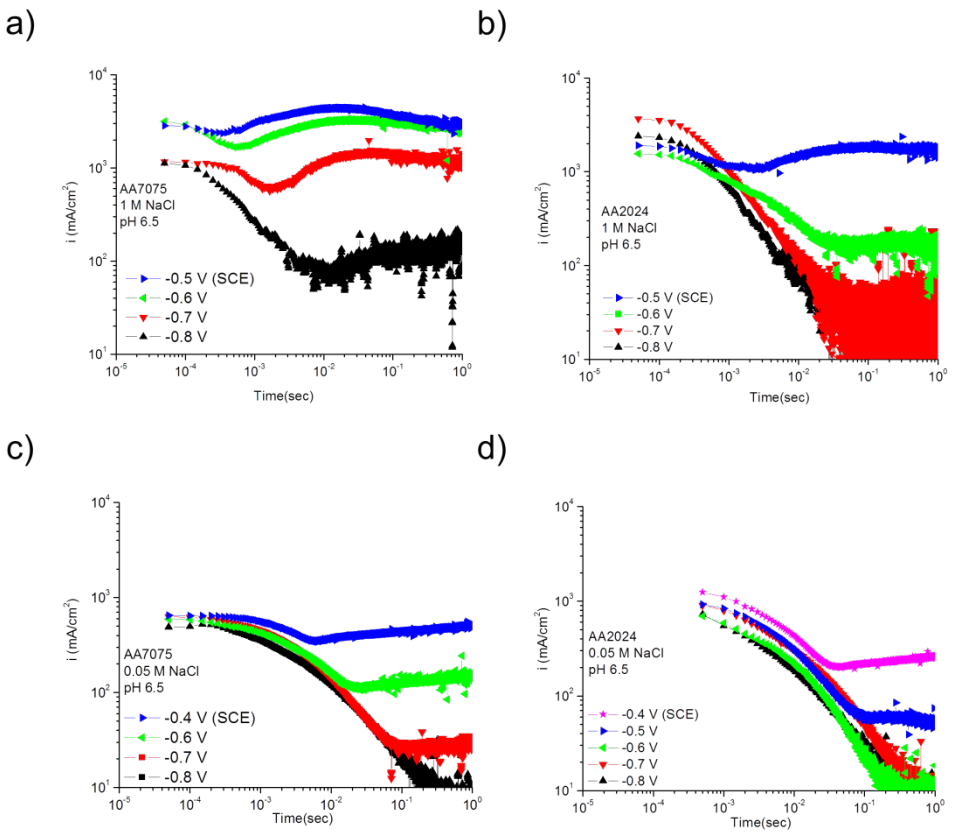

Figure 133. Net current transients from AA7075 (a) and AA2024 (b) in aqueous 1 M NaCl with pH adjusted to 6.5 with NaOH. Scratch potentials vary from -0.5 to -0.8 V vs. SCE. Current transients from AA7075 (c) and AA2024 (d) in aqueous 1 M NaCl with pH adjusted to 6.5. Scratch potentials vary from -0.5 to -0.8 V vs. SCE for (c) and -0.4 to -0.8 V vs. SCE for (d).

Figure 134 shows the effects of 0.1 M chromate and 0.1 M molybdate on the repassivation behavior of AA7075-T6 in aqueous 0.05 M NaCl solution with pH 6.5. A relatively low concentration of chloride and a large concentration of molybdate in a neutral solution result in no inhibition of either peak current density or depassivated anodic behavior onset. However, the onset of depassivated current behavior is increased from -0.7 V to -0.4 V_{SCE} when chromate is used. Even at -0.4 V the current density at 1 second is less than the uninhibited solution at -0.6 V_{SCE}. Peak current densities are summarized in Figure 134(b). Chromate and molybdate both raise the theoretical ohmic limit due to increased conductivity of the solutions. Figure 135

shows integration of the current density over several time periods for all investigated potentials. Chromate shows inhibition of net anodic charge passed over all integration periods while molybdate shows no inhibition of net anodic charge after scratching of AA7075.

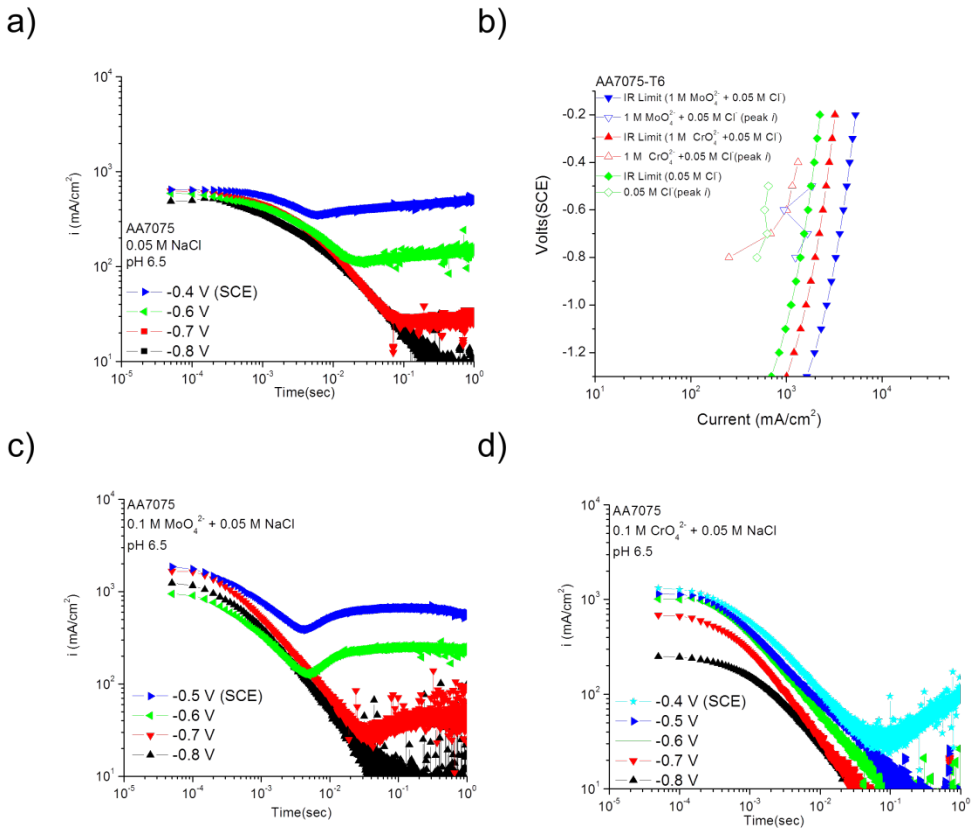

Figure 134. (a) Scratched electrode net anodic current densities for AA7075-T6 in 0.05 M NaCl solution with pH 6.5. (b) Calculated IR limit as compared to peak current density of scratched AA7075 electrodes at time zero after scratch. IR limit is calculated for an aqueous 0.05 M NaCl solution, a 0.1 M CrO_4^{2-} and 0.05 M NaCl solution, and 0.1 M MoO_4^{2-} and 0.05 M NaCl solution. (c) and (d) show scratched electrode current transients for AA7075-T6 with 0.1 M MoO_4^{2-} and 0.1 M CrO_4^{2-} additions, respectfully.

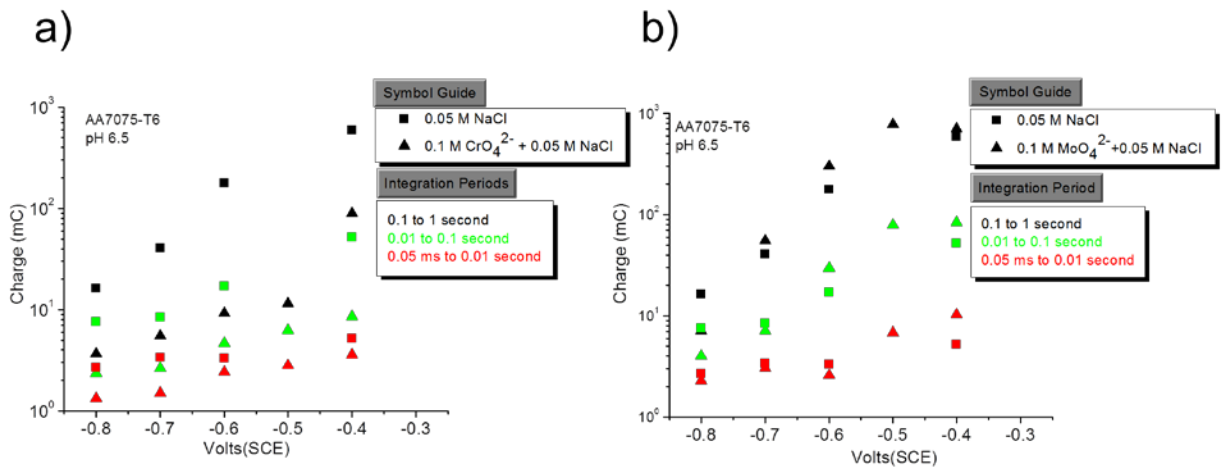

Figure 135. (a) Scratched electrode charge passed for AA7075-T6 in 0.05 M NaCl solution with a pH of 6.5 and 0.1 M CrO_4^{2-} and 0.05 M NaCl solution. (b) Scratched electrode charge passed for AA2024-T351 in 0.05 M NaCl solution with a pH of 6.5 and 0.1 M Na_2MoO_4 and 0.05 M NaCl solution. Integration of current over three periods from 0.05 milliseconds to 0.01 second, 0.01 to 0.1 second, and 0.1 to 1 second.

Figure 136 shows the effects of 0.1 M molybdate and 0.1 M chromate additions to aqueous 0.05 M NaCl, with a pH 6.5, on AA2024-T351. No inhibition of either peak current density or depassivated anodic behavior onset is observed for molybdate additions. Chromate inhibits the onset of depassivated current behavior, increasing onset from -0.7 V to -0.2 V_{SCE}. Peak current densities are summarized in Figure 136(b). Chromate and molybdate both raise the theoretical ohmic limit due to increased conductivity of the solutions. Figure 137 shows integration of the current density over several time periods for all investigated potentials. Chromate shows inhibition in charge passed over all integration periods while molybdate shows no inhibition of charge passed for AA2024-T351. The inhibition efficiency of chromate is greater for AA2024 then for AA7075.

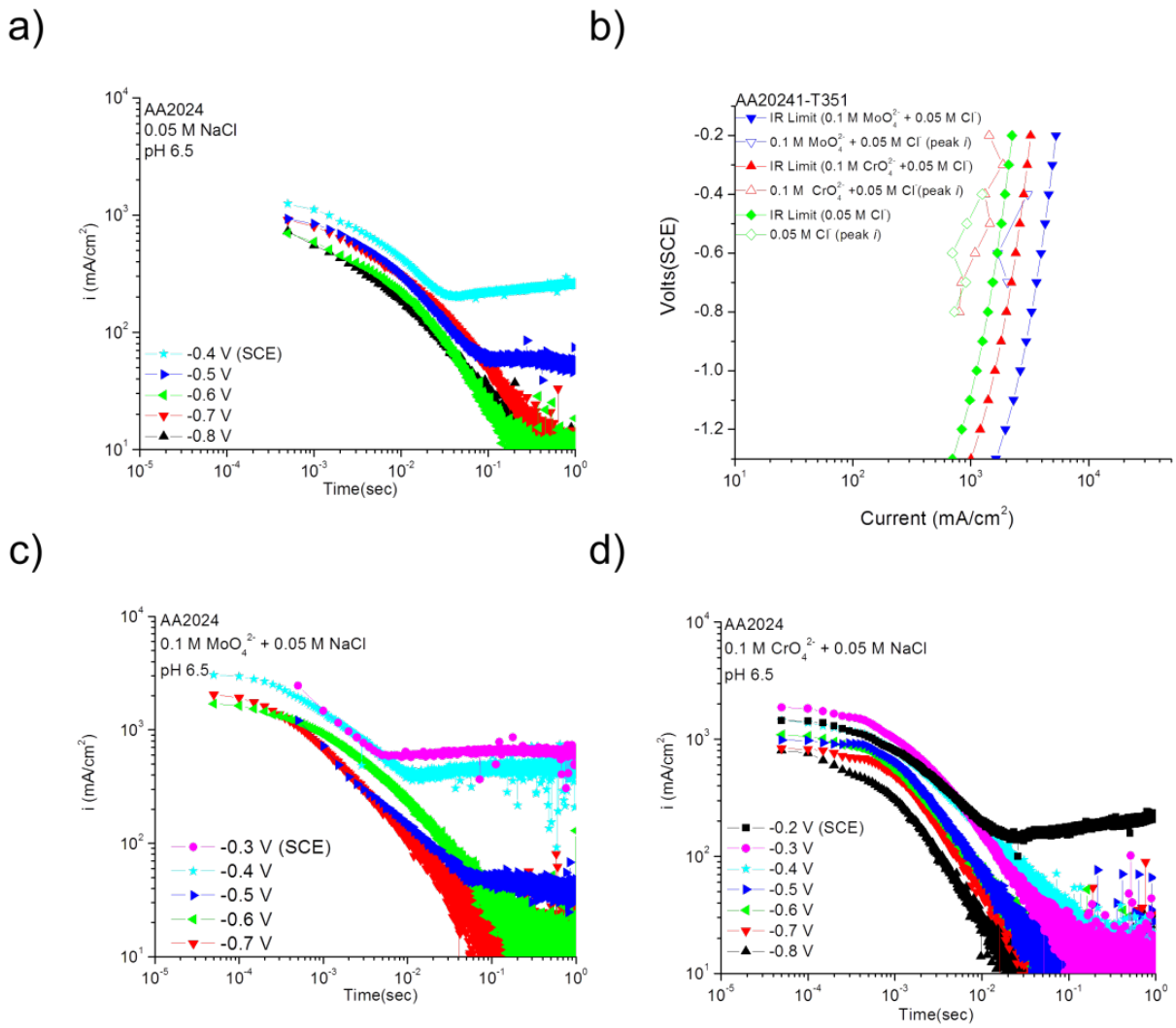

Figure 136. (a) Scratched electrode net anodic current densities for AA2024-T6 in 0.05 M NaCl solution with pH 6.5. (b) Calculated IR limit as compared to peak current density of scratched AA2024 electrodes at time zero after scratch. IR limit is calculated for an aqueous 0.05 M NaCl solution, 0.1 M CrO_4^{2-} and 0.05 M NaCl solution, and 0.1 M MoO_4^{2-} and 0.05 M NaCl solution. (c) and (d) show scratched electrode current transients for AA2024-T351 with 0.1 M $MoO_4^{2-}$and 0.1 M CrO_4^{2-} additions, respectfully.

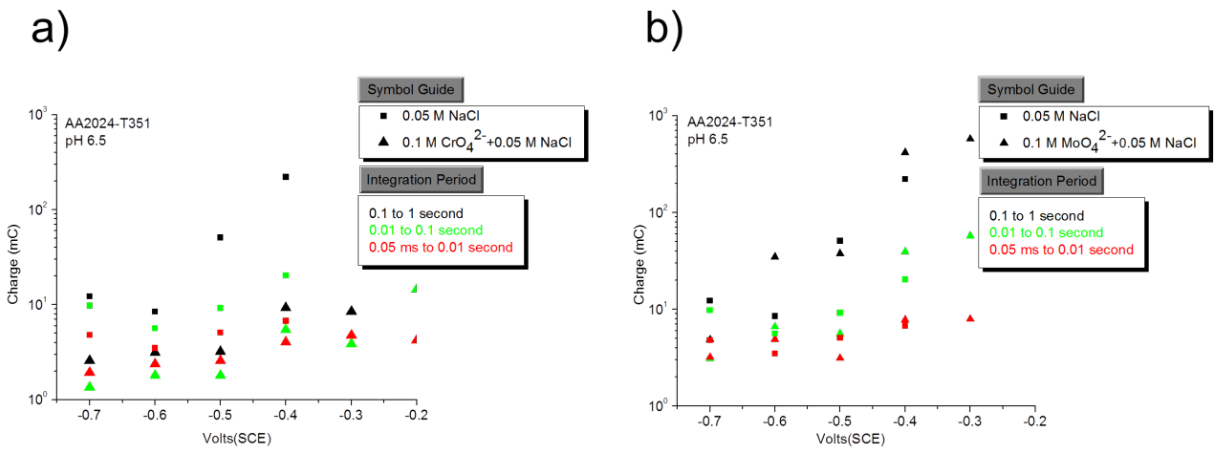

Figure 137. (a) Scratched electrode charge passed for AA2024-T351 in 0.05 M NaCl solution with a pH of 6.5 and 0.1 M CrO_4^{2-} and 0.05 M NaCl solution. (b) Scratched electrode charge passed for AA2024-T351 in 0.05 M NaCl solution with a pH of 6.5 and 0.1 M MoO_4^{2-} and 0.05 M NaCl solution. Integration of current over three periods from 0.05 milliseconds to 0.01 second, 0.01 to 0.1 second, and 0.1 to 1 second.

The Oxide Film Capacitance

Using Equation 28, the capacitance can be calculated assuming that the frequency applied is in the capacitance dominated region of frequency response.

$$C = 1 \,/\, 2\pi f |Z_{mag}| \qquad \textbf{Equation 28}$$

Figure 138 demonstrates that this is an acceptable assumption for the electrical parameters considered. Figure 138 (d) shows the calculated oxide barrier thickness in the presence of molybdate. When molybdate is in solution the capacitance measured suggests the formation of a thin film on the scratched surface over a large range of molybdate concentrations. Figure 139 shows the growth of a thick oxide when 5 mM chromate is present in aqueous 1 M NaCl solution. A rise in impedance can be seen in the first 20 seconds of data. However, the impedance has reached the limit of the instrument as seen in Figure 138 after 20 seconds have passed. It is encouraging that this behavior is apparent at very low chromate concentrations even in an aggressive 1 M chloride environment.

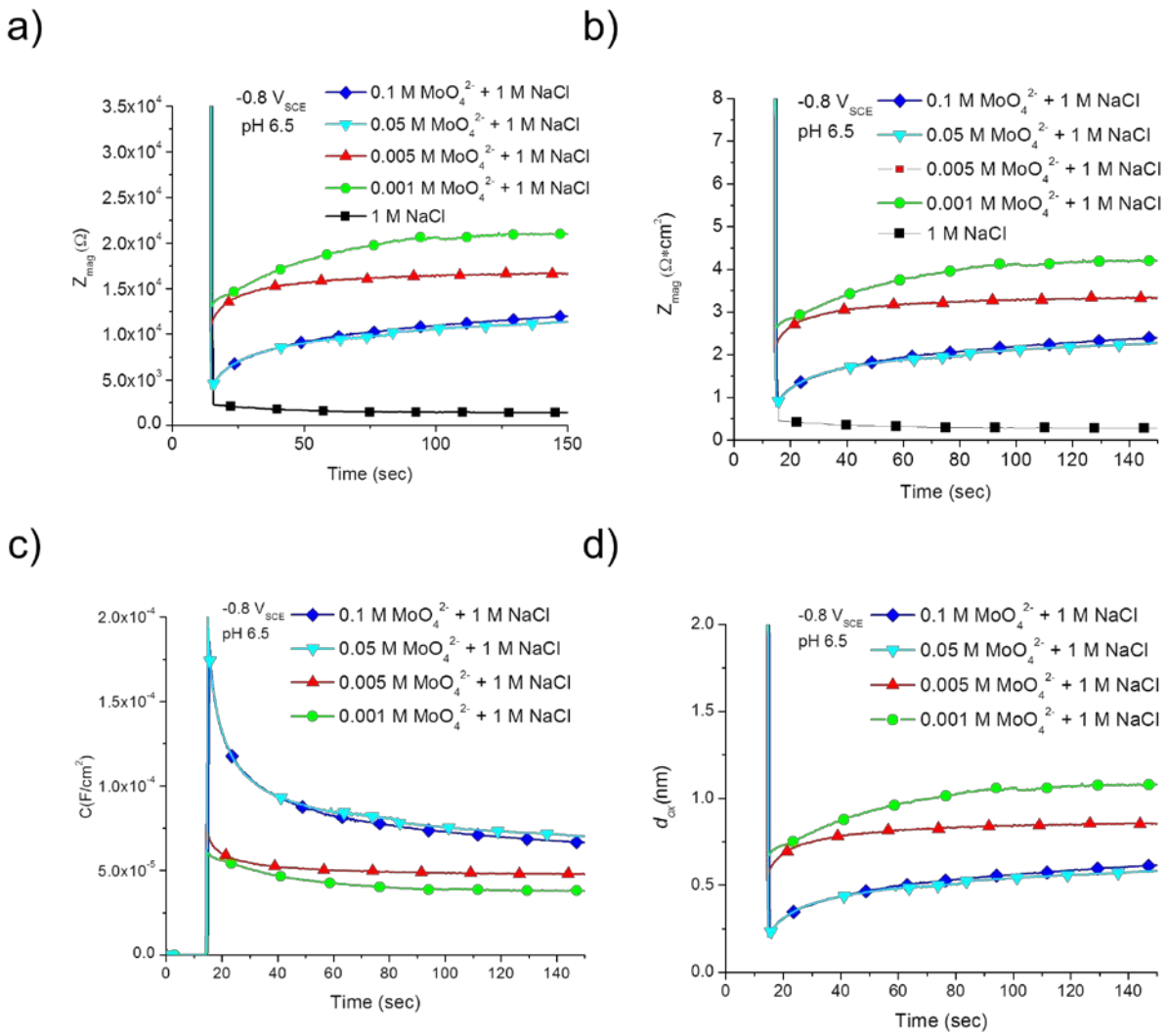

Figure 138. (a) Single frequency impedance measurements on AA2024 taken at -0.8 V_{SCE} in aqueous 1 M NaCl with a range of MoO_4^{2-} concentrations, all with adjusted pH of 6.5 at frequency 1000 Hz. These are impedance values as collected by the frequency response analyzer. (b) Single frequency impedance measurements from (a) corrected for scratched electrode area. (c) Calculated capacitance values from area corrected impedance values. (d) Oxide thickness calculated from film capacitance. The 1 M NaCl did not repassivate.

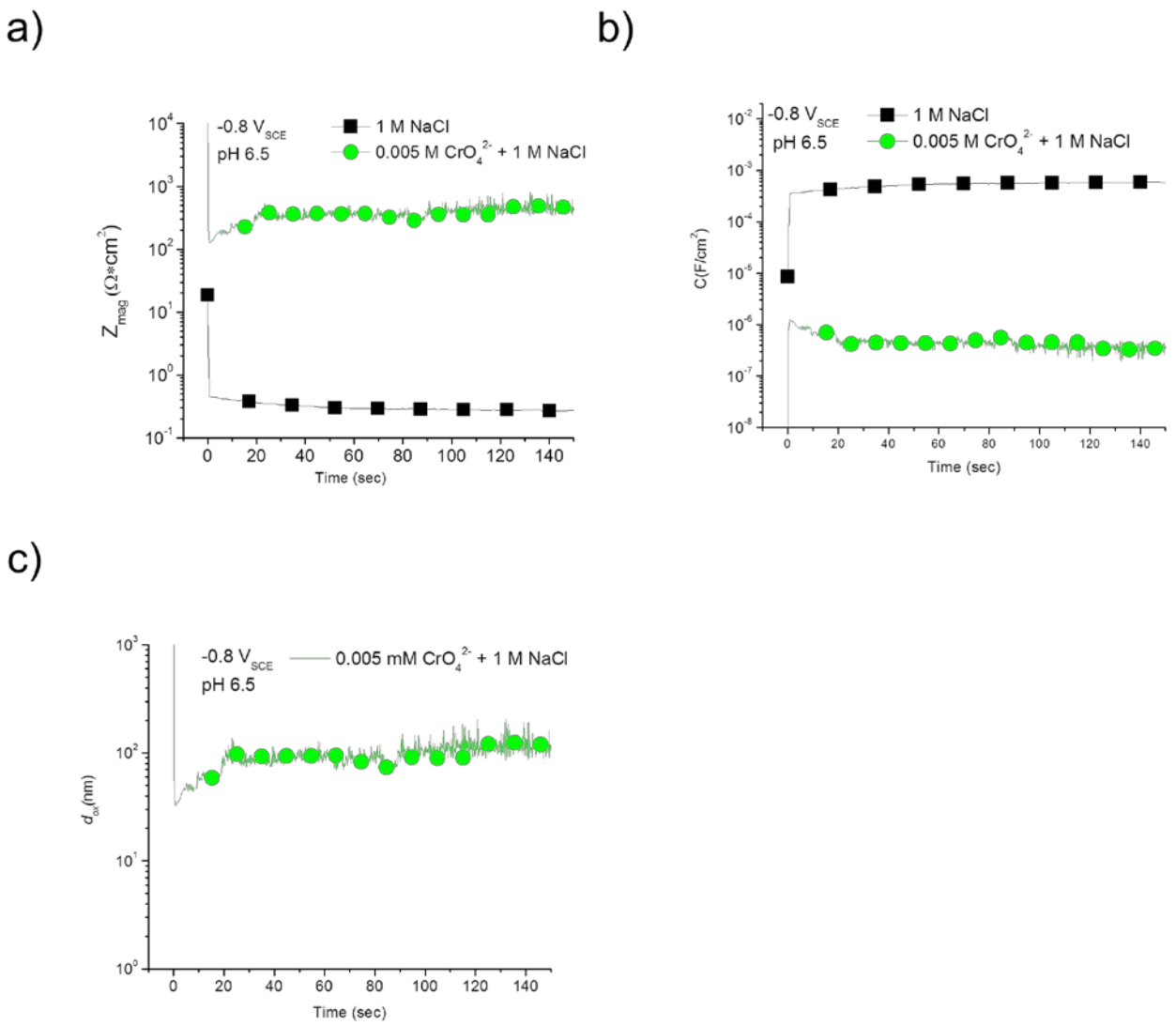

Figure 139. (a) Single frequency impedance measurements taken at -0.8 V_{SCE} in an aqueous 1 M NaCl and 5 mM CrO_4^{2-} solution corrected for scratched electrode area. Instrument limitations prevent data acquisition at long times in the solution shown and at all times at higher concentrations of chromate. This is due to small sample area and large oxide thickness. (b) Calculated capacitance values from area corrected impedance values. (c) Oxide thickness calculated from film capacitance. The 1 M NaCl solution did not repassivate.

Corrosion Inhibition of AA7075 and Carbon Steel 1018

Effect of Individual Inhibitors on AA7075

The effect of cerium, molybdate, vanadate and permanganate ions on the corrosion of AA7075 in the presence of chloride ions was investigated in this task. Both anodic and cathodic inhibition properties were elucidated in a series of screening tests. Correlations between the inhibitor concentration and corrosion properties were sought in order to allow for the development of an "intelligent" design tool that is capable of predicting corrosion inhibition efficiencies under different environmental conditions.

Anodic Inhibition

Anodic potentiodynamic polarization scans were carried out under deaerated conditions at various inhibitor levels to elucidate the anodic inhibitor efficiency of the proposed alternatives for hexavalent chrome. Representative anodic potentiodynamic scans measured in various inhibitor solutions containing 0.05 M NaCl and the corresponding inhibitor at different concentrations are shown in Figure 140.

The vanadate, molybdate and cerium inhibitors all showed anodic inhibition, especially at higher concentrations. Distinct passive ranges were observed in case of these inhibitors. In the presence of permanganate ions, however, no passive range and current densities higher than those of untreated AA7075 were observed, probably due to the strong oxidizing property of the permanganate.

Cathodic Inhibition

The effect of the inhibitors on the dominant cathodic reaction, the ORR on AA7075 was also investigated. Under non-deaerated conditions, in the presence of chloride ions, cathodic potentiodynamic polatization scans were carried out after the addition of various inhibitors in different concentrations. Representative scans are shown in Figure 141.

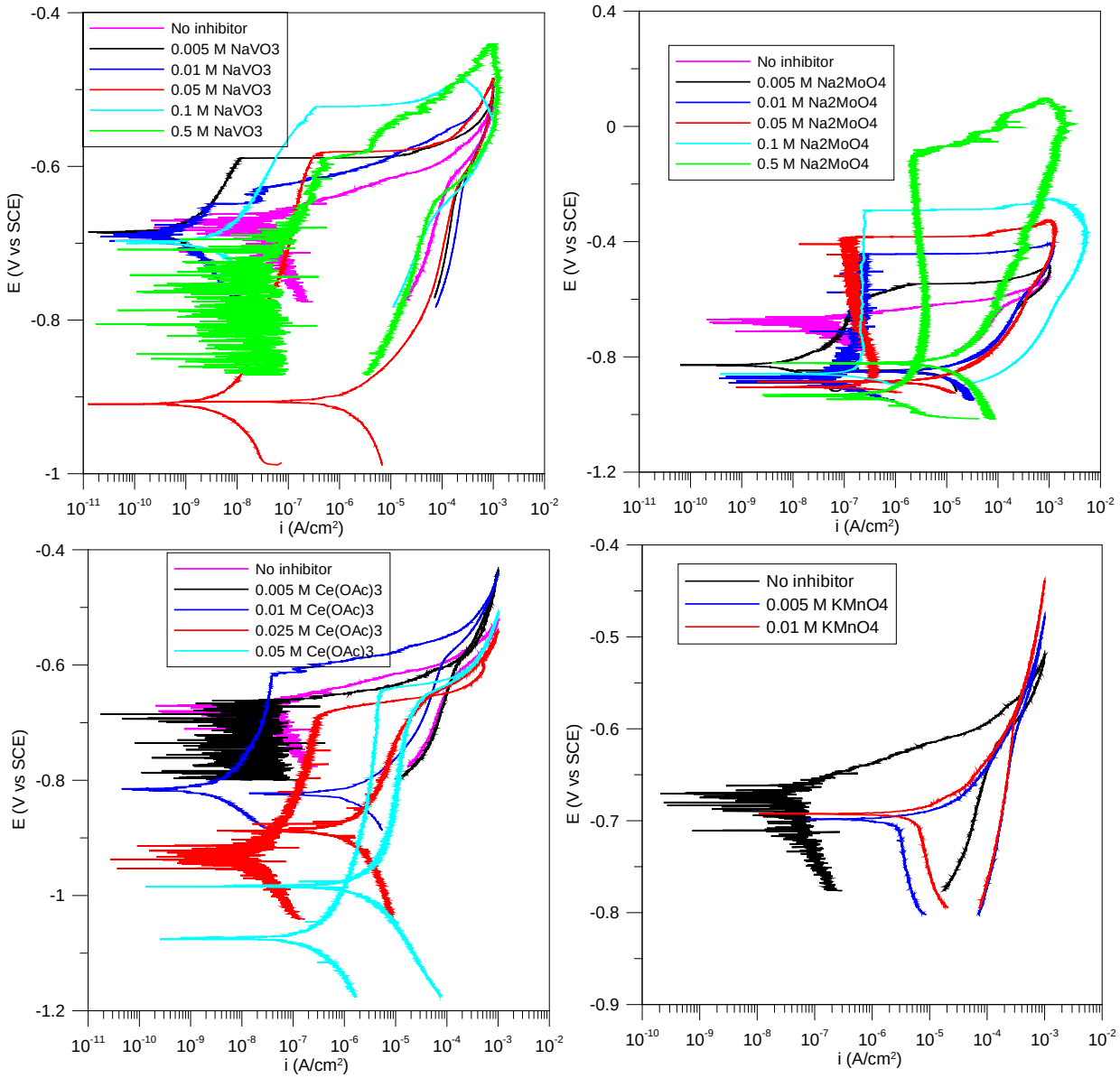

Figure 140. Representative anodic potentiodynamic polarization scans measured in 0.05 M NaCl solutions containing inhibitors at different concentrations.

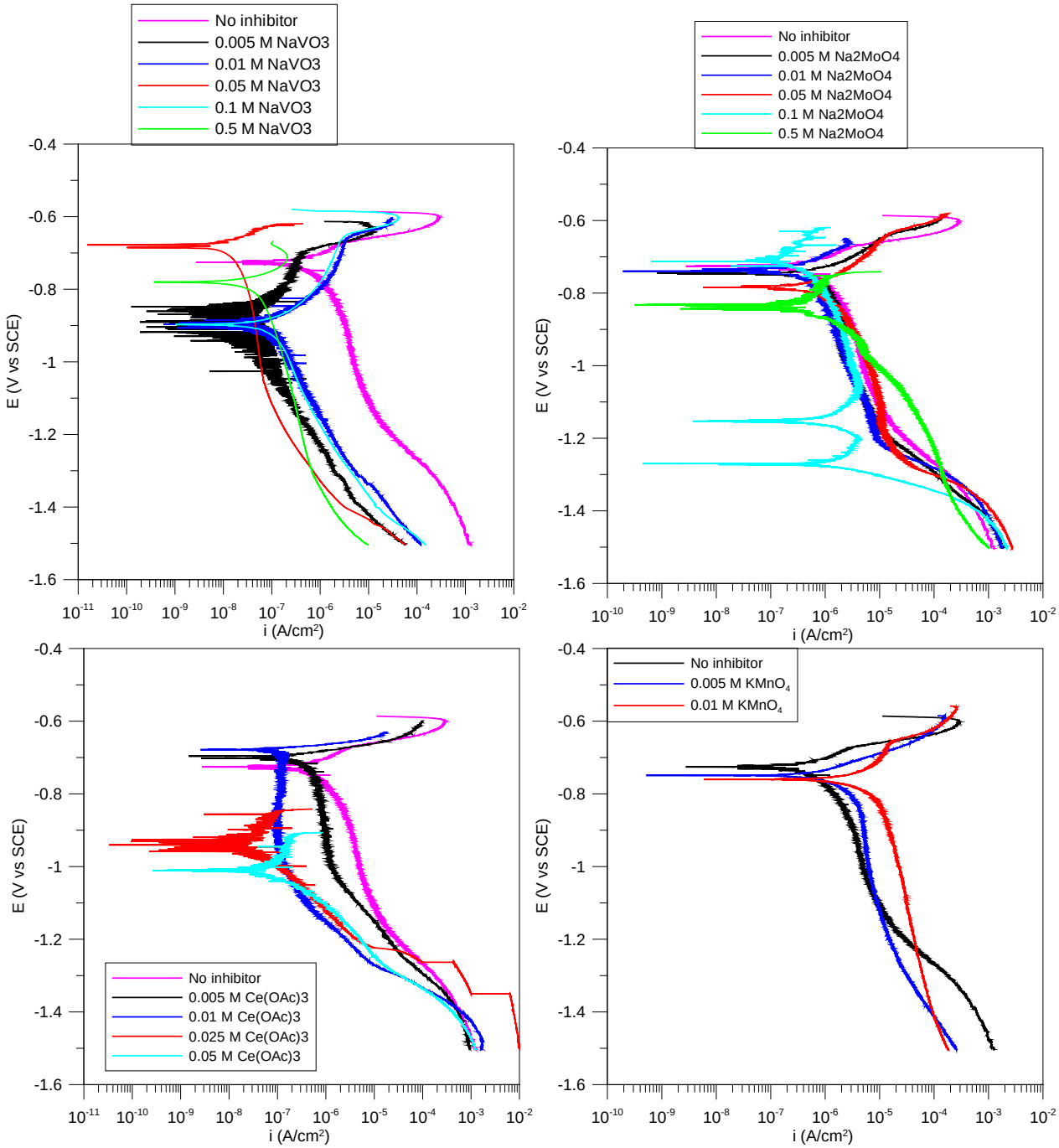

Figure 141. Cathodic potentiodynamic polarization scans of AA7075 in non-deaerated, 0.05 M NaCl solution containing various inhibitors at different concentrations.

Vanadate and cerium showed excellent cathodic inhibition of AA7075 by effectively reducing the cathodic current density compared to the uninhibited case. No apparent concentration dependence was found in either inhibitor. Molybdate slightly lowered the cathodic current density at lower concentrations. This effect, however, diminished at higher molybdate levels. The permanganate ions were found to increase the cathodic current density due to their highly oxidizing nature.

Chronoamperometric measurements were also carried out to further investigate the cathodic inhibition of cerium and vanadate ions. Current density vs. time curves of AA7075 exposed to 0.05 M NaCl with and without cerium or vanadate ions are shown in Figure 142. Significant reduction of the current density was found in case of both inhibitors confirming their excellent cathodic inhibitor properties. Figure 143 summarizes the measured current densities as a function of inhibitor concentration. No apparent concentration dependence was found. It was observed that at the highest cerium ion concentration, the inhibitor property diminished. This was probably due to the formation of thick cerium oxide precipitates, which do not possess barrier properties due to the presence of cracks and pores in their microstructure.

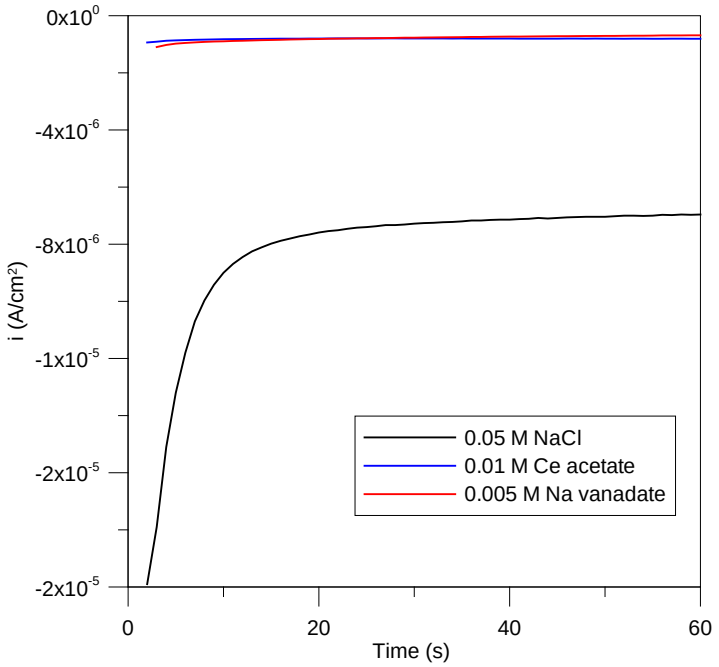

Figure 142. Chronoamperometric curves of AA7075 measured in non-deaerated, 0.05 M NaCl solution with and without inhibitors.

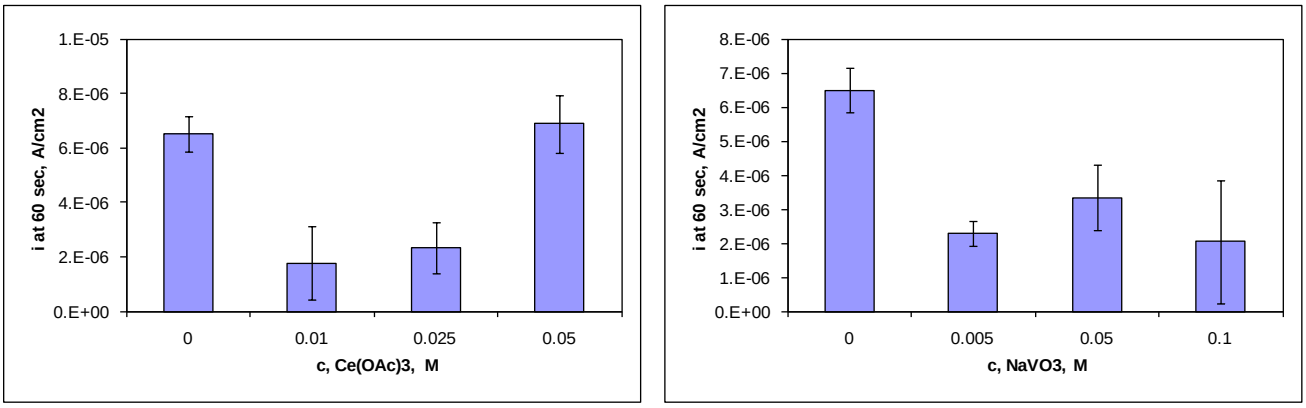

Figure 143. Cathodic current densities measured after 60 seconds of potentiostatic hold during chronoamperometric tests as a function of inhibitor concentrations.

Most of the inhibitors that were found to be effective in the case of AA2024 were also effective in the case of AA7075. Molybdate ions were found to be good anodic inhibitors, increasing E_{pit} with strong concentration dependence. Vanadate ions also were found to be good anodic inhibitors, although they did not show any concentration dependence, similarly to the anodic inhibition of AA2024. Cerium and vanadate ions are good cathodic inhibitors of both AA2024 and AA7075. Molybdate ions, however, were not as effective in inhibiting the ORR on AA7075 as in the case of AA2024. While the permanaganate ions were found to be good anodic and cathodic inhibitors of AA2024 at low concentrations, they did not inhibit the corrosion of AA7075.

OCP decreased logarithmically with the concentration cerium acetate, as shown in Figure 144. E_{pit} however remained constant, based upon the measurements shown in Figure 140.

The open circuit potentials, E_{pit} and ranges of passivity (i.e., $\Delta E_{pass} = E_{pit} - OCP$) were determined and plotted as a function of the inhibitor concentration on semilogarithmic plots as shown in Figure 144, Figure 145 and Figure 146, for cerium, molybdate and vanadate, respectively. No concentration dependence of the anodic properties was found in case of vanadates. However, strong concentration dependences were found in case of the molybdate and cerium ions. In the case of the molydate, E_{pit} of the AA7075 increased as the inhibitor concentration (c_{Mo}) increased according to Equation 29.

$$E_{pit} = 0.23 \times logc_{Mo} - 0.04 \; R^2 = 0.95 \qquad \textbf{Equation 29}$$

OCP did not show any concentration dependence. The range of passivity (ΔE_{pass}), thus, was directly dependent on the concentration, based on Equation 30.

$$\Delta E_{pass} = 0.27 \times logc_{Mo} + 0.89 \; R^2 = 0.93 \qquad \textbf{Equation 30}$$

OCP decreased logarithmically with the concentration cerium acetate, as shown in Figure 144. E_{pit} however remained constant, based upon the measurements shown in Figure 140. Consequently, the passive range increased logarithmically as a function of the cerium acetate concentration. The OCP and ΔE_{pass} concentration dependence are obtained using equations Equation 31 and Equation 32, respectively.

$$\mathrm{OCP} = -0.42 \times logc_{Ce} - 1.64 \;\; R^2 = 0.99 \qquad \textbf{Equation 31}$$

$$\Delta E_{pass} = 0.41 \times logc_{Ce} + 0.97 \;\; R^2 = 0.97 \qquad \textbf{Equation 32}$$

Based on the measured pH as a function of the inhibitor concentration (see Figure 16) and the speciation diagrams for vanadate (Figure 17), cerium (Figure 18) and molybdate (Figure 19), the predominant species can be found. The predominant cerium compound in 0.05 M cerium acetate is $Ce(CH_3COO)^{2+}$, while it is MoO_4^{2-} and $HMoO_4^-$ for molybdenum. The solution chemistry of vanadates is very complex and whil $V_2O_7^{4-}$ and VO_3OH^{2-} are the most plentiful compounds, other are also present in large quantity and the type of vanadium-based ion is highly dependent on the pH.

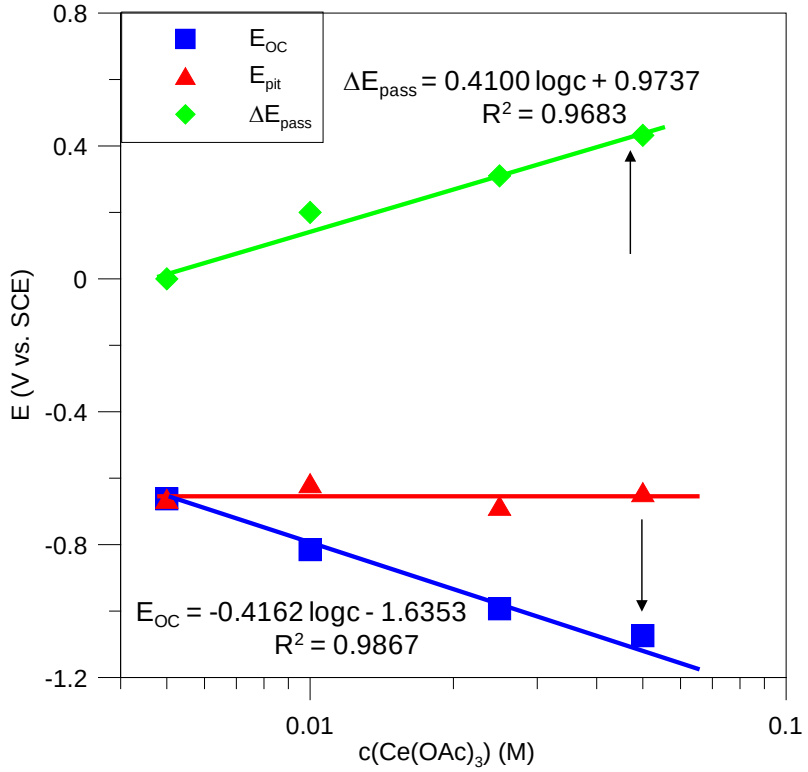

Figure 144. Measured open circuit potential, E_{pit} and resulting ΔE_{pass} for AA7075 in non-deaerated, 0.05 M NaCl solution containing cerium at different concentrations.

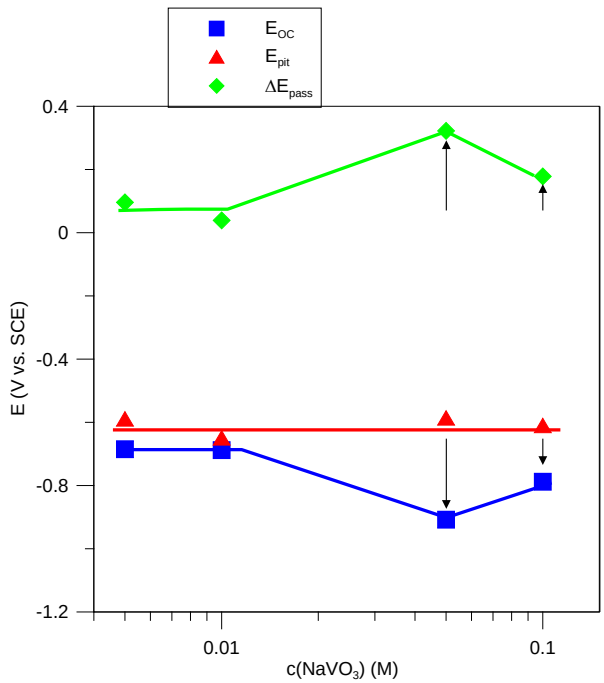

Figure 145. Measured open circuit potential, E_{pit} and resulting ΔEpass for AA7075 in non-deaerated, 0.05 M NaCl solution containing vanadate at different concentrations.

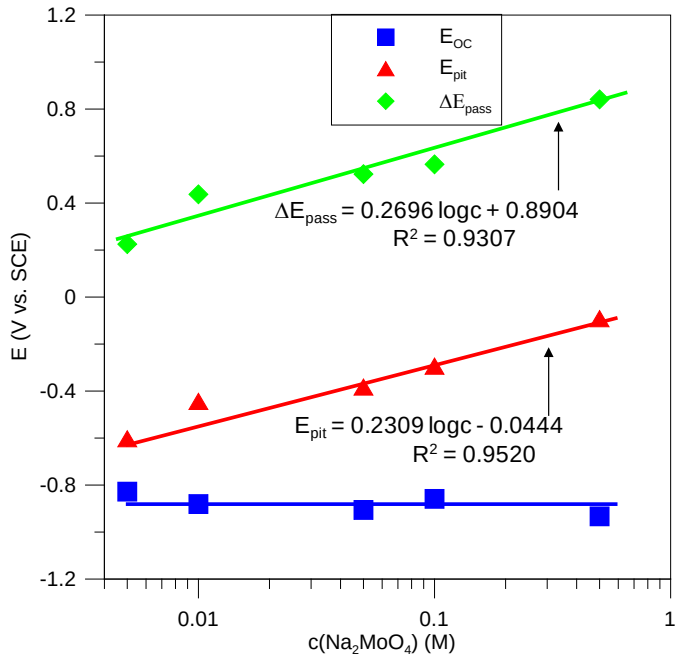

Figure 146. Measured open circuit potential, E_{pit} and resulting ΔEpass for AA7075 in non-deaerated, 0.05 M NaCl solution containing molybdate atdifferent concentrations.

Effect of Individual Inhibitors on 1018 Carbon Steel

The effect of cerium, vanadate, molybdate and permanganate ions on the anodic and cathodic behavior of 1018 carbon steel in the presence of chloride ions was investigated in this task.

Anodic Inhibition

Anodic potentiodynamic polarization scans were carried out in 0.05 M NaCl solution containing various inhibitors at different concentrations to assess the effect of these ions on the barrier properties of 1018 carbon steel. Representative polarization scans are shown in Figure 148. Vanadate was found to only affect the anodic behavior of 1018 carbon steel at very high inhibitor concentrations. Molybdate, on the other hand, had a significant effect on the barrier properties of the alloy, essentially passivating the surface at all inhibitor concentrations. Cerium and permanganate had no effect on the anodic behavior. In the case of molybdate, the passive current density was found to be inversely proportional to the inhibitor concentration according to the following logarithmic relationship (see Equation 33). The data points and logarithmic extrapolation are represented in Figure 147. Thus, the passive current density decreased with increasing inhibitor concentration.

$$logi_{pass} = -0.779 \times logc_{Mo} - 5.622 \qquad \textbf{Equation 33}$$

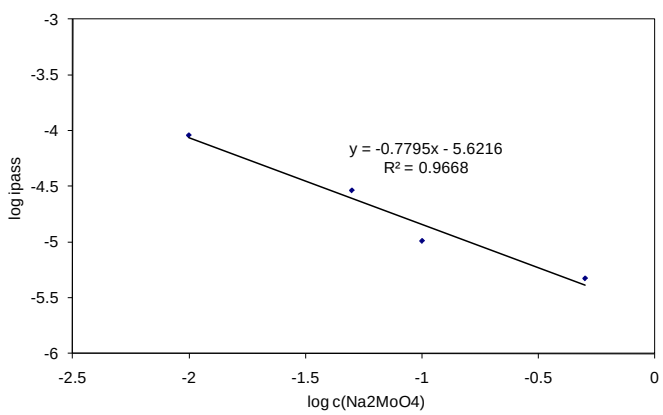

Figure 147. Passive current density (A/cm^2) of carbon steel 1018 in deaerated, 0.05 M NaCl solution containing molybdate at different concentrations, as a function of the concentration of sodium molybdate.

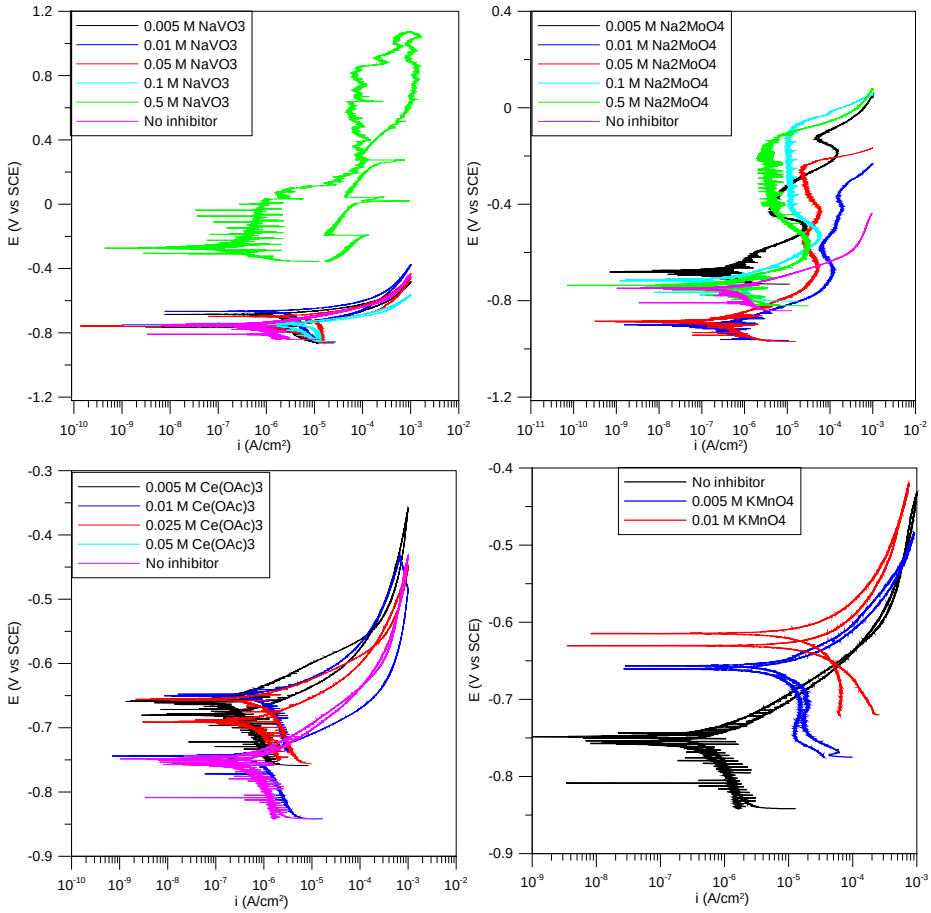

Figure 148. Anodic potentiodynamic polarization scans of 1018 carbon steel in deaerated, 0.05 M NaCl solution containing various inhibitors at different concentrations.

Cathodic Inhibition

Cathodic polarization scans were measured in 0.05 M NaCl solutions containing various inhibitors to assess the effect of the inhibitors on the ORR. Figure 151 shows examples of the scans. Vanadate did not have a significant effect on the ORR kinetics. Cerium was found to be an effective cathodic inhibitor at low concentrations, where a thinner, but more compact, pore-free cerium hydroxide layer forms on the surface of the alloy. Molybdates significantly lowered the cathodic current density throughout the investigated concentration range (0.005-0.5M). A linear relationship was found between the logarithm of the measured cathodic current density and the logarithm of the molybdate concentration (see Equation 34).

$$logi_{cath} = -0.233 \times logc_{Mo}$$ **Equation 34**

Permanganates were found to increase the measured cathodic current density.

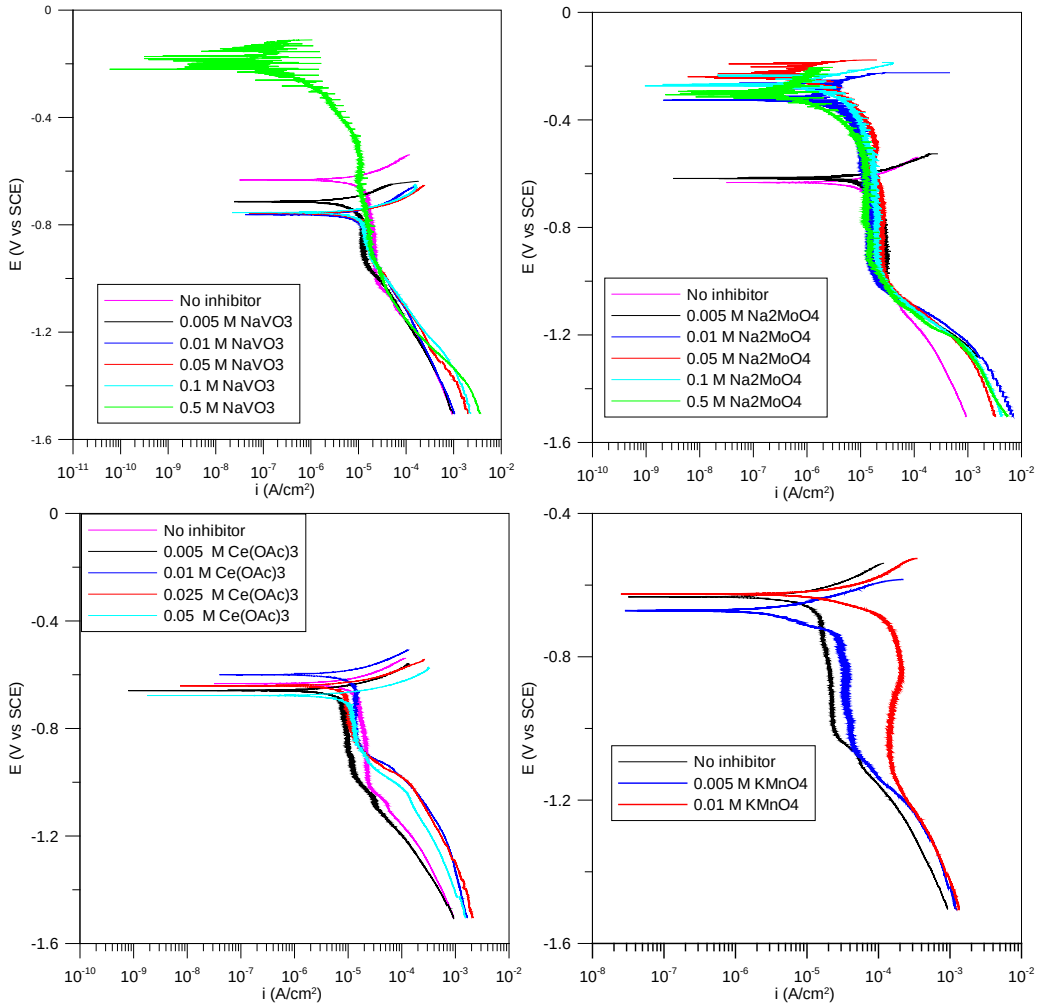

Figure 149. Cathodic potentiodynamic polarization scans of 1018 carbon steel measured in non-deaerated, 0.05 M NaCl solutions containing various inhibitors at different concentrations.

Chronoamperometric measurements performed on 1018 carbon steel in molybdate containing solutions did not confirm the cathodic inhibition provided by the molybdate ions that was seen in the polarization scans. This is probably due to the interference of the molybdate reduction reaction.

Effect of Inhibitor Combinations on AA7075 and 1018 Carbon Steel

The effect of selected inhibitor combinations on the electrochemical behavior of AA7075 and 1018 CS was investigated in this section. The inhibitor combinations were selected partly based on results of the study of the effect of individual inhibitors and partly based on literature sources.

Cerium and Vanadate Combination

The effect of vanadate and cerium inhibitor combinations on the electrochemical behavior of AA7075 and 1018 CS is described below.

1018 Carbon Steel

No synergistic effects on the anodic kinetics was found (not shown). OCP was significantly higher for V/Ce combinations than for single V and Ce inhibitors at the corresponding total inhibitor concentrations as shown in Figure 150.

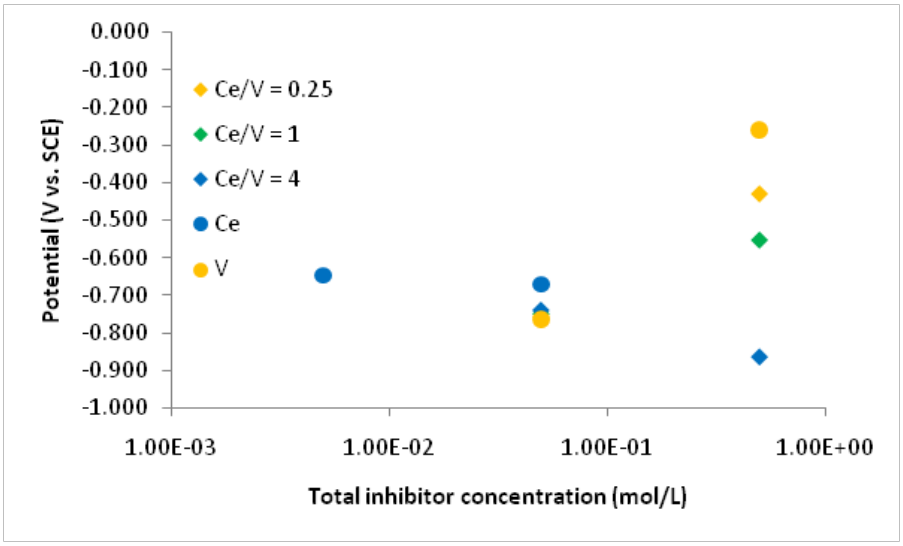

Figure 150. OCP of 1018 CS in non-deaerated, 0.05 M NaCl with single Ce and V inhibitors and V/Ce inhibitor combinations as a function of the total inhibitor concentration.

Figure 151 shows that the cathodic current densities were found to be significantly lower in the case of inhibitor combinations indicating synergistic effect on the cathodic inhibition of 1018 CS in Ce and V solutions.

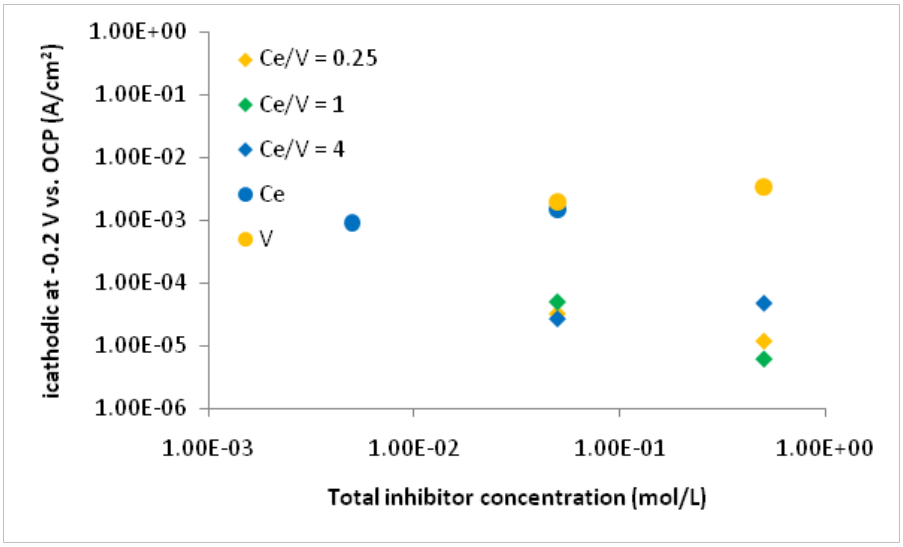

Figure 151. Cathodic current densities of 1018 CS at -0.2 V vs. OCP in 0.05 M NaCl with single Ce and V inhibitors and V/Ce inhibitor combinations as a function of the total inhibitor concentration.

Aluminum Alloy 7075

OCP of AA 7075 was constant (approximately -0.7 V vs. SCE) for the single inhibitors as well as for the Ce/V combinations, when the total concentration was 0.5 M as shown in Figure 152. It was found to be significantly lower for the single inhibitors (approximately -0.9 V vs. SCE and -1.1 V vs. SCE for V and Ce, respectively) than for the combinations (approximately -0.7 V vs. SCE) when the total concentration was 0.05 mol/L. The cathodic current densities at -0.2 V vs. OCP of AA 7075 for the inhibitor combinations were within the range of the single inhibitors for a total concentration of 0.05 mol/L (presented in Figure 153). No cathodic measurement was performed for Ce as a single inhibitor at a total concentration of 0.5 mol/L due to solubility limitations. However, an extrapolation of the data existing for Ce at 0.005 mol/L and at 0.05 mol/L indicated that the cathodic current densities of the inhibitor combinations were within the boundaries of those of the single inhibitors. E_{pit} of the inhibitor combinations were found to be higher than those of the single inhibitors as shown in Figure 154. The trend increased with the increase of the total inhibitor concentration. This resulted in an increase of E_{pit} of up to 0.2 V for a total inhibitor concentration of 0.5 mol/L.

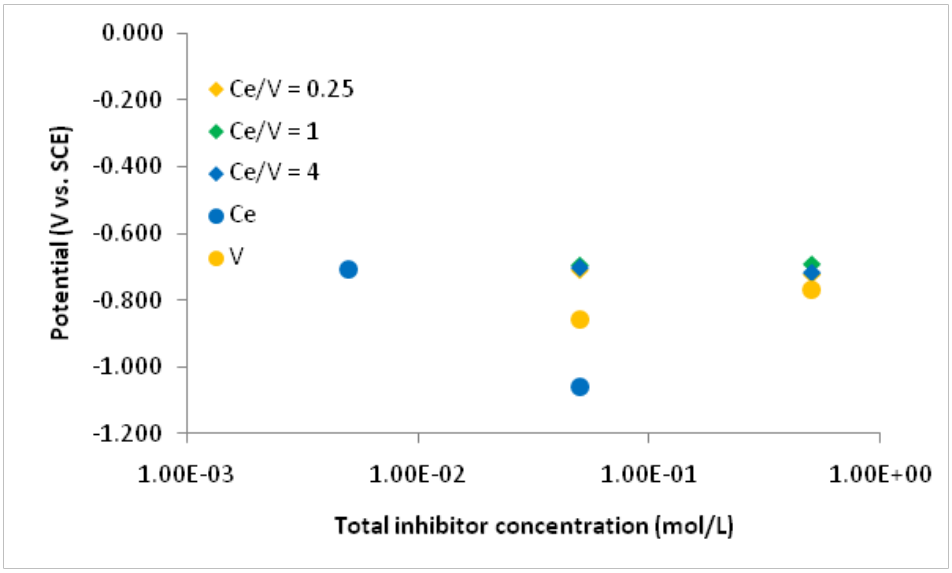

Figure 152. OCP of AA 7075 in non-deaerated, 0.05 M NaCl with single Ce and V inhibitor and V/Ce inhibitor combinations as a function of the total inhibitor concentration.

Figure 153. Cathodic current densities of AA 7075 at -0.2 V vs. OCP in 0.05 M NaCl with single Ce and V inhibitors and V/Ce inhibitor combinations as a function of the total inhibitor concentration.

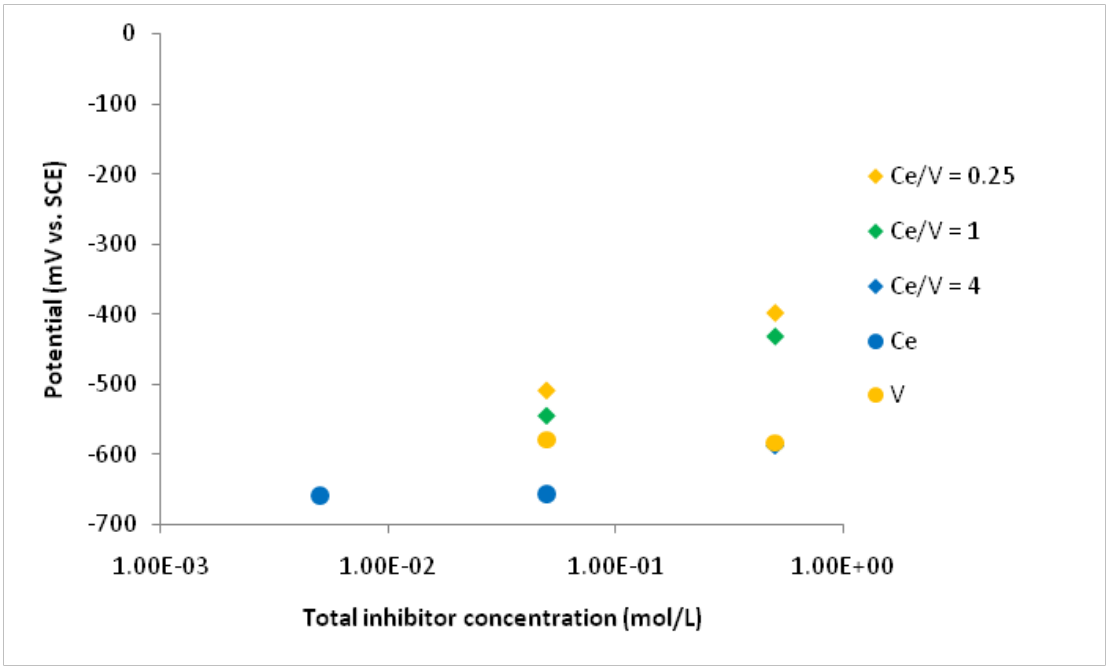

Figure 154. E_{pit} of AA 7075 in 0.05 M NaCl with single Ce and V inhibitors and V/Ce inhibitor combinations as a function of the total inhibitor concentration.

Cerium and Molybdate Combination

The effect of cerium and molybdate inhibitor combinations on the electrochemical behavior of 1018 CS and AA7075 is described below.

1018 Carbon Steel

OCP of 1018 CS for the individual inhibitors and the combinations are shown in Figure 155. The OCP of the Ce and Mo inhibitor combinations was found to be within the range of those measured in single inhibitor solutions.

E_{pit} of 1018 CS measured in solution containing Mo alone were higher than those found in Mo/Ce solution (not shown). E_{pit} measured in Ce solutions were the lowest. The cathodic current densities measured at -0.2 V vs. OCP were up to two orders of magnitude lower for the inhibitor combinations than for the single inhibitors as shown in Figure 156. The synergistic effect increased with increasing total inhibitor concentration.

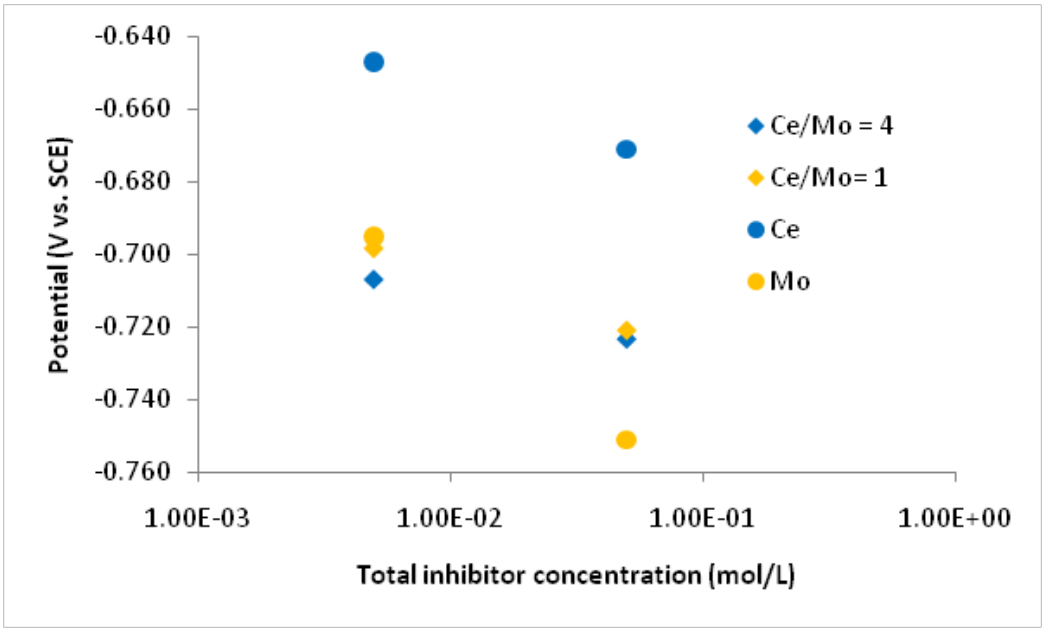

Figure 155. OCP of 1018 CS in 0.05 M NaCl with single Ce and Mo inhibitors and Ce/Mo inhibitor combinations as a function of the total inhibitor concentration.

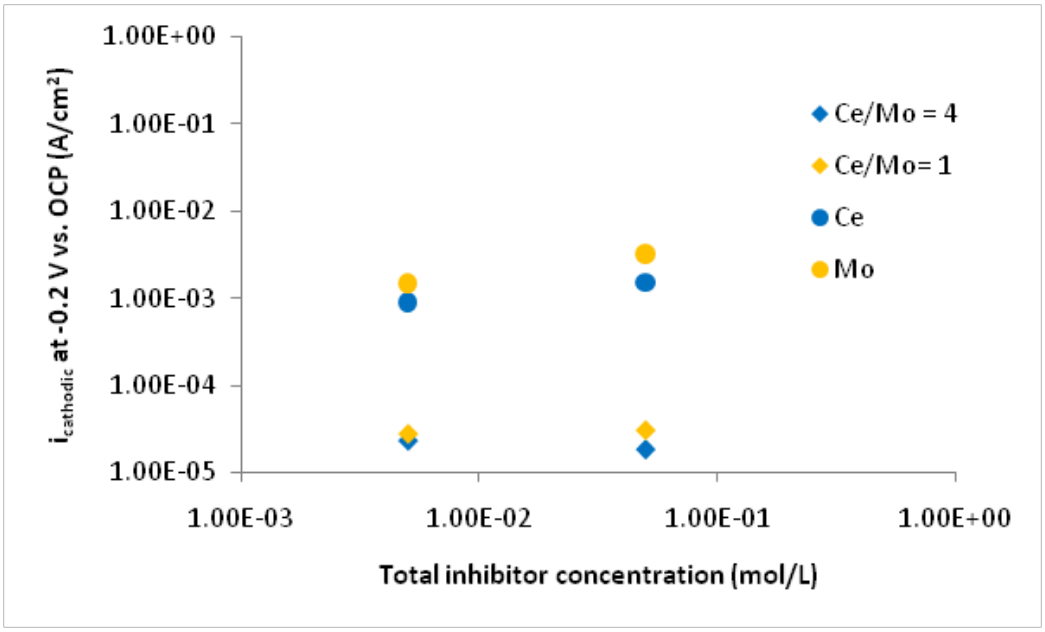

Figure 156. Cathodic currents of 1018 CS at -0.2 V vs. OCP in 0.05 M NaCl with single Ce and Mo inhibitors and Ce/Mo inhibitor combinations as a function of the total inhibitor concentration.

Aluminum Alloy 7075

The open circuit potentials, the cathodic current densities and E_{pit} of AA 7075 in inhibitor combinations solutions were all within the boundaries of those measured in the case of the individual inhibitors as shown in Figure 157, Figure 158 and Figure 159.

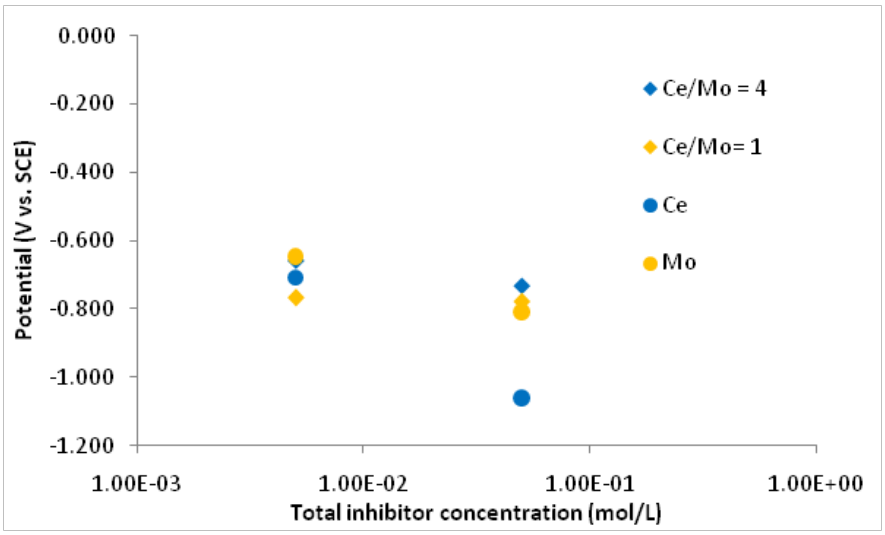

Figure 157. OCP of AA 7075 in 0.05 M NaCl with single Ce and Mo inhibitors and Ce/Mo inhibitor combinations as a function of the total inhibitor concentration.

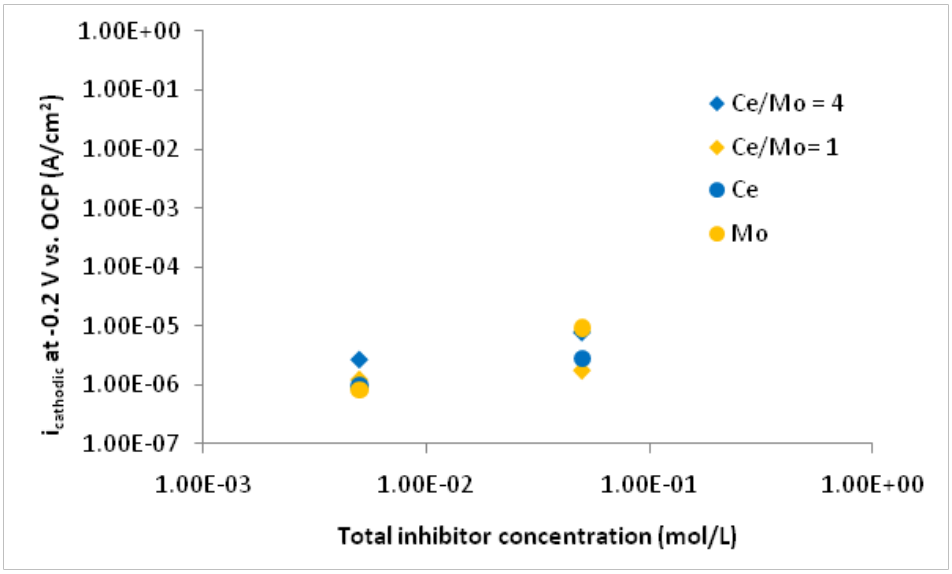

Figure 158. Cathodic currents of AA 7075 at -0.2 V vs. OCP in 0.05 M NaCl with single Ce and Mo inhibitors and Ce/Mo inhibitor combinations as a function of the total inhibitor concentration.

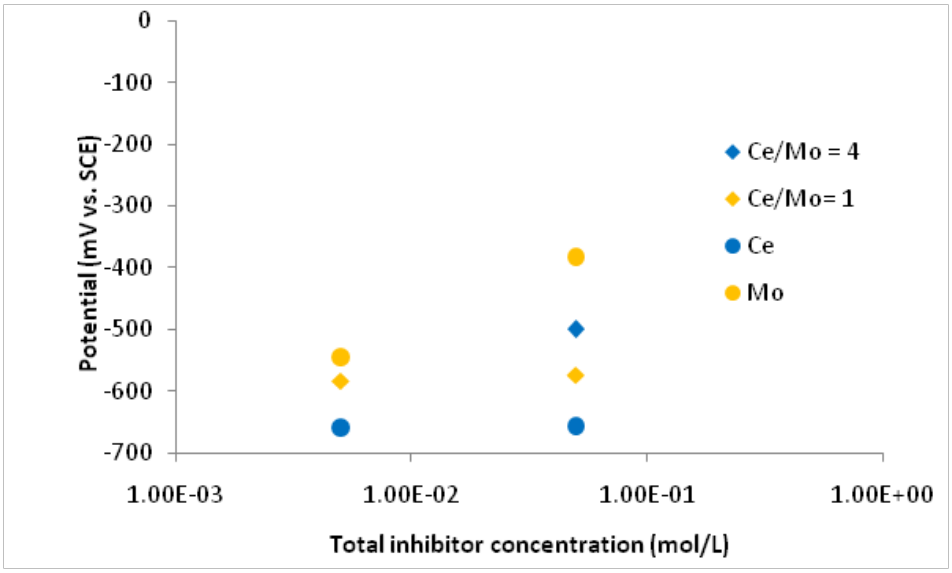

Figure 159. E_{pit} of AA 7075 in 0.05 M NaCl with single Ce and Mo inhibitors and Ce/Mo inhibitor combinations as a function of the total inhibitor concentration.

Investigation of the Effect of the Inhibitors on the Microstructural Heterogeneity of AA2024

Rotating Disc Arrays

The cathodic scans at 1000 rpm rotation rate in V, Ce and borate buffer solutions of arrays 1 through 4 are shown in Figure 160, Figure 161, Figure 162 and Figure 163. The cathodic inhibition effect of Ce on larger electrodes (500 microns, in arrays 1 and 2) was found to be less

significant than that of V (see Figure 160 and Figure 161). Furthermore, Ce appeared to be detrimental in the case of array 1, when compared to borate buffer (see Figure 160).

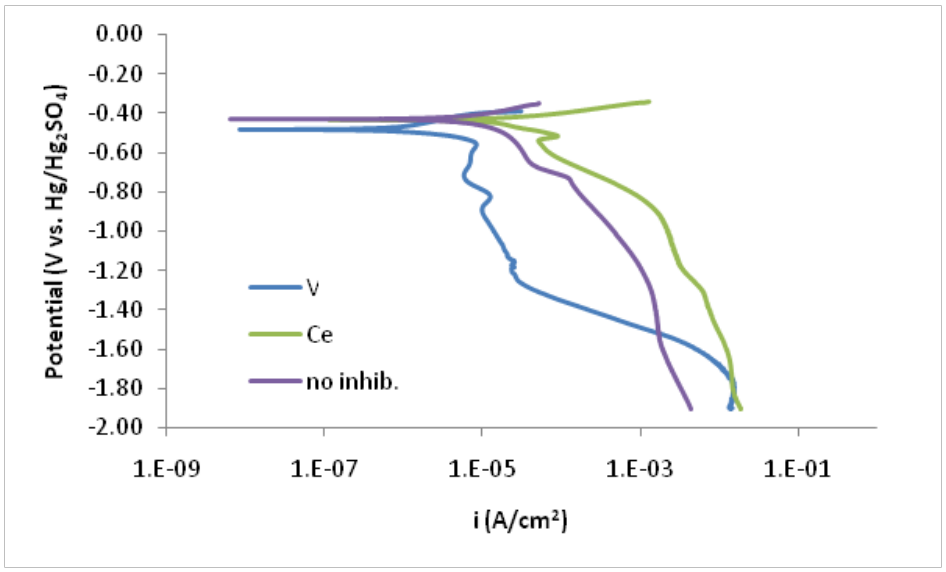

Figure 160. Cathodic polarization scans of array 1 at 1000 rpm with and without the presence of inhibitors.

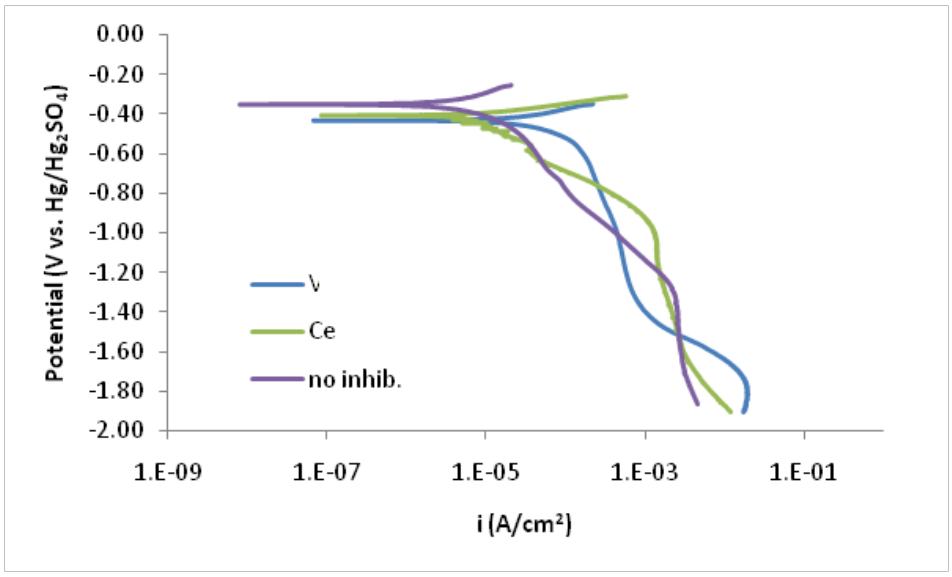

Figure 161. Cathodic polarization scans of array 2 at 1000 rpm.

Smaller electrodes in arrays 3 and 4 resulted in cathodic current densities lower in Ce and V inhibitor solutions than in borate buffer as shown in Figure 162 and Figure 163. The cathodic inhibition effect of V was found to improve as the electrode area increased and the distance between the electrodes decreased, when compared to borate buffer. The cathodic inhibition effect of Ce was more significant for smaller electrodes, independently from the distance between them.

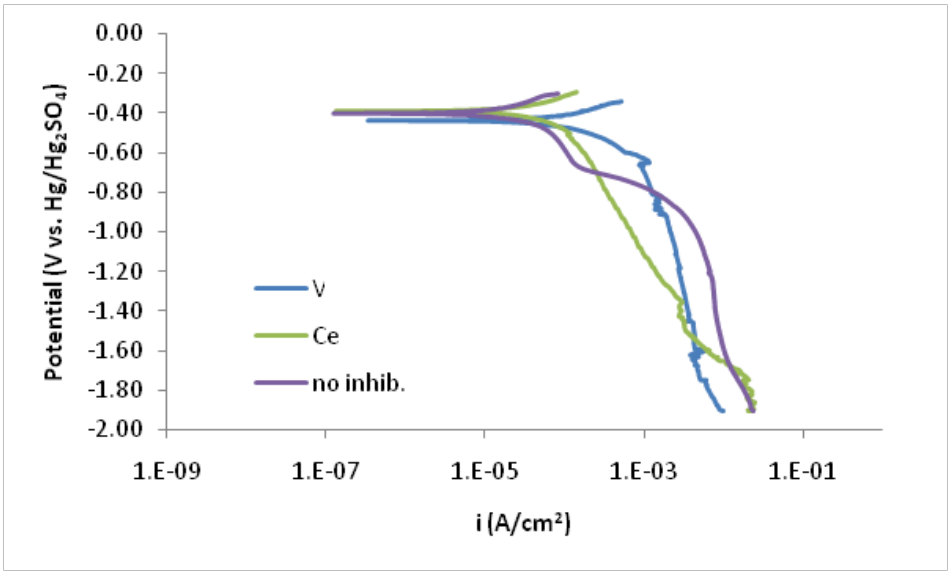

Figure 162. Cathodic polarization scans of array 3 at 1000 rpm.

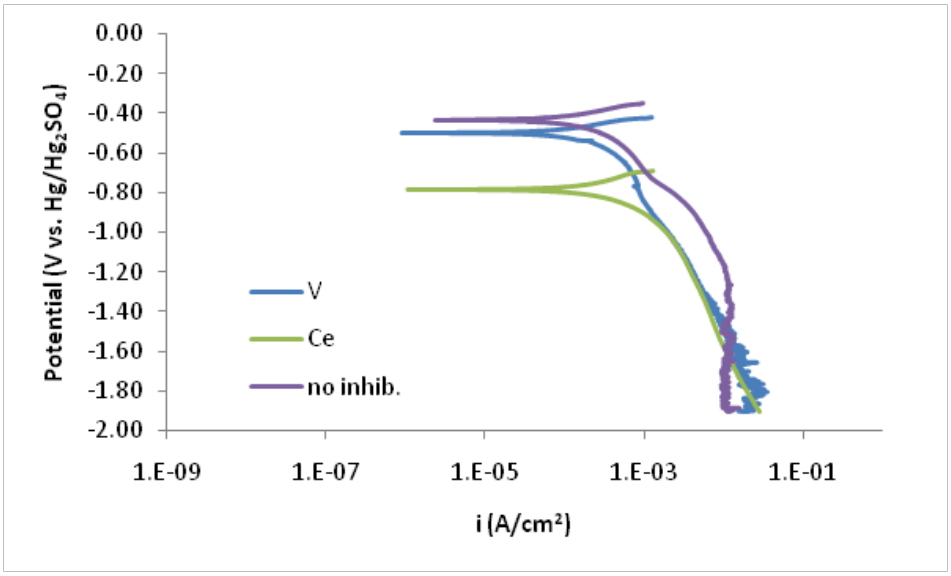

Figure 163. Cathodic polarization scans of array 4 at 1000 rpm.

Figure 164 and Figure 165 show the cathodic potentiodynamic polarization scans of all arrays measured at 1000 rpm in V and Ce solutions, respectively. As the distance between electrodes L increased (from array 1 to array 2, and from array 3 to array 4), with a constant electrode diameter, the cathodic current in V solution was found to decrease for small electrodes and to increase for large electrodes (see Figure 164). Correspondingly, the cathodic current in V solution decreased for a small L value (array 1 and 3) and increased for large L value (array 2 and 4), when the diameter of the electrodes increased. Consequently, the cathodic inhibition effect of V is more pronounced for a higher density of larger copper electrodes. As the distance between the electrodes, L, increased, the cathodic current in Ce solution decreased for large electrodes and increased for small electrodes (see Figure 165). The cathodic current in Ce solution increased for both small and large L value when the diameter of the electrodes

increased. Consequently, the cathodic inhibition effect of Ce was found to increase when the density of small electrodes increased. The opposite was observed for large electrodes, i.e. the cathodic current decreased when the distance between electrodes increased.

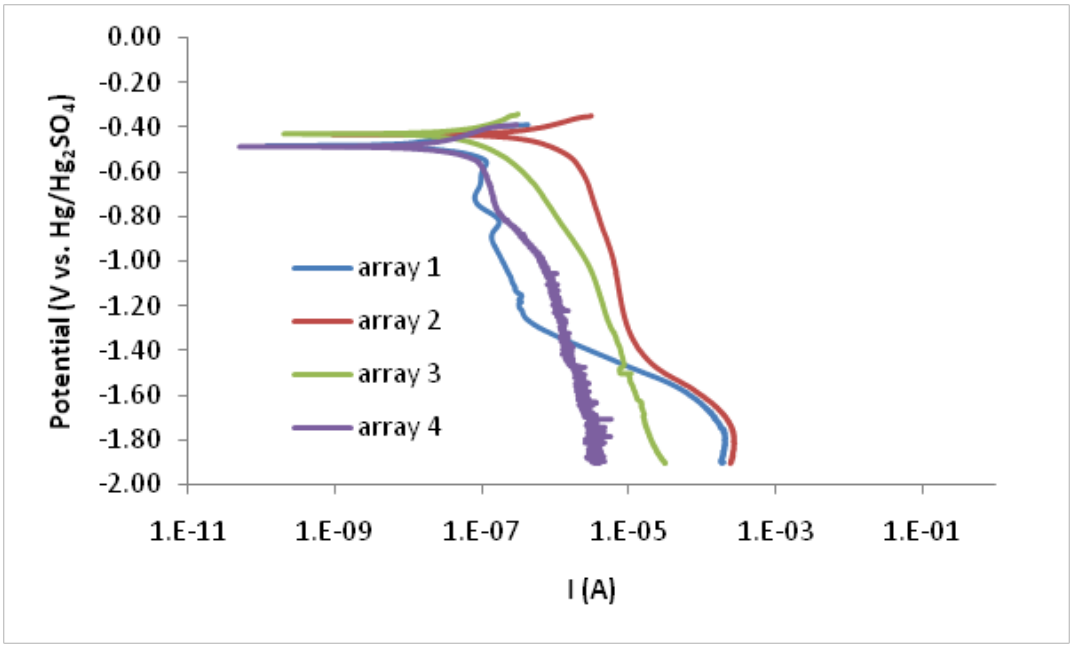

Figure 164. Cathodic polarization scans of all arrays in V solution at 1000 rpm.

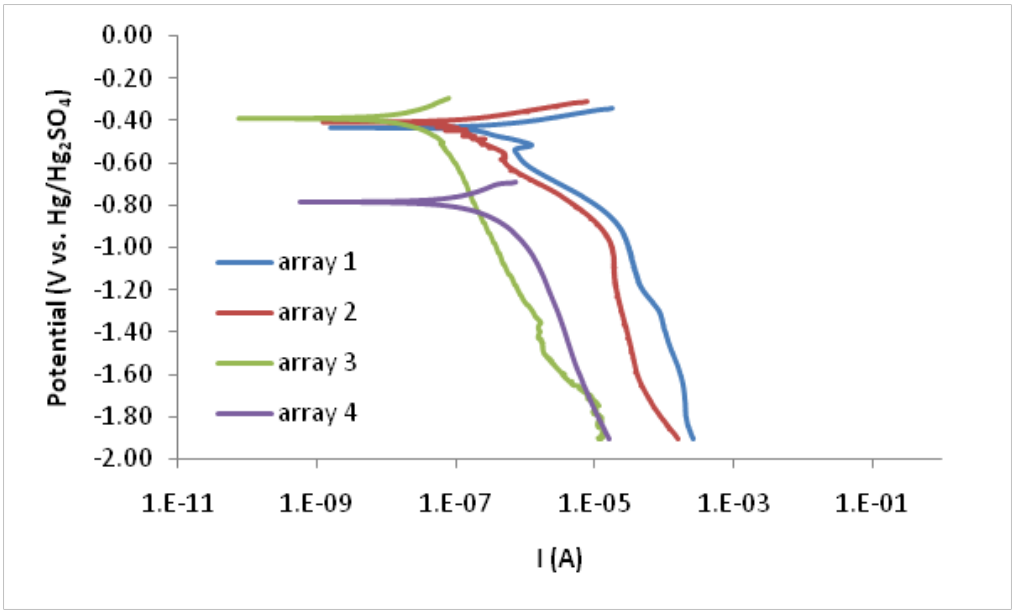

Figure 165. Cathodic polarization scans of all arrays in Ce solution at 1000 rpm.

Aluminum/Copper Multi-Electrode Array Study of Inhibitor

An aluminum/copper MEA was used in order to measure the individual anodic and cathodic current of an array that replicated Al-Cu alloys. The electrodes from the 100 wires array are galvanically connected through individual ZRAs. The currents are measured at – 0.8 V vs. OCP for two hours. The average anodic and cathodic current sums are plotted in order to assess the effect of the inhibitors based on their type, their concentration and their exposure process. All measurements were performed in a solution containing 0.05 M NaCl.

Figure 166 shows the effect of 0.05 M vanadate, cerium or molybdate combined in solution with 0.05 M NaCl compared to measurements performed in bare 0.05 M NaCl. Only vanadate resulted in a significant decrease of the anodic and cathodic current over time. The currents measured in cerium and molybdate treated solutions were similar to those found in untreated NaCl solution.

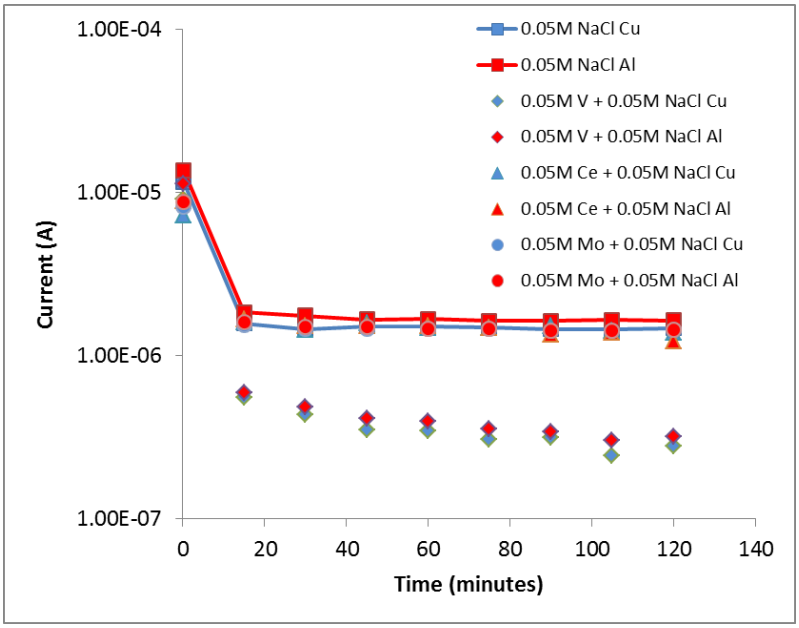

Figure 166. Effect of the type of inhibitors combined to 0.05 M NaCl on the measured anodic (Al, in red) and cathodic (Cu, in blue) total current as a function of time.

Figure 167 shows the effect of the concentration of vanadate when combined with 0.05 M NaCl. Vanadate was chosen because it was the only inhibitor that reduced the anodic and cathodic current. The measured currents are lower when the amount of vanadate in solution is lower. Based upon the measured pH as a function of the concentration, presented in Figure 16, and the speciation of vanadate in 0.01 M and 0.05 M sodium vanadate solutions (see Figure 17), the pH of vanadate/NaCl solution and the resulting vanadate speciation can be predicted. For the 0.005 M vanadate, the pH is expected to be just under 8 and it will be over 8.5 when the concentration is 0.05 M. Consequently, the predominant species ($V_4O_{12}^{4-}$, $V_3O_9^{3-}$ and VO_3OH^{2-}) will be independent from the vanadate solution concentration and is not the cause for the decrease in the measured currents.

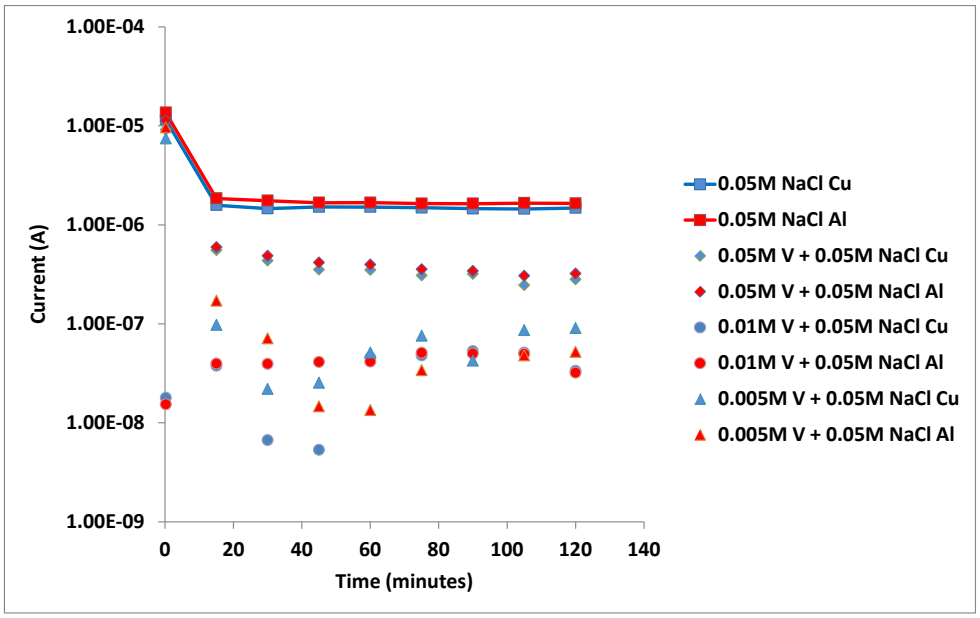

Figure 167. Effect of the concentration of vanadate combined to 0.05 M NaCl on the measured anodic (Al, in red) and cathodic (Cu, in blue) total current as a function of time.

Figure 168 and Figure 169 show the impact of the exposure process (combined vs. pre-exposed) for cerium and molybdate, respectively. It is obvious that pre-exposure to the inhibitor results in a significant drop of anodic and cathodic current by one order of magnitude.

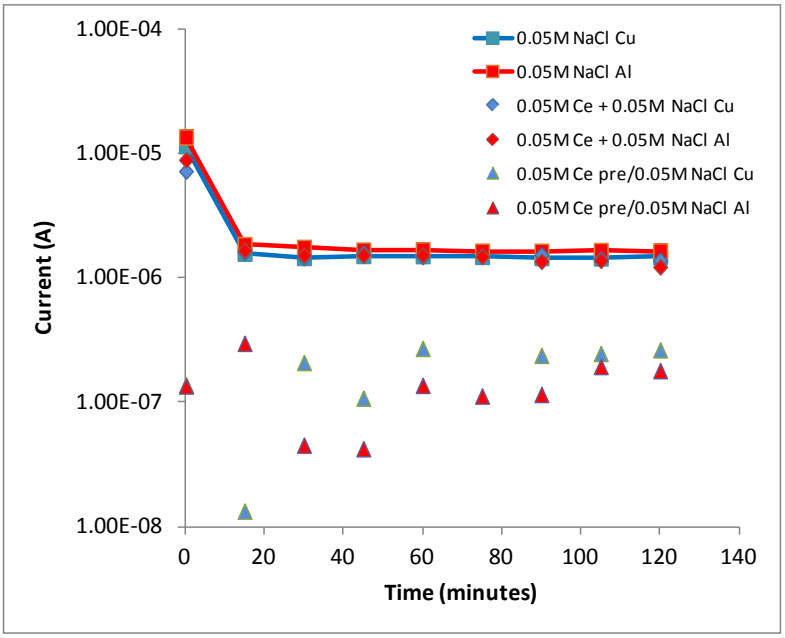

Figure 168. Comparison between pre-exposure and combination with cerium on the measured anodic (Al, in red) and cathodic (Cu, in blue) total current as a function of time.

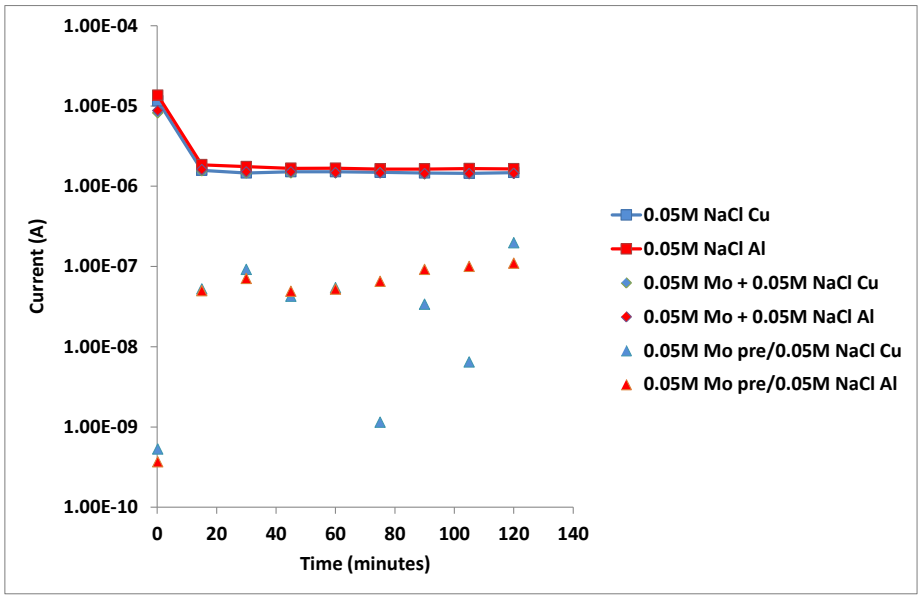

Figure 169. Comparison between pre-exposure and combination with molybdate on the measured anodic (Al, in red) and cathodic (Cu, in blue) total current as a function of time.

Figure 170 shows the effect of the concentration of vanadium and the impact of the exposure process. Higher currents were measured when the MEA was pre-exposed to 0.05 M vanadate than when the vanadate was combined with NaCl. But as, the concentration of vanadate was decreased to 0.005 M, lower currents were measured even after pre-exposure. The currents after pre-exposure to 0.005 M vanadate were lower than those measured in combined 0.05 M vanadate solution, but higher than in combined 0.005 M vanadate solution (see Figure 167).

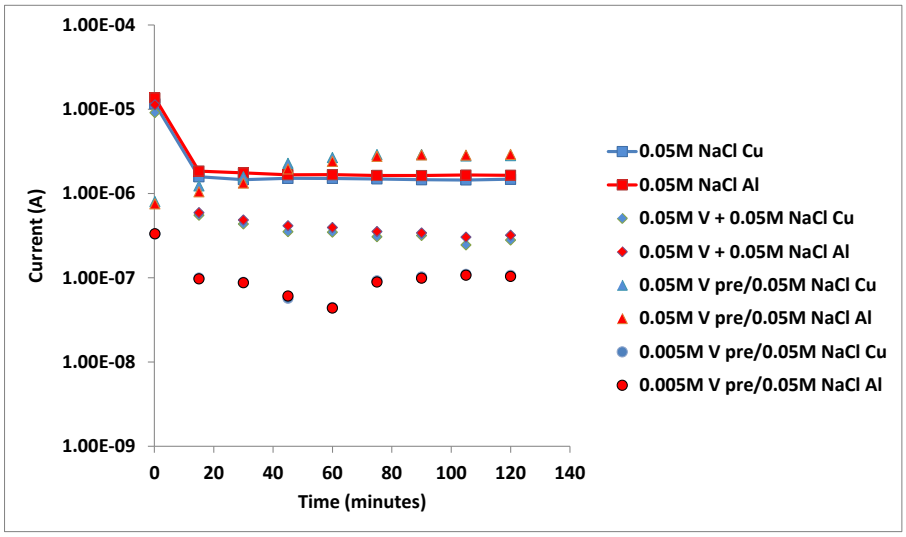

Figure 170. Effect of the concentration of pre-exposure vanadate on the measured anodic (Al, in red) and cathodic (Cu, in blue) total current as a function of time.

Inhibitor Interaction with AA7075

Auger electron spectroscopy was performed on AA7075 specimens after being exposed for 24 hours to 0.05 mol/L and 0.005 mol/L of cerium, vanadate and molybdate. The scans were performed on the fresh specimens after exposure as well as after 10 seconds sputtering and 30 seconds sputtering at 400 Å/min. The resulting scans of the bare specimens treated with cerium, vanadate and molybdate are shown in Figure 171, Figure 174 and Figure 177, respectively. The scans of the specimens sputtered for 10 seconds after being treated with cerium, vanadate and molybdate are shown in Figure 172, Figure 175 and Figure 178. The scans of the specimens sputtered for 10 seconds after being treated with cerium, vanadate and molybdate are shown in Figure 173, Figure 176 and Figure 179. The cerium, vanadium and molybdenum are indicated on each scans. The quantity of inhibitor measured was found to be independent of the inhibitor concentration at any measured depth.

EDS analysis of similarly treated specimens was performed in order to measure the quantity of inhibitor present on the surface. The results are presented in Figure 180, Figure 181 and Figure 182, for cerium, molybdate and vanadate, respectively. Ce1, Mo1 and V1 represent 0.05 mol/L of inhibitors and Ce2, Mo2 and V2 represent 0.005 mol/L. Semi-Quantitative results are summarized in

Figure 183. The inhibitors are proven to be present on the surface of the material and the quantity adsorbed is significantly dependent on the inhibitor solution concentration for cerium only.

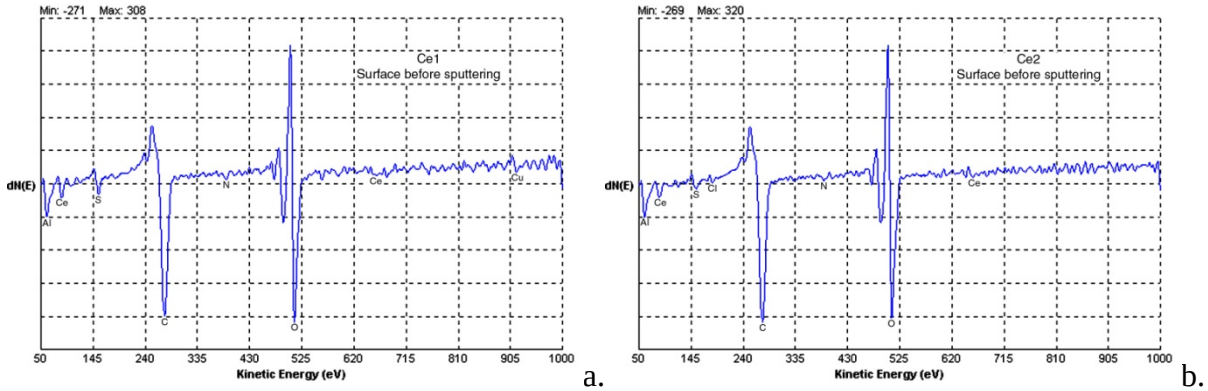

Figure 171. Auger electron Spectroscopy Scans of AA7075 after exposure to (a) 0.05 mol/L and (b) 0.005 mol/L cerium for 24 hours.

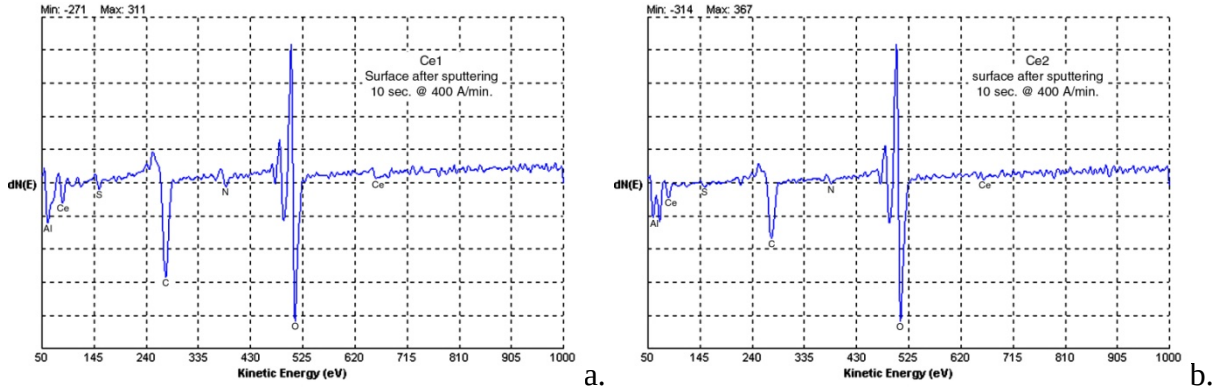

Figure 172. Auger electron Spectroscopy Scans of AA7075 after exposure to (a) 0.05 mol/L and (b) 0.005 mol/L cerium for 24 hours and 10 seconds at 400 Å/min sputtering.

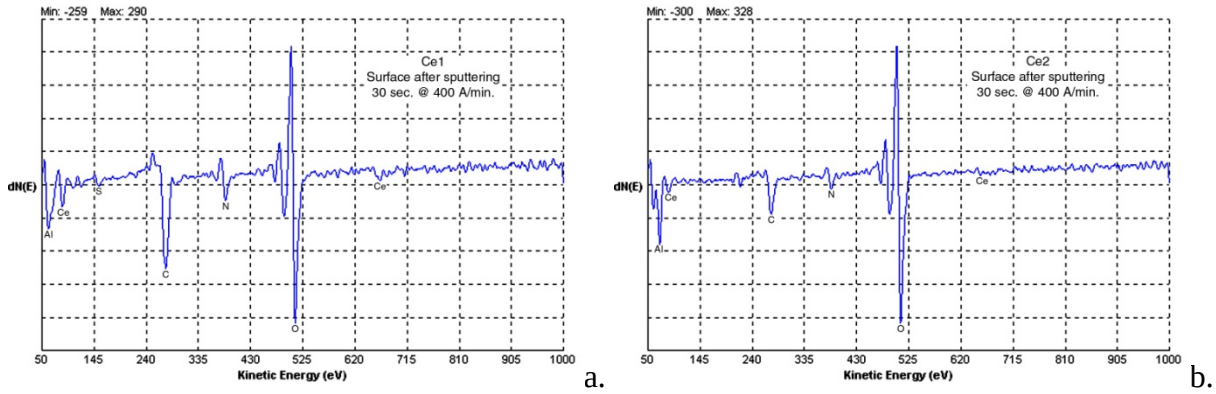

Figure 173. Auger electron Spectroscopy Scans of AA7075 after exposure to (a) 0.05 mol/L and (b) 0.005 mol/L cerium for 24 hours and 30 seconds at 400 Å/min sputtering.

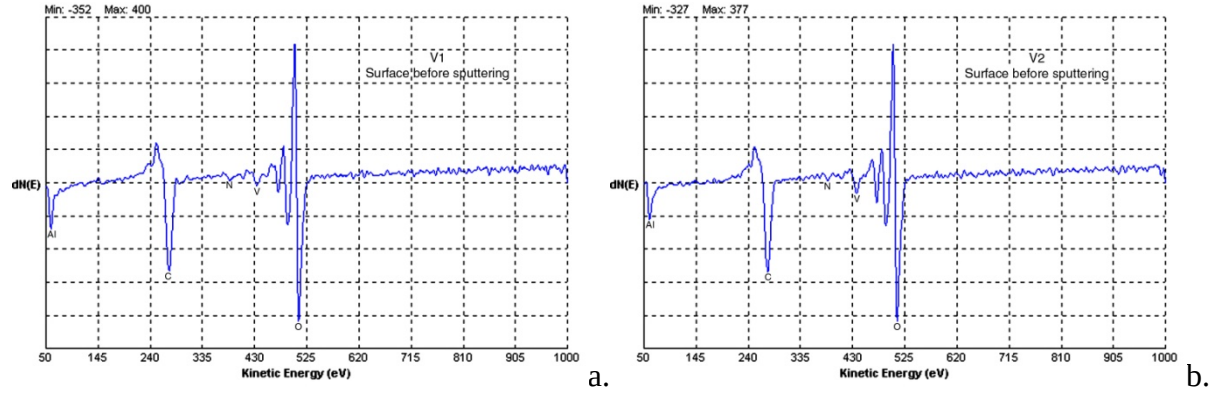

Figure 174. Auger electron Spectroscopy Scans of AA7075 after exposure to (a) 0.05 mol/L and (b) 0.005 mol/L vanadate for 24 hours.

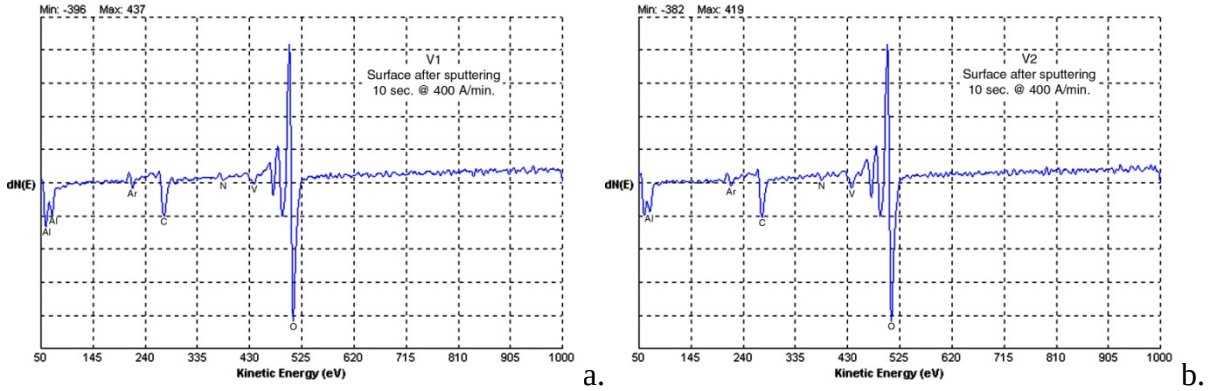

Figure 175. Auger electron Spectroscopy Scans of AA7075 after exposure to (a) 0.05 mol/L and (b) 0.005 mol/L vanadate for 24 hours and 10 seconds at 400 Å/min sputtering.

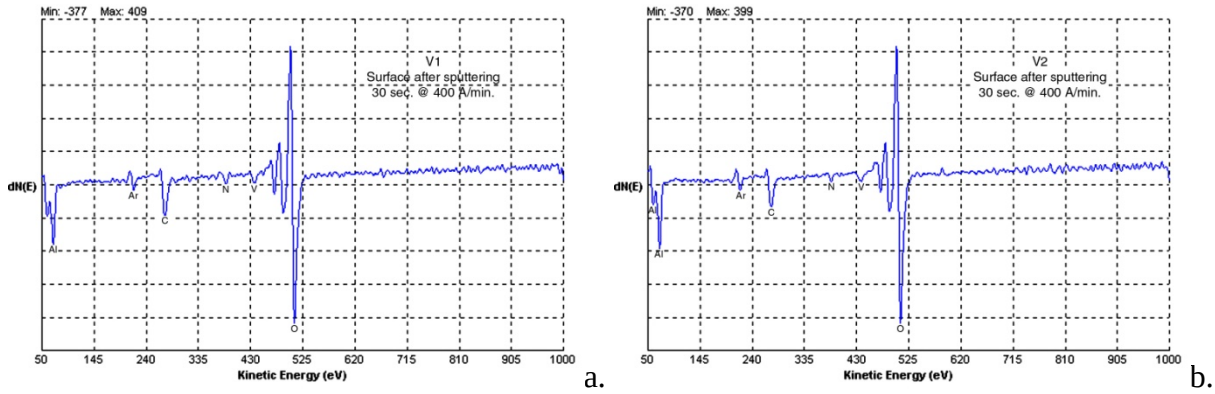

Figure 176. Auger electron Spectroscopy Scans of AA7075 after exposure to (a) 0.05 mol/L and (b) 0.005 mol/L vanadate for 24 hours and 30 seconds at 400 Å/min sputtering.

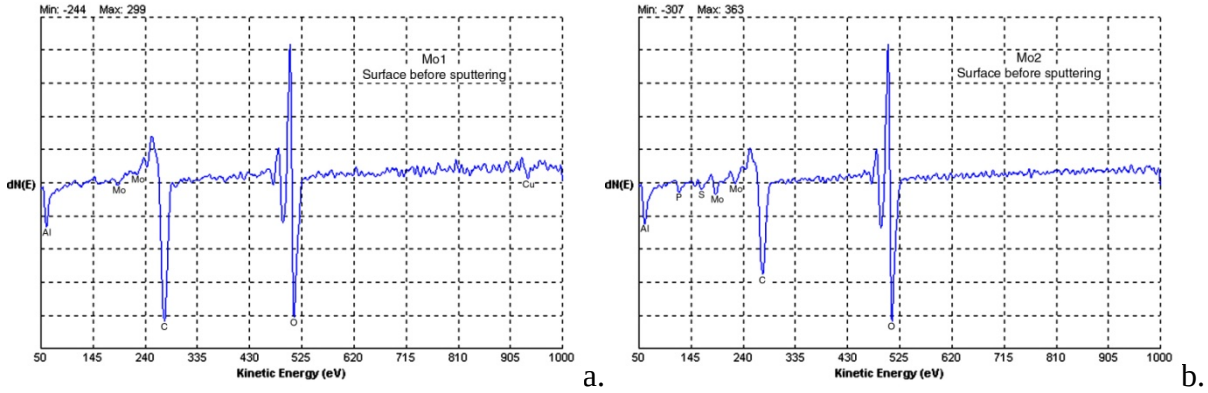

Figure 177. Auger electron Spectroscopy Scans of AA7075 after exposure to (a) 0.05 mol/L and (b) 0.005 mol/L molybdate for 24 hours.

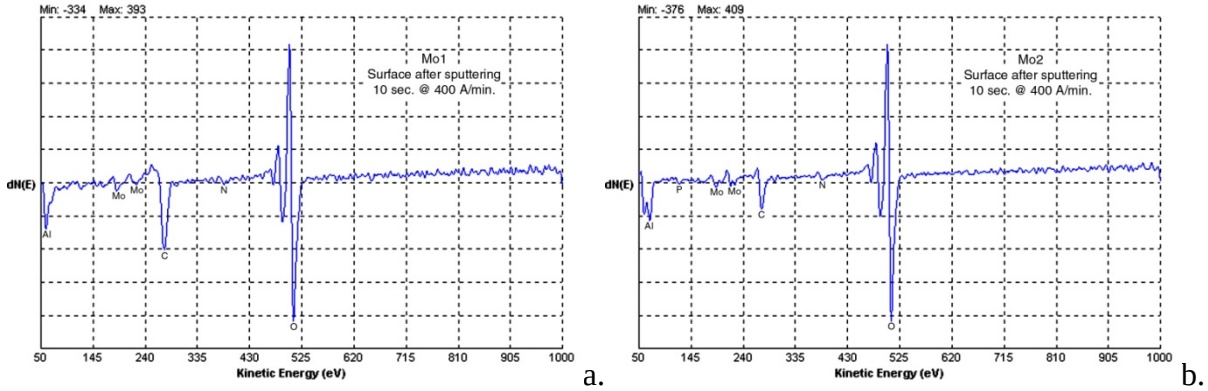

Figure 178. Auger electron Spectroscopy Scans of AA7075 after exposure to (a) 0.05 mol/L and (b) 0.005 mol/L molybdate for 24 hours and 10 seconds at 400 Å/min sputtering.

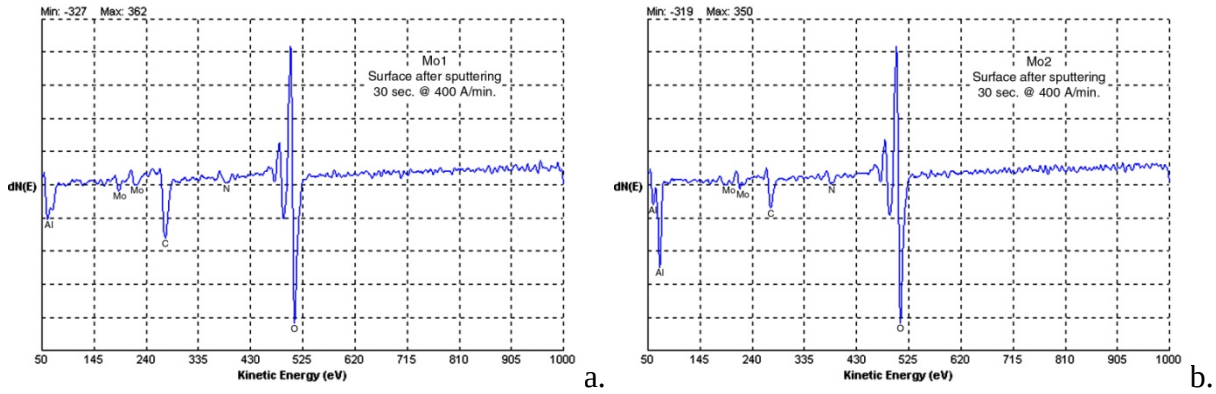

Figure 179. Auger electron Spectroscopy Scans of AA7075 after exposure to (a) 0.05 mol/L and (b) 0.005 mol/L molybdate for 24 hours and 30 seconds at 400 Å/min sputtering.

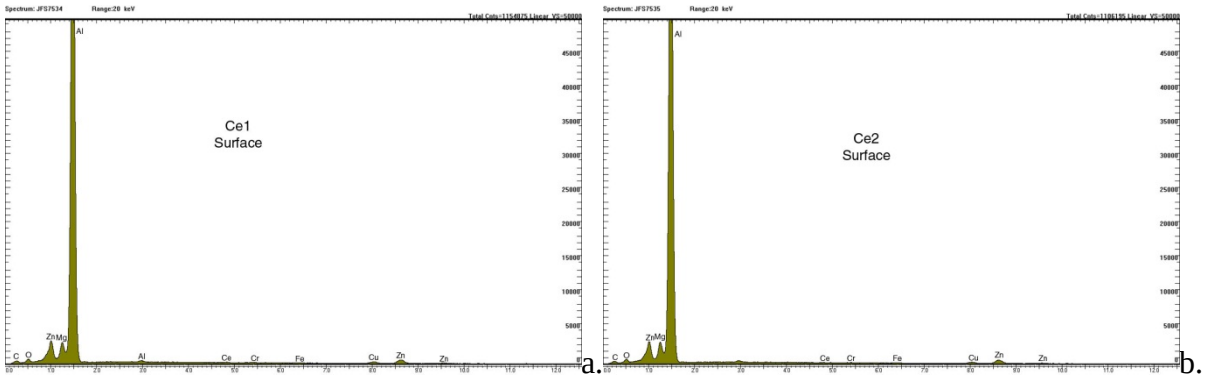

Figure 180. EDS of AA7075 after exposure to (a) 0.05 mol/L and (b) 0.005 mol/L cerium for 24 hours.

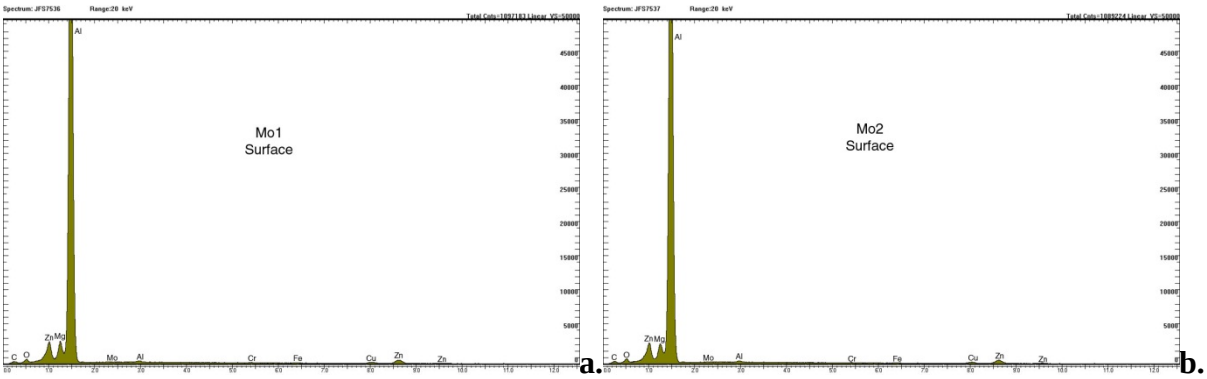

Figure 181. EDS of AA7075 after exposure to (a) 0.05 mol/L and (b) 0.005 mol/L molybdate for 24 hours.

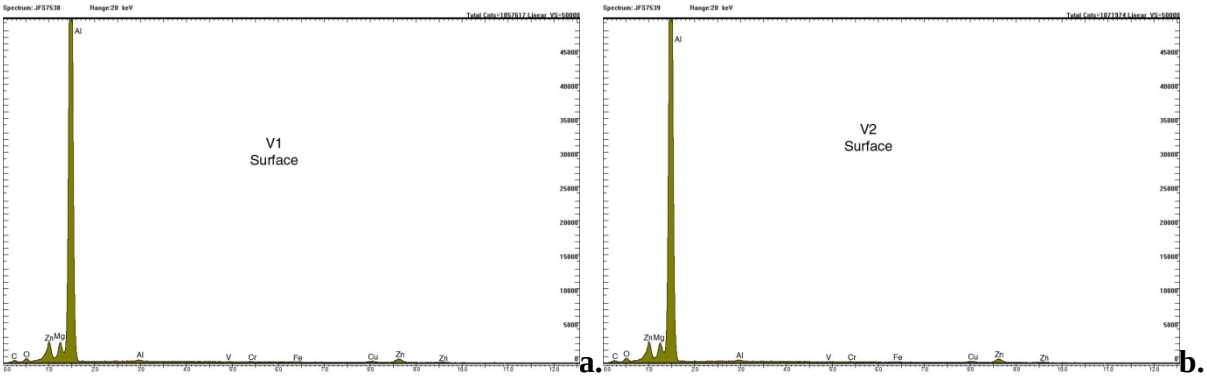

Figure 182. EDS of AA7075 after exposure to (a) 0.05 mol/L and (b) 0.005 mol/L vanadate for 24 hours.

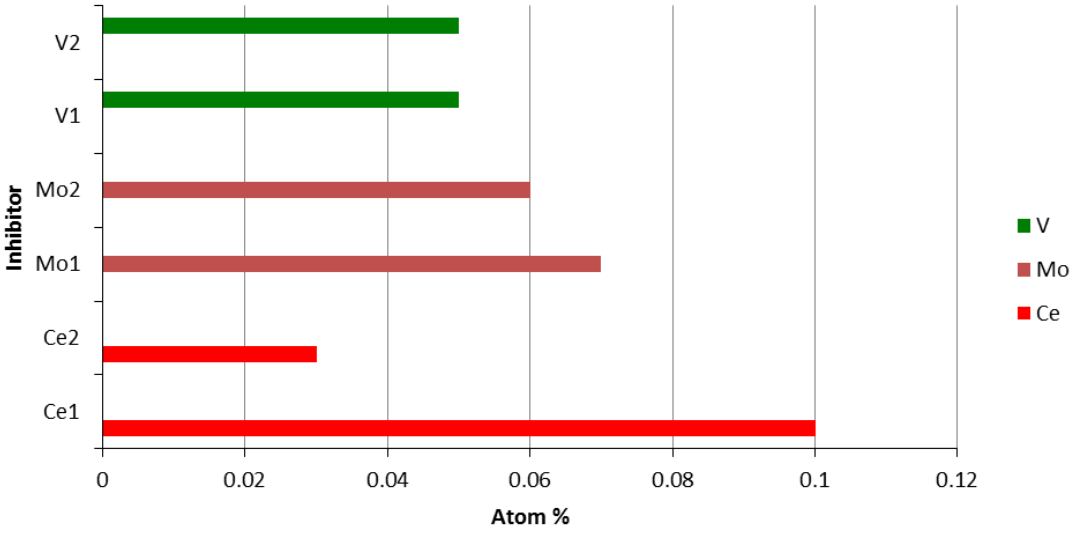

Figure 183. Surface analysis performed using EDS on AA7075 after 24 hours exposure to 0.05 mol/L (*inh*1) and 0.005 mol/L (*inh*2) molybdate, cerium and vanadate.

EDS mapping was performed on large area of AA7075 containing multiple intermetallic particles as well as on single particles. The specimens were exposed to 0.05 mol/L of inhibitor solution (cerium, molybdate or vanadate). EDS mapping was performed before and after exposure on the same or similar area. The mapping was performed for aluminum, iron and copper, in order to identify the type of IMC, as well as for the type of inhibitor used. The EDS maps before exposure are shown in Figure 184, Figure 187 and Figure 190. The large (approximately 200 μm^2) and small frames(approximately 25 μm^2) after exposure to the inhibitors are shown in Figure 185 and Figure 186, Figure 188 and Figure 189, and Figure 191 and Figure 192, for cerium, vanadate and molybdate, respectively.

In the case of cerium and molybdate, a very small number of precipitated particles were observed on the surface. The size of those precipitates was too small to allow for identification using EDS mapping, however, it may be hypothesized that they are inhibitors precipitates. It can also be assumed that the inhibitor precipitated homogeneously over the surface of the AA7075 specimens. Vanadate precipitates as vanadium-rich particles in large quantity over the surface independently form the presence of intermetallic particles.

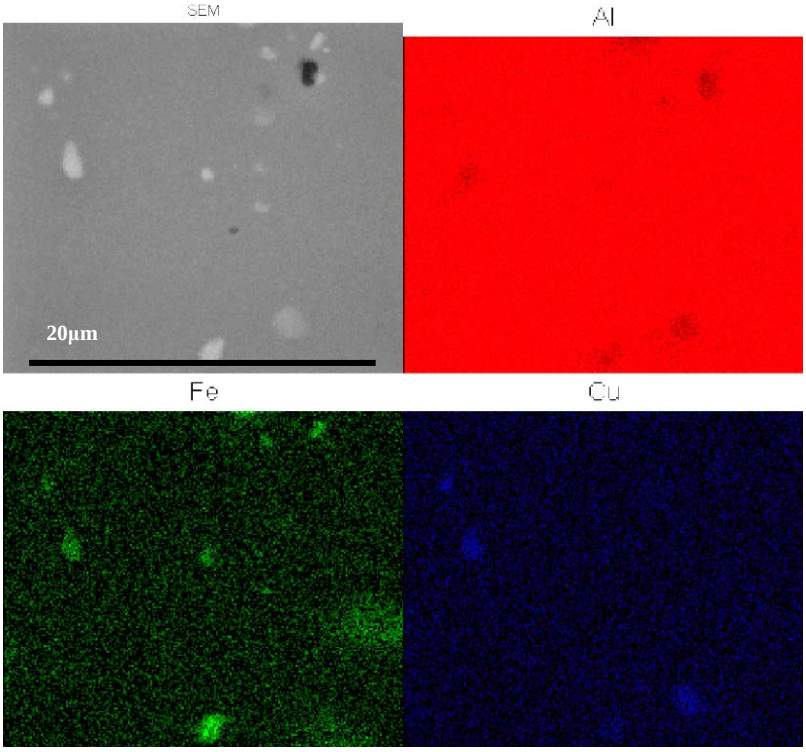

Figure 184. EDS mapping of AA 7075 before 24 hours immersion in 0.05 mol/L cerium acetate. 200 μm^2 frame.

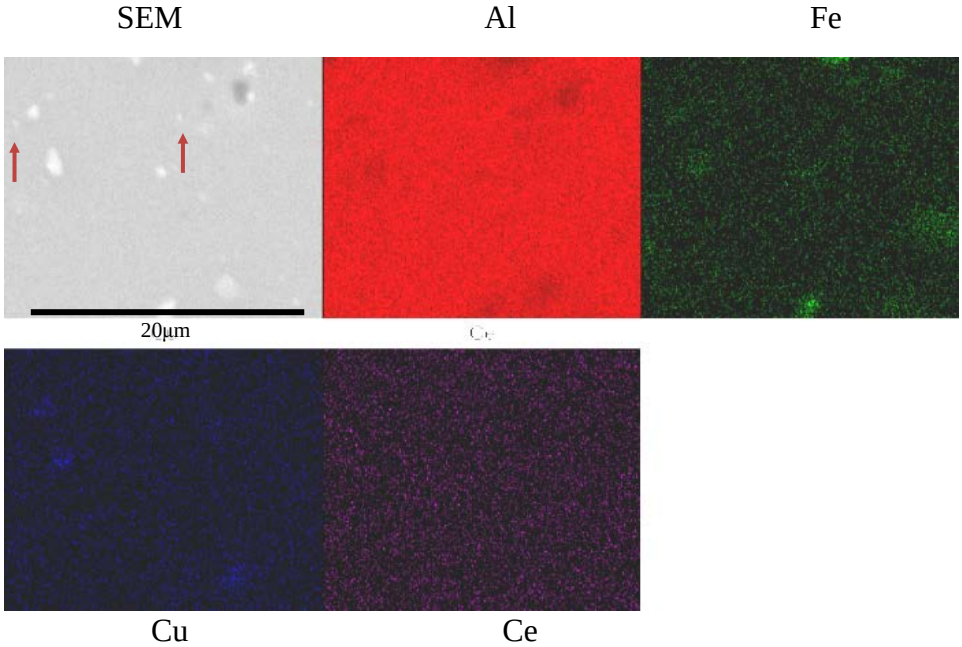

Figure 185. EDS mapping of AA 7075 after 24 hours immersion in 0.05 mol/L cerium acetate. 200 µm^2 frame. The hypothesized inhibitor precipitates are indicated with the red arrows.

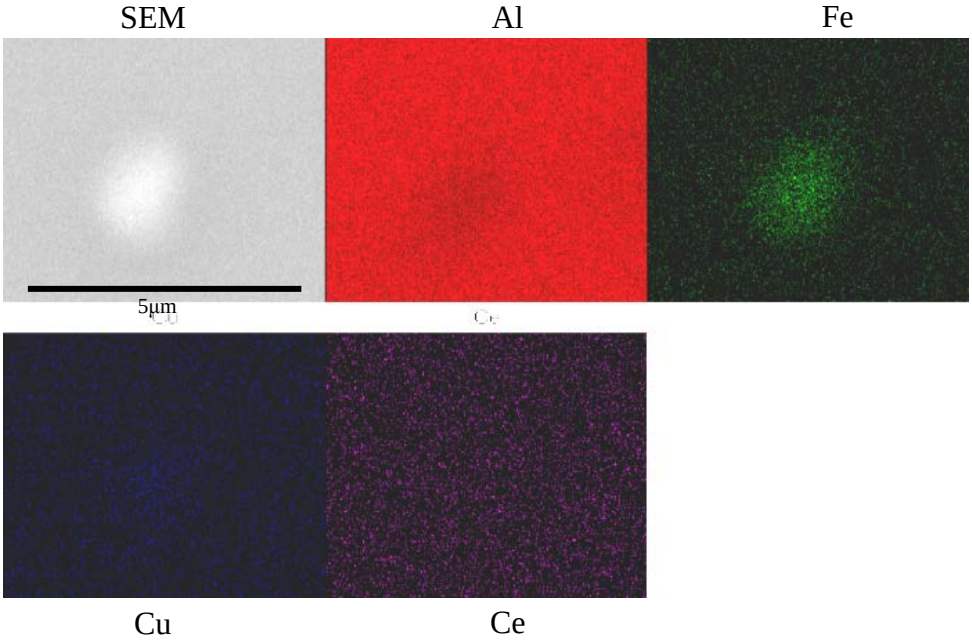

Figure 186. EDS mapping of AA 7075 after 24 hours immersion in 0.05 mol/L cerium acetate. 25 µm^2 frame.

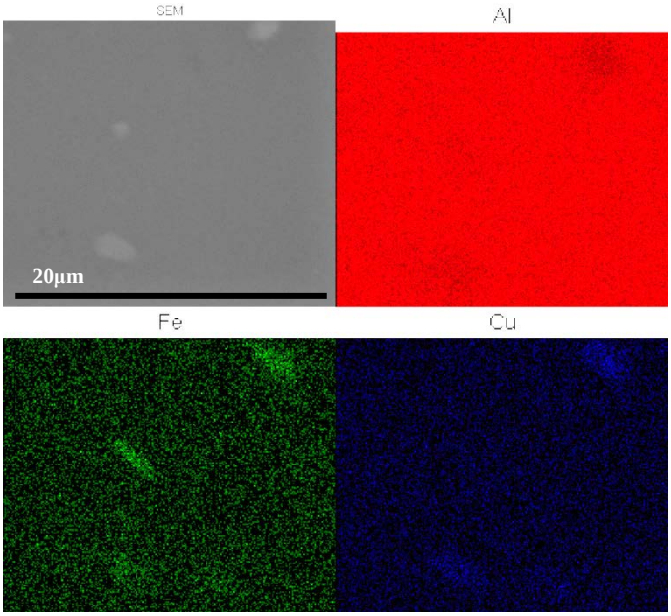

Figure 187. EDS mapping of AA 7075 before 24 hours immersion in 0.05 mol/L sodium vanadate. 200 µm^2 frame.

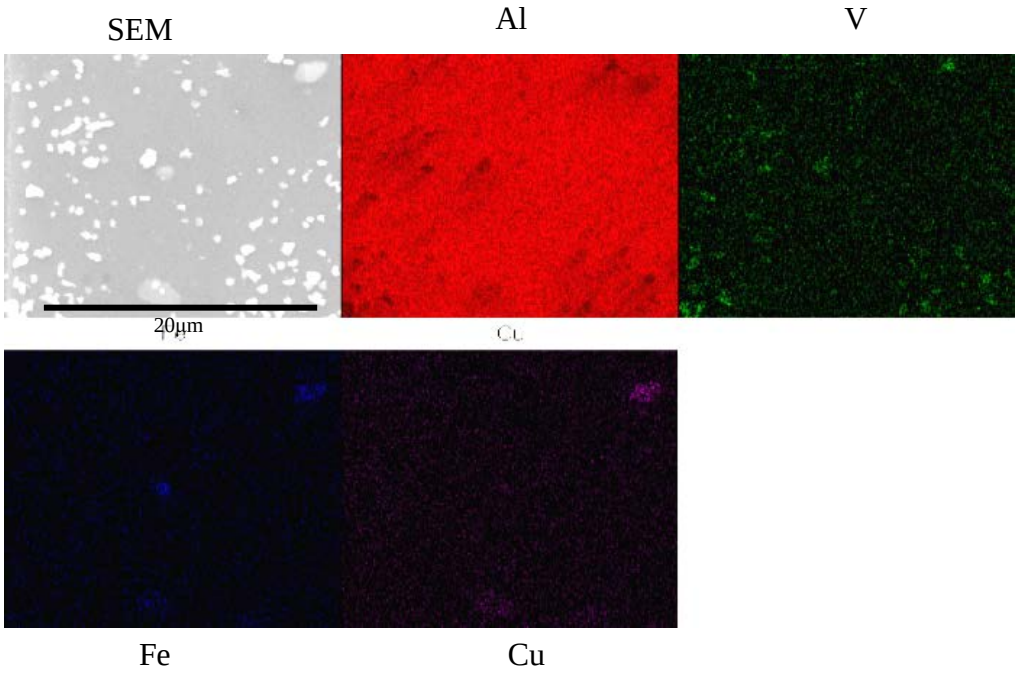

Figure 188. EDS mapping of AA 7075 after 24 hours immersion in 0.05 mol/L sodium vanadate. 200 µm^2 frame.

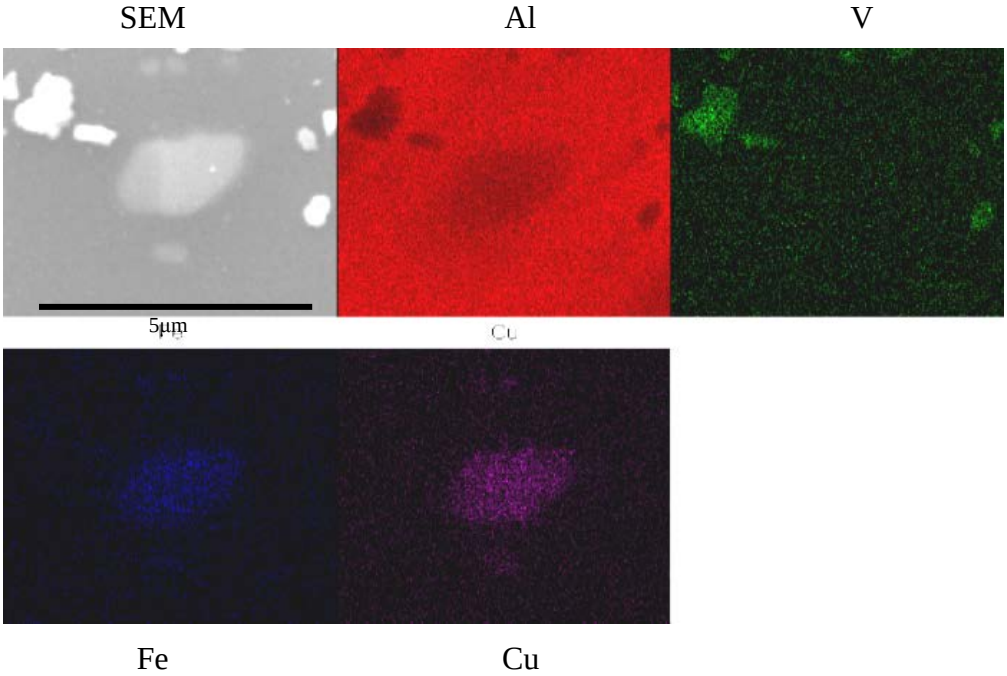

Figure 189. EDS mapping of AA 7075 after 24 hours immersion in 0.05 mol/L sodium vanadate. 25 µm^2 frame.

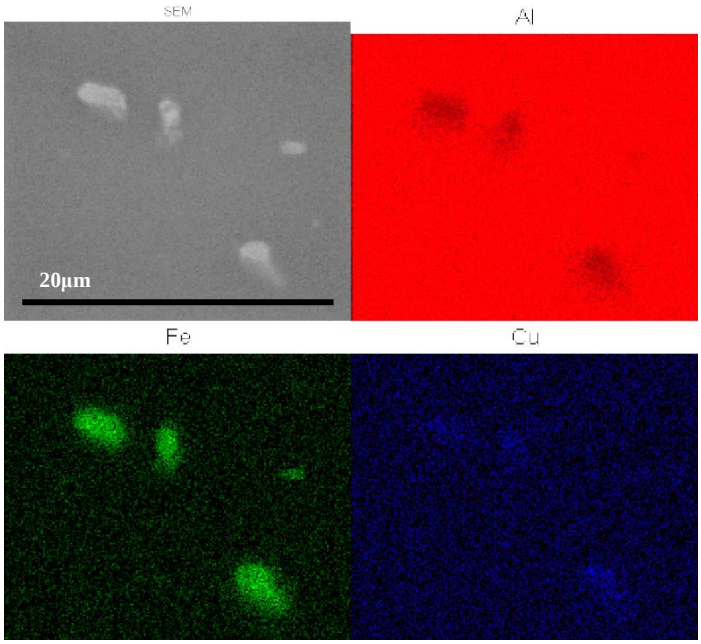

Figure 190. EDS mapping of AA 7075 before 24 hours immersion in 0.05 mol/L sodium molybdate. 200 µm^2 frame.

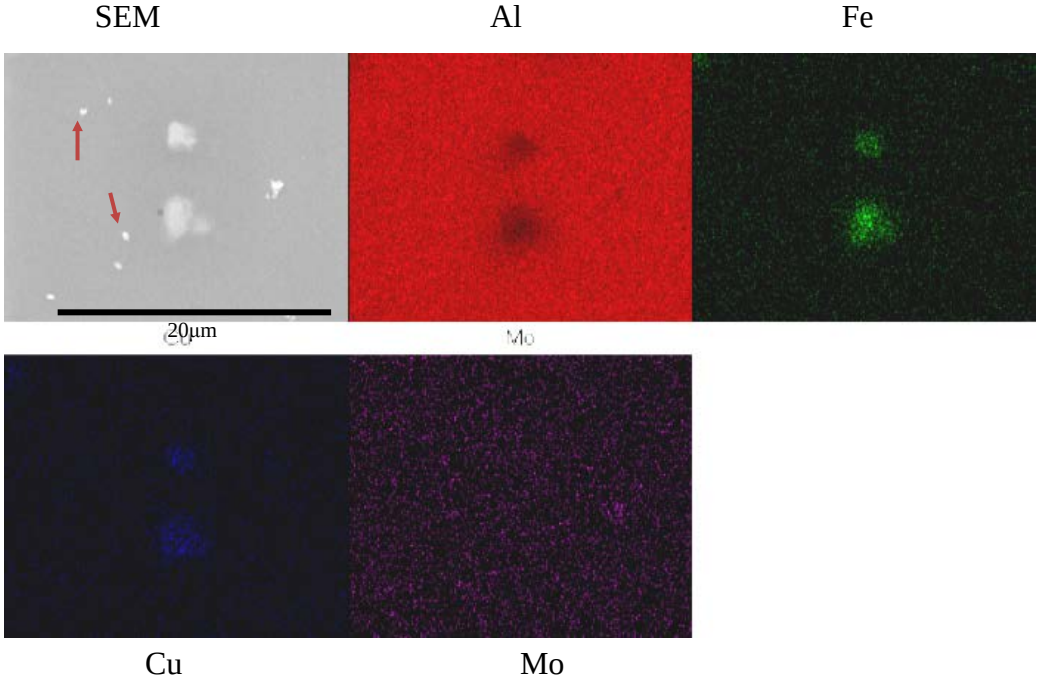

Figure 191. EDS mapping of AA 7075 after 24 hours immersion in 0.05 mol/L sodium molybdate. 200 µm^2 frame. The hypothesized inhibitor precipitates are indicated with the red arrows.

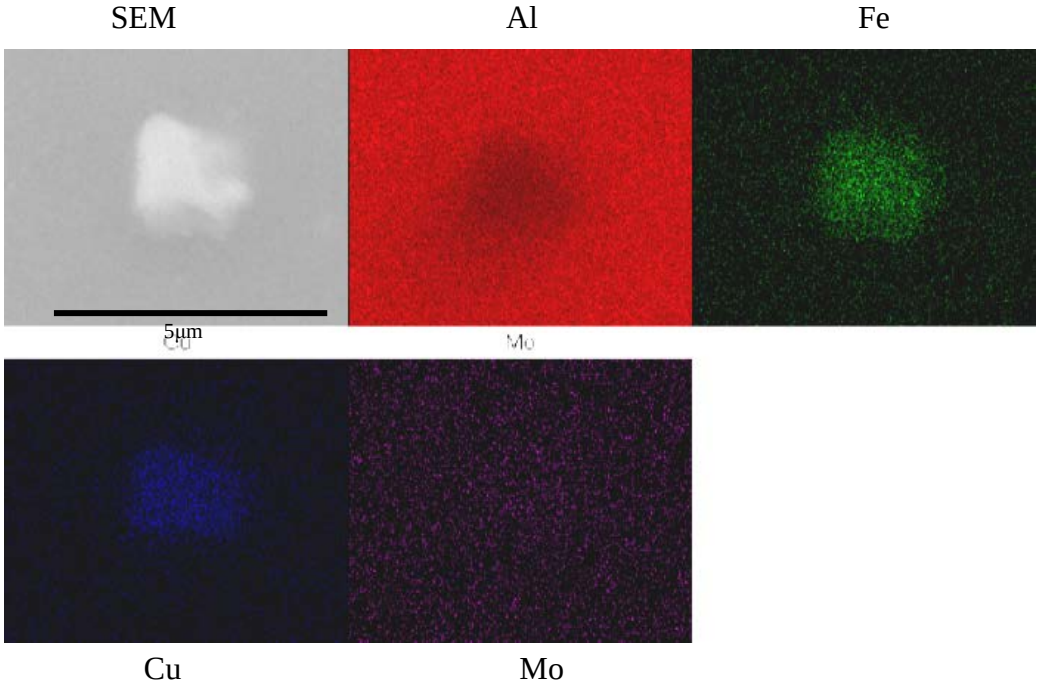

Figure 192. EDS mapping of AA 7075 after 24 hours immersion in 0.05 mol/L sodium molybdate. 25 µm^2 frame.

The presence of vanadium precipitates can be related to what has been observed on AA2024-T3 specimens (see Figure 57). Vanadate was found to result in vanadium-rich precipitate on the surface for both AA2024-T3 and AA7075. It was found that that the vanadium-rich particles precipitated preferentially on intermetallic particles in the case of AA2024-T3. However, in the case of AA7075, no preferential precipitation was observed. The density of vanadium-rich precipitates is much higher on AA7075 than for AA2024-T3, as can be observed by comparing Figure 54 with Figure 188.

Scanning Kelvin Probe (SKP)

Topographic and work function scans of copper before and after exposure to inhibitors and controlled relative humidity environment were performed using a SKP. The scans for a pure copper specimen before and after exposure to sodium molybdate are shown in Figure 193 and Figure 194, respectively. The scans for a specimen before and after exposure to sodium vanadate are shown in Figure 195 and Figure 196, respectively. It is possible to survey the surface morphology of the specimens using the topography scans. However the work function scans did not show any difference between the before and after state for either of the inhibitors.

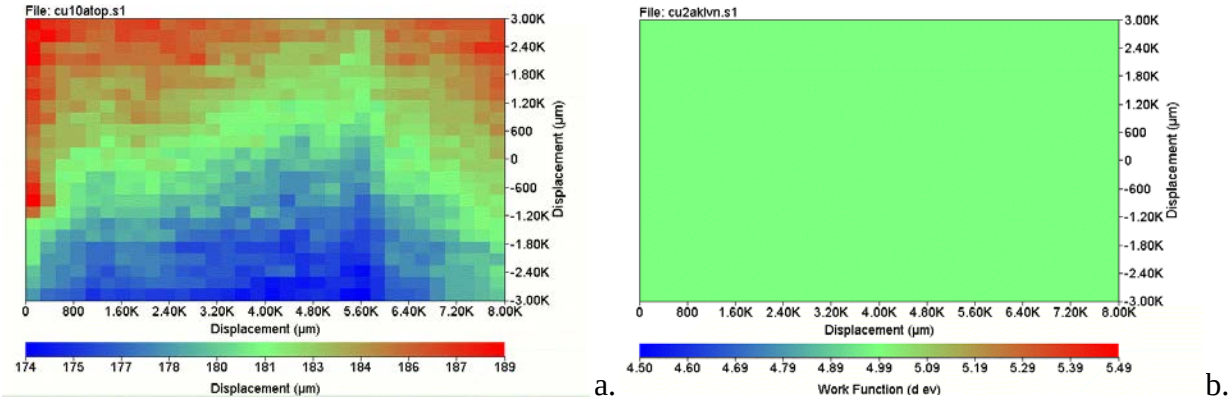

Figure 193. (a) topographic scan and (b) work function scan of a pure copper specimen before being exposed to 0.05 M sodium molybdate.

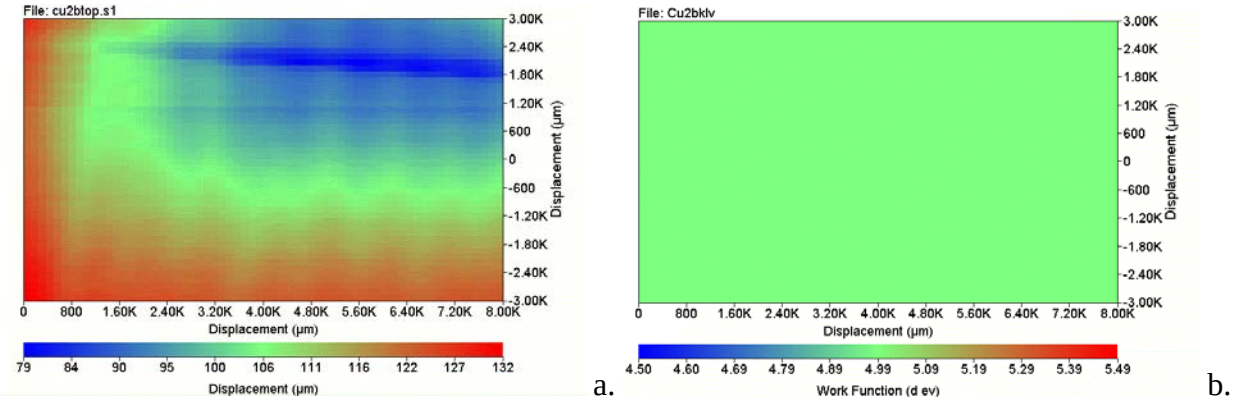

Figure 194. (a) topographic scan and (b) work function scan of a pure copper specimen after being exposed to 0.05 M sodium molybdate.

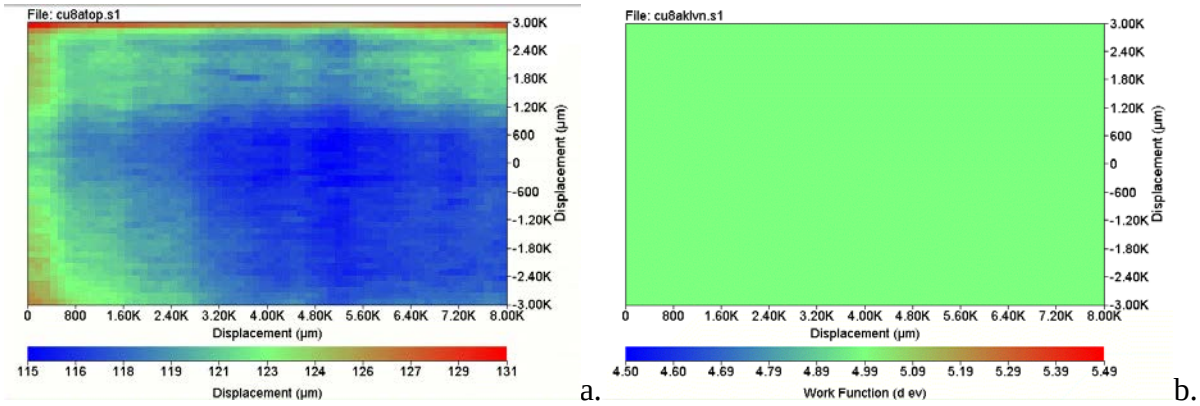

Figure 195. (a) topographic scan and (b) work function scan of a pure copper specimen before being exposed to 0.05 M sodium vanadate.

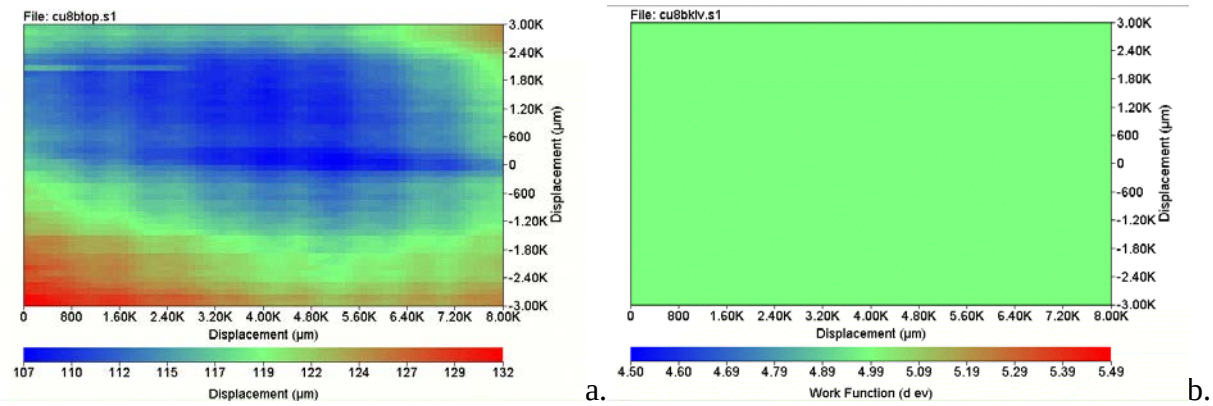

Figure 196. (a) topographic scan and (b) work function scan of a pure copper specimen after being exposed to 0.05 M sodium vanadate.

Mott-Schottky (M-S)

M-S experiments were used in order to determine the prevalent corrosion inhibition mechanism of the individual inhibitors in order to understand why they are effective in inhibiting corrosion of certain alloys. M-S analysis allowed the determination of the adsorption properties of chosen inhibitors onto oxide surface as a function of surface properties. M-S measurements can be performed on oxide films formed on the surface of alloys in solution as shown in Figure 18. M-S data provides information regarding the charge carrier density and the E_{FB} which is closely related to the surface energy of the solid. The flat band potential is taken as the point where the extrapolated line crosses the x-axis. A positive shift in flatband potential is accompanied by an increase in the localized E_{corr}. The inverse of the capacitance squared can be plotted against the potential, according to Equation 35. [C_{SC}, the capacitance of the space charge region; e, the dielectric constant of the passive film; e_0, the permittivity of free space; N, the donor density (electron donor concentration for an n-type semi-conductor or hole acceptor concentration for a p-type semi-conductor); E, the applied potential and E_{FB}, the flatband potential].

$$\frac{1}{C_{SC}^2} = \frac{2}{e\varepsilon\varepsilon_0 N}\left(E - E_{FB} - \frac{kT}{e}\right) \qquad \textbf{Equation 35}$$

The results of Mott-Schottky analysis in 0.05 M cerium acetate are shown in Figure 197. The slope of $1/C^2$ vs. potential is positive for both borate buffer (control) and Ce-acetate. Consequently, it can be concluded that the cerium treated oxide layer has the properties of a n-type semiconductor. The flatband potential measured on a passive film grown in cerium acetate is approximately 600 mV lower than that measured for a passive film grown in borate buffer. Consequently, cathodic inhibition by cerium is predicted to occur.

The effects of the type and concentration of inhibitor are shown in Figure 198: 0.05 M of vanadate results in a significant negative shift of the flatband potential. Consequently, it is expected that E_{pit} may increase based upon the semiconductor properties resulting from the interaction of the vanadate with the specimens oxide film layer. Addition of lower amount of inhibition (0.005 M) results in lower flatband potential for both cerium and vanadate. Furthermore, a lower flatband potential is still observed for vanadate than for cerium. Therefore, it is expected that cerium and vanadate will be more successful inhibitors at 0.005 M than 0.05 M, and vanadate will be a more successful inhibitor than cerium, independently from the concentration.

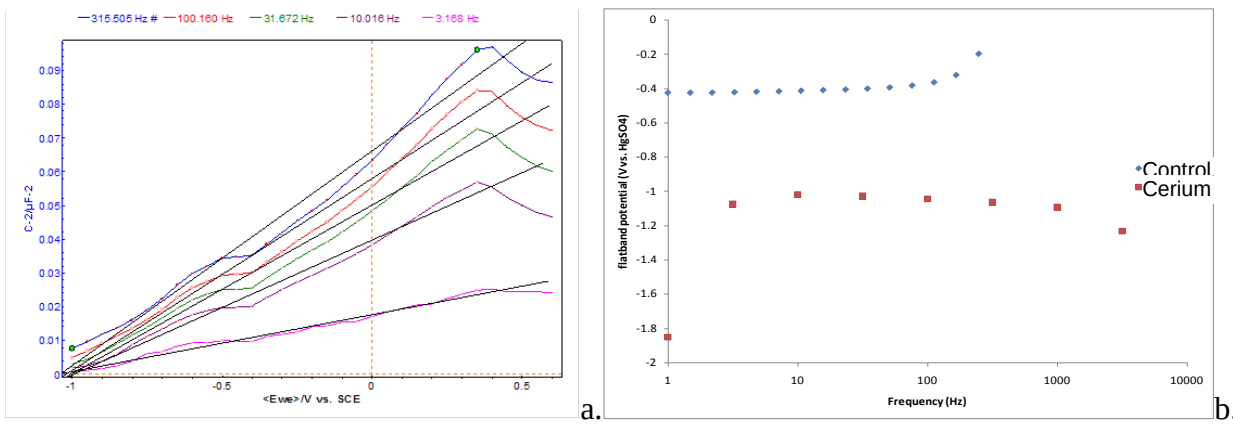

a. b.

Figure 197. Mott-Schottky analysis results in 0.05 M cerium acetate. (a) Evolution of $1/C^2$ as a function of the applied potential at various frequencies. (b) Flatband potential (V vs. $HgSO_4$) as a function of the frequency.

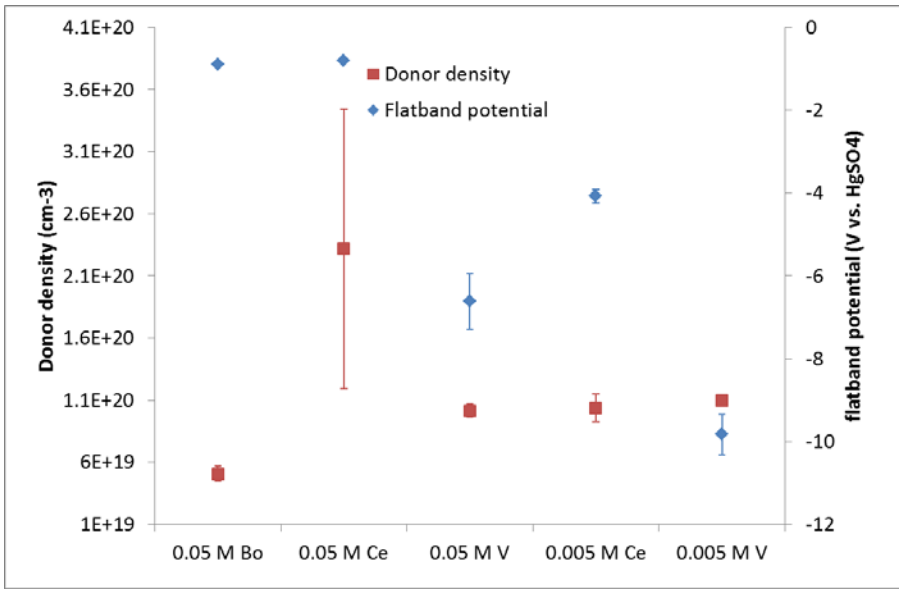

Figure 198. Donor density and flatband potential for 0.05 M and 0.005 M cerium acetate and vanadate.

Atmospheric MEA

MEAs (80% aluminum/20% copper) were exposed to controlled atmospheric environments after being treated with inhibitors. This was performed to assess the effect of cerium acetate, sodium vanadate and sodium molybdate during atmospheric corrosion.

The current was measured as the MEA was exposed to a high relative humidity for 3 hours followed by 2.5 hours at 45% relative humidity. Figure 199 shows the evolution of the total anodic and cathodic currents measured on a cerium-treated MEA with high level of relative humidity of 60%, 70%, 80% and 90%. Figure 200 and Figure 201 show the same measurements for a vanadate and a molybdate treated MEA, respectively. It can be noticed that the total current decreases overall as the value of the high relative humidity increases. The current drops drastically when the relative humidity is decreased to 45%. Figure 202 shows the evolution of the total current measured on an untreated MEA with high level of relative humidity of 60%, 70%, 80% and 90%. The total current measured on the untreated MEA decreases as the first part of the test is performed at a higher relative humidity. The current decreases when the relative humidity is shifted to 45%. However, the total current is not zero, unlike for the treated MEA. Furthermore, overall, the total current measured in the case of the untreated MEA is higher than for the cerium-treated MEA.

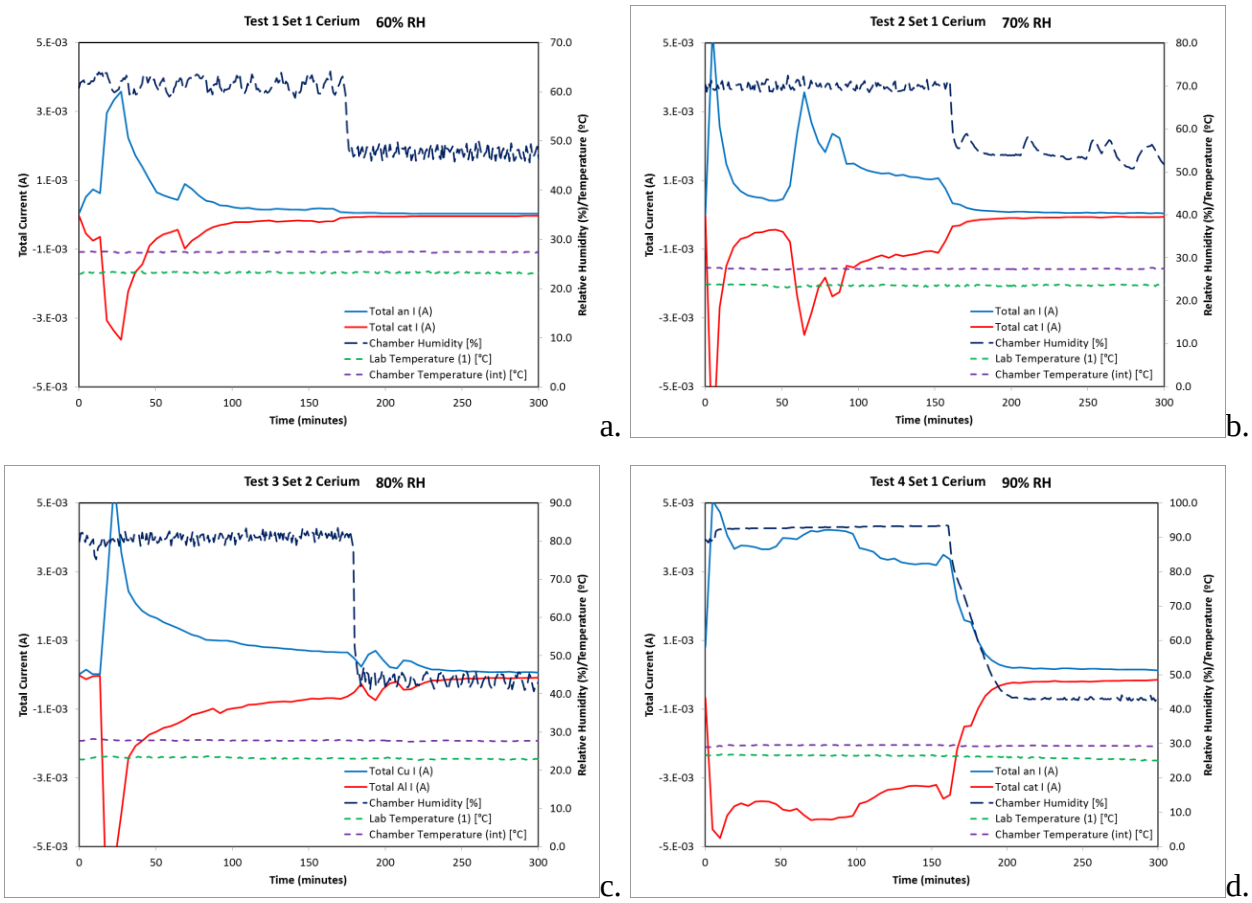

Figure 199. Total current measured on Al/Cu MEA treated with 0.05 M cerium acetate for 24 hours. The current are measured during (a) 3 hours at 60% RH and 2.5 hours at 45% RH, (b) 3 hours at 70% RH and 2.5 hours at 45% RH, (c) 3 hours at 80% RH and 2.5 hours at 45% RH, and (d) 3 hours at 90% RH and 2.5 hours at 45% RH. The test chamber relative humidity and temperature, and room temperature are also plotted.

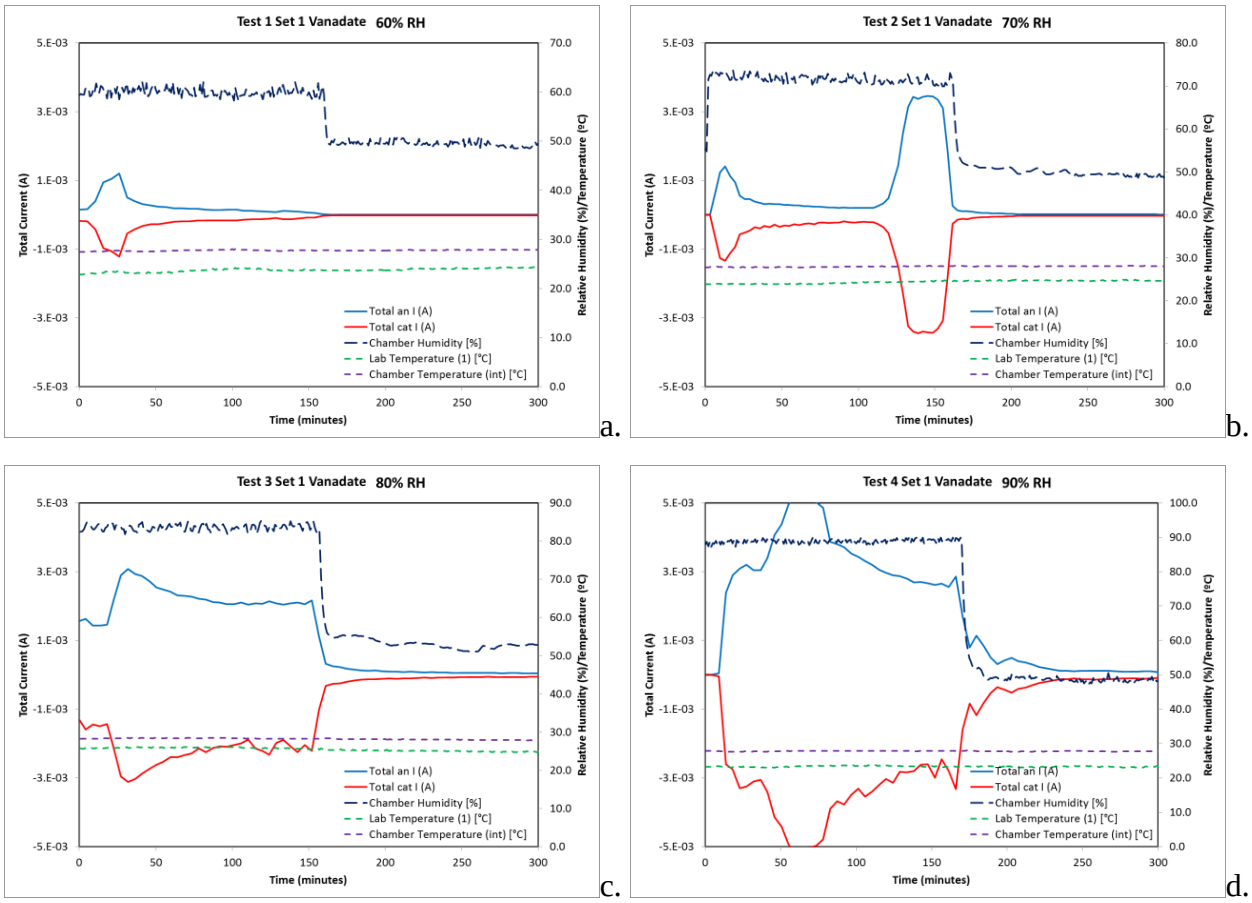

Figure 200. Total current measured on Al/Cu MEA treated with 0.05 M sodium vanadate for 24 hours. The current are measured during (a) 3 hours at 60% RH and 2.5 hours at 45% RH, (b) 3 hours at 70% RH and 2.5 hours at 45% RH, (c) 3 hours at 80% RH and 2.5 hours at 45% RH, and (d) 3 hours at 90% RH and 2.5 hours at 45% RH. The test chamber relative humidity and temperature, and room temperature are also plotted.

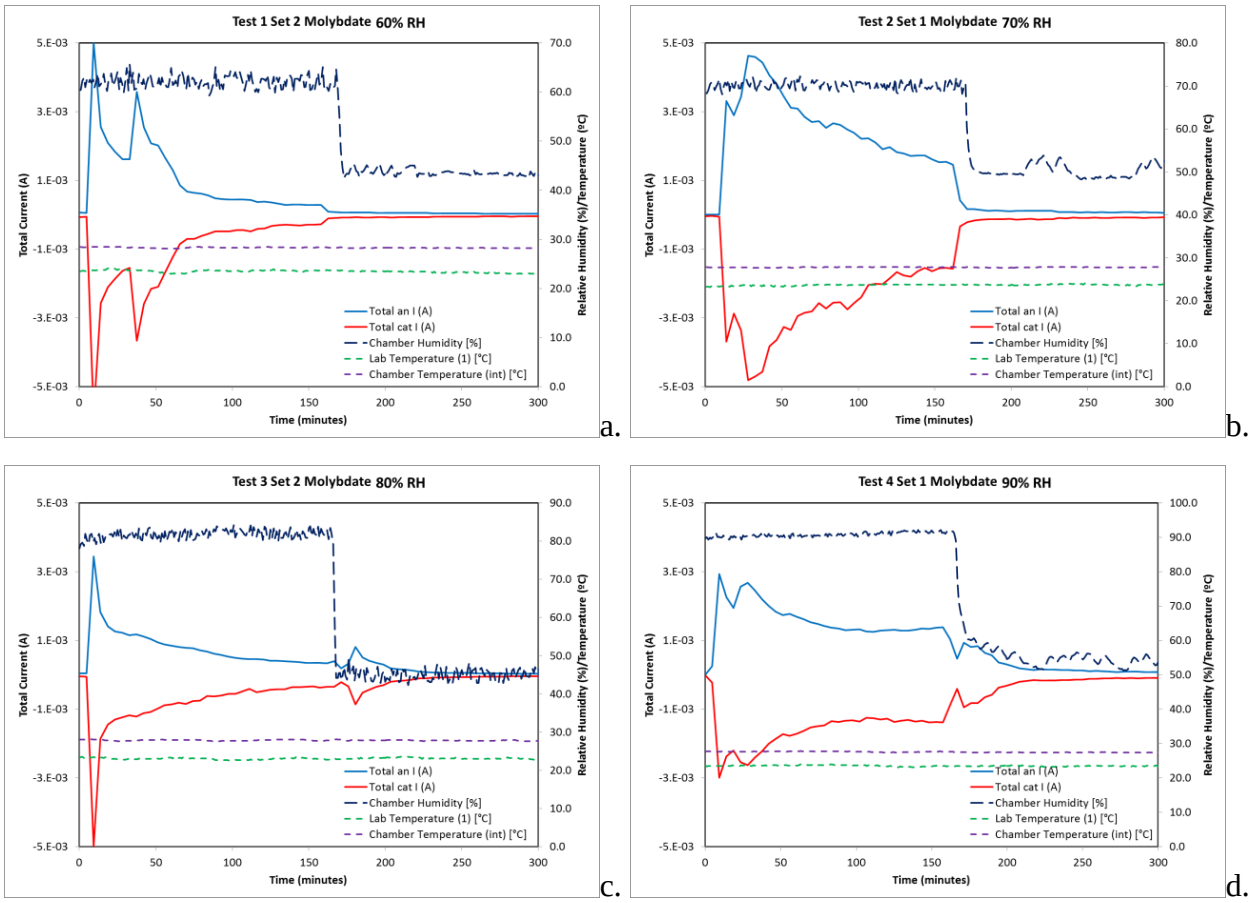

Figure 201. Total current measured on Al/Cu MEA treated with 0.05 M sodium molybdate for 24 hours. The current are measured during (a) 3 hours at 60% RH and 2.5 hours at 45% RH, (b) 3 hours at 70% RH and 2.5 hours at 45% RH, (c) 3 hours at 80% RH and 2.5 hours at 45% RH, and (d) 3 hours at 90% RH and 2.5 hours at 45% RH. The test chamber relative humidity and temperature, and room temperature are also plotted.

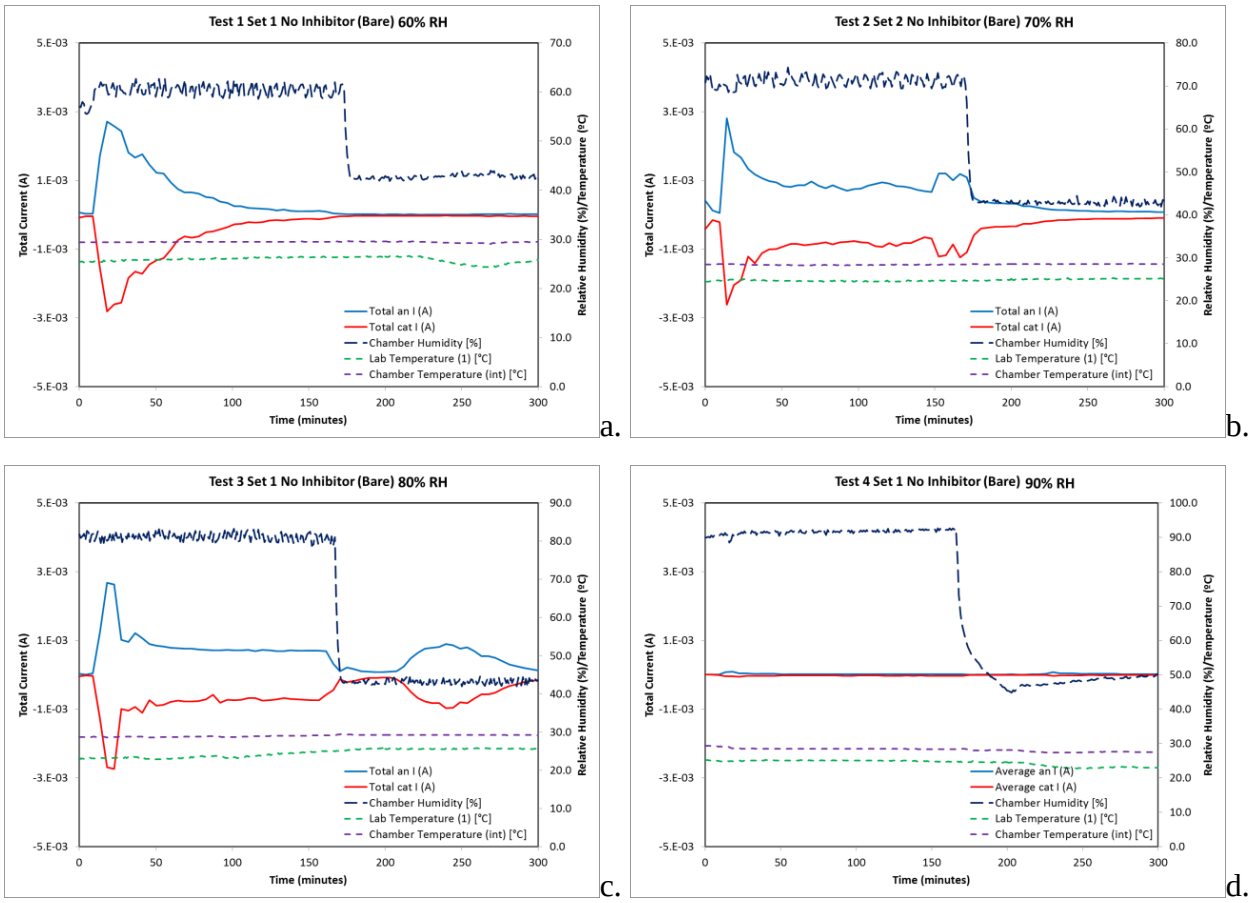

Figure 202. Total current measured on Al/Cu MEA untreated. The current are measured during (a) 3 hours at 60% RH and 2.5 hours at 45% RH, (b) 3 hours at 70% RH and 2.5 hours at 45% RH, (c) 3 hours at 80% RH and 2.5 hours at 45% RH, and (d) 3 hours at 90% RH and 2.5 hours at 45% RH. The test chamber relative humidity and temperature, and room temperature are also plotted.

In order to accurately compare the effect of the various inhibitors and relative humidity values, the total anodic charge was plotted at the end of the first relative humidity step (after 150 minutes (see Figure 203) and at the end of the test (after 330 minutes (see Figure 204)). The total anodic charge plots were also linearly fitted.

Both vanadate and cerium act as an inhibitor based upon the total anodic exchanged after 150 minutes exposure (Figure 203) and 330 minutes exposure (Figure 204) at lower relative humidity (60% and 70%). The total anodic charge measured on a molybdate treated MEA implies that it does not behave as an inhibitor on the Al/Cu MEA. At higher relative humidity (80% and 90%), vanadate and cerium lose their inhibitive capability. This is thought to be due to the fact that droplets of very high chloride concentration deliquesce, under which conditions the inhibitors cannot retain the inhibitor properties.

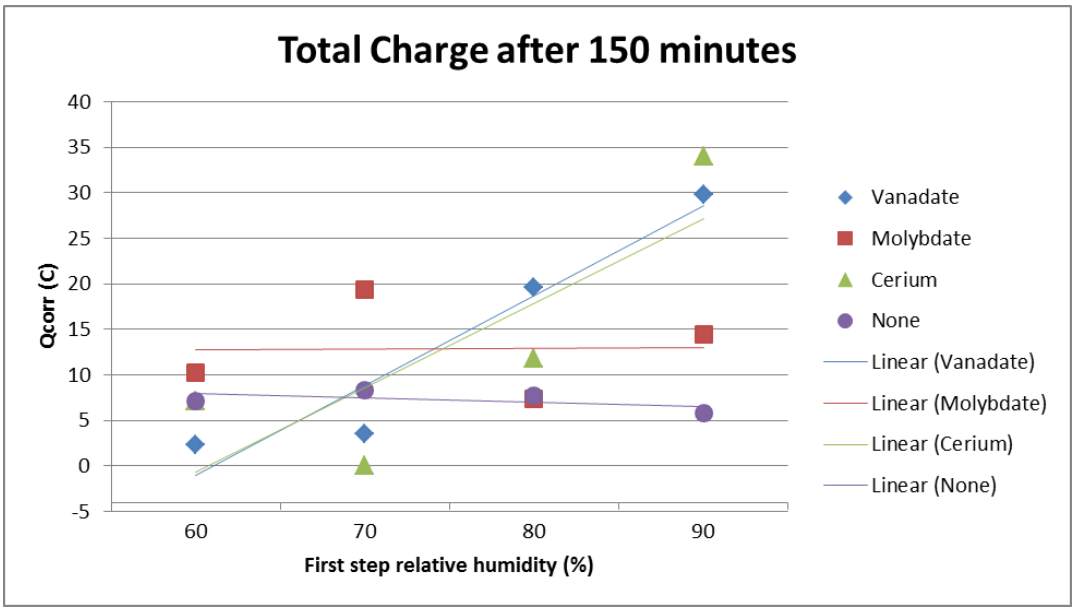

Figure 203. Total anodic charge as a function of the relative humidity and inhibitor treatment after 150 minutes exposure at high relative humidity.

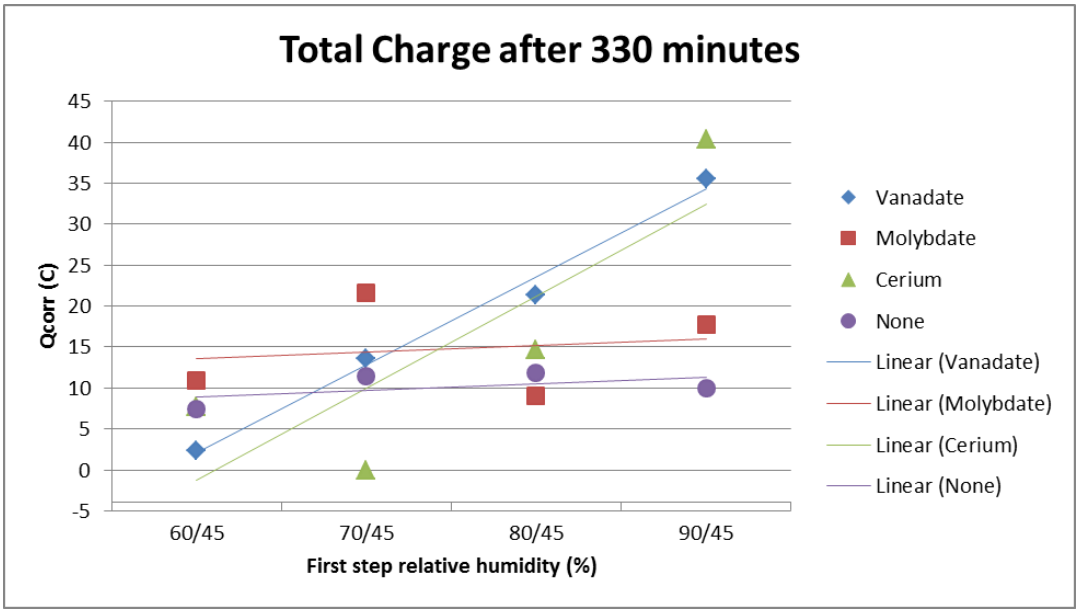

Figure 204. Total anodic charge as a function of the relative humidity and inhibitor treatment after 330 minutes exposure at high relative humidity.

Discussion

Corrosion Inhibition of AA2024 using Permanganate and Vanadate

Oxidation States of Manganese

The oxidation state of the manganese oxide deposits is critical to the understanding of this inhibitor system. If the oxidation state has a high valence state the E-pH diagrams in Figure 2 suggest that the oxide deposits may be electrochemically active and eligible for further reduction at the open circuit of AA2024. This activity can manifest itself as the reduction of the oxide deposits to lower valence state oxides accompanied by aluminum oxidation. These oxide reactions may have some impact on the corrosion inhibition. It is useful for the discussion to give a brief example of our understanding of these manganese deposits. A galvanostatic reduction at -20 μA/cm^2, conducted in pH 10 borate buffer is shown in Figure 51. The multiple potential waves indicate that the oxide is reduced from a high valence state.[87] Evidence of this is also shown in Figure 31 at OCP and 49 upon downward scan. The reversible potentials of several likely reactions are indicated in Figure 51. The reversible potential of $MnO_4^- + 4H + +3e^- \leftrightarrow MnO_2 + 2H_2O$ at 0.54 V vs. SCE is shown by the (· ·) line. The reversible potential for $MnO_2 + H_2O + e^- \leftrightarrow MnOOH + OH^-$ at 0.187 V vs. SCE is shown by the (– –) line. The reversible potential for $MnOOH + H_2O + e^- \leftrightarrow Mn(OH)_2 + OH^-$ at -0.385 V vs. SCE is shown by the (– · –) line. This reduction path is supported in literature concerning the reduction of manganese oxides.[86,87,144] Raman spectroscopy (Figure 52) shows that the manganese species present on the Cu and analyzed by galvanostatic reduction is the same as that reduced onto AA2024-T351 at open circuit. It is sufficient to state that the manganese oxide present on the surface of the AA2024 has a high valence state and the potential to be reduced. The reduction of the oxide may play a role in understanding all of the activity of the inhibitor in a corrosive environment. The reduction of Mn(III) to Mn(II) has been shown to involve an aqueous pathway which may enable a manganese oxide deposit to selfheal over active cathodic sites through a homogeneous chemical reaction. The speciation of this aqueous reaction pathway has not been proposed in the literature.[144]

Active Corrosion Inhibition

Galvanostatic reductions (Figure 51), cathodic polarizations (Figure 49), and open circuit potentials (Figure 31) all indicate the presence of a high valence manganese species present on the surface of the AA2024-T351. The reduction of these species after their deposition has been made clear and can occur spontaneously coupled to Al, Mg oxidation. Manganese oxide literature shows that the reaction mechanism between the Mn(III) and Mn(II) valence states occurs through an aqueous pathway.[144,145] Evidence includes visible color changes to filter paper surrounding manganese oxide electrodes as they are reduced between the (III) and (II) valence states as well as from the standard half-cell potential of the Mn(II)-Mn(III) system. This reaction suggests soluble aqueous Mn(III) species are released in when deposited oxides are further reduced. This leads to the possibility of the release and utilization of manganese species on AA2024 located adjacent to a manganese deposit. Details on the potential of manganese oxide deposits to protect remote AA2024 electrodes will be examined in further investigations.

Modes of MnO_4^- Inhibition: Anodic

While the ORR is inhibited by the presence of Mn-oxides that result from permanganate reduction, elevation of E_{pit} is speculated to require the presence of a manganese oxide film-barrier formed over the aluminum matrix as seen in Figure 39.

Figure 42 shows the trends in the extent of the passive region (ΔE where $\Delta E = E_{pit} - E_{corr}$) as a function of inhibitor concentration. In both pretreatment and solution phase tests, the inhibitor raises ΔE as the inhibitor concentration was decreased. This is an interesting and somewhat counter-intuitive observation. The interpretation of this behavior is that various amounts of $KMnO_4$ are reduced onto Cu-rich sites during pretreatment. Lower $KMnO_4$ levels may deposit with less residual/unreduced Mn(VII). This can lower the OCP and increase ΔE by lowering E_{Corr}. Higher levels may induce pitting prior to blockage. This speculation is supported by Figure 30. In-situ inhibitor at low concentrations in the presence of an activating ion such as Cl^- produces a statistical increase in E_{pit}. The principle reason for this increase is speculatively believed to be the protective manganese oxide covering the S-phase as seen in Figure 38. We have shown that both MnO_4^- and Mn^{2+} do not inhibit when they are in solution. The inhibition is not seen on AA2024-T351 samples that have been exposed to the permanganate-chloride solution for 1 hour. Speculatively, the 24 hour exposure prior to the anodic polarization allows for the growth of the manganese oxide film covering and protecting the aluminum matrix and the S-phase. This is supported by the lack of manganese species in pitted areas examined via EDS.

Modes of MnO_4^- Inhibition: Cathodic

Permanganate functions as a cathodic inhibitor by growing Mn oxide caps over copper-rich intermetallic particles (Figure 24 and 29). This process occurs quickly at the natural pH of the permanganate solution and does not require any Cl^- activation. The oxide growth by direct electrochemical reduction of permanganate over the copper-rich intermetallics greatly reduces the total cathodic current density i_{Tot} as well as the diffusion limited current density i_D when used as a pretreatment (Figure 45(a)). The MnO_4^- ion is reduced providing an additional cathodic reactant that increases the cathodic current density when present in solution (Figure 45(b)). We will now examine the pretreatment case in more detail.

Using a model first utilized by Jakab [29,90,146] that combines the Gueshi and Membrane models, we can examine the controlling variables that limit the reduction of dissolved oxygen on a planar electrode. Where the diffusion limited current density i_D^* on a homogeneous planar electrode is given by Equation 36.

$$i_D^* = \mathrm{n}FDC/\delta \qquad \textbf{Equation 36}$$

were n is the number of electrons in the electrochemical reaction, D is the diffusion coefficient of the reactant, C is the bulk concentration of the reactant, and δ is the diffusion-affected zone. In a RDE experiment δ is proportional to $\omega^{-1/2}$ where ω is the rotation rate of the planar electrode.[132] The Gueshi and Membrane models enable the extension of the description of i_D^* to heterogeneous electrodes. Two effects can occur when oxide caps are grown over the intermetallic particle. The first is a change in the geometry and spacing of active regions in the inactive matrix as described by Gueshi in Equation 37.

$$i_D = \frac{i_D^*}{\sigma^2 - 1}\left[\sigma e^{-lt} - 1 + \sqrt{\pi\sigma^2}\sqrt{\frac{lt}{\sigma^2 - 1}}\exp\left(\frac{lt}{\sigma^2 - 1}\right)\left\{erf\left(\sigma\sqrt{\frac{lt}{\sigma^2 - 1}}\right) - erf\left(\sqrt{\frac{lt}{\sigma^2 - 1}}\right)\right\}\right]$$

Equation 37

In Equation 37, l is a geometric term describing the active-inactive array, and σ is a term that relates to the coverage of aluminum matrix (shown in Figure 205), by active sites or the coverage of active intermetallic sites (*erf* is the Gauss error function). As the caps grow one effect is the exposure of the effective active region or IMCs is decreased. This can be seen in the SEM microscopy of the pretreated AA2024, Figure 26, as well as by examining the activation controlled current density, Figure 50.

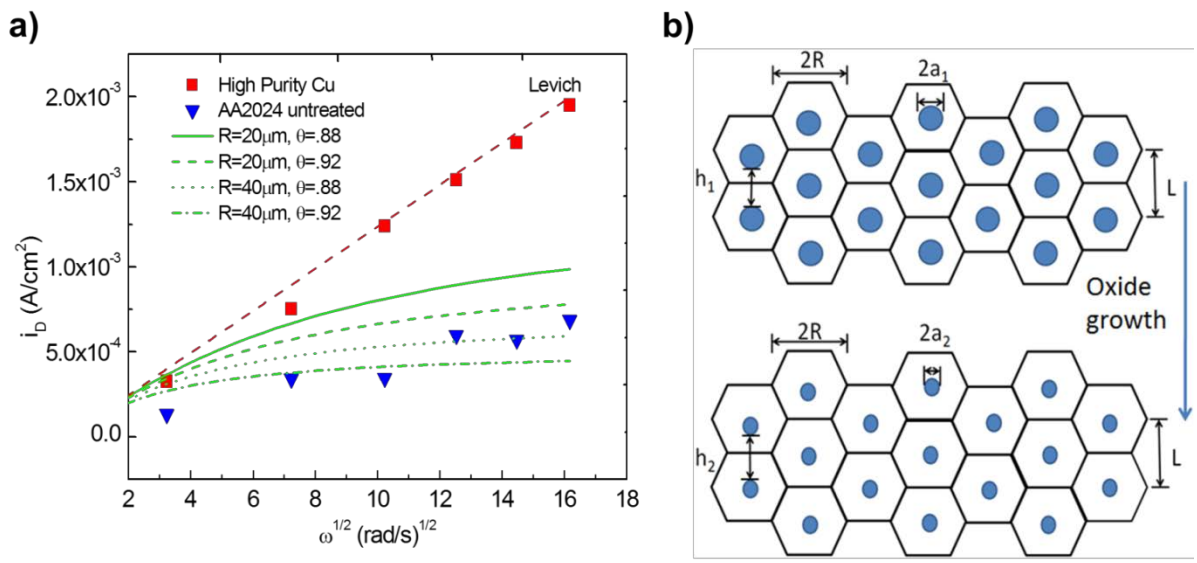

Figure 205. (a) Gueshi model showing effect of IMC special geometry in AA2024-T351 on modeled ORR kinetics and actual data values. (b) A schematic showing effect of decreasing active area in an inactive matrix.

The decrease in copper "surface coverage" decreases the size of the active sites and increases the spacing of the active sites in the Gueshi model. By examining Figure 205 the effect of copper coverage on ORR can be clearly seen. The coverage of the copper intermetallics by manganese oxides accounts for some of the ORR decrease seen on pretreated samples.

The second possible effect is the decreased rate of oxygen diffusion through the oxide barrier as opposed to through the electrolytic solution to the heterogeneous active sites. The membrane model treats the situation of two phase diffusion involving the oxygen diffusion boundary layer and the oxide. The model is described by Equation 38 and used by Ilevbare,[146]

$$i_D = nFc^o\left(\frac{1}{\left(1.61D_{sol}^{1/3}\nu^{1/6}/D_{sol}\omega^{1/2}\right) + \left(\chi_{ox}/D_{ox}\right)}\right)$$

Equation 38

where χ_{ox} is the oxide thickness, D_{sol} is the diffusion of O_2 in solution, D_{ox} is the diffusion of O_2 in the oxide, and ν is the kinematic viscosity of water. To examine the diffusion of oxygen through a porous manganese oxide film, manganese oxide films were grown over a highly pure copper RDE at a potential of -0.5 V vs. SCE. This potential was chosen to replicate the environment of the Cu-rich intermetallics on AA2024 which are held at the OCP of AA2024. Optical and scanning electron microscopy of the film can be seen in Figure 206 and the film was shown to be homogeneous in thickness and coverage. A cross-section of the film was taken to determine its thickness. Rotation-rate-ramp experiments were performed at a potential of -1 V vs. SCE on the sample in borate buffer and i_D from i_T were extracted. The result can be seen in Figure 207 compared to the model results for of the system. High-purity copper with a uniform manganese oxide film grown over the surface exhibits a large reduction in the ORR after the MnO_4^- is reduced. A potentiodynamic scan of high-purity copper with a manganese film electrodeposited over its surface (Figure 49) shows that at -1 V the ORR has been suppressed to a level approaching the HER reaction. The diffusion coefficient through the oxide film was estimated to be $1\times10^{-8}cm^2/sec$ using Equation 38, the rotation rate dependent mass limited current densities collected from the manganese oxide coated high-purity copper samples, the film thickness, and reasonable values for the remaining parameters.

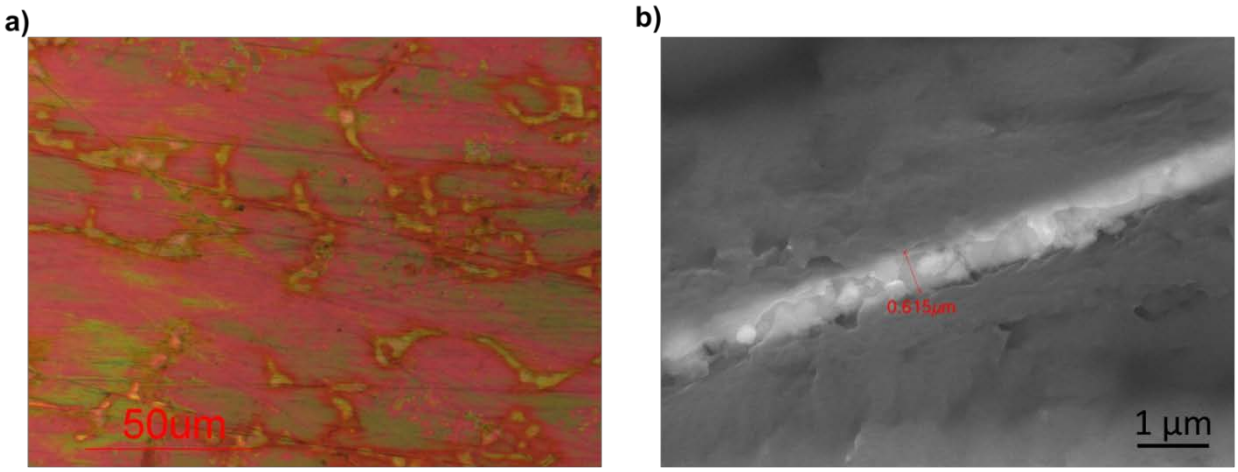

Figure 206. Optical (left) and scanning electron microscopy (right) of manganese oxide film grown over high-purity copper.

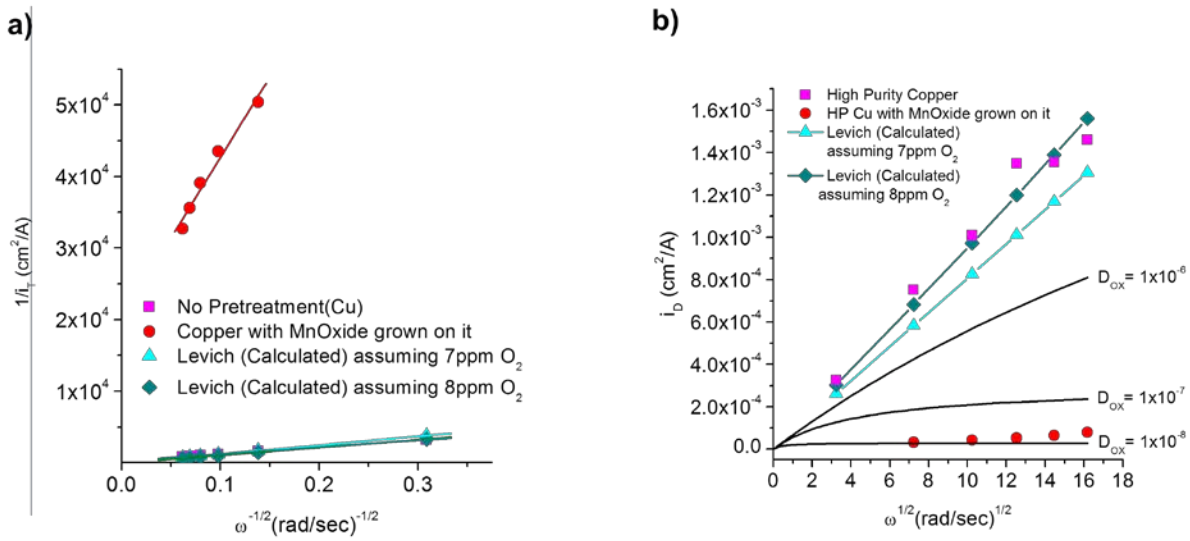

Figure 207. Membrane modeling of cathodic reaction kinetics in mass transport and mixed ORR regime for high-purity copper with a manganese oxide film grown on its surface from 0.1 M $KMnO_4$ solution at -0.5 V vs. SCE.

The combined model incorporates Gueshi[132] and membrane[146] analysis detailed above. The former handles the array of heterogeneous Cu sites while the latter treats the membrane over these sites. Equation 39 is the result of combining the two models and the description of reactant delivery to the face of a RDE (Equation 16).[29]

$$I_D = \frac{AnFDc^o\omega^{1/2}D^{2/3}}{1.61(\sigma^2-1)}\left(\frac{1}{\frac{1.61D_{sol}^{\frac{1}{3}}\nu^{\frac{1}{6}}}{D_{sol}\omega^{\frac{1}{2}}}+\left(\frac{\chi_{ox}}{D_{ox}}\right)}\right)$$
$$\times\left[\sigma e^{-l\left(\frac{2.592}{\pi\omega}\right)\left(\frac{\nu}{D_{sol}}\right)^{1/3}}-1+\sqrt{\pi\sigma^2}\times\sqrt{\frac{l\frac{2.592}{\pi\omega}\left(\frac{\nu}{D_{sol}}\right)^{1/3}}{\sigma^2-1}}\exp\left(\frac{l\frac{2.592}{\pi\omega}\left(\frac{\nu}{D_{sol}}\right)^{1/3}}{\sigma^2-1}\right)\right.$$
$$\left.\times\left\{\mathrm{erf}\left(\sigma\frac{l\frac{2.592}{\pi\omega}\left(\frac{\nu}{D_{sol}}\right)^{1/3}}{\sigma^2-1}\right)-\mathrm{erf}\left(\frac{l\frac{2.592}{\pi\omega}\left(\frac{\nu}{D_{sol}}\right)^{1/3}}{\sigma^2-1}\right)\right\}\right]$$

Equation 39

The effect of a number of controlling factors can be ascertained by exercising this model including the coverage of copper containing intermetallic particles (proportional to σ), the diffusion coefficient of O_2 through a [144] barrier oxide (D_{ox}), the thickness of the barrier oxide (χ_{ox}), the thickness of the Nernst diffusion layer (proportional to ω, the angular frequency of rotation), and the geometry and spacing of active regions in the inactive matrix (proportional to l). In equation 39 n is the number of electrons involved in the reaction, F is faradays constant, c^o is the bulk concentration of oxygen, and D_{sol} is the diffusion coefficient of O_2 in solution, and t is time at a fixed potential in the mass transport- limited regime.[90,132] This model accounts for the trends on permanganate treated 2024- T351 using reasonable values of these parameters.

Vanadate Speciation

There were discrepancies among the major species of the vanadate solutions identified using NMR and those were predicted by the thermodynamic software, Medusa.[137] Table 20 lists the five highest concentrations of vanadate species in solution with 50 mM NaCl as determined by Medusa between pH 6 and 8. At -577 ppm, the major peak identified experimentally by NMR corresponded to the $V_4O_{12}^{4-}$ species. This species was present at all concentrations of sodium vanadate in solution with 50 mM sodium chloride from pH 6.5 to 8.7, as identified by NMR spectrum (Table 21). However, the predicted hydroxyl vanadate species were not identified. Other researchers have also found $V_4O_{12}^{4-}$ as a dominant peak in chloride vanadates solutions[138,139] in the metavanadate range. The use of Medusa software without improving the chemical database for vanadate species' pKa should be avoided in favor of experimental determination of speciation.

While some minor species were unidentified, two identified species, $V_4O_{12}^{4-}$ and $V_5O_{15}^{5-}$, were present in all solutions except that $V_5O_{15}^{5-}$ was not present in 1 mM $NaVO_3$ plus 50 mM NaCl solution. These known species did not demonstrate pH sensitivity between pH 7 and 9. Of the unknown species, only one is likely to be of the V_1 family (only 1 vanadium atom per molecule)[95] of vanadium aqueous species due to its ppm reading.[94] This is the unknown peak detected in 150 mM $NaVO_3$ plus 50 mM NaCl (pH of 8.9) at -544 ppm. At a pH value below 9, a 10 ppm chemical shift occurs where the stable monomer of HVO_4^{2-} is protonated to $H_2VO_4^-$.[94] Likewise, the species listed for -568 ± 1 ppm represents a V_4 species whose presence as $HV_4O_{13}^{5-}$ or protonated $V_4O_{13}^{6-}$ is strongly pH dependent.[138,139]

From the chemical literature, there are a few facets of aqueous chemistry that are usually ignored in corrosion science, but must be considered for the speciation of vanadate inhibitors. Namely, all ions in solution including spectator ions such as Na^+ from NaCl dissociation have been suspected of affecting vanadate speciation.[95,138,139] While the amount of Na^+ in solution may not affect E_{pit} of AA2024, it will have an effect on the stability of different vanadate species.[95,138,139] Three molar Na^+ concentration stabilizes the higher charged polyatom ions (6-, 4-), which increases the stability of decavanadate ion $V_{10}O_{28}^{6-}$.[138] A similar effect was seen with increasing the KCl dissolved in a vanadate solution.[136] There is also a change in speciation related to Cl^- concentration. Chloride ions are more likely to complex with vanadate species than with OH^- or H_2O, so that the total Cl^- concentration will also have an effect on the final vanadate speciation.[91]

Decavanadates, which form in acid conditions, were shown by Iannuzzi to be weak inhibitors and to be slow to transform back into metavanadate species, which were found to be strong

inhibitors.[32] Moreover, in solutions with pH above 9, a Na^+ concentration greater than 100 mM will lead to ion pairing of HVO_4^{2-} and $V_2O_7^{4-}$ to create $NaHVO_4^-$ and $NaV_2O_7^{3-}$.[95] At a pH of 8.9 and a total Na^+ concentration of 200 mM, such as in 150 mM $NaVO_3$ plus 50 mM NaCl solutions, tests were performed in the Na^+ ion pairing region. In this environment, the sodium vanadate solutions would perform as well as non Na^+ ion paired vanadate cathodic inhibitors in lower Na^+ concentrations solutions and would perform better that non Na^+ ion paired anodic inhibitors in lower Na^+ concentrations solutions. In fact, the 150 mM $NaVO_3$ plus 50 mM NaCl solution performed the best during anodic inhibition tests of AA2024-T3 (Figure 63). It is unlikely that the ion paring effect itself resulted in inhibition. However, ion paring may have affected speciation stability. The dominant species in tested solutions with vanadate concentrations greater than 1 mM $NaVO_3$, $V_4O_{12}^{4-}$, does not change with increasing $NaVO_3$ concentration, but the quantity present does increase. As the total amount of all the other types of species is less than 30% (at the most) of the vanadate species in solution and the minor species vary in concentration, it is likely that the dominant species, $V_4O_{12}^{4-}$, is the responsible molecule or one of the responsible molecules leading to anodic inhibition. However, reduction in ORR occurred when $V_4O_{12}^{4-}$ was not the main aqueous species providing for cathodic inhibition.

There are differences in Na^+ and Cl^- concentrations between the Iannuzzi, Young and Frankel,[70] Ralston et al.,[67] and Ralston, Young and Buchheit,[71] and Iannuzzi and Frankel[93] work and the concentrations used in the current work. As a result of these differences, a different set of vanadate species will be present in the present work with different effects on inhibition.

Different vanadate species have been cited as effective inhibitors. However, in many of these studies, speciation was determined in the absence of sodium chloride. Iannuzzi and Frankel,[32] who evaluated speciation (monovanadate species, a single vanadium atom in the molecule, were dominant) in low concentration (0.001 to 5 mM) sodium vanadate solutions in the absence of sodium chloride, reported reductions in the cathodic current with increasing vanadate concentration up to 5 mM sodium vanadate in sodium chloride solution. Iannuzzi also reported increased inhibition of cathodic current in sodium chloride solutions containing monovanadate species (evaluation of speciation performed in the absence of sodium chloride).[31,32,93] While these inhibiting tetrahedrally coordinated vanadate solutions had monovanadate, as a minority species, there were present divanadate (2 vanadium atoms per molecule), tetravanadate (4 vanadium atoms per molecule), and pentavanadate (5 vanadium atoms per molecule) species.[32,70,93] In the present study, monovanadate species were not identified in the presence of sodium chloride. An unknown peak at -544 ppm may be a monovanadate species, but it was found only for the high vanadate concentration of 150 mM $NaVO_3$ plus 50 mM NaCl. It seems unlikely that monovanadates are wholly responsible for inhibition effect. Ralston, based on evaluation of speciation in the absence of sodium chloride, separated the inhibiting and noninhibiting vanadate species by the type of coordination that was associated with the vanadium atom.[67,71] Lack of inhibition in sodium chloride solutions was associated by Iannuzzi and Ralston with decavanadates, which have octahedral coordination.[31,32,67,70,71,93] Decavanadate species were not found nor specifically created for this present study. Inhibition in sodium chloride solutions was associated by Iannuzzi and Ralston with tetrahedrally coordinate vanadates, which exist within the subgroups: monovanadate, divanadate, tetravanadate, and pentavanadate. As all identified vanadates species in the presence of sodium chloride in the present study had tetrahedral coordination, this work supports the view that inhibition arises from tetrahedrally coordinated vanadate species.

Open Circuit Potential Inhibition with Coupled Anodic and Cathodic Reactions

The surface of AA2024 has local cathodes of copper intermetallic particles in an aluminum matrix. Missert et al.,[147] studied the change in surface acidity due to corrosion of S–phase intermetallics on AA2024-T3 in pH 6.5, 100 mM NaCl solutions. The pH only increased locally at S–phase undergoing dealloying. Localized alkaline regions, believed to be affiliated with IMPs, developed in response to the more acidic pitting sites.

In this study, exposure to vanadate plus sodium chloride solutions, led to a decrease in optically visible pitting sites with increasing vanadate concentration. Low concentration vanadate solutions (1, 5 and 10 mM $NaVO_3$) had yellow vanadate precipitates at and covering the pitting sites (Figure 56). As the local pH on the surface decreased during pitting, it is likely that metavanadates underwent a polymerization precipitation reaction due to the pH change. Both the matrix and intermetallic particles away from the pitting site did not show an increase in vanadium on the surface (Figure 57), as determined by EDS line scans. At higher vanadate concentrations, vanadium levels above background were seen on copper intermetallics inside pitting sites although no yellow precipitate was observed. The vanadium concentration at the aluminum matrix adjacent to pits did not increase. Nor did it increase at intermetallic particles away from the pitting sites. Adsorption of vanadate onto the surface likely occurred on both intermetallic compounds and the aluminum matrix. It is possible that during pit growth, vanadate molecules are chemically bonded to the intermetallic particles at the pitting sites and unless there is a localized decrease in surface pH elsewhere, it will not be found elsewhere on the surface. The yellow vanadate precipitates that attached to the surface during pit formation cannot be washed off with running water. However, the precipitation is not regarded to be the source of corrosion protection.

Anodic Inhibition Upon Anodic Polarization

For Al 99.99 %, there was a monotonic relationship between dissolved vanadate and increased E_{pit}, which is especially apparent after the 24 hour open circuit (Figure 60). There was a difference in E_{pit} due to the length of time at the open circuit before polarization for Al 99.99%. After only 1 hour, E_{pit} for specimens in 5 mM $NaVO_3$ and 10 mM $NaVO_3$ plus 50 mM NaCl are grouped together (Figure 59). A second group was formed for specimens in 50 mM $NaVO_3$ and 150 mM $NaVO_3$ plus 50 mM NaCl (Figure 60). Increasing the time at OCP from 1 to 24 hours led to a greater increase in E_{pit} for the specimens in different concentrations of vanadate in solution with 50 mM NaCl. The fact that E_{pit} increased on aluminum with vanadate suggests that the vanadate anion species compete with chloride in acidic pits and may not be exclusively associated with intermetallic compounds.

AA2024-T3 exhibited increased E_{pit} with increased vanadate concentration. AA2024-T3 did not exhibit the same monotonic relationship as aluminum during the anodic tests. The 1 hour open circuit behavior was different from the 24 hour open circuit behavior. For the 1 hour open circuit experiments, all vanadate concentrations were grouped together at the 80th percentile (Figure 62). The specimens in 5 mM $NaVO_3$ plus 50 mM NaCl solution had higher E_{pit} than specimens in solutions with the other vanadate concentrations at above the 40th percentile. This was not associated with a change in the majority vanadate species in solution. After a 24 hour open circuit exposure before the anodic testing, specimens in higher concentrations of vanadate in solution exhibited higher E_{pit} than specimens in the lower vanadate concentration solutions,

which formed a group (1, 5 and 10 mM $NaVO_3$). This is in contrast to the pitting behavior of pure aluminum specimens (Figure 63) in vanadate containing solutions, which showed a monotonic behavior after either a 1 hour or 24 hour open circuit exposure prior to anodic scans. As for aluminum, the average E_{pit} increased with 24 hour compared 1 hour at OCP for all vanadate concentrations. Half of the anodic tests performed in 50 or 150 mM $NaVO_3$ plus 50 mM NaCl, with a 24 hour open circuit, did not reach the pitting criteria when polarized to 0 V_{SCE}. The 24 hour exposure experiments of AA2024 in 50 mM NaCl plus various vanadate concentrations closely followed the E_{pit} results after a 24 hour open circuit where higher vanadate concentration greatly reduced pitting at open circuit potential. No pits were seen using the optical microscope for the 150 mM $NaVO_3$ plus 50 mM NaCl. Pits on AA2024 specimens were found at (Al-Cu-Mg) or adjacent to (Al-Cu-Mn-Fe) copper containing intermetallic particles. The fact that pit initiation on aluminum and AA2024-T3 is inhibited suggests that vanadate anion species inhibit both the pitting of aluminum matrix and intermetallic compounds of AA2024-T3.

The i_{pass} and E_{repass} were similar for AA2024-T3 and aluminum. While i_{pass} and E_{repass} were unrelated to inhibitor concentration, the passive potential range was related to vanadate inhibitor concentration and exposure time. The constant i_{pass} suggests that vanadate is not incorporated in the passive film or, if incorporated, that it does not affect i_{pass}. The low value of E_{repass} suggests that vanadate species in deep acidic pits, which may contain $AlCl_3$, are ineffective anodic inhibitors (Figure 61).

Vanadate pretreatments are ineffective in reducing the pitting corrosion of AA2024-T3 when the inhibitor is absent from solution at the time of pit formation. After 24 hour vanadate solution pretreatments on AA2024-T3 before testing in 50 mM NaCl, no statistical significant increase in E_{pit} was achieved. The average increase was approximately the same for all vanadate pretreatment concentrations and less than the lowest 1 hour open circuit average E_{pit} value for $NaVO_3$ plus 50 mM NaCl solutions. It is likely that vanadate must be in solution to increase the E_{pit}. The anion vanadate species present may compete with chloride anions during absorption. A physical absorption model rather than a chemical absorption model would explain this phenomenon.

Cathodic Inhibition due to Vanadate Solutions

The cathodic current density for ORR is either mass transport or charge transfer controlled.[9,28,90] In the mass transport limited regime, the rate of the electrochemical reaction is normally limited by the transport of molecules to or from the surface. In the charge transfer limited case, the regulation of the ORR is due to the passage of charge at the interface between the electrolyte solution and the electrode.[122] The cathodic polarizations in this study fall in the mixed or purely mass transport limited regime for ORR controlled reactions and the charge transfer regime for the HER controlled reactions. Vanadate may affect both regimes. Classical Koutecky-Levich and Levich studies shed light on these processes.

Koutecky-Levich plots were used to extract the effect of the inhibition in both the charge and mass transport ORR regimes. Levich plots for both the AA2024-T4 and Cu demonstrated that 1 mM $NaVO_3$ in 50 mM NaCl suppressed the ORR. The total cathodic current density was below the current density associated with the oxygen diffusion limit. It is possible that 1 mM of $NaVO_3$ or less is the critical vanadate concentration needed to reduce the effect of the ORR on

AA2024-T4[32] Ralston[67] and Iannuzzi[32] both found a reduction in the ORR when tetrahedrally coordinated vanadates were in solution during cathodic testing of AA2024. However, the kinetic regime was not elucidated. In this study, the vanadate inhibitors also affected the charge transport control regime. Other than using the Levich model, the AA2024–T4 electrode surface can be considered a large anode with cathodic sites.

One way to model an array of available cathodic sites on an alloy surface is to use the Gueshi model.[90,130,131] In the Gueshi model, the copper intermetallic particles are treated as the only sites on which the cathodic reaction occurs in a benign or inert aluminum matrix. The placement of these cathodic sites in an inert matrix is used to determine the limiting current density as function of cathodic site coverage. The areas of each site and the distance between sites are also variables in the model.[90] In Figure 208 is presented the theoretical limiting current density for various coverage of copper intermetallic sites on the aluminum matrix. As shown in Figure 208, AA2024-T3 in 50 mM NaCl had a low level of copper coverage in comparison to a pure copper surface represented by the black ideal Levich line. The addition of vanadate to the 50 mM NaCl, further reduced the approximate copper intermetallic coverage by a factor of 10 on AA2024-T4. In this model, all inhibitor concentrations gave the same result. The interpretation within the framework of this model was that vanadate adsorption blocks copper-rich ORR sites making it appear as if the array of copper-rich intermetallic compounds has a lower surface area. Such a reduction in effective copper coverage, θ, would produce a reduction in current density for both the mass transport and charge transfer controlled regimes. This interpretation is also consistent with Figure 75 because a charge transfer process would also be limited by a blocking agent. The charge transfer controlled cathodic current density, *i*, is given by Equation 40.

$$i = i_{act}\theta_{act} \qquad \textbf{Equation 40}$$

i_{act} is the current density on the active cathodic sites, and θ_{act} is the surface area of active cathodic sites. In addition, the diffusion concentration gradient dependance was removed, as seen in the Levich plot of this data (Figure 74). The limit of the rotation rate dependence occurred when the spacing between intermetallic compounds, L, equaled 20 μm. This model does not relate the reduction in copper intermetallic coverage, θ, directly to the solution's vanadate concentration.

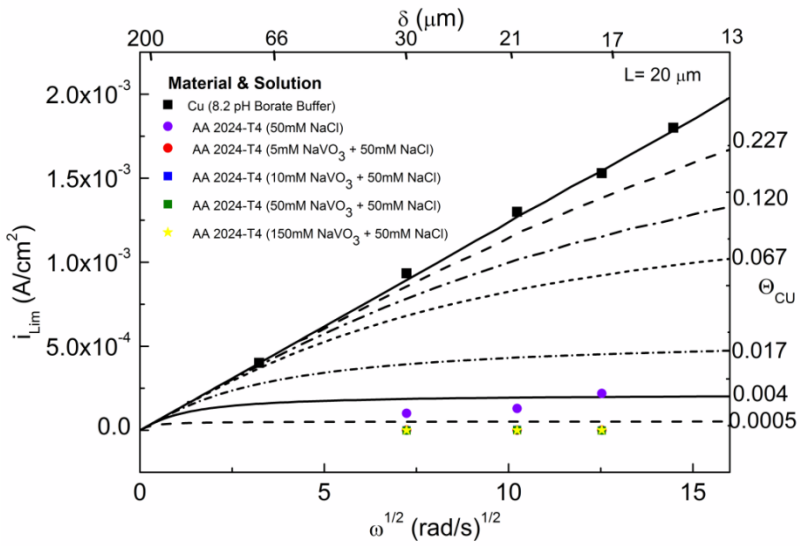

Figure 208. The limiting current density extracted from the total current for AA2024-T4 in open to the air 50 mM NaCl plus (0, 1, 5, 10, 50, 150 mM $NaVO_3$). δ is the O_2 diffusion boundary layer thickness perpendicular to the planer surface. L is the spacing between intermetallic compounds. The copper coverage θ is determined by the difference in current for the inhibited vs. uninhibited specimen divided by the current of the uninhibited specimen at a single potential in the ORR dominated potential range. Data place on top of theoretical limiting current density generated using the Gueshi model.[90]

An adsorption isotherm may be useful in modeling the change in coverage over the cathodic site. The use of an adsorption isotherm to model the effect of vanadate inhibition on the cathodic current density of AA2024-T3 was first proposed by Iannuzzi.[93] A Langmuir isotherm, which models the surface coverage, assuming no interactions between molecules on the surface, and the effect of surface charge on the absorption of molecules to the surface, was first employed.[93] The coverage of cathodic sites was determined by the current density at a given potential using the Equation 41 where θ is the coverage, i_{free} represents the current density for the inhibitor free experiment, and $i_{inhibitor}$ is the current density for the AA2024-T3 specimens tested in inhibitor bearing solutions[32]

$$\theta = 1 - \frac{i_{inhibitor}}{i_{free}} \qquad \textbf{Equation 41}$$

The copper coverage, θ, is related to the concentration of the vanadate concentration, C_{NaVO3}, by the Equation 42 in the Langmuir isotherm: [32]

$$\frac{\theta}{1-\theta} \quad vs \quad C_{NaVO_3} \qquad \textbf{Equation 42}$$

These plots were constructed at a potential where $i_{corr} > i_{HER}$ and $E_{Applied} < E_{corr}$. θ increased with concentration. It is also potential dependant, which was not seen previously. As seen in Figure 209, there is a decrease in coverage due to an increase in cathodic polarization potential. Potential dependance implies coulombic repulsion of negatively charged vanadate anions such as $V_4O_{12}^{4-}$ at negative potentials. Hurley et al., had seen a similar potential

dependance coverage phenomenon with ammonia vanadate in solution on copper surfaces.[148] An alternative explanation is that CuO and/or V^{5+} reduction limited vanadate adsorption.[149] The Temkin isotherm should be considered to model this behavior because a clear potential dependence is seen (Figure 209).

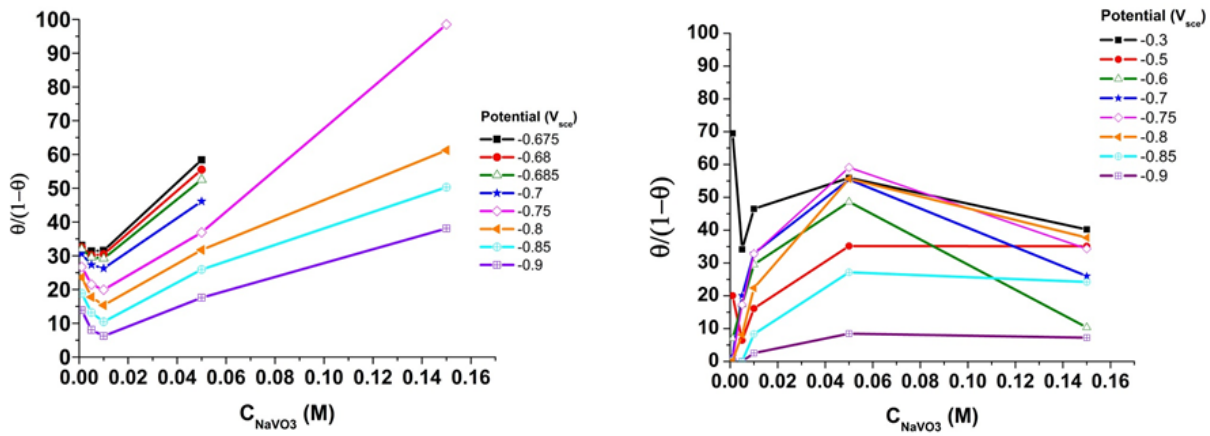

Figure 209. Plot of θ/(1-θ) versus C_{NaVO3}: (a) AA2024-T4 or (b) Cu in open to the air 50 mM NaCl plus various (1, 5, 10, 50, 150 mM) $NaVO_3$ solutions at different potentials. θ is the vanadate coverage on the surface. The rotation rate was 2,500 rpm.

The Temkin isotherm, which relates coverage to the relevant ion concentration and the heat of adsorption of the ion near zero coverage and ion absorption due to surface charge, was also used to model vanadate concentration to surface coverage. The Temkin isotherm relationship is given by Equation 43.

$$\theta = \frac{2.303RT}{r}\log C_{NaVO_3} + \frac{2.303RT}{r}\log K \qquad \textbf{Equation 43}$$

r is the Temkin parameter related to the heat of adsorption near zero coverage, K' is a constant, R is the Universal gas constant, and T is temperature. Instead of a constant heat of adsorption modeled by the Langmuir isotherm, the heat of absorption decreases as the coverage of the surface increases for the Temkin isotherm. For coverage values between 0.3 and 0.7, a linear relationship has been reported when this isotherm is obeyed.[150] As shown in Figure 210, the calculated coverage values were greater than 0.7, which is the upper limit for a linear relationship between coverage and vanadate concentration using the Temkin isotherm.

The Levich plot of Cu in various $NaVO_3$ plus 50 mM NaCl solutions (Figure 21) showed that higher vanadate concentrations had less of an effect than lower concentrations at reducing the ORR after a one hour open circuit. This may be due to a physical adsorption of large slow-moving vanadate molecules to the rotating surface and/or absence of the simple noncompetitive adsorption case of the Langmuir adsorption isotherm. At higher concentrations, it would be more difficult for the larger molecules to move to the electrode surface and displace small molecules such as OH^- and Cl^-. This same phenomenon of a one hour open circuit leading to better

inhibition for lower vanadate concentration was also apparent for AA2024-T3 anodic scans. An inhibition mechanism of molecule adsorption that is kinetically limited by molecular weight would explain why the AA2024-T4 Levich plots did not exhibit concentration dependance. AA2024-T4 has fewer cathodic sites to be covered and would thus need fewer molecules to reach the surface. Apparently, a concentration of 1 mM $NaVO_3$ plus 50 mM NaCl solutions is adequate for cathodic inhibition.

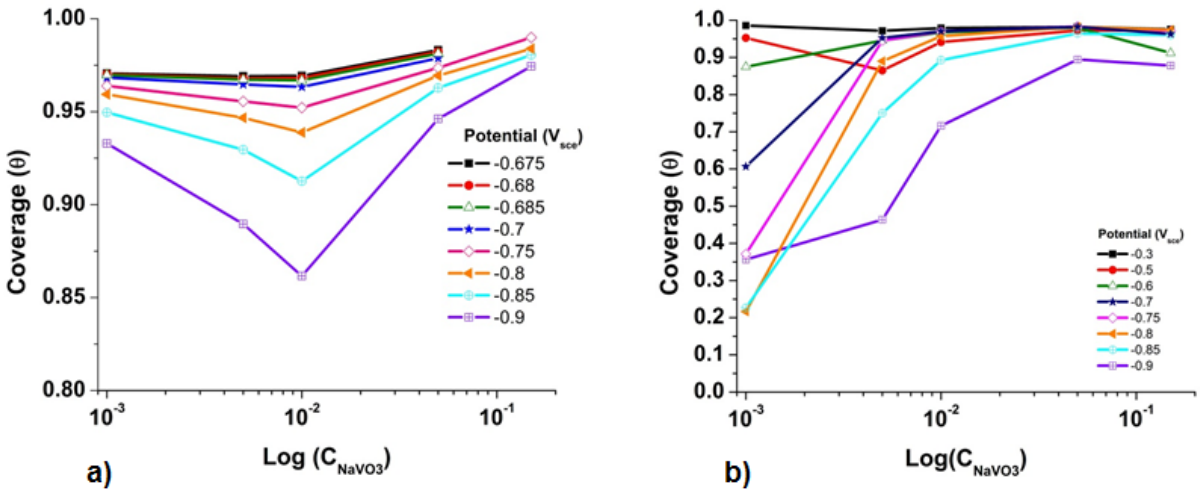

Figure 210. Plot of θ versus Log C_{NaVO3}: (a) AA2024-T4 or (b) Cu in open to the air 50 mM NaCl plus various (1, 5, 10, 50, 150 mM) $NaVO_3$ solutions at different potentials. The rotation rate was 2,500 rpm.

Corrosion Inhibition of AA2024 with Inhibitors Combination

Cerium-Permanganate Combinations

Open circuit and Anodic Inhibition by Cerium Permanganate Pretreatments

All inhibitor combinations show some decrease in current densities attributed to copper reduction. The suppression of copper replating as indicated by CV (Figure 89) correlates with the reduced damage observed in our OCP microscopy experiments when the cerium deposits are removed compared to untreated samples (Figure 84, 85, and 86). However, when permanganate is not used in the pretreatment, pitting attack through a cerium oxide layer occurs resulting in only a small reduction in current during the surface copper assay. The attack of the substrate through the observed cerium film appears to be mitigated by manganese deposits when dual inhibitor pretreatments are used and this is reflected in the CV data (Figure 89). When permanganate is used alone the reduction in current during the surface copper assay is almost an order of magnitude lower than when cerium is used alone. The greatest reduction in ΔE_{pass} is for permanganate or cerium-permanganate combinations. Cerium alone is less effective than permanganate possibly due to homogeneous chemical precipitation vs. direct permanganate reduction which effectively blocks IMC electrochemical MnO_4^- deposition. The oxidation state of the cerium oxide/hydroxide is unclear and further study needs to be done to determine if permanganate has oxidize the cerium deposits from cerium hydroxide to cerium oxide.

Diffusion Limited Current Density Inhibition by Cerium-Permanganate Pretreatments

Figure 94 (a) shows the true total cathodic current density on single inhibitor pretreatments of cerium and permanganate as well as combinations of the two. Cerium clearly shows a higher cathodic current density. This may result from the chemical precipitation reaction which can't be site specific that leads to the observed irregular cerium rich oxide or hydroxide film seen in Figure 80 (d). The cerium-permanganate combination pretreatments and the permanganate single inhibitor pretreatment have lower total cathodic current densities. The rotation rate dependence of the cathodic current density is not immediately obvious as it is in the cerium pretreatment. The reduction of manganese has a linear relationship with time and when subtracted out, reveals the rotation rate dependence seen in Figure 95 (a). The manganese reduction is removed from the diffusion limited current density analysis so that a better understanding of the ORR can be obtained leading to more information about the blockage of cathodic reaction sites. In Figure 95(a) $1/i_{Total}$ is plotted against one over the square root of rotation rate (ω). Here i_{Total} is the total current seen in Figure 94(a) minus the cathodic current due to manganese reduction. High rotation rates are on the left of the graph. The permanganate pretreated sample shows the lowest current density while the cerium pretreated samples shows the highest cathodic current density. The two step inhibitor pretreatments also show strong cathodic current inhibition. However, it is not as strong as permanganate pretreatment as a single inhibitor.

When the K-L correction is applied to the data, seen in Figure 95(b), the inhibition of diffusion limited cathodic current density due to permanganate pretreatment shows the highest inhibition, while cerium shows the lowest levels of inhibition. The homogeneous chemical reaction that leads to cerium deposition cannot be site specific and may leave gaps in coverage of constituent particles, the primary cathodic reaction sites. In contrast, the reduction reaction that leads to manganese oxide coverage is targeted to fast reacting cathodic sites and complete as it is the result of a cathodic reaction (Figure 211). Sites where cathodic reactions happen quickly will be sites were permanganate is reduced quickly, leading to blockage and deactivation of the cathodic reaction site. When cerium-permanganate dual inhibitor pretreatments are conducted the cerium may act to block this direct, targeted deposition leading to a slight decrease in the permanganate cathodic current inhibition efficiency.

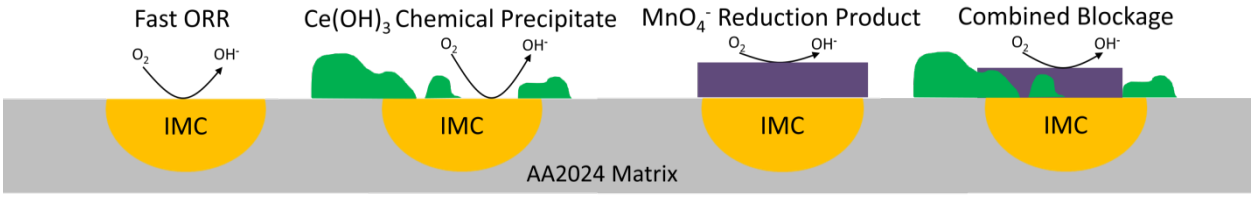

Figure 211. Schematic of different cathodic reaction inhibition mechanisms for the reduction of permanganate, the chemical precipitation of cerium hydroxide, and the effect of dual inhibitor pretreatment.

Vanadate-Cerium and Vanadate-Molybdate Combinations

Vanadate Speciation

Similar vanadate speciation results were obtained between the different vanadate-molybdate solution combinations. The major peak at -577 ppm identified experimentally by NMR corresponded to the $V_4O_{12}^{4-}$ species. This species was present at all concentrations of sodium vanadate and sodium vanadate-sodium molybdate combinations in solution with 50 mM sodium chloride from pH 7.9 to 8.4 (Table 25). Other researchers have also found $V_4O_{12}^{4-}$ as a dominant or majority species in chloride solutions containing vanadates[138,139] in the metavanadate range (approximately pH 6-9). As the total amount of all the other types of species (see Table 26) was less than 30% (at the most) of the vanadate species in solution and the minor species varied in concentration, it is likely that the dominant species, $V_4O_{12}^{4-}$, is one of the responsible molecules leading to inhibition.

NMR spectra peaks representing minority species were also similar between all vanadate and vanadate-molybdate combinations in 50 mM NaCl solutions. The ratio between the minor species present changed among the different vanadate-molybdate mixtures. It is expected that as the pH of the solution is increased, smaller vanadate molecules would become more numerous.[94] $H_2V_2O_7^{2-}$, $HV_2O_7^{3-}$, and $V_2O_7^{4-}$ are usually in a three way equilibrium in basic solutions with the majority species changing from $H_2V_2O_7^{2-}$ to $V_2O_7^{4-}$ as alkalinity is increased and dissolved vanadium salt concentration is decreased.[139] Due to line–broadening of the peaks, peaks for $HV_2O_7^{3-}$, and $V_2O_7^{4-}$ may have overlapped as there is only a l ppm separation between the peaks cited in the literature; thus, $HV_2O_7^{3-}$ may not have been visible as a separate peak in the NMR spectra obtained.[139] The minimal increase in pH and much larger increase in dissolved $NaVO_3$ resulted in the vanadate and molybdate-vanadate mixtures having a decrease in the $V_2O_7^{4-}$ and $H_2V_2O_7^{2-}$ species concentration, while the concentration of larger molecular weight molecules ($V_4O_{12}^{4-}$ and $V_5O_{15}^{5-}$) increased. The 10 mM $NaVO_3$ plus 40 mM Na_2MoO_4 in 50 mM NaCl solution had a larger percentage of the smaller molecule weight V_2 species as compared to the 40 mM $NaVO_3$ plus 10 mM Na_2MoO_4 plus 50 mM solution (Table 26). This occurred, even though the alkalinity of the solution slightly increased, which should have resulted in a high ratio of V_2 to V_5 species in solution.[94] A comparison of the species in the10 mM $NaVO_3$ plus 50 mM NaCl solution to those in the 10 mM $NaVO_3$ plus 40 mM Na_2MoO_4 plus 50 mM NaCl solution demonstrates that molybdate concentration has little effect on final pH of the solution, but it does increase the amount of higher molecular weight species in solution. It is important to note that no V–Mo compounds were found in the as made solution.

As vanadate and molybdate can react to form V-Mo compounds, the chemical mixtures have interactions that need to be considered in addition to the different chemical conditions which effect vanadate species. Vanadate speciation is affected by solution pH, cation type and concentration, chloride concentration and the total concentration of dissolved vanadium salt in solution.[91,95,136,138,139] Starting at pH values as high as 7, acidification of V–Mo mixed solutions can lead to the formation of V–Mo compounds in solution.[98] There is disagreement as to what species exist, but these compounds (whose exact formulae have not been agreed upon) are usually large molecules.[92,97,98] When the V:Mo ratio is high, Mo substitutes for two V atoms in decavanadate structures (octahedrally coordinated).[92,97,98] When the V:Mo ratio is low, Keggin species (tetrahedrally coordinated vanadium atom with octahedral clusters) and other isopolymolybdate structures with V atoms substitute for as much as two Mo atoms.[92,97,98] At a

V:Mo ratio almost equal to one, asymmetrical $(Mo_4V_5O_{27})^{5-}$ was found. However, analog chemical groups that form with only vanadium cations are not effective inhibitors.[31,32,67,70,71,93] Additionally, solid crystals of a V-Mo compound were found to precipitate out of solution during acidification.[97,98] No mixed species were found in the ^{51}VNMR analyses of the as prepared test solutions, but they may have formed during anodic polarization of the test surface during pitting experiments due to the decrease in solution pH during testing.

Decavanadates, which form in acid conditions, were shown by Iannuzzi to be weak inhibitors and to be slow to transform back into metavanadate species, which were found to be strong inhibitors.[32] Ralston correlated the lack of inhibition to the octahedral coordination of decavanadate species.[31,32,67,70,71,93] Decavanadate species were not found nor specifically created for this present study. Inhibition by vanadate in sodium chloride solutions was associated by Iannuzzi and Ralston with tetrahedrally coordinated vanadates, which exist within the subgroups: monovanadate, divanadate, tetravanadate, and pentavanadate. This work supports the view that inhibition arises from tetrahedrally coordinated vanadate species, because all identified vanadate species in the presence of sodium chloride in the present study had tetrahedral coordination.

Open Circuit Potential Inhibition with Coupled Anodic and Cathodic Reactions

In this study, exposure to vanadate inhibitor combinations plus sodium chloride solutions, led to a decrease in optically visible pitting sites with increasing vanadate concentration (see Figure 100). Pits on AA2024-T3 specimens were found at (Al-Cu-Mg) or adjacent to (Al-Cu-Mn-Fe) copper containing intermetallic particles. When AA2024–T3 specimens were exposed to 50 mM NaCl solutions containing 50 mM total inhibitor concentration, only the specimens exposed to the solution containing 50 mM $NaVO_3$ exhibited a reduction in the size and number of pits, and in the number of entrenched intermetallic particles. The 50 mM $Ce(C_2H_3O_2)_3$ pretreated surface showed similar discoloration by the entrenched particles as that of the 50 mM NaCl exposed surface. Cerium compounds were found to selectively deposit over Al-Cu-Mg intermetallic particles. However, the underlying Al-Cu-Mg particles were still attacked during the 24 hour exposure to chloride containing solutions (Figure 102). For the combination cerium pretreatment and vanadate in solution, vanadate at or higher than 25 mM $NaVO_3$ in solution resulted in no pits visible to the unaided eye on AA2024–T3 specimens. There was corrosion of parts of the intermetallic particle [Figure 100 (c), (d), (h), and (j)]. A yellow vanadium rich precipitate was only found on AA2024-T3 specimen that was pretreated in 40 mM $Ce(C_2H_3O_2)_3$ and evaluated in 10 mM $NaVO_3$ plus 50 mM NaCl solution. The reduction in visible pits correlates to an increase in vanadate in the test solution and not to the concentration of $Ce(C_2H_3O_2)_3$ used in the 2 hour pretreatment, for AA2024-T3 specimens exposed at open circuit potential.

As the local pH on the surface decreased during pitting, it is likely that metavanadates and molybdate underwent a polymerization precipitation reaction due to the pH change (Figure 100). The specimen exposed to 50 mM Na_2MoO_4 plus 50 mM NaCl had a white–orange Mo rich precipitate at pitting sites. Both the matrix and intermetallic particles away from the pitting site did not show an increase in vanadium or molybdenum on the surface (Figure 104), as determined by EDS line scans. AA2024-T3 specimens exposed to solutions containing a combination of vanadate-molybdate, both V and Mo are found at the pitting sites [Figure 103 (b)]. For specimens exposed to solutions containing 50mM vanadate, vanadium levels above background were seen on copper intermetallics inside pitting sites, although no yellow precipitate was observed. For specimens exposed to solutions containing both vanadate and

molybdate, vanadium and molybdenum concentrations did not increase at the aluminum matrix adjacent to pits nor at intermetallic particles away from the pitting sites. It is possible that during pit growth, vanadate and or molybdate molecules are bonded to the intermetallic particles at the pitting sites and unless there is a localized decrease in surface pH elsewhere, they will not be found elsewhere on the surface. Molybdenum was detected closer to the attacked intermetallic particle than V rich precipitates [Figure 103 (b)]. As in the case of the yellow vanadium precipitates attached to the surface during pit formation, molybdenum rich precipitates cannot be washed off with running water. However, the precipitation is not regarded to be the source of corrosion protection.

Anodic Inhibition Upon Anodic Polarization

E_{pit} increased for cerium pretreated Al 99.99 % specimens with increasing vanadate in solution [Figure 212 (a)]. Most Al specimens subjected to the combination cerium pretreatment and testing in vanadate containing solutions had equivalent or reduced average E_{pit} values after twenty-four hours of exposure as compared to 1 hour exposure. The fact that E_{pit} increased on aluminum with vanadate concentration but not with cerium pretreatment concentration suggests: 1) the 2 hour cerium pretreatment was ineffective as an anodic inhibitor; and 2) Ce precipitation blocks IMC from interaction with vanadate in solution.

Vanadate-molybdate inhibitor combinations increased the average E_{pit} to or above the values found on Al 99.99% specimens tested in 50 mM $NaVO_3$ plus 50 mM NaCl [Figure 212 (b)]. Similar to the specimens exposed to solution containing vanadate only, specimens exposed to solutions containing vanadate-molybdate mixtures had an increase in E_{pit} and E_{corr} as the open circuit exposure time increased. The highest average E_{pit} observed after a 1 hour open circuit exposures occurred on Al specimens exposed to solutions containing 40 mM Na_2MoO_4 plus 10 mM $NaVO_3$. Aluminum specimens had the highest E_{pit} after 24 hour open circuit exposures to solutions containing 50 mM Na_2MoO_4.

AA2024-T3 specimens with cerium acetate pretreatment and tested in 50 mM sodium chloride solutions with or without sodium vanadate did not display E_{pit} greater than those for specimens exposed to solutions containing 50 mM sodium vanadate [Figure 213 (a)]. E_{pit} increased and E_{corr} decreased with increasing vanadate concentration in the test solution for the specimens given a cerium pretreatment. This change in average E_{pit} was not associated with a change in the dominant vanadate species in solution. Additional testing of AA2024-T3 specimens at constant cerium pretreatment level and varying vanadate concentrations proved that 1) the increase in E_{pit} value was due to the amount of vanadate in solution; and, 2) higher cerium pretreatment concentration resulted in lower E_{pit} values for the same concentration of vanadate in solution (Figure 212).

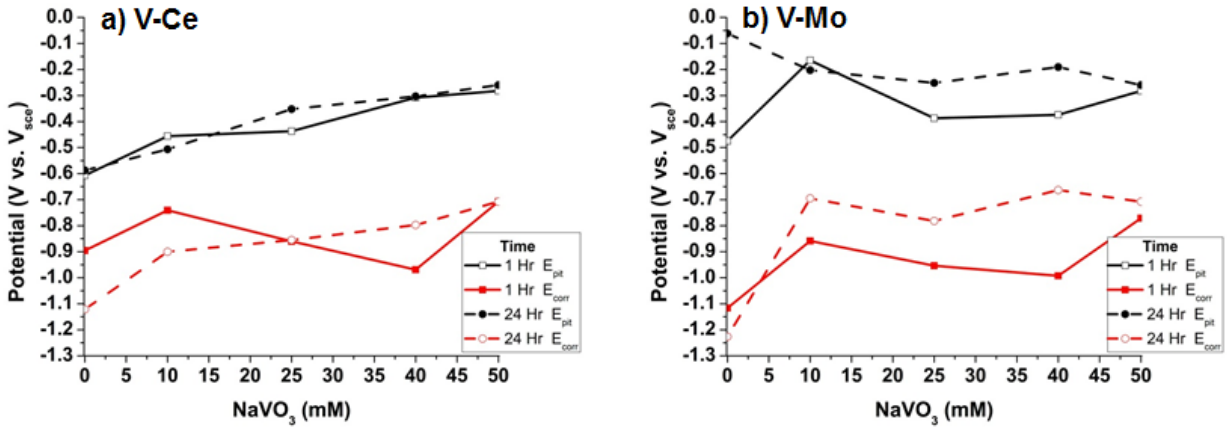

Figure 212. Plots of E_{pit} and E_{corr} for Al (99.99%) exposed to 50 mM of inhibitor plus 50 mM NaCl and with a 1 or 24 hour open circuit prior to an anodic polarization scan. a) A pretreatment in various concentrations of $Ce(C_2H_3O_3)$ followed by testing in various concentrations of $NaVO_3$ in the 50 mM NaCl solution lead to each surface having been exposed to a total of 50 mM of inhibitor between the two solutions. b) The test solution contained 50 mM of $NaVO_3$ and Na_2MoO_4 inhibitors in addition to 50 mM NaCl. The ratio of $NaVO_3$ and Na_2MoO_4 varied, but the total inhibitor concentration was kept constant at 50 mM.

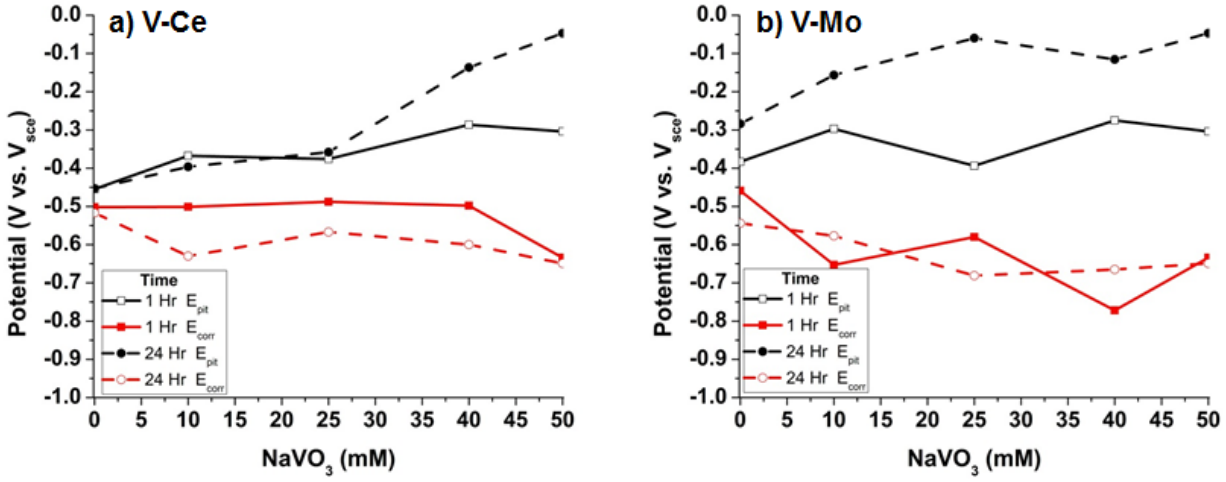

Figure 213. Plots of E_{pit} and E_{corr} for AA2024-T3 exposed to 50 mM of inhibitor plus 50 mM NaCl and with a 1 or 24 hour open circuit prior to an anodic polarization scan. a) A pretreatment in various concentrations of $Ce(C_2H_3O_3)$ followed by testing in various concentrations of $NaVO_3$ in the 50 mM NaCl solution lead to each surface having been exposed to a total of 50 mM of inhibitor between the two solutions. b) The test solution contained 50 mM of $NaVO_3$ and Na_2MoO_4 inhibitors in addition to 50 mM NaCl. The ratio of $NaVO_3$ and Na_2MoO_4 varied, but the total inhibitor concentration was kept constant at 50 mM.

The AA2024-T3 surfaces exposed to vanadate and/or molybdate inhibitors had average E_{pit} which increased with open circuit exposure time [Figure 213 (b)]. After 24 hours of exposure in 50 mM NaCl plus various inhibitor combinations, AA2024-T3 specimens showed increased E_{pit} values as compared to specimens after 1 hour open circuit exposures in the same solutions [Figure 110 (b)]. Unlike aluminum, AA2024-T3 specimens in solutions containing 50 mM Na_2MoO_4 inhibitor exhibited the lowest average E_{pit} and highest average E_{corr} values for all twenty-four hour open circuit test in solutions containing molybdate-vanadate combinations. The fact that pit initiation on aluminum and AA2024-T3 is inhibited suggests that vanadate anion species inhibit both the pitting of aluminum matrix and intermetallic compounds of AA2024-T3.

The i_{pass} and E_{repass} were similar regardless of material (AA2024-T3 or aluminum) or inhibitor combination. While i_{pass} and E_{repass} were unrelated to inhibitor concentration, the passive potential range was related to vanadate and/or inhibitor concentration and exposure time. The constant i_{pass} suggests that the inhibitors are not incorporated into the passive film or, if incorporated, that it does not affect i_{pass}. The low value of E_{repass} suggests that vanadate, molybdate, or cerium cation species in deep acidic pits, which may contain $AlCl_3$, are ineffective anodic inhibitors under acidic conditions (Figure 109, Figure 110, Figure 105, and Figure 106).

Cathodic Inhibition due to Vanadate Binary Combinations Solutions

The cathodic current density for ORR is either mass transport or charge transfer controlled.[9,28,90] In the mass transport limited regime, the rate of the electrochemical reaction is normally limited by the transport of molecules to or from the surface. In the charge transfer limited case, the regulation of the ORR is due to the passage of charge between the electrolyte solution and the electrode.[122] The cathodic polarization data in this study lies in the mixed or purely mass transport limited regime for ORR controlled reactions and the charge transfer regime for the HER controlled reactions. Vanadate inhibitor combinations my impact either control mechanism by altering existing rate limiting processes. Classical Koutecky-Levich and Levich studies shed light on these processes.

Koutecky-Levich plots were used to extract the effect of the inhibitor in both the charge and mass transport ORR regimes. Cu and AA2024-T4 specimens, in the same test solutions, exhibited dissimilar behavior. Fifty mM $NaVO_3$ was the best inhibitor of the cathodic current density on Cu at -0.8 V_{SCE} (Figure 123). The resulting cathodic current densities on Cu specimens for the inhibitor combinations evaluated were less than those for AA2024-T4 specimens evaluated in 50 mM $NaVO_3$ plus 50 mM NaCl solutions (Figure 123 and Figure 124). Levich plots for both AA2024-T4 and Cu demonstrated that both binary vanadate inhibitor combinations suppressed the oxygen reduction reaction. The total cathodic current was less than the current associated with the oxygen diffusion limit. These binary vanadate combinations removed the oxygen diffusion path length dependence for ORR dominated current for all 50 mM binary vanadate combinations as well as for 50 mM $NaVO_3$ exposed samples (Figure 125 and Figure 126). The lack of ORR inhibition from the use of 50 mM $Ce(C_2H_3O_2)_3$ pretreatment or 50 mM Na_2MoO_4 in 50 mM NaCl solutions was unexpected as prior researchers had found that exposure to these chemicals led to a reduction in the ORR current.[29] The prior experiments were completed in a Cl^- free borate buffer ($Na_2B_4O_7$ and H_3BO_3) at pH 8.2.[29] The dissociation of sodium tetraborate and boric acid in water resulted in the formation of $BH_2O_3^-$, $4[B(OH)_4]^-$, 3 H^+, $2Na^+$, and 3 H_2O molecules. The borate and molybdate molecules are much larger than Cl^- molecules, and can effectively compete with vanadate molecules and each other to cover the

copper intermetallic particles in the absence of chloride molecules. It is also possible that the metal surface selectively bonds to molybdate rather than borate ions. The increased competition from the solvent anions is hypothesized to result in an order of magnitude lower inverse total current density than found by Jakab et al.[29] Figure 214 presents the competition between anions for the Cu intermetallic particles on the surface of AA2024-T3.

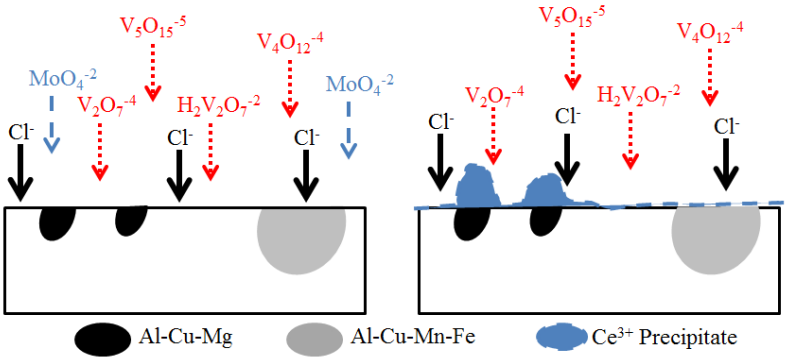

Figure 214. The competition of anions on a positively charged AA2024 surface. The cerium precipitate blocks anions from reaching the surface.

As presented in Figure 214, there are different anions attempting to adsorb onto the surface. The potential of zero charge, E_{PZC}, is the potential at which the surface has a net zero charge.[150] At potentials anodic to the E_{PZC}, anions will be attached to the positively charged surface. Voltages of -1248 mV_{SCE} and -1090 mV_{SCE} have been reported as the E_{PZC} for Al and Al 8 wt% Cu supersaturated alloy, respectively.[151] These two materials were also reported to have a pH_{ZC}, the pH when there is a net zero charge at the surface with no applied charge, of 8.6 and 8.61 for Al and Al 8 wt% Cu supersaturated alloy, respectively.[151,152] AA2024-T4, with 4.4 wt% copper, has a pH_{ZC} of 8. It is reasonable to expect the E_{PZC} of AA2024 to also be at a potential lower than the OCP and should lead to a positively charged AA2024 surface to which anions will be adsorbed at open potential. E_{PZC} correlates with the E_{pit} of aluminum alloys.[151] Thus, molybdate and vanadate must have successfully competed with chloride to adsorb onto the positively charged surface at open circuit as demonstrated by the increase in E_{pit} with time [Figure 109 (b) and Figure 110 (b)]. The theory of zero charge potential does not consider competition of anions (the selective adsorption of ion species over another nor the differences in molecular weight and resulting ionic mobility in solution).[151] All of the mentioned effects could lead to a change in the anion population at the surface with time.

Physical blockage of intermetallic particles could change the anion population at the surface of the material. Cerium precipitates act as a physical block to anions adsorption onto S-phase Al-Cu-Mg intermetallic particles. The removal of the cerium caps will allow vanadate anions to complete for occupancy on the S-phase. However, vanadate has no effect on E_{repass} and cannot stop the ongoing pitting.[153]

A possible mechanism for the reduction of availability cathodic sites for ORR is the adsorption of inhibitor anions to the surface. An adsorption isotherm can be used to model the change in coverage over the cathodic site. The use of an adsorption isotherm to model the effect of vanadate inhibition on the cathodic current density of AA2024-T3 was first proposed by Iannuzzi.[93] A Langmuir isotherm, which models the surface coverage, assuming no interactions

between molecules on the surface, and the effect of surface charge on the absorption of molecules to the surface, was employed.[93] The coverage of cathodic sites was determined by the current density at a given potential using Equation 44 where θ is the coverage, i_{free} represents the current density for the inhibitor free experiment, and $i_{inhibitor}$ is the current density over a 1 hour time period for the AA2024-T3 specimens tested in inhibitor bearing solutions.[32]

$$\theta = 1 - \frac{i_{inhibitor}}{i_{free}} \qquad \textbf{Equation 44}$$

The copper coverage, θ, is related to the concentration of the vanadate, C_{NaVO3}, by Equation 45 if the Langmuir isotherm is operative.[32]

$$\frac{\theta}{1-\theta} \quad vs \quad C_{NaVO_3} \qquad \textbf{Equation 45}$$

These plots were constructed in this study at a potential where $i_{ORR} > i_{HER}$ and $E_{applied} < E_{corr}$. The total inhibitor concentration in solution was kept constant at 50 mM (Na_2MoO_4 + $NaVO_3$). As θ coverage values were very high, the graphs in Figure 215 a) show asymptotic behavior and can provide useful information. As shown in Figure 215 a) and b), there is a decrease in coverage due to an increase in cathodic polarization potential. Potential dependence implies coulombic repulsion of negatively charged vanadate anions such as $V_4O_{12}^{4-}$ at negative potentials. Hurley et al., had seen a similar potential dependence coverage phenomenon with ammonia vanadate in solution on copper surfaces.[148] The Temkin isotherm was also considered to model this behavior.

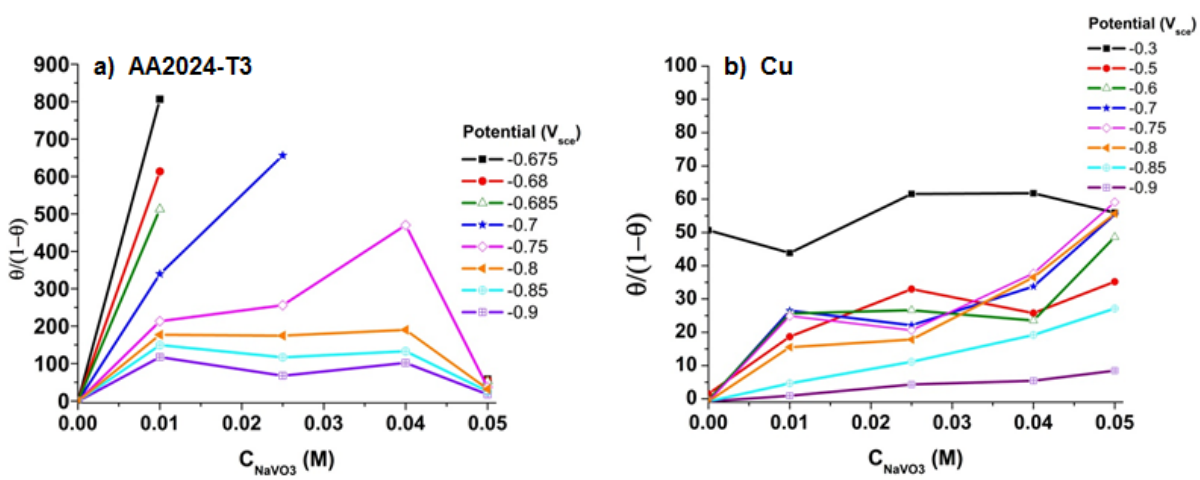

Figure 215. Coverage versus concentration of $NaVO_3$ at various cathodic potentials. Total inhibitor concentration of vanadate and molybdate equals 50 mM in 50 mM sodium chloride. a) AA2024-T4 and b) Cu.

The Temkin isotherm, which relates coverage to the relevant ion concentration and the heat of adsorption of the ion near zero coverage and ion absorption due to surface charge, also was used

to model vanadate concentration to surface coverage. The Temkin isotherm relationship is given by Equation 46.

$$\theta = \frac{2..303RT}{r}\log C_{NaVO_3} + \frac{2.303RT}{r}\log K' \qquad \textbf{Equation 46}$$

where r is the Temkin parameter related to the heat of adsorption near zero coverage, K' is a constant, R is the Universal gas constant, and T is temperature. Instead of a constant heat of adsorption modeled by the Langmuir isotherm, the heat of absorption decreases as the coverage of the surface increases for the Temkin isotherm. For coverage values between 0.3 and 0.7, a linear relationship has been reported.[150]

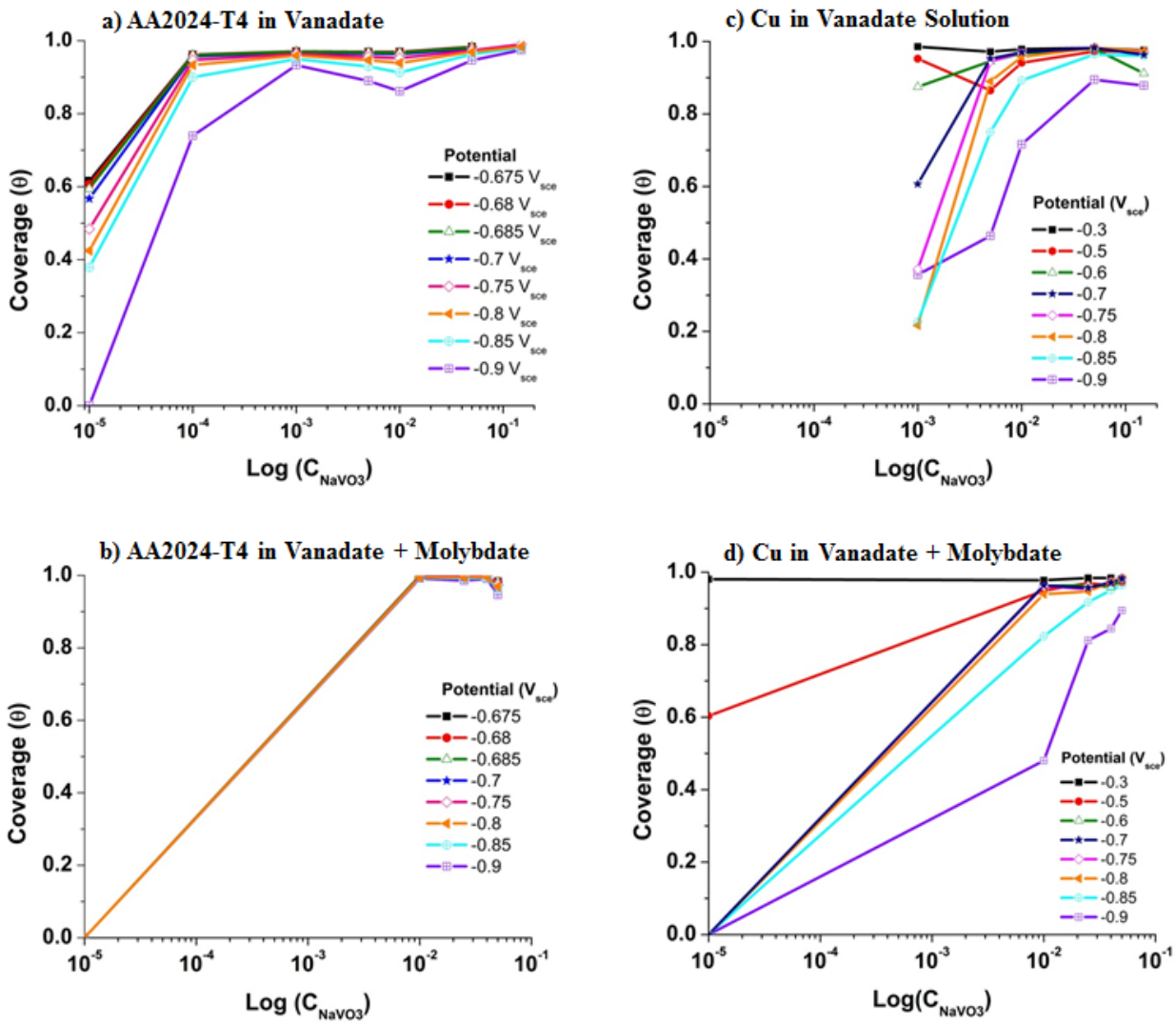

Figure 216. Coverage versus Log C_{NaVO3} at various cathodic potentials. Metals exposed to 50 mM sodium chloride with increasing vanadate concentration: a) AA2024-T4; and c) Cu. Total inhibitor concentration of vanadate and molybdate equals 50 mM in 50 mM sodium chloride: b) AA2024-T4 and d) Cu.

As shown in Figure 216, the calculated coverage values with greater than 1 mM vanadate in solution were greater than 0.7, which is the upper limit for a linear relationship between coverage and vanadate concentration using the Temkin isotherm. At these high coverage values (above 0.9), the coverage on AA2024-T4 specimens do not appear to be strongly potential dependent whereas that on Cu specimens is still potential dependent. Low concentrations of vanadate provide for better surface coverage of AA2024-T4 than the combination of vanadate and molybdate.

On AA2024-T4, the high surface coverage and lack of vanadate concentration dependence at different overpotentials may be due to the high 50 mM inhibitor concentration used in all tests and the absence of the simple noncompetitive adsorption case of the Langmuir adsorption isotherm. The physical adsorption of large slow-moving vanadate and molybdate molecules to the rotating surface and displacement of multiple smaller molecules such as OH^- and Cl^-, could be more difficult for the larger molecules. The increase in inhibition of vanadate-molybdate combinations as observed for the 24 hour versus the 1 hour anodic scans (Figure 117 and Figure 118) for AA2024-T3 may be associated with an inhibition mechanism of molecule adsorption that is slow or time dependent. As E_{pit} increased with time, there may also be adsorption selectivity with preference given to vanadate and molybdate anions once they reach the surface. Surface coverage did not follow the Langmuir isotherm and showed a strong dependence on the applied potential (Figure 215). This dependence of surface coverage on applied potential may be due to the surface having a higher positive charge and a stronger electric field as a result of the difference between the applied potential and E_{PZC}.

Effect of Molybdate on Repassivation AA2024 Using Scratch Repassivation Experiments

Under the chosen experimental conditions no inhibition of current density or total anodic charge after repassivation is observed in molybdate containing solutions. One explanation is that the chosen conditions for inhibition are not relevant to the actual scratch environment. There are other possibilities that can account for the benefit by molybdate. The first is that molybdate acts as a buffer in the scratch. The buffer properties of molybdate in reducing acid are shown in Figure 128. It is possible that the pH of the solution in the scratch is higher than was tested in these experiments. This could change the stability of the native aluminum oxide leading to decreases in current density. Another possibility is that the buffer capacity is overwhelmed by hydrolysis of aluminum cations resulting in a much lower pH in the scratch. At this lower pH, the stability of molybdate oxides increases to much higher potentials as shown in Figure 217. The result of a more stable molybdate oxide could be the growth of a more protective mixed aluminum-molybdate oxide barrier. A third possibility is that the charge must be assessed over a longer time period to observe inhibition of anodic charge.

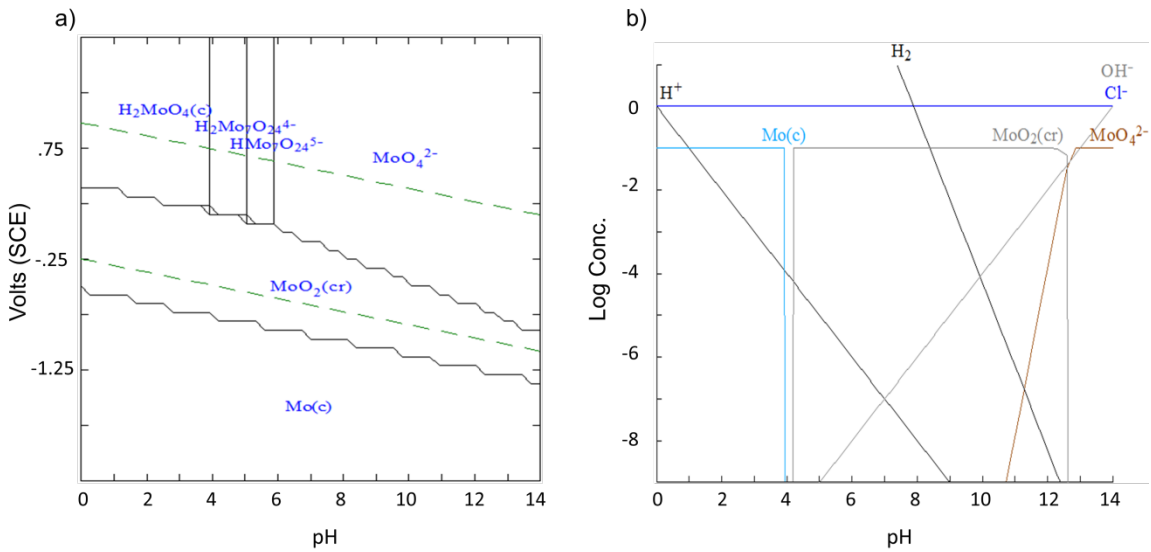

Figure 217. (a) E-pH diagram for 0.1 M molybdate and 1 M chloride solution showing the stability of molybdenum oxide over a large region of potential and pH with high potential stability in the low pH region. (b) Speciation of molybdate-chloride system at previously stated concentrations at -0.8 V vs. SCE.

There is a third mechanism through which molybdate might promote scratch repassivation. An oxide barrier may be present in the case of molybdate. The defective state of the oxide may result in high current densities. Figure 138 (a) shows the results of capacitance measurements for molybdate inhibited solutions. In the uninhibited solution the impedance magnitude was approximately 0.3 Ω-cm^2. When molybdate was added to solution at a range of concentrations from 1 mM to 1 M the impedance magnitude was shown to increase anywhere from 1.5 Ω-cm^2 to 3.0 Ω-cm^2. It is possible that the presence of an oxide results in a permeation barrier despite the large anodic dissolution rate.

Corrosion Inhibition of AA7075 and Carbon Steel 1018

Corrosion Inhibition with Single Inhibitors

Single corrosion inhibitors that have been considered as replacement for chromate for AA2024 were successfully transferred to AA7075 and carbon steel 1018. Cerium acetate, sodium molybdate and sodium vanadate behaved as anodic and/or cathodic inhibitor for AA7075 (see Figure 144, Figure 145 and Figure 146, respectively). Only E_{pit} increased with the concentration of molybdate, making it only an anodic inhibitor. The open circuit decreased, resulting in an increase of the passive range, with the concentration of cerium and vanadate. Furthermore, the presence of cerium and vanadate resulted in decrease of the cathodic current. Consequently, cerium and vanadate are both successful anodic and cathodic inhibitors.

The corrosion inhibitors had less of an effect on carbon steel 1018. Cerium and vanadate were failed as either anodic or cathodic inhibitors. Only molybdate was successful. It resulted in decreasing the passive current (see Figure 147) as well as the cathodic current making it both an anodic and cathodic inhibitor.

Corrosion Inhibition with Inhibitor Combinations

Inhibitors were combined in order to identify any possible synergistic behavior between them. Two combinations were studied, cerium acetate combined with sodium vanadate, and cerium acetate with sodium molybdate.

Only cerium/vanadate was partially successfully synergistic with AA7075. E_{pit} was found to be higher for cerium/vanadate than for either of its individual compounds. Both combinations were more successful with carbon steel 1018. E_{pit} measured in cerium/molybdate was higher than for cerium and lower than for molybdate. This is in accord with the single inhibitor measurements since cerium did not behave as an inhibitor for carbon steel 1018. However, the combination of cerium and molybdate resulted in a higher level of cathodic inhibition than either cerium (which did not behave as a single cathodic inhibitor) or molybdate. Cathodic inhibition synergy was also observed with cerium/vanadate for carbon steel 1018. Neither cerium nor vanadate acted as single cathodic inhibitor. It is therefore noticeable that both inhibitor combinations are more favorable inhibiting compounds than their single counterparts.

Synergistic behaviors have been proven to be occurring in certain cases and were especially successful for carbon steel 1018. However they were not accurately predicted during this project. Consequently, further studies to better understand how multi-compounds treatment may affect the speciation of either inhibitor should be pursued.

Investigation of the Effect of the Inhibitors on the Microstructural Heterogeneity of AA2024

Rotating Disc Arrays

Rotating disc arrays were used to study the impact of the density and size of copper intermetallic particles on the cathodic behavior. The arrays contained copper electrodes of various diameters and at various distances from each other. It was found that the cathodic inhibitor effects of vanadate increased as the density and diameter of the copper electrodes increased. This is consistent with the comparison between AA2024 and AA7075, Vanadate has been proven to be good cathodic inhibitor for AA2024, based upon the work that was performed at UVA (see Figure 75), and was more effective than for AA7075 (see Figure 141). AA2024 contains more copper than AA7075, and SEM analysis (such as Figure 54 for AA2024 and Figure 184 for AA7075) shows clearly that larger copper-rich intermetallic particles can be found in larger quantity in AA2024, resulting in vanadate being a better cathodic inhibitor for AA2024. Cerium cathodic inhibitive properties only increased when the density increased and the size of the intermetallic properties decreased.

Aluminum/Copper Multi-Electrode Array Study of Inhibitor

The aluminum/copper MEA was used to simulate copper-rich intermetallic particles in an aluminum-rich matrix. The comparison was more relevant to AA2024 than to AA7075 since it contains more copper and copper-rich precipitates. When the vanadate was combined with NaCl, it was found that better results were observed at lower concentration, 0.001 mol/L and 0.005 mol/L, rather than at 0.05 mol/L. This was consistent with the Levich analysis performed on AA2024 (see Figure 73 and Figure 70(d)), which concluded that the critical inhibitor concentration needed to suppress ORR is below 0.005 mol/L sodium vanadate.

Cerium and molybdate did not behave cathodic inhibitor when combined at 0.05 mol/L with NaCl. However, it was found that pretreatment resulted in a cathodic inhibition for both compounds at the same concentration. Pretreatment was only found to be effective for vanadate at lower concentration (0.005 mol/L compared to 0.05 mol/L), following the AA2024 Levich prediction. The effect of vanadate pretreatment on anodic behavior of AA2024 was also studied. It was found that it had no impact on E_{pit} (see Figure 65). Consequently, while pretreatment does not affect the anodic behavior, it will improve the cathodic behavior when vanadate concentration is below 0.005 mol/L.

It was mentioned above that vanadate speciation is also dependent on the presence of cations, which do not affect the corrosion mechanism otherwise. It may be postulated that preexposure in the absence of NaCl had an impact on the type of vanadate species adsorbed on the MEA surface.

Inhibitor Interaction with AA7075

EDS and Auger electron spectrometry have shown that cerium, molybdate and vanadate are all present on the surface of AA7075. However, only cerium was found to be dependent on the quantity of the inhibitor (0.05 and 0.005 mol/L) using surface EDS (see

Figure 183). When measuring the cathodic inhibition of these inhibitors using the Al/Cu MEA, the inhibitors concentration was found to have a significant effect when the MEA was pretreated. Based upon the surface EDS, it appears that the concentration role is not due to the amount of inhibitor on the surface but may be due to the species of inhibitors. This would be due to the fact that the pH of the solution is dependent on the concentration of the inhibitor (see Figure 16) and the inhibitor speciation is directly related to the pH (see Figure 17, Figure 18 and Figure 19).

Mott-Schottky

Mott-Schottky was performed on AA7075 specimens and the flatband potential can be derived from the results of the measurement. The flat band potential is taken as the point where the extrapolated line crosses the x-axis. The flatband potential is closely related to the surface energy of the solid. A positive shift in flatband potential is usually accompanied by an increase in localized corrosion. A negative shift such as the one measured on AA7075 (see Figure 198) in the presence of inhibitor and also when the concentration of the inhibitors decrease may be due to competitive adsorption of the inhibitor with the chloride. The effect of the inhibitor concentration is similar to that measured using the Al/Cu. It is also noteworthy that neither cerium nor molybdate were found to have an effect on anodic measurements. Consequently, the flatband potential shifts observed for AA7075 are more likely to be relevant to cathodic inhibiton.

Atmospheric MEA

Atmospheric test using the Al/Cu MEA were performed in order to assess the ability of the various inhibitor to perform at various relative humidity. Only vanadate and cerium were found to perform successfully at lower relative humidity (60 and 70%). At higher relative humidity, vanadate and cerium were not able to maintain inhibition, based upon the total charge exchanged. This was due to the fact that at higher relative humidity, the concentration of vanadate and cerium in solution is high and therefore they cannot perform as cathodic inhibitors.

Conclusions and Implications for Future Research/Implementation

Conclusions

Permanganate leads to an increase in the E_{pit} of AA2024 when partially oxidized manganese oxides were electrochemically deposited over the AA2024 aluminum matrix. Increases in OCP accompanied the elevated E_{pit}. Permanganate increased cathodic reaction rates when it was present in solution owing to the addition of this oxidizing cathodic reactant. However, when permanganate was used as a pretreatment and was electrochemically deposited as a lower valence state oxide on the IMCs, it decreased cathodic reaction rates. OCP was greatly reduced after pretreatment as copper-rich sites were covered with manganese oxides. The reduction of high valence manganese oxides may account for the slow decrease in the OCP. Copper replating was decreased after pretreatments. However, this effect did not occur to the same extent as when permanganate was added as a solution phase inhibitor. The manganese oxide has been shown to be present initially in a high valence state, most likely MnO_2. The reduction of this oxide to lower valence compounds has a number of effects including acting as an additional cathodic reactant which has the effect of complicating the cathodic reaction kinetics. The high valence oxide also provides a mechanism for the release of Mn(III) into solution.

The dominant species for almost all vanadate concentrations in 50 mM NaCl was $V_4O_{12}^{4-}$. However, there may also be a change in speciation due to chloride concentration.

Vanadate in 50 mM NaCl solutions increased the average E_{pit} values for both AA2024-T3 and 99.99% Al. While aluminum had a monotonic relationship with vanadate concentration after only 1 hour at open circuit, it took 24 hours for a similar correlation to occur on AA2024-T3. E_{pit} and the passive potential range increased with open circuit exposure time and with increasing vanadate concentration in the test solution. Vanadate increased E_{pit} for both pure aluminum and AA2024-T3, suggesting that vanadate species do more than protect intermetallic compounds in the aluminum matrix of alloys like AA2024. A lower limit of 5 mM $NaVO_3$ in the 50 mM NaCl solution was needed to elevate E_{pit} on AA2024-T3. Vanadate pretreatments of the surface of AA2024-T3 followed by rinsing in high-purity water did not have any benefit toward raising E_{pit} values during anodic polarization in 50 mM NaCl solution. The anionic vanadate inhibitor must be in solution during corrosion. This implies that the vanadate anions compete with chloride ions at pit sites but vanadate is not permanently enriched at surface sites by pretreatment.

Cathodic polarization tests indicated that the ORR was suppressed by vanadate for both Cu and AA2024-T4. The effective inhibitor concentration needed to suppress the ORR is at or below 1 mM $NaVO_3$ in solution with 50 mM NaCl.

An analysis using the Gueshi model demonstrated the effective area on which the ORR could occur on AA2024-T4 for all vanadate concentrations in 50 mM NaCl was reduced by a factor of 10 as compared to that for AA2024-T4 in 50 mM NaCl. ORR and, possibly, pitting are dependant on an inhibitor molecule adsorption mechanism. This mechanism is potential dependant but does not show the linear relationship between the coverage and log of

concentration of the Temkin isotherm. The relationship between vanadate concentration in solution, vanadate anion surface coverage, and inhibition is complex.

The effects of cerium-permanganate, vanadate-molybdate and vanadate-cerium combinations on corrosion inhibition of AA2024 were studied. High concentrations of cerium in the pretreatment package can lead to a homogeneous cerium enriched oxide surface. However, such a treatment shows little indication of being passive or suppressing corrosion. Cerium-permanganate pretreatments show insignificant anodic inhibition in pitting scans but reduced copper replating during open circuit corrosion. Permanganate pretreatments are effective at increasing ΔE (E_{pit}-OCP) mainly through reducing the OCP. Permanganate pretreatments are shown to have strong cathodic inhibition properties. Cerium-permanganate pretreatments show promise as cathodic inhibitors, in some cases reducing cathodic current density two and a half orders of magnitude when compared to AA2024-T351. However, no indication of a combined species was found and there is no reference to such a species in the literature. Cerium can act detrimentally to block permanganate oxide formation over copper rich intermetallic particles.

The dominant species for vanadate and molybdate in 50 mM NaCl were $V_4O_{12}^{4-}$ and MoO_4^{-2}. The addition of molybdate in vanadate solutions increased the percentage of $V_4O_{12}^{4-}$ present in solution.

Vanadate and molybdate solutions in 50 mM NaCl solutions increased the average E_{pit} for both AA2024-T3 and 99.99% Al. Vanadate and molybdate in solution increased E_{pit} for both pure aluminum and AA2024-T3 and decreased the pitting of the aluminum matrix of alloys like AA2024. This implies that the vanadate and molybdate anions compete with chloride ions at pit sites. This competition may be impacted by the molecular weight of the anions and selectivity of the surface to anion adsorption. The cerium pretreatments covered the Al-Cu-Mg particles with cerium and as a result, vanadate molecules could not reach the particles. When the coverage was degraded, lower E_{pit} occurred for specimens with higher pretreatment concentrations but the same vanadate concentration in solution. This also indicates that vanadate may need to be present at the surface before pitting initiates to be effective.

Cathodic polarization tests indicated that the ORR was most suppressed by vanadate for both Cu and AA2024-T4. ORR and, possibly, pitting are dependent on an inhibitor molecule adsorption mechanism. This mechanism is not potential dependent at high inhibitor concentrations and may not follow the Temkin isotherm. Surface coverage did not follow the Langmuir isotherm and showed a strong dependency on applied potential, which could result from the surface having a higher positive charge and a stronger electric field as the applied potential is increase above E_{PZC}. The relationship between vanadate and molybdate anion surface coverage and inhibition is complex.

The effect of inhibitor concentration and chloride concentration on the repassivation of AA2024, AA7075, and high purity aluminum has been investigated. Chromate is an inhibitor of net anodic scratch current densities as well as total charge after depassivation. This result is evident for both AA2024 and AA7075 at a neutral pH of 6.5. The net anodic charge passed in the presence of chromate is two orders of magnitude lower than uninhibited solution for AA2024 and one order of magnitude for AA7075. A thick oxide barrier is observed through a variation on the scratched electrode technique that exploits high frequency capacitance measurements to observe oxide regrowth. Scratch current density reduction by molybdate of either AA2024 or AA7075 was not

observed. However, the enhanced regrowth of an oxide has been observed through the capacitance measurements. Buffering is also operative. This suggests that there are multiple mechanisms through which inhibition occurs as both chromate and molybdate promote scratch repassivation.

Cerium acetate, sodium vanadate and sodium molybdate have been shown to have the potential to be applied to aluminum alloy 7075 and carbon steel 1018. Cerium and vanadate acted as anodic inhibitors for AA7075 by decreasing the OCP while molybdate increased E_{pit}. Furthermore, cerium and vanadate acted as cathodic inhibitor as the passive current was found to decrease. Molybdate alone was both an anodic and cathodic inhibitor for carbon steel 1018. The combination of cerium with vanadate, and cerium with molybdate resulted in synergistic effect for the anodic and cathodic inhibition with carbon steel. Synergy was only measured for AA7075 for cerium and vanadate, and it only impacted E_{pit}.

The cathodic effectiveness of the inhibitor has been found to increase for vanadate and cerium with the density of copper intermetallics particles. This was confirmed when comparing the ORR studies for AA2024 and AA7075, with AA2024 having a higher IMC density (as measured with SEM). Additional cathodic inhibition studies using 100 electrodes Al/Cu array revealed that the concentration and the pretreatment had an effect on the inhibitor properties. Lower concentration and pretreatment resulted in better cathodic inhibition. Pretreatment was found to also result in inhibitor-rich precipitates for vanadate and molybdate, as well as homogeneous precipitation for all inhibitors, using SEM and EDS mapping. It is suggested that lower concentration may result in a better homogeneous covering without precipitates. Consequently, the various compounds would be more useful when pretreated at low concentration. Cathodic studies on AA2024 predicted a critical inhibitor concentration of 0.05 M for vanadate which was confirmed with the Al/Cu MEA. Pretreatment was not effective for AA2024 during anodic testing due to competitive adsorption mechanism between vanadate and chloride. This is not the mechanism observed during cathodic inhibition.

During atmospheric testing, only vanadate and cerium behaved as inhibitor at lower relative humidity. It may be postulated that since molybdate did not act as an inhibitor, the prominent inhibition mechanism under those conditions would be cathodic (since molybdate was not found to act as a cathodic inhibitor for AA7075). When the relative humidity increases above 80%, cerium and vanadate stop acting as inhibitors. This is due to the higher inhibitor and chloride concentration that are expected on the surface after deliquescence as the relative humidity comes close to 100%. The local environment becomes more aggressive and the inhibitor concentration increases above the critical concentration.

Implications for Future Research/Implementation

Transfer of technology to other metallic alloys

Cerium, vanadate and molybdate, which had been successfully applied to AA2024, were shown to be partially transferable to AA7075 and carbon steel 1018. It was also shown that other permanganate acted as an anodic inhibitor by being deposited on AA2024 matrix which is very similar to that of other aluminum alloys such as AA7075. Furthermore, MEA studies successfully mimicked copper-rich intermetallic particles in an aluminum-rich matrix, which was applicable to AA2024 due to the localized corrosion mechanisms. The corrosion mechanisms on

AA7075 and carbon steel are different due to different microstructures (the copper-rich intermetallics particles present AA2024 do not exist in such large size and quantity in AA7075). It is suggested to continue the inhibitor technology transfer between aluminum alloys as well as to carbon steels (for which it was partly successful). Furthermore, it is recommended to focus on the corrosion mechanisms and microstructures using MEA that mimic new materials of interest.

Development of application techniques with combination of inhibitors

It was shown during this project that different inhibitors behaved in various ways depending on the type of treatment, e.g. in solution vs. pretreatment. Permanganate acted as a better cathodic inhibitor when AA2024 was pretreated, while vanadate was a better anodic inhibitor when in solution with NaCl. The overall corrosion protection of AA2024 can potentially be greatly improved by combining those two inhibitors. It was shown that combination of inhibitors with various behaviors can result in synergistic properties. It is therefore recommended to combine vanadate to permanganate in order to improve corrosion inhibition of AA2024.

However, practical application of the combination of vanadate and permanganate will require the development of application techniques to retain the cathodic properties of pretreated permanganate as well as the anodic behavior of vanadate in solution. This issue may not be limited to the combination of vanadate and permanganate. Any practical application of combination of corrosion inhibitors may lead to issues. It has been shown that the environmental conditions, such as concentration and pH, will impact drastically the speciation of the inhibitors and their efficiency. Therefore, when combining inhibitors, it is important to take into consideration the development of potentially detrimental competitive environmental conditions. This makes better designed, more advanced and fully tested application techniques a very important requirement for the practical development of combination of corrosion inhibitors.

It is therefore suggested that future work should 1) focus on developing advanced coating techniques that can help maintain the efficiency of the inhibitor species over long period of time; 2) confirm the synergistic properties of vanadate and permanganate when applied to AA2024, resulting in an improved inhibition of corrosion; 3) improve single inhibitor application techniques so that they can be applied to a combination of inhibitors requiring different treatments; and 4) use vanadate and permanganate to confirm that the improved application techniques can be used successfully to maintain the efficiency of two inhibitors.

Study of inhibitor combinations for aggressive atmospheric conditions

Cerium and vanadate have been shown to efficiently inhibit corrosion under atmospheric corrosion at lower relative humidity. However, their efficiency decreased as the relative humidity increased above 80%. This was due to two mechanisms: the increase in chloride concentration and the inhibitor quantity reaching the critical maximum concentration. Consequently, it was not possible to rely on a single compound to inhibit corrosion throughout the entire range of relative humidity that may exist in atmospheric conditions. Since synergistic corrosion inhibition behaviors have been observed, it is suggested that a combination of corrosion inhibition may result in a better protection over a wider range of environment.

Pretreatment with cerium and vanadate have already been shown to be successful solutions at lower relative humidity, therefore it is suggested that those two compounds are to be used as a basis for combination of inhibitors. The second inhibitor must be able to inhibit corrosion in high chloride environment and when present in high concentration. It was shown that vanadate acts as an anodic inhibitor without a maximum critical concentration when present in solution with NaCl, and should therefore be used as a potential secondary inhibitor. Permanganate pretreatment also resulted in anodic inhibition. This was due to oxidized manganese oxides being deposited over the aluminum-based matrix. Therefore, this is not a competitive mechanism against chloride adsorption and therefore, it may not be hindered by high chloride concentrations. Consequently, it is suggested to perform synergistic studies of combination of inhibitors under atmospheric conditions for AA2024 using either cerium or vanadate pretreatment as a first inhibitor, and vanadate in solution, or permanganate pretreatment as a second inhibitor.

Literature Cited

1. Kendig, M. W. & Buchheit, R. G. Corrosion Inhibition of Aluminum and Aluminum Alloys by Soluble Chromates, Chromate Coatings, and Chromate-Free Coatings. *Corrosion* **59,** 379 (2003).

2. Clark, W. J. & McCreery, R. L. Inhibition of Corrosion-Related Reduction Processes via Chromium Monolayer Formation. *Journal of the Electrochemical Society* **149,** B379–B386 (2002).

3. Ilevbare, G. O., Scully, J. R., Yuan, J. & Kelly, R. G. Inhibition of Pitting Corrosion on Aluminum Alloy 2024-T3: Effect of Soluble Chromate Additions vs Chromate Conversion Coating. *Corrosion* **56,** 227 (2000).

4. Xia, L., Akiyama, E., Frankel, G. S. & McCreery, R. L. Storage and Release of Soluble Hexavalent Chromium from Chromate Conversion Coatings Equilibrium Aspects of Cr VI Concentration. *Journal of the Electrochemical Society* **147,** 2556 (2000).

5. O'Brian, P. & Kortenkamp, A. The Chemistry Underlying Chromate Toxicity. *Transition Metal Chemistry* **20,** 636

6. *Occupational Exposure to Hexavalent Chromium; Final Rule*. 10099 (OSHA, 2006).

7. Mansfeld, F., Wang, Y. & Shih, H. Development of 'Stainless Aluminum'. *Journal of the Electrochemical Society* **138,** L74 (1991).

8. Chambers, B. D. & Taylor, S. R. The high throughput assessment of aluminium alloy corrosion using fluorometric methods. Part II – A combinatorial study of corrosion inhibitors and synergistic combinations. *Corrosion Science* **49,** 1597 (2007).

9. Ilevbare, G. O. & Scully, J. R. Mass-Transport-Limited Oxygen Reduction Reaction on AA2024-T3 and Selected Intermetallic Compounds in Chromate-Containing Solutions. *Corrosion* **57,** 134 (2001).

10. Szklarska-Smialowska, Z. Inhibition of Pitting Corrosion. in (NACE, 1989).

11. Kaesche, H. in (1971).

12. Pride, S. T., Scully, J. R. & Hudson, J. R. Metastable Pitting of Aluminum and Criteria for the Transition to Stable Pit Growth. *Journal of the Electrochemical Society* **141,** 3028 (1994).

13. Cinderey, R. J. & Burstein, G. T. The effects of chromate on the transient repassivation potential of aluminium in chloride solution. *Corrosion Science* **33,** 493 (1992).

14. Natishan, P. M., McCafferty, E. & Hubler, G. K. The Effect of pH of Zero Charge on the Pitting Potential. *Journal of the Electrochemical Society* **133,** 1061 (1986).

15. McCafferty, E. The electrode kinetics of pit initiation on aluminum. *Corrosion Science* **37,** 481 (1995).

16. Zhao, J., Frankel, G. S. & McCreery, R. L. Corrosion Protection of Untreated AA-2024-T3 in Chloride Solution by a Chromate Conversion Coating Monitored with Raman Spectroscopy. *Journal of the Electrochemical Society* **145,** 2258 (1998).

17. Stearns, D. M. & Wetterhahn, K. E. Intermediates produced in the reaction of chromium(VI) with dehydroascorbate cause single-strand breaks in plasmid DNA. *Chemical Research in Toxicology* **10,** 271 (1997).

18. Lay, P. A. & Levina, A. Activation of Molecular Oxygen during the Reactions of Chromium(VI/V/IV) with Biological Reductants: Implications for Chromium-Induced Genotoxicities1. *Journal of the American Chemical Society* **120,** 6704 (1998).

19. Vukasovich, M. S. & Farr, J. P. G. *Materials Performance* **25,** 9 (1986).

20. Jakab, M. A., Presuel-Moreno, F. & Scully, J. R. Critical Concentrations Associated with Cobalt, Cerium, and Molybdenum Inhibition of AA2024-T3 Corrosion: Delivery from Al-Co-Ce(-Mo) Alloys. *Corrosion Science* **61,** 246–263 (2005).

21. Alsaffar, A. H. *et al.* Effect of Molybdenum Ion-Implantation on the General and Pitting Corrosion Behavior of Pure Aluminum and a High-Strength Aluminum-Alloy. *Corrosion Science* **20,** 127 (1980).

22. Silva, J. W. J., Codaro, E. N., Nakazato, R. Z. & Hein, L. R. O. Influence of Chromate, Molybdate, and Tungstate on Pit Formation in Chloride Medium. *Applied Surface Science* **252,** (2005).

23. Moshier, W. C. & Davis, G. D. Interaction of Molybdate Anions with the Passive Flim on Aluminum. *Corrosion* **46,** 46 (1990).

24. Breslin, C. B., Treacy, G. & Carroll, W. M. Studies on the Passivation of Aluminium in Chromate and Molybdate Solutions. *Corrosion Science* **36,** (1994).

25. Maksimovskaya, R. I. & Maksinmov, G. M. 95Mo and 17O NMR Studies of Aqueous Molybdate Solutions. *Inorganic Chemistry* **46,** 3688–3695 (2007).

26. Zein El Abedin, S. Molybdate and Tungstate Anions o the Inhibition of Aluminium in Chloride Solutions. *Journal of Applied Electrochemistry* **31,** 711 (2001).

27. Emregül, K. C. & Aksüt, A. A. The Effect of Sodium Molybdate on the Pitting Corrosion of Aluminum. *Corrosion Science* **45,** 2415 (2003).

28. Presuel-Moreno, F., Jakab, M. A. & Scully, J. R. Inhibition of the Oxygen Reduction Reaction on Copper with Cobalt, Cerium, and Molybdate Ions. *Journal of the Electrochemical Society* **152,** B376 (2005).

29. Jakab, M. A., Presuel-Moreno, F. & Scully, J. R. Effect of Molybdate, Cerium, and Cobalt Ions on the Oxygen Reduction Reaction on AA2024-T3 and Selected Intermetallics: Experimental and Modeling Studies. *Journal of the Electrochemical Society* **153,** B244 (2006).

30. Buchheit, R. G., Guan, H., Mahajanam, S. & Wong, F. Active corrosion protection and corrosion sensing in chromate-free organic coatings. *Progress in Organic Coatings* **47,** 174 (2003).

31. Iannuzzi, M., Kovac, J. & Frankel, G. S. A study of the mechanisms of corrosion inhibition of AA2024-T3 by vanadates using the split cell technique. *Electrochimica Acta* **52,** 4032 (2007).

32. Iannuzzi, M. & Frankel, G. S. Mechanisms of corrosion inhibition of AA2024-T3 by vanadates. *Corrosion Science* **49,** 2371 (2007).

33. Moutarlier, V., Gigandet, M. P., Ricq, L. & Pagetti, J. Electrochemical characterisation of anodic oxidation films formed in presence of corrosion inhibitors. *Applied Surface Science* **183,** 1 (2001).

34. Virtanen, S., Iver, M. B., Sproule, G. I., Schmuki, P. & Graham, M. J. A surface analytical and electrochemical study on the role of cerium in the chemical surface treatment of stainless steels. *Corrosion Science* **39,** 1897 (1997).

35. Hinton, B. R. W. Corrosion inhibition with rare earth metal salts. *Journal of Alloys and Compounds* **180,** 15 (1992).

36. Arenas, M. A., Bethencourt, M., Botana, F. J., de Damborenea, J. & Marcos, M. Inhibition of 5083 aluminium alloy and galvanised steel by lanthanide salts. *Corrosion Science* **45,** 157

37. Aramaki, k. XPS and EPMA studies on self-healing mechanism of a protective film composed of hydrated cerium(III) oxide and sodium phosphate on zinc. *Corrosion Science* **45,** 199 (2003).

38. Hinton, B. R. W., Arnott, D. R. & Ryan, N. E. *Metals Forum* **7,** 211 (1984).

39. Arnott, D. R., Ryan, N. E., Hinton, B. R. W., Sexton, B. A. & Hughes, A. E. *Applied Surface Science* **22-23,** 236 (1985).

40. Aldykewicz, Jr., A. J., Isaacs, H. S. & Davenport, A. J. The Investigation of Cerium as a Cathodic Inhibitor for Aluminum-Copper Alloys. *Journal of the Electrochemical Society* **142,** 3342 (1995).

41. Mansfeld, F., Lin, S., Kim, S. & Shih, H. Corrosion Protection of Al Alloys and Al-Based Metal Matrix Composites by Chemical Passivation. *Corrosion* **45,** 615 (1989).

42. Arnott, D. R., Hinton, B. R. W. & Ryan, N. E. Cationic-Film-Forming Inhibitors for the Protection of the AA 7075 Aluminum Alloy Against Corrosion in Aqueous Chloride Solution. *Corrosion* **45,** 12 (1989).

43. Buchheit, R. G., Mamidipally, S. B., Schmutz, P. & Guan, H. Active Corrosion Protection in Ce-Modified Hydrotalcite Conversion Coatings. *Corrosion* **58,** 3 (2002).

44. Jakab, M. A. & Scully, J. R. On-demand release of corrosion-inhibiting ions from amorphous Al–Co–Ce alloys. *Nature Materials* **4,** 667 (2005).

45. Davenport, A. J. & Isaacs, H. S. X-Ray Absorption Study of Cerium in the Passive Film on Aluminum. *Journal of The Electrochemical Society* **136,** 1837 (1989).

46. Kolics, A., Besing, A. S., Baradlai, P. & Wieckowski. Cerium Deposition on Aluminum Alloy 2024-T3 in Acidic NaCl Solutions. *Journal of The Electrochemical Society* **150,** B512 (2003).

47. Hayes, S. A., Yu, P., O'Keefe, T. J., O'Keefe, M. J. & Stoffer, J. O. The Phase Stability of Cerium Species in Aqueous Systems I. E–pH Diagram for the Ce–HClO4–H2O System. *Journal of The Electrochemical Society* C623 (2002).

48. Yu, P., Hayes, S. A., O'Keefe, T. J., O'Keefe, M. J. & Stoffer, J. O. The Phase Stability of Cerium Species in Aqueous Systems II. The Ce(III/IV)–H2O–H2O2/O2 Systems. Equilibrium Considerations and Pourbaix Diagram Calculations. *Journal of The Electrochemical Society* C74 (2006).

49. Edington, J., O'Keefe, M. J. & O'Keefe, T. J. Formation of Cerium Oxide/Hydroxide on Copper Substrates by Spontaneous Immersion Process. *Journal of The Electrochemical Society* **154,** D563 (2007).

50. Hughes, A. E. *et al.* Factors Influencing the Deposition of Ce–based Conversion Coatings, part I: The Role of Al3+ Ions. *Surface and Coatings Technology* **203,** 2927 (2009).

51. Lau, D. *et al.* Factors Influencing the Deposition of Ce-based Conversion Coatings, Part II: The Role of Localised Reactions. *Surface and Coatings Technology* **203,** 2937 (2009).

52. Bellezze, T., Roventi, G. & Fratesi, R. Electrochemical study on the corrosion resistance of Cr III-based conversion layers on zinc coatings. *Surface and Coatings Technology* **155,** 221 (2002).

53. Zhang, X. *et al.* Comparison of the morphology and corrosion performance of Cr(VI)- and Cr(III)-based conversion coatings on zinc. *Surface and Coatings Technology* **199,** 2005 (92).

54. Ilevbare, G. O., Schneider, O., Kelly, R. G. & Scully, J. R. In Situ Confocal Laser Scanning Microscopy of AA 2024-T3 Corrosion Metrology - I. Localized Corrosion of Particles. *Journal of the Electrochemical Society* **151,** B453 (2004).

55. Schneider, O., Ilevbare, G. O., Scully, J. R. & Kelly, R. G. In Situ Confocal Laser Scanning Microscopy of AA 2024-T3 Corrosion Metrology - II. Trench Formation Around Particles. *Journal of the Electrochemical Society* **151,** B465 (2004).

56. Scully, J. R., Knight, T. O., Buchheit, R. G. & Peebles, D. E. Electrochemical Characteristics of the Al2Cu, Al3Ta and Al3Zr Intermetallic Phases and their Relevancy to the Localized Corrosion of Al Alloys. *Corrosion Science* **35,** 185 (1993).

57. Wei, R. P., Liao, C. M. & Gao, M. A transmission electron microscopy study of constituent-particle-induced corrosion in 7075-T6 and 2024-T3 aluminum alloys. *Metallurgical and Materials Transactions A* **29,** 1153 (1998).

58. Chen, G. S., Gao, M. & Wei, R. P. Microconstituent-induced pitting corrosion in aluminum alloy 2024-T3. *Corrosion* **52,** (1996).

59. Harlow, D. G. & Wei, R. P. A probability model for the growth of corrosion pits in aluminum alloys induced by constituent particles, Engineering Fracture Mechanics. *Engineering Fracture Mechanics* **59,** 305 (1998).

60. Buchheit, R. G., Grant, R. P., Hlava, P. F., McKenzie, B. & Zender, G. L. Local dissolution phenomena associated with S phase (Al2CuMg) particles in aluminum alloy 2024-T3. *Journal of the Electrochemical Society* **144,** 2621 (1997).

61. Buchheit, R. G. *et al.* The electrochemistry of intermetallic particles and localized corrosion in Al alloys. *JOM-Journal of the Minerals Metals & Materials Society* **53,** 29 (2001).

62. Kim, S., Burns, J. T. & Gangloff, R. P. Fatigue crack formation and growth from localized corrosion in Al-Zn-Mg-Cu. *Engineering Fracture Mechanics* **76,** 651 (2009).

63. Pidaparti, R. M. & Patel, R. R. Correlation between corrosion pits and stresses in Al alloys. *Materials Letters* **62,** 4497 (2008).

64. Sankaran, K. K., Perez, R. & Jata, K. V. Effects of pitting corrosion on the fatigue behavior of aluminum alloy 7075-T6: modeling and experimental studies. *Materials Science & Engineering A* **297,** 223 (2001).

65. Twite, R. L. & Bierwagen, G. P. Review of alternatives to chromate for corrosion protection of aluminum aerospace alloys. *Progress in Organic Coatings* **33,** 91 (1998).

66. Robertson, W. D. Molybdate and Tungstate as Corrosion Inhibitors and the Mechanism of Inhibition. *Journal of the Electrochemical Society* **98,** 94 (1951).

67. Ralston, K. D., Chrisanti, S., Young, T. L. & Buchheit, R. G. Corrosion inhibition of aluminum alloy 2024-T3 by aqueous vanadium species. *Journal of the Electrochemical Society* **155,** C350 (2008).

68. Jakab, M. A., Presuel-Moreno, F. & Scully, J. R. Critical Concentrations Associated with Cobalt, Cerium, and Molybdenum Inhibition of AA2024-T3 Corrosion: Delivery from Al-Co-Ce(-Mo) Alloys. *Corrosion* **61,** 246 (2005).

69. Iannuzzi, M. & Frankel, G. S. Inhibition of Aluminum Alloy 2024 Corrosion by Vanadates: An In Situ Atomic Force Microscopy Scratching Investigation. *Corrosion* **63,** 672 (2007).

70. Iannuzzi, M., Young, T. & Frankel, G. S. Aluminum alloy corrosion inhibition by vanadates. *Journal of the Electrochemical Society* **153,** B533 (2006).

71. Ralston, K. D., Young, T. L. & Buchheit, R. G. Electrochemical Evaluation of Constituent Intermetallics in Aluminum Alloy 2024-T3 Exposed to Aqueous Vanadate Inhibitors. *Journal of the Electrochemical Society* **156,** C135 (2009).

72. Lizlovs, E. A. Molybdates as Corrosion-Inhibitors in Presence of Chlorides. *Corrosion* **32,** 263 (1976).

73. Pourbaix, M. *Atlas of Electrochemical Equilibria in Aqueous Solution*. (NACE, 1974).

74. Baek, Y. & Frankel, G. S. Electrochemical quartz crystal microbalance study of corrosion of phases in AA2024. *Journal of the Electrochemical Society* **150,** B1 (2003).

75. Bibber, J. W. US Patent 4895608 (1990). (1990).

76. Bibber, J. W. US Patent 5554231 (1996). (1996).

77. B117 - Standard Practice for Operating Salt Spray (Fog) Apparatus. (2009).

78. Bibber, J. W. A Chrome Free Conversion Coating and Sealant for Aluminum and Its Alloys. in (NACE).

79. Crouse, M., Vasanth, K. L., Miller, A. E. & Pujar, M. G. Evaluation of Potassium Permanganate (KMnO4) as a Green Corrosion Inhibitor/Sealant for Anodized Al 2024 and Al 6061 at Different pH Values. in (NACE, 2002).

80. Kulinich, S. A., Farzaneh, M. & Du, X. W. Growth of corrosion-resistant manganese oxide coatings on an aluminum alloy. *Inorganic Materials* **43,** 956 (2007).

81. Danilidis, I., Davenport, A. J. & Sykes, J. M. Characterisation by X-ray absorption near-edge spectroscopy of KMnO4-based no-rinse conversion coatings on Al and Al alloys. *Corrosion Science* **49,** 1981 (2007).

82. Danilidis, I., Hunter, J., Scamans, G. M. & Sykes, J. M. Effects of inorganic additions on the performance of manganese-based conversion treatments. *Corrosion Science* **49,** 1559 (2007).

83. Swain, H. A., Lee, C. & Rozelle, R. B. Determination of the solubility of manganese hydroxide and manganese dioxide at 25.deg. by atomic absorption spectrometry. *Analytical Chemistry* **47,** 1135 (1975).

84. Buciuman, F., Patcas, F., Craciun, R. & Zahn, D. R. T. Vibrational spectroscopy of bulk and supported manganese oxides. *Physical Chemistry Chemical Physics* **1,** 185 (1999).

85. Danilidis, I., Hunter, J., Scamans, G. M. & Sykes, J. M. Effect of silica nano-particles on the performance of manganese-based conversion treatments. *Corrosion Science* **50,** 3038 (2008).

86. Demishima, B. A. L., Ohtsuka, T., Konna, H. & Sato, N. Xps Study of the Mno2 Electrode in Borate Solution during the Discharge Process. *Electrochimica Acta* **36,** 1485 (1991).

87. Demishima, B. A. L., Ohtsuka, T. & Sato, N. A Study of the Discharge Process of Manganese Oxide in Borate Solution Using Insitu Techniques. *Electrochimica Acta* **38,** 341 (1993).

88. Gassa, L. M., Mishima, H. T., Demishima, B. A. L. & Vilche, J. R. An electrochemical impedance spectroscopy study of electrodeposited manganese oxide films in borate buffers. *Electrochimica Acta* **42,** 1717 (1997).

89. Ho, W. H. & Yen, S. K. Characterization of Electrolytic Manganese Oxide Coating on Pt for Lithium Battery Applications. *Journal of the Electrochemical Society* **152,** A506 (2005).

90. Jakab, M. A., Little, D. A. & Scully, J. R. Experimental and Modeling Studies of the Oxygen Reduction Reaction on AA2024-T3. *Journal of the Electrochemical Society* **152,** B311 (2005).

91. Baes, C. F. & Mesmer, R. E. *The Hydrolysis of Cations*. (Rovert E. Krier, Malabar, Florida, 1986).

92. Pope, M. T. *Heteropoly and Isopoly Oxometalates*. (Springer-Verlang, New York, 1983).

93. Iannuzzi, M. & Frankel, G. S. Corrosion Inhibition of 2024-T3 by Vanadates. *ECS Transactions* **31,** 127 (2007).

94. Heath, E. & Howarth, O. W. Vanadium-51 and Oxygen-17 Nuclear Magnetic Resonance Studey of Vanadate(V) Equilibria and Kinetics. *Journal of the Chemical Society, Dalton Transactions* 1069 (1981).

95. Sigel, H. & Sigel, A. *Metal Ions in Biological Systems: Volume 31 Vanadium and Its Role in Life*. (Marcel Dekker, Inc., New York, 1995).

96. Chambers, B. D. & Taylor, S. R. Multiple Electrode Methods to Massively Parallel Test Corrosion Inhibitors for AA2024-T3. in *Corrosion* (NACE, 2006).

97. Maksimovskaya, R. I. & Chumachenko, N. N. 51V and 17O NMR Studies of the Mixed Metal Polyanions in Aqueous V–Mo Solutions. *Polyhedron* **6,** 1813 (1987).

98. Howarth, O. W., Petterson, L. & Andersson, I. Aqueous Molybdovanadates at High Mo: V Ratio. *Journal of the Chemical Society, Dalton Transactions* **7,** 1799 (1991).

99. Goldman, M. E., Unlu, N., Shiflet, G. J. & Scully, J. R. Selected Corrosion Properties of a Novel Amorphous Al-Co-Ce Alloy System. *Electrochemical and Solid-State Letters* **8,** B1 (2005).

100. Morrison, R. S. *Electrochemistry at Semiconductor and Oxidized Metal Electrodes*. (Plenum Press, 1980).

101. Schmuki, P. & Bohni, H. Illumination Effects on the Stability of the Passive Film on Iron. *Electrochimica Acta* **40,** 775 (1995).

102. Menezes, S., Haak, R., Hagen, G. & Kendig, M. Photoelectrochemical Characterization of Corrosion Inhibiting Oxide Films on Aluminum and Its Alloys. *Journal of the Electrochemical Society* **136,** 1884 (1989).

103. Noufi, R. N., Kohl, P. A., Frank, S. N. & Bard, A. J. Semiconductor Electrodes: XIV . Electrochemistry and Electroluminescence at n-Type Formula in Aqueous Solutions. *Journal of the Electrochemical Society* **125,** 246 (1978).

104. Lenhart, S., Urquidi-Macdonald, M. & Macdonald, D. D. Photo-inhibition of passivity breakdown on nickel. *Electrochimica Acta* **32,** 1739

105. Montemor, M. F., Ferreira, M. G. S., Hakiki, N. E. & Da Cunha Belo, M. Chemical composition and electronic structure of the oxide ®lms formed on 316L stainless steel and nickel based alloys in high temperature aqueous environments. *Corrosion Science* **42,** 1635 (2000).

106. Natishan, P. M., McCafferty, E. & Hubler, G. K. Localized corrosion behavior of aluminum surface alloys produced by ion implantation and ion beam mixing. *Materials Science & Engineering A* **116,** 41 (1989).

107. Dunn, D. S. & Sridhar, N. In Situ Study of Salt Film Stability in Simulated Pits of Nickel by Raman and Electrochemical Impedance Spectroscopies. *Journal of the Electrochemical Society* **144,** 4243 (1997).

108. Xia, L. & McCreery, R. L. Chemistry of a Chromate Conversion Coating on Aluminum Alloy AA2024-T3 Probed by Vibrational Spectroscopy. *Journal of the Electrochemical Society* **145,** 3083 (1998).

109. Dunn, D. S. *et al.* Development of a Surface-Enhanced Raman Technique for Biomarker Studies on Mars. *Applied Spectroscopy* **61,** 25 (2007).

110. Tormoen, G., Burket, J., Dante, J. & Sridhar, N. Monitoring the Adsorption of Volatile Corrosion Inhibitors in Real Time with Surface-Enhanced Raman Spectroscopy. *Corrosion* **62,** 1082 (2006).

111. Ford, F. P., Burstein, G. T. & Hoar, T. P. Bare Surface Reaction Rates and Their Relation to Environment Controlled Cracking of Aluminum Alloys. *Journal of The Electrochemical Society* **127,** 1325 (1980).

112. Rudd, W. J. & Scully, J. C. The function of the repassivation process in the inhibition of pitting corrosion on aluminium. *Corrosion Science* **20,** 611 (1980).

113. Kolman, D. G. & Scully, J. R. On the Repassivation Behavior of High-Purity Titanium and Selected alpha, beta, and beta + alpha Titanium Alloys in Aqueous Chloride Solutions. *Journal of The Electrochemical Society* **143,** 1847 (1996).

114. Lillard, R. S., Vasquez, G. & Bahr, D. F. The Kinetics of Anodic Dissolution and Repassivation on Stainless Steel 304L in Solutions Containing Nitrate. *Journal of The Electrochemical Society* **158,** C194 (2011).

115. Burstein, G. T. & Davies, D. H. The Effects of Anions on the Behavior of Scratched Iron Electrodes in Aqueous-Solutions. *Corrosion Science* **20,** 1143 (1980).

116. Burstein, G. T. & Marshall, P. I. Growth of Passivating Films on Scratched 304l Stainless-Steel in Alkaline-Solution. *Corrosion Science* **23,** 125 (1983).

117. Devicharan, C., Vasquez, M. J., Gary, P. H. & Clive, R. C. Studies on the repassivation behavior of aluminum and aluminum alloy exposed to chromate solutions. *Surface and Interface Analysis* **35,** 226 (2003).

118. Lee, H. C., Xu, F., Jeffcoate, C. S. & Isaacs, H. S. Cyclic polarization behavior of aluminum oxide films in near neutral solutions. *Electrochemical and Solid-State Letters* **4,** B31 (2001).

119. Schmutz, P. & Frankel, G. S. Influence of dichromate ions on corrosion of pure aluminum and AA2024-T3 in NaCl solution studied by AFM scratching. *Journal of The Electrochemical Society* **146,** 4461 (1999).

120. Kolman, D. G. & Scully, J. R. An Assessment of the Crack Tip Potential of Beta-Titanium Alloys During Hydrogen Environmentally Assisted Crack Propagation Based on Crack Tip and Passive Surface Electrochemica Measurements. *Corrosion Science* **42,** 1863–1879 (2000).

121. Scully, J. R., Silverman, D. C. & Kendig, M. W. *Electrochemical Impedance: Analysis and Interpretation*. (1993).

122. Hamann, C., Hamnett, A. & Vieltich, W. *Electrochemistry*. (Air Academy Press, 2000).

123. Scully, J. R., Frankenthal, R. P., Hanson, K. J., Siconolfi, D. J. & Sinclair, J. D. Localized Corrosion of Sputtered Aluminum and Al-0.5-Percent Cu Alloy Thin-Films in Aqueous Hf Solution .2. Inhibition by CO2. *Journal of The Electrochemical Society* **137,** 1373 (1990).

124. Walter, G. W. A review of impedance plot methods used for corrosion performance analysis of painted metals. *Corrosion Science* **26,** 681 (1986).

125. Dante, J., Tormoen, G. & Sridhar, N. In-Situ Measurements of Volatile Corrosion Inhibitor (VCI) Performance, Paper No. 06400. in *Corrosion 2006* (NACE, 2006).

126. Kiemele, M. J., Schmidt, S. R. & Berdine, R. J. *Basic Statistics*. (Air Academy Press, 2000).

127. G16 - Standard Guide for Applying Statistics to Analysis of Corrosion Data. (2009).

128. Bastek, P. D., Newman, R. C. & Kelly, R. G. Measurement of Passive Film Effects on Scratched Electrode Behavior. *Journal of The Electrochemical Society* **140,** 1884 (1993).

129. Chambers, B. D. & Taylor, S. R. The high throughput assessment of aluminium alloy corrosion using fluorometric methods. Part I – Development of a fluorometric method to quantify aluminium ion concentration. *Corrosion Science* **49,** 1584 (2007).

130. Gileadi, E. *Electrode Kinetics for Chemists, Chemical Engineers and Materials Scientists*. (John Wiley & Sons, 1993).

131. Bard, A. J. & Faulkener, L. R. *Electrochemical Methods: Fundamentals and Applications*. (John Wiley & Sons, 2001).

132. Gueshi, T., Tokuda, K. & Matsuda, H. Voltammetry at partially covered electrodes: Part I. Chronopotentiometry and chronoamperometry at model electrodes. *Journal of Electroanalytical Chemistry* **89,** 247 (1978).

133. Tokuda, K., Gueshi, T. & Matsuda, H. Voltammetry at partially covered electrodes: Part III. Faradaic impedance measurements at model electrodes. *Journal of Electroanalytical Chemistry* **102,** 41

134. Nakayama, S., Kaji, T., Shibata, M., Notoya, T. & Osakai, T. Which is easier to reduce, Cu2O or CuO. *Journal of the Electrochemical Society* **154,** C1 (2007).

135. Sykes, A. G. & Cruywagen, J. J. *Advances in Inorganic Chemistry*. (Academic Press, 2000).

136. Amado, A. M., Aureliano, M., Ribeiro-Claro, P. J. A. & Teixeira-Dias, J. J. C. Combined Raman and 51V NMR Spectroscopic Study of Vanadium (V) Oligomerization in Aqueous Alkaline Solutions. *Journal of Raman Spectroscopy* **24,** 699 (1993).

137. Puigdomenech, I. Hydra/Medusa Chemical Equilibrium Database and Plotting Software. (2004). at <http://www.kemi.kth.se/medusa/>

138. Petterson, L., Andersson, I. & Hedman, B. A potentiometric and 51V–NMR study of equilibria in the H+–HVO42- system in 3.0 M–Na(ClO4) medium covering the range 1 ≤-lg[H+] ≤10*,. *Chemica Scripta* **25,** 309 (1985).

139. Petterson, L., Hedman, B., Andersson, I. & Ingri, N. A potentiometric and 51V NMR study of equilibria in the H+–HVO42- system in 0.6 Na(cl) medium covering the range 1≤-lg[H+]≤10*. *Chemica Scripta* **22,** 254 (1983).

140. Boag, A. *et al.* How Complex is the Microstructure of AA2024–T3. *Corrosion Science* **51,** 1565 (2009).

141. Al-Ghamdi, S. The effect of aqueous phase inhibitors on mitigating potential-dependant hydrogen environmental assisted cracking of an ultra-high strength steel, in Materials Science and Engineering. (2010).

142. Chen, G. S. Microconstituent-induced pitting corrosion in aluminum alloy 2024-T3. *Corrosion* **52,** (1996).

143. Little, D. A., Connolly, B. J. & Scully, J. R. An electrochemical framework to explain the intergranular stress corrosion behavior in two Al-Cu-Mg-Ag alloys as a function of aging. *Corrosion Science* **49,** 347 (2007).

144. Kozawa, A. & Yeager, J. F. The Cathodic Reduction Mechanism of Electrolytic Manganese Dioxide in Alkaline Electrolyte. *Journal of the Electrochemical Society* **112,** 959 (1965).

145. Messaoudi, B., Joiret, S., Keddam, M. & Takenouti, H. Anodic behaviour of manganese in alkaline medium. *Electrochimica Acta* **46,** 2487 (2001).

146. Ilevbare, G. O. & Scully, J. R. Oxygen Reduction Reaction Kinetics on Chromate Conversion Coated Al-Cu, Al-Cu-Mg, and Al-Cu-Mn-Fe Intermetallic Compounds. *Journal of the Electrochemical Society* **148,** B196 (2001).

147. Buchheit, R. G., Kelly, R. G., Missert, N. & Shaw, B. A. *Real–time Observation of Localized pH Changes During Corrosion of Aluminum Alloy 2024–T3*. (The Electrochemical Society, 2004).

148. Hurley, B., Qiu, S. & Buchheit, R. G. Raman Spectroscopy Characterization of Aqueous Vanadate Species Interaction with Aluminum Alloy 2024–T3 Surfaces. *Journal of the Electrochemical Society* **158,** C125 (2011).

149. Barrado, E., Rardo, R., Castrillejo, Y. & Vega, M. Electrochemical Behavior of Vanadium Compounds at a Carbon Paste Electrode. *Journal of Electroanalytical Chemistry* **427,** 35 (1997).

150. McCafferty, E. *Introduction to Corrosion Science*. (Springer, 2010).

151. Bockris, J. O. & Kang, Y. The Protectivity of Aluminum and Its Alloys with Transition Metals. *Journal of Solid State Electrochemistry* **1,** 17 (1997).

152. Devereux, O. F., Libsch, T. A., Choo, Y. H. & Bambri, A. K. The Effect of Environmental pH on the Failure Strain of Anodic Films Formed on The Aluminium Alloy 2024. *Corrosion Science* **15,** 361 (1975).

153. Wilson, A. & Scully, J. R. Evaluation of Vanadate and Vanadate Combinations as Hexavalent Chromate Inhibitor Replacements for Corrosion Inhibition of AA 2024. in *NACE DoD* (2011).

Appendices

List of Scientific/Technical Publications

Talks

Bocher, F., Jakab, M. "Scientific Understanding of the Mechanisms of Non-Chromate Corrosion Inhibitors" NACE Corrosion Conference 2012, Salt Lake City, UT (2012).

Wilson, A. Scully, J. R. "Mechanism of Protection of Selected Chromate-Free Inhibitor Combinations on AA2024: Vanadate-Based Combinations" TTC Conference, Charlottesville, VA (July 2012).

Madden, S. B. Scully, J. R. "The Effects of Chromate, Molybdate, and Other Selected Inhibitors on Crack Tip Corrosion Inhibition" ECS PRiME , Waikiki, HI (2012).

Bocher, F., Jakab, M. "Scientific Understanding of the Mechanisms of Non-Chromate Corrosion Inhibitors" NACE Corrosion Conference 2011, Houston, TX (2011).

Wilson, A. Scully, J. R. "Evaluation of Vanadate and Vanadate Combinations as Hexavalent Chromate Inhibitor Replacements for Corrosion Inhibition of AA 2024" NACE DoD Corrosion Conference, Palm Springs, CA (July 2011).

Wilson, A. Scully, J. R. "Evaluation of Vanadate and Vanadate Inhibitor Combinaitons for Corrosion Inhibition of AA 2024" NACE Corrosion Conference 2011, Houston, TX (March 2011).

Madden, S. B. Scully, J. R. "Permanganate and Permanganate Inhibitor Combinations as an Environmentally Friendly Corrosion Inhibitor Replacements for AA2024" NACE DoD Corrosion Conference, Palm Springs, CA (2011).

Madden, S. B. Scully, J. R. "Investigation of Selected Inhibitor Combinations as an Environmentally Friendly Corrosion Inhibitor Strategy for AA2024" University Corrosion Collaboration Meeting, UAFA, Colorado Springs, CO (January 2011).

Madden, S. B. Scully, J. R. "Permanganate and Permanganate Inhibitor Combinations as Environmentally Friendly Corrosion Inhibitor Replacements for AA2024-T351" NACE Corrosion Conference 2011, Houston, TX (2011).

Scully, J. R., Madden, S. B. "Investigation of Potassium Permanganate as an Environmentally Friendly Corrosion Inhibitor on AA2024" NACE DoD Corrosion Conference, Palm Springs, CA (2011).

Bocher, F., Jakab, M. "Scientific Understanding of the Mechanisms of Non-Chromate Corrosion Inhibitors" NACE Corrosion Conference 2010, San Antonio, TX (2010).

Wilson, A. Scully, J. R. "Investigation Of Vanadate and Vanadate-Secondary Inhibitor Combinations As An Environmentally Friendly Inhibitor Strategy For AA2024" SERDP Inter-program Review at OSU, Columbus, OH (July 2010).

Madden, S. B. Scully, J. R. “Investigation of Permanganate and Permanganate Inhibitor Combinations as an Environmentally Friendly Corrosion Inhibitor Strategy for AA2024” SERDP Inter-program Review at OSU, (July 2010).

Papers

Bocher, F., Dante, J., Jakab, M. “Transfer of Aluminum Alloy 2024 Environmentally Friendly Inhibitors of Corrosion to Aluminum Alloy 7075 and Carbon Steel 1018” In Progress.

Bocher, F., Dante, J., Jakab, M. “Effect of Microstructure Properties on Aluminum Alloy 2024 Environmentally Friendly Inhibitors of Corrosion” In Progress.

Madden, S. B. Scully, J. R. “Investigation of Permanganate as an Environmentally Friendly Inhibitor of Corrosion on Aluminum 2024-T351” In Progress for Submission to ECS as of 1/3/2012.

Wilson, A. Scully, J. R. " Evaluation of Vanadate and Vanadate Combinations as Hexavalent Chromate Inhibitor Replacements for Corrosion Inhibition of AA 2024” NACE DoD 2011 Conference Proceedings, July 2011. Palm Springs, CA.

Madden, S. B. Scully, J. R. "Investigation of Permanganate as an Environmentally Friendly Inhibitor of Corrosion on Aluminum 2024-T351” NACE DoD 2011 Conference Proceedings, July 2011. Palm Springs, CA.

Posters

Wilson, A. “Evaluation of Vanadate and Vanadate Inhibitor Combinations for Corrosion Inhibition of AA 2024” NACE DoD Corrosion Conference, Palm Springs, CA (2011).

Madden, S. B. “Permanganate and Permanganate Inhibitor Combinations as an Environmentally Friendly Corrosion Inhibitor Replacements for AA2024” NACE DoD Corrosion Conference, Palm Springs, CA (2011).

Wilson, A. “Evaluation of Vanadate and Vanadate Combinations as Hexavalent Chromate Inhibitor Replacements for Corrosion Inhibition of Aluminum Alloy AA 2024” NACE Corrosion Conference 2011, Houston, TX (2011). 1st Place Marcel Pourbaix Category.

Madden, S. B. “Permanganate and Permanganate Inhibitor Combinations as an Environmentally Friendly Corrosion Inhibitor Replacements for AA2024” NACE Corrosion Conference 2011, Houston, TX (2011) 2nd Place Marcel Pourbaix Category.

Wilson, A. “Evaluation of Vanadate as a Hexavalent Chromate Inhibitor Replacement for Corrosion Inhibition of AA 2024” NACE Corrosion Conference 2010, San Antonio, TX (2010). 3rd Place Marcel Pourbaix Category.

Madden, S. B. “Investigation of Potassium Permanganate as an Environmentally Friendly Corrosion Inhibitor on AA2024” NACE Corrosion Conference 2010, San Antonio, TX (2010).

Madden, S. B. Scully, J. R. “Investigation of Permanganate and Permanganate Inhibitor Combinations as an Environmentally Friendly Corrosion Inhibitor Strategy for AA2024” Gordon Research Conference, Aqueous Corrosion, New London, NH (2010).